

U.S. Patent No. 7,128,988
Declaration in Support of Petition for *Inter Partes* Review

UNITED STATES PATENT AND TRADEMARK OFFICE

BEFORE THE PATENT TRIAL AND APPEAL BOARD

TDK Corporation,
Petitioner

v.

Lambeth Magnetic Structures, LLC
Patent Owner

Patent No. 7,128,988
Issue Date: October 31, 2006
Title: MAGNETIC MATERIAL STRUCTURES,
DEVICES AND METHODS

Inter Partes Review No. _____

**DECLARATION OF DR. ROBERT SINCLAIR IN SUPPORT OF
PETITION FOR *INTER PARTES* REVIEW**

UNDER 35 U.S.C. §§ 311-319 AND 37 C.F.R. § 42.100 *et seq.*

TABLE OF CONTENTS

I.	INTRODUCTION	1
II.	BACKGROUND AND QUALIFICATIONS	2
III.	MATERIALS CONSIDERED	5
IV.	LEGAL STANDARDS	6
V.	BRIEF OVERVIEW OF THE '988 PATENT	9
	A. Summary of the '988 Patent	9
	B. '988 Patent Prosecution History	11
	C. '988 Patent Claims	13
	D. '988 Patent Filing Date	24
VI.	STATE OF THE ART	24
VII.	ANALYSIS OF THE PRIOR ART	32
	A. J. Shen, M. Klaua, P. Ohresser, H. Jenniches, J. Barthel, Ch. V. Mohan, J. Kirschner, "Structural and magnetic phase transitions of Fe on stepped Cu (111)," Phys. Rev. B 56, 17 (1997) ("Shen")	34
	B. U.S. Patent No. 6,023,395 to Dill et al. ("Dill")	37
	C. U.S. Patent No. 5,465,185 ("Heim")	42
	D. D.N. Lambeth, W. Yang, H. Gong, D.E. Laughlin, B. Lu, L.L. Lee, J. Zou, P.S. Harlee, "Magnetic Media Performance: Control Methods for Crystalline Texture and Orientation," Mat. Res. Soc. Symp. Proc. Vol. 517, 181-192 (1998) ("Lambeth I")	42
	E. U.S. Patent No. 5,862,022 to Noguchi et al. ("Noguchi")	44
VIII.	SHEN, ALONE OR IN COMBINATION WITH DILL, RENDERS OBVIOUS CLAIMS 1 AND 27 OF THE '988 PATENT	45
	A. Claim Charts	45
	B. Shen, Alone or in Combination With Dill, Renders Obvious Claim 1	45
	C. Shen, Alone or in Combination With Dill, Renders Obvious Claim 27	53

IX.	DILL, IN COMBINATION WITH SHEN ALONE OR IN FURTHER COMBINATION WITH HEIM, RENDERS OBVIOUS CLAIMS 1, 3, 6-19, 21-24, 27-30, 34 AND 38 OF THE '988 PATENT.....	54
A.	Claim Charts.....	54
B.	Dill in Combination With Shen Renders Obvious Claim 1	54
C.	Dill in Combination With Shen Renders Obvious Claim 3	64
D.	Dill in Combination With Shen Renders Obvious Claim 6.....	65
E.	Dill in Combination With Shen Renders Obvious Claim 7	65
F.	Dill in Combination With Shen Renders Obvious Claim 8	66
G.	Dill in Combination With Shen Renders Obvious Claim 9	68
H.	Dill in Combination With Shen Renders Obvious Claim 10	70
I.	Dill in Combination With Shen Renders Obvious Claim 11	70
J.	Dill in Combination With Shen and Heim Renders Obvious Claim 12	72
K.	Dill in Combination With Shen Renders Obvious Claim 13	74
L.	Dill in Combination With Shen Renders Obvious Claim 14.....	76
M.	Dill in Combination With Shen and Heim Renders Obvious Claim 15	78
N.	Dill in Combination With Shen and Heim Renders Obvious Claim 16	82
O.	Dill in Combination With Shen Renders Obvious Claim 17	85
P.	Dill in Combination With Shen Renders Obvious Claim 18.....	86
Q.	Dill in Combination With Shen Renders Obvious Claim 19	86
R.	Dill in Combination With Shen and Heim Renders Obvious Claim 21	87
S.	Dill in Combination With Shen Renders Obvious Claim 22.....	89
T.	Dill in Combination With Shen and Heim Renders Obvious Claim 23	90
U.	Dill in Combination With Shen Renders Obvious Claim 24.....	92
V.	Dill in Combination With Shen Renders Obvious Claim 27	92

W. Dill in Combination With Shen Renders Obvious Claim 2893

X. Dill in Combination With Shen Renders Obvious Claim 2993

Y. Dill in Combination With Shen Renders Obvious Claim 3094

Z. Dill in Combination With Shen Renders Obvious Claim 3494

AA. Dill in Combination With Shen Renders Obvious Claim 3895

X. DILL IN COMBINATION WITH SHEN AND LAMBETH I
RENDERS OBVIOUS CLAIMS 2, 25, 26, AND 31 OF THE
'988 PATENT.....96

A. Claim Chart96

B. Dill in Combination With Shen and Lambeth I Renders
Obvious Claim 2.....96

C. Dill in Combination With Shen and Lambeth I Renders
Obvious Claim 25.....98

D. Dill in Combination With Shen and Lambeth I Renders
Obvious Claim 26.....99

E. Dill in Combination With Shen and Lambeth I Renders
Obvious Claim 31.....102

XI. DILL IN COMBINATION WITH SHEN AND NOGUCHI
RENDERS OBVIOUS CLAIM 39 OF THE '988 PATENT103

A. Claim Chart103

B. Dill in Combination With Shen and Noguchi Renders Obvious
Claim 39103

XII. CONCLUSION.....105

Exhibit List for Declaration of Dr. Robert Sinclair

Exhibit Description	Exhibit
<i>PCT Publication No. WO 03/021579</i>	A
<i>Jin (U.S. Patent No. 5,998,048)</i>	B
<i>Kadau I (K. Kadau, R. Meyer, P. Entel, “Molecular-Dynamics Study of Thin Iron Films on Copper,” Surface Review and Letters 6, 1, 35-43 (1999));</i>	C
<i>Pinarbashi (U.S. Patent No. 6,295,187)</i>	D
<i>P. Álvarez-Alonso, A. Pérez-Checa, I.R. Aseguinolaza, J. Alonso, A.V. Svalov, V.A. Chernenko, J.M. Barandiarán, “Fabrication of Patterned Ferromagnetic Shape Memory Thin Films,” Key Engineering Materials, Vol. 644, pp. 219-22, May 2015.</i>	E
<i>Pierre Villars, Material Phases Data System (MPDS), CH-6354 Vitznau, Switzerland; SpringerMaterials; sd_0555891 (Springer-Verlag GmbH, Heidelberg, 2014), http://materials.springer.com/isp/crystallographic/docs/sd_0555891 originally accessed: 29-08-2015; copy dated 19_09_2015.</i>	F
<i>W. F. Smith “Principles of Materials Science and Engineering” McGraw-Hill, New York (1990, 1996), p. 94 et seq.;</i>	G
<i>Metals Handbook, Volume 8, American Society for Metals, p. 251 et seq. (1973)</i>	H
<i>L. J. Swartzendruber et al., J. of Phase Equilibria, vol. 12, pp. 288-312 (1991);</i>	I
<i>Curriculum Vitae of Dr. Robert Sinclair</i>	J

1. I, Robert Sinclair, Ph.D., submit the following declaration (the “Declaration”) in connection with the proceeding identified above.

I. INTRODUCTION

2. I have been retained by counsel for TDK Corporation (“TDK”) as a technical expert in connection with the proceeding identified above. I submit this Declaration in support of Petitioner TDK’s Petition for *Inter Partes* Review (“Petition”) of United States Patent No. 7,128,988 (“the ’988 patent”) (Ex. 1001) against Patent Owner Lambeth Magnetic Structures, LLC (“Lambeth”). All “Ex. 10__” cites herein are to the Exhibits to the Petition. All “Ex. _” cites with letters A through I herein are to Exhibits to this Declaration.

3. I understand that Lambeth has filed a patent infringement lawsuit in the U.S. District Court for the Western District of Pennsylvania alleging infringement by Toshiba Corporation, Toshiba America Information Systems, Inc., Toshiba America Electronic Components, Inc., and Toshiba Of Canada, Ltd. (collectively “Toshiba”) of claims 1, 3, 6, 8, 11, 12, 17, 19, 23, 27, 28, and 29 (the “asserted claims”) of the ’988 patent. *Lambeth Magnetic Structures, LLC v. Toshiba Corp.*, Civil Action No. 2:14-cv-01526-CB (W.D. Pa.).

4. For the purposes of this Declaration, I will address the asserted claims of the ’988 patent and selected other claims of the ’988 patent. I have omitted

from my analysis several claims that, in my view, cannot reasonably be asserted against Toshiba. However, inclusion of a claim in my analysis is not an indication that I believe it could reasonably be asserted against Toshiba. If, at any time in the future, additional claims are asserted by Lambeth against Toshiba, I reserve the right to amend or supplement this Declaration accordingly.

II. BACKGROUND AND QUALIFICATIONS

5. My curriculum vitae is attached (Ex. J). I am a professor of Materials Science and Engineering at Stanford University. At Stanford, I head a research group studying microelectronic and magnetic thin film microstructure. We primarily use transmission electron microscopy (“TEM”) to image materials of interest at the atomic level. Doing so provides microstructural information necessary for the understanding of structural, electrical, and magnetic properties of those materials. We routinely examine materials of interest both to magnetic data storage and devices relating to that application.

6. I joined the faculty of the Department of Materials Science and Engineering at Stanford in 1977. I have been a professor there ever since. I have also directed Stanford’s Nanocharacterization Lab from 2002-2013. I became the Chair of the Department of Materials Science and Engineering in 2004 and served in that capacity until 2014. During the time I have been at Stanford, my research

has touched on various aspects of magnetic materials, materials used in the context of data storage, and thin film deposition.

7. Prior to being at Stanford, I held research positions at the University of Newcastle-upon-Tyne and the University of California, Berkeley. Before that, I received my B.S. and Ph.D. degrees in Materials Science from Cambridge University (UK).

8. I have authored around 250 refereed, scientific journal articles and over 200 conference proceedings in materials and physical science. Of these, I would estimate that approximately 30 percent directly or indirectly concern magnetic materials and/or thin film applications of magnetic materials. I have also authored six edited works and seven book chapters. Several of these touched upon some aspect of magnetic materials and/or thin film deposition.

9. For my research and work as an educator, I have received a number of awards. These awards include the Robert Lansing Hardy Gold Medal of the Metallurgical Society of the American Institute of Mining, Metallurgical, and Petroleum Engineers (AIME), the Eli Franklin Burton Award of the Electron Microscopy Society of America, an Alfred P. Sloan Foundation Fellowship, and the Marcus E. Grossman Award of the American Society for Metals. I have also received two awards for Excellence in Undergraduate Teaching at Stanford, and most recently the Distinguished Scientist Award (Physical Sciences) of the

Microscopy Society of America in 2009, and the David M. Turnbull Lectureship of the Materials Research Society in 2012.

10. In addition, I am very active in several professional societies. These societies include the Materials Research Society (MRS) and the Microscopy Society of America (MSA). I am also active in the organization of symposia and workshops on electron microscopy. Recent examples include the workshops on “Advanced and In Situ Microscopies of Functional Nanomaterials and Devices (IAMNano)” held in Krakow, Poland (2012), Rio de Janeiro, Brazil (2014), and Hamburg, Germany (2015) and the international conferences on “Remote Electron Microscopy and In Situ Studies,” held at Stanford University (2008), Gothenburg, Sweden (2010), Pittsburgh, Pennsylvania (2011), and Lisbon, Portugal (2013). I have also organized numerous symposia at electron microscopy and materials research conferences and workshops. I was also invited to serve as Chair of the U.S. National Research Council’s Committee on Smaller Facilities from 2003-2006, which is a rare responsibility on behalf of the National Academy of Sciences (NAS). This culminated in a 230 page report entitled “Midsize Facilities: Infrastructure for Materials Research” published by NAS in 2006.

11. During my tenure at Stanford University, I have been actively involved in teaching and education, as well as scientific research, at both the undergraduate and graduate level. For instance, I have taught a course on

“Introduction to Materials Science” to undergraduates since 1977, which includes the structure and magnetic properties of materials and has involved approximately 3,000 students over the years. Likewise I have taught graduate courses on “Atomic Arrangements in Solids,” “Nanocharacterization of Materials,” and “Transmission Electron Microscopy.”

12. I am being paid at an hourly rate for my work on this matter. I have no personal or financial stake or interest in the outcome of the present proceeding.

III. MATERIALS CONSIDERED

13. I have considered information from various sources in forming my opinions. Besides drawing from almost three decades of research and development in the area of distributed computing systems, I also have reviewed the following documents: (a) the '988 patent (Ex. 1001); (b) the prosecution file history of the '988 patent (including Ex. 1002); (c) PCT Publication No. WO 03/021579, the publication of international application, PCT /US02/27327, to which the '988 patent claims priority (Ex. A); (d) J. Shen, M. Klaua, P. Ohresser, H. Jenniches, J. Barthel, Ch. V. Mohan, J. Kirschner, “Structural and magnetic phase transitions of Fe on stepped Cu (111),” Phys. Rev. B 56, 17, 134-143 (1997) (“Shen”) (Ex. 1011); (e) U.S. Patent No. 6,023,395 (“Dill”) (Ex. 1009); (f) U.S. Patent No. 5,998,048 (“Jin”) (Ex. B); (g) K. Kadau, R. Meyer, P. Entel,

“Molecular-Dynamics Study of Thin Iron Films on Copper,” *Surface Review and Letters* 6, 1, 35-43 (1999) (“Kadau I”) (Ex. C); (h) D.N. Lambeth, W. Yang, H. Gong, D.E. Laughlin, B. Lu, L.L. Lee, J. Zou, P.S. Harllee, “Magnetic Media Performance: Control Methods for Crystalline Texture and Orientation,” *Mat. Res. Soc. Symp. Proc. Vol. 517*, 181 192 (1998) (“Lambeth I”) (Ex. 1013); (i) U.S. Patent No. 5,862,022 (“Noguchi”) (Ex. 1014); (j) U.S. Patent No. 6,295,187 (“Pinarbashi”) (Ex. D); (k) U.S. Patent No. 5,465,185 (“Heim”) (Ex. 1012); (l) TDK’s Petition for *Inter Partes* Review of the ’988 patent (the “Petition”), to which this Declaration is being submitted as Exhibit No. 1006; and (m) the other documents and references as cited herein. I reviewed the Petition in detail and agree with both its analysis and conclusions.

IV. LEGAL STANDARDS

14. I have relied on instructions from counsel as to the applicable legal standards to use in arriving at my opinions in this Declaration.

15. I have been informed and understand that patent claims are construed from the perspective of one of ordinary skill in the art at the time the claimed invention was made and that, during this proceeding, claims are to be given their broadest reasonable construction consistent with the specification.

16. I have been informed and understand that a patent claim is invalid because of anticipation when every element of the claim is described in a single prior art reference, such that the elements are arranged as required by the claim. I have been informed and understand that the description of a claim element in a prior art reference can be express or inherent. For a prior art reference to describe a claim element inherently, the claim element must be necessarily present. Probabilities are not sufficient to establish inherency.

17. I have also been informed and understand that the subject matter of a patent claim is obvious if the differences between the subject matter of the claim and the prior art are such that the subject matter as a whole would have been obvious at the time the invention was made to a person having ordinary skill in the art to which the subject matter pertains. I have also been informed that the framework for determining obviousness involves considering the following factors: (i) the scope and content of the prior art; (ii) the differences between the prior art and the claimed subject matter; (iii) the level of ordinary skill in the art; and (iv) any objective evidence of non-obviousness.

18. I further understand that the claimed subject matter would have been obvious to one of ordinary skill in the art if, for example, it results from the combination of known elements according to known methods to yield predictable results, the simple substitution of one known element for another to obtain

predictable results, the use of a known technique to improve similar devices in the same way, or the application of a known technique to a known device ready for improvement to yield predictable results. I have also been informed that the analysis of obviousness may include recourse to logic, judgment, and common sense available to the person of ordinary skill in the art that does not necessarily require explication in any reference. I understand that so-called “secondary considerations of non-obviousness,” must be considered in an obviousness analysis. I understand that an analysis including these secondary considerations helps to prevent the forbidden use of hindsight in determining whether a patent claim is obvious. I understand that secondary considerations of non-obviousness include: (a) a long-felt but unresolved need for the invention; (b) commercial success of the invention; (c) copying of the invention; (d) praise and recognition of the invention by others; (e) licensing of the rights to the invention; and (f) unexpected results. In rendering my opinions, I followed these guidelines.

19. In my opinion, a person of ordinary skill in the art pertaining to the '988 patent at the relevant date would have an undergraduate degree in materials science, physics, or chemistry, and two to four years of experience in the design of magnetic materials. Relevant professional or practical experience or degrees in other subject areas where a person would gain experience with distributed computing systems may also suffice.

20. Based on my education and experience in the field of materials science set forth above, I believe I am qualified to provide opinions about how one of ordinary skill in the art at the relevant time would have interpreted and understood the '988 patent and the prior art discussed herein.

V. BRIEF OVERVIEW OF THE '988 PATENT

A. Summary of the '988 Patent

21. The '988 patent (Ex. 1001), titled "Magnetic Material Structures, Devices and Methods," issued from the national stage of International Patent Application No. PCT/US02/27327, which was filed on August 29, 2002. The '988 patent entered the national stage in the United States under 35 U.S.C. § 371 (c) on August 29, 2003. The '988 patent issued on October 31, 2006.

22. The '988 patent is directed to "a structure to achieve uniaxial magnetocrystalline orientation via the use of the (110) texture of body centered cubic (bcc) or body centered cubic derivative crystal thin film structures."

(Ex. 1001, 12:58-13:2.)¹ In particular, the '988 patent describes “the invention” as “orientation control of bcc and bcc derivative materials.” (Ex. 1001, 13:4-8.) “The invention” is applied in various devices to cause “good orientation, high magnetization, high permeability and low losses.” (Ex. 1001, 13:4-8.)

23. The '988 patent focuses on achieving “uniaxial [magnetic] anisotropy,” which the '988 patent defines as the situation in which the “anisotropy energy density function only contains a single maximum and a single minimum” when the magnetization angle is rotated 180°. (Ex. 1001, 1:56-60.) The '988 patent explains that whether or not a thin magnetic film will exhibit uniaxial anisotropy is related to film structure, specifically to the presence and orientations of so-called crystallographic “variants.” (*Id.*, 14:34-55.) Variants form as thin, crystal films grow epitaxially on a particular surface. (*Id.*) Different crystal variants tend to form during formation of the films in order to minimize the interfacial and surface energy of the newly forming film. It is possible to influence

¹ The '988 patent uses the term “bcc-d” structure, which the '988 patent defines as “either a bcc or a bcc derivative crystal structure.” (Ex. 1001, 14:66-67.) One of ordinary skill in the art would have understood this phrase to denote an elemental crystal having a bcc structure or a crystalline compound having a structure that is based on the bcc structure.

or determine the number and type of variants by controlling various parameters during the film deposition process. (*Id.*, 14:48-65.)

24. The inventor of the '988 patent purports to have discovered an entirely new system or set of six variants in a particular film growth regime, specifically the growth of bcc-d structured films on a (111) plane surface. (*Id.*, 14:49-53.) There is one important and allegedly unique advantage of the system. This six-variant system allegedly allows achieving uniaxial anisotropy by breaking the symmetry of the crystallographic variants. (*Id.*, 14:49-55.) The '988 patent asserts that prior known crystallographic variants for this materials system would not yield uniaxial anisotropy even where symmetry is broken.

B. '988 Patent Prosecution History

25. On August 29, 2003, Application No. 10/415,757 (the “757 Application”) (Ex. 1002) entered the national stage in the U.S. Patent and Trademark Office (“USPTO”) under 35 U.S.C. § 371 (c). The original application had 65 total claims, including 8 independent claims. The Applicant canceled all claims and provided a new claim set via preliminary amendment on March 23, 2004. On September 8, 2005, the Examiner issued a restriction requirement with respect to those claims. In response to that requirement, on September 19, 2005, the Applicant chose to prosecute the claim set directed to “magnetic material[s] structure and magnetic device.”

26. On December 19, 2005, the USPTO issued a Non-Final Rejection rejecting claims 118-30, 134-37, and 140-58 based on 35 U.S.C. § 102 as being anticipated by or, in the alternative, under 35 U.S.C. § 103, as being obvious in view of Lambeth, et al. (U.S. Patent No. 6,248,416) (“Lambeth ’416.”). (Ex. 1003.) The Examiner also indicated that claims 131-33, 138, and 139 contained allowable subject matter and further rejected claim 157 under 35 U.S.C. § 112.

27. On March 17, 2006, the Applicant responded to the Office Action. (Ex. 1004.) In the response, the Applicant amended claim 157 to overcome the rejection under 35 U.S.C. § 112. (*Id.*, p. 12.) The Applicant traversed the rejections under 35 U.S.C. § 102/103 by arguing that Lambeth ’416 did not disclose uniaxial symmetry broken structure because Lambeth ’416 relates to the growth of an (fcc) magnetic layer. (*Id.*, p. 14.) The Applicant argued that (fcc) magnetic structures cannot achieve such symmetry. (*Id.*) The Applicant further argued that, though Lambeth ’416 “did disclose the use of a (111) template under a (110) bcc layer, . . . only 3 variants were found . . . [and such a] 3 variant system will not yield the desirable uniaxial symmetry broken magnetic properties of the present invention.” (*Id.*) Applicant further made the statement that the “claimed substrate . . . is not considered by the Applicant to be novel.” (*Id.*, p. 15.)

28. In response to Applicant's arguments, the Examiner issued a notice of allowance on July 28, 2006, of all pending claims directed toward the elected species. (Ex. 1005.) The only reasons given for allowance were that "Lambeth '416 fails to teach or suggest a uniaxial symmetry broken structure and a hexagonal (111) atomic template with a bcc-d magnetic layer (*see* Applicant's arguments in the response filed 3/17/06)." (*Id.*, p. 3.) The Applicant paid the issue fee on September 13, 2006, and the '757 Application issued as U.S. Patent No. 7,128,988 on October 31, 2006. The Applicant filed a Request for a Certificate of Correction on November 3, 2010, to add a priority claim to U.S. Provisional Application No. 60/315,920, filed on August 29, 2001. The Certificate Issued on December 7, 2010.

C. '988 Patent Claims

29. Lambeth has asserted independent claims 1 and 27 and dependent claims 3, 6, 8, 11, 12, 17, 19, 23, 28, and 29 of the '988 patent against Toshiba. I understand the Petition challenges the patentability of claims 1-3, 6-19, 21-31, 34, 38, and 39. I address these claims below. Claim 1 is representative of the independent claims of the '988 patent.

1. [a] A magnetic material structure comprising:
a substrate;

[b] at least one bcc-d layer which is magnetic,

[c] forming a uniaxial

[d] symmetry broken structure; and

[e] at least one layer providing a (111) textured

[f] hexagonal atomic template disposed between said substrate and said bcc-d layer.

2. The magnetic material structure recited in claim 1, wherein said substrate is single crystal.

3. The magnetic material structure recited in claim 1, wherein a surface of said substrate is amorphous or polycrystalline.

6. The magnetic material structure recited in claim 1, wherein the layer providing said hexagonal atomic template is formed from a fcc-d or hcp crystalline material.

7. The magnetic material structure recited in claim 1, wherein the layer providing said hexagonal atomic template is magnetic.

8. The magnetic material structure recited in claim 1,

wherein said bcc-d layer is epitaxially grown on said (111) textured hexagonal atomic template and has a (110) crystalline texture, and at least one crystalline grain of said (111) textured hexagonal atomic template has epitaxially grown thereon at least two and not more than four dominate (110) orientational variants.

9. The magnetic material structure according to claim 1, further comprising:

a second layer providing a (111) textured hexagonal atomic template, wherein said second layer is magnetic.

10. The magnetic material structure according to claim 1, further comprising: a second bcc-d layer which is non-magnetic.

11. The magnetic material structure according to claim 1, further comprising: a second bcc-d layer which is magnetic.

12. The magnetic material structure according to claim 1, further comprising:

a second bcc-d layer

wherein the crystalline orientation of the second bcc-d layer is epitaxially determined by said bcc-d layer.

13. The magnetic material structure according to claim 1, further comprising:

a second bcc-d layer; and a second layer providing a (111) textured hexagonal atomic template wherein said second layer providing a (111) textured hexagonal atomic template is disposed between said bcc-d layers.

14. The magnetic material structure according to claim 1, further comprising:

a second bcc-d layer, which is magnetic; and

at least one oxide layer between said bcc-d layers.

15. The magnetic material structure according to claim 1, further comprising:

a second and a third bcc-d layers which are non-magnetic;

a fourth bcc-d layer which is magnetic;

and at least one oxide layer between said second bcc-d layer and said third bcc-d layer

wherein said second and third bcc-d layers are disposed between said first and fourth bcc-d layers.

16. The magnetic material structure according to claim 1, further comprising:

a second bcc-d layer which is magnetic;

a second (111) textured hexagonal atomic template layer between said bcc-d layers; and

at least one oxide layer between said bcc-d layers.

17. The magnetic material structure recited in claim 1, wherein said bcc-d layer forming a uniaxial symmetry broken structure is composed of Fe or FeCo or an alloy of Fe or FeCo.

18. The magnetic material structure recited in claim 1, wherein said bcc-d layer forming a uniaxial symmetry broken structure is composed of an alloy of Fe or FeCo having one or more of the elements Al, B, Cr, C, Cu, Ni, N, Nb, Mo, V, Si, Ta, and Ti.

19. The magnetic material structure recited in claim 1, wherein the layer material forming said (111) textured hexagonal atomic template is composed of Ag, Al, Au, Cu, fcc-Co, fcc-CoCr, Ir, Ni, NiFe, Pt, Rh, Pd, hcp-Co, Gd, Re[,] Ru, Tb, Ti, or alloys of one of these materials combined with at least one element.

21. The magnetic material structure according to claim 1, further comprising:

a coupling layer; and

a second bcc-d layer which is magnetic

wherein the coupling layer material antiferromagnetically couples the bcc-d layers.

22. The magnetic material structure according to claim 1, further comprising:

a second bcc-d layer which is magnetic; and

a third bcc-d layer disposed between the bcc-d layers which are magnetic.

23. The magnetic material structure according to claim 1, further comprising:

a second bcc-d layer which is magnetic; and

a second (111) textured hexagonal atomic template layer

wherein said second (111) textured hexagonal atomic template is disposed between said bcc-d layers.

24. The magnetic material structure according to claim 1, further comprising:

at least one magnetic hcp Co alloy layer.

25. The magnetic material structure according to claim 1, further comprising:

at least one magnetic hcp Co alloy layer;

wherein said hcp Co alloy has a (1011) crystalline texture.

26. The magnetic material structure according to claim 1, wherein:

said substrate is a (111) crystalline textured single crystal; and

a surface of said single crystal provides a layer providing the (111) textured hexagonal atomic template

disposed between the bulk of said substrate and said at least one bcc-d layer.

27. A magnetic device having incorporated therein a magnetic material structure material comprising:

a substrate;

at least one bcc-d layer which is magnetic,
forming a uniaxial
symmetry broken structure; and
at least one layer providing a (111) textured
hexagonal atomic template disposed between said substrate and
said bcc-d layer.

28. The magnetic device recited in claim 27, wherein the device is a
magnetic data storage system.

wherein the device is a magnetic data storage system.

29. The magnetic device recited in claim 27,

wherein the device is a data storage magnetic recording
transducer.

30. The magnetic device recited in claim 27, wherein the device is at
least one of:

an anisotropic magnetoresistive sensor; a spin valve magnetoresistive sensor; a magnetic tunnel junction magnetoresistive sensor and a data storage magnetic playback transducer.

31. The magnetic device recited in claim 27, wherein the device is at least one of:

a data storage magnetic recording media; a data storage magnetic recording media incorporating an oriented soft magnetic layer; and a data storage magnetic recording media incorporating an oriented hard magnetic layer.

34. The magnetic device recited in claim 27, wherein the device is at least one of:

an electronic circuit inductive component and an electronic circuit inductive transformer component.

38. The magnetic device according to claim 27, further comprising:

at least one hard magnetic layer; wherein said at least one bcc-d layer which is magnetic, forming a uniaxial symmetry broken structure, is disposed between said (111) textured hexagonal atomic template and said at least one hard magnetic layer.

39. The magnetic device according to claim 27, further comprising:

at least one hard magnetic layer; wherein said at least one hard magnetic layer is disposed between said substrate and said at least one bcc-d layer.

30. As discussed in ¶ 24, *supra*, and explored in more detail below, the independent claim 1 system can be schematically represented as follows:

∴ To other layers

[1b] magnetic bcc-d layer:	(110)(bcc)
[1e] (111) textured hexagonal template:	(111)(fcc) or (0002)(hcp)

∴ To substrate [1a] and other layers

(Schematic A: Structure in claim 1 of the '988 patent.)

The '988 patent provides (111) (fcc) or (0002) (hcp) as two examples of the claimed (111) textured hexagonal template. (Ex. 1001, 14:55-57.) Although the '988 patent does not explicitly label (111)(fcc) and (0002)(hcp) as surface

structures, one of ordinary skill in the art would have understood that to be the meaning.

D. '988 Patent Filing Date

31. The '988 patent is the national stage of International Patent Application No. PCT/US02/27327, which was filed on August 29, 2002, and properly designated in the United States for national stage entry. Application No. PCT/US02/27327 entered national stage in the United States one year later, on August 29, 2003. Therefore, I have been advised by counsel, under 35 U.S.C. § 371 (c), the '988 patent is entitled to the August 29, 2001 filing date of Provisional Application No. 60/315,920.

VI. STATE OF THE ART

32. Generally, and in the context of the '988 patent (Ex. 1001), “magnetic materials” are those that retain their own magnetic fields. The direction of the internal field is referred to as “magnetization” or “magnetization direction.” The magnetic materials relevant to sensors, magnetic recording (*e.g.*, read/write heads) and many other devices are generally in thin film form or stacks of thin films. They are typically grown onto a substrate by various vapor phase deposition techniques which include both physical vapor deposition (PVD) or chemical vapor deposition (CVD). Controlling the deposition processing can allow control of the

structure and magnetic properties of the resulting films, so long as structure/property relationships in the films are well-understood. Depending on the application, the thin film material can be employed while it remains on the substrate or can be removed from the substrate.

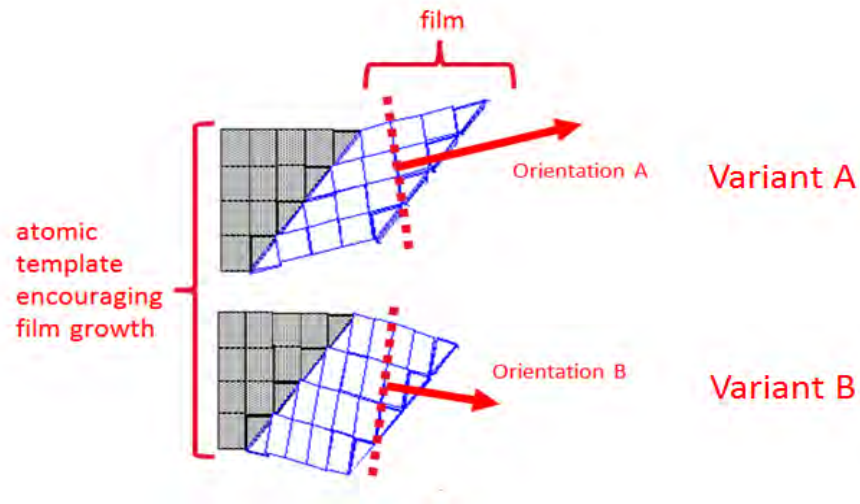
33. Many magnetic devices employ the natural crystalline anisotropy associated with the crystal structure of the magnetic material. “Magnetic anisotropy” is a material’s overall preference for a particular magnetization direction. A more anisotropic material will often have a greater preference. “Uniaxial anisotropy” is a severe form of anisotropy represented by a preference for a single axis such as the “easy magnetization axis.” One such property could be the “easy” magnetization axis in which the material is more easily magnetized by an applied magnetic field in one specific crystallographic direction. When there is only one such axis, the “easy magnetization axis,” the material is said to have “uniaxial anisotropy.” As has been known for at least fifty years, magnetic anisotropy, and uniaxial anisotropy in particular, is advantageous in magnetic recording. Magnetic recording heads, for example, need to sustain magnetization in a particular direction, regardless of the influence of exterior magnetic fields. A write head incorporating a material with uniaxial anisotropy will not easily change its magnetization direction under the influence of local fields. (*See, e.g., Ex. 1007, pp. 81-171.*)

34. Because of their very nature, crystalline materials have various symmetries associated with their structure, in which the atomic arrangements in separate but well-defined crystallographic orientations are identical resulting in identical magnetic or other physical or chemical properties. Materials with cubic symmetry such as (bcc), body-centered cubic structure, and (fcc), face-centered cubic structure, have the highest degree of symmetry of all known materials. There are exact interangular relationships between these “crystallographically equivalent” directions.

35. The underlying substrate on which a thin film is grown, often referred to as a “template” or an “atomic template,” will often dictate the film’s structure and symmetry. In the absence of a template’s “encouragement” to grow with a particular structure, a thin film will generally adopt the “natural” structure of the material the thin film comprises. As discussed above, so-called “body centered cubic” (bcc) and “face centered cubic” (fcc) structures are common among magnetic materials. It was well-known that when (bcc) structure phases grow in, or on, (fcc) structure phases that certain specific orientation relationships between the crystal structures are preferred. When the atoms in the two crystal phases have similar diameter (such as in (fcc) and (bcc) iron, (fcc) Ni, (fcc) Cu, (fcc) and (hcp) Co, (bcc) Cr and others) the most common orientation relationship is that described by G. Kurdjumov and G. Sachs (*Z. Phys.*, vol. 64, p. 325 (1930)). In this case, the

closest packed planes and close packed directions are parallel. In crystallographic nomenclature this can be written as (fcc) (111) is parallel to (bcc) (110) for the close packed planes, and (fcc) $[1\bar{1}0]$ is parallel to (bcc) $[1\bar{1}1]$ for the close packed directions. As described in Shen, there are six possible (bcc) variants for each (fcc) close packed plane, “six kinds of atomic relationship between the bcc(110) and fcc(111) structure.” (Ex. 1011, p. 137, ¶ 1; FIG. 4.) Shen describes these six variants as “KS domains,” where “KS” stands for “Kurdjumov-Sachs.” (*Id.*) One of ordinary skill in the art would have understood that these six crystallographic variants (KS domains) discussed by Shen in the (111)(fcc)/(110)(bcc) system are the same set of six crystallographic variants identified by the '988 patent. (Ex. 1001, 14:47-62.)

36. So-called crystallographic “variants” form naturally in films deposited on surfaces. The variants are crystals having the same structure, but different orientations relative to the atomic template on which the variants grow. Below is a schematic illustration of two crystallographic variants (A and B) each grown on the same atomic template, but having different orientations.



(Variant Growth Schematic adapted from Ex. E, pp. 219-22.)

37. The orientation of a crystallographic variant can dictate its preferred magnetization direction. Moreover, variants forming on the same surface as part of a single film do not necessarily have the same preferred magnetization direction. When they do not, the presence of multiple, opposing variants may lessen or diminish the degree of magnetic anisotropy in the film. For this reason, increasing the volume fraction of certain variants over others has been a known way to increase magnetic anisotropy for decades. (*See, e.g.*, Ex. 1008, p. 5777 (teaching enhancing anisotropy “by either nucleating favorable variants or increasing the volume fraction of the favorable variants.”).) The ’988 patent describes a “symmetry broken” structure in terms of crystallographic variants. (*See, e.g.*, Ex. 1001, 23:37-41.) More specifically, the ’988 patent describes a “symmetry broken” structure as one that does not include equal amounts of all variants in a

particular variant system, such as the six variant system found in (110)(bcc) films when grown on (111)(fcc) surfaces. (*Id.*) Therefore, one of ordinary skill in the art would have understood the meaning of ordinary meaning of a “symmetry broken” structure to be a structure with unequal volumes of crystallographic variants in either a three or six variant system.

38. The highest degree of crystallographically preferred orientation is obtained when a single crystal thin film is grown epitaxially onto an underlying perfect single crystal substrate. The directionally determined properties of the thin film material are then determined by the crystallographic orientation of the thin film, as imposed by growth on the underlying substrate, and the crystallographic symmetry associated with specific directions normal to and within the thin film material.

39. In many practical magnetic thin film sensors and related devices, the substrate is generally not a single crystal. It may be polycrystalline with random orientations, polycrystalline with preferred orientations, or even amorphous with no regular crystalline structure. Likewise, in many practical magnetic thin film sensors and related devices, an underlayer crystalline material is often grown first on the substrate to impart crystallographic preferred orientation on the subsequently grown magnetic thin film. It has been known for decades in materials science and physics that thin films can be grown under appropriate

conditions so that there is a preferred growth direction in the thin film (*i.e.*, perpendicular to the thin film plane) with its associated crystallographic symmetries. In the vast majority of cases, the thin films are polycrystalline with their crystal sizes determined by the growth conditions and with random orientations of the crystals “in plane.”

40. It has also been known for decades that there are specific growth methods whereby the random crystallographic orientations of the polycrystalline thin film material can be reduced to achieve preferred growth orientations, with associated anisotropic preferred magnetic properties. These include employing a stepped substrate or a substrate with polished grooves, depositing the thin film at an oblique angle to the substrate, depositing a magnetic thin film in an applied, defined magnetic field, etc. The degree of preferred orientation is dependent on the exact conditions used involving multiple parameters such as deposition rate, substrate temperature, background vacuum conditions, surface cleanliness and so on. A “preferred orientation” in plane is achieved under special combinations of circumstances and is very rarely, if ever, exactly perfect.

41. Manipulation of structures of thin films used in magnetic device applications has been routine for decades. (Ex. 1001, 1:1-12:56.) In particular, it was well-understood in the art long before August 2001 that an “atomic template,” *i.e.*, an underlying material surface as a structural scaffold, can be used to build,

grow, or deposit² an overlying layer that follows the crystalline structure of the template. (*Id.*) Influencing film structure is important, technologically, for a number of reasons, not the least of which is to improve magnetic properties of the grown film(s). (*Id.*; *see also* Ex. 1010, p. 9365.)

42. One very common film growth substrate is a hexagonally close packed (hcp) surface. “Close packed” means an arrangement of atoms in which the density is highest and the atoms are surrounded in the plane by the maximum number of neighbors (*i.e.*, six each), as shown in Shen’s Fig. 4, reproduced in ¶ 49 below. Several kinds of hexagonally close-packed surface have been used for film growth, but one of the most common is (111)(fcc). (*See, e.g.*, Ex. 1010, p. 9375.) Using these surfaces as templates can be advantageous because their high atomic density, and other properties, facilitate known structural variations in thin films grown on their surfaces. For the purposes of growing thin films, different hexagonally close-packed surfaces provide equivalent or nearly equivalent surface templates. For example, film growth will likely not be very sensitive to differences between (111)(fcc) and (0002)(hcp) close packed surfaces, which both provide a (111) textured hexagonal close packed surface template.

² Note that one of ordinary skill in the art would have used these terms somewhat interchangeably.

43. The basic film structure of a (bcc) magnetic film grown on a hexagonally close packed surface, such as (111)(fcc) or (0002)(hcp) is common for reasons mentioned above. Moreover, some common ferromagnetic materials, such as Fe, have a natural (bcc) structure at room temperature. (*See, e.g.*, Ex. H, p. 251 *et seq.*; *see also* Ex. G, p. 94 *et seq.*) Other common magnetic materials, such as Ni, have a natural (fcc) structure. When bcc materials form films on close-packed surfaces, they tend to form a (110) orientation of the bcc crystalline structure, *i.e.*, the closest packed bcc (110) plane lies on and parallel to the close packed fcc (111) plane.

44. Use of a hexagonal atomic template, such as (111)(fcc), for growing magnetic thin films was well known long before the August 29, 2001 effective filing date of the '988 patent. Moreover, as the '988 patent shows at least in FIG. 3, crystallographic variants in this very system had been characterized before 2001. (Ex. 1001, 10:20-11:27; 11:33-12:54.) Also, their relationship to properties such as magnetic anisotropy was understood before 2001.

VII. ANALYSIS OF THE PRIOR ART

45. There are a number of patents and publications that constitute prior art to the '988 patent. The primary prior art references used in the invalidity grounds,

together with their filing date, are set forth in the table below. A description of these prior art references follows.

Ground	Reference(s)	Basis	Claims
1	Shen and Dill	35 U.S.C. §103	1 and 27
2	Dill and Shen	35 U.S.C. §103	1, 3, 6-11, 13-14, 17-19, 22, 24, 27-30, 34, and 38
3	Dill, Shen, and Heim	35 U.S.C. §103	12, 15, 16, 21, and 23
4	Dill, Shen, and Lambeth I	35 U.S.C. §103	2, 25, 26, and 31
5	Dill, Shen, and Noguchi	35 U.S.C. §103	39

46. As I discussed above, it is my understanding that, for the purposes of this proceeding, the earliest priority date that the '988 patent can claim is August 29, 2001. (*See V(D) supra.*)

47. In the following sections, I provide a brief summary of each of the prior art references in my analysis. Based on the filing dates and/or publication dates of the below-listed prior art, it is evident that each of them is prior art to the '988 patent.

A. J. Shen, M. Klaua, P. Ohresser, H. Jenniches, J. Barthel, Ch. V. Mohan, J. Kirschner, “Structural and magnetic phase transitions of Fe on stepped Cu (111),” Phys. Rev. B 56, 17 (1997) (“Shen”)

48. J. Shen et al. published a scientific paper in the journal Physical Review B titled “Structural and magnetic phase transitions of Fe on stepped Cu (111)” on November 1, 1997. Shen discloses that the (111)(fcc)/(bcc) system has symmetry breaking (dominance of two KS variants over the other four) (Ex. 1011, p. 137, ¶ 1; FIG. 4) and substantially increasing magnetization of the overlying layer. (*Id.*, p. 134, ¶ 4 (5).) In a (111)(fcc)/(bcc) material, there are six possible crystalline orientation variants. The ’988 patent explains that “symmetry broken structure” means that the layer “do[es] not contain an equal amount of all six of the [possible] (110) textured bcc-d variants [*i.e.*, “KS domains”].” (Ex. 1001, 23:38-41.) This would also have been understood as the meaning by one of ordinary skill in the art. Shen discloses that symmetry breaking increases the magnetic field required to saturate the layer and contributes to uniaxial anisotropy, improving the magnetic properties of the bcc layer. (*Id.*, p. 139, left column.) Later, the ’988 patent defines “the invention” as orientation control [*i.e.*, symmetry breaking] of bcc and bcc derivative materials,” allowing “new devices to be constructed, which have... high magnetization....” (Ex. 1001, 13:2-8.)

49. More specifically, Shen discloses the bi-layer materials system of (bcc) Fe grown on Cu(111), *i.e.*, (111)(fcc)Cu / (bcc) Fe. (*See, e.g.*, Ex. 1011, FIG. 1.)

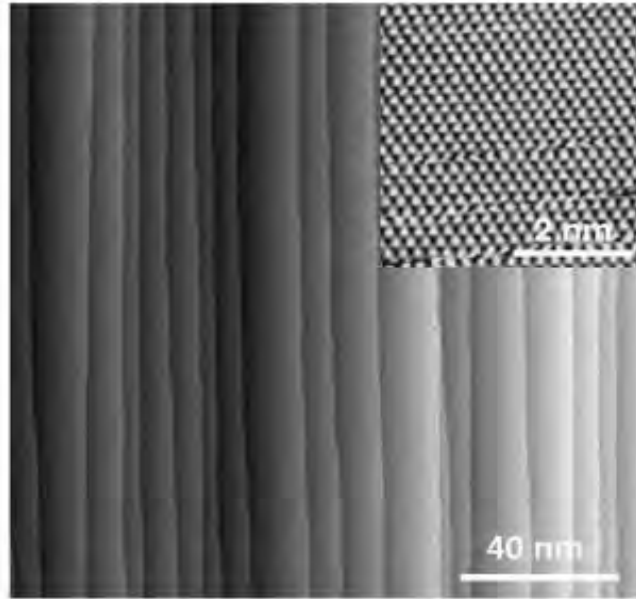


FIG. 1. STM topography image of a well-prepared Cu(111) vicinal surface. The atomic steps are parallel and oriented along $\langle 011 \rangle$ direction. The inset is an atomically resolved image ($I_t = 0.25$ nA, $V_{bias} = 10$ mV) recorded from a terrace showing the six-fold symmetry of the Cu(111) surface.

(*Id.*, FIG. 1.)

50. The Fe films were deposited in an MBE preparation chamber (Ex. 1011, p. 135, ¶ 1) on top of the surface of the substrate which was cut at a slight 1.2° miscut with respect to the (111) orientation (*id.*, p. 134, ¶ 2; p. 135, ¶ 2) in order to form steps (*id.*, FIG. 1). The Fe films were grown epitaxially on the (111)(fcc) surface, which has a hexagonal structure. Shen shows both epitaxial growth and the hexagonal structure in FIG. 4.

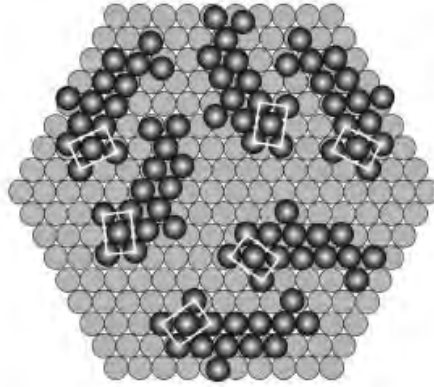


FIG. 4. Demonstration of the Kurdjumov-Sachs superstructure. Upper left: LEED pattern of the 2.7-ML film at the beam energy of 90 eV. Upper right: Simulated LEED pattern of Fe bcc(110) on Cu(111) with Kurdjumov-Sachs orientation. Note the consistency between the experimental and the simulated LEED patterns. Bottom: real-space schematic view of the six KS domains on the Cu(111) substrate.

(*Id.*, FIG. 4.)

51. Therefore, Shen discloses the following structure:

[1b] Fe layer grown on Cu(111):	(110)(bcc)
[1e] Cu(111) surface:	(111)(fcc)
⋮	To bulk Cu substrate [1a]

(Schematic B: Structure in Shen.) Shen discloses that both the structure and magnetic properties of the films depend on their thickness, which Shen reports in terms of “ML,” or monolayers of Fe. (*See, e.g., id.*, FIG. 2 and caption showing “morphological evolution” of the Fe overlayer “with increasing thickness.”) Shen also discloses that the Fe films have a well-defined “easy magnetization axis.” (*Id.*, pp. 138-39, ¶ 3.) Shen further reports that changes in properties relate to a change in Fe film structure with thickness, specifically a transition from (fcc) to bcc structure with increasing film thickness. (*Id.*, FIG. 3; p. 136, ¶ 1.)

52. Shen explains that the morphological evolution of the Fe films, along with the fact that they are grown on steps of Cu(111) with a particular orientation (*i.e.*, along the $\langle 011 \rangle$ direction), results in breaking the symmetry of the Fe films. (*Id.*, p. 137, ¶ 1, emphasis added; *see also* FIG. 4.) More particularly, Shen discloses that the “two [Kurdjumov-Sachs, or ‘KS’] domain configurations [in the (bcc) ferromagnetic layer] which are parallel to the [Cu(111)] steps should be more favored as compared to the other four [KS] domains.” (*Id.*, p. 137, ¶ 1; FIG. 4.) Therefore, symmetry is broken because of a preference for two of the (bcc) ferromagnetic layer’s six possible variants (*i.e.*, KS domains). The structural transition includes symmetry breaking and causes “[t]he magnetization of the transformed bcc Fe films [to sharply increase by] about four to five times larger than the extrapolated value from the low thickness fcc Fe films.” (*Id.*, p. 134, ¶ 4 (5).)

B. U.S. Patent No. 6,023,395 to Dill et al. (“Dill”)

53. Frederick Dill et al. filed a U.S. patent application titled “Magnetic Tunnel Junction Magnetoresistive Sensor With Instack Biasing” on May 29, 1998. This application issued as U.S. Patent No. 6,023,395 (“Dill”) on February 8, 2000.

54. Dill discloses embedding a (111)(fcc)/(bcc) layer structure, with a uniaxial (bcc) layer, in a multi-layer device, such as a magnetic tunnel junction (MTJ). (*See* ¶ 56, *infra.*) Dill discloses that adding this structure to the MTJ and

Example 1 from (Ex. 1009, 9:47-53; 8:29-57.)		
...various other layers...		
Interface layer of layer 118:	Co ₍₃₀₎ Fe ₍₇₀₎ (bcc)	“[first] bcc-d layer which is magnetic”
Bulk layer of layer 118:	Ni ₍₄₀₎ Fe ₍₆₀₎ (fcc)	“[first] (111)...hexagonal atomic template”
AF layer 116:	Mn ₍₅₀₎ Fe ₍₅₀₎ (fcc)	(111)...hexagonal atomic template
Template layer 112:	Ni ₍₈₁₎ Fe ₍₁₉₎ (fcc)	(111)...hexagonal atomic template
...various other layers...		
Substrate G1:	Al ₂ O ₃	

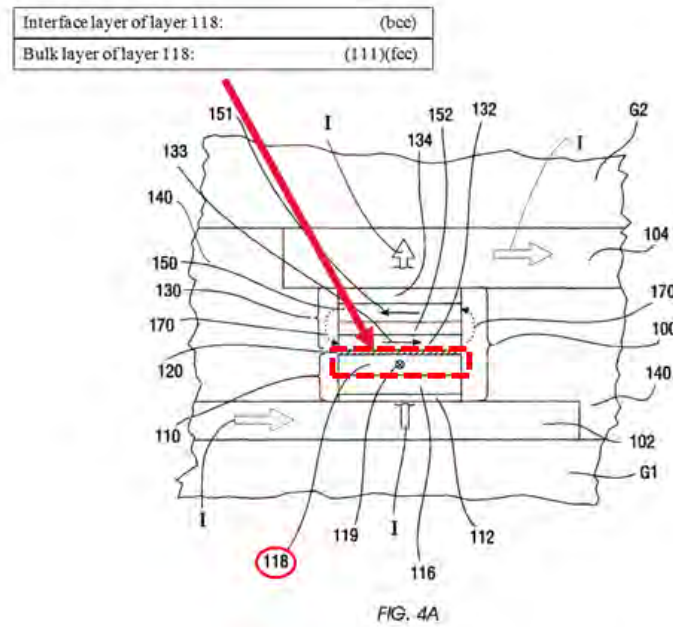
Certain aspects of the above structure can be represented by the following simplified Schematic C:

∴ To rest of layers in stack (FIG. 4A)

Interface layer of layer 118:	(bcc)
Bulk layer of layer 118:	(111)(fcc)

∴ To layers 116, 112, and substrate (G1)

(Schematic C: Film structure for Dill, Example 1.)



(Ex. 1009, FIG. 4A, annotated.)

Example 2 from (Ex. 1009, 9:65-10:3; 9:47-53; 8:29-57.)			
...various other layers...			
Upper layer of layer 118:	$\text{Co}_{(30)}\text{Fe}_{(70)}$	(bcc)	
Thin metal layer of 118:			
Lower layer of layer 118:	$\text{Co}_{(30)}\text{Fe}_{(70)}$	(bcc)	“[first] bcc-d layer which is magnetic”
AF layer 116:	$\text{Mn}_{(50)}\text{Fe}_{(50)}$	(fcc)	“[first] (111)...hexagonal atomic template”
Template layer 112:	$\text{Ni}_{(81)}\text{Fe}_{(19)}$	(fcc)	(111)...hexagonal atomic template
...various other layers...			
Substrate G1:	Al_2O_3		

In Example 1, Dill discloses a $\text{Ni}_{81}\text{Fe}_{19}$ “template layer 112” that is “(111)...fcc” material, that directs the (111) (fcc) crystalline growth of an overlying $\text{Mn}_{50}\text{Fe}_{50}$

AF layer 116. (*Id.*, 8:35-47; FIG. 4A *supra.*) A “fixed layer” 118 near the middle of the layer stack, is grown onto AF layer 116. (*Id.*) In this example, layer 118 is divided into two layers, a lower “bulk” layer grown on (fcc) (111) layer 116 and an “interface” layer grown on the bulk layer. (*Id.*, 9:37-59.) In one example, the bulk layer is $\text{Ni}_{40}\text{Fe}_{60}$, and the interface layer is $\text{Co}_{30}\text{Fe}_{70}$ or $\text{Co}_{40}\text{Fe}_{60}$ (*id.*), making the bulk layer naturally (fcc) material and the interface layer naturally (bcc) material. (*See, e.g.,* Ex. F.) Also, one of ordinary skill in the art would have understood that the bulk and interface layers are both magnetic. Therefore, Dill discloses an (fcc)[bulk layer of layer 118]/(bcc)[interface layer of layer 118] structure embedded in a magnetic layer stack to form a magnetic device. Dill also discloses that the (fcc) structure of layer 118 is influenced by the structure of underlying (fcc) AF layer 116, and that the (fcc) structure of layer 116 is determined by (fcc)(111) “seed layer” 112. (*Id.*, 8:37-41; FIG. 4A.) Dill further discloses that uniaxial anisotropy is “induce[d]” in layer 118 by growing the layer under the influence of a magnetic field in the direction 119. (*Id.*, 10:47-52; FIG. 4A.) Dill discloses a number of different layer stacks and devices employing the (111)(fcc)/(bcc) structure discussed above. (*See, e.g., id.*, FIGs. 4A, 4B, and 6; *see also* Example 2 summarized above; *see also* magnetic layer variations and substitutions discussed from 5:22-7:52.) According to Dill, each of these

multilayer devices benefits from the ability of that structure to “provide[] a linear response to the magnetic fields from the recorded medium.” (*Id.*, 3:2-4.)

C. U.S. Patent No. 5,465,185 (“Heim”)

57. U.S. Patent No. 5,465,185 (“Heim”) (Ex. 1012) issued on November 7, 1995. Heim discloses a magnetoresistive spin valve sensor with an improved pinned ferromagnetic layer and magnetic recording system using the sensor. (*Id.*, Title.) The structure includes a multi-film laminated pinned ferromagnetic layer (*id.*, Abstract) which “comprises a first Ni₈₁Fe₁₉ film 72 having a thickness of 30 Å formed directly on the copper spacer layer 65, a 5 Å ruthenium (Ru) film 73 deposited onto the first Ni-Fe film 72, and a second Ni₈₁Fe₁₉ film 74 of 30 Å thickness formed on the Ru film 73.” (*Id.*, 5:19-23.) Heim discloses that separating layer 73 in this configuration is an “AF [antiferromagnetically] coupling film” that antiferromagnetically couples films 72 and 74. (*Id.*, 6:13-17.) Heim further discloses that the “AF coupling film” 73 can be comprised of a number of materials besides Ru, including Cr. (*Id.*, 7:3-10.)

D. D.N. Lambeth, W. Yang, H. Gong, D.E. Laughlin, B. Lu, L.L. Lee, J. Zou, P.S. Harllee, “Magnetic Media Performance: Control Methods for Crystalline Texture and Orientation,” Mat. Res. Soc. Symp. Proc. Vol. 517, 181-192 (1998) (“Lambeth I”)

58. David N. Lambeth et al. published a scientific paper in the Materials Research Society Proceedings titled “Magnetic Media Performance: Control

Methods for Crystalline Texture and Orientation” on April 15, 1998 (“Lambeth I”). Lambeth I provides “an overview of the guiding media design philosophy and discuss[es] materials issues, multi-layered thin film material structures and processing techniques which are used to control the microstructure and magnetic properties of Co-alloy films.” (Ex. 1013, Abstract.)

59. More specifically, Lambeth I discloses particular methods for controlling microstructure of magnetic films and devices/structures made with such films. The disclosed methods include manipulating the “underlayer” structure of deposited films in order to ensure a particular structure, phase composition, and orientation of the resulting film. (*Id.*, p. 185, ¶ 1.) Lambeth I discloses that the “choice of the underlayer texture upon which to perform epitaxial growth is critical” in determining the orientation, crystalline quality, and grain size in resulting films. (*Id.*) Lambeth I provides an overview of several relationships between the structure of the underlayer and the structure and properties of the resulting overlayer. (*See, e.g., id.*, pp. 186-88.) In particular, Lambeth I discloses that single crystalline underlayers, and/or underlayers with a particular crystallographic orientation such as (111), can result in superior quality overlayer films. (*Id.*, p. 188.)

E. U.S. Patent No. 5,862,022 to Noguchi et al. (“Noguchi”)

60. Kiyoshi Noguchi et al. filed a U.S. patent application titled “Ferromagnetic Tunnel Junction, Magnetoresistive Element and Magnetic Head” on Sep. 19, 1997. This application issued as U.S. Patent No. 5,862,022 (“Noguchi”) on January 19, 1999.

61. Noguchi discloses a “ferromagnetic tunnel junction” comprising multiple configurations of magnetic layers (Ex. 1014, 12:53-67; Abstract; *see also*, *e.g.*, FIGs. 1, 6, 10, and 21.)

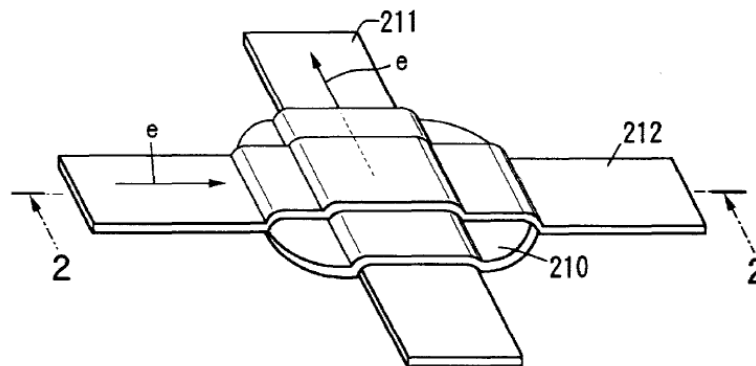


FIG. 1

(*Id.*, FIG. 1.)

62. Noguchi’s device shares similar goals and structure with the MTJ of Dill. For example, Noguchi discloses, like Dill, that tunneling junctions and layer stacks can be used in conjunction with magnetoresistive read heads (MRs). (*Id.*,

1:13-22.) Noguchi's MR includes ferromagnetic films and magnetic domain control films. (*Id.*, 12:53-67; FIGs. 6-8.) The magnetic domain control films "prevent a disturbing influence of an external magnetic field" (*id.*, 15:52-57) in the ferromagnetic films. Noguchi further discloses using the structure in a variety of other devices, including an "inductive magnetic conversion element." (*Id.*, 20:37-55.)

VIII. SHEN, ALONE OR IN COMBINATION WITH DILL, RENDERS OBVIOUS CLAIMS 1 AND 27 OF THE '988 PATENT

A. Claim Charts

63. The Petition sets forth claim charts (Petition, Sections VI(A) and (B)) citing disclosures in Shen and Dill that demonstrate how these prior art references render obvious claims 1 and 27 of the '988 patent. I fully agree with the claim charts. The following sections include additional analysis that demonstrates how Shen, alone or in combination with Dill, renders these claims obvious.

B. Shen, Alone or in Combination With Dill, Renders Obvious Claim 1

64. The preamble for claim 1 recites "[a] *magnetic material*." To the extent this preamble is a limitation, Shen discloses this limitation. For example, Shen discloses an Fe film ("magnetic material") deposited on a "copper

substrate.”³ (Ex. 1011, p. 135, ¶¶ 2-3.) Shen discloses that the Fe film is a “magnetic” material. (*See, e.g., id.*, Title; Abstract.)

65. Claim 1 recites that the magnetic material comprises “*a substrate.*” Shen discloses that an Fe film is deposited on a “copper substrate.” (*See, e.g., id.*, p. 135, ¶¶ 2-3.)

66. Claim 1 recites “at least one *bcc-d layer which is magnetic.*” Shen discloses this limitation.

67. Shen discloses that the Fe film has a “bcc(110)” structure. More specifically, as the film thickness increases above a “critical thickness,” the film material changes from (fcc) to bcc structure. (*Id.*, Abstract; pp. 137-38, ¶ 2; FIG. 4 and caption; FIG. 5; p. 138, ¶¶ 1-3; p. 139, ¶ 2.) Shen presents experimental results that confirm the bcc structure. (*See, e.g., id.*, FIG. 3 and caption.) Shen acknowledges that the Fe films are “magnetic,” by discussing their “magnetic properties” (*Id.*, p. 138, ¶ 3; p. 140, ¶ 3; p. 142, ¶ 3) and presenting experimental results demonstrating “[t]he magnetization of both the (fcc) Fe films and the bcc Fe films.” (*Id.*, ¶ 1, FIG. 9 and caption.)

³ Shen uses the terms “copper substrate” and “Cu(111) substrate” interchangeably. (*See, e.g., Ex. 1011, caption of FIG. 4.*) Accordingly, I will do so here as well.

68. Claim 1 recites that the magnetic bcc-d layer “[forms] *a uniaxial structure.*” The ’988 patent describes “‘uniaxial’ anisotropy to exist if the anisotropy energy density function only contains a single maximum and a single minimum as the magnetization angle, θ , is rotated by 180 degrees from a physical axis” (Ex. 1001, 1:56-60), which a person of ordinary skill in the art would have understood to be demonstrated if the material has one easy magnetization axis. Shen discloses this limitation.

69. Shen consistently refers to the easy axis in the disclosed films as singular. For example, Shen discloses that the (fcc) to (bcc) structural transition observed in the Fe films caused “the easy magnetization direction [to switch] from perpendicular to in plane.” (Ex. 1011, p. 139; *also, id.*, pp. 140-41, ¶ 3, “The film thus may have a[n] in-plane easy magnetization axis . . .”). In other words, Shen discloses that in this example the Fe films, whether they have (fcc) or bcc structure, are uniaxial in that they have a single, easy magnetization direction. Shen confirms this by referring to “a” or “the” easy axis in both the (fcc) films and the (bcc) films. (Ex. 1011, Abstract; p. 139, top of right column.)

70. Shen explained that, though the bcc Fe layers have an easy magnetization axis and the easy axis is in the plane of the Fe layer, Shen’s available equipment was not able to measure the specific direction of the axis in the layer plane, other than to say that it is not in the direction of the substrate steps.

(Ex. 1011, p. 139, ¶ 1.) Even if Shen was unable, for technical reasons, to establish the specific direction of the easy axis, one of ordinary skill in the art would still have understood from the disclosure above that Shen discloses that the Fe films have a preferred easy axis and, therefore, they have uniaxial anisotropy.

71. Dill also discloses a magnetic device with a bcc magnetic layer that is uniaxial. Dill further discloses that operation of the magnetic device can be improved by predetermining and “induc[ing]” that direction to cooperate with operation of the device. Specifically, as discussed in ¶ 56 *supra*, Dill discloses a fixed layer 118 that is bcc and magnetic and also discloses inducing uniaxial anisotropy in the layer. And Dill discloses a method for inducing this uniaxial anisotropy. In fact, the very method Dill discloses is identified by the '988 patent as a method “[to] achieve a single uniaxial anisotropy.” (Ex. 1001, 4:60-65.) Moreover, one of ordinary skill in the art would have recognized this method as achieving uniaxial anisotropy.

72. It would have been obvious to a person of ordinary skill in the art at the time of the effective filing date of the '988 patent to modify Shen's (bcc) Fe layer (Ex. 1001, FIG. 4) by using Dill's method to form a predetermined uniaxial structure.

73. Specifically, Shen discloses a magnetic film structure of Cu(111)/(bcc) Fe, where the (bcc) Fe layer is grown on Cu(111) and has an easy

magnetization axis. (Ex. 1011, FIG. 4; pp. 140-41, ¶ 3.) Dill discloses growing ferromagnetic layer 118 in the presence of a magnetic field to induce an easy magnetization axis aligned in the direction of an applied field.

(Ex. 1009, 10:47-10:52.) Dill further indicates that inducing uniaxial anisotropy this way may be “beneficial.” (*Id.*) Although Dill does not explicitly describe the benefit, one of ordinary skill in the art would have understood that the benefit is to create a more reliable magnetization along a particular direction that will be less easily changed under the influence of external magnetic fields.

74. Applying a field to induce uniaxial anisotropy during the growth of Shen’s (bcc) Fe layer would be straight-forward and predictable. Shen’s (bcc) Fe layer is uniaxial and grown on an (fcc) Cu(111) substrate (*see, e.g.*, Ex. 1011, pp. 138-39, ¶ 3). Similarly, Dill’s ferromagnetic layer 118 is grown on layer 116 (Ex. 1009, 8:37-41), which is fcc(111).

75. Therefore, a person of ordinary skill in the art would have been able to modify Shen’s (bcc) Fe layer (Shen, FIG. 4) by growing it in a magnetic field such that it has a uniaxial structure, as disclosed by Dill.

76. Claim 1 recites that the bcc-d layer forms a “*symmetry broken structure*.” Shen discloses this limitation.

77. As discussed in ¶ 48, *supra*, the ’988 patent explains that “symmetry broken structure” means that the layer “do[es] not contain an equal amount of all

six of the possible (110) textured bcc-d variants [*i.e.*, “KS domains”].” (Ex. 1001, 23:38-41) This would also have been understood as the meaning by one of ordinary skill in the art. Shen discloses that the Fe films have a symmetry broken structure (dominance of two crystalline variants) (Ex. 1011, p. 134, ¶ 4 (5)) and have improved magnetic properties (*see* ¶ 48, *supra*). Further, Shen discloses a method of breaking the symmetry by enhancing certain variants and minimizing others in the (bcc) layer. (*See* ¶¶ 51-52, *supra*.)

78. Specifically, Shen discloses that when the (bcc) Fe layer is grown on the Cu(111) substrate, there are six crystallographic variants of the (bcc) Fe that might possibly grow. These variants are referred to as “Kurdjumov-Sachs domains” or “KS domains.” However, Shen discloses that two of the six variants were preferentially grown on the stepped (111) surface [*i.e.*, symmetry was broken in the Fe layer]. (Ex. 1011, p. 137, right column; FIG. 4.)

[T]he STM images have shown that there are more domains elongated along the step direction than the other two $\langle 011 \rangle$ directions. . . . The two domain configurations which are parallel to the [substrate] steps should be more favored as compared to the other four domains.

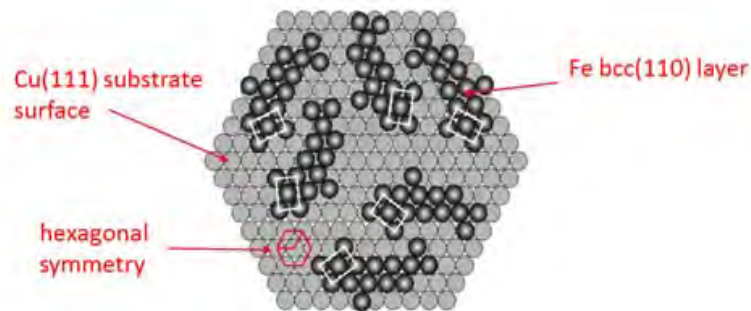
(*Id.*, p. 137; FIGs. 2(f)-(g) and 4.)⁴ Shen discloses that symmetry breaking increases the magnetic field required to saturate the layer and contributes to the uniaxial anisotropy, improving the magnetic properties of the bcc layer. (*Id.*, p. 139, left column.) Shen also discloses that the structural transition from (fcc) to (bcc) in the Fe films results in a “four to five times” increase in magnetization of the Fe films. (Ex. 1011, p. 134, ¶ 4 (5); *see also* pp. 140-41, ¶ 3; p. 137, ¶ 2.)

79. Claim 1 recites “at least one *layer providing a (111) textured hexagonal template.*” Shen discloses this limitation.

80. For example, Shen discloses that the copper substrate, “Cu(111),” has a (111) texture. Shen consistently and repeatedly refers to the (111) texture of the Cu(111) surface. (*See, e.g.*, Ex. 1011, p. 135, ¶¶ 2-3; Abstract; FIGs. 1, 2, and 3.) A topographic image of the “Cu(111)” surface shows that the surface provides a hexagonal template. (*Id.*, FIG. 1 and caption, reproduced above in ¶ 49.) Shen shows the same surface schematically in a “real-space schematic view of the six KS domains on the Cu(111) substrate.” (*Id.*, FIG. 4, *infra*, and caption.)

⁴ Shen acknowledges that the dominance of the two particular KS domains should also, “in principle,” give different spot intensities in the measured LEED pattern, but the actual LEED data has insufficient resolution to show this definitively. (Ex. 1011, p.137, right column; FIG. 4, upper left.)

81. I have annotated a part of that figure below in order to show the hexagonal pattern.



(Ex. 1011, FIG. 4, annotated.)

82. Moreover, one of ordinary skill in the art would have understood that (111) texture in (fcc) material would have a hexagonal structure. (*See, e.g.,* Ex. G, p. 94 *et seq.*) In fact, the '988 patent indicates that (111) (fcc) is one example of a “(111) textured hexagonal atomic template.” (Ex. 1001, 14:55-58.)

83. Shen discloses that the Cu(111) substrate is fcc. For example, Shen explains that, when the Fe layer grown on Cu(111) is relatively thin, the films “adopt the fcc *structure from the* [Cu(111)] *substrate.*” (Ex. 1011, Abstract, emphasis added.) Shen also refers to the (fcc) structure of the Cu(111) substrate numerous times throughout the text. (*See, e.g.,* Ex. 1011, p. 136, ¶ 1; p. 137, ¶¶ 1-2.)

84. Claim 1 recites that *the template is “disposed between said substrate and said bcc-d layer.”* Shen discloses this limitation. The '988 patent explains

that a “layer...disposed between said substrate and said bcc-d layer” could be the top surface of the substrate. For example, dependent claim 26 recites “[the] surface of said single crystal provides a layer providing the (111) textured hexagonal atomic template disposed between the bulk of said substrate and said at least one bcc-d layer.”

85. Shen discloses that the top surface of the Cu(111) substrate provides the (111) textured hexagonal atomic template. (*See* ¶¶ 18-21, *supra*.)

86. Finally, by disclosing that the layer stack is (fcc) Cu(111)/bcc Fe (110), Shen discloses that the surface of the Cu(111) substrate is disposed between the underlying body of the substrate and the overlying bcc-d Fe layer.

C. Shen, Alone or in Combination With Dill, Renders Obvious Claim 27

87. Claim 27 of the '988 patent is identical to claim 1, apart from the additional limitation that the magnetic material structure must be incorporated into a “*magnetic device*.” As discussed in VIII(B) *supra*, Shen, alone or in combination with Dill, discloses all the limitations of claim 1. Shen also discloses the additional limitation of claim 27 that the magnetic structure can be incorporated into a “magnetic device.”

88. The '988 patent defines a “magnetic device” broadly in a way that one of ordinary skill in the art would have understood to encompass a layered structure of at least one magnetic material. For example, the '988 patent refers to “magnetic

media” as a “device,” even though the medium is nothing more than layers of magnetic material with a “preferred orientation ratio.” (Ex. 1001, 32:32-47.) Therefore, because Shen discloses a magnetic material bi-layer with a preferred orientation (*i.e.*, a net orientation preference in the direction of <110> steps of Cu(111)) (Ex. 1011, p. 137, ¶ 1; FIG. 4.), the Cu(111)/Fe(bcc) bi-layer of Shen is a “magnetic device.”

IX. DILL, IN COMBINATION WITH SHEN ALONE OR IN FURTHER COMBINATION WITH HEIM, RENDERS OBVIOUS CLAIMS 1, 3, 6-19, 21-24, 27-30, 34 AND 38 OF THE '988 PATENT

A. Claim Charts

89. The Petition sets forth claim charts (Petition, Sections VI(B) and (C)) citing disclosures in Dill and Shen that demonstrate how the combination of Dill and Shen alone, or in further combination with Heim, renders obvious claims 1, 3, 6-19, 21-24, 27-30, 34 and 38 of the '988 patent. I fully agree with the claim charts. The following sections include additional analysis that demonstrates how the combination of Dill and Shen alone, or in further combination with Heim, renders these claims obvious.

B. Dill in Combination With Shen Renders Obvious Claim 1

90. For at least the following reasons, Dill in combination with Shen renders obvious claim 1 of the '988 patent.

91. The preamble for claim 1 recites “[a] *magnetic material*.” To the extent this preamble is a limitation, Dill discloses this limitation.

92. For example, Dill discloses a magnetic tunnel junction (“MTJ”) magnetoresistive (“MR”) read head (“magnetic material”) that includes a magnetic layer stack on a substrate. (Ex. 1009, 5:26-31; FIG. 4A.) One of ordinary skill in the art would readily have understood that an MTJ read head includes “magnetic material.”

93. As discussed in ¶ 56, *supra*, Dill discloses two examples of an MR layer stack, schematically summarized in the following tables of layers:

Example 1 from (Ex. 1009, 9:47-53; 8:29-57.)		
	...various other layers...	
Interface layer of layer 118:	Co ₍₃₀₎ Fe ₍₇₀₎ (bcc)	“[first] bcc-d layer which is magnetic”
Bulk layer of layer 118:	Ni ₍₄₀₎ Fe ₍₆₀₎ (fcc)	“[first] (111)...hexagonal atomic template”
AF layer 116:	Mn ₍₅₀₎ Fe ₍₅₀₎ (fcc)	(111)...hexagonal atomic template
Template layer 112:	Ni ₍₈₁₎ Fe ₍₁₉₎ (fcc)	(111)...hexagonal atomic template
	...various other layers...	
Substrate G1:	Al ₂ O ₃	

Example 2 from (Ex. 1009, 9:65-10:3; 9:47-53; 8:29-57.)			
...various other layers...			
Upper layer of layer 118:	Co ₍₃₀₎ Fe ₍₇₀₎	(bcc)	
Thin metal layer of 118:			
Lower layer of layer 118:	Co ₍₃₀₎ Fe ₍₇₀₎	(bcc)	“[first] bcc-d layer which is magnetic”
AF layer 116:	Mn ₍₅₀₎ Fe ₍₅₀₎	(fcc)	“[first] (111)...hexagonal atomic template”
Template layer 112:	Ni ₍₈₁₎ Fe ₍₁₉₎	(fcc)	(111)...hexagonal atomic template
...various other layers...			
Substrate G1:	Al ₂ O ₃		

94. Claim 1 recites that the magnetic material comprises “*a substrate.*” Dill discloses that the MTJ includes a “G1 alumina layer as the substrate.” (*See, e.g., id.*, 10:29-32; Example 1 or Example 2 above.)

95. Claim 1 recites “at least one *bcc-d layer which is magnetic.*” Dill discloses this limitation.

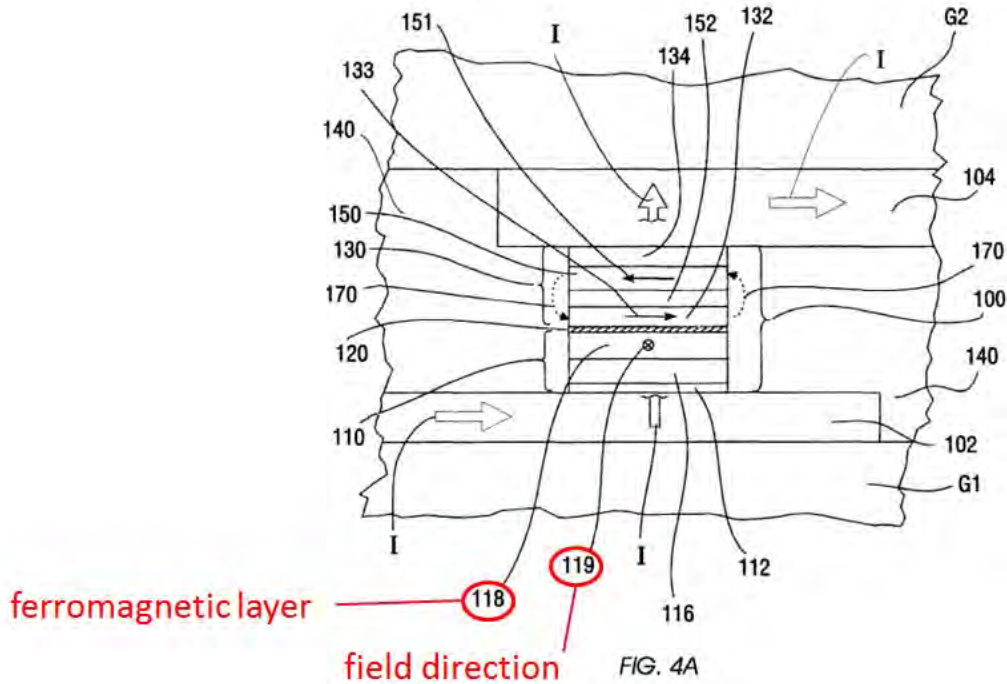
96. In Example 1, as schematically represented above, layer 118 has two layers: 1) a lower, bulk layer (hereinafter, the “bulk layer of layer 118” or “bulk layer of 118”) and 2) an upper, interface layer (hereinafter, the “interface layer of layer 118” or “interface layer of 118”) grown thereon. (*Id.*, 9:47-59.) The interface layer of 118 is Co₃₀Fe₇₀ or Co₄₀Fe₆₀. (*Id.*) One of ordinary skill in the art would have known that the natural crystal structure of the interface material is bcc

and magnetic. (*See, e.g.*, Ex. H, p. 251 *et seq.*; Ex. G, p. 94 *et seq.*; Ex. F.) The bulk layer of layer 118 is Ni₄₀Fe₆₀. (Ex. 1009, 9:47-59.) This material naturally has (fcc) structure and is magnetic.

97. In Example 2, as schematically represented above, layer 118 is comprised of a thin metal layer separating two ferromagnetic layers, a lower layer of 118 and an upper layer of 118. (*Id.*, 9:65-10:4.) Each ferromagnetic layer is comprised of “Ni, Co, Ni-Fe alloys, Co-Fe alloys, or Ni-Fe-Co ternary alloys” (*id.*) such as the Co₃₀Fe₇₀ or Co₄₀Fe₆₀ discussed above, which as discussed in ¶ 96 *supra* is (bcc) material.

98. Claim 1 of the '988 patent recites that the bcc-d layer “form[s] *a uniaxial ... structure.*” Dill discloses this limitation.

99. Dill discloses that layer 118 is “grown in a [magnetic] field oriented along [a particular] direction 119 in FIG 4A,” “to induce in the fixed [layer] 118, sensing [layer] 132 and biasing [layer] 150 ...appropriate magnetic anisotropies.” (Ex. 1009, 10:47-10:59.) FIG 4A shows the field direction 119 used to induce uniaxial anisotropy in layer 118:



(Ex. 1009, FIG. 4A, annotated.)

100. One of ordinary skill in the art would readily have understood that growing ferromagnetic layer 118 under the influence of such a field “to induce in the fixed [layer] 118 ... [an] appropriate magnetic anisotrop[y]” creates a preferred uniaxial magnetic anisotropy in the interface layer of 118. In fact, the ’988 patent recognizes “depos[iting a magnetic film] in the presence of an applied magnetic field” as one way of “achiev[ing] a single uniaxial anisotropy” in the film by ensuring that the film’s “resulting single magnetic easy axis is aligned along the applied magnetic field.” (Ex. 1001, 4:60-65, “Background of the Invention” discussing the prior art.) Similarly, U.S. Patent No. 5,998,048 to Jin (Ex. B) (“Jin”) discloses applying “magnetic fields during the deposition of the films

comprising Co-Fe-Cr-N to induce magnetic anisotropy” through “preferential ordering of atoms to form an easy direction of magnetization.” (Ex. B, 5:48-65; 11:1-9.)

101. Dill discloses that, in Example 1, ferromagnetic layer 118 is also exchanged coupled, in the same direction as the easy axis (*i.e.*, in the direction of applied field 119). (Ex. 1009, 11:62-12:15.) However, one of ordinary skill in the art would have known that exchange coupling and uniaxial anisotropy can coexist, and, in fact, complement one another, in the same layer. In addition to Dill, another example of providing exchange coupling as a complement to uniaxial anisotropy to ensure magnetization along a particular direction is disclosed by U.S. Patent No. 6,295,187 to Pinarbashi (Ex. D). More specifically, Pinarbashi provides a “highly stabilized pinned layer structure” by simultaneously exchange coupling and pinning with stress induced uniaxial anisotropy. Pinarbashi discloses that, when temperature effects degrade the pinning strength, the stress induced uniaxial anisotropy “maintains the orientation of the magnetic moment of the AP pinned layer” in the desired direction. (Ex. D, 1:3-30.)

102. Claim 1 recites that the “bcc-d layer which is magnetic” forms a “*symmetry broken structure.*” Dill in combination with Shen discloses this limitation.

103. As shown in Example 1 above, Dill discloses that the following layers are grown in sequence: (111) (fcc) template layer 112, (111) (fcc) layer 116, (111) (fcc) bulk layer of 118, and (bcc) interface layer of 118. (*Id.*, 8:37-41; 9:37-59; FIG. 4A; *see also* ¶¶ 107-13, *infra*). Particularly, the (bcc) interface layer of 118 is grown on a “bulk [Ni₄₀Fe₆₀] layer” that is (111) (fcc). (Ex. 1009, 8:29-57; 9:37-59).

104. As discussed in ¶ 48, *supra*, Shen discloses a bcc layer (disposed onto a (111) (fcc) layer) that has broken symmetry. Shen also discloses that the magnetic properties of the bcc layer are improved. (*See* ¶ 48, *supra*.) It would have been obvious to a person of ordinary skill in the art at the time of the effective filing date of the '988 patent to use Dill's (111)(fcc) bulk layer of layer 118 / (bcc) interface layer of layer 118 to form broken symmetry in the interface layer to improve the magnetic properties of the interface layer. (*See* ¶¶ 48-52, *supra*.) For example, one of ordinary skill in the art would have known Shen's teaching that creating the disclosed symmetry broken layer would increase the magnetic field required to saturate the layer and would contribute to magnetic anisotropy. (*Id.*) One of ordinary skill in the art would have also understood that the structural transition from (fcc) to (bcc) in the Fe films dramatically increases the magnetization of the layer. (*Id.*)

105. Specifically, Shen discloses a magnetic material layered structure formed by growing a (bcc) magnetic layer on a stepped (111) (fcc) surface. (Ex. 1011, FIG. 4; FIG. 5; p. 138, ¶¶ 1-2; p. 139, ¶ 2.) Shen discloses that the (bcc) films have broken symmetry because two of the six possible crystallographic variants are favored in the growth. (Ex. 1011, p. 137, ¶ 1; FIG. 1.)

106. Dill's (bcc) interface layer of 118 was grown onto the (fcc) bulk layer of 118, to form the (111)(fcc)/(bcc) structure as disclosed by Shen.⁵ (Ex. 1009, FIG. 4A; Ex. 1011, FIGs. 2 and 4.) Shen discloses that broken symmetry is formed in such a (111)(fcc)/(bcc) structure. (Ex. 1011, p. 134, ¶ 4; p. 137, ¶ 1.) Also in Dill's Example 2 (*see* ¶ 96, *supra*), the (bcc) lower ferromagnetic layer of 118 was grown onto the (111)(fcc) AF layer 116,⁶ a (111)(fcc)/(bcc) structure. It would have been obvious to use the teaching of Shen to form broken symmetry in the (bcc) layers of Dill's examples in order to gain improvement in magnetic properties as discussed in ¶ 104, *supra*.

⁵ Note that here and in the Petition, the (111)(fcc)/(bcc) structure formed according to the teachings of Shen discussed *supra* is referred to as "Shen's symmetry broken (111)(fcc)/(bcc) structure."

⁶ I say "*lower* ferromagnetic layer" here because it is the lower of the two ferromagnetic layers of 118, not because it is lower than AF layer 116.

107. Claim 1 recites “at least one *layer providing a (111) textured hexagonal template.*” As discussed in ¶ 56, *supra*, Dill discloses that layers 112, 116, and bulk layer of 118 are all (111) textured hexagonal templates.

108. In Example 1, the “template layer 112” is “fcc (111) Ni₈₁ Fe₁₉.” (Ex. 1009, 8:37-41.) Because layer 112 is (111) textured fcc, it has a hexagonal texture and is a “(111) textured hexagonal atomic template,” according to the definition provided by the ’988 patent. (Ex. 1001, 14:55-58.) Dill discloses that layer 116 is grown directly on layer 112, and layer 112 “encourages” the growth of AF layer 116 by providing the template for layer 116. (Ex. 1009, 8:29-57.) Dill further discloses that the antiferromagnetic (“AF”) layer 116 is Mn₅₀Fe₅₀. (*Id.*) One of ordinary skill in the art would have understood that Mn₅₀Fe₅₀ is naturally (fcc). Because (fcc) layer 116 is grown directly on layer 112, one of ordinary skill in the art would have understood that the (fcc) (111) hexagonal texture of template layer 112 is imparted to layer 116. Moreover, because the bulk layer of layer 118 is Ni₄₀Fe₆₀ and grown on (fcc) layer 116, one of ordinary skill would have understood that the bulk layer of layer 118 also has a (111) (fcc) textured hexagonal atomic template. (¶ 56 *supra*; Ex. 1009, 8:29-57; 9:37-59.)

109. In Example 1, layers 112 and 116 and the bulk layer of 118 each provide a (111) textured hexagonal atomic template.

Example 1 from (Ex. 1009, 9:47-53; 8:29-57.)		
...various other layers...		
Interface layer of layer 118:	Co ₍₃₀₎ Fe ₍₇₀₎ (bcc)	“[first] bcc-d layer which is magnetic”
Bulk layer of layer 118:	Ni ₍₄₀₎ Fe ₍₆₀₎ (fcc)	“[first] (111)...hexagonal atomic template”
AF layer 116:	Mn ₍₅₀₎ Fe ₍₅₀₎ (fcc)	(111)...hexagonal atomic template
Template layer 112:	Ni ₍₈₁₎ Fe ₍₁₉₎ (fcc)	(111)...hexagonal atomic template
...various other layers...		
Substrate G1:	Al ₂ O ₃	

110. This is because, as shown above, each of the layers has an (111)(fcc) structure as a result of being grown in seed layer 112 which Dill explicitly discloses as having such a structure. (See Ex. 1009, 8:37-41.)

111. In Example 2 discussed in ¶¶ 108-09, AF layer 116 provides an fcc (111) hexagonal atomic template to the (bcc) lower layer of 118. (*Id.*)

Example 2 from (Ex. 1009, 9:65-10:3; 9:47-53; 8:29-57.)		
...various other layers...		
Upper layer of layer 118:	Co ₍₃₀₎ Fe ₍₇₀₎ (bcc)	
Thin metal layer of 118:		
Lower layer of layer 118:	Co ₍₃₀₎ Fe ₍₇₀₎ (bcc)	“[first] bcc-d layer which is magnetic”
AF layer 116:	Mn ₍₅₀₎ Fe ₍₅₀₎ (fcc)	“[first] (111)...hexagonal atomic template”
Template layer 112:	Ni ₍₈₁₎ Fe ₍₁₉₎ (fcc)	(111)...hexagonal atomic template
...various other layers...		
Substrate G1:	Al ₂ O ₃	

112. Claim 1 recites that *the template is “disposed between said substrate and said bcc-d layer.”* Dill’s Example 1 shows this limitation, with the bulk layer of 118 disposed between the interface layer of 118 and the substrate, and Example 2 shows this limitation with AF layer 116 disposed between the lower layer of 118 and the substrate. (*See* Ex. 1009, FIG. 4A.)

C. Dill in Combination With Shen Renders Obvious Claim 3

113. Claim 3 of the ’988 patent recites: “The magnetic material structure recited in claim 1, wherein a surface of said *substrate is amorphous or polycrystalline.*” The combination of Dill and Shen renders obvious this limitation.

114. Dill discloses depositing the MTJ MR layers on a layer of Au metal that is deposited on the surface of an “alumina substrate” (Ex. 1009, 8:43-48). Although Dill does not explicitly disclose that the Al₂O₃ layer is polycrystalline, one of ordinary skill in the art would have understood the Al₂O₃ substrate is polycrystalline because Dill’s reference to the Al₂O₃ substrate as an “alumina” substrate would have been understood as polycrystalline. Moreover, one of ordinary skill in the art would have understood that the Au metal is deposited onto the polycrystalline Al₂O₃ layer and that this would naturally create a polycrystalline Au surface.

D. Dill in Combination With Shen Renders Obvious Claim 6

115. Claim 6 of the '988 patent recites: “The magnetic material structure recited in claim 1, wherein the *layer providing said hexagonal atomic template is formed from a fcc-d or hcp crystalline material.*” Dill discloses this limitation.

116. As discussed above and shown in Example 1, Dill's layers 112 and 116 each has (fcc) structure and provides a (111) textured hexagonal atomic template. Specifically, Dill discloses that “template layer 112” is “(111)... (fcc) Ni₈₁ Fe₁₉,” and because AF layer 116 is Mn₅₀Fe₅₀ grown on layer 112, the crystalline structure of AF layer 116 is “encourage[d]” by underlying layer 112. Because layer 116 is grown on (111)(fcc) layer 112, one of ordinary skill in the art would have known that layer 116's structure is also (111)(fcc). (Ex. 1009, 8:29-57; *see also, e.g.*, Ex. H, p. 251 *et seq.*; Ex. I, pp. 288-312; Ex. G, p. 94 *et seq.*)

E. Dill in Combination With Shen Renders Obvious Claim 7

117. Claim 7 of the '988 patent recites: “The magnetic material structure recited in claim 1, wherein *the layer providing said hexagonal atomic template is magnetic.*” Dill discloses this limitation.

118. As discussed in IX(B) and IX(D) *supra* and shown in Example 1, the bulk layer of layer 118 is Ni₄₀Fe₆₀, grown onto (111)(fcc) AF layer 116 and

“provid[es] said hexagonal atomic template.” (Ex. 1009, 9:47-53; 8:29-57.)

Ni₄₀Fe₆₀ is magnetic material. Therefore the bulk layer of 118 is “magnetic.” (See, e.g., Ex. 1009, 7:65; 9:65-67; 8:29-57; 9:37-10:4.)

F. Dill in Combination With Shen Renders Obvious Claim 8

119. Claim 8 of the '988 patent recites “wherein said *bcc-d layer* [of claim 1] *is epitaxially grown on said (111) textured hexagonal atomic template.*”

The combination of Dill and Shen discloses this limitation.

120. As discussed in IX(B) *supra*, Dill discloses that the bulk layer of 118 provides a (111) textured hexagonal atomic template to the (bcc) interface layer of 118, which is grown thereon. (Ex. 1009, 8:29-57; 9:37-57.) One of ordinary skill in the art would have known that in this context, the term “grown on” (*id.*, 8:46) means epitaxially grown on, with layers 112 and 116, the bulk layer of 118, and the interface layer of 118 epitaxially grown on their respective underlayers. For the same reason, one of ordinary skill in the art would also have understood that the lower ferromagnetic layer of layer 118 is epitaxially grown on layer 116.

121. Even if Dill does not explicitly disclose that the (bcc) interface layer of 118 was epitaxially grown on the (111) (fcc) bulk layer of 118 or that the (bcc) lower ferromagnetic layer of layer 118 was epitaxially grown on layer 116, Shen discloses that such epitaxial growth is part of forming Shen’s symmetry broken (111)(fcc)/(bcc) structure discussed in IX(B) *supra*. Specifically, Shen discloses

growing the bcc Fe(110) layer on the Cu(111) substrate and shows that this is epitaxial growth in FIG. 4. (Ex. 1011, pp. 136-37; FIG. 4.)

122. Claim 8 also recites that “*the bcc-d layer...has a (110) crystalline texture.*” Dill does not explicitly disclose the crystalline texture of the interface layer of 118. However, as discussed in ¶¶ 102-06, *supra*, it would have been obvious to a person of ordinary skill in the art at the time of the effective filing date of the '988 patent to combine the teachings of Shen and Dill to improve the magnetic properties of Dill's (bcc) interface layer of 118 (*see also* ¶¶ 48-52, *supra*). Shen discloses that Shen's symmetry broken (111)(fcc)/(bcc) structure formed a (110) structure in the (bcc) layer. (*See, e.g.*, Ex. 1011, FIG. 4.)

123. More specifically, Shen discloses that when the bcc layer is more than 2 or 3 ML (atomic monolayers) thick, the bcc layer in the (111) (fcc)/(bcc) structure forms a (110) crystalline texture. (*Id.*, pp. 140-41, ¶ 3.) Likewise, Dill discloses an example in which the interface layer of layer 118 is 2 nm thick. (Ex. 1009, 9:53-54.) An atomic monolayer is on order of 0.2 nm thick. Therefore, the exemplary interface layer portion of layer 118 is approximately 10 ML thick.

124. Therefore, one of ordinary skill in the art would have understood from Dill that the interface layer of layer 118 forms a (110) crystalline texture.

125. Claim 8 also recites “at least *one crystalline grain of said (111) textured hexagonal atomic template has epitaxially grown thereon at least two*

and not more than four dominate (110) orientational variants.” Dill does not explicitly disclose the number of orientational variants in the interface layer of 118 after it is grown on the bulk layer of 118.

126. However, as discussed in IX(B) *supra*, Dill discloses the following (111)(fcc)/(bcc) structure: (fcc) (111) bulk layer of 118/(bcc) interface layer of 118. As discussed in VIII(B) *supra*, Shen grows a (bcc) ferromagnetic layer onto a stepped (111)(fcc) layer to form a (110) crystalline texture in the top bcc layer with two dominant growth orientational variants. (Ex. 1011, pp. 136-37; FIG. 4.) Therefore, the combination of Dill and Shen discussed in IX(B) *supra* discloses an interface layer of 118 grown on the bulk layer of 118, to cause broken symmetry (*see* X(B) *supra*), to form a (bcc) film with two dominant (110) orientational variants. To the extent that growing the layers of Dill according to the disclosure in Shen does not provide such variants, it would have been obvious to grow the interface layer of layer 118 to provide the variants as disclosed in Shen to improve magnetic properties in the interface layer of layer 118. (*See* X(B) *supra*.)

G. Dill in Combination With Shen Renders Obvious Claim 9

127. Claim 9 of the '988 patent recites: “The magnetic material structure according to claim 1, further comprising: *a second layer providing a (111) textured hexagonal atomic template*, wherein said second layer is *magnetic*.” Dill discloses this limitation, as summarized in Example 1 (below)

Example 1 from (Ex. 1009, 9:47-53; 8:29-57.)		
	...various other layers...	
Interface layer of layer 118:	Co ₍₃₀₎ Fe ₍₇₀₎ (bcc)	“[first] bcc-d layer which is magnetic”
Bulk layer of layer 118:	Ni ₍₄₀₎ Fe ₍₆₀₎ (fcc)	“[first] (111)...hexagonal atomic template”
AF layer 116:	Mn ₍₅₀₎ Fe ₍₅₀₎ (fcc)	(111)...hexagonal atomic template
Template layer 112:	Ni ₍₈₁₎ Fe ₍₁₉₎ (fcc)	(111)...hexagonal atomic template
	...various other layers...	
Substrate G1:	Al ₂ O ₃	

128. Template layer 112 is “a second layer providing a (111) textured hexagonal atomic template” that is magnetic. This is because layer 112 is (fcc) Ni₈₁Fe₁₉ and has a (111) structure (Ex. 1009, 8:29-57), which the '988 patent defines as a (111) textured hexagonal template (Ex. 1001, 14:55-58.) Moreover, one of ordinary skill in the art would have known layer 112 to be a hexagonal, magnetic template, at least because of layer 112's (111)(fcc) structure and because both Ni and Fe, and their alloys, are magnetic. Alternatively, Dill discloses a “sensing ferromagnetic layer 132” that is Ni₈₁Fe₁₉, which provides a (111) textured hexagonal atomic template to (bcc) Cr spacer layer 152. (*See, e.g.*, Ex. 1009, 8:50-53; FIG. 4A.) One of ordinary skill in the art would have known that Ni₈₁Fe₁₉ has an (fcc) structure and is magnetic.

H. Dill in Combination With Shen Renders Obvious Claim 10

129. Claim 10 of the '988 patent recites: “The magnetic material structure according to claim 1, further comprising: *a second bcc-d layer which is non-magnetic.*” Dill discloses this limitation, as summarized in Example 1.

Example 1 from (Ex. 1009, 9:47-53; 8:29-57.)		
	...various other layers...	
Interface layer of layer 118:	Co ₍₃₀₎ Fe ₍₇₀₎ (bcc)	“[first] bcc-d layer which is magnetic”
Bulk layer of layer 118:	Ni ₍₄₀₎ Fe ₍₆₀₎ (fcc)	“[first] (111)...hexagonal atomic template”
AF layer 116:	Mn ₍₅₀₎ Fe ₍₅₀₎ (fcc)	(111)...hexagonal atomic template
Template layer 112:	Ni ₍₈₁₎ Fe ₍₁₉₎ (fcc)	second (111)...hexagonal atomic template
	...various other layers...	
Substrate G1:	Al ₂ O ₃	

130. For example, Dill discloses a spacer layer 152 that is made of chromium (Cr) metal. (Ex. 1009, 8:50-57.) The '988 patent indicates that Cr is a “non-magnetic bcc [material].” (Ex. 1001, 10:57-60.)

I. Dill in Combination With Shen Renders Obvious Claim 11

131. Claim 11 of the '988 patent recites: “The magnetic material structure according to claim 1, further comprising: *a second bcc-d layer which is magnetic.*” Dill discloses this limitation in an alternate of Example 1.

Example 1 from (Ex. 1009, 9:37-53; 8:29-57.)		
...various other layers...		
Bulk layer of sensing layer 132:		
Interface layer of 132:	Co ₍₄₀₎ Fe ₍₆₀₎ (bcc)	“second bcc-d layer which is magnetic”
Tunnel barrier 120:	Al ₂ O ₃	
Interface layer of layer 118:	Co ₍₃₀₎ Fe ₍₇₀₎ (bcc)	“[first] bcc-d layer which is magnetic”
Bulk layer of layer 118:	Ni ₍₄₀₎ Fe ₍₆₀₎ (fcc)	“[first] (111)...hexagonal atomic template”
AF layer 116:	Mn ₍₅₀₎ Fe ₍₅₀₎ (fcc)	(111)...hexagonal atomic template
Template layer 112:	Ni ₍₈₁₎ Fe ₍₁₉₎ (fcc)	(111)...hexagonal atomic template
...various other layers...		
Substrate G1:	Al ₂ O ₃	

132. Dill discloses an exemplary “alternative sensing ferromagnetic layer 132” “comprised of a thin Co or Co_(100-x)Fe_(x) or Ni_(100-x)Fe_x (x is approximately 60) layer at the interface between the sensing ferromagnetic layer 132 and the tunnel barrier layer 120.” (Ex. 1009, 9:37-41; FIG.4A.) Because “x is approximately 60,” the composition of this interface layer is approximately Co₄₀Fe₆₀, an Fe-rich alloy of FeCo. One of ordinary skill in the art would have understood that the layer has the (bcc) structure. (*See, e.g.*, Ex. F.) And with both Co and Fe being magnetic, one of ordinary skill in the art would have understood that their alloys are also magnetic.

J. Dill in Combination With Shen and Heim Renders Obvious Claim 12

133. Claim 12 of the '988 patent recites: “The magnetic material structure according to claim 1, further comprising: *a second bcc-d layer . . .*” Dill discloses this limitation as summarized in Example 2.

Example 2 from (Ex. 1009, 8:14-22; 10:57-60; 9:65-10:3; 9:47-53; 8:29-57.)			
...various other layers...			
Upper layer of layer 118:	Co ₍₃₀₎ Fe ₍₇₀₎	(bcc)	
Thin metal layer of 118:	Cr	(bcc)	“second bcc-d layer”
Lower layer of layer 118:	Co ₍₃₀₎ Fe ₍₇₀₎	(bcc)	“[first] bcc-d layer which is magnetic”
AF layer 116:	Mn ₍₅₀₎ Fe ₍₅₀₎	(fcc)	“[first] (111)...hexagonal atomic template”
Template layer 112:	Ni ₍₈₁₎ Fe ₍₁₉₎	(fcc)	(111)...hexagonal atomic template
...various other layers...			
Substrate G1:	Al ₂ O ₃		

134. As discussed in ¶ 97 *supra* and shown in Example 2, Dill discloses an alternative example of layer 118 that includes two ferromagnetic layers of (bcc) Co₃₀Fe₇₀ “separated by a thin metallic layer, which results in antiferromagnetic coupling of the two ferromagnetic layers.” (Ex. 1009, 9:65-10:4.) One of ordinary skill in the art would have known that, in this example, the spacer layer must be non-magnetic in order to allow AF coupling of the ferromagnetic layers.

135. Dill does not explicitly specify the spacer layer in this example of layer 118, but Dill discloses that the thin metal layer is non-magnetic metal that separates and couples two ferromagnetic layers. Dill cites Heim as providing further information about the “type of laminated fixed layer” of layer 118, including the above-mentioned thin metal layer. (Ex. 1009, 9:60-10:4.) Because Dill cites Heim for the laminate structure and because Heim discloses the same ferromagnetic structure as disclosed in Dill, it would have been obvious for a person of ordinary skill to use this information from Heim, including that the thin layer can be Cr. (Ex. 1012, 7:3-10.) Similarly, Dill discloses another non-magnetic metal spacer layer 152 that separates and couples the ferromagnetic sensing layer 132 and its ferromagnetic bias layer 150. (Ex. 1009, 8:14-22.) The non-magnetic spacer layer between layers 132 and 150 is chromium. Dill discloses that Cr layer 152 couples layers 150 and 132 to “maintain a generally single domain state” in film 132. (Ex. 1009, 8:14-22.) Also, the '988 patent explains that Cr is an example of what is claimed as a “non-magnetic bcc [material].” (Ex. 1001, 10:57-60.)

136. In this example, the first ferromagnetic film of layer 118 is the claimed first “bcc-d layer,” and the Cr spacer of layer 118 is the claimed “second bcc-d layer.” Alternatively, the “second bcc-d layer” is the second ferromagnetic film of layer 118, grown onto the Cr spacer of layer 118.

137. Claim 12 of the '988 patent further recites “wherein *the crystalline orientation of the second bcc-d layer is epitaxially determined by said [first] bcc-d layer.*” Dill discloses this limitation.

138. As discussed in ¶¶ 135-36, *supra*, the chromium spacer and both ferromagnetic films of layer 118 have a (bcc) structure, and one of ordinary skill in the art would have known that the Cr spacer layer would grow epitaxially on and have its crystalline orientation epitaxially determined by the lower ferromagnetic film. Because the upper ferromagnetic film is grown on the Cr thin metal layer, one of ordinary skill in the art would have known that its structure would be determined by the thin metal layer and, therefore, also epitaxially determined by the lower ferromagnetic film (first bcc-d layer). Therefore, it would have been obvious to one of ordinary skill in the art to have a second bcc-d layer (the Cr spacer layer of layer 118 or the upper ferromagnetic film of 118) whose bcc-d crystalline orientation is epitaxially determined by the first bcc-d layer (lower ferromagnetic film).

K. Dill in Combination With Shen Renders Obvious Claim 13

139. Claim 13 of the '988 patent recites: “The magnetic material structure according to claim 1, further comprising: *a second bcc-d layer.*” Dill discloses this limitation as summarized in Example 1.

Example 1 from (Ex. 1009, 8:51-52; 9:41-42; 9:47-53; 8:29-57.)			
...various other layers...			
Spacer layer 152:	Cr	(bcc)	“second bcc-d layer”
Bulk layer of sensing layer 132:	Ni ₈₁ Fe ₁₉	(fcc)	second “(111)...hexagonal atomic template”
Interface layer of 132:	Co ₍₄₀₎ Fe ₍₆₀₎	(bcc)	
Tunnel barrier 120:	Al ₂ O ₃		
Interface layer of layer 118:	Co ₍₃₀₎ Fe ₍₇₀₎	(bcc)	“[first] bcc-d layer which is magnetic”
Bulk layer of layer 118:	Ni ₍₄₀₎ Fe ₍₆₀₎	(fcc)	“[first] (111)...hexagonal atomic template”
AF layer 116:	Mn ₍₅₀₎ Fe ₍₅₀₎	(fcc)	(111)...hexagonal atomic template
Template layer 112:	Ni ₍₈₁₎ Fe ₍₁₉₎	(fcc)	(111)...hexagonal atomic template
...various other layers...			
Substrate G1:	Al ₂ O ₃		

140. For example, Dill discloses a layer 152 that is made of chromium (Cr) metal. (Ex. 1009, 8:50-57.) The '988 patent indicates that Cr is an example of what is claimed as a “non-magnetic bcc [material].” (Ex. 1001, 10:57-60.) Therefore, layer 152 is the claimed “second bcc-d layer.”

141. Claim 13 of the '988 patent further recites “*a second layer providing a (111) textured hexagonal atomic template.*” Dill discloses this limitation.

142. For example, Dill discloses that sensing layer 132 is Ni₈₁Fe₁₉. (Ex. 1009, 8:51-52; 9:41-42.) One of ordinary skill in the art would have known that Ni₈₁Fe₁₉ naturally has an (fcc) structure and is magnetic. (See, e.g., Ex. H, p. 251 *et seq.*; Ex. I, pp. 288-312; Ex. G, p. 94 *et seq.*) In addition, one of ordinary skill in the art would also have known that this particular composition, Ni₈₁Fe₁₉,

would naturally form a (111)(fcc) structure. (*Id.*) Therefore, alternative sensing layer 132 would be the claimed “second layer providing a (111) textured hexagonal template.”

143. Claim 13 of the '988 patent further recites “wherein said *second layer providing a (111) textured hexagonal atomic template is disposed between said bcc-d layers.*” Dill discloses this limitation.

144. Example 1 summarized above shows that layer 132 (the “second layer providing a (111) textured hexagonal atomic template”) is located between layer 152 (the “second bcc-d layer”) and layer 118 (the first “bcc-d layer”).

145. Moreover, FIG. 4A shows that layer 132 is disposed between layers 118 and 152.

L. Dill in Combination With Shen Renders Obvious Claim 14

146. Claim 14 of the '988 patent recites: “The magnetic material structure according to claim 1, further comprising: *a second bcc-d layer, which is magnetic.*” Dill discloses this limitation as summarized in Example 1.

Example 1 from (Ex. 1009, 8:51-52; 9:41-42; 9:47-53; 8:29-57.)		
	...various other layers...	
Spacer layer 152:	Cr	(bcc)
Bulk layer of sensing layer 132:	Ni ₍₈₁₎ Fe ₍₁₉₎	(fcc)
Interface layer of 132:	Co ₍₄₀₎ Fe ₍₆₀₎	(bcc) “second bcc-d layer, which is magnetic”
Tunnel barrier 120:	Al ₂ O ₃	“oxide layer between”
Interface layer of layer 118:	Co ₍₃₀₎ Fe ₍₇₀₎	(bcc) “[first] bcc-d layer which is magnetic”
Bulk layer of layer 118:	Ni ₍₄₀₎ Fe ₍₆₀₎	(fcc) “[first] (111)...hexagonal atomic template”
AF layer 116:	Mn ₍₅₀₎ Fe ₍₅₀₎	(fcc) (111)...hexagonal atomic template
Template layer 112:	Ni ₍₈₁₎ Fe ₍₁₉₎	(fcc) (111)...hexagonal atomic template
	...various other layers...	
Substrate G1:	Al ₂ O ₃	

147. For example, Dill discloses an alternative sensing layer 132 that includes an interface layer of 132 that is Co₍₄₀₎Fe₍₆₀₎. (Ex. 1009, 9:37 41.) One of ordinary skill in the art would have known that both Co and Fe are magnetic, as are their alloys. Therefore, one of ordinary skill in the art would have known this layer to be magnetic. As shown in the phase diagram for this material, one of ordinary skill in the art would have understood that the natural state of Co₍₄₀₎Fe₍₆₀₎ is bcc. (See, e.g., Ex. H, p. 251 *et seq.*; Ex. I, pp. 288-312; Ex. G, p. 94 *et seq.*)

148. Claim 14 further recites “*at least one oxide layer between said bcc-d layers.*” Dill discloses this limitation.

149. For example, Dill discloses a “tunnel barrier layer 120” (“at least one oxide layer between said bcc-d layers”) that is comprised of the oxide Al_2O_3 . (Ex. 1009, 8:49-51.) As shown at least in Example 1 above, tunnel barrier 120 is disposed between ferromagnetic fixed layer 118 (which includes the first bcc-d layer) and layer 132 (which includes the second bcc-d layer). This is also shown in FIG. 4A of Dill. (Ex. 1009, FIG. 4A.)

M. Dill in Combination With Shen and Heim Renders Obvious Claim 15

150. Claim 15 of the '988 patent recites: “The magnetic material structure according to claim 1, further comprising: *a second and a third bcc-d layers which are non-magnetic.*” Dill discloses this limitation as summarized in Example 2.

Example 2 from (Ex. 1009, 13:35-38; 9:65-10:3; 9:47-53; 8:29-57.)			
Cap layer 134:	Cr	(bcc)	
Top layer of 150:	Co ₍₃₀₎ Fe ₍₇₀₎	(bcc)	
Thin metal layer of 150:			
Bottom layer of 150:	Co ₍₃₀₎ Fe ₍₇₀₎	(bcc)	“fourth bcc-d layer which is magnetic”
Spacer layer 152:	Cr	(bcc)	“third bcc-d layer” which is non-magnetic
Sensing layer 132:	Co ₍₄₀₎ Fe ₍₆₀₎	(bcc)	
Tunnel barrier 120:	Al ₂ O ₃		“oxide layer between”
Upper layer of layer 118:	Co ₍₃₀₎ Fe ₍₇₀₎	(bcc)	
Thin metal layer of 118:	Cr	(bcc)	second bcc-d layer which is non-magnetic
Lower layer of layer 118:	Co ₍₃₀₎ Fe ₍₇₀₎	(bcc)	“[first] bcc-d layer which is magnetic”
AF layer 116:	Mn ₍₅₀₎ Fe ₍₅₀₎	(fcc)	“[first] (111)...hexagonal atomic template”
Template layer 112:	Ni ₍₈₁₎ Fe ₍₁₉₎	(fcc)	(111)...hexagonal atomic template
			...various other layers...
Substrate G1:	Al ₂ O ₃		

151. As discussed in ¶¶ 96-97, 134-35 and shown in Example 2 above, Dill discloses that an alternative example of layer 118 includes two ferromagnetic layers of (bcc) Co₃₀Fe₇₀ “separated by a thin metallic [spacer] layer” (Ex. 1009, 9:65-10:4), where it would have been obvious for the spacer layer to be Cr (*id.*; see also Ex. 1012, 7:3-10), which is non-magnetic and (bcc) (Ex. 1001, 10:57-60). (See ¶¶ 134-35, *supra.*) Because the film is “thin” and has a natural (bcc) structure, one of ordinary skill would have understood that it would conform to the

(bcc) crystalline structure of the underlying $\text{Co}_{30}\text{Fe}_{70}$ layer. In this example, the lower ferromagnetic film of layer 118 is the claimed *first “bcc-d layer”* and the Cr spacer of layer 118 is the claimed *“second bcc-d layer...which [is] non-magnetic.”*

152. Similarly, Dill also discloses a layer 152 that is made of chromium (Cr) metal. (Ex. 1009, 8:50-57.) As discussed above, one of ordinary skill in the art would have known that Cr is a (bcc) material that is non-magnetic, and the '988 patent indicates as much. Therefore, layer 152 is the claimed *“third bcc-d layer...which [is] non-magnetic.”*

153. Claim 15 further recites *“a fourth bcc-d layer which is magnetic.”* Dill discloses this limitation.

154. For example, Dill first discloses a “biasing ferromagnetic layer 150” that is a single ferromagnetic layer located over the sensing layer 132. (Ex. 1009, 8:51-54.) Dill then discloses an improved layer 150 that “secures the magnetic moment” of layer 150 (Ex. 1009, 13:8-11) by forming layer 150 from “a bilayer of a ferromagnetic layer of permalloy covered with an antiferromagnetic layer of FeMn.” (Ex. 1009, 13:35-38.) Dill also discloses a tri-layer laminate structure (for layer 118) that will “increase[] further” the stability of one of the ferromagnetic layers. (Ex. 1009, 9:65-10:4, emphasis added.) As discussed in ¶ 134 *supra*, in this example the laminate structure includes two (bcc) ferromagnetic layers separated by a thin metal layer. It would have been obvious to one of ordinary

skill in the art to apply the “further” increased stability of the layer laminate structure (for layer 118) to the merely increased stability of layer 150 to form a tri-layer laminate layer 150, like the tri-layer laminate layer 118. In this case, as shown in Example 2 above, layer 150 would be a laminate of a $\text{Co}_{(30)}\text{Fe}_{(70)}$ layer / a thin metal layer / a $\text{Co}_{(30)}\text{Fe}_{(70)}$ layer.

155. The lower ferromagnetic layer of layer 150 is $\text{Co}_{(30)}\text{Fe}_{(70)}$ which is naturally (bcc) and magnetic. The layer is grown directly on the Cr spacer layer 152, which is also naturally (bcc). Therefore, one of ordinary skill in the art would have known that it is natural that the lower ferromagnetic layer of layer 150 is (bcc) and that Dill discloses the “fourth bcc-d layer which is magnetic” limitation.

156. Claim 15 further recites “*at least one oxide layer between said second bcc-d layer and said third bcc-d layer.*” Dill discloses this limitation.

157. Dill discloses a “tunnel barrier layer 120” that is comprises of the oxide Al_2O_3 . (Ex. 1009, 8:49-51.) As summarized in Example 2 above, tunnel barrier 120 is disposed between layer 118 (that includes the second “bcc-d [layer] which [is] non-magnetic”) and layer 152 (the third “bcc-d [layer] which [is] non-magnetic”).

158. Claim 15 further recites “wherein said *second and third bcc-d layers are disposed between said first and fourth bcc-d layers.*” Dill discloses this limitation.

159. As summarized in Example 2 above, the Cr thin metal layer of layer 118 (“second...bcc-d layer”) and Cr layer 152 (“third bcc-d layer”) are located between the lower ferromagnetic layer of layer 118 (“first...bcc-d layer”) and the lower ferromagnetic layer of layer 150 (“fourth bcc-d layer”). This is also shown explicitly in FIG. 4A of Dill. (Ex. 1009, FIG. 4A.)

N. Dill in Combination With Shen and Heim Renders Obvious Claim 16

160. Claim 16 of the '988 patent recites: “The magnetic material structure according to claim 1, further comprising: *a second bcc-d layer which is magnetic.*” Dill discloses this limitation as summarized in Example 2.

Example 2 from (Ex. 1009, 9:37-41; 9:65-10:3; 9:47-53; 8:29-57.)			
...various other layers...			
Sensing layer 132:			
Interface layer of 132	Co ₍₄₀₎ Fe ₍₆₀₎	(bcc)	“second bcc-d layer which is magnetic”
Tunnel barrier 120:	Al ₂ O ₃		“oxide layer between”
Upper layer of layer 118:			
Thin metal layer of 118:	Ru	(hcp)	second (111)...hexagonal atomic template
Lower layer of layer 118:	Co ₍₃₀₎ Fe ₍₇₀₎	(bcc)	“[first] bcc-d layer which is magnetic”
AF layer 116:	Mn ₍₅₀₎ Fe ₍₅₀₎	(fcc)	“[first] (111)...hexagonal atomic template”
Template layer 112:	Ni ₍₈₁₎ Fe ₍₁₉₎	(fcc)	(111)...hexagonal atomic template
...various other layers...			
Substrate G1:	Al ₂ O ₃		

161. For example, Dill discloses an alternative sensing layer that includes an interface layer of layer 132 that is bcc and magnetic. (Ex. 1009, 9:37-41.) With “x [being] approximately 60,” the interface layer of layer 132 is Co₍₄₀₎Fe₍₆₀₎ (*id.*), because both Co and Fe are magnetic, as are their alloys, one of ordinary skill in the art would have known this layer to be magnetic. One of ordinary skill in the art would have understood that the natural state of Co₍₄₀₎Fe₍₆₀₎ is bcc. (*See, e.g.,* Ex. F.)

162. Claim 16 further recites “*a second (111) textured hexagonal atomic template layer between said bcc-d layers.*” Dill discloses this feature.

163. In the example discussed in ¶ 97, *supra*, layer 118 comprises a thin metal layer separating two (bcc) layers of $\text{Co}_{30}\text{Fe}_{70}$. (Ex. 1009, 9:47-53; 9:65-10:4.) Dill cites Heim as providing further information about the “type of laminated fixed layer” of layer 118, including the above-mentioned thin metal layer. (Ex. 1009, 9:60-10:4.) Because Dill cites Heim for the laminate structure and because Heim discloses the same ferromagnetic structure as disclosed in Dill, it would have been obvious for a person of ordinary skill to use this information from Heim, including that the thin layer can be Ru. (Ex. 1012, 5:16-27; *see also* ¶ 135, *supra*.) One of ordinary skill in the art would have known from the relevant phase diagram that the natural structure of Ru grown on a (bcc) surface is (hcp) that provides a (111) hexagonal atomic template. (*See, e.g.*, Ex. G, p. 94 *et seq.*) Therefore, in this example the metal layer of 118 is “a second (111) textured hexagonal atomic template layer.”

164. Because the Ru thin metal layer of layer 118 separates the two ferromagnetic layers of layer 118, it is disposed above the lower ferromagnetic layer of layer 118 (the first “bcc-d layer”). As summarized for Example 2 above, the Ru thin metal layer of layer 118 (“second layer providing a (111) textured hexagonal atomic template”) is disposed below the $\text{Co}_{(40)}\text{Fe}_{(60)}$ interface layer of layer 132 (the “second bcc-d layer”). The metal layer of 118 is located between

the lower ferromagnetic layer of layer 118 (the first “bcc-d layer”) and the interface layer of layer 132 (the “second bcc-d layer”).

165. Claim 16 further recites “at least one *oxide layer between said bcc-d layers.*” Dill discloses this limitation.

166. Dill discloses an Al₂O₃ “tunnel barrier layer 120.” (Ex. 1009, 8:49-51.) As summarized for Example 2 above, tunnel barrier 120 is disposed between biasing layer 150 (with the “second bcc-d layer which is magnetic”) and fixed layer 118 (with the first “bcc-d layer which is magnetic”).

167. FIG. 4A further shows that layer 120 is disposed between layers 150 and 118.

O. Dill in Combination With Shen Renders Obvious Claim 17

168. Claim 17 of the '988 patent recites: “The magnetic material structure recited in claim 1, wherein said *bcc-d layer forming a uniaxial symmetry broken structure is composed of Fe or FeCo or an alloy of Fe or FeCo.*” Dill in combination with Shen discloses this limitation.

169. For example, as discussed in IX(B) *supra*, Dill in combination with Shen discloses in Example 1 that the interface layer of layer 118 is (bcc) and provides a uniaxial symmetry broken structure (first “bcc-d layer”). Also, the

interface layer is $\text{Co}_{(100-x)}\text{Fe}_{(x)}$ (x is approximately 60). (Ex. 1009, 9:47-59.)

Therefore, the interface layer is “an alloy of Fe or FeCo” as claimed.

P. Dill in Combination With Shen Renders Obvious Claim 18

170. Claim 18 of the '988 patent recites: “The magnetic material structure recited in claim 1, wherein said *bcc-d layer forming a uniaxial symmetry broken structure is composed of an alloy of Fe or FeCo having one or more of the elements Al, B, Cr, C, Cu, Ni, N, Nb, Mo, V, Si, Ta, and Ti.*” Dill discloses this limitation.

171. For example, as discussed in IX(B) *supra*, Dill discloses in Example 2 that the layer 118 “can be ... form[ed] from a lamination of two ferromagnetic layers, such as Ni, Co, Ni-Fe alloys, Co-Fe alloys, or Ni-Fe-Co ternary alloys, separated by a thin metallic layer” (See ¶¶ 56, 93, 108-09, 111, *supra*; see also Ex. 1009, 9:65-10:3; 9:47-53; 8:29-57.) As discussed above, the lower ferromagnetic layer provides a uniaxial symmetry broken structure (first “bcc-d layer”). (*Id.*) The same layer can contain Ni and, therefore, is “an alloy of Fe ... having ... Ni” as claimed. (*Id.*)

Q. Dill in Combination With Shen Renders Obvious Claim 19

172. Claim 19 of the '988 patent recites: “The magnetic material structure recited in claim 1, wherein *the layer material forming said (111) textured*

hexagonal atomic template is composed of Ag, Al, Au, Cu, fcc-Co, fcc-CoCr, Ir, Ni, NiFe, Pt, Rh, Pd, hcp-Co, Gd, Re, Ru, Tb, Ti, or alloys of one of these materials combined with at least one element.” Dill discloses this limitation.

173. For example, as discussed in IX(B) *supra*, Dill discloses in Example 1 that the bulk layer of layer 118 “form[s] said (111) textured hexagonal atomic template” and is composed of $\text{Ni}_{(100-x)}\text{Fe}_{(x)}$ (x is approximately 60), which is an alloy of Fe and Ni as claimed.

R. Dill in Combination With Shen and Heim Renders Obvious Claim 21

174. Claim 21 of the '988 patent recites: “The magnetic material structure according to claim 1, further comprising: *a coupling layer.*” Dill discloses this limitation, as summarized for Example 2 below.

Example 2 from (Ex. 1009, 9:37-41; 9:65-10:3; 9:47-53; 8:29-57.)			
...various other layers...			
Upper layer of layer 118:	$\text{Co}_{(30)}\text{Fe}_{(70)}$	(bcc)	“second bcc-d layer which is magnetic”
Thin metal layer of 118:	Ru	(hcp)	“coupling layer” and AF coupling
Lower layer of layer 118:	$\text{Co}_{(30)}\text{Fe}_{(70)}$	(bcc)	“[first] bcc-d layer which is magnetic”
AF layer 116:	$\text{Mn}_{(50)}\text{Fe}_{(50)}$	(fcc)	“[first] (111)...hexagonal atomic template”
Template layer 112:	$\text{Ni}_{(81)}\text{Fe}_{(19)}$	(fcc)	(111)...hexagonal atomic template
...various other layers...			
Substrate G1:	Al_2O_3		

175. Dill discloses that fixed layer 118 (“bcc-d layer which is magnetic”) can be formed “from a lamination of two ferromagnetic layers [*i.e.*, a first and a second bcc-d layer]” that are separated by a “thin metallic layer” (“coupling layer”) “which results in antiferromagnetic coupling of the two ferromagnetic layers.” (Ex. 1009, 9:60-10:3.)

176. Claim 21 further recites “*a second bcc-d layer which is magnetic.*” Dill discloses this limitation.

177. For example, Dill discloses that fixed layer 118 (“bcc-d layer which is magnetic”) can be formed “from a lamination of two ferromagnetic layers [*i.e.*, a first and a second bcc-d layer], such as Ni, Co, Ni-Fe alloys, Co-Fe alloys, or Ni-Fe-Co ternary alloys.” (Ex. 1009, 9:60-10:3.) One of ordinary skill in the art would have known that at least Fe and some of its alloys are (bcc) and magnetic. (*See, e.g.*, Ex. H, p. 251 *et seq.*; Ex. G, p. 94 *et seq.*)

178. Claim 21 further recites “wherein the coupling layer material *antiferromagnetically couples the bcc-d layers.*” Dill discloses this limitation.

179. For example, Dill discloses that the “thin metallic layer” (“coupling layer”) “results in antiferromagnetic coupling of the two ferromagnetic layers [*i.e.*, a first and a second bcc-d layer].” (Ex. 1009, 9:60-10:3.)

S. Dill in Combination With Shen Renders Obvious Claim 22

180. Claim 22 of the '988 patent recites: “The magnetic material structure according to claim 1, further comprising: *a second bcc-d layer which is magnetic.*” Dill discloses this limitation as shown in the summary of Example 2 below.

Example 2 from (Ex. 1009, 9:37-41; 9:65-10:3; 9:47-53; 8:29-57.)			
...various other layers...			
Sensing layer 132:			
Interface layer of 132	Co ₍₄₀₎ Fe ₍₆₀₎	(bcc)	“second bcc-d layer which is magnetic”
Tunnel barrier 120:	Al ₂ O ₃		
Upper layer of layer 118:	Co ₍₃₀₎ Fe ₍₇₀₎	(bcc)	“third bcc-d layer...between”
Thin metal layer of 118:		(hcp)	
Lower layer of layer 118:	Co ₍₃₀₎ Fe ₍₇₀₎	(bcc)	“[first] bcc-d layer which is magnetic”
AF layer 116:	Mn ₍₅₀₎ Fe ₍₅₀₎	(fcc)	“[first] (111)...hexagonal atomic template”
Template layer 112:	Ni ₍₈₁₎ Fe ₍₁₉₎	(fcc)	(111)...hexagonal atomic template
...various other layers...			
Substrate G1:	Al ₂ O ₃		

181. For example, Dill discloses an alternative ferromagnetic sensing layer that includes an interface layer of layer 132 that is bcc and magnetic. (Ex. 1009, 9:37-41.) With “x [being] approximately 60,” the interface layer of layer 132 is Co₍₄₀₎Fe₍₆₀₎, which one of ordinary skill in the art would have understood to be bcc (*id.*) and magnetic (“second bcc-d layer which is magnetic”) in its normal state.

182. Claim 22 further recites “*a third bcc-d layer disposed between the bcc-d layers which are magnetic.*” Dill discloses this feature.

183. Dill discloses an example of layer 118 has a lower ferromagnetic layer of 118 (“[first] bcc-d layer”) and an upper ferromagnetic layer of 118 (“third bcc-d layer”), separated by a metallic layer. (Ex. 1009, 9:65-10:4.)

184. As summarized for Example 2 above, the upper ferromagnetic layer of 118 (“third bcc-d layer”) is disposed between the lower ferromagnetic layer of 118 (“[first] bcc-d layer which is magnetic”) and the layer added to layer 132 (“second bcc-d layer which is magnetic”).

T. Dill in Combination With Shen and Heim Renders Obvious Claim 23

185. Claim 23 of the '988 patent recites: “The magnetic material structure according to claim 1, further comprising: *a second bcc-d layer which is magnetic;* and *a second (111) textured hexagonal atomic template layer.*” Dill discloses this limitation as summarized for Example 2 below:

Example 2 from (Ex. 1009, 9:37-41; 9:65-10:3; 9:47-53; 8:29-57.)			
...various other layers...			
Upper layer of layer 118:	Co ₍₃₀₎ Fe ₍₇₀₎	(bcc)	“second bcc-d layer”
Thin metal layer of 118:	Ru	(hcp)	second (111)...hexagonal atomic template
Lower layer of layer 118:	Co ₍₃₀₎ Fe ₍₇₀₎	(bcc)	“[first] bcc-d layer which is magnetic”
AF layer 116:	Mn ₍₅₀₎ Fe ₍₅₀₎	(fcc)	“[first] (111)...hexagonal atomic template”
Template layer 112:	Ni ₍₈₁₎ Fe ₍₁₉₎	(fcc)	(111)...hexagonal atomic template
...various other layers...			
Substrate G1:	Al ₂ O ₃		

186. See, in particular, the “upper layer of layer 118” and the “thin metal layer of 118” *supra*.

187. More specifically, as discussed in IX(B) *supra*, Dill discloses the example of lower ferromagnetic layer of 118 and the upper ferromagnetic layer of 118 that are Co₃₀Fe₇₀ and are naturally bcc materials and magnetic (the “[first] bcc-d layer which is magnetic” and the “second bcc-d layer which is magnetic,” respectively), and intervening metal layer of 118 is Ru and in this example naturally provides a “second (111) textured hexagonal atomic template.”

188. Claim 23 further recites “wherein said *second (111) textured hexagonal atomic template is disposed between said bcc-d layers.*” Dill discloses this limitation.

189. As shown in the summary for Example 2 above, the Ru metal layer of layer 118 (“second (111) textured hexagonal atomic template layer”) is disposed below the $\text{Co}_{(30)}\text{Fe}_{(70)}$ upper layer of layer 118(the “second bcc-d layer”).

190. Because the Ru thin metal layer of layer 118 separates the two ferromagnetic layers of layer 118, it is disposed above the interface layer of layer 118 (the first “bcc-d layer”).

191. This is further shown in the summary for Example 2 above.

U. Dill in Combination With Shen Renders Obvious Claim 24

192. Claim 24 of the '988 patent recites: “The magnetic material structure according to claim 1, further comprising: at least *one magnetic hcp Co alloy layer.*” Dill discloses this limitation. For example, Dill discloses an example in which layer 150 is $\text{Co}_{75}\text{Pt}_{13}\text{Cr}_{12}$, which one of ordinary skill in the art would have understood has an hcp crystalline structure and is magnetic. (Ex. 1009, 8:52-53; *see, e.g.,* Ex. G, p. 94 *et seq.*)

V. Dill in Combination With Shen Renders Obvious Claim 27

193. Claim 27 of the '988 patent is identical to claim 1, apart from the additional limitation that the magnetic material structure must be incorporated into a “*magnetic device.*” As discussed in IX(B) *supra*, the combination of Dill and Shen discloses all the limitations of claim 1. Dill also discloses the additional

limitation of claim 27 that the magnetic structure must be incorporated into a “magnetic device.”

194. For example, Dill discloses a magnetic tunnel junction (“MTJ”) magnetoresistive (“MR”) read head (i.e., a “magnetic device”) in the form of a layer stack that includes a “gap layer G1 substrate” (“substrate”). (Ex. 1009, 5:26-31; FIG. 4A.) One of ordinary skill in the art would readily have understood that an MTJ and an MR read head are devices that both incorporate or include at least one “magnetic material.”

W. Dill in Combination With Shen Renders Obvious Claim 28

195. Claim 28 recites: “The magnetic device recited in claim 27, wherein the device is *a magnetic data storage system.*” Dill discloses this limitation.

196. For example, Dill discloses that the MTJ of the invention could be used in “heads for magnetic recording systems.” (Ex. 1009, 1:41-43.)

X. Dill in Combination With Shen Renders Obvious Claim 29

197. Claim 29 of the ’988 patent recites: “The magnetic device recited in claim 27, wherein the device is *a data storage magnetic recording transducer.*”

Dill discloses this limitation.

198. For example, Dill discloses that the magnetic film structure is used in “heads for magnetic recording systems” (Ex. 1009, 1:41-43) and, more

specifically, in an “MR read head” of a “read/write . . . transducer” that also includes an “inductive write head.” (*See, e.g.*, Ex. 1009, 4:22-25; 5:23-25.)

Y. Dill in Combination With Shen Renders Obvious Claim 30

199. Claim 30 of the '988 patent recites: “The magnetic device recited in claim 27, wherein the device is at least one of: an anisotropic magnetoresistive sensor; a spin valve magnetoresistive sensor; a *magnetic tunnel junction magnetoresistive sensor* and a data storage magnetic playback transducer.” Dill discloses this limitation.

200. For example, Dill is entitled “Magnetic Tunnel Junction Magnetoresistive Sensor . . . “ and discloses that the device in FIG. 4A is a magnetic tunnel junction (“MTJ”) for a magnetic read head (i.e., a magnetic data storage system). (Ex. 1009, Title; 3:57-59; 3:7-41; Abstract; *see also* 7:53-56.)

Z. Dill in Combination With Shen Renders Obvious Claim 34

201. Claim 34 of the '988 patent recites: “The magnetic device recited in claim 27, wherein *the device is* at least one of: an electronic circuit inductive component and an *electronic circuit inductive transformer component.*” The combination of Dill with Shen discloses this limitation. Dill discloses that the magnetic film structure is used in “heads for magnetic recording systems” (Ex. 1009, 1:41-43.) and, more specifically, in an “MR read head” of a “read/write

. . . transducer” that also includes an “inductive write head.” (*See, e.g.*, Ex. 1009, 4:22-25; 5:23-25.)

AA. Dill in Combination With Shen Renders Obvious Claim 38

202. Claim 38 of the '988 patent recites: “The magnetic device according to claim 27, further comprising: at least *one hard magnetic layer*.” The combination of Dill with Shen discloses this limitation.

203. For example, Dill discloses an example in which bias layer 150 is $\text{Co}_{75}\text{Pt}_{13}\text{Cr}_{12}$. (Ex. 1009, 8:52-53.) One of ordinary skill in the art would have understood that this material is magnetically hard.

204. Claim 38 further recites “wherein said at least one *bcc-d layer* which is magnetic, forming a uniaxial symmetry broken structure, is *disposed between* said *(111) textured hexagonal atomic template* and said at least one *hard magnetic layer*.” Dill discloses this limitation.

205. As discussed in ¶¶ 95-105 *supra*, Dill discloses that the interface layer of layer 118 is a bcc-d layer which is magnetic, forming a uniaxial symmetry broken structure. As discussed in IX(B) *supra*, Dill discloses that the interface layer of 118 in Example 1 is **grown onto** the bulk layer of 118, which provides a (111) textured hexagonal atomic template to the interface layer of 118. As shown in FIG. 4A, Dill discloses that the interface layer of 118 is **disposed beneath** bias layer 150. Therefore, the interface layer of 118 (“bcc-d layer which is

magnetic...broken symmetry structure”) is *disposed between* the bulk layer of 119 (the “(111) textured hexagonal atomic template”) and bias layer 150 (the “hard magnetic layer”).

X. DILL IN COMBINATION WITH SHEN AND LAMBETH I RENDERS OBVIOUS CLAIMS 2, 25, 26, AND 31 OF THE '988 PATENT

A. Claim Chart

206. The Petition sets forth a claim chart (Petition, Section VI(D)) citing disclosures in Dill, Shen, and Lambeth I that demonstrate how this combination of prior art references renders obvious the above-referenced claims. I fully agree with the claim chart. The following sections include additional analysis that demonstrates how the combination renders obvious each of these claims.

B. Dill in Combination With Shen and Lambeth I Renders Obvious Claim 2

207. Claim 2 of the '988 patent recites: “The magnetic material structure recited in claim 1, wherein said substrate is *single crystal*.” The combination of Dill and Shen with Lambeth I renders obvious this limitation.

208. Dill discloses depositing the MTJ MR layers on the surface of an “alumina...substrate.” (Ex. 1009, 10:19-34.) Even if Dill does not teach or suggest that the substrate is single crystal, Lambeth I does.

209. Lambeth I discloses the advantages of using a single crystal substrate to control crystalline texture and orientation when growing magnetic thin films. (Ex. 1013, Title; Abstract.) Specifically, Lambeth I discloses that “utilizing single crystal Si as a substrate” to grow magnetic films on top of “fcc metals,” including those of Au metal as used by Dill, “with a very high degree of epitaxy.” (*Id.*, p. 189.) Lambeth I discloses that this “maximize[s] the coercivity” and “minimize[s] the media noise . . . [and helps] to control the easy axes orientations.” (*Id.*) Lambeth I further discloses that the “fcc” metal films can “easily be used to epitaxially grow other quasi-single crystal films of similar or differing crystalline structure,” and gives the example of magnetic films of Co metal. (*Id.*, pp. 189-90.)

210. It would have been obvious to a person of ordinary skill in the art at the time of the effective filing date of the '988 patent to grow Dill's magnetic structure on a single crystalline material, according to Lambeth I.

211. Dill discloses growing a magnetic layer stack on a substrate. (Ex. 1009, 5:26-28.) Similarly, Lambeth I discloses forming magnetic structures, including multilayer structures, on a substrate. (Ex. 1013, p. 190, ¶ 1; FIG. 5.)

212. Growing Dill's multilayer structures on a single crystal substrate would be straightforward and predictable. One of ordinary skill in the art would have known that layer stacks can be grown on single crystal surfaces.

213. Therefore, it would have been obvious to a person of ordinary skill in the art to try growing Dill's layered structure on a single crystal surface, as disclosed by Lambeth I to "maximize the coercivity and . . . minimize the media noise . . . [and help] to control the easy axes orientations." (Ex. 1013, p. 189.)

C. Dill in Combination With Shen and Lambeth I Renders Obvious Claim 25

214. Claim 25 of the '988 patent recites: "The magnetic material structure according to claim 1, further comprising: at least one *magnetic hcp Co alloy layer*." Dill discloses this limitation.

215. As discussed in IX(U) *supra*, Dill discloses an example in which layer 150 is $\text{Co}_{75}\text{Pt}_{13}\text{Cr}_{12}$, which one of ordinary skill in the art would have understood has an hcp crystalline structure and is magnetic. (Ex. 1009, 8:52-53.)

216. Claim 25 also recites "wherein said *hcp Co alloy has a (1011) crystalline texture*."

217. Lambeth I discloses that the anisotropy of Co magnetic layers can be improved by growing selected crystalline textures, such as the (1011) texture. (Ex. 1013, p. 189, ¶ 1; p. 190.) Therefore, Lambeth I discloses a "magnetic hcp Co alloy layer" with "a (1011) crystalline texture."

218. It would have been obvious to a person of ordinary skill in the art at the time of the effective filing date of the '988 patent to grow Dill's Co-alloy of

layer 150, a “magnetic hcp Co alloy layer,” to have “a (1011) crystalline texture,” according to Lambeth I.

219. Dill discloses growing a magnetic layer stack on a substrate. (Ex. 1009, 5:26-28.) Similarly, Lambeth I discloses forming magnetic structures, including multilayer structures, on a substrate. (Ex. 1013, p. 190, ¶ 1; FIG. 5.) Because of the similarity in structures, growing Dill’s Co-containing interface layer to achieve the (1011) texture according to Lambeth I would be straightforward and predictable.

220. Therefore, a person of ordinary skill would grow Dill’s Co-containing interface layer of layer 118, a “magnetic hcp Co alloy layer” to have “a (1011) crystalline texture,” according to Lambeth I. Doing so would “grow Co-alloy and underlayer crystalline grains of considerable perfection and appropriate texture to avoid compromising the crystalline [magnetic] anisotropy.” (Ex. 1013, p. 189.)

D. Dill in Combination With Shen and Lambeth I Renders Obvious Claim 26

221. Claim 26 of the ’988 patent recites: “The magnetic material structure according to claim 1, wherein: said *substrate is a (111) crystalline textured single crystal; and a surface of said single crystal provides a layer providing the (111) textured hexagonal atomic template.*” Dill in combination with Shen and Lambeth I discloses this limitation.

222. Dill discloses depositing the MTJ MR layers on the surface of an “alumina...substrate” (Ex. 1009, 10:19-34), which is not a single crystal, that has been coated with Au metal (*id.*, 8:43-48). However, it would have been obvious in view of Lambeth I to grow Dill’s multilayer structures on a single crystal. (*See X(B) supra.*)

223. Lambeth I discloses that the substrate can be a single crystal with a (111) surface. (Ex. 1013, p. 190, ¶ 1; FIG. 5 and caption.) Lambeth I further discloses that the single crystal Si structure provides a system “to control the easy axes orientations” to maximize the coercivity and minimize the noise in the film. (*Id.*, p. 189, ¶ 1.) One of ordinary skill in the art would have known that a Si (111) surface provides a (111) textured hexagonal atomic template. For these reasons, it would have been obvious to a person of ordinary skill in the art at the time of the effective filing date of the ’988 patent to try growing Dill’s layer stack on Lambeth I’s single crystal Si(111).

224. Dill discloses growing a magnetic layer stack on a substrate. (Ex. 1009, 5:26-28.) Similarly, Lambeth I discloses forming magnetic structures, including multilayer structures, on a substrate. (Ex. 1013, p. 190, ¶ 1; FIG. 5.) Because of the similarity in structures, growing Dill’s layer stack on a single crystal (111) surfaced substrate would be straightforward and predictable.

E. Dill in Combination With Shen and Lambeth I Renders Obvious Claim 31

227. Claim 31 recites: “The magnetic device recited in claim 27, wherein the device is at least one of a *data storage magnetic recording media*; a data storage magnetic recording media incorporating an oriented soft magnetic layer; and a data storage magnetic recording media incorporating an oriented hard magnetic layer.” The combination of Dill and Lambeth I discloses this limitation.

228. As discussed above in Sections VIII(B) and (C), Shen in combination with Dill discloses a multi-layer device with broken symmetry and improved magnetic properties. However, neither Shen nor Dill explicitly discloses that the layered device can be used as data storage media.

229. Lambeth I discloses controlling growth and texture in magnetic film structures (Ex. 1013, Title; Abstract) for use in “Magnetic Media” (*id.*). Lambeth I discloses the relationship between “media thin film microstructure” and “microstructural properties” in media performance. (*Id.*, p. 182.)

230. Therefore, Lambeth I discloses “recording magnetic media” for which the “media thin film microstructure” can improve the “achievable areal recording density” and “media signal to noise ratio.” (*Id.*)

231. It would have been obvious to a person of ordinary skill in the art at the time of the effective filing date of the '988 patent to apply Shen's

(111)(fcc)/(bcc) structure and broken symmetry (Ex. 1011, FIG. 4) to improve magnetic properties in the “recording magnetic media” disclosed by Lambeth I.

232. Shen discloses breaking symmetry in multi-layered, magnetic structures deposited on a substrate. (Ex. 1011, FIG. 4.) Lambeth I discloses forming magnetic structures, including multilayer structures, on a substrate. (Ex. 1013, p. 190, ¶ 1; FIG. 5.) Because of the similarity in structures, applying Shen’s teachings to Lambeth I’s magnetic media would be obvious, straightforward and predictable.

XI. DILL IN COMBINATION WITH SHEN AND NOGUCHI RENDERS OBVIOUS CLAIM 39 OF THE ’988 PATENT

A. Claim Chart

233. The Petition sets forth a claim chart (Petition, Section VI(E)) citing disclosures in Dill, Shen, and Noguchi that demonstrate how this combination of prior art references renders obvious claim 39. I fully agree with the claim chart. The following sections include additional analysis that demonstrates how the combination renders obvious that claim.

B. Dill in Combination With Shen and Noguchi Renders Obvious Claim 39

234. Claim 39 of the ’988 patent recites: “The magnetic device according to claim 27, further comprising: at least one *hard magnetic layer...disposed*

between said substrate and said...bcc-d layer.” The combination of Dill with Shen and Noguchi discloses this limitation.

235. Even if Dill does not disclose the claimed hard magnetic layer, it would be obvious to add the hard magnetic layer of Noguchi to Dill. Like Dill, Noguchi discloses forming an “MR element” (“magnetic material”), including “ferromagnetic tunnel junction 21” and a substrate 4 (“substrate”). (Ex. 1014, 14:55-15:10; FIGs. 6-8.) The MR includes first ferromagnetic film 211 and magnetic domain control films 214 and 215 (“hard magnetic layer”). (*Id.*, 12:53-67; FIGs. 6-8.) Noguchi discloses that using such hard magnetic films “prevent[s] a disturbing influence of an external magnetic field” (*id.*, 15:52-57) and that they may be provided to “ferromagnetic film 211.” (*Id.*, 15:46-48.) Therefore, it would have been obvious to a person of ordinary skill in the art at the time of the effective filing date of the ’988 patent to use the “hard magnetic layer” (214 and 215), as taught by Noguchi, in Dill’s magnetic layered structure (FIG. 4A). Because of the similarity in structure and function, applying Noguchi’s “hard magnetic layer” (214 and 215) to Dill’s magnetic layered structure (FIG. 4A) would be straightforward and predictable.

236. In FIG. 12, Noguchi shows magnetic domain control films 214 and 215 disposed between the substrate 4 and ferromagnetic layer 211:

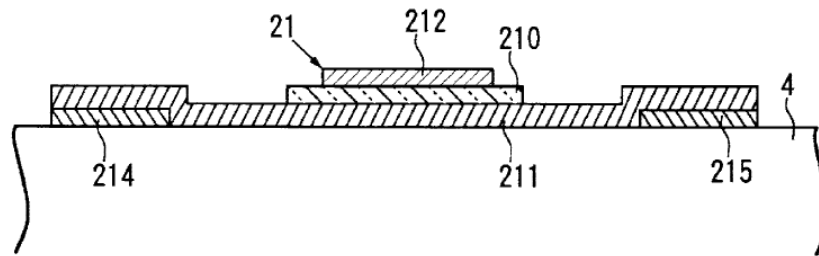


FIG. 12

(Ex. 1014, FIG. 12.)

237. Because Noguchi discloses disposing magnetic domain control films 214 and 215 (“hard magnetic layer”) between (bcc) first ferromagnetic film 211 and substrate 4, it would have been obvious to place the magnetic domain control films 214 and 215 (“hard magnetic layer”) between Dill’s (bcc) bulk layer of 118 (“bcc d layer which is magnetic, forming a uniaxial symmetry broken structure”) and the substrate G1. Doing so would have “prevent[ed] a disturbing influence of an external magnetic field.” (Ex. 1014, 15:52-57.)

XII. CONCLUSION

238. For at least the preceding reasons, I believe that each of claims 1-3, 6-19, 21-31, 34, 38, and 39 of the ’988 patent is invalid pursuant to 35 U.S.C. §§ 102 and/or 103.

239. I may testify about any of the preceding topics at a deposition or hearing.

240. I reserve the right to respond to any declarations that are submitted by Lambeth's expert witnesses or to any testimony by Lambeth's fact or expert witnesses, whether at deposition or at trial.

 10.5.15

Robert Sinclair, Ph.D.

(19) World Intellectual Property Organization
International Bureau



(43) International Publication Date
13 March 2003 (13.03.2003)

PCT

(10) International Publication Number
WO 03/021579 A1

(51) International Patent Classification⁷: **G11B 5/64**,
5/66, 5/667, 5/673

(21) International Application Number: PCT/US02/27327

(22) International Filing Date: 29 August 2002 (29.08.2002)

(25) Filing Language: English

(26) Publication Language: English

(30) Priority Data:
60/315,920 29 August 2001 (29.08.2001) US

(71) Applicant and

(72) Inventor: **LAMBETH, David, N.** [US/US]; 118 Buckingham Road, Pittsburgh, PA 15215 (US).

(74) Agents: **BYRNE, Richard, L.** et al.; Webb Ziesenheim Logsdon Orkin & Hanson, P.C., 700 Koppers Building, 436 Seventh Avenue, Pittsburgh, PA 15219-1818 (US).

(81) Designated States (*national*): AE, AG, AL, AM, AT (utility model), AT, AU, AZ, BA, BB, BG, BR, BY, BZ, CA,

CH, CN, CO, CR, CU, CZ (utility model), CZ, DE (utility model), DE, DK (utility model), DK, DM, DZ, EC, EE (utility model), EE, ES, FI (utility model), FI, GB, GD, GE, GH, GM, HR, HU, ID, IL, IN, IS, JP, KE, KG, KP, KR, KZ, LC, LK, LR, LS, LT, LU, LV, MA, MD, MG, MK, MN, MW, MX, MZ, NO, NZ, OM, PH, PL, PT, RO, RU, SD, SE, SG, SI, SK (utility model), SK, SL, TJ, TM, TN, TR, TT, TZ, UA, UG, US, UZ, VC, VN, YU, ZA, ZM, ZW.

(84) Designated States (*regional*): ARIPO patent (GH, GM, KE, LS, MW, MZ, SD, SL, SZ, TZ, UG, ZM, ZW), Eurasian patent (AM, AZ, BY, KG, KZ, MD, RU, TJ, TM), European patent (AT, BE, BG, CH, CY, CZ, DE, DK, EE, ES, FI, FR, GB, GR, IE, IT, LU, MC, NL, PT, SE, SK, TR), OAPI patent (BF, BJ, CF, CG, CI, CM, GA, GN, GQ, GW, ML, MR, NE, SN, TD, TG).

Published:

— with international search report

For two-letter codes and other abbreviations, refer to the "Guidance Notes on Codes and Abbreviations" appearing at the beginning of each regular issue of the PCT Gazette.

(54) Title: MAGNETIC MATERIAL STRUCTURES, DEVICES AND METHODS

(57) Abstract: A thin film magnetic structure, magnetic devices, and method of producing the same, wherein (110) textured, symmetry broken body centered cubic or body centered cubic derivative crystalline structures epitaxially grown on hexagonal shaped templates, in the presence of a symmetry breaking mechanism is provided to promote oriented uniaxial magnetic properties from a series of successively deposited film layers, result in new oriented magnetic layer structures and microstructures and thus improved magnetic devices and device performance.



WO 03/021579 A1

Magnetic Material Structures, Devices And Methods

BACKGROUND OF THE INVENTION

1. Field of the Invention

This invention is directed to magnetic material
5 structures, methods for making magnetic material structures
and devices made from magnetic material structures.

2. Description of the Prior Art

As the home, office, transportation system, business
10 place and factory become more automated and electronically
connected, and as electronic devices and appliances such as
computers, communication devices, wireless communication
devices, electronic games, entertainment systems, personal
15 data assistants, transportation vehicles, manufacturing
tools, shop tools, and home appliances become more
sophisticated there is, and will be, an ever-increasing
demand for higher performance and low cost electronic
circuits, sensors, transducers, data storage systems and
20 other magnetic devices which employ magnetic thin film
materials. In order for these devices to remain
competitive in the market place each product generation
must be higher performing, unobtrusive and, usually, less
expensive than the previous. Hence there are ever
increasing demands for technical improvements in the
25 materials and structure of these devices.

For all of these applications the magnetic material
has an improved performance if the magnetic properties can
be better controlled during the construction. Two familiar
properties, which are sometimes considered to be intrinsic
30 magnetic properties, are the saturation magnetization, M_s ,
and the magnetocrystalline anisotropy energy density
constants (usually denoted by a subscripted K symbol). The
meaning of magnetic anisotropy energy is that the
magnetization would have a preferred direction, or
35 directions, of orientation. That is, the energy of the
system is minimal when the magnetization vector points
along certain directions. These directions are referred to
as the magnetic easy axes while the magnetic hard axes

coincide with magnetic orientations where the energy is maximized. However, it should be noted that the magnetic anisotropy is not actually an intrinsic property in the sense that the materials are commonly not made perfectly. Nevertheless, good performance in device applications is almost always dependent upon there being a single preferred magnetic orientation or anisotropy direction and so in the manufacturing process one strives to achieve a desired uniaxial anisotropy. An objective of the present invention is to provide new mechanisms for controlling the magnetocrystalline anisotropy of thin magnetic films. By doing so the performance of almost all magnetic devices are envisioned to be improved.

In general the anisotropy energy is a function of the orientation of the magnetization vector with respect to a given physical axis. Here, we define a "uniaxial" anisotropy to exist if the anisotropy energy density function only contains a single maximum and a single minimum as the magnetization angle, θ , is rotated by 180 degrees from a physical axis. Likewise we define an "ideal uniaxial" anisotropy energy to exist if the energy equation has only a $\sin^2(\theta)$ or $\cos^2(\theta)$ dependence. Materials and device processing to achieve a desired orientation or anisotropy is commonly difficult and sometimes impossible, perhaps because heretofore the mechanism for achieving anisotropic orientation has not been well understood. Furthermore, uniform control of the orientation of the magnetic anisotropy is often difficult to achieve and maintain in a manufacturing process where many different desired material properties must be obtained simultaneously.

Background for Oriented Soft Magnetic Films

In magnetic devices, for example, such as sensors, transducers, transformers, inductors, signal mixers, flux concentrators, recording media keepers, data recording and playback transducers it is common that the magnetic

response to a driving field possess high sensitivity and at the same time, low coercivity (H_c). Or stated simply, the material possesses essentially non-hysteretic behavior. For this type of behavior the device is constructed so that the applied field is directed along the hard magnetic axis of a uniaxial magnetic material. This results in the minimization of coercivity and hysteric effects, which are many times associated with magnetic domain wall motion of materialsthat are multi-axial. For example, a material, which has bi-axial anisotropy, will have two easy and two hard magnetic axes and will exhibit hystersis and losses. In many of these applications a linear, or near linear response is also advantageous, while in other applications, such as signal mixers, a controlled non-linear response is desire. To obtain a linear magnetic response, requires both applying a field along the magnetic hard axis and that the anisotropy energy density function not only be uniaxial, but that it also have simple $\sin^2(\theta)$ or negative $\cos^2(\theta)$ dependence, where, θ , is the angle measured between the magnetization vector direction and the physically determined magnetic easy axis. Since there is the mathematical identity, $\sin^2(\theta) = 1 - \cos^2(\theta)$, and since the origin in the energy function is arbitrarily defined the use of $\sin^2(\theta)$ or $-\cos^2(\theta)$ yield equivalent physical behavior. Item [1] of Figure 1 illustrates the squared sinusoidal anisotropy energy density curve shape versus the angle of the magnetization vector with respect to the easy axis located at zero degrees. Figure 2 illustrates the response of the components of the magnetization, M_x and M_y , as a function of applied field, $H_x = H_a$, along the hard magnetic axis direction, x. The linear curve kinks only at the point [2] where the magnetization becomes saturated, or fully aligned with the applied field. For this special uniaxial anisotropy this occurs at the applied field value of H_k along the x direction, which is known as the anisotropy field. These response curves are sometimes referred to as hysteresis loops even though they exhibit no

hysteresis. It is the shape of the $\sin^2(\theta)$ energy function that causes the response, M_x , along the hard axis to be linear and to be fully reversible. M_y is the response in the y direction to an applied field in the x direction.

5 The curve shape shown is quadratic for applied field magnitudes less than H_k , where M_y is zero for larger magnitude fields. The quadratic behavior is necessary for linear M_x since $M_s^2 = M_x^2 + M_y^2$, where M_s is the total, constant, saturation magnetization vector magnitude. If

10 the anisotropy energy is uniaxial, but is not governed by the, ideal, $\sin^2(\theta)$ functional form then the magnetic response is not linear. However, heretofore, the applicant knows of no real material examples exhibiting both a uniaxial energy curve and a non-linear M_x versus H_x

15 behavior.

Materials exhibiting the $\sin^2(\theta)$ energy density functional form are often referred to as having Stoner-Wohlfarth behavior after the famous ideal uniaxial single domain magnetization theory. However, thin films are

20 commonly multi-domain even though they might exhibit the $\sin^2(\theta)$ functional energy form on a localized basis. Unless the hard axis direction is the same at all points in a sample and the applied driving field is exactly parallel to the hard axis then domain wall motion can commonly be

25 observed. This motion results in coercivity mechanisms and hysteretic energy losses. The lossless behavior of samples represented by Figure 2 is due to the magnetization rotating in response to the applied field rather than a response via domain wall motion. Multi-axis anisotropy

30 materials always switch via wall motion and so suffer losses.

It is also well known that, for soft uniaxial thin films, by first applying a field along the easy axis, and then by keeping a constant bias field in this direction, to

35 eliminate 180 degree domain walls, one can force all of the material to appear to be single domain as the hard axis is then driven. Hence, because of this bias field, $H_b = H_y$, in

the easy axis direction the application of any finite H_x field along the hard axis can never quite drive the magnetization vector completely to the energy maximum [3] and the response will always be reversible and so lossless.

5 This is not the case for materials with multiple anisotropy axes. For uniaxial materials the rotational response is key to many sensor devices and it is common in various forms of magnetoresistive sensors to provide a bias field along the easy axis by either applying a small field or by exchange

10 coupling the magnetic sensor material to a hard magnetic material that has been so oriented to provide an effective bias field.

For some sensor applications, such as anti-theft devices, and special electronic mixing circuit devices,

15 soft, low loss, magnetic properties are desired simultaneously with a specific non-linear response. In these applications, the driving field has historically, and most commonly, been directed along an easy axis or in the direction of the lowest magnetic anisotropy energy. In

20 this direction magnetic domain wall motion is usually significant. This domain wall motion commonly results in a highly non-linear response or even in strong hysteretic behavior.

Certain anti-theft, article surveillance, article

25 identification or inventory control devices rely upon detecting harmonic signals, which are generated by this non-linear behavior or upon materials being driven in to saturation. One of many examples, of this type of surveillance system and tag is described in U.S. Patent No.

30 3,747,086. This type of tag response has also been disclosed as enabling multiple bits of information to identify objects in U. S. Patent No. 5,538,803 Other article tag devices are based upon the magnetoelastic effect and mechanical resonance, where coupling exist

35 between the magnetization and the mechanical strain in the material. An example, of this type of tag is disclosed in U.S. Patent No. 4,510,489. In these later devices it is desirable to drive the magnetization towards a hard axis so

that rotation of the magnetization dominates and magnetic hysteretic losses are minimized. By using this mode, and by using the field to drive the device at its mechanical resonance frequency significant amounts of energy can be stored in the device. Hence, even after the drive field has been removed the mechanical vibration continues, the magnetoelastic properties are then used to invert the process to transmit a magnetic field as the mechanical stress causes the magnetization vector direction to rotationally oscillate synchronously with the mechanical vibration. This time dependent magnetic dipole radiates a magnetic field at the distinct resonance frequency, which can be detected to verify the tag's existence. Uniaxial anisotropy is needed in such a device to achieve low losses. Due to the magnetoelastic coupling between the mechanical strain and the magnetic moment orientation the fundamental of the mechanical resonance frequency is emitted as an oscillating magnetic dipole field. However, if the uniaxial anisotropy is non-ideal and results in a non-linear response then the harmonics would also be available for detection in the presence of a drive signal. This is advantageous, but there have never been available materials from which to form such a device before.

Likewise, in analog mixer circuit devices a non-linear response is desired. When two separate sinusoidal signals are simultaneously imposed on a nonlinear circuit device component a multiplication process results in a beating of the two signals. This results in additional harmonics at the sum and difference frequencies of the initial signals. Hence, the information contained in a modulated carrier frequency signal can be shifted to a beat frequency. Typically this is done to shift the information carrying bandwidth to a higher carrier frequency bandwidth (modulation) or bring the information carrying bandwidth signal back down to a bandwidth located near, or nearer to, zero frequency for demodulation. These techniques of frequency shifting are common to telecommunication and signal processing and in many other signal processing

applications. The non-linear circuit response, circuit components, and circuit implementation used to perform these signal mixing processes are described in many electrical engineering circuit textbooks. Two example texts
5 are "Electronic Communications Techniques" by P. H. Young and "Physics of Semiconductor Devices" by S. M. Sze. Ideally the non-linear device used to mix the signals is efficient, low loss, and low noise. Usually non-linear Silicon active devices are used for this. In the past when
10 magnetic devices were used for this application domain wall motion caused both losses to the signal and induced noise. A magnetic material with non-linear response that operates by low loss magnetization rotation rather than by domain wall motion is very desirable.

15 For most all transducer and sensor applications, which require low anisotropy values in order to provide large sensitivity, the use of cubic crystalline materials are common. However, due to the three fold crystalline symmetry of cubic materials, achieving a single axis of
20 anisotropy energy density, which is almost always essential to obtaining the desired low loss, low noise, magnetic properties, is difficult. Thin, or thick, film materials are commonly employed. For example many devices, such as data storage playback transducers or field transducers,
25 commonly utilize face centered cubic, fcc, thin film crystalline materials. Should these materials be prepared with a (001) crystalline texture the anisotropy energy, as a function of angle in the film plane is bi-axial, has multiple easy and hard axes in the film plane yielding a
30 non-linear and hysteretic magnetic response resulting in noisy signals. Hence, a (111) crystalline texture is desired, where it can be mathematically shown for the case of the magnetization being confined to the (111) texture plane, that due to the crystalline three fold symmetry of
35 the projection of the {111} crystalline directions into the film plane, the cubic material will possess no net first order anisotropy energy density. Even for only moderate saturation magnetization thin films, the magnetization is

essentially confined to the film plane by the demagnetization forces associated with the planar film shape.

To achieve a single uniaxial anisotropy in a cubic material with (111) texture the material is usually subjected to a thermal treatment, or is deposited directly, in the presence of an applied magnetic field. The resulting single magnetic easy axis is aligned along the applied magnetic field, while the hard axis is perpendicular to this applied field. Furthermore the M_x versus H_x response function is a linear response. While the mechanism for the cause of this induced magnetic anisotropy is not well understood it is often argued that an atomic pair ordering mechanism occurs to break the symmetry of the directions in the (111) plane for each grain of the material. That is, on a local scale inside each grain, pairs of atoms align along the applied field during the deposition, or the annealing process, to reduce the magnetic field energy. Interestingly, annealing in a field of different orientation can often alter this induced anisotropy direction demonstrating that the orientation inducing mechanism is reversible. It is believed that this localized ordering allows fcc materials such as the NiFe alloys, permalloy, to have a small induced uniaxial anisotropy. Magnetic thin film body centered cubic, bcc, or bcc derivative materials, such as Fe, FeCo, FeAl, and similar compositions, are seldom used in such applications because the required (111) crystalline texture never develops during deposition of the bcc symmetric crystals.

It is well understood that during the growth of thin metal films certain texture orientations tend to appear. These are driven by the minimization of surface energy and surface bonding considerations and are modified by surface mobility issues, which can be somewhat controlled by substrate and processing conditions. One simple rule of thumb is that the film surface energy is minimized when the atomic surface configuration is the most closely packed. For a fcc crystal the atoms in the surface are most closely

packed in the (111) plane and so this texture is the most likely. The (001) texture is less energetically likely, but is possible where as the high surface energy (110) texture never seems to occur. On the other hand, for a bcc

5 crystal the atomic surface most closely packed is the (110) texture and this commonly appears, the (001) texture is the next lowest energy and is sometimes induced, but the high surface energy (111) texture never seems to occur. Hence, for fcc crystals we refer to the (111) texture as being

10 natural where as for the bcc crystal we refer to the (110) texture as being naturally occurring. If a low surface energy substrate is chosen, such as an amorphous metal, which tends to wet to the depositing material, the fcc (111) texture and the bcc (110) texture naturally occur. On

15 the other hand, if the substrate is non-wetting, such as an oxidized surface where the depositing material tends to bond to the oxygen atoms to limit the atomic surface mobility, then it is common to see limited orientation in the deposited films or at best a set of mixed textures.

20 The fcc crystal tends to form only weak (111) and (001) textures while the bcc crystal tends to form only weak (110) and (001) textures. For magnetic cubic crystalline thin film grains with (110) or (001) texture there are multiple easy or hard axes in the film plane of the grain.

25 In addition, because each grain has a random in-plane orientation relative to other grains, these polycrystalline magnetic materials result in an ensemble of grains with multiple, random, anisotropy axes. These materials yield both a non-linear response, as well as, high coercivity associated with losses and noise. Hence, bcc or bcc

30 derivative materials, which almost always grow with (110) or (001) texture, are seldom used for devices. For this reason the high saturation magnetization value of bcc materials have largely been unavailable to the device

35 designer who wishes to avoid domain wall motion.

One need only consult the very authoritative text, "Physics of Ferromagnetism, 2nd Edition" by Soshin Chikazumi, pages 299-309, on thermally induced anisotropy

of permalloy to see that the degree of understanding of the cause of uniaxial anisotropy in cubic materials is poor. Professor Chikazumi details the literature on the subject and notes that one theory attempts to explain this
5 "phenomena in terms of "directional order," or an anisotropic distribution of different atomic pairs such as Ni-Ni, Fe-Fe, or Ni-Fe." The logic is that the atomic spacing between the Ni-Fe pair is smaller than the other possible pairs and so a lattice distortion results from the
10 atomic pairing. A magneto-crystalline uniaxial anisotropy is then proposed to result from the magneto-elastic energy associated with the resulting lattice distortion. Professor Chiakazumi also outlines a second theory in which it is "assumed that ordering occurred by the growth of
15 distinct volumes of the ordered phase, and explains the induced anisotropy as the result of shape anisotropy of the second phase." Geometrical grain shapes, other than spherical, could generate considerable shape anisotropy energy. It should be pointed out however, that no physical
20 evidence supporting either of these theories has been provided.

Shape anisotropy is an intellectually comforting explanation, as this phenomenon is quite observable in elongated magnetic particles such as used in magnetic
25 particulate data storage tapes and bar shaped permanent magnets. In these, the magnetic easy axis is aligned with the longer dimension. However, while Professor Chiakazumi illustrates that a rather complex pair ordering model with dipole-dipole interactions proposed by Neel can be used to
30 qualitatively explain field induced anisotropy, there is no quantitative agreement and he comments "The reasons why quantitative agreement is not obtained may lie in the approximate estimates of various quantities and in failure to attain complete thermal equilibrium." Nevertheless, he
35 comments regarding the texture of the materials that "magnetic annealing is most effective for, $\langle 111 \rangle$ annealing, less effective for $\langle 110 \rangle$, and least effective for $\langle 100 \rangle$." In this statement he is referring to the parallel

orientation of the applied field and the crystalline directions during the annealing process.

Very recently a publication; "Soft High Saturation Magnetization ($\text{Fe}_{0.7}\text{Co}_{0.3}$)_{1-x}N_x Thin Films For Inductive Write Heads," IEEE Transactions On Magnetics, Vol. 36, No. 5, September 2000, by N. X. Sun and S. X. Wang, claimed to achieve orientation of the bcc like material during deposition in an applied magnetic field. The publication appears to indicate that the Nitrogen content was necessary, induced strain into the films, and created a small grain structure as it shifted the angle of, and broadened, the (110) x-ray diffraction peak. They also indicated that a "significant amount" of a second crystalline magnetic phase, Fe_4N , appeared in the films. As Chikazumi suggests perhaps this anisotropy behavior is due to the strain or shape or pair ordering associated with the second phase. It is interesting to note that they obtained this orientation on an oxidized Si (100) textured substrate and by the applicant's standards the FeCoN (110) texture is weak. They went on to indicate that by sandwiching the FeCoN film between two permalloy films the hard axis coercivity could be decreased, but they did not indicate or offer any evidence that the orientation of the FeCoN film was improved by depositing upon the permalloy. In fact, a comparison of hard axis hysteresis loops for films prepared with and without the permalloy films indicate similar anisotropy fields necessary to saturate the magnetization. This would indicate that the permalloy layer did not improve the orientation in their structure.

Background For Orientation with Hard Magnetic Films

It should be noted that unlike field sensing and energy transforming devices that usually require soft magnetic materials, devices such as magnetic recording media and permanent magnets demand higher uniaxial anisotropy energy in order to achieve high coercivity H_c , and a preferred orientation in order to achieve a high

remnance value. For motors or actuators this directly affects the amount of work that a device can deliver while for recording media it directly affects the output signal level and signal pulse width, or flux transition width, and, hence, the recording density. Even in some of these hard magnet applications it is desirable to incorporate soft magnetic materials to enhance overall performance. For example, perpendicular thin film recording media has long been discussed as a future replacement for longitudinal thin film media. However, in order for a recording system to function properly it is desirable that a soft magnetic keeper layer, or underlayer, be placed on the opposite side of the perpendicular hard magnetic recording layer from the recording head. This soft layer then provides a flux return path, or flux concentrator, for the recording head fields, as well as, a flux closure path for stabilizing the recorded bits against demagnetization energies after the head is removed. The former enables recording heads to function with higher coercivity media and with better resolution, while the later provides improved stability to the recorded patterns by eliminating a portion of the self-demagnetization energy associated with perpendicular recording. In longitudinal recording media a soft magnetic layer would also improve the stability of the recorded patterns by reducing the self-demagnetization energy of the hard recording layer. However, heretofore, no soft magnetic underlayer has been found to be a satisfactory keeper layer for either perpendicular or longitudinal media as no good method of controlled the anisotropy orientation has been available. Soft magnetic underlayers, without a uniform and controlled anisotropy direction, results in domain wall induced media noise via domain wall motion Barkhausen phenomena. As the magnetic head passes over the media data it effectively shorts out the stray media bit fringe fields causing the magnetic patterns in the soft magnetic underlayers to relax to new positions. If there are significant domain walls involved in this process they commonly break loose from

localized pinning defects causing sudden changes in their magnetic configuration. This Barkhausen phenomena causes noise signals to appear in the data playback head. For either perpendicular or longitudinal hard disk recording, where the recorded bit or flux patterns have been wider across the recorded track than the bit length, the desired anisotropy configuration for the soft layer is for the hard magnetic axis to be along the recorded track so that the easy axis lies across the track direction. Hence, for a traditional hard disk system this implies that the easy axis of the soft film should be directed radially, while the hard axis is directed circumferentially. Since the easy axis of the soft magnetic layer of this configuration is at 90 degrees to the fields produced by the flux transitions of the hard recording layer, the magnetization vector of the soft magnetic layer rotates by spin rotation and the noise generating domain wall motion is avoided. Having a uniaxial soft magnetic underlayer with radial orientation will solve a long-standing technical problem. As data storage areal densities are pushed forward, magnetic grain sizes have been reduced to the extent that the magnetic recorded state is near the thermal stability limit. Hence, even longitudinal recording stability and the transition length also benefit from the use of a soft magnetic underlayer to reduce the bit transition demagnetizing effects. Again, because of domain wall motion generates noise the ideal orientation of the soft underlayer easy axis should be radial to minimize the potential for domain wall noise. Similarly, anisotropy orientation control can benefit magnetic tape and x-y addressable data storage systems by providing a keeper layer wherein the magnetization vector is rotated by spin rotation and domain wall motion is minimized. This invention, of oriented soft magnetic materials, represents a significantly improving future magnetic media.

Background For Hard Magnetic Film Orientation

Modern hard disk longitudinal media consists of a polycrystalline thin film composed essentially of uniaxial grains randomly oriented in the substrate plane. Playback by averaging the signals from the randomly oriented grains results in an isotropic response around the disk radius. This orientation randomness has been necessary to avoid the twice around modulation during disk rotation of a non-isotropic media. By mechanically grooving the disk surface prior to deposition of the thin film layers some small amount of orientation along the circumferential direction is sometimes observed. However, the orientation ratio, OR, of the hard magnetic remanence along the track to the radial remanence is seldom more than 1.2 and more often typically less than 1.1 and has been decreasing as substrates have been made smoother and media films made thinner to enable higher areal recording densities. Likewise, the ratio of the coercivities in the two directions is also sometimes referred to as the orientation ratio, OR, and its maximum value is also typically similar to that of the magnetic remanence ratios. The origin of this hard magnetic material orientation has been in dispute for several years. While it has been argued by some that it originates from a slight preference of the c-axis of the hexagonal close packed, hcp, cobalt alloy to lie along the grooved direction, it has also been shown to diminish or vanish if the disk is thermally cycled before media deposition, but after the mechanical grooving. This latter phenomenon has resulted in some arguing that the orientational origin is due to a thermal stress development between the substrate and the film layers as the substrate stress associated with the grooves relaxes from the heat used, or generated, during the deposition. In US Patent 5,989,674, Marinero et al. outlines several patents and publications claiming to reveal the cause of media orientation and then invokes stress, shape and even crystalline orientation to claim a cause for orientation during the deposition of an hcp cobalt alloy on a mechanically grooved substrate. Others had claimed to

achieve small orientation ratios by deposition of the media materials at an oblique angle to the disk surface. See for example, U.S. Patent No. 4,776,938. While this approach has shown some effect it has not resulted in a significantly improved OR over grooved substrates and the deposition methods described are significantly inefficient in the deposition of material. Furthermore, the crystallographic origin of this orientation effect has also never been clearly stated or proven and it is possible that it is due to particle shape effects. In spite of it's the patent description a number of years ago the method is not a technology that is currently used in production.

Nevertheless, from wherever the orientation originates, it has been proven to be beneficial to magnetic recording for achieving higher resolution and shorter magnetic flux transition lengths and better thermal stability. There is little doubt that a greater degree of this orientation is of benefit to future hard disk data storage systems. Likewise, in particulate tape the individual acicular magnetic particles are commonly oriented physically during the wet coating process to have their long axis, and hence their easy magnetic axes, to lie along the track direction. This results in a higher signal level, shorter transition length, and higher recording densities. It is an interesting observation, that for best performance, the easy axis orientation of the hard magnetic media layer, whether longitudinal or perpendicular media, should be along the applied head field direction, while the easy axis orientation of an associated soft keeper layer should be across the recording track, perpendicular to the applied head field direction for longitudinal media; in order to enjoy the benefits of magnetic moment rotation instead of domain wall motion to avoid the Barkhausen noise phenomena of the soft keeper layer.

Background for epitaxial thin film growth

One of the most often cited concepts is that thin films prefer to grow with the atoms arranged on the thin film surface to minimize the atomic bonding energy. This implies that the most stable atomic crystalline surface grows when the surface atoms form the densest arrangement consistent with the crystalline structure. This means that for the fcc lattice, and fcc derivatives, the (111) texture develops in a thin film because the atoms are the most closely packed on this crystalline plane. The next most commonly occurring texture would be the (001) while the (110) texture would be seen only rarely. On the other hand for the bcc, and bcc derivatives, the (110) texture preferentially develops, as it is the most closely packed crystalline plane. The next most commonly occurring texture is the (001), while the (111) texture is never observed. In rare instances, such as described in U.S. Patent No. 5,693,426 it was found that for some materials the B2, bcc derivative, crystalline structure may form a (112) texture if deposited under the correct conditions. However, even the B2 crystal will easily form the (110) texture on non-oxidized surfaces, where the initially deposited atoms have high surface mobility during the film growth. Likewise, for hexagonal close packed (hcp) crystals the (0002) texture is the most closely packed and most commonly develops.

Likewise, there are several publications describing the epitaxial relationships, which prevail when a second crystalline material is deposited directly upon an underlayer. U.S. Patent No. 6,248,416 discusses a number of these. Assuming that the atomic lattice spacing of the first material and the second material sufficiently match a number of second layer texture following relationships to the first layer texture have been found. However, if the atomic lattice matching is not sufficient then epitaxial growth does not occur. For example, U.S. Patent No. 6,248,416, which is incorporated herein by reference, Lambeth et al. have discussed, non-ferromagnetic, Cr

textures grown as quasi-epitaxial single crystal thin films on clean, non-oxidized, single crystal Si substrates.

The textures developed on these substrates are extremely strong indicating a high degree of order and single orientation. In this patent, and in other publications, it has been shown that two different fcc materials can epitaxially grow upon each other with the same texture. Likewise, two different bcc materials can epitaxially grow upon each other with the same texture. Likewise, two different hcp materials can epitaxially grow upon each other with the same texture. More interesting, however, is the case when one crystalline material class is deposited upon a different crystalline material class. Not only is crystalline texture induced into the second layer by the epitaxial growth on the first layer, the texture, and the in-plane orientation of the second layer is determined by the first layer texture and orientation. For example, U. S. Patent 6,248,416 shows that a clean Si (001) single crystal can induce fcc Ag (001) texture and if bcc Cr is grown on this then (001) texture results. The authors then showed that hcp Co (11 $\bar{2}$ 0) texture grows on the Cr (001) texture and that the possible c-axes orientations is predetermined, to be only two possible directions, by the crystalline directions of the single crystal Si wafer. Likewise, they showed that if a Si (110) textured single crystal is used as the substrate then the highly unusual fcc Ag (110) texture develops and on this, the unusual bcc Cr (112) texture, develops. Co (10 $\bar{1}$ 0) texture is induced by this Cr surface and the in-plane single Co c-axis lies parallel to the Cr \langle 110 \rangle direction. Another epitaxial texture relationship described in U. S. Patent 6,248,416 is noted. If the initial single crystal Si substrate is (111) the epitaxial fcc Ag will be (111) textured and oriented in the plane in the same directions as the Si crystal. If another fcc, such as Cu or Ni, is deposited upon this then it too will be epitaxial and so carry the (111) texture and orientation. Each of these textures is strongly oriented because the layer below it is strongly oriented and one can

continue the epitaxial growth of one layer on the next. They also described how this structure, with the use of a Ti layer can be used to grow hard magnetic perpendicular Co (0002) texture films. They did not describe how Cr would
 5 grow on these (111) texture fcc layers or the Co (0002) textured layer. Nevertheless in separate publications H. Gong et al, (H. Gong, W. Yang, M. Rao, D.E. Laughlin and D.N. Lambeth, "Epitaxial growth of quad-crystal Co-alloy magnetic recording media," *IEEE Transactions on Magnetics*,
 10 35(5), 1999, pp.2676-2663), as well as, G. Zangari et al (G. Zangari, B. Lu, D. E. Laughlin and D. N. Lambeth, "Structure and Magnetic Properties of Sm-Co Thin Films on Cr/Ag/Si Templates," *Journal of Applied Physics*, Vol. 85 (8), April 15, 1999, pp. 5759-5761), noted that upon the
 15 (111) single crystal Si substrate and subsequent epitaxial (111) textured fcc layers when a bcc Cr was deposited a strong Cr (110) texture resulted. However, the atomic arrangement of the (110) bcc crystalline plane is rectangular while the fcc atomic arrangement of the (111)
 20 crystalline plane has hexagonal symmetry. Gong et al notes, as does Zangari et al, that there are three possible ways (variants) for the bcc Cr (110) plane to orient on this atomic hexagonally arrange surface. These crystalline planes and crystalline directions are illustrated in Figure
 25 3. These three orientations correspond to when the <001> directions of the (110) textured Cr lie exactly parallel to the <110>, or perpendicular to the <112>, directions of the hexagonal atomic lattice plane of the (111) textured fcc. They summarized these three Cr (110) orientational variant
 30 relationships with the fcc underlayer via the following notation:

35	Cr(110) [001]		Ag(111) [<u>110</u>]		Si(111) [<u>110</u>],
	Cr(110) [001]		Ag(111) [<u>101</u>]		Si(111) [<u>101</u>],
	Cr(110) [001]		Ag(111) [<u>011</u>]		Si(111) [<u>011</u>].

Their publications, as well as U. S. Patent 6,248,416, were focused upon hard hcp and soft fcc magnetic structures that
 40 could be grown and they show no evidence of working with

anything but non-magnetic bcc materials such as Cr. Upon each of these three Cr variants four possible hcp Co (1011) quad-crystal variants were obtained. This Co layer then contains grains with four possible easy axes directions when grown on each Cr variant. As a result, the Co quad-crystal structure consists of grains, each with one of twelve possible easy axis directions. There are four Co orientational possibilities for each of the three possible Cr variants.

Figure 3 illustrates the positions of the three bcc Cr (110) orientational variants [4] relative to the fcc (111) epitaxial template [5]. Example $\langle 001 \rangle$ bcc directions and an example $\langle 112 \rangle$ fcc direction are shown along with other relevant crystallographic directions. Hence, the public literature, states that there are three possible Cr variants that can grow on the (111) fcc textured substrate. The same result would apply to any size single crystal provided it is (111) textured fcc and the lattice constants are sufficiently matched to induce the epitaxial growth. Hence, since polycrystalline fcc films, grown on a non-single crystal substrate, with strong (111) texture, contain a large number of single crystal grains, one could obtain the same result for each individual grain. However, if the grain were small enough, it is possible that only one or two of the three possible bcc (110) textured orientational variants might grow on a given grain, but it is also possible, depending upon the deposition processing conditions, that all three variants could coexist on a single fcc (111) textured grain. Furthermore, since the probability of growth for each variant is equal then a sufficiently large sample will contain an equal volume of each variant and a magnetic material will appear to have symmetrical orientational magnetic properties. This would be true if the epitaxial growth occurred on a single crystal substrate or if the final film were polycrystalline and had been grown on a non-single crystal substrate.

These effect will now be explained in terms of the anisotropy energy density.

Magnetic Anisotropy Energy of (110) Textured Thin Films

5 To understand the magnetic properties of (110) textured magnetic bcc materials grown on a (111) texture fcc substrate we consider the expression for the cubic magnetocrystalline anisotropy energy when the magnetization is confined to the thin film plane of a single crystal of cubic material. Consider the in-plane unit cell atomic surface [6] of a single variant of the (110) textured film grown in Figure 3. Figure 4 shows the magnetocrystalline energy plotted, where the magnetization is confined to the (110) crystalline plane, as a function of angle for this single variant for $K_1 > 0$ and $K_2 = 0$. The magnetocrystalline energy density is given by $E_{110}(\theta)$ (See "Physics of Ferromagnetism, 2nd Edition" by Soshin Chikazumi, pages 249-256), where:

$$20 \quad E_{110}(\theta) = K_1 \left\{ \frac{1}{4} \sin^4(\theta) + \sin^2(\theta) \cos^2(\theta) \right\} + K_2 \left\{ \frac{1}{4} \sin^4(\theta) \cos^2(\theta) \right\} + \text{higher K terms.}$$

Or when expanded into the harmonics of θ ,

$$25 \quad E_{110}(\theta) = \frac{1}{32} K_1 \{ 7 - 4 \cos(2\theta) - 3 \cos(4\theta) \} + \frac{1}{128} K_2 \{ 2 - \cos(2\theta) - 2 \cos(4\theta) - \cos(6\theta) \},$$

where θ is the magnetization vector direction measured from the $\langle 100 \rangle$ bcc direction in the film plane, and K_1 and K_2 are the first and second order magnetocrystalline anisotropy energy density constants, respectively. The higher order energy terms are usually much smaller and are neglected here.

35 For pure Fe, K_1 is often quoted to be about $+4.7 \times 10^5$ erg/cc, but can be tailored by chemical additions. On the other hand the disordered bcc form of $\text{Co}_{50}\text{Fe}_{50}$ is believed to be about -1.5×10^5 erg/cc while the ordered bcc

derivative, B2, form of $\text{Co}_{50}\text{Fe}_{50}$ is about zero. Interestingly, the K_1 value for both the ordered and disordered alloys are about the same when the Co atomic percent is 35% or less. $K_1 \sim +1 \times 10^5$ erg/cc for $\text{Co}_{35}\text{Fe}_{65}$ and approaches the Fe value for Co content of less than 25%. This alloy is of particular interest due to its very high M_s value and interesting anisotropy properties as a function of composition. See "Modern Magnetic Materials Principles and Applications" by R. C. O'Handley, pages 190, 192 for anisotropy constants and page 145 for saturation magnetization values. The higher order anisotropy constants, such as K_2 , are less well known, but are usually smaller in magnitude and are weighted less heavily in the energy expression. Only in cases where the role of K_1 tends to vanish do the K_2 terms seem to play a significant role in these calculations. In the description of variant sets which will follow below, it is important to note the 2θ harmonics will play a dominate role while the 4θ harmonic tends to cancel out. Furthermore, the 6θ harmonic of the second order anisotropy energy term is weighted significantly less than the 2θ or 4θ harmonic. Hence, in most cases the effect of this 6θ harmonic can be neglected. While one skill in the field of magnetism will understand that the higher order anisotropy energy densities may play a small role in this invention, for simplicity of explanation they will be neglected in the following derivations.

While the smallest energy minimum for the function ($K_1 > 0$) is at the in-plane $\langle 100 \rangle$ direction there are two equal maximums along the in-plane $\langle 111 \rangle$ directions [7]. Hence, there is a localized minimum [8] located between the two $\langle 111 \rangle$ directions and directed along the $\langle 110 \rangle$ direction. Hence, this texture does not yield uniaxial behavior and is subject to domain wall motion resulting in highly non-linear switching for all directions of applied field when the sample is driven near to saturation. There is a reasonably a large region of monotonic behavior on

this energy curve where the response conceivably could be reversible and low loss if the magnetic configuration was single domain orientation. Conceptually if the magnetization is initially all pointed along the $\langle 001 \rangle$ direction and then is rotated toward one of the in-plane $\langle 111 \rangle$ hard axes by an applied field the process could be reversible, hence lossless, until the magnetization approached the hard axis. However, as the magnetization crossed the in-plane $\langle 111 \rangle$ direction it would then abruptly jump towards the localized energy minimum at the in-plane $\langle 110 \rangle$ direction. This jump is not reversible and so represents a lossy process. Since a 90-degree domain almost always wall exists, or forms, between the magnetization pointing along the in-plane $\langle 001 \rangle$ and $\langle 110 \rangle$ directions then wall motion dominates any possible rotational mechanism. Grain boundaries or defects in the film structure would cause localized wall motion jumps, again resulting in loss mechanisms.

In the 0 to 180 degree region of the energy plot, Figure 4, we see, for the case of $K_1 > 0$, the one minimum [9], two maximums [7], and a localized minimum [8] corresponding to the single $\langle 100 \rangle$, two $\langle 111 \rangle$ and single $\langle 110 \rangle$ directions, respectively, of variant [6] of Figure 3. These extremes would invert if the $K_1 < 0$. Clearly, this curve does not satisfy our definition for a uniaxial magnetic material.

SUMMARY OF THE INVENTION

The present invention is directed generally to oriented thin film magnetic materials and devices including magnetic sensors, transducers, electronic circuit components, recording heads, recording media, and data storage systems, incorporating the said, thin film oriented magnetic materials and, more particularly, crystallographically oriented thin film materials and oriented magnetic layer structures utilizing materials such as iron, nickel, and cobalt, and alloys of the same. In

particular, this invention deals with a structure to achieve uniaxial magnetocrystalline orientation via the use of the (110) texture of body centered cubic (bcc) or body centered cubic derivative crystal thin film structures. In general, the bcc or bcc derivative materials have higher saturation magnetizations than face centered cubic and the invention of orientation control of bcc and bcc derivative materials allows new devices to be constructed, which have good orientation, high magnetization, high permeability and low losses. These devices are used to detect or determine magnetic fields, store and retrieve data, and to transform energy or perform electronic signal processing. Improved magnetic properties or orientation of the magnetic properties of the materials when used in such devices result in better technical performance or allows for the construction of smaller, faster or less expensive systems. In most existing magnetic devices, with designs utilizing traditional magnetic materials structures, the performance is significantly improved by simply replacing the traditional magnetic material structure with the new structure described herein.

BRIEF DESCRIPTION OF THE DRAWINGS

The advantages of the present invention can be better understood by reference to the drawings in which:

Figure 1 shows a plot of the magnetic anisotropy energy density for the uniaxial Stoner-Wohlfarth model.

30

Figure 2 shows the magnetic hard axis response function, M_x , to an applied field along the hard axis, H_x , for the uniaxial Stoner-Wohlfarth model; and the magnetic easy axis response function, M_y , to an applied field along the hard axis, H_x , for the uniaxial Stoner-Wohlfarth model.

35

Figure 3 shows an illustration of the historical three orientational variant arrangement of the (110) crystal

plane of a bcc crystal in comparison to the atomic arrangement of the (111) crystal plane of an fcc crystal.

5 Figure 4 shows a plot of the magnetic anisotropy energy density versus magnetization direction in the plane for the (110) texture plane of a cubic crystal, where the first order anisotropy energy density constant, K_1 , is positive.

10 Figure 5 shows an illustration of two of the six possible orientational variants of the (110) crystal plane of a bcc-d crystal in comparison to the atomic arrangement of the (111) crystal plane of a hexagonal lattice template crystal.

15 Figure 6 shows a plot of the magnetic anisotropy energy density versus the in-plane magnetization direction for the specific case of three (b1, b2, and c1) coupled (110) variants, of the six bcc-d (110) textured variants
20 when $K_1 > 0$ and $\delta = 7.5$ degrees. Only one energy minimum and one energy maximum per 180 rotation occurs.

25 Figure 7 shows a plot of the magnetic anisotropy energy density versus the in-plane magnetization direction for the specific case of two (a1 and c2) coupled (110) variants, of the six possible bcc-d (110) textured variants when $K_1 > 0$ and $\delta = 5.26$ degrees. Only one energy minimum and one energy maximum per 180 rotation occurs.

30 Figure 8 shows a plot of the magnetic anisotropy energy density versus the in-plane magnetization direction for the specific case of four (a2, b1, b2 and c1) coupled (110) variants, of the six possible bcc-d (110) textured variants when $K_1 > 0$ and $d = 5.26$ degrees. Only one energy
35 minimum and one energy maximum per 180 rotation occurs.

Figure 9 shows the magnetic hard axis response function, M_x , and the magnetic easy axis response function,

M_y , for an applied field along the hard axis, H_x , for the coupled variant pair (a1 and c2) when $K_1 > 0$ and $\delta = 5.264$ degrees.

5 Figure 10 shows a plot of the magnetic anisotropy energy density versus the in-plane magnetization direction for the specific case of three (b1, b2, and c1) coupled (110) variants, of the possible six bcc-d (110) textured variants when $K_1 > 0$ and $\delta = 5.264$ degrees. Only one
10 energy minimum and one energy maximum per 180 rotation occurs.

Figure 11 shows a plot of the magnetic anisotropy energy density versus the in-plane magnetization direction
15 for the specific case of two (a1 and b2) coupled (110) variants, of the six possible bcc-d (110) textured variants when $K_1 > 0$ and $\delta = 5.264$ degrees. Two energy minimums and two energy maximums per 180 rotation occurs.

20 Figure 12 shows a sketch of the coordinate system for defining the angle of atomic motion during angle of incidence deposition. The substrate plane is x-y and the depositing materials arrive along r. The angle of deposition, ω , is defined as the angle between the z-axis
25 and r vector.

Figure 13 is a schematic illustration of a new sputtering cathode geometry relative to a disk surface for angle of incidence deposition.

30

Figure 14 is X-ray pole figure data demonstrating the existence of six bcc-d (110) textured variants with $\delta = 5.264$ where variant a1 and c2 dominate the other four variants to produce a symmetry broken structure. Also
35 shown are the three Ag (220) peaks. The sample was produced using angle of incidence deposition.

Figure 15 shows the uniaxial magnetic hard axis response, M_x , function, and easy axis response function, M_y , data to an applied field along the hard axis, H_x , for an Fe ($K_1 > 0$) sample prepared with the easy axis along the hexagonal template $\langle 112 \rangle$ direction. The symmetry breaking mechanism was an applied magnetic field along the $\langle 112 \rangle$ direction.

Detailed Description Of The Preferred Embodiments

The material structures of the invention can be embodied in both magnetically hard and soft magnetic devices including magnetic field sensors, transducers, electronic circuit components, magnetic solid state memory, antitheft devices, recording heads, recording media, and data storage systems, incorporating the said, thin film oriented magnetic materials and, more particularly, crystallographically oriented thin film materials and oriented magnetic layer structures utilizing materials such as iron, nickel, and cobalt, and alloys of the same. These structures are especially useful where the embodiment of the device requires special magnetic orientation, specific linear or non-linear response, or a low loss response.

By carefully controlling the epitaxial growth conditions of (110) crystalline textured bcc or bcc derivative thin film materials on highly oriented (111) hexagonal atomic templates the applicant has invented a new set of six crystalline variants with special orientational relationships. By the selection and the growth of a very special exchange coupled subset of these six orientational variants a symmetry broken uniaxial magnetic thin film is obtained. The (111) textured fcc, (111) textured fcc derivative, or an (0002) textured hcp crystals are examples of the (111) textured hexagonal atomic template. In each of these cases the atoms of the template are close packed. When a highly oriented (111) hexagonal template is available a highly oriented bcc or bcc derivative (110) texture structure can be epitaxially grown. With the combination of being highly oriented and the use of special

processing techniques the six new variants can be constructed. Since under many circumstances the bcc and the bcc derivative materials form a single class of behavior, we shall consider the notation "bcc-d" to
5 represent either a bcc or a bcc derivative crystal structure. Likewise, the notation "fcc-d" shall be used to represent either an fcc or fcc derivative crystal structure. For example, here materials with the NaCl
10 prototype structure are considered to be a fcc derivative as there is a close packed hexagonal pattern of atoms in the (111) plane. The (111) plane of atoms of these fcc-d and (0002) plane of hcp crystals are always close packed and so are different from the (111) atomic crystal planes of many fcc Bravais lattices, which are not close packed.
15 For example, the Si, diamond structure, substrate is a member of the fcc Bravais lattice F3dm space group. Likewise, the C15 (Strukturbericht designation) is a member of the F3dm group, which does not have a close packed (111) plane. From Figure 3 one can see that there are three
20 hexagonal template $\langle 110 \rangle$ directions similar to [10]. It was found that, by carefully controlling the epitaxial film growth conditions, a strongly (110) textured bcc-d crystal could be made to grow with one of its $\langle 111 \rangle$ directions parallel to the hexagonal template $\langle 110 \rangle$ directions. This
25 orientation is different than was obtained by the processing of Gong and Zangari. In our processing the bcc-d $\langle 110 \rangle$ directions are no longer parallel to the hexagonal template $\langle 112 \rangle$ directions.

Before discussing the new 6 crystalline (110) textured bcc-d variant system it is worthwhile to further analyze the 3 crystalline (110) textured variant system. The energy expression for the single variant, $E_{110}(\theta)$ was given earlier and discussed in the context of Figure 4. It is important to point out that if there were two dominate variants of this (110) textured bcc on the same (111) textured fcc crystal surface and if they were magnetically coupled by being in contact or via another magnetic material being in contact with each of them then the magnetization vector of each of the variants would tend to move or rotate together. Likewise, if there were all three variants, as illustrated by [4] in Figure 3 and espoused for Cr, in both the Gong and Zangari literature, and the three variants were magnetically coupled the magnetization of each would tend to move with the others. Of course Cr has no magnetic moment and so neither Gong nor Zangari discussed this. The anisotropy energy density equation for equal amounts of each of these three crystalline variants, with the magnetization rotating together would be written as the sum of each of the variants:

$$E_3'(\theta) = \{E_{110}(\theta) + E_{110}(\theta - 60) + E_{110}(\theta - 120)\} / 3.$$

Here θ is the angle of the magnetization vector with respect to the $\langle 100 \rangle$ direction of the original single variant [6]. Because the underlayer in-plane fcc $\langle 112 \rangle$ directions are at 60 degree intervals, the two other bcc (110) texture variant easy axes are located at 60 degree intervals with respect to the first. By simple trigonometry it can be shown that the sum of the energy of these three variants is a constant of $(7/32)K_1$ and has no θ dependence. Hence, there are no net anisotropy directions. However, in actual materials, since domain walls can form, the localized anisotropy of each variant, in combination

with material defects, results in a significant coercivity and lossy behavior.

Because the reference point in any energy calculation is arbitrarily chosen one can always add a constant to the energy function without changing the predicted physical behavior. Also, since the combined energy in the three variant case just discussed is a constant, it is obvious that if there were only two coupled variants the energy function would be simply proportional to the negative of the single variant case. Writing this statement mathematically:

$$\{E_{110}(\theta) + E_{110}(\theta - 60) + E_{110}(\theta - 120)\} / 3 = 7/32.$$

Hence, for a material with only two variants

$$E_2'(\theta) = \{E_{110}(\theta - 60) + E_{110}(\theta - 120)\} / 2 = 21/64 - E_{110}(\theta) / 2.$$

Therefore, after normalizing the energy density by the appropriate unit volume of material, the energy curve of the two, coupled variants is simply 1/2 the inverted energy curve of the single variant of the same total unit volume of material. The curve shape and energy minimums and maximums interchange position and so the hard axes and easy axes directions would interchange. Any localized easy axis or energy minimum, such as [8], would become a localized hard axis or energy maximum. Recall that the constant in the energy expressions is arbitrary and has no effect on the physical response so it can be considered to be equal to zero in any analysis. Hence, the response of a magnetically coupled pair of these variants appears as a single variant material with a change in sign of the K_1 value and a decrease in the amplitude of the differences in the energy extremes by a factor of 1/2. Hence, whether the material of a (110) textured cubic magnetic material is composed of a single variant, two coupled variants or three coupled variants the magnetocrystalline anisotropy energy density function does not yield uniaxial behavior, but a

form of bi-axial behavior. Therefore, when there are three possible variants of bcc magnetic material located at 60 degree intervals, as advocated for the non-magnetic bcc Cr by Gong et al and Zangari et al, and whether a (110) textured cubic magnetic film is polycrystalline or is epitaxially grown on a single crystal, it cannot possess uniaxial behavior. Hence, the M versus H response function will have coercivity and lossy behavior. Furthermore, uniaxial behavior cannot be obtained even if the volumes of each of the three variants are arbitrarily selected. When the volumes of the three variants are not equal we herein refer to the sample as being "symmetry broken."

It is also clear that should all three variants be present, but that either one or more than one be of more volume than the others then the energy properties of the larger volume variants will be dominate. To clarify this, simply consider the case of Figure 3 where 6 has a volume fraction of 1/2 while the other two equal volume variants have a volume fraction of 1/4 each. Then 1/2 of the volume of 6 is equal to the volume of each of the other two. So the energy terms from these three quarters of the total volume would be equally portioned and sum to a constant. This then would leave the remaining 1/2 of variant 6 to provide an energy curve of the shape of Figure 4. Hence, we herein referred to the larger volume variants as being "dominate."

It is important to note that nowhere in U. S. Patent 6,248,416 or in Gong et al or Zangari et al, was the use of any magnetic bcc or bcc derivative thin film discussed. Nor were magnetic bcc or bcc derivative materials investigate or advocated as the magnetic layer. If they had been investigated, and found to have the same three variant crystalline orientational relationships that were found for bcc (110) Cr when placed on a (111) fcc layer, the magnetic properties would have had to have been lossy and to have significant coercivity. Furthermore, they never suggested that they obtained a sample situation where the volumes of each of the variants were not equal. Hence,

at no time did they discuss a symmetry broken variant system nor a dominate variant system.

Likewise it is important to note that in their discussion of FeCoN thin films Sun and Wang provided no evidence regarding any (110) textured variants. Furthermore, they offered no explanation for the anisotropy the observed and because their anisotropy fields appeared to be the same whether or not permalloy was placed under their CoFeN film their results were not dependent upon on any ordered variant structure. Furthermore, their results showed a strained lattice and a significant Fe₄N second phase indicating a possible anisotropy mechanism associated with strain or shape effects as discussed by Chikazumi.

It is well known that crystallographic twinning can form at the (112) planes of the bcc-d. These (112) planes contain both a <110> and a <111> direction. Hence a pair of bcc-d twins can form with an interface along the plane containing the thin film surface normal and containing one of the hexagonal template <110> directions. In this arrangement the hexagonal template <110> directions coincides with one of the bcc-d <111> directions. Hence, for bcc-d (110) texture films that have grown with a <111> direction parallel to a hexagonal template <110> direction, there are two possible variants. Since there are three possible hexagonal template <110> directions, then there three possible sets of twins. Hence, we are lead to the concept that there are 6 possible bcc-d variants that could be grown. However these variants do not have to be in a twinned configuration to exist. For clarity, only two of these six possible variants are shown in Figure 5. The other four variants can be constructed by rotating the positions of these two by 60 and 120 degrees. This sketch is meant to be illustrative in showing the orientation of the variants and it is to be understood that a single variant would extend over a considerable some of atomic distances.

The angle formed between the bcc-d <111> direction and the bcc-d <100> direction is given by $\arctan(\sqrt{2}) = 54.736$.

degrees. Likewise, the angle between the $\langle 111 \rangle$ direction and the $\langle 110 \rangle$ direction is $\arctan(1/\sqrt{2}) = 35.264$ degrees. The sum of these two angles is of course 90 degrees and forms the angle between the $\langle 100 \rangle$ and $\langle 110 \rangle$ directions.

5 The importance of this 54.736 degree angle value is that it differs from the 60 degree interval of the $\langle 110 \rangle$ directions of the hexagonal template by 5.264 degrees. In contrast to the three variants observed by Gong and Zangari, the $\langle 100 \rangle$ directions of the proposed six bcc-d variants do not lie

10 parallel to any of the hexagonal template $\langle 110 \rangle$ directions. Furthermore, where as for the Gong and Zangari symmetrical arrangement where none of the $\langle 111 \rangle$ bcc directions lie parallel to the hexagonal template $\langle 110 \rangle$ directions, for our new variants one of the bcc-d $\langle 111 \rangle$ directions lies

15 parallel to one of the hexagonal template $\langle 110 \rangle$ directions and the bcc-d $\langle 100 \rangle$ direction does not lie parallel to the $\langle 110 \rangle$ hexagonal template. Hence, for a coordinate system where $\theta = 0$ at the hexagonal template direction $[110]$, the bcc-d variant crystal $\langle 100 \rangle$ directions and easy magnetic

20 axis ($K_1 > 0$) lie at angles of $\beta_i = 0 \pm \delta, 60 \pm \delta$ and $120 \pm \delta$ degrees where $\delta = 60 - \arctan(\sqrt{2}) = 5.264$ degrees. In Figure 5, it is also important to note the orientation of the two $\langle 111 \rangle$ directions of each of the two the bcc-d variants. They match the 60 and 120 degree hexagonal template $\langle 110 \rangle$

25 directions, but near the 0 degree axis they differ from the $\langle 110 \rangle$ axis by + and - 2δ . When exchange coupled this variant pair will be represented by an energy function $E_{2-ai1c2}(\theta)$ in the discussion below.

For a (110) textured bcc-d crystalline structure

30 containing six equally occurring magnetically coupled variant volumes the anisotropy energy density function is written as:

$$E_6(\theta) = \{E_{110}(\theta \pm \delta) + E_{110}(\theta - 60 \pm \delta) + E_{110}(\theta - 120 \pm \delta)\} / 6,$$

35

where the + and - signs are to represent two functions for each angle in this expression. As before, it can be

mathematically shown that the total anisotropy energy of this symmetrically balanced arrangement of six variants, six E_{110} energy terms, has no angular dependence and so the anisotropy energy density function is a constant, $K_1(7/32)$.

5 However, of particular interest here are the cases when only an odd or even numbers of particular variants are coupled. It is important to consider that any one or more of the six variants could possibly grow on a hexagonal template and it is not a requirement that they appear in

10 twin pairs or of a balanced, equal amounts of material. However, for clarity, during the discussion of the next few paragraphs we will consider the amounts of material in each variant of a coupled group of variants to be balanced to be equal. That is to say, for example, if there are only

15 three variants coupled together we shall assume that the volume of each of the three is equal.

If there is only one of the six variant then the energy density function simply reduces to that of $E_{110}(\theta)$ shifted by the particular variant offset angle

20 β_i . Likewise, if there are five of the six variants then, similarly to the earlier logic and ignoring the unimportant energy constant offset or origin, the resulting normalized energy density function is negative 1/5th the energy function peak to peak value of the missing variant. As

25 shown in Figure 4, since the $E_{110}(\theta)$ function has two maximums, one minimum and a localized minimum (for $K_1 > 0$, or two minimums, one maximum and a localized maximum for $K_1 < 0$), these two possible sets of coupled variants yield energy functions that do not represent uniaxial magnetic

30 material behavior. There are three other possible sets of numbers of coupled variants; two, three, and four variants per combination. However, there is more than one way to form each of these, as there are six variants to choose from. Here, we continue to consider each of the variants

35 in a set to be balanced or of equal volume of material.

As stated before there are six possible bcc-d variants each with a single crystalline $\langle 100 \rangle$ direction in the plane (and easy magnetic axis when $K_1 > 0$) lying at one of the

six angles $\beta_i = +0 \pm \delta, +60 \pm \delta$ and $+120 \pm \delta$ degrees. We shall denote these six possible variants by the names: $a_1(60+\delta)$, $a_2(60-\delta)$, $b_1(0+\delta)$, $b_2(0-\delta)$, $c_1(120+\delta)$, and $c_2(120-\delta)$, where the angle in the corresponding parenthesis represents the angular location of the bcc-d $\langle 100 \rangle$ direction for the given variant relative to the $\langle 110 \rangle$ direction [10] of the hexagonal template. We see that, for example, the a_1 and a_2 variants are located at, or deviate by, $+\delta$ and $-\delta$ degrees, respectively, from the 60 degree position of the $\langle 110 \rangle$ direction of the hexagonal template.

Special Case: $\delta = 7.5$ Degrees

Before discussing the energy density curves for the various other combinations of variants it is informative to consider three particular sets of two couple variants of the possible fifteen cases of pairs. However, we now consider the special case when the deviation angle of the variant, δ , is not equal to $60 - \arctan(\sqrt{2}) = 5.264$ degrees, but is exactly equal to 7.5 degrees. The three particular sets of energy density functions of interest are written as:

$$\begin{aligned}
 E_{2_b1a2}''(\theta) &= \{E_{110}(\theta - 0 - 7.5) + E_{110}(\theta - 60 + 7.5)\} / 2, \\
 E_{2_a1c2}''(\theta) &= \{E_{110}(\theta - 60 - 7.5) + E_{110}(\theta - 120 + 7.5)\} / 2, \text{ and} \\
 E_{2_c1b2}''(\theta) &= \{E_{110}(\theta - 120 - 7.5) + E_{110}(\theta - 0 + 7.5)\} / 2.
 \end{aligned}$$

The subscripted energy function notation, for example, $E_{2_b1a2}''(\theta)$ represents the two variants b_1 and a_2 coupled as a pair. The quotation mark, "", is used to denote this special $\delta = 7.5$ degree case. We see that in each of these three cases the coupled variants are phase shifted by exactly 45 degrees from each other. It can easily be shown, by trigonometry for this particular $\delta = 7.5$ degree angle, that for each of these pairs, which are separated by 45

degrees phase angle, the only dependence on θ is of the form of $\cos^2(\theta)$. In particular, it can be shown that:

$$\begin{aligned} E_{2_b1a2}''(\theta) &= (K_1/64) \{14 - 8\cos(45) + 16\cos(45)\cos^2(\theta + 60)\}, \\ 5 \quad E_{2_a1c2}''(\theta) &= (K_1/64) \{14 - 8\cos(45) + 16\cos(45)\cos^2(\theta)\}, \text{ and} \\ E_{2_c1b2}''(\theta) &= (K_1/64) \{14 - 8\cos(45) + 16\cos(45)\cos^2(\theta - 60)\}. \end{aligned}$$

$E_{2_a1c2}''(\theta)$, for example, represents a coupled pair of variants that has a Stoner-Wohlfarth hard axis at zero degrees and easy axis at 90 degrees, while the individual variants have their easy axes ($\langle 100 \rangle$ directions for $K_1 > 0$) angled at $+67.5$ and 112.5 degrees. In other words, each of these paired variants result in an energy function that is of the same functional form as the uniaxial Stoner-Wohlfarth model with an easy axis ($K_1 > 0$) angle located half between the easy axis directions of the two individual variant easy axis locations. This Stoner-Wohlfarth behavior only occurs because of the coupling of the two variants and their specific $60 - 2\delta = 45$ degree orientation with respect to each other. It is also clear that if the anisotropy energy density constant $K_1 < 0$ the direction of the resulting easy and hard axes of the coupled pair of variants invert.

Each of these paired variants not only results in a uniaxial energy function, but, as discussed earlier for figure 2, in a zero loss hard axis driven M_x versus H_x response function and a non-linear, quadratic M_y versus H_x response function. (To a reasonable approximation this will turn out to also be the case for $\delta = 60 - \arctan(\sqrt{2}) = 5.264$ degrees.) Each of these three coupled pairs ($\delta = 7.5$) represents an ideal way to construct an ideal uniaxial response from a (110) textured bcc-d magnetic material. As before, because the sum of the energy functions of all six possible variants is equal to a constant, $K_1(7/32)$, then in each of these three paired variant cases the sum of the remaining four variant energy functions is equal to $-1/4$ of

the sum of the paired variants. Hence, there are three particular sets of four coupled variants that sum to yield a Stoner-Wohlfarth type energy function, however because of the negative sign, its hard and easy axes are rotated by 90 degrees relative to the corresponding coupled pair and the peak to peak energy amplitude swing is 1/2 that of the coupled pair case. Hence, these three sets of four coupled variants result in, a Stoner-Wohlfarth, linear and lossless M versus H response functions when driven along the net hard axis. From a notation standpoint we should state that the coupled variants represented by the energy function $E_{2-b1a2}(\theta)$ and corresponding $E_{4-a1b2c1c2}(\theta)$ are complements. After all, similarly to before

$$E_6(\theta) = \{2E_{2-a1c2}(\theta) + 4E_{4-b1a2b1c2}(\theta)\} / 6 = K_1 (7/32) = \text{constant.}$$

It should also be noted that there are twelve other possible combinations of pairs of coupled variants and that none of them yield a uniaxial energy function. Some are worst than others in terms of the depth of the localized energy minimum. Likewise, the corresponding twelve other possible complementary foursomes of coupled variants cannot yield uniaxial behavior, because they can be written in terms of the non-uniaxial coupled pairs of crystallographic variants. This analysis now only leaves the twenty possibilities for sets of three coupled variants to be considered. By similar logic as used before, ten of them are complements (negatives) of the other ten. Fourteen of them have either double minimums or maximums and localized extremes. The other six satisfy the definition of uniaxial anisotropy energy functions, but each does contain a wavy portion[11] of the energy curve located about midway between, and only on one side of, the single minimum and the single maximum. A response curve when driven at an angle between this wavy portion and the hard axis would be nearly lossless, but non-linear over large portions of the response curve. If driven along an angle constrained to the

smooth part of the curve near the hard axis [12] the response would be lossless and more linear over just this portion of the drive. A representative plot of one of these six energy curves, $E_{2_a1b2}(\theta)$, is shown in Figure 6.

5 In summary, not including the previously discussed six singular variants and the null case of all six, there are fifty six possible combinations of equally weighted variants. Hence, when the variant phase angle is set to 7.5 degrees, there are six possible balanced variant
10 combinations that will yield exact Stoner-Wohlfarth like energy curves and corresponding M versus H response functions, plus there are six possible balanced variant combinations that will yield uniaxial, but wavy energy density functions. All others yield non-uniaxial behavior.

15 For completeness, we briefly consider the effect of higher order anisotropy energy terms. An energy expression example, for the uniaxial case of a coupled pair of variants, when the second order anisotropy energy density constant, K_2 , is non-zero, is given by:

20

$$E_{2_a1c2}(\theta) = (K_1/64) \{14 - 8\cos(45) + 16\cos(45)\cos^2(\theta)\} + (K_2/64) \{1 - \cos(45)/2 + \cos(45)\cos^2(\theta) + \cos(45)\cos(6\theta)/2\}.$$

We investigated this function and found that the
25 effect of the 6θ harmonic is of most significance to the uniaxial behavior when the magnitude of K_2 is comparable to or larger than the magnitude of K_1 . However, for many materials this is not the case and in most cases K_2 is so insignificant that it is unknown. For example, for iron,
30 it is sometimes reported that $|K_1/K_2| > 5$, but in some publications it is unmeasurable. Nevertheless, if needed, a similar analysis could be conducted including K_2 .

Special Case: $\delta = 5.264$ Degrees

35

We now return to the case where the variant phase angle δ , is given by $60 - \arctan(\sqrt{2}) = 5.264$ degrees. The

5.264 degree phase angle is not largely different from the 7.5 degree value and the resulting energy curves for the same combinations of variants, but using 5.264 degree phase shifts, are similar to the special 7.5 degree cases just discussed. Uniaxial energy density curves are obtained for the same three sets of pairs of variants as observed before, but using the smaller δ value:

$$\begin{aligned}
 E_{2_b1a2}(\theta) &= \{E_{110}(\theta-0-5.264) + E_{110}(\theta-60+5.264)\}/2, \\
 10 \quad E_{2_a1c2}(\theta) &= \{E_{110}(\theta-60-5.264) + E_{110}(\theta-120+5.264)\}/2, \text{ and} \\
 E_{2_c1b2}(\theta) &= \{E_{110}(\theta-120-5.264) + E_{110}(\theta-0+5.264)\}/2.
 \end{aligned}$$

We also note that each of these energy functions, or variant pairs, is the same if simply phase shifted by 60 degrees on the hexagonal atomic template,

$$E_{2_b1a2}(\theta) = E_{2_a1c2}(\theta+60) = E_{2_c1b2}(\theta+120).$$

Likewise there are three sets of corresponding; complementary variant foursomes that yield similar, but inverted and reduced amplitude differences, energy curves. Furthermore, each of these energy functions, or variant foursomes, is the same if simply phase shifted by 60 degrees on the hexagonal atomic template.

As an example of the functional shape we use $K_1=1$, $K_2=0$ and plot in Figure 7 the anisotropy energy density function for:

$$E_{2_a1c2}(\theta) = \{E_{110}(\theta-60-5.264) + E_{110}(\theta-120+5.264)\}/2.$$

And, in Figure 8 is plotted the anisotropy energy density function for the complement coupled variant set, corresponding to the foursome variant combination:

$$\begin{aligned}
 E_{4_b1a2c1b2}(\theta) &= \{E_{110}(\theta-0-5.264) + E_{110}(\theta-60+5.264) + \\
 35 \quad &E_{110}(\theta-120-5.264) + E_{110}(\theta-0+5.264)\}/4.
 \end{aligned}$$

As discussed earlier, ignoring the additive constant, the anisotropy energy density function of Figure 8 has a peak to peak difference of is just $-1/2$ the amplitude difference of the energy density function represented in Figure 7. While these functions are very similar to the $\sin^2(\theta)$ or the $\cos^2(\theta)$ dependence of the Stoner-Wohlfarth model the curvature around the maximum and the minimum can be seen to differ. They are uniaxial in behavior, but the hard axis magnetic response function is somewhat non-linear, but free of lossy processes. The curve shape at the extremes invert, and so the easy and hard axes deviations, from the Stoner-Wohlfarth model, interchange, when $K_1 < 0$.

The M_x [13] versus H_x and the M_y [14] versus H_x response curves corresponding to $E_{2-a1c2}(\theta)$ are plotted in Figure 9. The M_x versus H_x curve (solid) shows the non-linearity resulting from δ not exactly equaling 7.5 degrees. However it represents a lossless response. The M_y response curve shows similarity to the quadratic behavior of the Stoner-Wohlfarth response. For completeness, Figure 10 is provided to show the $E_{2-b1b2}(\theta)$ coupled variant energy curve for $\delta=5.264$ degrees, which is analogous to that of Figure 6 where $\delta = 7.5$ degrees. The curve is almost flat on the right side of the maximum. However, it still represents a uniaxial material. From these comparisons we can see that for $\delta = 5.264$ degrees there are also 12 possible uniaxial coupled variant sets.

If portions of a film are constructed from a coupled variant pair, for example $E_{2-a1c2}(\theta)$, and other portions of the film are constructed from a coupled variant foursome, for example $E_{4-b1a2c1b2}(\theta+90)$, rotated 90 degrees then they both have a common easy and hard axis. The two film portions must not be strongly coupled so that the two separate coupled variant sets function independently. Then the two non-linear response functions can average to yield a net response function that is nearly linear. However we have found that the response of physical samples may

contain some waviness. It is important to realize that to achieve the rotation of the foursome the templates for the two portions of the material need to be rotated relative to each other by 90 degrees so that the hard axes of the two material portions coincide. Of course because the hexagonal template repeats every 60 degrees of rotational it implies that the template actually only needs to be rotated 30 degrees to be equivalent to a 90 degree shift. This is because the symmetry breaking mechanism is common for both variant sets. Of course it is obvious that other variant sets, perhaps not balanced, can occur for template orientations between the 0 and 30 degree directions and may yield near linear behavior. This concept, of utilizing more than one group of different sets of coupled variants in a single sample, is very powerful as it enables the development of nearly linear magnetic response functions even for polycrystalline (110) textured bcc-d films epitaxially grown on polycrystalline, randomly oriented, (111) hexagonal atomic templates. This means that even though a single crystal substrate will yield the best and most easily understood performance, having a single crystal is not a requirement to achieve the near linear and low loss magnetic response function. The requirement is only that each group of coupled variants be selected and placed upon an appropriately rotated polycrystalline grain template so as to produce a nearly common hard magnetic axis for the entire sample. When a non-single crystalline substrate is used for the deposition of a highly (111) textured polycrystalline hexagonal atomic template the films will consist of individual grains with random in-plane orientation. The technique to obtaining the same easy and hard magnetic axis behavior across an entire polycrystalline sample is to induce the appropriate (110) textured bcc-b coupled uniaxial variant set for each of the randomly oriented hexagonal templates. The method of achieving this is to provide an energetically driven growth process that preferentially selects the appropriate coupled variant set for each hexagonal template orientation being

use. In the experimental results that are to follow we have used both a magnetic field applied along the desired easy axis direction during magnetic variant film deposition or angular vacuum vapor deposition of the bcc-d material to
5 select a direction for the crystallographic orientation growth. Deposition in an applied field was found to yield superior uniaxial behavior. However, unique subsets of the many variant sets were obtained in both cases. These methods result in a controlled uniaxial behavior for the
10 magnetic film. Other methods of supplying an energetically favored crystallographic growth direction may include chemical plating in an applied magnetic field, chemical plating from a bath solution which flows along the substrate in a particular direction, deposition on a miss
15 cut single crystal substrate, and deposition upon a strained, or distorted hexagonal template.

We believe that just as there is a preference for the formation of lowest energy atomic arrangements that can cause preferred crystalline textures, there is a similar
20 mechanism in the symmetry breaking mechanisms to cause orientation in of the crystalline directions in the film plane. In particular, on a surface the resulting texture is usually the most close packed atomic arrangement. Hence, for angle depositions of bcc-d materials one would
25 expect the $\langle 111 \rangle$ directions to tend to align with the direction of the depositing material. Furthermore, it has been found that since there are two $\langle 111 \rangle$ directions in the bcc-d (110) texture plane and multiple, $\langle 110 \rangle$ hexagonal template directions there is some latitude as to whether
30 one of the $\langle 111 \rangle$ directions align exactly with the $\langle 110 \rangle$ template direction parallel to the deposition direction or that it align with one of the $\langle 110 \rangle$ directions at + or - 60 degrees. The later is usually the case for unaxial materials. Also, the energies of film formation must be
35 just balanced against the surface bonding energies otherwise this symmetry breaking will not occur. Likewise, we have found that unless the processing conditions are just right not only will the variants not be symmetry

broken, but the variant set will be the three variants discussed by Gong and Zangari rather than the six new ones. By adjusting these competing energies the desired film structure can be obtained. Adjustment parameters include
5 deposition rate, substrate temperature, vacuum quality against film oxidation, and hexagonal template atomic spacing and material composition. We have found that it is not necessary to achieve magnetic coupling between variants to achieve a symmetry broken structure. However, in order
10 to achieve a uniaxial magnetic behavior the appropriate set of variants must be exchange coupled. The exchange coupling may be directly between the individual touching variants when their size and spacing is such that the exchange length is comparable or not too small compared to
15 variant grain size. However, more preferred is to place a magnetic hexagonal template material directly in contact with the magnetic bcc-d film to assist the exchange coupling via the hexagonal shaped layer. Furthermore, while it has been observed that the hexagonal magnetic
20 exchange coupling layer may be placed either under or on top of the magnetic bcc-d layer it is most preferred to place it under the films and so also use it as the hexagonal atomic template. It is also viable to build multiple alternating layers of hexagonal templates and bcc-d
25 magnetic layers.

To illustrate that not all variant sets yield a uniaxial energy function a three variant set, $E_{3-b1b2c1}$, example is plotted in Figure 11. Clearly this is not uniaxial, but bi-axial behavior.

30 Clearly there are a large number of possible ways of coupling sets of variants to achieve a lossless magnetization response function. For epitaxial growth on single crystal substrates the resulting hard and easy axes are correlated to the substrate directions. However, for
35 polycrystalline substrates the epitaxially grown films contain multiple variant sets corresponding to the crystalline orientations of the individual hexagonal template grains. The appropriate set of couple variants

are selected for the particular orientated polycrystalline hexagonal template via processing conditions and symmetry breaking mechanism. These coupled variant sets do not have to be equally weighted in volume in the sample. Also key, 5 for used of both random in-plane oriented polycrystalline hexagonal template films, and for single crystalline substrates is the concept that the variants of the selected coupled set be sufficiently strongly magnetically coupled so that the magnetization vector of each of the variants of 10 the set rotates together. The coupling is most likely via magnetic exchange coupling. Hence, we adopt the phrase "uniaxial symmetry broken" to denote the crystallographic characteristics of these uniaxial and nearly uniaxial, bcc-d materials, which have low coercivity and, so, low loss 15 magnetic properties. A crystallographically "symmetry broken" material is defined to exist when individual, variant sets do not contain an equal amount of all six of the (110) textured bcc-d variants. We use the phrase "symmetry breaking mechanism" to describe the energetic 20 process by which a "symmetry broken" crystalline structure is obtained. Because of the conceptual complexity and multiplicity of these systems, we have only discussed at length the cases where the variants of a coupled set of variants are equally weighted (balanced) in volume of 25 material. This does not have to be the situation and other interesting energy functions and response curves can be obtained for these cases. One trivial, but important case can be envisioned by considering a film composed of the six coupled variants. If the volume of each variant is equal 30 then, as noted before, the energy density function is a constant and has no θ dependence. However, if two of the six variants are of different volume than the other four then uniaxial behavior can result. Consider the simple case when the two variants with different volumes of 35 material are selected as one of the three Stoner-Wohlfarth variant pairs ($E_2''(\theta)$ or $E_2(\theta)$). If the quantity of material for this pair is slightly greater than the other four variants then this would break the symmetry and

uniaxial behavior would result. However, the energy density difference between the minimum and the maximum would be decreased by the relative difference in volume of materials. For example, of the six couple variants suppose
5 that each of variants of the Stoner-Wohlfarth like coupled pair occupied 30% of the total volume and each of the other four variants occupied 10% of the total volume. Then this would result in a minimum to maximum energy difference equal to 40% of what would be obtained when all the
10 material was in just the Stoner-Wohlfarth like pair. Hence, the magnetic response function would be more sensitive to the applied field as the minimum to maximum energy difference would be smaller for the total magnetic volume. This represents a method of adjusting the slope,
15 also called the magnetic relative permeability, of the magnetic response function.

In many magnetic devices it is advantageous to have multiple thin film layers. Many times they need to magnetically or electronically interact and so there needs
20 to be specifically anisotropy orientational relationships between them. For example, to minimize noise signal it is extremely useful to apply a controlling force along the easy axis of a magnetoresistive sensor in order to stabilize the device against the formation or motion of
25 magnetic domain walls in the sensor material. This is sometimes accomplished by placing a hard magnetic material at the ends of a rectangular shaped device to provide a small magnetostatic field or to exchange couple to the soft film. Likewise, in these devices there is a need to bias
30 the magnetization into a partially rotated state. This allows the magnetization to swing both positive and negative toward the hard axis and tends to avoid signal clipping or extreme non-linearities. In this anisotropic magneto resistance device the signal resistance varies with
35 the orientation angle of the magnetization relative to the current flow direction. Hence, a second layer of controlled hardness or anisotropy, when placed in contact or proximity of the first layer, can provide these

stabilizing or orienting effects. Likewise, in a spin valve or magnetic tunnel junction type magnetoresistive sensor the electron spin transport across an interface between the two stacked magnetic layers is effected via the relative orientation of the two magnetic layers. R. C. O'Handley's text, "Modern Magnetic Materials and Principles and Applications" discusses the structures and mechanisms of these magnetoresistive effects as well as other magnetic applications. This technology is now well developed for field sensors, magnetic data storage playback heads and is rapidly being developed for Magnetic Random Access Memory (MRAM). When the magnetization of the two magnetic layers is aligned the electrical resistance is minimized as spin transport across the interface is enabled or enhanced. For example, sensing an external field is accomplished by pinning one layer against rotation while leaving the other free to rotate or designing a structure where the two films are antiparallel and both of them are allowed to rotate toward a common direction as the applied field is increased. When the two layers are not aligned the available conduction spin states are not common and the conductivity is minimized. In these types of devices a variety of orientation geometries have been discuss in the literature, but for all of these the signal always depends upon the field induced magnetization orientation changes between the stacked magnetic layers. In some device geometries there are multiple magnetic layers, more than two, and the magnetoresistance effect is determined via the conduction between the multiple film interfaces. Hence the signal determining applied field or magnetic state is determined by the field induced angle difference between the pairs of layers. Clearly, the incorporation of layers in which the anisotropy can be better controlled is essential to improving these types of devices. The uniaxial symmetry broken magnetic layer technology invented, and discussed here, is of considerable value for each of these devices. A third, hard magnetic layer structure, antiferromagnetic, or synthetic antiferromagnetic layer constructed from hard

magnetic layers can be used to pin or exchange couple to one or more of the sensor magnetic layers. Control of the anisotropy of this layer is likewise of value in the device designs. By choosing the composition of two layers to have
5 differing anisotropy constants one layer essentially appears hard to rotate while the layer with the lower anisotropy constant can appear to be magnetically softer and freer to rotate. Later in this application, we will discuss another method of using the uniaxial symmetry
10 broken technology to orient hard disk magnetic media. This same approach can also be used to create or orient these hard or antiferromagnetic layer structures.

A new integrated circuit technology is emerging based upon the spin transport process and upon the orientation of
15 magnetic layers similar to those just discuss. This technology is sometimes referred to as spintronics. The most simple of these concepts is a magnetic spin transistor whose conduction is a function of magnetic spins injected into a current controlling junction region. The current
20 controlling concept is analogous to the carrier control or field control produced in a bipolar or field effect transistor. However, for spintronics, the orientation of a magnetic moment in the junction region of the device determines the spin dependent injection of the electronic
25 carriers. Hence, control of the orientation and the magnetic state of these layers is essential. It is envisioned that transistors can be constructed as well as electronic logic and state devices. Furthermore, because with proper design magnetic states can remain after
30 electrical power is removed, it is envisioned that these devices can possess memory functionality. These future electronic devices may come in unforeseen designs and functionality, but one aspect is assured. Control of the anisotropy energy density and anisotropy orientation will
35 be critical. The uniaxial symmetry broken mechanism can provide a methodology for controlling these angles and magnetic states.

Other magnetic circuit components, which can benefit from improved anisotropy control, include inductive properties. These are envisioned to include small traditional inductor geometries of magnetic materials in proximity of current carrying conductors. The permeability of the magnetic materials enable the additional storage of energy and so can be used to manipulate signal waveforms as in filters or to transfer or convert power to alternative voltage or current levels. Thin film structures would be especially useful at the microcircuit scale where high frequencies would normally eliminated the use of bulk magnetic materials. Both inductors and transformers are envisioned where serpentine pathways of layers of conductors and magnetic materials would be used to form the magnetic devices. The design needs to incorporate a considerable degree of magnetic flux path closure in order to achieve a reasonably high extrinsic permeability and, hence, efficiency. For linear signal transfer a near linear magnetic response is desirable, whereas for power transfer this is not as critical an issue. On the other hand, an analog signal mixer, as is commonly employed in radio communication, requires a non-linear response, which can be obtained from a uniaxial material via the easy axis response to a hard axis drive field in the presence of a bias field along the easy axis. However, important to each of these devices is that the magnetic losses be minimal. Otherwise the devices inject noise into the signal, tend to over heat as energy is dissipated in each cycle, and possess a limited frequency response. Clearly the uniaxial symmetry broken mechanism can provide a methodology for controlling the magnetic anisotropy and orientation and so enable these desirable device attributes.

Another magnetic field sensor, which utilizes the non-linear response function and benefits tremendously from a lossless process and high frequency operation, is known as the fluxgate. Fluxgates are commonly used to sense the earth's field and are extensively used in the well drilling process to monitor direction of the drilling process. This

is especially important for deep well drilling such as in the oil industry where the cost of pulling the drill is quit significant. Having a robust field sensor to provide information for avoiding hitting certain materials is quite valuable. There are a number of physical designs for these devices. However, they all work on the simple concept of driving one magnetic axis and inductively measuring the time rate of change of the magnetization induced by the external magnetic field along an orthogonal axis. A non-linear response yields a signal, which is proportional to both the external field and drive frequency; and, is a second harmonic to the drive field frequency. Since the response is proportional to the drive frequency, the signal amplitude, for a small applied field, can be increase considerably via the use of a high frequency drive. However, if the material has losses the drive frequency is limited and if the losses are due to the Barkhausen phenomena associated with domain wall motion then the measurement sensitivity is also noise limited. If the magnetic material has a lossless uniaxial response, as obtained by a uniaxial symmetry broken structure, then device can be operated to higher frequencies and with better sensitivity to external fields.

Another family of magnetic devices can be used for article surveillance and article identification and are commonly referred to as tags. Some of these devices operate on the principle of non-linear response and others operate on the principles of linear response employing energy storage for later radiation. The control of the anisotropy energy density and direction is essential in each. The non-linear response devices typically allow the switching of the magnetic state abruptly via wall motion, which generated large amounts of harmonics of the driving field, which are then detected via picked up via electromagnetic sensing antennas. In the simplest manifestation the non-linear response tag is simply a strip of very soft magnetic material with a uniaxial anisotropy

direction. This is easily produced utilizing our uniaxial symmetry broken material structures.

The linear tags work on the principle of coupling the magnetization orientation to the mechanical resonance of acoustic vibrations in the tag. This is done via the magnetoelastic properties, which is a complement property to magnetostriction, of the materials. For these materials a large magnetostriction coefficient is desired. When the magnetization is rotated away from the easy axis by a drive field along the hard axis the material either elongates or contracts depending upon the coefficient sign. This shape change is equivalent to an acoustic wave traveling along the tag. When the acoustic wave reaches the end of the material it tends to reflect backwards. Hence, if the tag is driven with magnetic field that oscillates with a period corresponding to the acoustic transit time between the ends of the tag, resonance is obtained. Likewise, if the drive field is fixed the length of the tag can be adjusted to match. For bulk material devices, where there is no substrate, the acoustic properties are determined by the acoustic properties of the magnetic material. However, if the magnetic material is laminated with another material or deposited upon a substrate then the acoustic propagation properties are determined by the combined properties of the magnetic material and the laminate or substrate. However, the acoustic resonance condition, of the combined set of materials, must still be matched to the magnetic field driving frequency. Tag detection occurs after the magnetic drive field is discontinued. Due to the acoustic resonance the tag continues to elongate and contract at the mechanical resonance frequency. Via magnetostrictive coupling to the acoustic vibrations the magnetization vector oscillates at the mechanical frequency, generating a magnetic field at the very specific mechanical resonance frequency, which can be detected by the detection antennas. As with the magnetoresistive field sensors the magnetoelastic tag device works best if a DC bias field is employed to tilt the magnetization from the easy axis. In

this manner the magnetization vector oscillates about the bias point, which avoid frequency doubling and improves efficiency and sensitivity. For thin films, deposited on thin Si substrates, or very thin substrates etched from Si structures, the high mechanical Q of the Si further improves the mechanical resonance process. A multitude of resonance frequencies can be utilized if substrates of different lengths are employed. The Micro-Electro-Mechanical structure, MEMS technology, is ideally suited to be incorporated in such a device when a multitude of unique tags are desired. Resonance beams of various lengths can be micro-machined on to a single substrate for a single device. The magnetoelastic material deposited on to all of the beams. Just as with electronic circuit technology many of these devices can be processed on a Si wafer in parallel. When this device is driven by an oscillating magnetic field only those beams with the length corresponding to the driving field frequency vibrate and store energy. By sweeping the drive frequency and then electronically listening via an antenna for the radiated magnetic field response each of the beams sequentially, or by applying an impulse field and then observing the various response frequencies, a very unique signal signature can be obtained. Various acoustical MEMS structures can be designed to allow a generic MEMS structure, which can be programmed after the devices are constructed. For example, via mechanical dampening of predetermined beams of specific lengths of a given device, a unique signal signature can be obtained. Hence, from a single MEMS processed Si substrate thousands of unique tag devices can be constructed. Hence, it is conceivable to label each product with unique tag device, each with a unique signal signature. Critical to any of these devices for operation is the control and orientation of the uniaxial magnetic anisotropy energy. The uniaxial symmetry broken magnetic material structure is ideal for this application.

Also, as discussed earlier, in hard disk media it is potentially valuable to have a soft keeper layer in close

proximity to the hard media layer. By using a uniaxial material and controlling the orientation of this layer relative to the recording track, and to the preferred direction of the hard memory layer, can yield improved areal densities via improved media noise, SNR, PW50, thermal stability, and overwrite properties. We have also found that the use of the orientation determining bcc-d variants as an underlayer can result in some control of the orientation of the hard magnetic layer.

By investigating the epitaxial growth of various film stacks on single crystal substrates we have found that there are some unique epitaxial relationships that have heretofore not been invented or utilized, as well as, some which enable unique characteristics when combined with the newly invented coupled variant structures.

We investigated three Si crystal substrate texture orientations, (100), (110), and (111) by first depositing epitaxial Ag on to these cleaned surfaces. Some epitaxial relationships are already known from U. S. Patent 6,248,416, Heng, Zangari, and similar publications where, for example, the growth of Cu(fcc) on Ag(fcc); permalloy(fcc) on Ag(fcc) or Cu(fcc); Co(fcc) on Cu(fcc) or permalloy(fcc); Cr(bcc) on Ag(fcc); Ti(hcp) on Ag(fcc); or Co(hcp) on Cr(bcc) or Ti(hcp) were studied extensively. However, nowhere in these works was any evidence presented of depositing bcc-b magnetic materials nor of the observation of any symmetry broken structures disclosed. We have observed symmetry broken structures by applying symmetry breaking methods and controlling the deposition process conditions. For example, we have used both deposition in an applied field and deposition at an angle on highly oriented hexagonal templates to obtain highly textured symmetry broken iron, iron compounds and iron alloys.

Also, we have found, as has been disclosed in the literature, that we can epitaxially grow one bcc-d on another and again on another while maintain the strong texture and orientational relationships between each of the

bcc-d on each of the three Si crystalline textures, $\langle 100 \rangle$, $\langle 111 \rangle$, and $\langle 110 \rangle$. There are also other relationships. Epitaxial fcc Ag, Au or Al always forms the same texture as the Si substrate surface. On this fcc-d substrate, a
5 number of epitaxial relationships can be obtained for the following layers. Upon these layers yet other epitaxial relationships are formed. When a bcc-d is grown on another bcc-d the same texture results. When fcc-d is grown on fcc-d the same texture results. However, when bcc-d materials
10 are epitaxially grown upon, denoted by "/", fcc-d materials of a give texture the following texture relationships result:

bcc-d texture/fcc-d texture

(100)/(100)

15 (110)/(111)

(112)/(110).

When fcc-d materials are epitaxially grown on bcc-d the following texture relationships result:

fcc-d texture/bcc-d texture

20 (100)/(100)

(111)/(110)

(110)/(112).

When hcp materials, such as Co alloys, are epitaxially grown on bcc-d the following relationships result:

25 hcp texture/bcc-d texture

($11\bar{2}0$)/(100)

($10\bar{1}1$)/(110)

($10\bar{1}0$)/(112).

When Ti is epitaxially grown on fcc the resulting Ti is hcp
30 and the following texture relationship can resulted:

hcp Ti texture/fcc texture

(0002)/(111).

However, the bulk phase diagrams of Co alloys show both an hcp phase at low temperatures and an fcc phase at somewhat
35 higher, but not extreme, temperatures and so it is possible to grow either hcp or fcc Co. When grown on an fcc underlayer we found the epitaxial Co to most commonly form the fcc phase and texture of the underlayer. Hence, it

behaved just as other fcc-d materials deposited upon fcc-d templates. However, when formed on bcc-d it formed the hcp phase and the texture relationships noted above resulted. When Co is epitaxially grown on another hcp it is hcp and
5 has the same texture and orientation as the underlayer hcp.

In each of these cases, except for the case of the six bcc-d variant structures under discussion, the in-plane orientational relationships were as denoted in U. S. Patent 6,248,416, and publications by Heng and by Zangari.
10 However, we have invented some new relationships involving oxides, which enable the construction of new devices. For the three fcc metals, Cr, Fe, and Al; and for selected alloys of these, we have found that the surface of the metals can be formed as oxides and then when the same metal
15 is then deposited upon this surface oxide the second metal layer sometimes epitaxially grows and assumes the texture and in-plane orientation nearly as though the first metal layer had not been oxidized. This statement was found to be true for all three of the Si substrate textures
20 investigate. However, the Si(111) is the most stable against oxidation followed by Si(100) followed by the least stable S(110). And so when growing epitaxial films, by our current techniques, usually the films that develop on Si(111) are of the highest quality and their resulting textures of the
25 following layers are also of higher quality. Hence, they are also the easiest to analyze. Because of the high degree of texture and lack of large angle grain boundaries, when these metals are exposed to oxygen they appear to passivate uniformly with a thin oxide layer and then cease
30 to be consumed into oxides. It is estimated that even for a reasonable exposure to atmospheric conditions the oxides can be as thin as 1 to 3 nanometers, but could also be grown thicker by direct epitaxial oxide deposition or with the addition of heat or moisture during a post deposition
35 exposure to oxygen. While extremely thin and difficult to measure each of these oxides may form the rhombohedral corundum crystalline phase commonly designate as prototype α -Al₂O₃. Interestingly enough α -Cr₂O₃ and α -Fe₂O₃ form a

continuous solid solution. It was found that when the first metal was a Cr alloy, then oxidized, and the second metal was Fe, that the second metal formed, to a limited degree, the same texture and orientation as the first. The same
5 was true when the Fe was the first metal and the Cr was the second. However, when the Fe was oxidized on its surface many of its magnetic properties were degraded. In addition, there are many additional elements that can be added to Cr, Fe, or Al and then be oxidized into the same crystal
10 structure. For example, both α -V₂O₃ and α -Ti₂O₃ phases exist. The α -V₂O₃ forms a solid solution with α -Fe₂O₃. Also limited amounts of Al can be added to Fe and the α -Al₂O₃ crystalline structure still results when oxidize. Likewise, it is known that FeTiO₃, MnTiO₃, CoTiO₃, NiTiO₃
15 can be added to α -Fe₂O₃. There are a large number of other metals that in small quantities can be added to the Cr, Fe, or Al and when oxidized still result in the α -Al₂O₃ structure. However, it should be recalled that in our samples the oxide is very thin and it was difficult to
20 determine the exact crystal structure. It is possible that more than one oxide structure can pass the texture and orientation of the first metal layer to the second. Fe and Cr both also form the cubic spinel structure, A₁B₂O₄, and there are many transition metals, and combinations of
25 metals, that can be added to these to still form the spinel. There is also the possibility that the oxides formed are more than one crystal structure. CrO₂ is a tantalizing possibility as its nearly half filled conduction band is essentially half filled with a single
30 magnetic spin orientation and so holds tremendous potential in a spin valve or tunneling structure. The corundum, however, is an excellent candidate for the oxide due to its stability and is commonly known to form on Fe, Cr and Al metal surfaces. While amorphous oxides also form, it is
35 hard to believe that the strong texture could be passed from one metal to the other via an amorphous oxide.

Furthermore, for the $\langle 110 \rangle$ bcc-d texture, we have found that the texture of the six variants discussed propagates the variant crystalline orientations if one bcc-d is placed directly on another metallic bcc-d or if it was placed upon the oxidized surface as just discussed. Hence, it is possible to develop a first symmetry broken uniaxial bcc-d layer, epitaxially grow a second symmetry broken bcc-d layer, oxidize it, and then grow yet another bcc-d layer on the oxide with the same texture as the first bcc-d. Some interesting magnetic arrangements can be constructed from these layer-to-layer texture relationships. If the two variant sets that have been epitaxially grown on top of one another, and have anisotropy energy constants of the same sign, then the easy axes are aligned. However, an interesting case arises if one layer has a positive and the other a negative anisotropy energy density constant. This results in the two layers having easy axes at 90 degrees to one another. This means that one orientation can be induced by the symmetry breaking mechanism and then by using a bcc-d with the opposite anisotropy constant sign the easy axes of the second layer is rotated 90 degrees with respect to the first bcc-d layer even without the use of a process that would normally be required to break the symmetry of the second bcc-d film. Furthermore, the thickness of a non-magnetic bcc-d layer, which can be placed between these two magnetic layers, can be used to adjust the magnetic exchange coupling between the layers. This can be adjusted from being strong to weak as this non-magnetic layer is made thicker. Adjusting this non-magnetic layer thickness and the thickness-saturation magnetization product of each of the two magnetic layers adjusts both the angle between the magnetization vectors and the in-plane orientation of the two magnetic layers. Hence, because exchange coupling strength between the two magnetic bcc-d layers can be controlled by selecting the coupling material or by controlling the coupling layer thickness the net magnetic easy axis orientation of the coupled film structure can be selected. These features are

useful in a variety of magnetic device designs as they allow the angle between the two magnetic layers, as well as the stiffness to changes in the angle, to be varied without the use of an additional hard or anti-ferromagnetic layer. This type of behavior is of use in device construction such as spin valves or spend dependent tunneling devices.

We also found that a strong (111) fcc-d texture develops when grown on the six variants of the bcc-d. Furthermore, the in-plane orientation assumes the same direction as the underlying hexagonal (hex) template. Hence, a layer structure such as

bcc-d(110)/fcc-d(111)/bcc-d(110)/hex(111)/Ag(111)/Si(111)

is viable, where either, or both, of the bcc-d layers are symmetry broken by the use of the symmetry breaking mechanism. (Here we use the notation that the film on the left of the "/" is deposited after the film on the right of the "/". From the tilt angle of the "/" it is easy to recall which layer is on top.) Of course this approach also applies when the substrate is polycrystalline via the grain orientation averaging process. Furthermore, when both layers are made uniaxial, the easy axes of the two magnetic bcc-d layers can be adjusted relative to each other by using the symmetry breaking mechanism at different angles for each layer. In another, example, a multiple layer epitaxial uniaxial layer structure can be formed as

bcc-d/Cr/O/Cr/bcc-d/hex(111)/substrate.

Again, here, the "/" symbol denotes a layer change, while the "O" layer represents the exposure of the prior film surface to oxygen or air. The bcc-d layers are magnetic, (110) textured, and symmetry broken. This Chromium example represents a non-magnetic bcc-d material that is epitaxially grown on the magnetic bcc-d layer and allows an oxide layer that does not contact the magnetic layer. This

structure allows the two magnetic layers to be electrically insulated from each other via the oxide layer and yet uniaxial behavior is obtained by utilizing the symmetry broken structure. Implied in this structure, but not shown, are the variant exchange coupling materials or layers. For example a magnetic hex (111) layer. In fact, it is not uncommon that the hex (111) layer structure is composed of more than one layer. Likewise, an fcc-d magnetic variant coupling layer, such as NiFe, can be placed on top of the final bcc-d layer.

For very thin oxide layers spin dependent electrical tunnel conduction devices have been constructed as a large effect magnetic field sensor. These devices, just as with the spin valve device, rely upon the electronic transport being sensitive to the relative orientation of two magnetic layers. However, in tunneling devices the current is directed perpendicular to the film plane and tunneling must occur through the oxide. Traditionally, these are usually constructed from fcc Co or permalloy magnetic layers with an Al oxide insulator layer. The use of an Al oxide as the insulator is widely published upon. However, deposition of the oxide has been hard to control and oxidation of a deposited, very thin polycrystalline Al oxide layer usually results in conduction pin holes. Sometimes the Al has been deposited as a metal and then post oxidized, but because of the limited quality of the underlying metal texture uniformity of the polycrystalline oxide is still a problem. The oxide layer thickness should only be about 1 to 2 nanometers in order for the tunneling energy barrier to be a reasonable value. Clearly the highly oriented films used to make the oxide structure listed above, where the Al is used to replace, or in addition to, the first Cr layer would benefit the spin dependent tunneling device. This is especially true when constructed upon the single crystal Si substrate. The uniaxial properties of the symmetry broken structure enable a considerably simpler device or construction process to be developed.

Yet another, example, of a multiple epitaxial set of layers allows both an oxide insulator, O to separate a conductor, such as fcc Ag or Cu, from the two magnetic layers

5

bcc-d/Cr/O/Cr/Ag/Cr/O/Cr/bcc-d/hex(111)/substrate.

For brevity, the texture and orientation relationships are not shown, but are understood to exist as discussed above.

10 When the Ag conductor carries a current, the two magnetic bcc-d layers guide the magnetic flux generated in a close path around the conductor (e.g. Ag). In this configuration each or both magnetic layers may be uniaxial with anisotropy directions equal or different. Providing the

15 relative magnetic permeability is greater than one and that lithographically defined current paths have been constructed this represents a compact electronic thin film inductor; and with the use of additional conductors and magnetic layers multiple turn electronic transformers can

20 be constructed. Inductance is proportional to the magnetic relative permeability. We have found that relative permeabilities exceeding 10 are quite viable and in some structures exceeded several hundred in our uniaxial, symmetry broken bcc-d film structures. Furthermore, for

25 thin metallic magnetic films the maximum operational frequency is either determined by the ferromagnetic resonance frequency or by eddy currents, if the structures are made thick. Our modeling indicates the it is quite reasonable to expect operational frequencies of a few

30 Gigahertz using Fe or Fe alloys. For uniaxial materials the resonance frequency is proportional to the root of the cross product of the saturation magnetization, M_s , and the anisotropy field, H_K . For linear uniaxial materials $H_K = 2K_u/M_s$. Hence, the ferromagnetic resonance frequency is

35 proportional to the anisotropy energy density, while the permeability is related to the inverse of this. For thicker films where the operational frequency might be limited by eddy currents, making chemical additions of only

a few percent of secondary materials, such as Si, N, C, or Al to Fe or FeCo can increase the resistivity substantially. For example 3% Si by weight in Fe results in a 5 fold decrease in conductivity. The penetration depth, or skin depth, of eddy currents is inversely proportional to the square root of the inverse permeability-conductivity-frequency product. Our estimates indicate that for the proposed geometry that the thickness of the magnetic layer will have to approach one or microns before the eddy currents limit the operational frequency. Hence, inductors, transformers, and sensors made utilizing these symmetry broken material structures should function in the Giga Hertz range.

It should be stated again that due to the variety of symmetry broken coupled variant sets and the fact that epitaxial growth should be viewed as happening on each individual grain of a polycrystalline material these texture relationships and the device concepts apply to both polycrystalline film structures and single crystal structures prepared on single crystal substrates such as Si. Likewise, other single crystal substrates can be used to produce the uniaxial symmetry broken thin film structures with exceptionally strong texture orientation, such as the commonly available Ge and GaAs, can be used provided that the texture is chosen to present the hex (111) template and that epitaxial thin film grown is obtained.

Yet another example of a device that can benefit from the symmetry broken structure is the growth of magnetic recording media. Here the hard magnetic layer is usually composed of hcp Co alloys such as CoCrTa, CoCrPt, CoCrPtTa, CoCrPtB, CoCrPtCuB and the like. In each of these the desired crystal structure is hcp to enable a high anisotropy energy density constant. Traditionally, hcp Co is grown on Cr or Cr alloy underlayers to control the crystalline texture and disk substrate is mechanically textured (scratched) along the recording direction to achieve a preferred orientation ratio to be greater than

one, when compared to that perpendicular to the recording direction. Having a hard disk recording media oriented preferential along the recording direction results in a higher coercivity and better thermal stability. It is well documented that upon a Cr (110) textured underlayer hcp Co alloys develop (10 $\bar{1}$ 1) crystalline texture. The texture is referred to as the Co alloy quad-crystal because there are four possible c-axis orientations on a single crystal Cr grain with (110) texture. This is not the ideal hcp texture because the hcp c axis, which is the magnetic easy axis, is tilted in or out of the film plane by about 28 degrees. Nevertheless, this texture has been used extensively for media and if it were oriented along the recording field direction it would be of considerable benefit. Because of the demagnetization field of thin films the magnetization vector lies in the projection of the c-axis into the plane of the film. This then reduces the possible number of in-plane projections of c-axis orientations on a single Cr (110) textured crystallite to two. They are at angles of + and - the $\arctan(1/\sqrt{2}) = 35.26$ degrees with respect to the bcc-d $\langle 100 \rangle$ directions. If one considers the bcc-d coupled variant pairs as template underlayers for epitaxial Co alloy growth then the symmetry broken films provide a template with preferred direction for the Co alloy to grow upon. This technique of selecting a textured and oriented underlayer provides a pathway to achieve hard disk oriented media. Consider, the coupled variant pair, $E_{2-a1c2}(\theta)$. This symmetry broken coupled variant pair has the its $\langle 111 \rangle$ crystal lattice directions, that are parallel to the (111) hexagonal template $\langle 110 \rangle$ directions, along the $\theta = 60$ and 120 directions. From Figure 5 it is easy to see the $\langle 100 \rangle$ directions of the two bcc-d cells. When a Co alloy quad-crystal is grown, the projection of the c-axis is approximately at $+40.3$ or -40.3 degrees with respect to the bcc-d $\langle 100 \rangle$ direction.

Table 1 lists all of the possible quadcrystal structure Co alloy in-plane easy axes directions when grown

on all of the six possible bcc-d variants discussed. An ideal, hcp $c/a = 2\sqrt{2/3} = 1.63$, crystalline unit cell was assumed for these angle calculations. As an example to understanding the calculations in Table 1 consider the first variant, a_1 . The $\langle 100 \rangle$ direction is listed as 65.26 degrees in Figure 5. Hence, the two in-plane Co c-axis projections would be at approximately 105.6 and 25.0 corresponding to the + and - entries in the first row of Table 1. Considering only the two variants of the symmetry broken $E_{2_{a_1c_2}}$ coupled variant of Figure 5 one can predict the Co alloy magnetocrystalline anisotropy directions which will be selected from those of Table 1.. These two bcc-d variants, whether coupled or not, would induce the eight possible Co alloy variants associated with obtaining two quadcrystals. There would be four for each of the two a_1 and c_2 bcc-d variants. However, because the out of plane demagnetization forces would drive the magnetization vector into the thin film plane, the four c-axes projections in the film plane would be 105.6 and 25 degrees for a_1 and 155 and 74.4 degrees for c_2 . Since the later two are closer to the 90 degree direction than the first two are to the 0 degree direction the net coercivity along the 90 degree direction is higher than that along the 0 degree position. Clearly, the recording tract should be oriented along the 90 degree direction to obtain an magnetic orientation ratio greater than one. Unlike the soft magnetic films it is desirable, for good SNR, that the four possible hcp cobalt orientations be individual grains, which are decoupled. For this reason it is best if a non-magnetic symmetry broken bcc-d provide the template for the Co alloy to grow. However, a magnetic bcc-d symmetry broken template can first be grown and then the non-magnetic variant template can be epitaxially grown on this. As discussed earlier, while not necessary in all media structures it may also be desirable to have a soft magnetic keeper layer below the oriented hard magnetic layer. The ideal easy axis direction for the keeper would be perpendicular to the recording track so that the stray fields from the recorded bits drive

the keeper layer magnetization along its hard axis. However, the easy axis for the E_{2_a1c2} example is also at the 90 degree position. As discussed earlier however, it is easily reoriented to the 0 degree position by choosing a material with a $K_1 < 0$. Due to the manufacturing constrains of a circular disk, the preferred symmetry breaking method is to deposit the bcc-d material radially on the round disk surface and at an angle relative to the substrate normal. Our findings are that a symmetry broken structure can be obtained even for polycrystalline films provided the (111) hexagonal template is highly textured and the deposition angle with respect to the substrate normal is constrained to be within $15 \leq \Omega \leq 75$ degrees from the normal. The incident angle is shown in Figure 12, where the arriving bcc-d material travels along -r, which is at an angle Ω with respect to a normal (z) to the substrate plane (x-y). When the deposition material arrives at grazing angle, 75 degrees, the efficiency of deposit decrease, but the symmetry breaking method is very effective. When the deposition angle is near the normal, 15 degrees, the deposition efficiency is superior but the symmetry breaking tends to diminish. The application of a magnetic field is also very effective symmetry breaking method, but a bcc-d layer with $K_1 > 0$ and a field directed along the track direction to achieve the E_{2_a1c2} are required. Due to the standard manufacturing process of simultaneous deposition of materials on both sides of the disk a radially directed or circumferentially directed field is not very conducive to incorporation in to modern hard disk media manufacturing process.

Table 1

Variant name	bcc-d <100> direction angle relative to template, $\theta=0$, <110> direction.	Two in-plane projected QuadCrystal projected c-axes angles relative to template <110> direction, $\theta=0$.	
		+	-
a1	65.264	100.529	30.000
a2	54.736	90.000	19.471

b1	5.264	40.529	-30.000
b2	-5.264	30.000	-40.529
c1	125.264	160.529	90.000
c2	114.736	150.000	79.471

Also, we found that by first depositing a metal
 5 wetting layer on a typical hard disk substrate surface that
 strong (111) texture could be obtain. The increased atomic
 surface mobility provided by the wetting layer allows the
 close packed texture to form from a hexagonal template
 material such as fcc Ag, Cu, Ni, NiFe or even a hcp Co
 10 alloy. A non-magnetic Co alloy of $Co_{1-x}Cr_x$, where
 $25_{at\%} < x < 50_{at\%}$ is preferred if exchange coupling of the bcc-d
 is not desired. It was found that a deposited amorphous
 metallic layer provided an excellent wetting layer.

In particular, in any application where a wet layer
 15 was desired, a amorphous compositions of NiP or materials
 that under bulk material equilibrium conditions would form
 C15 or C14 crystal structures seem to form excelled
 amorphous wetting layers when vacuum deposited. Examples
 of the C15 and C14 structures are $Cr_{1-x}Ta_x$ and $Cr_{1-x}Nb_x$, or
 20 $Fe_{1-x}Ta_x$ and $Fe_{1-x}Nb_x$ where $55 < x < 75$ atomic percent. It is
 noteworthy that in the Cr-Ta alloys the equilibrium phase
 diagram shows a high temperature to low temperature phase
 transition from a crystal structure of C14 to C15. It is
 believed by the author that the pairing of these complex
 25 equilibrium crystal structure enhance the propensity for an
 amorphous film to form in the non-equilibrium thin film
 deposition process. In each hexagonal atomic template
 material case, fcc-d or hcp, the use of these amorphous
 layers resulted in strong, (111) or (0002), texture
 30 respectively. In the case of these two C15 materials it
 was found that they could be exposed to oxygen and a
 reasonably strong texture still developed. Hence, the
 grain sizes of the hexagonal template layer and following
 layers could be made smaller in a process controlled
 35 manner.

While a cylindrical geometry is not needed for magnetic media that is not to be used in a disk format, it is needed for modern hard disk media. In order to achieve uniform and symmetric deposition, with preferred magnetic orientation around a disk substrate structure, a new vacuum sputtering cathode was devised. Figure 13 illustrates a cross-sectional view of a rod shaped sputtering target [15] composed of bcc-d material for deposition on to a disk substrate. A shield [16] and magnets [17] to facilitate a sputtering plasma at low Ar gas pressures surround the target. A disk substrate [18] is held on axis with the sputtering target, but at a distance to cause the sputtered material [27] to arrive at the disk surface along a radial direction and at an angle of incidence. Ar gas is introduced into the vacuum chamber via a pathway [26] between the target and a water cooled shield. This concentrates the sputtering gas [25] in the vicinity of the sputtering target and minimizes it in the vicinity of the disk substrate. The sputtering gas also provides a cooling mechanism to transfer heat from the target to the water cooled shield. A low gas pressure is desired to enable a scattering mean free path of the sputtered material to be comparable to, or longer than, the distance from the target to the disk substrate. This prevents the randomization of the direction of the sputtered material by avoiding gaseous collisions. Sputtering wears the target in a predefined and somewhat conical shape causing a deposition path from the target to the disk at the desired range of incident angles between 15 and 75 degrees. However, it has been found that a more narrow angle distribution centered about 45 degrees is preferred. The target rod diameter is small compared to the desired inside disk recording diameter and so the material leaving the target essentially follows a radial path toward the disk at all locations on the disk surface. In combination with the target surface profile shape, the disk to target distance is adjusted to set the deposition angle. To avoid non-uniformity produced by the magnetic fields of the sputtering cathode magnets the

magnet structure may be rotated around the target rod during the deposition process. While not needed for this current work it is envisioned that the target wears smoothly to a somewhat conical point allowing the target to
5 be advanced, relative to the magnets, toward the disk center along a normal path from the disk surface and center during the deposition of any one disk. This allows for adjustment of the deposition angle and deposition rate at various positions along the radius of the disk. Likewise,
10 the advancement of the overall position of the target relative to the magnets allows for continuous replacement of the worn target. This allows deposition on to many disks before the vacuum must be opened to replace the consumed targets. An interesting benefit arises from
15 spinning the sputtering magnets around the target. The magnetic fields from the magnets can be so arranged to provide a small, but non-negligible, magnetic field at the disk surface directed around the circumference of the disk. This directionally provides, a second symmetry breaking
20 mechanism, in addition to the deposition at an angle, an energy mechanism of deposition in a magnetic field to help promote bcc-d orientation of the magnetic material. For magnetic bcc-d material with $K_1 > 0$ the promoted easy axis from both symmetry breaking mechanism coincides.

25 Methods and structures to obtain an oriented hard Co alloy using the symmetry broken structures have been invented. It is also clear that these can be used to pin, via exchange coupling, the soft magnetic layers in many of the magnetic devices utilizing a soft magnetic layer.

30 To further confirm the information already described in this invention description a selected set of physically constructed materials and the analysis of these materials will be described in more detail.

A large number of thin film sample structures were
35 fabricated and analyzed. Four types of substrates were initially utilized: Si(111), Si(110), Si(100) and glass. The substrates were carefully cleaned via intensive washing with solvents such as acetone, toluene, and isopropyl

alcohol and then washed with detergent and hot water. They were then rinsed extensively with distilled water, isopropyl alcohol, distilled water and were blown dry. This removed all organic residues, water and most
5 extraneous metals from the substrates. The Si substrates were then etched for approximately 30 seconds in 49% Hydrofluoric acid and blown dry. The substrates were attached to a carrier and were quickly introduced into the vacuum system via a load lock system. The HF etch of the
10 Si is well known to leave a residual hydrogen bonding on the Si surface and temporarily prevent oxidation. The vacuum deposition system was both cryogenically and turbomolecularly pumped. A vacuum base pressure of 1×10^{-7} Torr or better was commonly obtained. Via a vacuum manipulator,
15 the substrate carrier was attached to one of three heated carrier positions to await thin film deposition.

The substrate carrier mount facilitated approximately a 7-inch radius planetary motion in a vertical plane. There were three possible positions for the substrate
20 carriers to be mounted; two on the planetary circle and one in the center on the planetary axis. Four magnetron sputtering target positions allowed up to four different materials to be deposited at various angles of deposition, each multiple times if needed, during one deposition
25 sequence. Three targets were arranged along the edge of an approximately 7-inch radius circle, which was aligned with the planetary positions of the substrate carrier positions. In this manner the three targets and the two concentric substrate holders could be brought into alignment to face
30 each other for normal angle deposition or the substrates could be rotated into any arbitrary position on the planetary circle for angular deposition. For example, one target could be located at the equivalent position of three
35 AM on the face of an imaginary clock and the substrate carrier, which was spaced an adjustable distance along the normal to the planetary plane, could be rotated to any position on the opposing imaginary clock face. The substrate carrier could be move away or toward the targets

over approximately a 7-inch swing, with a minimum spacing of less than 2 inches. The fourth target was located at the center of the planetary motion axis and in a plane with the other targets. Likewise, the third substrate carrier position was located at the planetary center in the substrate carrier plane. The carriers could be moved from a planetary position to the center and back via the mechanical manipulator in a time frame of less than one minute allowing layer to layer epitaxial growth.

10 The one and two inch diameter targets were usually small compared to the distance between the targets and the substrates. In a similar manner to that discussed for Figure 13, the Argon gas was introduced at the target surface allow a plasma while increasing the mean free path length in the rest of the chamber, and so to limit scattering, of the depositing material. A secondary gas flow such as N or H could also be introduced via the same path or another to allow interaction with the deposited layers. Each substrate carrier position was independently heated and monitored and the temperature could be varied from room temperature to about 350 degrees C. Except when experiments were performed on multiple substrate textures simultaneously, the temperature was selected to optimize the process for the particular single crystal substrate texture chosen. The substrates were heated prior to and during the deposition and to a limited degree, the temperature could be changed as each layer was deposited. The sputtering cathodes were DC powered with up to 500 watts available. The physical dimensions when a bcc-d was deposited from the center cathode to a substrate that was on the planetary circle allowed angles of deposition ranging from 75 to 33 degrees measured from the substrate normal. For smaller angles the substrate was mounted at 45 degrees to the substrate carrier and then the target to carrier angle was adjusted. Also, under some circumstances deposition at smaller angles could be accomplished by using a target and substrate position both on the planetary circle, but with the substrate rotated relative to the

target. Of course the distance between the target and the substrate could also be adjusted, but this did create a potential difference in deposition rate.

While a large number of deposition conditions were investigated it was soon found that working with layers that were 20 to 100 nm thick facilitated easier optical, magnetic and microstructure analysis. Hence, most of the bcc-d films were prepared at 20 nm to 200nm thickness. Most of the Ag layers on Si substrates were 40 nm thick and sometimes a second Ag or Cr layer or both was deposited as a final capping layer to prevent corrosion of the magnetic layers. Hexagonal template thickness varied and could be as thin as 1 nm and were made as thick as 40 nm. Typically a magnetic exchange coupling hexagonal template was kept minimally thick, 1 to 5 nm so that the bulk magnetic properties were not significant compared to the bcc-d magnetic properties. This facilitated easier interpretation of the magnetic data.

Commonly investigated materials included: Ag, Cu, Ni, NiFe, Al, Co and CoCrTa, which are fcc; Cr, Fe, Nb, NiAl, FeCo, which are all bcc-d, and Ti and CoCrTa, which are hcp.

Other bcc-d materials, which may be used to alloy with Fe or FeCo include W, Mo, V, Cr, Ti, Ta, Si, Al, N, Cu and B. Other fcc-d materials, which may be used include CoCr, Au, Pt, Rh, Pd, and Ir, while other hcp materials, which may be used includes Re, Ru, Gd, Ti and Tb . The materials of choice are chosen for there chemical, magnetic, or lattice matching properties. Considerable flexibility in atomic lattice constant is sometimes desirable to achieve epitaxial growth.

The following example notation will be used to designate the sequence of film layers that were prepare:

bcc/hcp/bcc-d/bcc-d<55,<xyz>/hex/fcc/Sub(tex).

Again, the notation is that the film on the left of the "/" is deposited after the film on the right of the "/". From

the tilt angle of the "/" it is easy to recall which layer is on top. The "tex" symbol represents the single crystal substrate texture used. The <55 represents the angle that the bcc-d is deposited and the number specifies the angle from the film normal. In general when used, the < symbol represents that a symmetry breaking mechanism is being employed. Likewise, if a magnetic field, H_a , is used to break the symmetry then the field is applied along the hexagonal crystal direction <xyz>. Likewise, when an angle of deposition is used to break the symmetry the in-plane direction of deposition material is also denoted to follow the <xyz> crystal direction.

Hence, as written in the example expression immediately above, fcc would be first deposited on the substrate at a normal angle, then the hexagonal template would be deposited at a normal angle, then at an angle to the plane normal of 55 degrees and parallel to the hex template <xyz> direction the bcc-d would be deposited. Then a second bcc-d would be deposited, then an hcp would be deposited and finally a bcc would be deposited last. If a surface was oxidized by exposure or an oxide was deposited then we would write that layer as a "O".

U. S. Patent 6,248,416 and the Gong and Zangari publications demonstrated that the textures and epitaxial relationships mentioned earlier could be grown on Si. This invention relates to the growth of six bcc-d variants rather than three, as was found by U. S. Patent 6,248,416 and Gong and Zangari, the exchange coupling of the variants, and in the symmetry breaking of the coupled variant sets so that they do not have equal variant volume weighting. That is, to obtain symmetry breaking, the three variants, in the Gong and Zangari publications, or the six variants, as describe here, are not balanced.

We first investigate the epitaxial growth of the bcc-d textures even though the surface of the first metal, when exposed to air, has formed an oxide. The key for this aspect of this invention to be assured is that the underlying crystallinity of the film exhibits extremely

uniform oriented texture and, while we do not address it here with physical evidence, we believe this leads to the underlying film being very dense. When a film has extremely high texture, then for some textures the grain boundaries are of low angle or there is little space between the grains. This assures that the film surface tends to passivate rather than oxidize down the grain boundaries to force the film from the substrate via expansion. This is extremely important for polycrystalline materials like Fe, which tend to oxidize badly.

First we provide a perspective for the degree of texture obtained by observing a θ - 2θ x-ray diffraction scan of a conventional polycrystalline film structure:

Hcp-CoCr₁₂Ta₂/Cr/glass

This is a classic, but simple structure sometimes sputtered for hard disk media. Upon examination of the X-ray scan we found that two peaks exist. Cr(110) had a peak height of about 150 counts and the resulting Co-alloy quad-crystal (10 $\bar{1}$ 1) peak height of 25 counts and a uni-crystal (10 $\bar{1}$ 0) peak height of 40 counts resulted. The base line was rather noisy and there were no other discernable peaks. We use the same scan time and X-ray anode current and voltage for all of the θ - 2θ X-ray diffraction scan examples to be discussed.

Four samples were made simultaneously each with a different substrate: glass, Si(100), Si(110), Si(111) where the Si was cleaned and HF treated as mentioned before. They were introduced into the vacuum system and quickly heated to approximately 165 degrees C before the first Ag deposition was made. The layer composition was:

Hcp-CoCr₁₂Ta₂(58nm)/Fe(37nm)<45/O/Fe(37nm)<45/Ag(40nm)/sub

Where the value given in the parenthesis is the nominal film thickness in nanometers. There was an oxidation exposure step in the process. This required that

after the first two film depositions the sample be briefly removed from the vacuum system. In the following table the entries are listed as (X-ray counts)/(X-ray texture)

99C15-19-2: CoCr ₁₂ Ta ₂ (58nm)/Fe(37nm)<45/O/Fe(37nm)<45/Ag(40nm)/sub			
CoCr ₁₂ Ta ₂ (58nm)/	Fe(37nm)/	Ag(40nm)	Substrate
50/(10 <u>1</u> 1)	200/(110)	600/(111)	glass
1450/(11 <u>2</u> 0)	3500/(100)	1.6x10 ⁴ /(100)	Si(100)
1600/(10 <u>1</u> 0)	1400/(112)	9000/(110)	Si(110)
600/(10 <u>1</u> 1)	1.4x10 ⁴ /(110)	>10 ⁵ /(111)	Si(111)

5

Other than from the single crystal substrate or second order diffraction peaks there were no other diffraction peaks observed indicating the strong singular texture orientation of each layer. The textures behaved just as predicted and discussed earlier. These results confirm that bcc-d Fe grows with the same textures as Cr when deposited on a hexagonal template or each of the other single crystal textures. Since the second layer Fe would have had the same peaks as the first, the absence of any additional peaks, along with the strength of the peaks, is a good indicator that the texture, even when the second layer of Fe is grown on the oxidized surface is identical to the that of the first layer. However, since the peaks would collinear with the first film peaks there remains the question whether as to whether or not there are any second layer peaks at all. The hcp-Co alloy peaks and their strength compared to those on glass tell us that epitaxial growth of the second layer of Fe on the Fe-O was very good and provided an excellent template for the Co alloy film growth. This to confirms the texture of the second Fe layer is identical to that of the first layer of the Fe. The epitaxial growth over the oxide is confirmed for all of these textures, including the use of glass as a substrate.

25

This later case is largely due to the excellent texture of the Ag(111) on the glass. In separated experiments the strength of the Ag(111) texture has been seen to improve several fold over the value of that directly on glass when
5 a wetting layer of amorphous Cr_{35}Ta was deposited upon the glass prior to the Ag. It also should be stated that the lattice match between Cr or Fe, which has virtually the same atomic lattice spacing, and Ag is not particularly good. Since another hexagonal template material (fcc-d or
10 hcp) could epitaxially grown on Ag better than the bcc-d we investigate this. Hexagonal templates of Cu, Ni, NiFe, and a combination layer fcc-Co on top of Cu, when place upon the Ag templates were all found to produce a stronger Fe or Cr texture.

15 To further investigate the oxide located between two different materials the following film structures were constructed:

99C15-19-3: CoCr ₁₂ Ta ₂ (58nm)/Cr(40nm)/O/Fe(37)<45/Ag(40nm)/sub				
CoCr ₁₂ Ta ₂ (58nm)/	Cr(40nm)/	Fe(37nm)/	Ag(40nm)	Substrate
50/(1010) 25/(1120)	50/(100)	250/(110)	>600/(111)	glass
1450/(1120)	2900/(100)	1900/(100)	1.8x10 ⁴ /(100)	Si(100)
75/(1010) 30/(1120)	750/(112)	700/(112)	1.3x10 ⁵ /(110)	Si(110)
40/(1120)	30/(100)	6500/(110)	1.2x10 ⁵ /(111)	Si(111)

From this table we can see that for Si(100) epitaxy over the oxide was excellent, however there does not appear to be much, if any, epitaxy via the oxide when Si(111) is used. It appears the the Cr epitaxy on the Fe-O was quite good for the Si(110) however the Co texture was not particularly impressive. To within experimental error the time and temperatures used to prepare this sample were the same as were used on the Fe-O-Fe samples (99C15-19-2) discussed just before this one.

The roles of Cr and Fe were interchange and the experiment repeated.

99C15-19-4: CoCr ₁₂ Ta ₂ (58nm)/Fe(37nm)/O/Cr(40)<45/Ag(40nm)/sub				
CoCr ₁₂ Ta ₂ (58nm)	Fe(37nm)/	Cr(40nm)/	Ag(40nm)	Substrate
35/(1120)	25/(100)	150/(110)	300/(111)	glass
1800/(1120)	1600/(100)	4000/(100)	1.1x10 ⁴ /(100)	Si(100)
60/(1010) 20/(1120)	?(112)	1350/(112)	5000/(110)	Si(110)
100/(1011)	?(110)	3.1x10 ⁴ /(110)	8.5x10 ⁴ /(111)	Si(111)

15

Here we see that the Cr grew highly textured on the Ag and the Fe(100) grew well on the Cr-O. However it is not clear if much of the Fe (112) grew as the peak was broad and the Cr and Fe peaks lie extremely close together and would be difficult to observe. It appears that there was some enhanced epitaxial growth of the Fe(110), but it was difficult to discern as the Cr(110) was over whelming. Nevertheless the Co (10 $\bar{1}$ 1) peak was the only one present. In the Si(110) case the fact that any Co (10 $\bar{1}$ 0) texture appeared is strong evidence that some of the Fe was (112) texture.

Overall we see that for the particular deposition temperature, deposition rate, and in general these particular processing conditions it was found that Fe/O/Fe epitaxially grew for all three of the Si textures. We found similar results for Cr/O/Cr. For the Cr/O/Fe/Ag/Si it appears that Cr(100) texture grew well and the Cr(112) texture grew somewhat. The Cr(110) texture did not grow well. Hence, it appears the bcc-d epitaxially grows well on the oxide of itself. Also the bcc-d (100) texture appears to grow well even on other members. The (110) and the (111) textures grow, but not as enthusiastically. We varied the processing temperature for the deposition of Ag on Si and found that the ideal temperature varied considerably with the Si orientation. The processing latitude was even more dramatic. Si(111) substrates could be processed at higher temperatures before it oxidized and this improved some of the later depositions. The Si(100) textured substrate had the next broadest process temperature range and the Si(110) substrate had the narrowest and least tolerable process temperature range. This is logical as this surface is the most unstable for an fcc Bravais lattice or for an fcc-d lattice. Each substrate texture had its own optimum temperature and temperature range and the particular temperature was dependent upon the deposition rate and humidity during the time interval just prior to placing the substrate in the vacuum system. We found the HF etched Si surface quality

to be very dependent upon the environment prior to the Si reaching the vacuum system. Hence, optimizing all of the conditions simultaneously were difficult, but when it was done the results showed that epitaxial growth through the oxide on the other Si textures is significantly improved. Fortunately the (111) surface is the most stable for the hexagonal template materials and this allowed for larger latitude of temperature and deposition rate. This allows the optimization of the temperature for the oxide to be grown for each material combination.

Evidence of the six variant structures is demonstrated next. In fact, the E_{2-a1c2} variant set is shown. The following film structure was made by angle of incident deposition. Two samples were prepared simultaneously, but with slightly different angles of deposition, different thicknesses, but most importantly at different angles relative to the template lattice plane direction. This was accomplished by mounting two substrates on the same carrier, but at different hex template angles. The deposition direction was along the $\langle 110 \rangle$ for sample 0909-6 and along the $\langle 112 \rangle$ template direction for sample 0909-5. The structure is defined here:

Sample name: 0909-6
Ag(200nm)/Cr(40nm)/Fe(37nm) $\langle 45 \langle 110 \rangle$ /Cu(10nm)/Ag(40nm)/Si(111)

Sample name: 0909-5
Ag(200nm)/Cr(40nm)/Fe(60nm) $\langle 55 \langle 112 \rangle$ /Cu(10nm)/Ag(40nm)/Si(111)

It should be pointed out that the Cu hexagonal template is non-magnetic and so does not provide the exchange coupling needed to cause uniaxial M-H curves. Nevertheless, it is shown below that the needed variant pair was obtained. If the Cu were replaced with fcc-Co, Ni or NiFe, or if the Ni or NiFe were deposited on top of the Fe then the coupled pair would be exchange coupled. In this example, the final thick Ag and Cr layers were applied to avoid the possibility of corrosion of the Fe after the

sample was made. It was found that these layers, especially the Cr was very effective at preventing corrosion. The sample was stored for one year without obvious corrosion of the Fe. We conclude this based upon
5 the fact that while Fe magnetic properties are very sensitive to oxidation they did not change. The protective Ag layer did discolor some.

A X-ray pole figure analysis was performed. This test allows one to rotate the sample while setting the x-ray
10 diffraction angle to a specific reflection plane. The Fe is (110) textured so the (100) planes are tilted at 45 degrees to the surface of the film. The sample was tilted to 45 degrees and then θ - 2θ was set to reflect from the (100) crystal planes. The sample was then rotated through
15 360 degrees and the signal was monitored. According to Figure 3, as espoused by Gong and Zangari, if there are only three possible variants then there should be three peaks observed for each 180 degrees of rotation and they would be equally spaced at 60 degree intervals. These
20 would repeat during the second 180 of rotation. However, if there are six variants as advocated in this invention then Figure 5 is of relevance and six peaks would be seen per 180 degrees of rotation; and 12 would be seen during the full 360 degree rotation. If the variants are equally
25 weighted by volume of material and the substrate were perfectly cut then all the variants of the set would be seen. We have observed both types of sets. Hence, not all samples have the potential of being represented by the energy equations associated with the six variant set. The
30 Gong and Zangari three variant set is the most commonly observed as the energy mechanism for rotating the crystal planes and then splitting the diffraction peaks is non-trivial to accomplish. Figure 14 shows the pole figure analysis for sample 0909-6. Careful analysis of the data
35 shows the peak height of the a1 and the c2 variants are more than a factor of two higher than any of the other variant diffraction peaks. However, the relevant quantity of measure is the area under the peak curve and this is a

very time consuming and difficult measurement, but shows a considerable larger fraction of material being in these two variants. In theory the scan should only show the Fe(100) diffraction peaks as the θ - 2θ angle was set specifically for this crystal plane. However there is a Ag (220) diffraction line near by and because the peak is so very strong the tails of these six peaks also show. Likewise, there is slight evidence of the very strong Si(400) peak. The angle between pairs of the six bcc-d variants was experimentally determined to be $2\delta = 2(5.26)$ degrees, as discussed at length earlier. However the angle between the peaks in the pole Figure 14 is smaller because of the coordinate frame rotations required to go from the (110) and (100) planes. In the figure the spread between any pair of peaks should be $\sim 2(3.74) = 7.5$ degrees. This is exactly what is observed. This data is strong evidence of both the six variant concepts and of the symmetry breaking mechanism. For sample 0909-5 where the deposition direction projection was the $\langle 112 \rangle$ direction along the hexagonal template the results were not as clearly defined. It appeared that there were again two dominant variants of the six. However they were represented by $E_{2-a_1b_2}$. For reference, the pole figure peaks for these variants, a_1 and b_2 , along with the other four, are also noted on Figure 14 while the corresponding bi-crystal energy curve for $E_{2-a_1b_2}$ was illustrated in Figure 11. Clearly, even if magnetically coupled, this variant pair does not yield uniaxial behavior at all. Hence, angle of incident deposition along the $\langle 112 \rangle$ template direction yields an entirely different result. In summary, when deposited onto a (111) textured single crystal substrate and using angle of deposition along the directions just described as a symmetry breaking mechanism, then one set of variants yields uniaxial behavior and the other set does not. To achieve uniaxial behavior via the symmetry breaking method requires proper orientation of the template and deposition direction. However, in both orientation cases the variant symmetry was broken.

It was found that even when a hexagonal template of non-magnetic material was employed it was possible to have exchange coupled variants and to obtain the uniaxial symmetry broken behavior. Samples of structure just as described when processed at different deposition rates and temperatures yielded different grain sizes and magnetic exchange between them was possible. It was also found that deposition at an angle could result in grain morphologies, which possessed particle shape anisotropy. However, by studying the films deposited along both the $\langle 112 \rangle$ and $\langle 110 \rangle$ hexagonal template directions it was found that the symmetry breaking process and uniaxial behavior caused by the crystalline orientation still existed along with the anisotropy associated with grain shape effects. Using the proper, strongly textured and matched atomic lattice spacing, hexagonal template to induce good epitaxial growth significantly helped to minimize particle shape effects.

A similar set of experiments was conducted with a magnetic hexagonal template and an applied field. That is, rather than using the angle of incident deposition as the symmetry breaking mechanism, a magnetic field was used. Ni was used at the hexagonal template and placing permanent magnets on the substrate carrier in the vicinity of the substrates generated an applied field in the 100 Oe range. The sample structure was:

Ag(200nm)/Cr(40nm)/Fe(50nm) $\langle 45 \rangle$ /Ni(5nm)/Ag(40nm)/Si(111)

The resulting variant set for the case when the field was applied generally along the hexagonal template $\langle 112 \rangle$ direction was $E_2\text{-}a_1c_2$, whereas, if the field were applied generally along the $\langle 111 \rangle$ direction then one of the complement four-element variant sets with uniaxial behavior was selected. However, it was difficult to observe by x-ray pole figure measurement techniques, exactly which set of four variants dominated. Nevertheless, from the magnetic response it was determined to be one of the symmetry broken uniaxial sets. Hence, unlike the angle of

incident deposition technique, when the symmetry is broken using a magnetic field mechanism, uniaxial behavior is obtain when the field is directed along either of the hexagonal template crystal directions; $\langle 110 \rangle$ or $\langle 112 \rangle$.

5 While the hard axis permeability, when the symmetry breaking field was along the $\langle 110 \rangle$ direction, which caused the four variant set to appear, should have been higher than for the two variant set it was difficult to say this was the case. The coercivity was higher and the uniaxial

10 magnetic response function was not as ideal. These magnetic effects indicate the greater difficulty in preparing the four variant set where the processing latitude is more sever. The magnitude of the applied field varied over some of the samples prepared and very small, ~

15 1.5 to 2 mm, size segments of the samples were studied for their individual magnetic properties. Hence, these segments represent individual samples prepared with various applied magnetic field magnitude and direction. From these measurements it was estimated that the magnetic field

20 symmetry breaking mechanism was causing an observable degree of symmetry breaking for fields as small as 10 Oe. It should be mentioned that the applicant became concerned that the earth's magnetic field or some other stray magnetic field might be influencing the findings. The stray

25 fields were measured in the vicinity of the substrate carrier and found to be less than or approximately one Oe, which was comparable to the measured earth's magnetic field intensity. Nevertheless, experiments were conducted where the sample substrate was mounted to a sample carrier

30 containing the applied field magnets. Then during the deposition process the substrate carrier and, hence, the applied field magnets and sample were rotated together. This provided a constant applied field while the rotation provided an averaging mechanism for any stray applied

35 fields. Likewise, a similar experiment was carried out with out any applied field, but employing the angle of incidence symmetry breaking technique. For both symmetry breaking techniques the magnetic results were found to be unchanged

from samples prepared without the rotation process. Hence, applicant was convinced that stray fields were not playing any significant role in the experimental results.

We anticipate that achieving the four variant uniaxial results would be much easier to obtain if we had a better vacuum system and did not have to passivate the Si via H bonding from the HF-etching technique. It is well known that the silicon oxide sublimates from Si at about 850 degrees C leaving behind a clean Si surface. If the process were preformed in an ultra high vacuum system a cleaner substrate would be available for the initial Ag deposition. We anticipate this would result in higher quality films and film structures and better control of the overall process.

Magnetic response curve measurements were made for these samples. Because the magnetic field from the permanent magnets was not perfectly uniform over the sample the symmetry breaking mechanism was not perfectly aligned with the hexagonal template $\langle 112 \rangle$ direction. Nevertheless, it was estimated that the field direction did not vary by more than 10 degrees over the measured sample and it was in much better alignment over the majority of the sample. This was sufficiently aligned to demonstrate the symmetry breaking mechanisms via the magnetic response curves. Figure 15 shows the M_x and M_y versus H_x response of one of the two variant exchange coupled, uniaxial symmetry broken samples using the structure:

Sample name: LS1425_2cx

Ag(200nm)/Cr(40nm)/Fe(50nm) $\langle H \langle 112 \rangle \rangle$ /Ni(5nm)/Ag(40nm)/Si(11
30 1)

The coercivity of the Ni alone was measured and found to be comparable to the 10 Oe observed for the hard axis loop of this sample. Hence, it is observed that exchange coupling the film variants is not sufficient to achieve a low coercivity. The exchange coupling layer must also be magnetically soft. Permalloy, a well known soft NiFe alloy was substituted for the Ni and the coercivity was found to

drop to less than 1.0 Oe. However, interestingly, even using the Ni template the sample exhibited lossless behavior if high drive fields were not used to drive the sample all the way to saturation. In a separate measurement
5 from Figure 15, the sample was first driven along the easy axis to remove most of the domain walls and then driven along the hard axis, but only to approximately 80% of the field needed to saturate the sample. This minor loop response showed coercivities of less than one Oe, which was
10 approximately the resolution limit of the measurement instrument. Figure 15 clearly shows a non-linear uniaxial type of response function when the sample was driven into saturation and uniaxial result similar to the ideal of Figure 2. This statement applies both to the narrow hard
15 axis loop, M_x vs. H_x [19] and the somewhat quadratic M_y easy axis [20] response. The hard axis loop, M_x , illustrates the potential near linear behavior, while the M_y response illustrates the non-linear response.

Other, similar composition and layer structured,
20 samples made by angle of incident deposition showed no measurable coercivity or losses for the minor hard axis loop. In these cases permeabilities ranging from 80 to over 1000 were observed.

Hard disk media samples were prepared using a
25 production hard disk media vacuum system, but by a similar, but less ideal than previously described, angle of incidence deposition technique. The source bcc-d material was delivered in a radial pattern over the entire disk at angles varying over the surface of the disk. This was
30 accomplished by depositing from a standard sputtering target but by masking a large portion of the disk with a circular mask with a hole in the center. Hence, the sputtered material exited the hole at an incident angle and essentially radially. Several samples were prepared with
35 layer constructions made as follows:

LSSDK-0505-1

Cr(40nm)/Fe(40nm)~45/Cu(20nm)/Cr₃₅Ta(20nm)/glass-ceramic

and

LSSDK-0505-2

CoCrPt (20nm) / Cr (40nm) \sim 45 / Cu (20nm) / Cr₃₅Ta (20nm) / glass-ceramic

5 The magnetic properties of the first sample (Fe) exhibit anisotropic behavior with an OR of greater than one and provided confidence to proceed with sample 0505-2. The Fe was changed to Cr so as to not obscure the magnetic results of the harder CoCrPt alloy with the properties soft
10 Fe. Of the samples prepared OR ranging from 1.05 to 1.15 were obtained when dividing the circumferential coercivity by the radial. This is as desired, and the over all coercivity was in the range of 2500 Oe. Because of the polycrystalline hexagonal template layer and the mixed
15 amorphous and ceramic substrate has a very large interfering set of diffraction peaks no X-ray data was taken.

Those of ordinary skill in the art will appreciate that a number of modifications and variations can be made
20 to specific aspects of the material structures, devices, method and apparatus of the present invention without departing from the scope of the present invention. Such modifications and variations are intended to be covered by the foregoing specification and the following claims.

25

1. A magnetic material structure comprising:
a substrate;
at least one bcc-d magnetic layer forming a symmetry
broken structure; and
5 at least one layer providing a (111) textured
hexagonal atomic template disposed between said substrate
and said symmetry broken bcc-d material structure.
2. A magnetic material structure comprising:
10 a substrate;
at least one bcc-d magnetic layer forming a uniaxial
symmetry broken structure; and
at least one layer providing a (111) textured
hexagonal atomic template disposed between said substrate
15 and said symmetry broken bcc-d material structure.
3. The magnetic material structure recited in claim 2
wherein said substrate is single crystal.
- 20 4. The magnetic material structure recited in claim 2
wherein said substrate surface is amorphous or
polycrystalline.
5. The magnetic material structure recited in claim 4
25 wherein said amorphous surface is formed from an alloy of
NiP, $\text{Cr}_x\text{Ta}_{1-x}$, $\text{Cr}_x\text{Nb}_{1-x}$, $\text{Fe}_x\text{Ta}_{1-x}$, or $\text{Fe}_x\text{Nb}_{1-x}$ and $55 < x < 75$.
6. The magnetic material structure recited in claim 4
wherein said amorphous surface is oxidized and is formed
30 from $\text{Cr}_x\text{Ta}_{1-x}$, $\text{Cr}_x\text{Nb}_{1-x}$, $\text{Fe}_x\text{Ta}_{1-x}$, or $\text{Fe}_x\text{Nb}_{1-x}$ and $55 < x < 75$.
7. The magnetic material structure recited in claim 2
wherein the layer forming said hexagonal atomic template is
formed from a fcc-d or hcp crystalline material.
35
8. The magnetic material structure recited in claim 2
wherein the layer forming said hexagonal atomic template is
magnetic.

9. The magnetic material structure according to claim 2 further comprising
at least one second magnetic layer wherein the second
5 layer forms a hexagonal atomic surface.
10. The magnetic material structure according to claim 2 further comprising
at least one second bcc-d layer.
10
11. The magnetic material structure according to claim 2 further comprising
at least one second magnetic bcc-d layer.
- 15 12. The magnetic material structure according to claim 2 further comprising
at least one second bcc-d layer wherein the
crystalline orientation of the second layer is epitaxially
determined by the first bcc-d layer.
20
13. The magnetic material structure according to claim 2 further comprising
at least one second bcc-d layer; and
at least one second hexagonal (111) template wherein
25 said hexagonal template is disposed between the first bcc-d
layer and the second bcc-d layer.
14. The magnetic material structure according to claim 2 further comprising
at least one second magnetic bcc-d layer; and
30 at least one oxide layer between said first bcc-d
layer and said second bcc-d layer.
15. The magnetic material structure according to claim 2
35 further comprising
at least one second and third non-magnetic bcc-d
layers;
at least one fourth magnetic bcc-d layer; and

at least one oxide layer between said second non-magnetic bcc-d layer and said third non-magnetic bcc-d layer wherein second and third non-magnetic layers are disposed between said first and fourth magnetic bcc-d layers.

16. The magnetic material structure according to claim 2 further comprising

at least one second and third non-magnetic hexagonal template layers;

at least one fourth magnetic bcc-d layer; and

at least one oxide layer between said second non-magnetic layer and said third non-magnetic layer wherein second and third non-magnetic layers are disposed between said first and fourth magnetic bcc-d layers.

17. The magnetic material structure recited in claim 2 wherein said symmetry broken bcc-d is composed of Fe or FeCo or an alloy of Fe or FeCo.

18. The magnetic material structure recited in claim 2 wherein said symmetry broken bcc-d is composed of an alloy of Fe or FeCo and one or more of the elements Cr, Si, N, C, Cu, Nb, and Al.

19. The magnetic material structure recited in claim 2 wherein said symmetry broken bcc-d is composed of an alloy of Fe or FeCo and one or more of the elements Al, B, Cr, C, Cu, Ni, N, Nb, Mo, V, Si, Ta, Ti and Nb.

20. The magnetic material structure recited in claim 2 wherein the layer material forming said hexagonal atomic template is composed of Ag, Cu, Ni, fcc-Co, NiFe, Al, hcp-Co, or Ti, or their alloys.

21. The magnetic material structure recited in claim 1 wherein the layer material forming said hexagonal atomic template is composed of Ag, Al, Au, Cu, fcc-Co, fcc-CoCr, Ir, Ni, NiFe, Pt, Rh, Pd, hcp-Co, Gd, Re Ru, Tb, or Ti, or
5 their alloys
22. The magnetic material structure according to claim 2, further comprising
at least one second bcc-d layer; wherein first and
10 second bcc-d layers are magnetic with anisotropy energy density constants of opposite sign.
23. The magnetic material structure according to claim 2, further comprising
15 at least one second bcc-d layer;
at least one third bcc-d layer;
wherein first and third bcc-d layers are magnetic and second bcc-d layer material is antiferromagnetic.
- 20 24. The magnetic material structure according to claim 2 further comprising
at least one second magnetic symmetry broken bcc-d layer; and
at least one second hexagonal (111) template wherein
25 said second hexagonal template is disposed between the first bcc-d layer and the second bcc-d layer.
25. The magnetic material structure according to claim 2 further comprising
30 at least one Co alloy magnetic hcp layer; wherein Co alloy has a (1011) crystalline texture.
26. A magnetic material structure comprising:
a (111) textured single crystal substrate; and
35 at least one bcc-d magnetic layer forming a uniaxial symmetry broken structure; wherein the bcc-d magnetic layer is disposed upon the (111) textured substrate.

27. A magnetic material structure comprising:
at least one (111) textured hexagonal atomic template;
and
at least one (110) textured bcc-d magnetic layer
5 forming a symmetry broken structure disposed upon said
(111) textured hexagonal atomic template.
28. A magnetic device incorporating therein the magnetic
material structure of claims 1, 2, 26 or 27.
10
29. The magnetic device recited in claim 24 wherein the
device is a magnetic data storage system.
30. The magnetic device recited in claim 24 wherein the
15 device is a data storage magnetic recording transducer.
31. The magnetic device recited in claim 24 wherein the
device is a data storage magnetic playback transducer.
- 20 32. The magnetic device recited in claim 24 wherein the
device is a data storage magnetic recording media.
33. The magnetic device recited in claim 24 wherein the
device is a data storage magnetic recording media
25 incorporating an oriented soft magnetic layer.
34. The magnetic device recited in claim 24 wherein the
device is data storage magnetic recording media
incorporating an oriented hard magnetic layer.
30
35. The magnetic device recited in claim 24 wherein the
device is a data storage magnetic random access memory.
36. The magnetic device recited in claim 24 wherein the
35 device is an article surveillance tag.
37. The magnetic device recited in claim 24 wherein the
device is a magnetoelastic article surveillance tag.

38. The magnetic device recited in claim 24 wherein the device is a magnetoelastic multiple harmonic generating article surveillance tag.
- 5
39. The magnetic device recited in claim 24 wherein the device is a non-linear response multiple harmonic generating article surveillance tag.
- 10
40. The magnetic device recited in claim 24 wherein the device is an electronic circuit inductive component.
41. The magnetic device recited in claim 24 wherein the device is a signal mixing electronic circuit component.
- 15
42. The magnetic device recited in claim 24 wherein the device is a magnetic fluxgate sensor.
43. The magnetic device recited in claim 24 wherein the device is a anisotropic magnetoresistive sensor.
- 20
44. The magnetic device recited in claim 24 wherein the device is a spin valve magnetoresistive sensor.
- 25
45. The magnetic device recited in claim 24 wherein the device is a magnetic tunnel junction magnetoresistive sensor.
46. The magnetic device recited in claim 24 wherein the device is an electronic circuit inductive transformer component.
- 30
47. The magnetic device recited in claim 24 wherein the device is an electronic spin tunneling digital logic circuit component.
- 35

48. An magnetic recording media device comprising;
substrate;
at least one hard magnetic recording layer;
at least one (111) textured hexagonal atomic template;
5 and
a soft magnetic keeper layer composed of at least one
bcc-d magnetic layer forming a uniaxial symmetry broken
structure disposed between said hexagonal atomic template
and said hard magnetic recording layer.
10
49. An magnetic recording media device comprising;
substrate;
at least one (111) textured hexagonal atomic template;
at least one symmetry broken (110) textured bcc-d
15 layer; and
at least one oriented hard magnetic recording layer;
where in said bcc-d layer is disposed between said hard
magnetic layer and said hexagonal atomic template and said
hexagonal atomic template is disposed between said bcc-d
20 layer and said substrate.
50. An apparatus for depositing a disk media layer
structure comprising;
a rod shaped sputtering target of diameter smaller
25 than the inside disk recording diameter;
a shield and permanent magnet structure surrounding
said sputtering target;
a gas pathway between said sputtering target and said
shield; and
30 a gas exit near one end of the sputtering target;
wherein the apparatus delivers vacuum disposed
material symmetrically from near an end surface of said
target rod in a generally radial direction to the hard disk
media substrate at an angle of incidence angle of between
35 15 and 75 degrees.
51. An apparatus recited in claim 50

wherein said disk media layer structure is an oriented soft magnetic keeper layer.

52. An apparatus recited in claim 50

5 wherein said disk media layer structure is an oriented media underlayer.

53. A method of producing a symmetry broken bcc-d structure comprising:

10 providing a (111) textured hexagonal atomic template;
providing at least one bcc-d layer;
depositing a bcc-d crystalline material on said (111) textured hexagonal atomic template while employing at least one symmetry breaking mechanism;
15 forming a bcc-d (110) crystalline textured film; and
forming a symmetry broken crystalline structure containing at least one dominate (110) orientational variant and not more than five dominate variants.

20 54. A method of producing a symmetry broken bcc-d structure recited in claim 53, wherein

at least one said dominate (110) orientational variant has a $\langle 111 \rangle$ crystalline direction in the plane of the said texture at approximately +5.26 or -5.26 degrees relative a
25 $\langle 110 \rangle$ direction of the said (111) textured hexagonal atomic template in the plane of the template.

55. A method of producing a symmetry broken bcc-d structure recited in claim 53, wherein

30 said symmetry breaking mechanism is deposition of said bcc-d material upon said (111) textured hexagonal atomic template at an angle of incidence angle between 15 and 75 degrees.

35 56. A method of producing a symmetry broken bcc-d structure recited in claim 55, wherein

said angle of incidence is directed generally along the (111) textured template $\langle 110 \rangle$ direction.

57. A method of producing a symmetry broken bcc-d structure recited in claim 53, wherein
said symmetry breaking mechanism is deposition of said
5 bcc-d material upon said (111) textured hexagonal atomic template in an applied magnetic field.
58. A method of producing a symmetry broken bcc-d structure recited in claim 57, wherein
10 said applied magnetic field is directed generally along the (111) textured template <112> direction.
59. A method of producing a symmetry broken bcc-d structure recited in claim 57, wherein
15 said applied magnetic field is directed generally along the (111) textured template <111> direction.
60. A method of producing a symmetry broken bcc-d structure recited in claim 57, wherein
20 said applied magnetic field is of magnitude 10 Oe or greater.
61. A method of producing a symmetry broken bcc-d structure recited in claim 53, further comprising:
25 providing at least one second thin film bcc-d material; and
forming at least one second symmetry broken bcc-d crystalline structure containing at least one dominate (110) orientational variant and not more than five dominate
30 variants.
62. A method of producing a symmetry broken bcc-d structure recited in claim 61, wherein
said first and said second bcc-d materials have
35 anisotropy energy density constants of opposite sign.

63. A method of producing a symmetry broken bcc-d structure recited in claim 61, wherein

said first and said second bcc-d materials have anisotropy energy density constants of the same sign.

5

64. A method of producing a symmetry broken bcc-d structure recited in claim 61, further comprising:

forming at least one oxide layer between said first bcc-d layer and said second bcc-d layer, to form an electrical insulation barrier.

10

65. A method of producing a symmetry broken bcc-d structure recited in claim 61, further comprising:

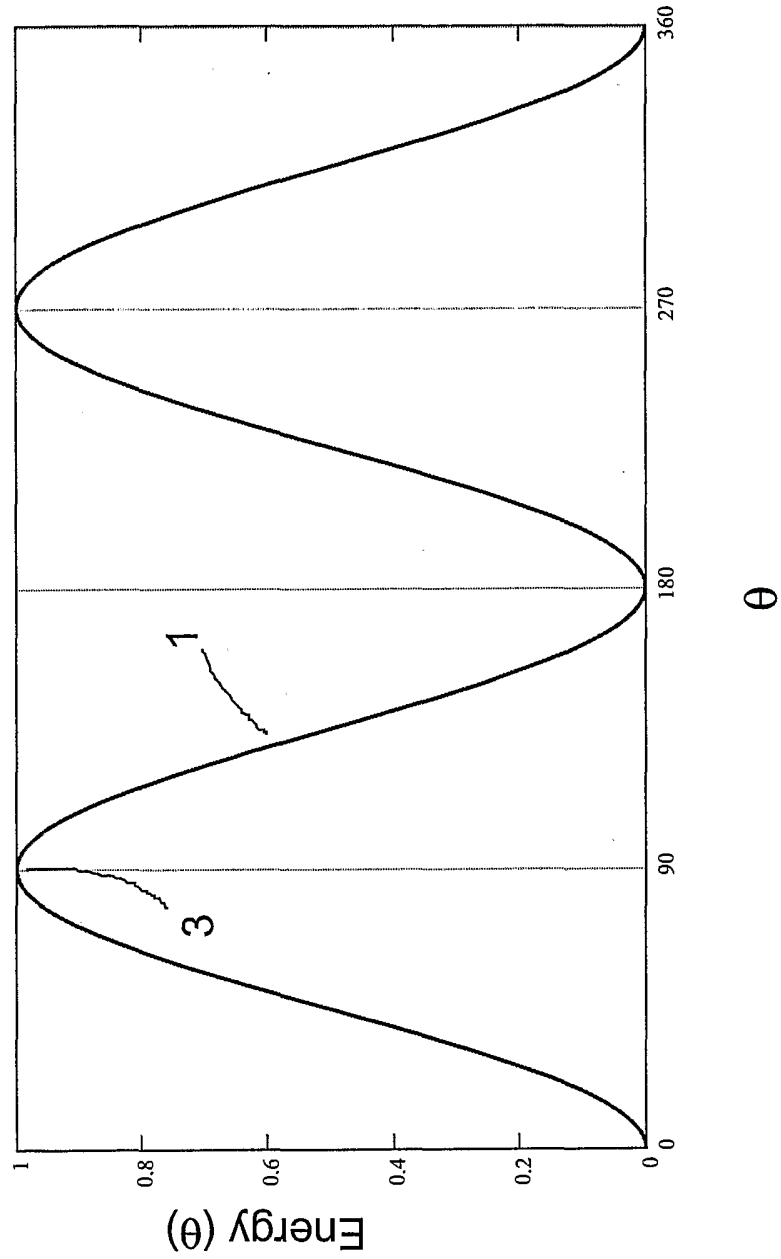
forming at least one second (111) textured hexagonal atomic template between said first bcc-d layer and said second bcc-d layer.

15

20

25

Figure 1



PRIOR ART

2/15

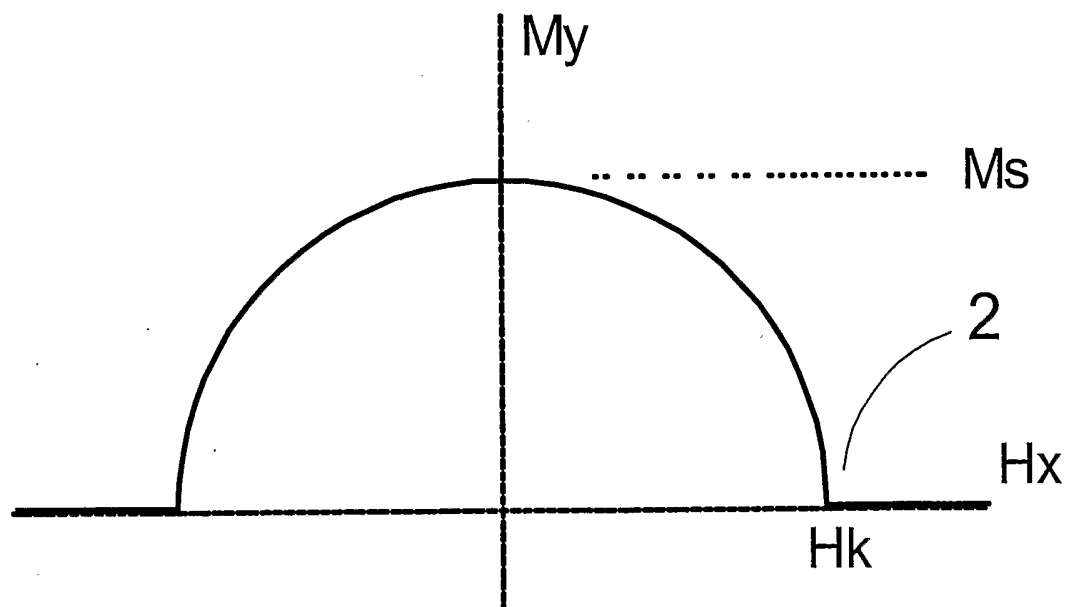
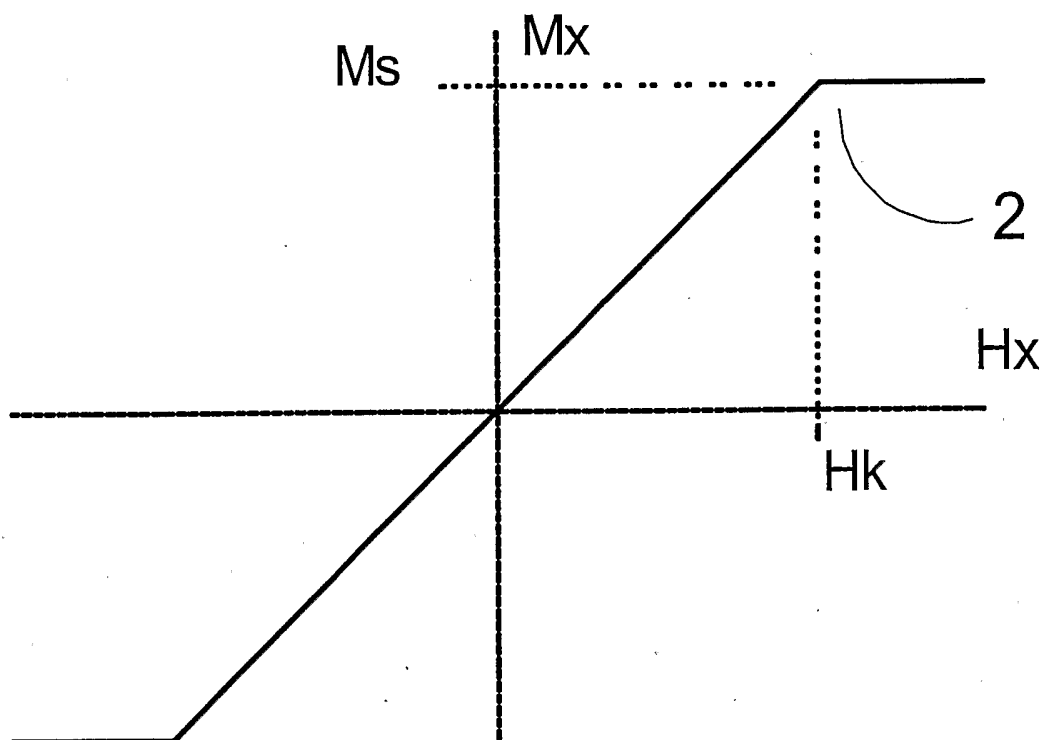


Figure 2

PRIOR ART

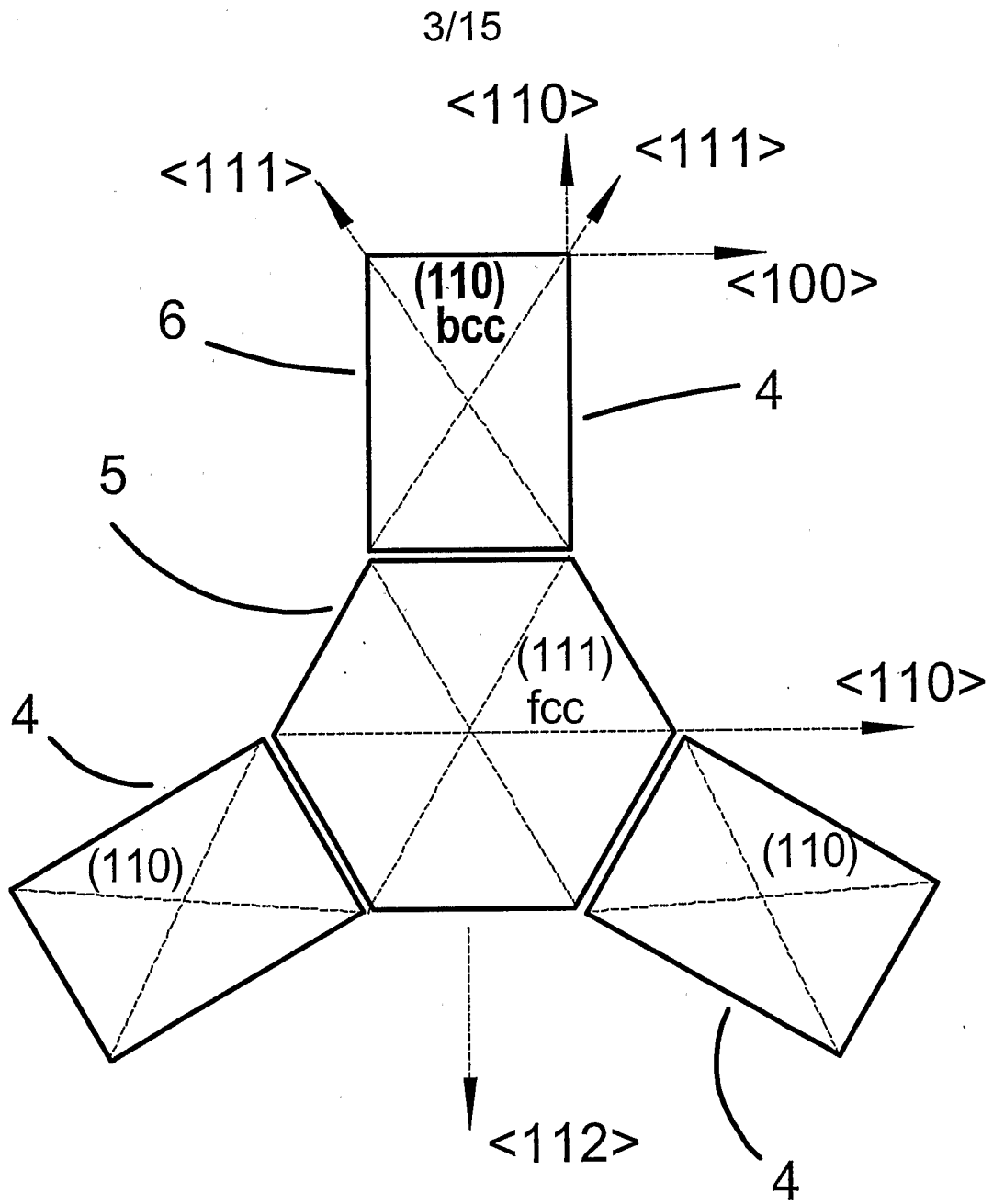
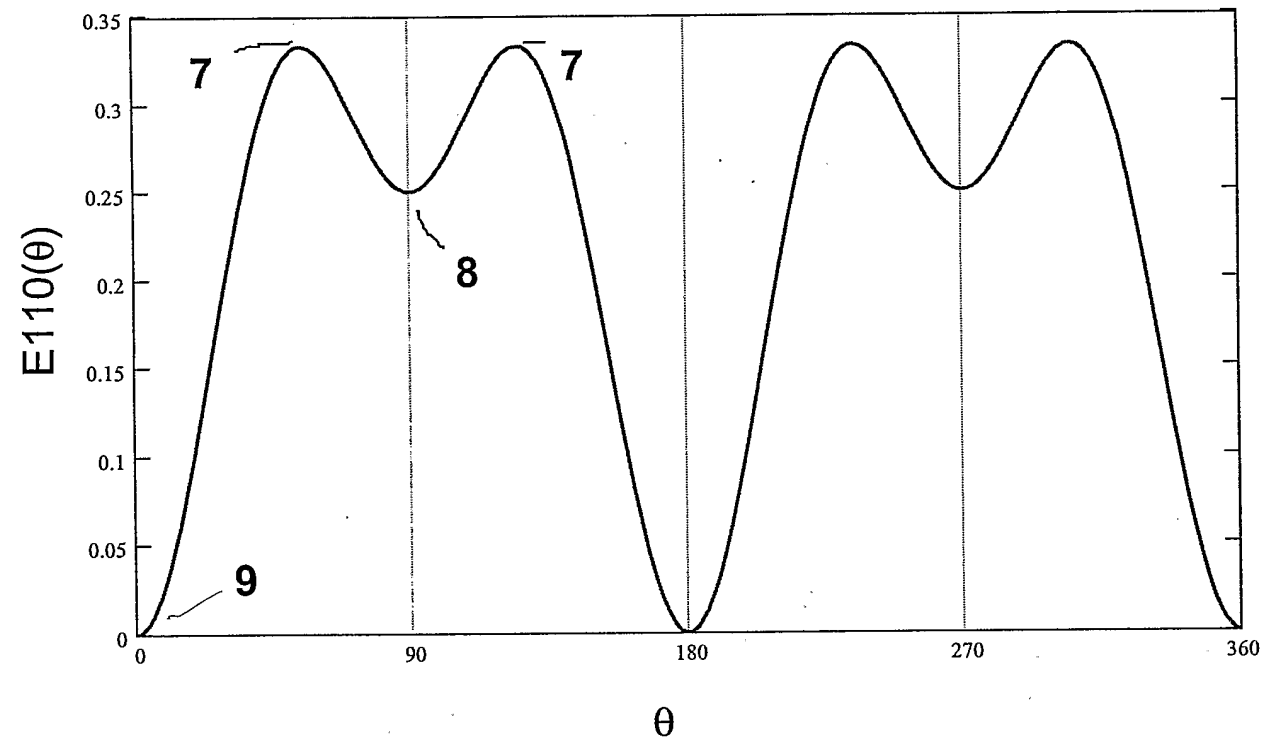


Figure 3

PRIOR ART

Figure 4



4/15

5/15

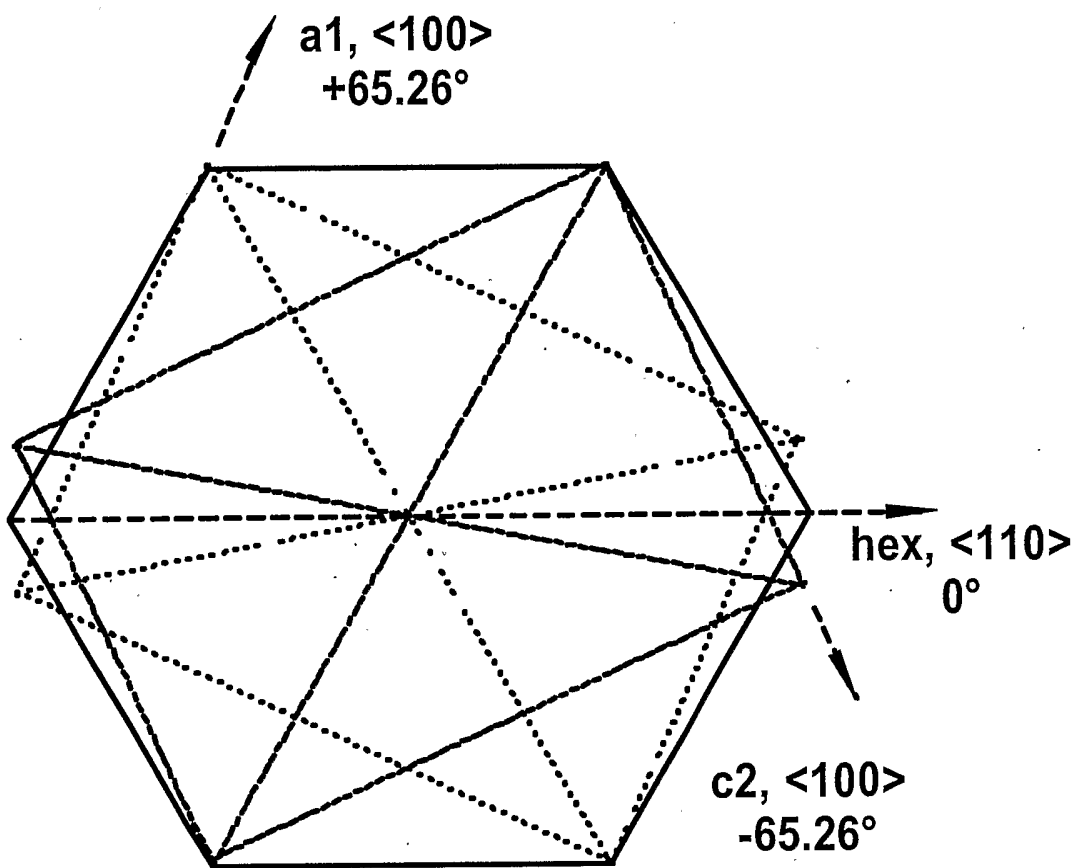
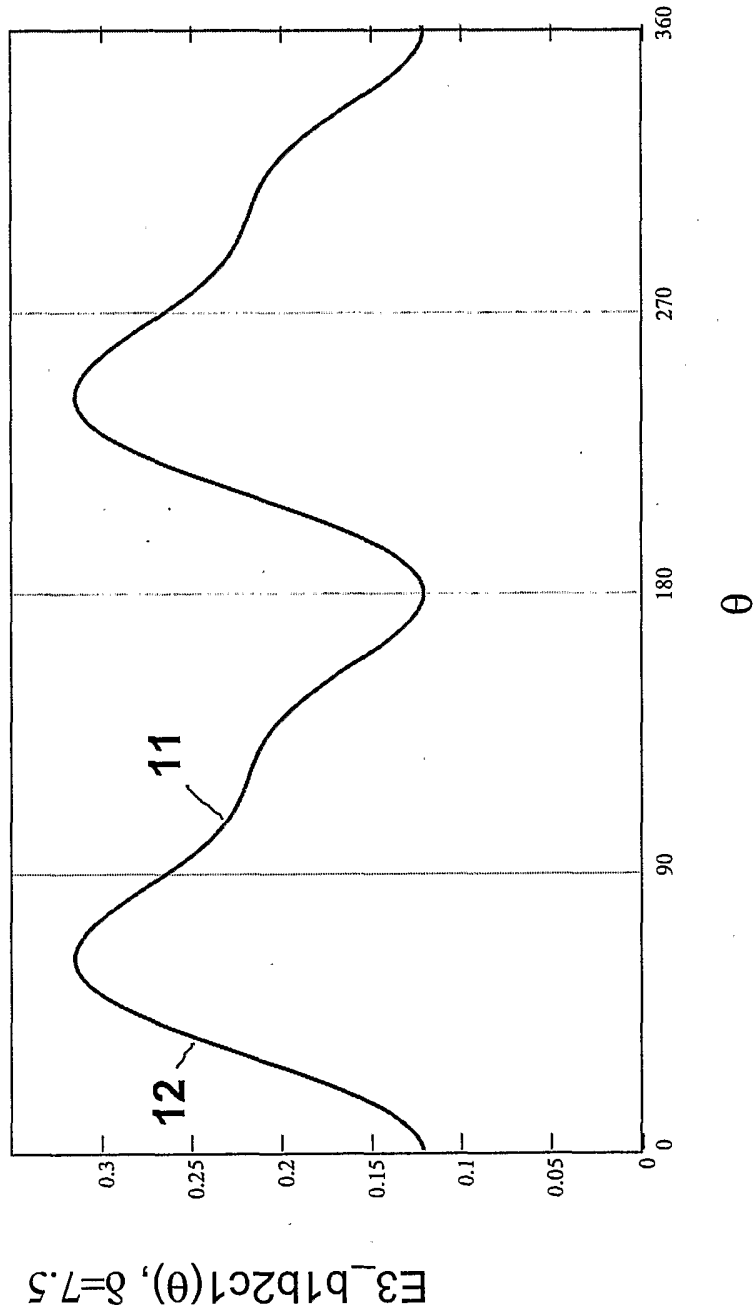


Figure 5

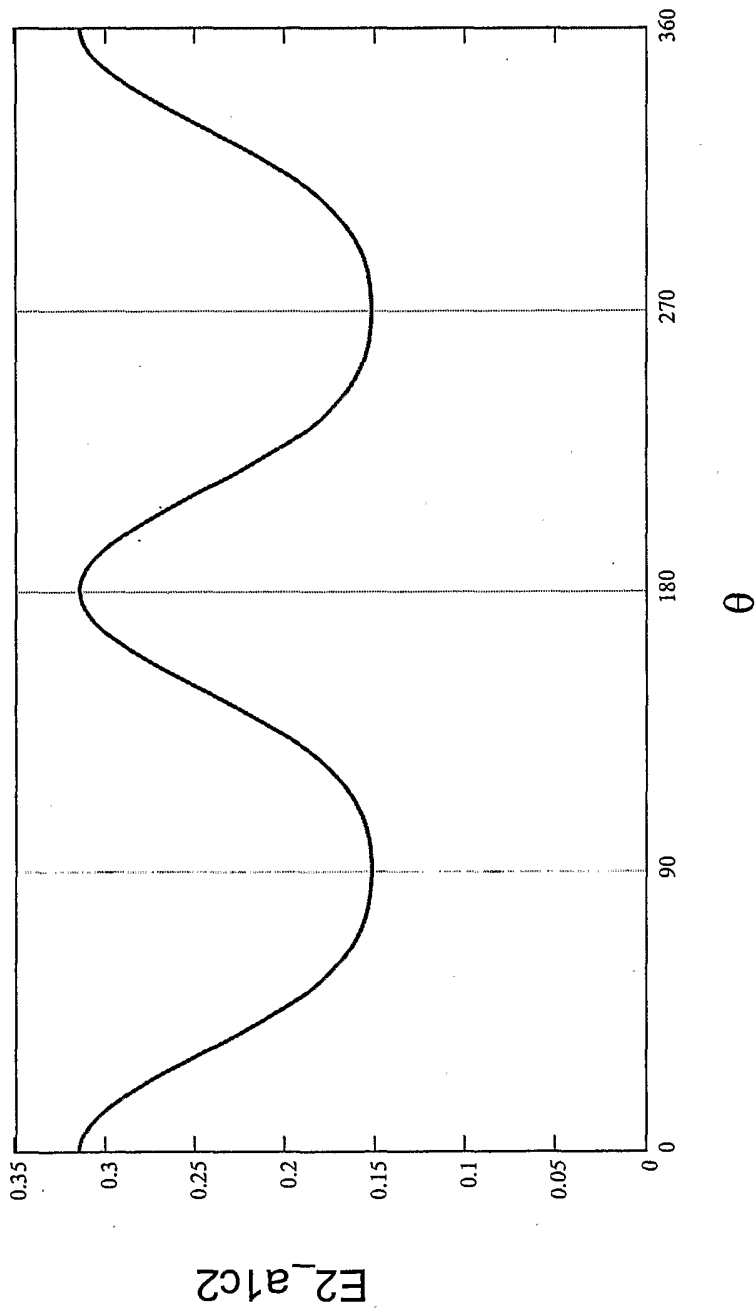
6/15

Figure 6



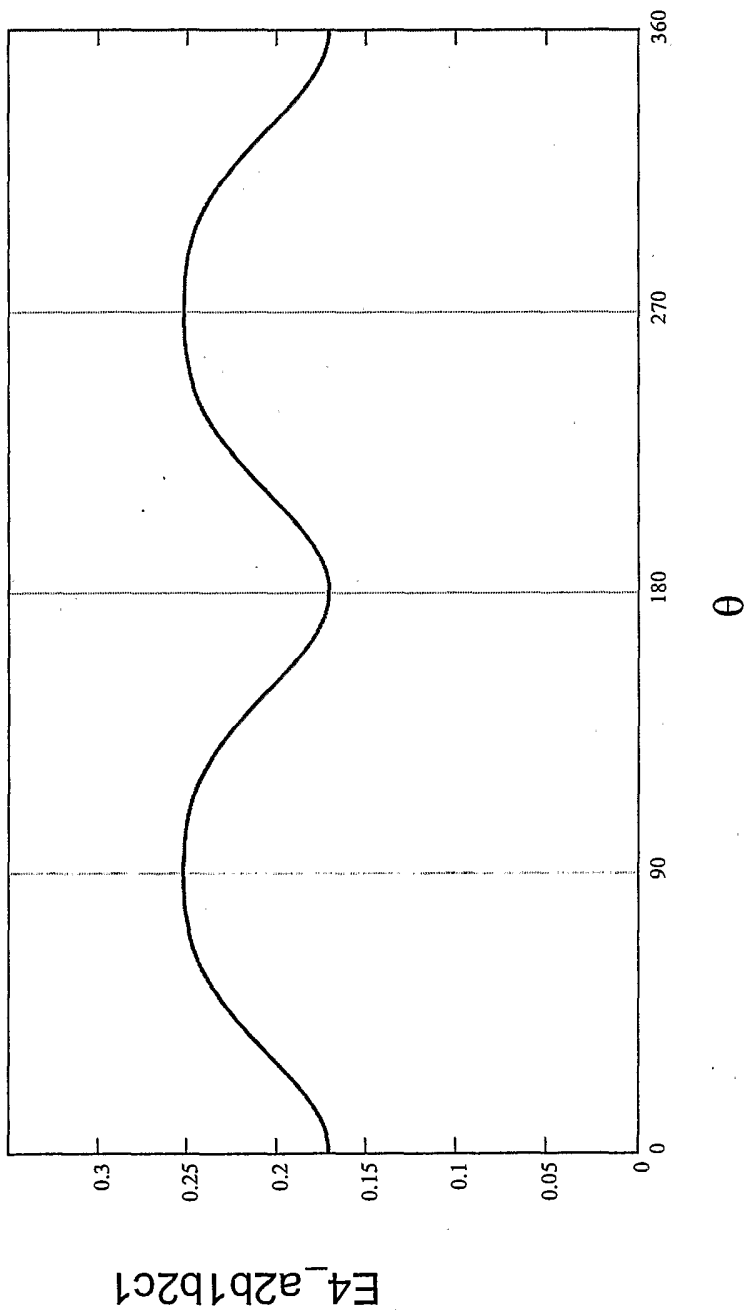
7/15

Figure 7



8/15

Figure 8



9/15

Normalized Magnetization Vs. Hard Axis Field, Hx

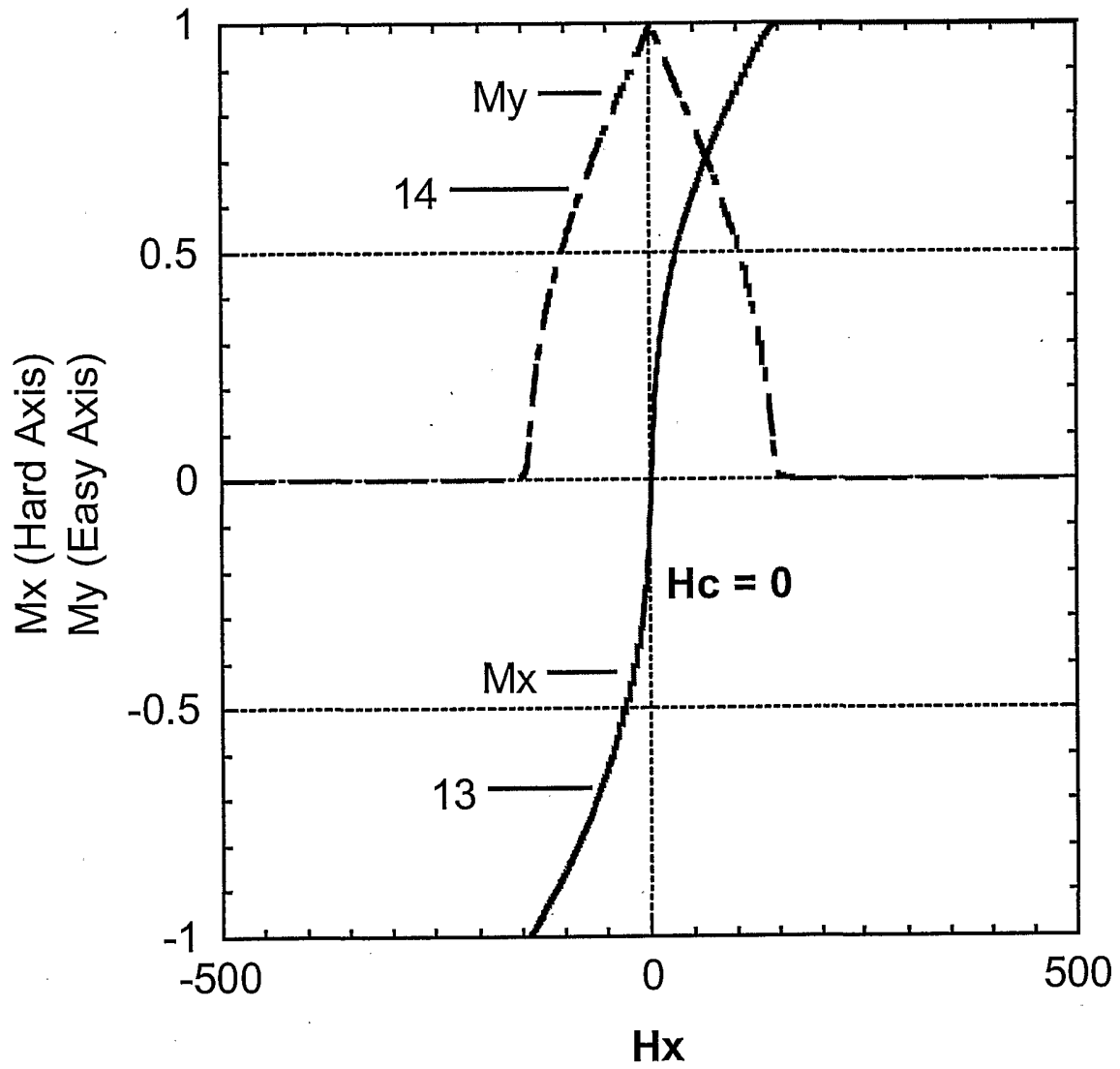
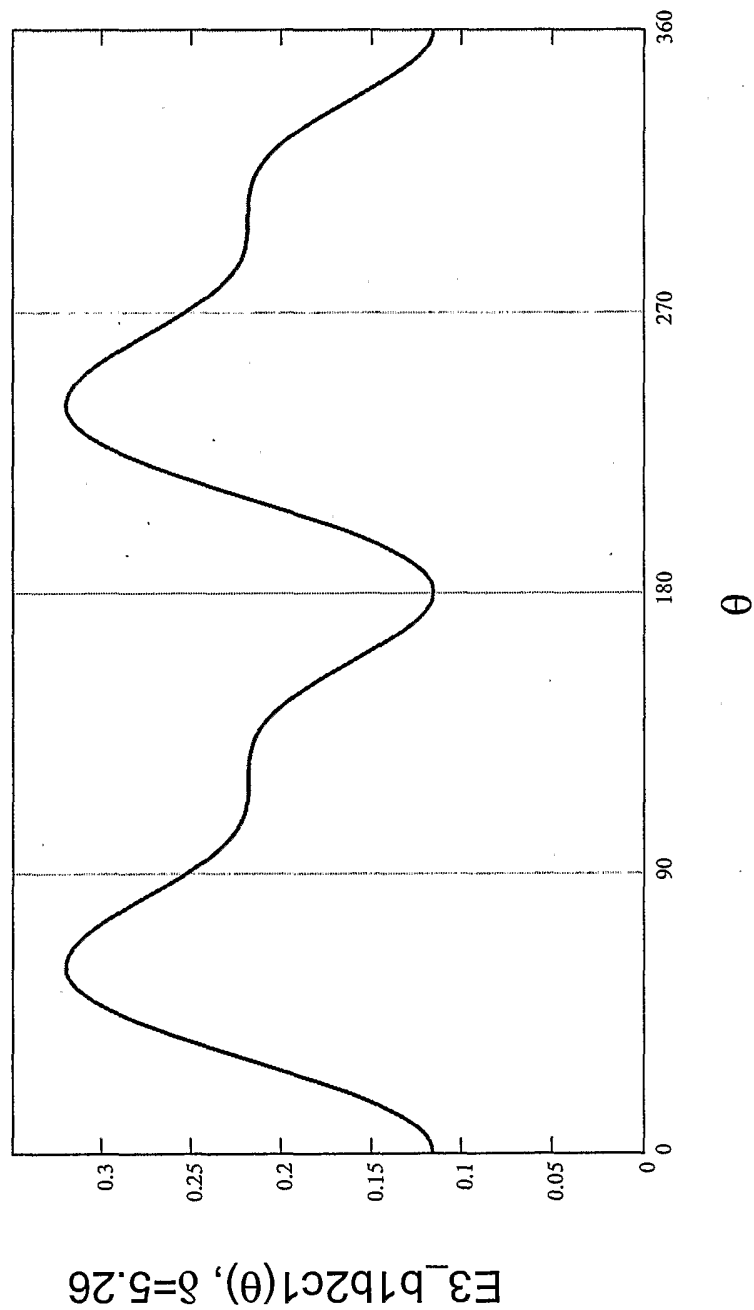


Figure 9

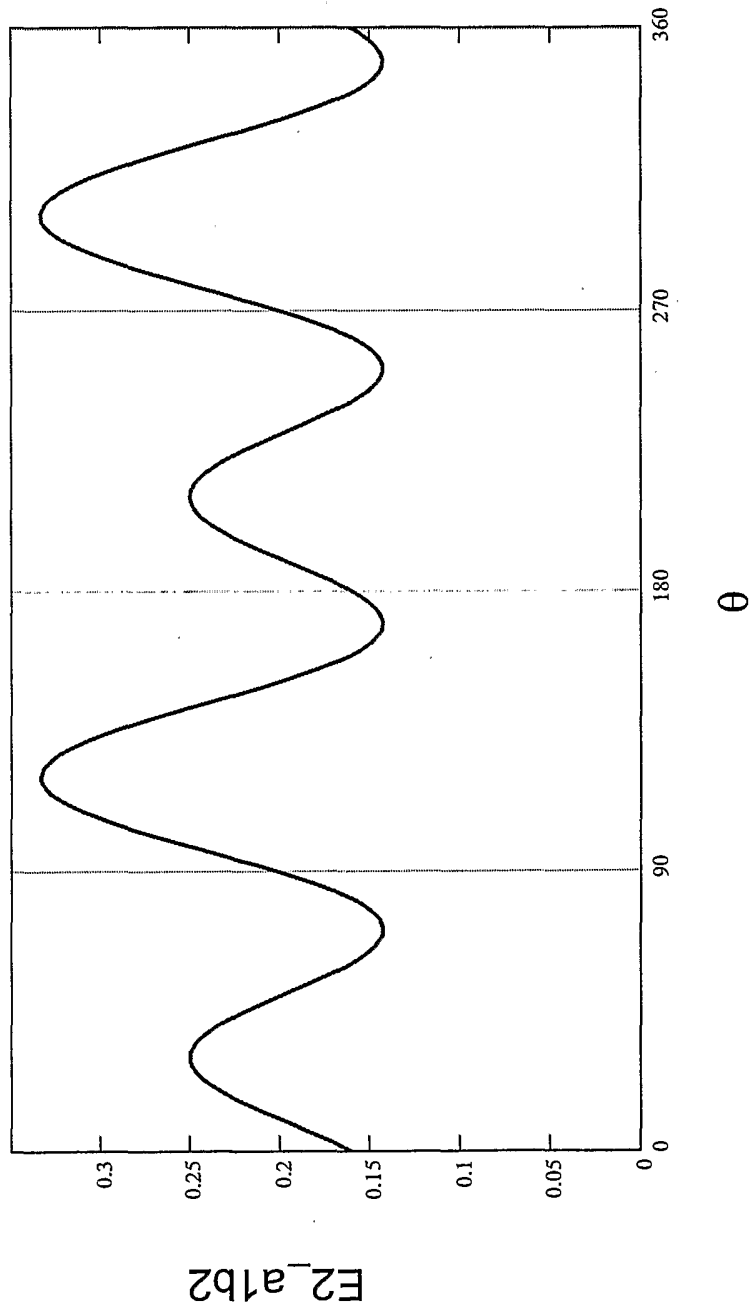
10/15

Figure 10



11/15

Figure 11



12/15

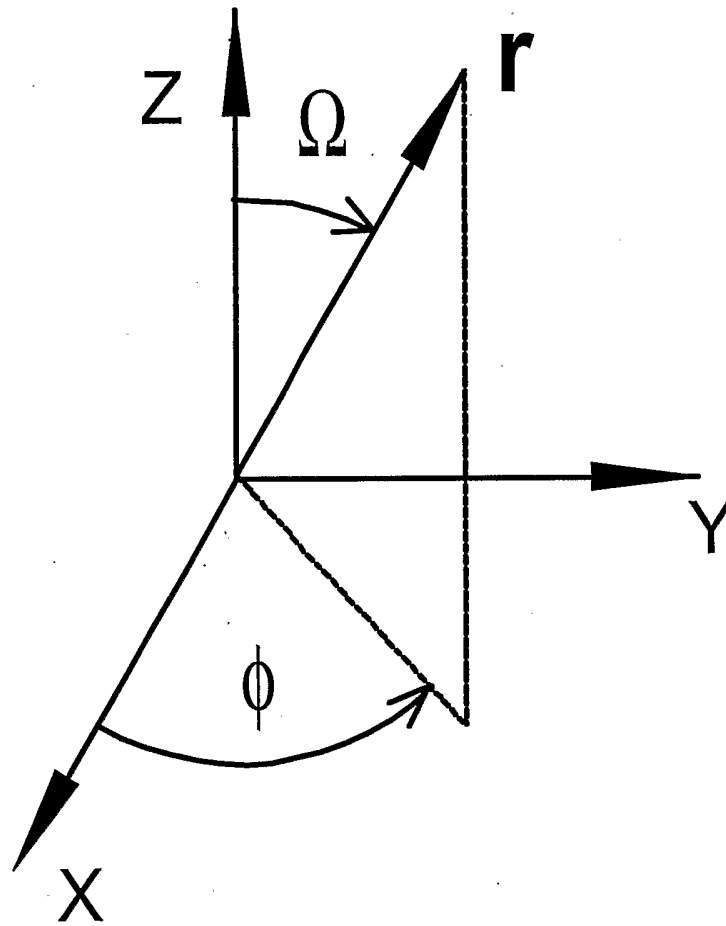
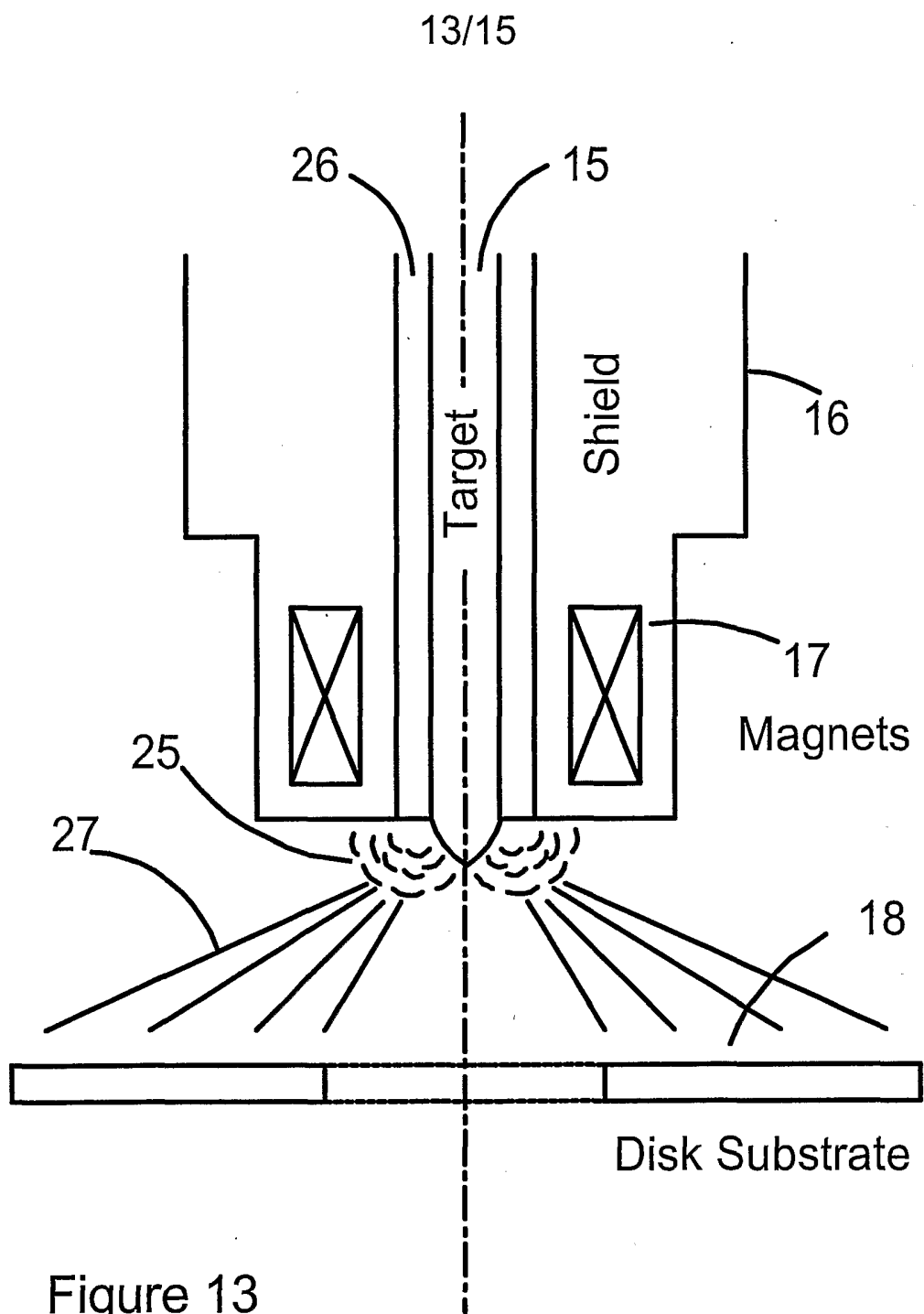


Figure 12



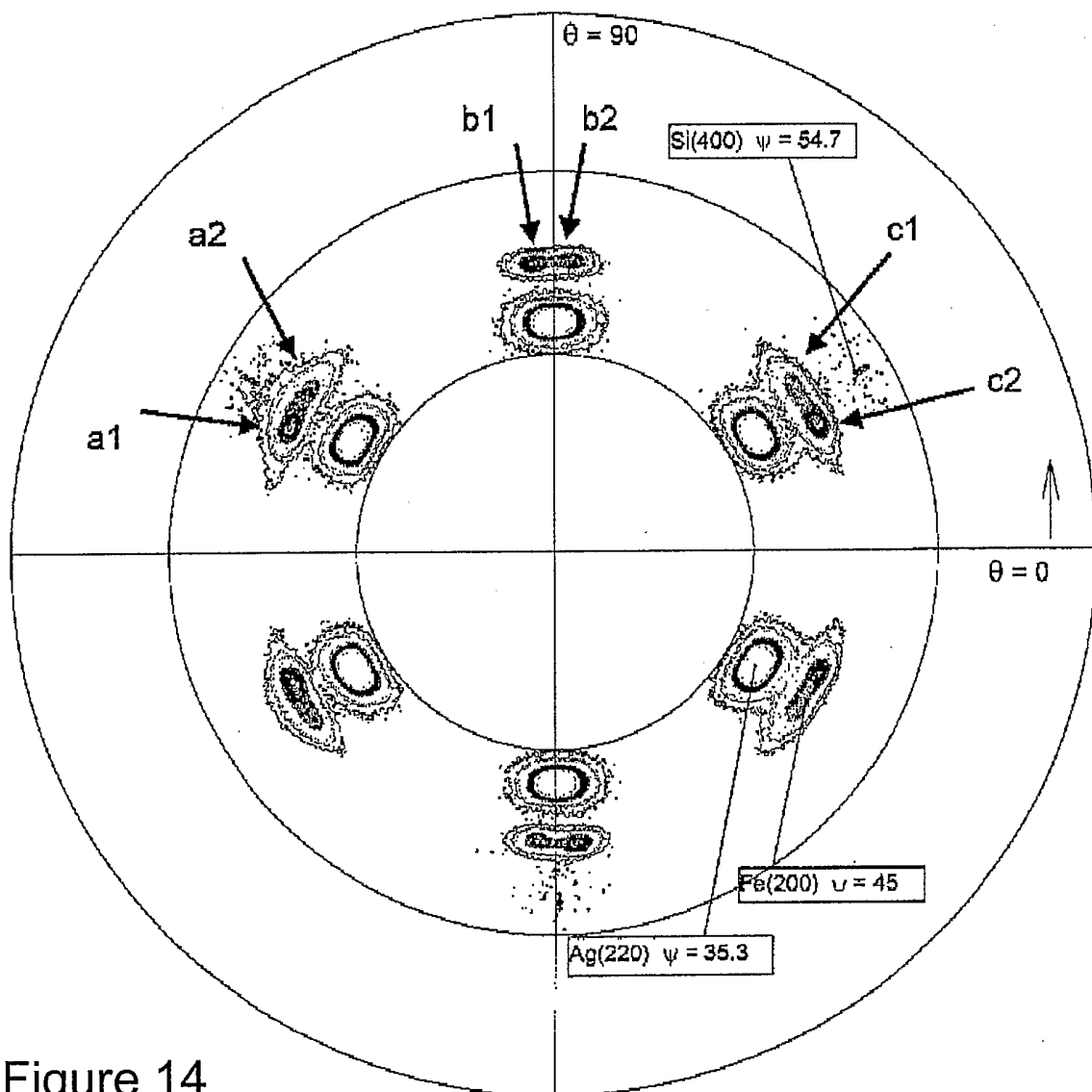


Figure 14

15/15

Normalized Magnetizations Vs. Hard Axis Field, Hx (Oe)

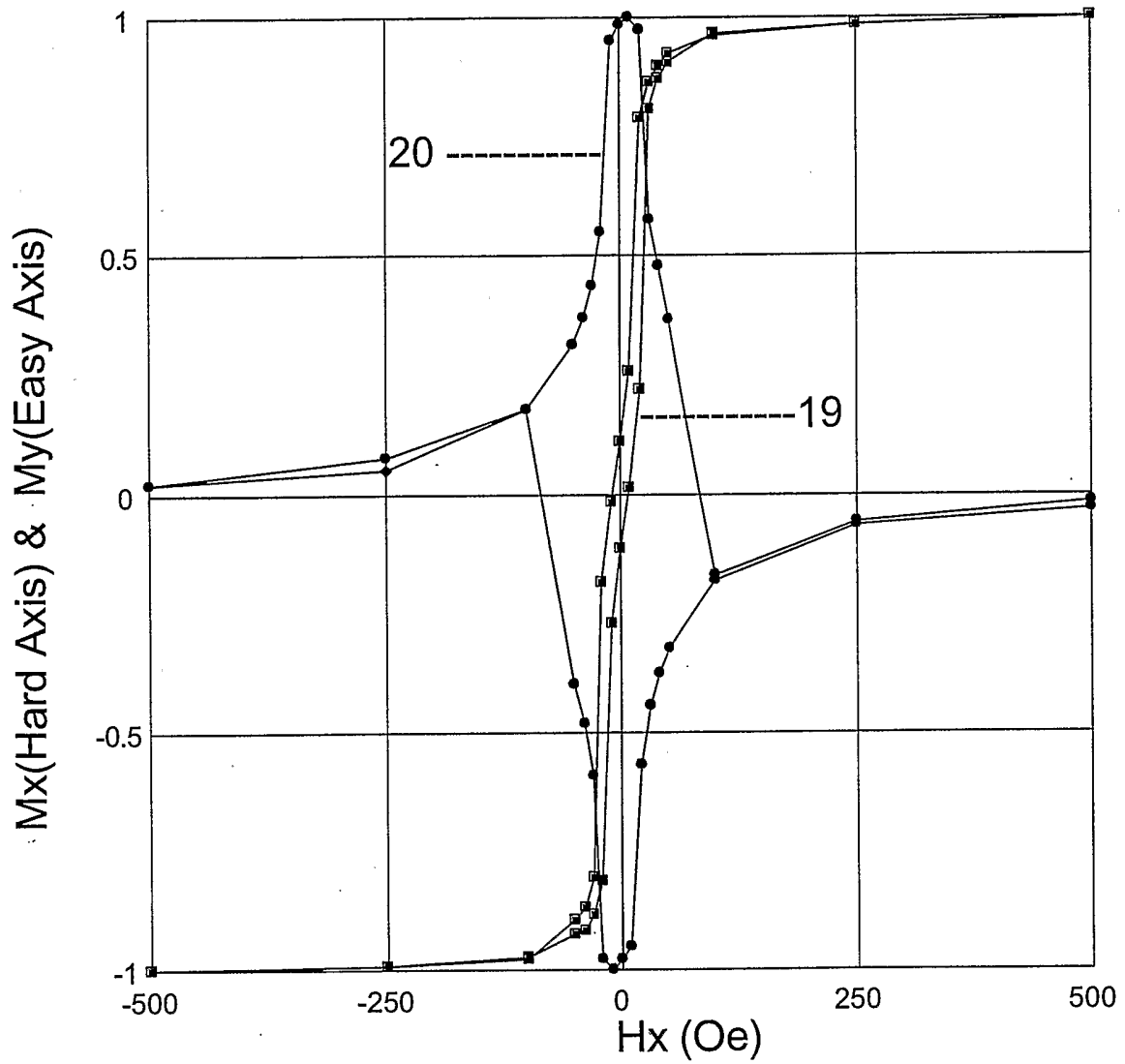
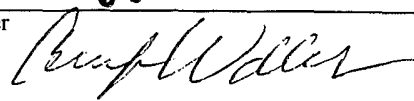


Figure 15

INTERNATIONAL SEARCH REPORT

International application No.

PCT/US02/27327

A. CLASSIFICATION OF SUBJECT MATTER		
IPC(7) : G11B 5/64, 5/66, 5/667, 5/673		
US CL : 428/668, 694TS, 694TM		
According to International Patent Classification (IPC) or to both national classification and IPC		
B. FIELDS SEARCHED		
Minimum documentation searched (classification system followed by classification symbols) U.S. : 428/668, 694TS, 694TM		
Documentation searched other than minimum documentation to the extent that such documents are included in the fields searched		
Electronic data base consulted during the international search (name of data base and, where practicable, search terms used)		
C. DOCUMENTS CONSIDERED TO BE RELEVANT		
Category *	Citation of document, with indication, where appropriate, of the relevant passages	Relevant to claim No.
Y	WO 99/24973 (LAMBETH et al) 20 May 1999 (20.05.1999), pages 15 - 17, 22, 34, 35 41, 44, 51 and 53.	1-12, 17-21, 25-28, 48-61 and 63
Y	US 6,248,416 B1 (LAMBETH et al) 19 June 2001 (19.06.2001), columns 13, 20, 21 and 27.	21-12, 17-21, 25-28, 48-61 and 63
Y	US 6,146,776 A (FUKUZAWA et al) 14 November 2000 (14.11.2000), column 8, lines 32 - 49 and Figures.	1-65
Y	JP 08-204253 A (FUJIKATA et al) 9 August 1996 (09.08.1996), Entire Derwent Abstract Translation.	1-65
Y	US 6,097,579 (GILL) 01 August 2000 (01.08.2000), columns 1, 2, 6 and 8, and Figures.	13-16, 23, 24, 29-47, 61 and 63-65
Y	US 6,262,869 B1 (LIN et al) 17 July 2001 (17.07.2001), columns 3 and 9, and Figures.	13-16, 23, 24, 29-47, 61 and 63-65
<input type="checkbox"/> Further documents are listed in the continuation of Box C. <input type="checkbox"/> See patent family annex.		
* Special categories of cited documents:		
"A"	document defining the general state of the art which is not considered to be of particular relevance	"T" later document published after the international filing date or priority date and not in conflict with the application but cited to understand the principle or theory underlying the invention
"E"	earlier application or patent published on or after the international filing date	"X" document of particular relevance; the claimed invention cannot be considered novel or cannot be considered to involve an inventive step when the document is taken alone
"L"	document which may throw doubts on priority claim(s) or which is cited to establish the publication date of another citation or other special reason (as specified)	"Y" document of particular relevance; the claimed invention cannot be considered to involve an inventive step when the document is combined with one or more other such documents, such combination being obvious to a person skilled in the art
"O"	document referring to an oral disclosure, use, exhibition or other means	"&" document member of the same patent family
"P"	document published prior to the international filing date but later than the priority date claimed	
Date of the actual completion of the international search 04 November 2002 (04.11.2002)		Date of mailing of the international search report 06 DEC 2002
Name and mailing address of the ISA/US Commissioner of Patents and Trademarks Box PCT Washington, D.C. 20231 Facsimile No. (703)305-3230		Authorized officer Kevin Bernatz  Telephone No. (703) 308-0661

INTERNATIONAL SEARCH REPORT

International application No.

PCT/US02/27327

Box I Observations where certain claims were found unsearchable (Continuation of Item 1 of first sheet)

This international report has not been established in respect of certain claims under Article 17(2)(a) for the following reasons:

1. Claim Nos.:
because they relate to subject matter not required to be searched by this Authority, namely:

2. Claim Nos.:
because they relate to parts of the international application that do not comply with the prescribed requirements to such an extent that no meaningful international search can be carried out, specifically:

3. Claim Nos.:
because they are dependent claims and are not drafted in accordance with the second and third sentences of Rule 6.4(a).

Box II Observations where unity of invention is lacking (Continuation of Item 2 of first sheet)

This International Searching Authority found multiple inventions in this international application, as follows:

1. As all required additional search fees were timely paid by the applicant, this international search report covers all searchable claims.
2. As all searchable claims could be searched without effort justifying an additional fee, this Authority did not invite payment of any additional fee.
3. As only some of the required additional search fees were timely paid by the applicant, this international search report covers only those claims for which fees were paid, specifically claims Nos.:

4. No required additional search fees were timely paid by the applicant. Consequently, this international search report is restricted to the invention first mentioned in the claims; it is covered by claims Nos.:

Remark on Protest

- The additional search fees were accompanied by the applicant's protest.
- No protest accompanied the payment of additional search fees.



US005998048A

United States Patent [19]

[11] Patent Number: **5,998,048**

Jin et al.

[45] Date of Patent: **Dec. 7, 1999**

- [54] **ARTICLE COMPRISING ANISOTROPIC CO-Fe-CR-N SOFT MAGNETIC THIN FILMS**
- [75] Inventors: **Sungho Jin**, Millington; **Timothy J. Klemmer**, Watchung; **Thomas Henry Tiefel**, deceased, late of North Plainfield, by Linda J. Tiefel, administratrix; **Robert Bruce Van Dover**, Maplewood; **Wei Zhu**, Warren, all of N.J.
- [73] Assignee: **Lucent Technologies Inc.**, Murray Hill, N.J.
- [21] Appl. No.: **09/033,204**
- [22] Filed: **Mar. 2, 1998**
- [51] Int. Cl.⁶ **G11B 5/66**
- [52] U.S. Cl. **428/694 T**; 428/694 TS; 428/694 TM; 428/900; 427/128; 427/129; 427/130; 427/131; 204/192.2
- [58] Field of Search 478/694 T, 694 TS, 478/694 TM, 900; 427/128-131; 204/192.2

E. Haftek and J. A. Barnard, Microstructure and Magnetic Properties of FeTaN Films, *IEEE Transactions on Magnetics*, vol. 30,, No. 6, Nov. 1994, pp. 3915-3917.

Nobuyuki Ishiwata, Chizuko Wakabayashi, and Haruo Urai, "Soft Magnetism of High-Nitrogen-Concentration FeTaN Films", *J. Appl. Phys.* 69(8), Apr. 15, 1991, pp. 5616-5618.

Jiang-Ching Lin, Lih-Juann Chen, Chi-Jen Chen, "Effects of Nitrogen Content on the Microstructure and Magnetic Properties of FeTaN Films", *IEEE Transactions on Magnetics*, vol. 30, No. 6, Nov. 1994, pp. 3912-3914.

G. Qiu, E. Haftek and J. A. Bernard, "Magnetic Properties and Crystal Structure of High Moment FeTaN Materials For Thin-Film Recording Heads," *J. App. Phys.* 73 (10), May 1993, pp. 6573-6575.

Book, *Magnetic Materials*, by R. S. Tebble and D. J. Craik, publisher, Wiley-Interscience, a division of John Wiley & Sons Ltd., London, New York, Sydney, Toronto 1969.

Book, *Magnetic Thin Films*, by Ronald F. Soohoo, Associate Professor, Division of Engineering and Applied Science, The California Institute of Tecnology, publisher, Harper & Row, New York, Evanston and London, 1965.

Book, *Thin Ferromagnetic Films*, by M. Prutton, publisher, Washington Butterworths, 1964.

Primary Examiner—Leszek Kiliman
 Attorney, Agent, or Firm—John M. Harman

[56] References Cited

U.S. PATENT DOCUMENTS

5,114,800 5/1992 Shimizu 428/692

OTHER PUBLICATIONS

Charles Sullivan, Seth R. Sanders, "Microfabrication of Transformers and inductors for High Frequency Power Conversion", 1993 IEEE, , pp. 33-41.

Masato Mino, Toshiaki Yachi, Aiko Tago, Keiichi Yanagisawa and Kazuhikio Sakakibara, "A New Planar Microtransformer for Use in Micro Switchcing Converters", *IEEE Transactions on Magnetics*, vol. 28, No. 4, Jul. 1992, pp. 1969-1973.

Noriyuki Kataoka, Masami Hosokawa, Akihisa Inoue, and Tsuyoshi Masumoto, "magnetic Properties of Fe-Based Binary Crystalline Alloys Produces by Vapor Quenching", *Journal of Applied Physics*, vol. 28, No. 3, Mar. 1989, pp. L462-L464.

[57] ABSTRACT

The invention is embodied in an anisotropic, soft magnetic thin film article comprising a cobalt-iron-chromium-nitrogen (Co-Fe-Cr-N) alloy. The thin film is formed such that the alloy has a relatively high saturation magnetization ($4\pi M_s$), e.g., greater than approximately 8 kilogauss (kG), a relatively low coercivity (H_c), e.g., less than approximately 2.0 oersteds (Oe), a relatively high squareness ratio (M_r/M_s), e.g., greater than approximately 0.90, and a relatively high anisotropy field (H_k), e.g., greater than approximately 20 Oe, in an as-deposited condition or, alternatively, with a relatively low temperature treatment, e.g., below approximately 300° Celsius. The inventive films are suitable for use in electromagnetic devices, e.g., in microtransformer cores, inductor cores and in magnetic read-write heads.

21 Claims, 5 Drawing Sheets

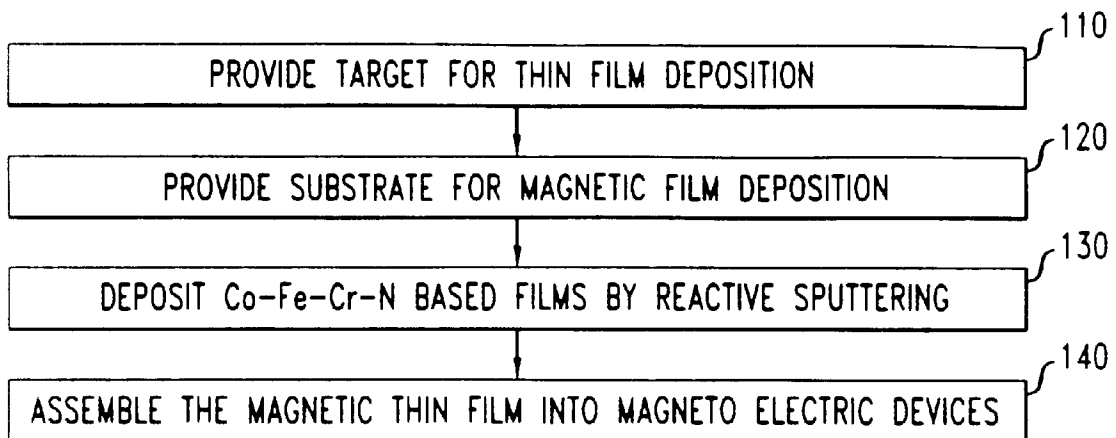


FIG. 1

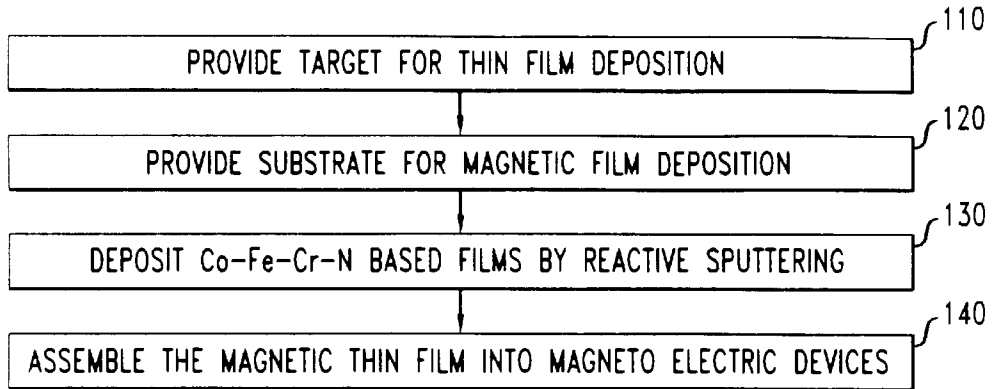


FIG. 2A

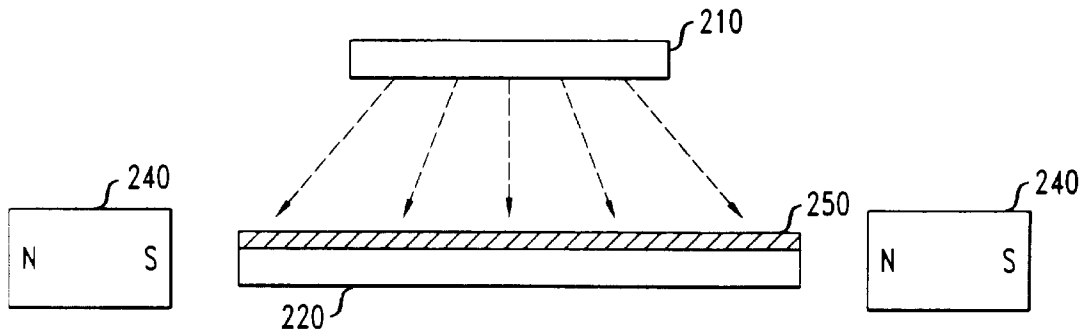


FIG. 2B

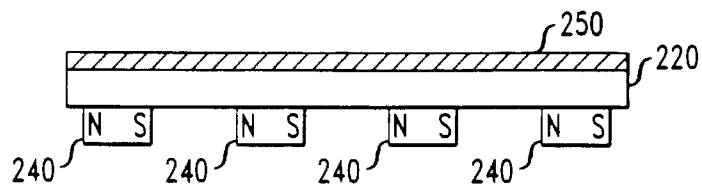


FIG. 3A

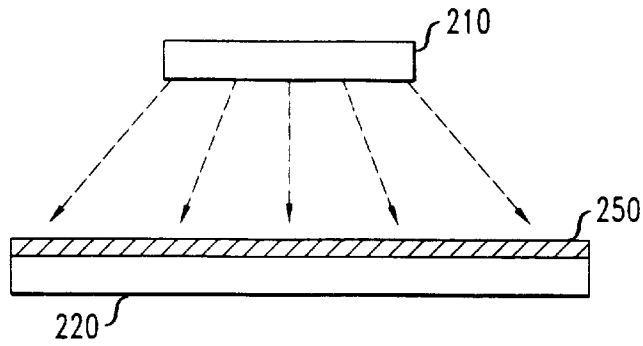


FIG. 3B

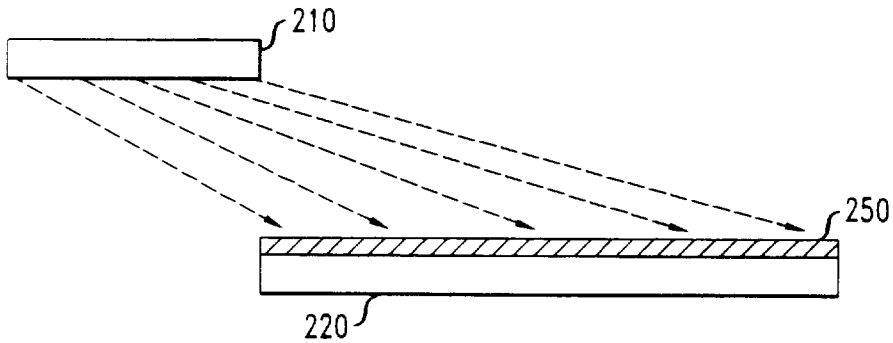


FIG. 3C

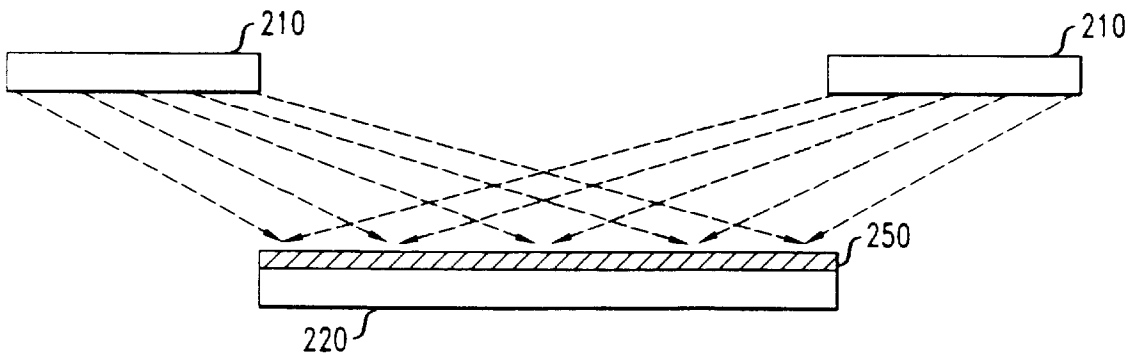


FIG. 4

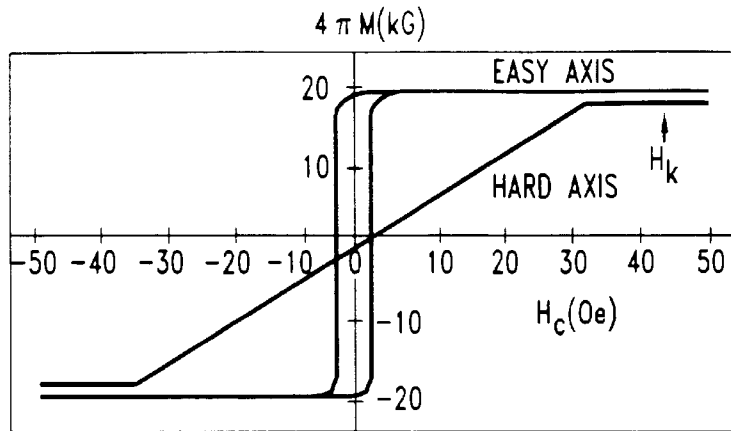


FIG. 5

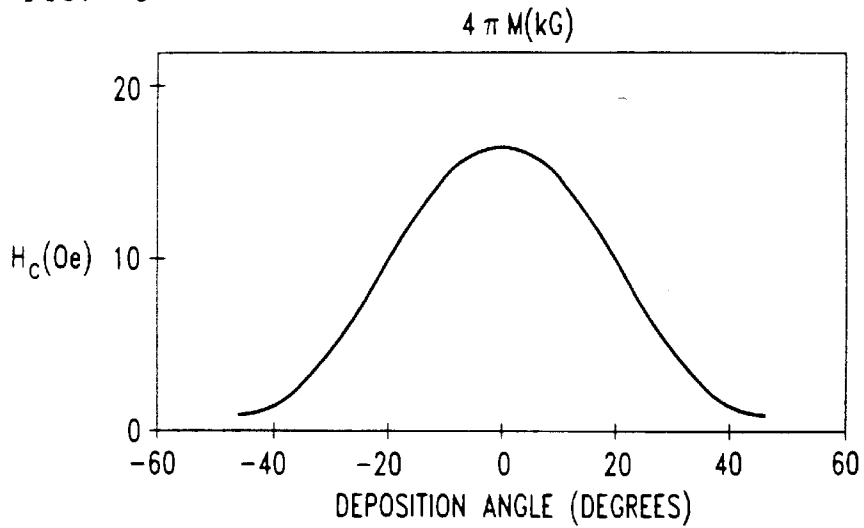


FIG. 6

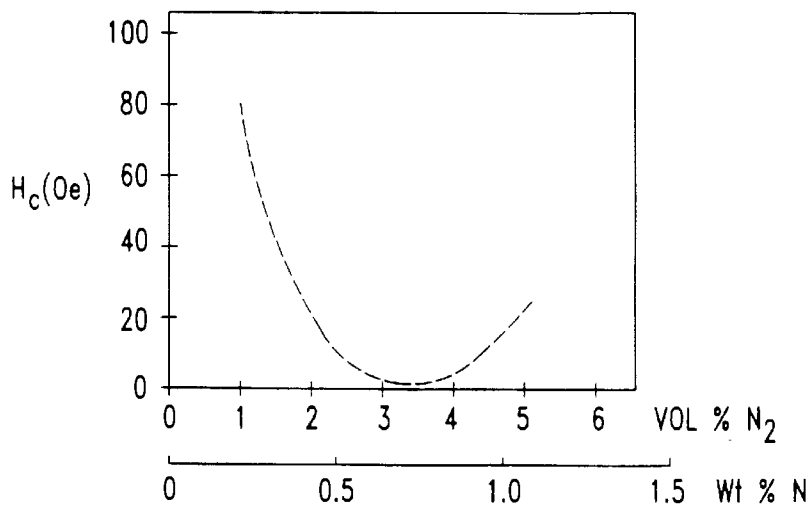


FIG. 7A

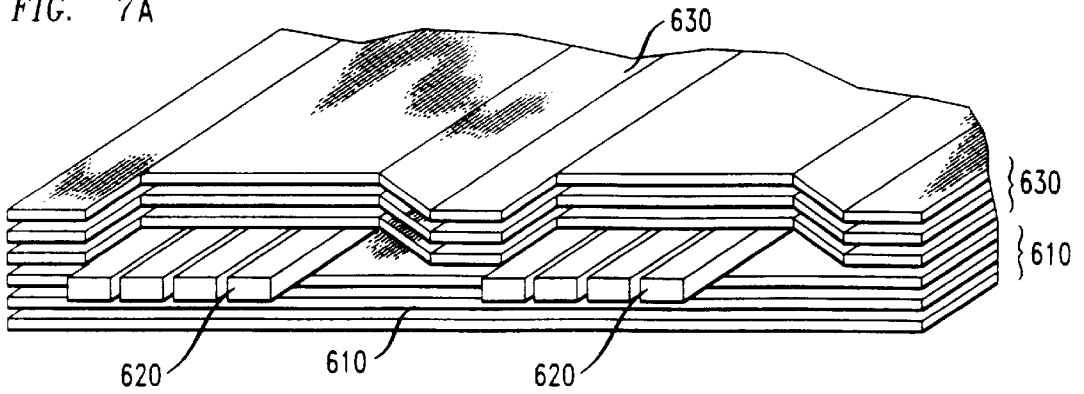


FIG. 7B

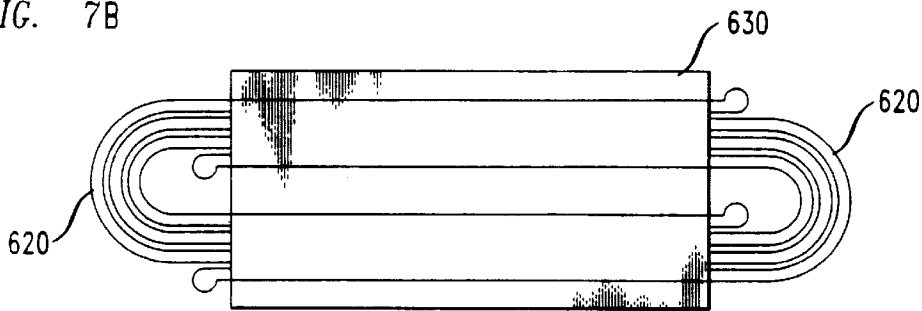


FIG. 8A

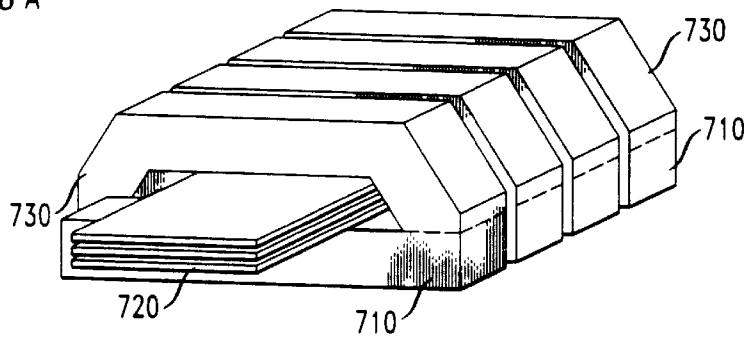


FIG. 8B

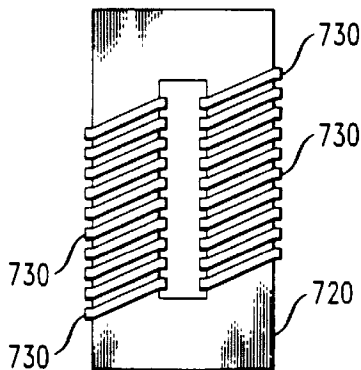


FIG. 9A

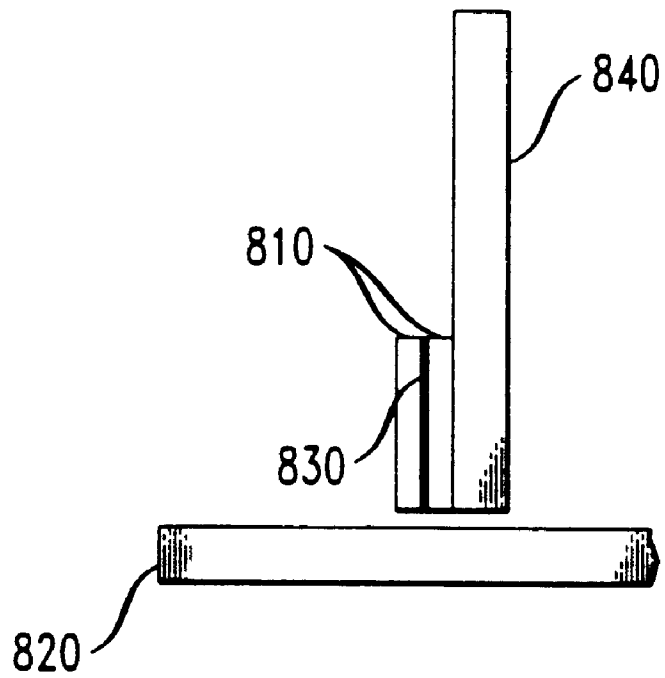
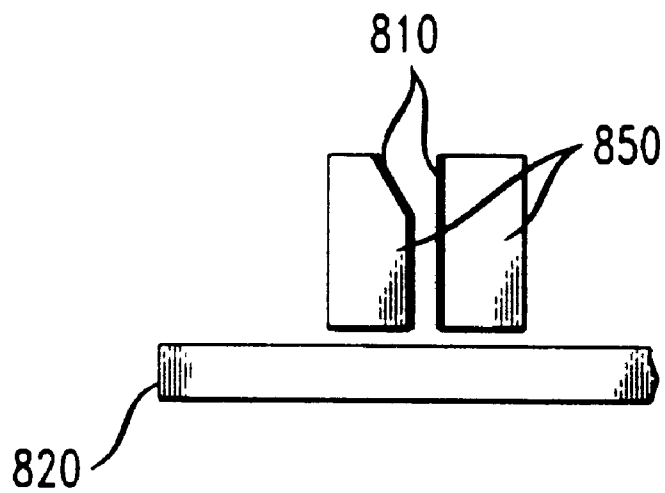


FIG. 9B



**ARTICLE COMPRISING ANISOTROPIC
CO-FE-CR-N SOFT MAGNETIC THIN
FILMS**

BACKGROUND OF THE INVENTION

1. Field of the Invention

The invention relates to thin films of magnetically soft alloys. More particularly, the invention relates to articles comprising these alloys and methods for making such articles.

2. Description of the Related Art

Thin film soft magnetic materials are useful in modern, high-frequency, electromagnetic devices, e.g., as a field-amplifying component in the read-write head of magnetic disk memories in computers or as a core in microtransformers and inductors. Among the desired properties of these films are relatively high saturation magnetization ($4\pi M_s$), low coercivity (H_c), high permeability, high electrical resistivity and high corrosion resistance. Various applications of soft magnetic thin films are described, e.g., in books *Magnetic Thin Films* by R. F. Soohoo, Harper and Row, 1965; *Thin Ferromagnetic Films* by M. Prutton, Butterworth, 1964; and in articles such as C. R. Sullivan and S. R. Sanders, IEEE Trans. on Power Electronics, Proc. 24th Annual Power Electronics Specialists Conf., p. 33-40, June 1993; and T. Yachi et al., IEEE Trans. Magn. 28, 1969-1973 (1992).

Among conventional soft magnetic thin films, nickel-iron (Ni-Fe) based films such as 80% Ni-20% Fe (permalloy) are useful because of their favorable magnetic properties and zero magnetostriction characteristics. Iron-based films such as iron-tantalum (Fe-Ta), iron-zirconium (Fe-Zr) and iron-hafnium (Fe-Hf) alloys generally exhibit saturation magnetizations ($4\pi M_s$) of approximately 15-20 kilogauss (kG) as compared to approximately 10 kG for the 80% Ni permalloy films (see, e.g., N. Kataoka et al., Japanese J. Appl. Phys. 28, L462-L464, 1989, Trans. Jap. Inst. Metals 31, 429, 1990). However, iron-based films exhibit poorer soft magnetic properties and require post-deposition heat treatment.

To obtain improved soft magnetic properties, nitrogen-containing films of these iron-based alloys such as iron-tantalum-nitrogen (Fe-Ta-N) have been prepared. See, e.g., E. Haftek et al., IEEE Trans. Magn. 30, 3915-3917 (1994); N. Ishiwata et al., J. Appl. Phys. 69, 5616 (1991); J. Lin et al., IEEE Trans. Magn. 30, 3912-3914 (1994); and G. Qiu et al., J. Appl. Phys. 73, 6573 (1993). However, although desirable magnetic softness, e.g., a coercivity (H_c) of less than approximately 2 oersteds (Oe) (for microtransformer applications), is obtainable in these nitrogen-containing films, it is apparent from the aforementioned articles that such desirable soft magnetic properties are difficult to obtain in an as-deposited form, but are possible after post-deposition heat treatment at high temperatures.

However, such heat treatment of deposited films is an additional processing step that needs to be avoided if possible, not only from a manufacturing cost point of view but also because of the complications of having to expose various other components and materials in the devices to high temperatures. Therefore, it is desirable for the required soft magnetic properties in the films to be obtained in the as-deposited condition, or at worst, with a very low temperature heat treatment below approximately 150° Celsius.

Desirable high-frequency properties for soft magnetic films include relatively high permeability and low power

loss. There are several sources of loss in ferromagnetic materials, including hysteresis loss, eddy current loss and ferromagnetic resonance (FMR) loss.

Hysteresis loss is reduced or minimized, e.g., by avoiding magnetic domain wall displacement, such as by performing alternating current (AC) operation of the magnetic films in the magnetically hard-axis so that magnetization only by spin rotation is used. Such mode of operation is accomplished most conveniently by providing a strong anisotropy (H_k) and a square magnetic hysteresis (M-H) loop. For example, see co-pending application Ser. No. 08/595,543, filed Feb. 2, 1996 now U.S. Pat. No. 5,780,175 and assigned to the assignee of the present invention.

Eddy current loss increases in proportion to the square of the operating frequency, and thus plays an important role in the high-frequency applications. Eddy current loss is reduced, e.g., by increasing the field penetration depth (skin depth) with relatively high electrical resistance in the magnetic material, either by using a thin film configuration or by selecting relatively high resistivity materials.

The occurrence of ferromagnetic resonance (FMR) in high-frequency ranges such as approximately 10 megahertz (MHz) or greater in most of the soft magnetic materials generally causes the magnetic permeability to drop off and the magnetic loss to increase by orders of magnitude, often spanning a frequency range from approximately 1-2 orders of magnitude. Such behavior is conventional for Ni-Zn ferrites. For example, see generally R. S. Tebble and D. J. Craik, *Magnetic Materials* (Wiley, New York, 1969), p. 598.

Ferromagnetic resonance (FMR) occurs when the frequency of the applied AC field matches the characteristic precession frequency of spins in the magnetic material. This precession frequency, f_r , is determined by the total anisotropy field (H_k) experienced by the spins. For a thin film, for which the demagnetizing field (H_d) along the z direction is approximately equal to the saturation magnetization ($4\pi M_s$), the FMR frequency is expressed as

$$f_r = 2\pi\gamma(H_k - 4\pi M_s)^{1/2},$$

where γ is the gyromagnetic constant ($2\pi\gamma = 2.8$ MHz/Oe), and H_k is the in-plane anisotropy field. This relation applies for the case when the AC field is applied in the plane of the film perpendicular to the easy-axis. In order to raise the FMR frequency so that ferromagnetic resonance does not interfere with the high-frequency operation of the magnetic materials, a higher anisotropy field (H_k) and higher saturation magnetization ($4\pi M_s$) are needed. Typically, values of the anisotropy field (H_k) up to approximately 10-15 oersteds (Oe) are obtainable, but anisotropy fields (H_k) higher than 15 Oe in soft magnetic films generally are difficult to obtain. However, in high-frequency applications such as in wireless cellular communications, magnetic films with FMR frequencies of at least approximately 1 gigahertz (GHz) are desired.

Therefore, it is desirable to have soft magnetic thin films with greater saturation magnetization ($4\pi M_s$) and greater anisotropy fields (H_k) than conventional soft magnetic thin films.

SUMMARY OF THE INVENTION

The invention is embodied in anisotropic, soft magnetic thin films comprising a cobalt-iron-chromium-nitrogen (Co-Fe-Cr-N) alloy and methods for making them. The thin films are formed such that the alloy has a relatively high saturation magnetization ($4\pi M_s$), e.g., greater than approximately 8 kilogauss (kG), a relatively low coercivity (H_c), e.g., less than approximately 2.0 oersteds (Oe), a relatively

high squareness ratio (M_r/M_s), e.g., greater than approximately 0.90, and a relatively high anisotropy field (H_k), e.g., greater than approximately 20 Oe. The soft magnetic properties are obtained in an as-deposited condition or, alternatively, with a relatively low temperature treatment, e.g., below approximately 300° Celsius. Thin films according to embodiments of the invention are suitable for use, e.g., in electromagnetic devices such as in microtransformer cores, inductor cores and in magnetic read-write heads.

BRIEF DESCRIPTION OF THE DRAWING

FIG. 1 is a simplified block diagram of a method for making soft magnetic thin films comprising Co—Fe—Cr—N according to embodiments of the invention;

FIGS. 2a–b are diagrams showing various configurations of depositing thin films in the presence of an applied magnetic field according to embodiments of the invention;

FIGS. 3a–c are diagrams showing various configurations of oblique angle thin film deposition in the absence of an applied magnetic field according to embodiments of the invention;

FIG. 4 is a graphical diagram of the magnetic hysteresis (M-H) loops along the easy and hard-axis direction of magnetization of as-deposited Co—Fe—Cr—N alloy films according to embodiments of the invention;

FIG. 5 is a graphical diagram illustrating magnetic coercivity, H_c , as a function of film deposition angle for Co—Fe—Cr—N films according to an embodiment of the invention;

FIG. 6 is a graphical diagram of magnetic coercivity, H_c , as a function of nitrogen flow rate in an argon (Ar) carrier gas during a reactive sputtering process for Co—Fe—Cr—N alloy films according to embodiments of the invention;

FIGS. 7a–b are perspective and top views, respectively, of a pot-core type microtransformer comprising Co—Fe—Cr—N films according to embodiments of the invention;

FIGS. 8a–b are perspective and top views, respectively, of a toroid type microtransformer comprising Co—Fe—Cr—N films according to embodiments of the invention; and

FIGS. 9a–b are side, cross-sectional views of a magnetic recording head comprising Co—Fe—Cr—N films according to embodiments of the invention.

It is to be understood that the drawings are to illustrate the concepts of the invention and are not to scale.

DETAILED DESCRIPTION

FIG. 1 is a simplified block diagram of a method for making soft magnetic thin films comprising cobalt-iron-chromium-nitrogen (Co—Fe—Cr—N) in accordance with embodiments of the invention. A first step 110 is to provide an alloy target or targets from which the inventive magnetic thin films are to be deposited, e.g., by chemical or physical deposition such as by sputtering, evaporation, molecular beam epitaxial growth, ion beam deposition and laser ablation.

For example, deposition by sputtering is amenable to large-scale industrial manufacturing. The sputtering target (shown as 210 in FIG. 2a), which typically is in the form of a round plate, in one embodiment, has an alloy composition similar to the desired film composition and, in another embodiment, has composite sections of different metals or alloys on the target surface to be sputtered away. Alternatively, the film deposition is accomplished by using multiple targets, e.g., by co-sputtering from two or more

targets with different compositions chosen so that the final composition of the deposited film on the substrate corresponds to the desired composition. For example, as will be discussed in greater detail hereinbelow, in data shown in FIG. 6, co-sputtering with two targets was used, e.g., a Co-9.6%Fe-4.4%Cr (in weight %) target on one side and a Fe-4.5%Cr target on the other side separated by approximately 6 inches.

According to one embodiment of the invention, diode sputtering or triode sputtering is used for deposition of the inventive films. Triode sputtering often is used instead of diode sputtering because triode sputtering uses lower bias voltage and lower argon (Ar) pressure, thus allowing easier control of the sputter deposition and the formation of desired nanocrystalline microstructure in the inventive soft magnetic films comprising Co—Fe—Cr—N.

According to another embodiment of the invention, nitrogen (N) is incorporated into the alloy film by reactive deposition, i.e., by continuously supplying a specific partial pressure of nitrogen gas in the background Ar gas carrier during the sputtering process. The nitrogen atoms are believed to go into the thin film structure both by reaction with one or more of the metallic elements in the form of a nitride, such as Cr-nitride or Fe-nitride, and/or by dissolution in the form of interstitial solute atoms in the alloy crystal lattice.

According to another embodiment of the invention, nitrogen is supplied by alloying it directly into the sputtering targets or by adding it to the films after deposition, e.g., by ion implantation. Accordingly, thin films of inventive alloys, prepared by any suitable technique, are subjected to nitrogen implantation with appropriate doses and processing temperatures.

In the case of using a single alloy target for sputtering, the composition of the target according to embodiments of the invention is, e.g., cobalt (Co) within the range from approximately 10–90 weight %, typically within the range from approximately 20–80 weight %, more typically within the range from approximately 30–60 weight %, iron (Fe) within the range from approximately 10–90 weight %, typically within the range from approximately 20–80 weight %, more typically within the range from approximately 30–60 weight %, chromium (Cr) in the range from approximately 0–15 weight %, typically within the range from approximately 1.0–12.0 weight % and more typically within the range from approximately 1.5–8.0 weight %. If nitrogen (N) is to be added to the sputtering target, the alloy target includes nitrogen within the range from approximately 0–10 weight %, depending on the concentration of the nitrogen gas used during the sputtering.

The next step 120 is to provide a substrate onto which one or more soft magnetic films according to embodiments of the invention are to be deposited. A clean and smooth non-magnetic substrate surface is desired, e.g., for microtransformer-type applications. Substrate materials include, e.g., semiconductors such as silicon (Si) and gallium-arsenide (Ga—As), and other materials such as glass, quartz, ceramic, polymer and polyimide. A silicon substrate is convenient if other semiconductor electronic integrated circuit (IC) circuitry and interconnection features are to be integrated on portions of the same substrate. The IC circuits are fabricated, e.g., either before or after the deposition of the soft magnetic films.

For use in microtransformer or inductor applications, especially for high-frequency devices (e.g., $f=1-1000$ megahertz or greater), Co—Fe—Cr—N thin films according to

embodiments of the invention are formed, e.g., into a multilayer, patterned Configuration with dielectric spacer layers, such as spin-coated or spray-coated and optionally photolithographically patterned polyimide films, interleaved therebetween. Alternatively, the thin films are formed by vacuum or CVD deposition of dielectric films such as aluminum oxide (Al₂O₃), aluminum nitride (AlN), silicon dioxide (SiO₂) and yttrium oxide (Y₂O₃). The multilayer configuration of magnetic thin films according to embodiments of the invention provides high electrical resistance for the film layers so as to reduce eddy current loss, e.g., during high-frequency operation.

In such multilayer arrangement, typically more than one substrate material is involved. For example, after depositing the first magnetic layer comprising Co—Fe—Cr—N on, e.g., a silicon (Si) substrate, a polyimide insulation layer is deposited on the first magnetic layer and thus becomes the next substrate for the remaining magnetic layers. Also, because the magnetic properties of alloys and compounds often are influenced by crystallographic texture and lattice parameters, it is possible to choose the substrate material to provide epitaxial growth with accompanying lattice parameter modifications, to induce growth texture (such as a columnar structure) or to induce desired degrees of crystallization.

The next step 130 is to deposit thin films comprising Co—Fe—Cr—N, e.g., by reactive sputtering in a nitrogen-containing atmosphere. According to embodiments of the invention, the amount of nitrogen used is within the range from approximately 0.2–30.0% in volume in argon (Ar), and often within the range from approximately 0.5–10.0% in volume with a total (Ar+N₂) gas pressure of approximately 10⁻² to 10⁻⁴ Torr. The sputtering target(s) are subjected to a bias voltage in the range from approximately 20–500 volts, typically within the range from approximately 50–200 volts.

For microtransformer or inductor applications involving multilayer deposition and temperature-sensitive dielectric spacer layers such as polyimide, the substrate temperature typically is kept at or near ambient temperature. Alternatively, the substrate temperature is kept below approximately 150° Celsius (a temperature above which many polymers or polyimides begin to suffer damage with undesirable chemical or structural changes). For other device applications in which temperature-degradable materials are not involved, higher substrate temperatures generally are used.

Other embodiments of the present invention use one or more magnetic fields during the deposition of the films comprising Co—Fe—Cr—N to induce magnetic anisotropy in the desired direction. Since the inventive films have soft magnetic properties, a relatively low field is applied to introduce preferential ordering of atoms to form an easy direction of magnetization for higher permeability, lower coercivity (H_c), and a more square magnetic hysteresis (M-H) loop shape. The magnitude of the applied field is within the range from approximately 2–5000 oersteds (Oe), typically within the range from approximately 10–500 Oe. Since the deposition temperature for the inventive films often is near ambient temperature, the magnetic fields are applied conveniently, e.g., by placing one or more electromagnets or permanent magnets near the substrate. Such is done without fear of solenoid wire insulation damage or loss of magnetism in permanent magnets upon heating toward or above the Curie temperature.

In the case of magnetron sputtering, the stray magnet field itself in the deposition system is used conveniently to induce

anisotropy. As shown in FIGS. 2a–b, if an additional field is to be applied, one or more permanent magnets is used because of the relative simplicity of placing magnets either on the sides of or beneath substrate 220 during the deposition. Various permanent magnets 240 are acceptable, including those made of relatively high coercivity materials samarium-cobalt (Sm—Co), neodymium—iron—boron (Nd—Fe—B), barium-ferrite and iron-chromium-cobalt (Fe—Cr—Co), all of which reduce self-demagnetization in small or short magnet configurations. Multiple magnet arrays, such as shown in FIG. 2b, generally provide a stronger field to the substrate regions between the magnets than, e.g., the magnet arrangement shown in FIG. 2a. If a relatively uniform in-plane field is desirable over the substrate area, it is possible to replace the small magnets shown in FIG. 2a with a single magnet having a size comparable to that of the substrate.

In the case of multilayer deposition, the thickness of the layers comprising Co—Fe—Cr—N are within the range, e.g., from approximately 0.001–10.0 microns, typically within the range from approximately 0.01–2.0 microns. Higher frequency operations generally require thinner magnetic films to reduce eddy current loss. The insulating (dielectric) spacers, such as nitride or oxide ceramic films or plastic or polyimide films formed between the magnetic layers, typically are within the range from approximately 0.001–1.0 microns. The number of magnetic layers in use depends on the total amount of magnetic flux required and the thickness of each layer, but typically is between approximately 1–1000 layers.

The composition of the inventive films include, e.g., cobalt (Co) within the range from approximately 10–90 weight %, typically within the range from approximately 20–80 weight %, more typically within the range from approximately 30–60 weight %; iron (Fe) within the range from approximately 10–90 weight %, typically within the range from approximately 20–80 weight %, more typically within the range from approximately 30–60 weight % balance; chromium (Cr) within the range from approximately 0–15.0 weight %, typically within the range from approximately 1.0–12.0 weight %, and more typically within the range from approximately 1.5–8.0 weight %; and nitrogen (N) in the range from approximately 0.1–10 weight %, typically within the range from approximately 0.2–8 weight %, more typically in the range from approximately 0.3–5.0 weight %. Also, the inventive films may contain one or more impurity elements such as copper (Cu), nickel (Ni), tantalum (Ta), titanium (Ti), zirconium (Zr), hafnium (Hf), vanadium (V), molybdenum (Mo), niobium (Nb) and tungsten (W), cerium (Ce), yttrium (Y), lanthanum (La), carbon (C), aluminum (Al) and silicon (Si), with individual element amounts of less than approximately 1 weight % and typically less than approximately 0.5 weight %, and with total element amounts less than approximately 3 weight % and typically less than approximately 0.5 weight %.

Structurally, the inventive film includes a nanocrystalline or near-amorphous structure with an average crystallite size (grain-size), e.g., of less than approximately 1000 angstroms (Å), typically less than approximately 500 Å, and more typically less than approximately 200 Å. Also, the inventive film exhibits suitable soft magnetic properties in the as-deposited condition without having to undergo post-deposition heat treatment. For example, the coercivity (H_c) of the inventive films often is less than approximately 5 oersteds (Oe), and typically less than approximately 2 Oe. Also, the saturation (4πM_s) often is greater than approximately 12 kilogauss (kG), typically greater than approximately 15 kG, and more typically greater than approximately 18 kG.

The inventive films also exhibit squareness ratios (M_r/M_s), e.g., of at least approximately 0.90 and typically greater than approximately 0.95. Also, the anisotropy field (H_k) often is at least approximately 15 Oe, typically greater than approximately 30 Oe, and more typically greater than approximately 50 Oe.

Some of the processing and properties of the inventive films are described in the examples given below.

EXAMPLE 1

Thin films comprising the inventive Co—Fe—Cr—N alloy were deposited on 4 inch diameter (100) Si wafer substrates by triode DC magnetron sputtering, using the co-sputtering process illustrated generally in FIG. 3c, with two 2.25 inch diameter targets having approximate compositions of 86%Co-9.5%Fe-4.5%Cr (in weight %) and 95.5%Fe-4.5%Cr, respectively, and using a reactive process in a nitrogen-containing atmosphere. The sputtering chamber first was pumped down to approximately 2×10^{-7} Torr, and then the reactive sputtering was performed under a gas atmosphere with an initial pressure (Ar+N₂) of approximately 5×10^{-3} Torr and a gas flow rate of approximately 50 cubic centimeters per minute. The amount of nitrogen in the argon gas was approximately 2.5% in volume, which resulted in a nitrogen content in the deposited film of approximately 0.6 weight %. A bias voltage of approximately 140 volts was applied to both targets. The Si substrate was kept at ambient temperature during sputtering. The rate of sputter deposition was approximately 100 Å per minute. The films were approximately 1000 Å thick.

The magnetic hysteresis (M-H) loops were measured using a Vibrating Sample Magnetometer (VSM). The M-H loops were measured as a function of the in-plane orientation to determine the direction of easy and hard magnetization. Because the co-sputtering process targets are placed approximately 6 inches apart, the deposited Co—Fe—Cr—N films have a concentration gradient from one end to the other (e.g., from the Co-rich end to the Fe-rich end). Small samples, each approximately 0.125 inch square, were cut from various locations of the substrate to represent a spectrum of the gradient composition. Table 1 shows the easy-axis magnetic properties of some selected samples cut from the Si wafer. The approximate compositions also are given in the table.

TABLE 1

Magnetic Properties of Co-Sputtered Co—Fe—Cr—N Films in the As-Deposited Condition								
Composition (wt %)				$4\pi M_s$	Squareness	H_c	H_k	
Co	Fe	Cr	N	(kilogauss)	(M_r/M_s)	(Oe)	(Oe)	
83.6	10.6	4.5	1.3	14.8	0.98	6.6	32	
54.0	40.2	4.5	1.3	16.2	0.98	2.9	80	
42.7	51.5	4.5	1.3	19.3	0.99	1.9	73	
36.5	57.7	4.5	1.3	18.6	0.97	3.1	68	
14.9	79.3	4.5	1.3	17.2	0.95	3.2	72	
2.7	91.5	4.5	1.3	16.2	0.97	2.7	57	

As is evident from Table 1, thin films according to embodiments of the invention exhibit, in the as-deposited condition, advantageous soft magnetic properties with relatively square M-H loops, high saturation magnetization ($4\pi M_s$), low coercivity (H_c) and high anisotropy fields (H_k). Of particular interest is the thin film with an estimated composition of approximately 42.7%Co-51.5%Fe-4.5%Cr-1.3%N in weight %.

EXAMPLE 2

A thin film comprising the inventive Co—Fe—Cr—N alloy, e.g., with a composition of 49.7%Co-44.5%Fe-4.5%Cr-1.3%N (in weight %) was deposited on a silicon (Si) substrate from a single alloy target by triode magnetron sputtering. The nitrogen content in the argon gas was approximately 2.5% in volume. The mixed gas was blown directly onto the substrate at a distance of approximately 1 inch. A bias voltage of approximately 140 volts was applied to the single alloy target. The substrate was kept at ambient temperature. The rate of deposition was approximately 100 Å per minute. The film thickness was approximately 1000 Å.

Referring now to FIG. 4, magnetic hysteresis (M-H) loops along the in-plane easy-axis and the hard-axis of the thin film are shown. The easy-axis M-H loop exhibits advantageous soft magnetic properties of the film in the as-deposited condition. For example, such advantageous properties include a relatively high saturation magnetization ($4\pi M_s$) of approximately 19 kG, a relatively low coercivity (H_c) of approximately 0.87 Oe, and a relatively high squareness ratio (M_r/M_s) of approximately 0.98. The hard-axis loop, obtained in a 90° rotated direction, exhibits an advantageously closed loop and an anisotropy field (H_k) of approximately 35 Oe. The ferromagnetic resonance (FMR) frequency is estimated to be approximately 2.2 gigahertz (GHz).

It should be noted that the alloy films according to embodiments of the invention have relatively well-defined easy-axis and hard-axis orientations, typically both in-plane and approximately 90 degrees apart. For minimal power loss in high-frequency applications, it is advantageous to have the hard-axis loop as closed as possible and with a coercivity (H_c) along the hard-axis of less than approximately 5 Oe, typically less than approximately 2 Oe, and more typically less than approximately 1 Oe, and with the remanent induction as close to zero as possible, with a squareness ratio (M_r/M_s), typically less than approximately 0.1 and typically less than 0.02.

EXAMPLE 3

A film comprising the inventive Co—Fe—Cr—N alloy and having a thickness of approximately 1000 Å was deposited on a silicon (Si) substrate using a diode sputtering system. The target-to-substrate incident angle was tilted to be approximately 45 degrees. The nitrogen gas content in argon was at approximately 17 volume %. The mixed gas was fed into the deposition chamber with a distance to the substrate of approximately 6 inches. The resultant film in the as-deposited condition yielded advantageously highly anisotropic, magnetic properties, e.g., an anisotropy field (H_k) of approximately 230 Oe, a saturation magnetization ($4\pi M_s$) of approximately 10 kG, a squareness ratio (M_r/M_s) of approximately 0.97, and a coercivity (H_c) of approximately 18 Oe. The ferromagnetic resonance frequency of this film is estimated to be approximately 4.2 GHz.

It is evident from the Examples 1–3 described above that advantageously highly anisotropic, soft magnetic properties are obtainable in the as-deposited condition for films according to embodiments of the invention prepared by either co-sputtering or single alloy sputtering. Such combinations of relatively high saturation magnetization ($4\pi M_s$), low coercivity (H_c), high squareness ratios (M_r/M_s) and high anisotropy fields (H_k) are advantageous for use in many electromagnetic devices, such as in microtransformers, recording heads and high-frequency telecommunication devices.

The advantageous squareness ratio of the loop, the strong anisotropy and the unusually high anisotropy field values in films according to embodiments of the invention are believed to be the result of the inventive alloys and the unique processing procedures employed. The addition of chromium (Cr), especially in combination with oblique incident film deposition, appears to be advantageous in enhancing the magnetic anisotropy and electrical resistivity. Also, the presence of Cr is believed to help the formation of desirable nanocrystalline structure and microstructural texture for strong in-plane anisotropy fields. Such presence also is believed to improve soft magnetic properties, e.g., a lower coercivity (H_c), by reducing magnetocrystalline anisotropy or magnetostriction.

Furthermore, according to embodiments of the invention, increasing the angle of sputter deposition during the formation of the invention alloys advantageously improves their magnetic properties. For purposes of discussion herein, the terms "angle of sputter deposition" or "sputter deposition angle" or "deposition angle" are intended to include the angle at which the sputtered atoms arrive at and impinge on the substrate.

For example, FIG. 3 illustrates various deposition angle configurations according to embodiments of the invention. In FIG. 3a, a target 210 is centered above a substrate 220. In this configuration, the portion of a film 250 near the periphery of the substrate is deposited with a greater inclined angle than the portion of film 250 deposited near the center of the substrate. The angular difference affects the magnetic properties of the film, e.g., as shown in FIG. 5. The plot in FIG. 5 was derived from a film having a thickness of approximately 1000 Å, with a composition of Co-45%Fe-4.5%Cr-0.6%N (weight percent). For an angular difference of approximately 45 degrees, an advantageously low coercivity value (H_c) of approximately 2 Oe or less is achieved, while for an angular difference of approximately 0 degrees, a disadvantageously high coercivity value (H_c) of approximately 18 Oe occurs.

To keep a sufficiently high deposition angle, the target and the substrate should be laterally displaced, e.g., as shown in FIG. 3b. In the case of co-sputtering, two or more targets may be placed laterally away from the substrate position, e.g., as shown in FIG. 3c. According to embodiments of the invention, sputter deposition angles of at least approximately 10 degrees should be maintained. Alternatively, maintaining sputter deposition angles of at least approximately 20 degrees or even at least approximately 40 degrees are advantageous.

Referring now to FIG. 6, the magnetic coercivity, H_c , of the inventive films comprising Co—Fe—Cr—N as a function of nitrogen content (in volume %) in the Ar gas sputtering atmosphere is shown. The coercivity value, H_c , of the films depends on the nitrogen content, with the lowest coercivity often being obtained by sputtering at a nitrogen gas content of approximately 2.5 volume %, which corresponds to approximately 0.6 weight % nitrogen atoms in the film. An insufficient nitrogen content is ineffective for preventing grain growth of the alloy matrix and results in an increased coercivity value. However, a nitrogen content too great (e.g., more than approximately 5 weight %) reduces the saturation magnetization ($4\pi M_s$) and also increases the coercivity. Thus, there appears to be a moderate, optimal range of nitrogen content for a given alloy composition.

The addition of Cr to a Co—Fe—N alloy film improves the soft magnetic properties of the film. Such improvements include, e.g., a lower coercivity (H_c), a more square mag-

netic hysteresis (M-H) loop, and a higher anisotropy field (H_k) in the as-deposited condition. Also, such additions reduce or eliminate the need for post-deposition heat-treatment.

According to an alternative embodiment of the invention, the inventive films are given a low-temperature heat treatment to further improve the soft magnetic properties. To reduce the damage to insulating layers such as polyimide, heat treatment temperatures below approximately 300° Celsius and typically below approximately 150° Celsius are used. Also, to reduce surface oxidation during the heat treatment, a vacuum atmosphere of greater than approximately 10^{-4} Torr is used. However, a vacuum atmosphere less than approximately 10^{-4} Torr is used, e.g., if the top surface of the film is protected by oxidation-resistant coatings such as Cr, Al, oxide, or nitride films.

According to another embodiment of the invention, the inventive films are formed as a composite structure with a different type of magnetic layer. For example, the composite structure has one or more exchange bias films made of, e.g., one or more antiferromagnetic, ferromagnetic or ferrimagnetic materials, that are added directly on the surface of the soft magnetic film. For example, a thin film of Fe-50% manganese antiferromagnetic alloy is added onto some or all of the soft magnetic layers comprising Co—Fe—Cr—N to shift the magnetic hysteresis (M-H) loop by more than the coercivity of the soft magnetic film (i.e., by at least approximately 2 Oe). Also, the thin film of Fe-50% manganese antiferromagnetic alloy is added to allow for high-frequency operation (e.g., approximately 0.1–10 GHz) of the soft magnetic films in the internal bias-field mode with minimal magnetic domain wall motion.

Some of the inventive Co—Fe—Cr—N films exhibit highly square, easy-axis loop characteristics in combination with closed, hard-axis loop shapes and relatively high, easy-axis coercivity, e.g., greater than approximately 10–30 Oe. Such high coercivity is desirable in operations that are free of domain-wall motion because the high coercivity provides the stability of easy-axis saturation against stray fields and thus makes it unnecessary to add antiferromagnetic bias films.

The last step 140 in FIG. 1 is to assemble the magnetic thin film within electromagnetic devices such as microtransformers, saturable transformers, inductors and recording heads. Step 140 comprises appropriately sizing the substrate (which contains a deposited and optionally patterned single layer, multilayer or composite-structured magnetic film), adding appropriate interconnection and conductor circuitry if needed, and assembling the film within the electromagnetic devices.

Referring now to FIGS. 7a–b, various views of a pot-core type microtransformer comprising the inventive films comprising Co—Fe—Cr—N are shown. To form such transformer, a multiplicity of soft magnetic film layers 610 (laminations with polyimide or other insulating layers there between) first is deposited, then a patterned conductor layer 620 (e.g., containing Cu lines) is added above magnetic film layers 610, and then more magnetic film laminations 630 are deposited, as shown.

FIGS. 8a–b show various views of a toroidal microtransformer according to an embodiment of the invention. Here, a conductor layer 710 in the form of parallel segments first is prepared, then a magnetic film lamination 720 comprising Co—Fe—Cr—N is deposited thereon, and then a top conductor layer 730 in the form of parallel segments is added for connection with segments of conductor layer 710 to form the toroidal winding configuration as shown.

For certain applications, films comprising Co—Fe—Cr—N are deposited in such a way that the easy-axis of magnetization coincides with the direction of the applied field from the windings. For very high-frequency applications (e.g., frequencies of approximately 10 MHz or greater), magnetization switching by domain wall motion typically is not desired and hence the magnetically hard direction is used so that coherent spin rotation mode is operational.

For this reason, in-plane uniaxial magnetic anisotropy and the accompanying square magnetic hysteresis (M-H) loop shape typically is used. The uniaxial anisotropy, which is induced, e.g., by thin film deposition in the presence of magnetic fields, is defined, e.g., in terms of the anisotropy field (H_k), which is represented by the field in which the hard-axis magnetization loop reaches saturation. See, for example, FIG. 4, which is discussed hereinabove.

According to embodiments of the invention, anisotropy fields (H_k) in the inventive films are advantageously high, e.g., in the range from approximately 15–200 Oe and typically in the range from approximately 30–100 Oe. However, too high of an anisotropy field, e.g., greater than approximately 500 Oe, reduces the high-frequency permeability, which is proportional to the saturation magnetization divided by the anisotropy field value ($4\pi M_s/H_k$) in the hard-axis operation. Also, too low of an anisotropy field, e.g., less than approximately 10 Oe, causes the ferromagnetic resonance frequency to be reduced and to interfere with operating frequency ranges. Therefore, too much magnetic softness (i.e., a very low anisotropy value) typically is disadvantageous for high-frequency operation of devices comprising the inventive films.

A relatively high “squareness” of the magnetic hysteresis (M-H) loop in the easy-axis direction is advantageous for high-frequency applications (e.g., greater than 0.5 GHz), as devices comprising the inventive films advantageously are saturated essentially into a single domain state along the easy-axis, and then are operated in a high-frequency alternating current (AC) mode in the hard-axis direction to reduce or minimize the domain wall motion. In this manner, devices with the inventive films comprising Co—Fe—Cr—N have a “squareness” (as defined by the ratio of the remanent magnetization, M_r , to the saturation magnetization, M_s) of at least 0.90 and typically at least 0.95.

FIGS. 9a–b show cross-sectional views of electromagnetic devices having embodiments of the invention incorporated therein. A cross-sectional view of a recording read-write head comprising an embodiment of the inventive film is illustrated in FIG. 9a. The soft magnetic film **810** serves to amplify the magnetic signal from the recorded magnetic memory bit information in the magnetic disk or tape **820** such that the inductive sense coil or magnetoresistive sensor **830** generates a higher output signal. Shown also is the substrate **840** upon which soft magnetic film **810** is formed.

Alternatively, as shown in FIG. 9b, the inventive film is used as the high-magnetization material in the metal-in-gap (MIG) type head configuration. In this embodiment, the head **850** is made of, e.g., ferrite.

It will be apparent to those skilled in the art that many changes and substitutions can be made to the thin films and their incorporation into the electromagnetic devices herein described without departing from the spirit and scope of the invention as defined by the appended claims.

What is claimed is:

1. An article, comprising:

a non-magnetic substrate; and

an anisotropic, magnetically soft film supported by said substrate, said film including an alloy of cobalt-iron-chromium-nitrogen (Co—Fe—Cr—N) and having a saturation magnetization ($4\pi M_s$) of at least approximately 8 kilogauss (kG), an anisotropy field (H_k) within the range from approximately 15 to 300 oersteds (Oe) and a magnetic hysteresis (M-H) loop squareness ratio (remanent magnetization, M_r , to saturation magnetization, M_s) of at least approximately 0.90, wherein said alloy contains, by atomic percentage, at least approximately 15% cobalt (Co), and wherein said article has been heat treated at a temperature of no more than approximately 150° Celsius.

2. The article as recited in claim 1, wherein said film has an anisotropy field (H_k) greater than approximately 50 Oe, and has a ferromagnetic resonance (FMR) frequency greater than approximately 1 gigahertz (GHz).

3. The article as recited in claim 1, wherein said Co—Fe—Cr—N alloy includes chromium (Cr) within the range from approximately 0 to 15 weight %.

4. The article as recited in claim 1, wherein said Co—Fe—Cr—N alloy contains cobalt (Co) within the range from approximately 20 to 80 weight %, iron (Fe) within the range from approximately 20 to 80 weight %, chromium (Cr) within the range from approximately 1 to 12 weight %, and nitrogen (N) within the range from approximately 0.2 to 8.0 weight %.

5. The article as recited in claim 1, wherein said film further comprises a plurality of thin film layers and wherein said article further comprises a corresponding plurality of dielectric spacer layers formed between said thin film layers in such a way that a multilayer structure is formed.

6. The article as recited in claim 5, wherein said plurality of dielectric spacer layers further comprises polyimide or ceramic insulators.

7. The article as recited in claim 1, wherein said film is formed on said substrate in such a way that the average grain structure size of said film is less than approximately 500 angstroms (Å).

8. The article as recited in claim 1, further comprising one or more exchange bias films formed on said film, said exchange bias films selected from a group consisting of antiferromagnetic, ferromagnetic and ferrimagnetic material.

9. The article as recited in claim 1, wherein said article is part of an electromagnetic device selected from a group consisting of a microtransformer, an inductor and a magnetic read-write head.

10. The article as recited in claim 1, wherein said article is for use at an operating frequency of at least approximately 10 megahertz (MHz), and wherein said film is saturated along an easy-axis of magnetization into a single domain state and then operated in an alternating current (AC) field along a hard-axis of magnetization.

11. The article as recited in claim 1, wherein said film has an easy-axis coercive force of at least approximately 30 oersteds (Oe).

12. A method for making a magnetically soft thin film article, said method comprising the steps of:

providing a non-magnetic substrate; and

depositing at least one anisotropic, magnetically soft thin film in such a way that said non-magnetic substrate supports said film, said film including an alloy of cobalt-iron-chromium-nitrogen (Co—Fe—Cr—N) and

13

having a saturation magnetization ($4\pi M_s$) of at least approximately 8 kilogauss (kG), an anisotropy field (H_k) within the range from approximately 15 to 300 oersteds (Oe) and a magnetic hysteresis (M-H) loop squareness ratio (remanent magnetization, M_r , to saturation magnetization, M_s) of at least approximately 0.90, wherein said alloy contains, by atomic percentage, at least approximately 15% cobalt (Co), and wherein said article has been heat treated at a temperature of no more than approximately 150° Celsius.

13. The method as recited in claim 12, wherein said Co—Fe—Cr—N alloy includes chromium (Cr) within the range from approximately 0 to 15 weight %.

14. The method as recited in claim 12, wherein the Co—Fe—Cr—N alloy contains cobalt (Co) within the range from approximately 30 to 60 weight %, iron (Fe) within the range from approximately 30 to 60 weight %, chromium (Cr) within the range from approximately 1 to 12 weight %, and nitrogen (N) within the range from approximately 0.7 to 5.0 weight %.

15. The method as recited in claim 12, wherein said depositing step is selected from the group consisting of sputtering, evaporation, molecular beam epitaxial growth, ion beam deposition and laser ablation.

16. The method as recited in claim 12, wherein said forming step further comprises depositing the elements of

14

said alloy without nitrogen on said substrate, and then adding nitrogen to said alloy by ion implantation.

17. The method as recited in claim 12, wherein said forming step further comprises sputter-depositing said magnetically soft thin film on said substrate with a deposition angle of at least approximately 10 degrees.

18. The method as recited in claim 12, wherein said forming step further comprises sputter-depositing said magnetically soft thin film on said substrate at ambient temperature and in the presence of an applied magnetic field having a strength greater than approximately 2.0 oersteds (Oe).

19. The method as recited in claim 12, further comprising, after said depositing step, the step of heat treating said magnetically soft thin film below a temperature of approximately 150° Celsius.

20. The method as recited in claim 12, wherein said depositing step further comprises depositing a plurality of magnetically soft thin film layers interleaved with corresponding plurality of dielectric spacer layers.

21. The method as recited in claim 12, further comprising the step of incorporating said magnetically soft thin film into an electromagnetic device selected from the group consisting of a microtransformer core, an inductor core, and a magnetic read-write head.

* * * * *

MOLECULAR-DYNAMICS STUDY OF THIN IRON
FILMS ON COPPERK. KADAU,* R. MEYER† and P. ENTEL‡
*Theoretische Tieftemperaturphysik, Gerhard-Mercator-Universität Duisburg,
Lotharstraße 1, 47048 Duisburg, Germany*

Received 26 May 1998

We have studied the structural stability of thin γ -iron films on Cu(001) and Cu(111) substrates using molecular-dynamics simulations in combination with a semiempirical model. Experimentally, the stability of such films has turned out to depend on (growth) temperature and film thickness. On increasing the thickness or decreasing the temperature the films undergo a structural change to the bcc structure, which is well reproduced by our simulations. An analysis of the local atomic environment of the films after the structural transformation shows that, especially on Cu(001), only parts of the film accomplish the transformation into the bcc structure. Considerations of the atomic displacements during the transformation allow us to give an explanation of the different stability of the films on Cu(001) and Cu(111) as well as the observed orientational relationships.

1. Introduction

The structural and magnetic properties of thin films usually differ from those of the corresponding bulk materials. This allows the study of systems under conditions which cannot be realized by bulk systems. A well-known example of this is the stabilization of fcc (γ -)iron on a copper substrate.

Bulk γ -Fe is only stable between 1184 and 1666 K, while at lower temperatures the stable phase is bcc (α -)iron.¹ Despite this, numerous experimental investigations have shown that it is possible to grow thin γ -Fe films epitaxially on Cu(001) or Cu(111) surfaces at room temperature.²⁻¹¹ The structural and magnetic properties of such films are still under discussion, due to the complex magnetic behavior of γ -Fe. Nevertheless, there is much experimental evidence that in the case of Fe on Cu(001) three different growth regimes have to be distinguished.^{4,8} Films with a thickness of less than approximately five monolayers (ML) grown near or below room

temperature show an fct-like structure with complex superstructures and a high-moment ferromagnetic state.^{9,12} In the region of $\approx 5-10$ ML a layer-by-layer growth of nearly isotropic fcc-Fe films is observed for growth at room temperature. In this regime the films show an antiferromagnetic layer-coupling in the interior of the films¹³ and a ferromagnetic coupling of the surface layers.^{4,8,12} Above a thickness of about 10 ML the fcc structure transforms into a twinned bcc structure.⁷ Many different values for the maximum thickness of stable γ -Fe films on Cu(001) have been reported. The reason for these discrepancies is that the onset of the structural transformation depends on several parameters. It has been shown that lower growth temperatures lead to a lower critical thickness of the films, while a higher background pressure (for example by CO molecules) stabilizes the fcc structure. Moreover, subsequent cooling of γ -Fe films grown at room temperature might lead to the formation of the bcc structure as well as mild

*E-mail: kai@thp.Uni-Duisburg.DE

†E-mail: ralf@thp.Uni-Duisburg.DE

‡E-mail: entel@thp.Uni-Duisburg.DE

PACS: 68.55.-a, 68.35.Rh, 61.43Bn

sputtering does.⁷ The maximum thickness of isotropic γ -Fe films on Cu(111) surfaces is significantly lower than on Cu(001). Values between 2.3 and 6 ML have been observed.^{3,10,11} Films thicker than these values undergo a structural transformation to the bcc structure similar to the case of Fe/Cu(001).

In this paper we focus on the stability of γ -Fe films on Cu(001) and Cu(111) surfaces. We have not looked at the differences between the first two growth regimes of Fe/Cu(001). These differences are certainly connected with changes in the magnetic structure of the films, which are beyond the scope of the model used in our computations. The rest of this paper is organized as follows. In the next section we give a short description of the model and the computational methods used in our calculations. The results obtained from computer simulations of Fe films on Cu(001) and Cu(111) are presented in Sec. 3. Finally, a short summary of the results is given in Sec. 4.

2. Computational Methods

In this study we used the method of molecular-dynamics (MD) simulations to investigate the structural stability of thin iron films on copper substrates. MD simulations have turned out to be a useful tool in the study of equilibrium and nonequilibrium phenomena of solids, like thermal properties, crack propagation, the contact mechanism, structural transformations, surface phonons, and many others.

Any kind of atomistic computer simulation requires a reliable model for the description of the interactions between the atoms. In our simulations we have made use of a model based on the embedded-atom method (EAM) of Daw and Baskes,^{14,15} since this method is able to give a better description of the elastic properties of metals than ordinary pair potentials do. Within our simulations the energy of the system is written as

$$E = \sum_i F_{\alpha_i}(\rho_i) + \sum_i \sum_{j \neq i} \frac{Z_{\alpha_i}(r_{ij})Z_{\alpha_j}(r_{ij})}{r_{ij}}, \quad (1)$$

where the indices i and j denote individual atoms; $\alpha_i, \alpha_j = \text{Fe, Cu}$ refer to the species of the corresponding atoms, and r_{ij} is the separation of atoms i and j . The function F_{α_i} represents the embedding energy of atom i depending on the background charge density

$$\rho_i = \sum_{j \neq i} \rho_{\alpha_j}^{\text{at}}(r_{ij}), \quad (2)$$

which is superposition of the contributions $\rho_{\alpha_j}^{\text{at}}$ of all atoms j except i . The second term of Eq. (1) is a screened Coulomb potential with the effective charges Z_{α_i} .

The functions F_{α_i} and Z_{α_i} are cubic spline functions which have been fitted empirically to the properties of pure iron and copper. In the case of iron we fitted these functions using the experimental data of the lattice constant, cohesive energy, vacancy formation energy, elastic constants and some phonon frequencies of α -Fe. Details of these calculations and the parameters of the resulting functions can be found in Ref. 16. It has to be noted that this EAM potential is based on the data of ferromagnetic α -Fe only. As a consequence, this potential is best suited for a description of the high-moment ferromagnetic state of γ -Fe.¹⁷ Nevertheless, this model has successfully been applied in simulations of the bcc-to-fcc transformation in iron-nickel alloys and should therefore also be suitable within the context of this work. For copper we used the functions of Gui *et al.*,¹⁸ which were obtained by a fit to the experimental data of the lattice constant, cohesive energy, vacancy formation energy and elastic constants of copper. In both cases the atomic contributions to the background charge density $\rho_{\alpha_j}^{\text{at}}$ are calculated with the help of the wave functions of the valence electrons in free atoms tabulated by Clementi and Roetti.¹⁹

In an atomistic MD simulation of a solid, the classical equations of motions of the atoms are numerically integrated and thermodynamical averages are calculated from the resulting trajectories.²⁰ For the integration of the equations of motions we adopted the velocity Verlet algorithm (see, for example, Ref. 20) with a time increment of 1.5 fs and the Nosé-Hoover thermostat method, which leads to a canonical distribution of the atomic configurations.²¹ Artificial surface effects have been minimized through the use of periodic boundary conditions in the directions perpendicular to the film normal, while changes in the size and shape of the simulation cell were allowed using the scheme of Parrinello and Rahman.²²

The initial configurations of our simulations consisted of regular arrangements of atoms on a perfect fcc lattice with randomly chosen velocities

according to the Maxwell-Boltzmann distribution. The following geometries have been used: 7 ML Fe on Cu(001), 15 ML Fe on Cu(001), 6 ML Fe on Cu(111) and 14 ML Fe on Cu(111). Since every real film inevitably contains a number of defects, we introduced about 2% of vacancies into the systems. This high concentration was chosen in order to guarantee a significant number of vacancies in the simulation box and to emulate the effect of other defects like dislocations and grain boundaries. The influence of these defects has been studied by additional simulations of defect-free films in the case of Fe/Cu(001). The total size of the configurations was about 21^3 lattice constants, containing approximately 37 000 atoms. The surface normal was oriented along the z -axis of the simulation cell. Actually, our systems contained two free surfaces: one iron surface at the top of the system and one copper surface at the bottom. However, we have studied only the iron surface except for the relaxation of the interlayer spacing, which we have analyzed at both surfaces as well as in the vicinity of the Fe/Cu interface. In order to check for finite-size effects, additional simulations have been carried out using configurations with a lateral size of 10, 15, 30 and 40 lattice constants.

At the beginning of the simulation runs the initial configurations had to be equilibrated at the desired temperature. In order to do this, we simulated the systems over a period of 500 simulation steps and rescaled the instantaneous temperature of the systems at every 50th step. Afterwards the normal parts of the simulation runs began, which consisted of a sequence of successive short simulations with a length of 300 time steps. From the mean positions of the atoms during these runs we calculated the percentage of iron atoms with a local bcc environment. The simulation runs ended when no significant change of this value was observed for a longer period. The structure of the local environment of an atom was determined by the following procedure. An atom was assumed to have a bcc environment if the standard deviation of the distance of its ten nearest neighbors was larger than $0.02 a_B$. Here we make use of the fact that the first nearest-neighbor shell of the bcc lattice contains only eight atoms while the fcc lattice has a coordination number of 12. Therefore, the 12 nearest neighbors of an atom in an fcc environment all belong to the same neighbor shell, whereas in a bcc environment two different neighbor shells are involved. Two

points have to be noted. First, our method for the determination of the local environment of an atom fails in the case of a surface atom due to the different coordination of these atoms. Therefore, we have discarded the surface atoms in the calculation of the percentage of bcc iron. Second, it is rather important that we have used mean atomic positions averaged over 300 simulation steps. If one uses the actual positions of the atoms at one time, thermal fluctuations lead to a much broader distribution of the neighbor separations, making it impossible to distinguish between local crystal structures. Problems arise from the diffusion of atoms in the case of the presence of vacancies. If an atom moves into the position of a neighboring vacancy, the mean position of this atom calculated during the hopping process is almost meaningless. This might lead to a slight overestimation of the fraction of atoms with a bcc environment. However, since such processes are rather rare, the resulting error is small and should not influence the observed general tendencies.

3. Results

3.1. Fe on Cu(001)

The interatomic potentials we used in our simulations have only been constructed on the basis of bulk properties of iron and copper. Therefore, it seemed appropriate to check the reliability of the EAM model in the context of surface phenomena. In order to do this, we compared the interlayer distances near the surface predicted by the model with experimental results. As will be discussed below, simulations of the configurations with 7 and 15 ML Fe/Cu(001) without vacancies showed no structural change at 300 K. From these simulations we derived an inward relaxation of the first copper layer by 3%. This is somewhat larger than the experimental values, which are in the range of 1–2%, but compares well with the results of other interatomic potentials (see Ref. 23 and references therein). At the iron surface we found an inward relaxation of the outermost layer by nearly 7%. In this case the experimentally observed value depends on the magnetic structure of the film. Wuttig *et al.* report an inward relaxation of 2% for a 5 ML film, whereas they found a considerable outward relaxation in films with 6–11 ML Fe/Cu(001).⁷ This difference is caused by the antiferromagnetic coupling in the interior of

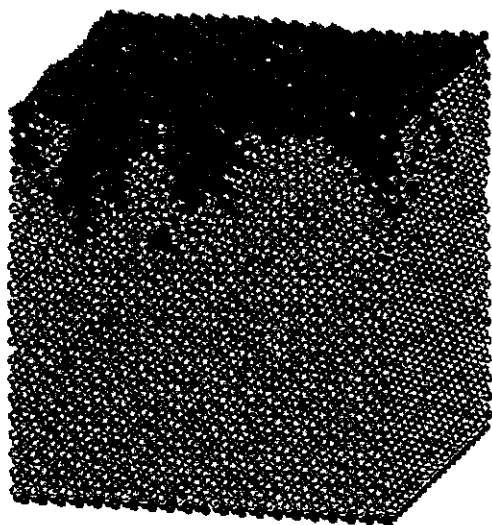


Fig. 1. Resulting configuration of 15 ML Fe/Cu(001) with 2% vacancies after a simulation time of 13.5 ps. The blue atom indicates a local bcc environment, while atoms with an fcc environment are drawn in orange.

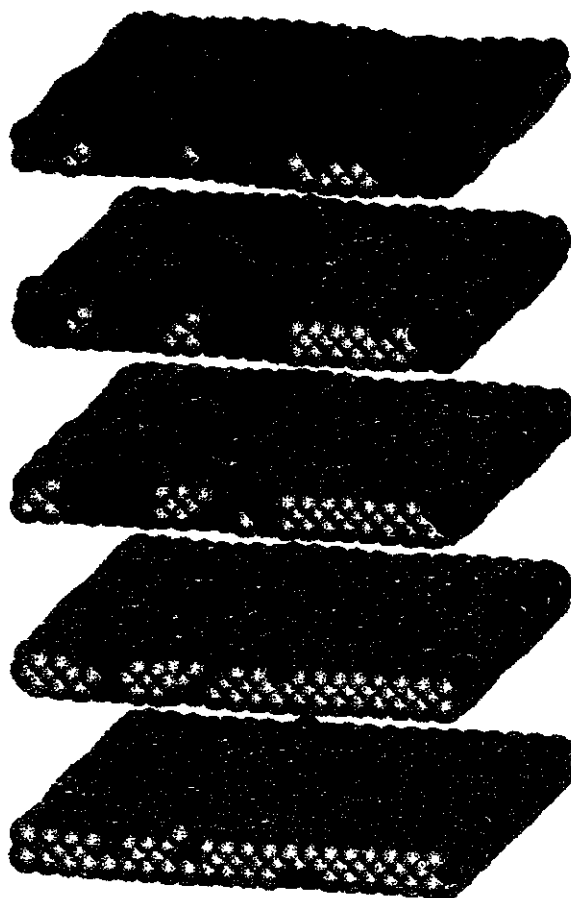


Fig. 2. Iron film from Fig. 1 drawn slicewise.

the thicker films, which reduces the layer separation of the deeper layers. Again, it turns out that the EAM model is best suited for a description of ferromagnetic γ -Fe. The large value of the relaxation we find is a consequence of the fact that the EAM model predicts rather low elastic constants for γ -Fe at low temperatures.¹⁷ In addition to the relaxation of the surface layers, we also studied the interlayer distances near the iron-copper interface in our systems. Here we find a pronounced increase of the separation of the first two iron layers by 6%. Although this effect might be an artifact of the short interaction range of the repulsive pair potentials in the EAM model, it would be interesting to check this result experimentally.

The main subject of this work is the investigation of the structural stability of iron films on copper substrates. Figure 1 shows the resulting (stable) configuration of the system with 15 ML Fe/Cu(001) and 2% vacancies after simulation over a period of 13.5 ps. The blue color indicates atoms with a local bcc environment, while atoms with an fcc environment are drawn in orange. From this figure it is clearly visible that not all of the iron atoms transformed into the bcc structure and that the amount of bcc iron decreases in the interior of the film. The resulting complicated domain structure consisting of channels of α -Fe going down from the surface can be seen in detail in Fig. 2, where the iron film is shown slicewise. The fact that only a part of the film transformed into the bcc structure has also been observed in experiments.²⁴ However, to the best of our knowledge no experiments have so far revealed the topology of the resulting domain structure.

In Figs. 3 and 4 the surface structures of the initial configuration and the transformed film are compared. While in Fig. 3 the regular square structure of the fcc unit cells can be seen, the stretched hexagons drawn in Fig. 4 are characteristic of $(110)_{\text{bcc}}$ planes. The occurrence of two different orientations of the hexagons is a consequence of the fact that the transformed film possesses a twin structure with $(\bar{1}12)$ twinning planes and $[1\bar{1}1]$ shear directions. This twin system is rather typical of the bcc structure.²⁵ The formation of twin variants reduces the atomic movement necessary for accomplishing the structural transformation. Without the twinning plane the transformation of fcc into bcc would require a macroscopic deformation of the

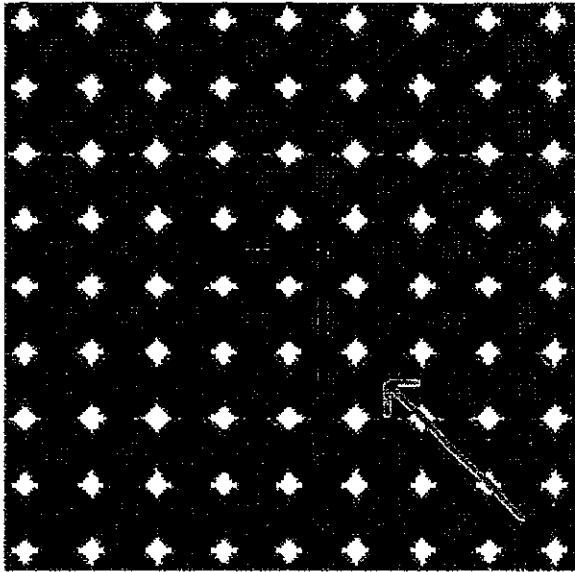


Fig. 3. Surface of the initial configuration of the system in Fig. 1. The dark arrow indicates the $[010]_{fcc}$ direction, the light arrow $[\bar{1}10]_{fcc}$.

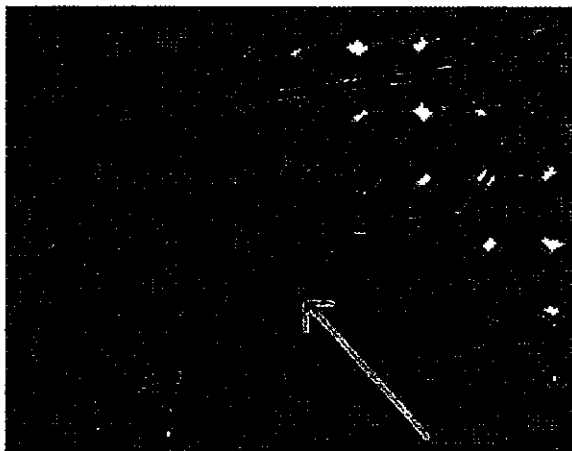


Fig. 4. Surface of the system in Fig. 1. The distorted hexagons are typical of $(110)_{bcc}$. The dark arrow indicates the $[001]_{bcc}$ direction, the light arrow $[1\bar{1}1]_{bcc}$.

iron film, which is rather unfavorable since the copper substrate retains its fcc structure. We generally find from our simulations a separation of 5–10 $(\bar{1}12)_{bcc}$ planes between the twinning planes. The same width has been found in simulations of systems with lateral sizes of 10, 15, 30 and 40 lattice constants. This shows that the width of the stripes is not influenced by finite-size effects, but is determined by the transformation process and elastic energies. If one compares Figs. 3 and 4, one can see that the

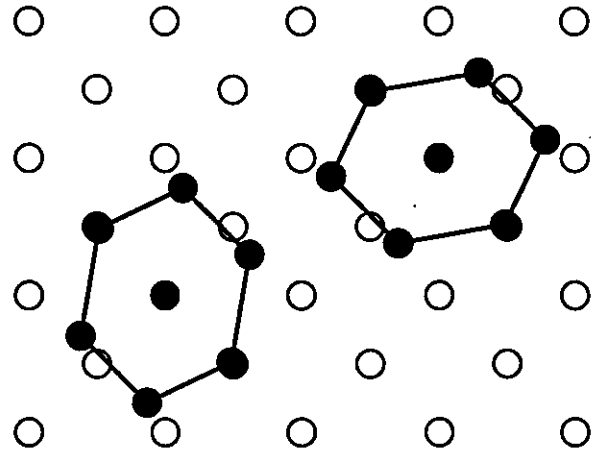


Fig. 5. Formation of $(110)_{bcc}$ hexagons (full circles) in Pitsch orientation from a $(001)_{fcc}$ plane (open circles).

close-packed $[110]_{fcc}$ direction is transformed into the $[1\bar{1}1]_{bcc}$ direction without any rotation. This orientational relationship combined with the plane condition $(001)_{fcc} \parallel (110)_{bcc}$, given by the film geometry, is called the Pitsch orientation.²⁶ It has experimentally been observed by Wuttig *et al.*⁷ in their scanning-tunneling-microscopy investigations of Fe/Cu(001). These authors also report the formation of twin variants similar to those we find in our simulations. The orientational relationships are further illustrated by Fig. 5, which schematically shows two variants of the distorted hexagons of the $(001)_{bcc}$ planes in comparison to the $(001)_{fcc}$ planes. The lattice constants have been chosen in such a manner that the atomic volumes of the two structures are equal, which nearly meets the situation of bcc iron and fcc copper. From Fig. 5 it can be seen that two other crystallographically equivalent variants of the bcc structure could be formed. However, due to the finite size of the systems, only two variants occurred simultaneously in the simulations.

The amount of iron atoms transformed from fcc into bcc, which we found in our simulations, depends both on temperature and on the thickness of the film. In Table 1 we present the results which we obtained from simulations of Fe films on Cu(001) with 2% vacancies at 50 and 300 K. The fcc structure remained more or less stable in both films at the higher temperature (the small fractions of α -Fe we observed are probably artefacts of diffusion processes), whereas at 50 K both films partially transformed into the

Table 1. Percentage of iron transformed from fcc into bcc in a Fe/Cu(001) film with 2% vacancies after a simulation time of 9 ps.

ML Fe	50 K	300 K
7	13.68%	0.49%
15	43.28%	0.03%

bcc structure, with the thicker film showing a significantly higher amount of α -Fe. This behavior reflects the experimental observation that the fcc structure of Fe/Cu(001) gets more and more unstable with increasing film thickness and/or decreasing temperature. However, some differences between our simulations and experimental results have to be noted. In contrast to our simulations, most experimental investigations did not show a stable fcc structure in films with a thickness of 15 ML Fe/Cu(001) at room temperature. Different results are probably related to higher background pressures. This discrepancy is probably caused by the permanent perturbation of the surface and the unavoidable presence of surface steps under experimental conditions. The neglect of these effects might artificially stabilize the fcc structure in the simulation. So far the small fraction of α -Fe we found in the thin film at 50 K has also not been observed in experiments. The corresponding bcc regions appear directly at the surface of the film. It is, therefore, likely that they are connected with the wrong interlayer relaxation at the surface and are caused by the insufficient treatment of magnetic effects by our model.

So far we have presented only results obtained from configurations containing 2% vacancies. Simulations using configurations without defects yielded somewhat different results. In Table 2 the amount of transformed iron atoms in these films is reported. From this table it can be seen that the amount of transformed iron atoms in these perfect films is strongly reduced with respect to Table 1. More serious than this difference in the amount of transformed iron, however, is the fact that the orientational relationship, which we observed in the films with defects, does not hold for the perfect films. While still the $(001)_{\text{fcc}}$ planes are transformed into $(110)_{\text{bcc}}$ planes, i.e. $(001)_{\text{fcc}} \parallel (110)_{\text{bcc}}$, the relationship $[100]_{\text{fcc}} \parallel$

Table 2. Percentage of iron transformed from fcc into bcc in a Fe/Cu(001) film without vacancies after a simulation time of 9 ps.

ML Fe	50 K	300 K
7	1.32%	0.00%
15	17.93%	0.00%

$[1\bar{1}0]_{\text{bcc}}$ holds instead of $[110]_{\text{fcc}} \parallel [1\bar{1}1]_{\text{bcc}}$. These orientational relationships correspond exactly to the well known purely distortive Bain transformation. A schematic view of both possible variants is given in Fig. 6. However, we did not observe the formation of a twinned structure, but instead growth of symmetrically arranged isolated islands of α -Fe within the matrix of γ -Fe.

An explanation of the different transformation behavior of films with and without defects might be given by the total displacement of the atoms during the transformation. The energy of the interface between a region of α -Fe and the copper substrates or the surrounding γ -Fe matrix should be approximately proportional to the square of the displacement (misfit) of the atoms. The sum of the squared displacements of the atoms of one hexagon in Fig. 5 is 0.24 in terms of the fcc lattice constant, while in Fig. 6 it is only 0.14 (the sum of the absolute values of the displacements are 1.02 and 0.89 fcc lattice constants, respectively). Therefore, it is clear that

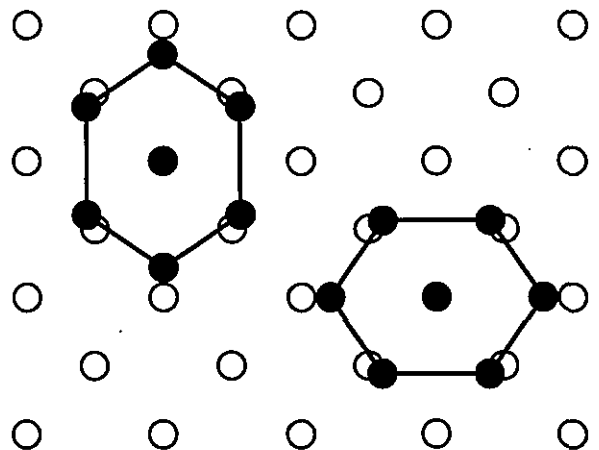


Fig. 6. Formation of $(110)_{\text{bcc}}$ hexagons (full circles) in Bain orientation from a $(001)_{\text{fcc}}$ plane (open circles).

the system without vacancies prefers the transformation according to Fig. 6. However, what is then the reason for the different behavior of Fe/Cu(001) with defects? The vacancies give the system much more freedom to shield the elastic stress originating from the interface. Thus, the influence of other factors on the transformation path might grow due to the presence of defects. An important difference between the Pitsch orientation and the Bain orientation is the fact that the Pitsch orientation is a shearlike transformation while the Bain transformation is purely distortive. Hence the Pitsch orientation might be realized in systems with defects due to a lower activation energy along the transformations path. Another advantage of the Pitsch orientation is that it leads to the formation of long homogeneous stripes. The resulting twin structure requires much less interface energy between the different variants of α -Fe than the spotlike islands formed in the case of the Bain transformation.

Our explanation of the transformation behavior given above is supported by simulations of Fe/Ni(001),²⁷ similar to the simulations presented in this work. In these simulations the Bain orientation occurs only as an intermediate phenomenon during the precipitation of the transformation. With an increasing amount of α -Fe, more and more regions of the system switch to the Pitsch orientation. After the transformation is completed, only this orientation is present, regardless of the presence of vacancies. On the Ni substrate the sum of the squared displacements of the atoms at the interface gives values of 0.21 and 0.12 for the Pitsch and the Bain orientation, respectively (the same units as before). Thus, according to our arguments, the realization of the Pitsch orientation on the nickel substrate requires less energy than on the copper substrate and can even be realized without the help of the vacancies.

3.2. Fe on Cu(111)

From simulations of Fe/Cu(111) films containing 2% vacancies we found that γ -Fe is generally less stable on this surface than on Cu(001). The amount of iron transformed into the bcc structure in these films is presented in Table 3. The presence of small amounts of α -Fe at 300 K and in the thin film at 50 K should have the same reasons as in the case of Fe/Cu(001),

Table 3. Percentage of iron transformed from fcc into bcc in a Fe/Cu(111) film with 2% vacancies after a simulation time of 9 ps.

ML Fe	50 K	300 K
6	8.43%	1.10%
14	91.673%	1.46%

which have already been discussed. The orientational relationships we observed in these simulations are $(111)_{\text{fcc}} \parallel (110)_{\text{bcc}}$ and $[\bar{1}\bar{1}0]_{\text{fcc}} \parallel [1\bar{1}\bar{1}]_{\text{bcc}}$, which is the Kurdjumov-Sachs orientation. This is in accordance with experimental observations.^{3,10,11} As in the case of Fe/Cu(001) (with defects), the structural transformation in the simulations of Fe/Cu(111) led to the formation of two variants of the bcc structure forming a twin system. Here, too, the finite size of the system prohibited the formation of all crystallographically equivalent variants. In Fig. 7 we show the formation of the distorted hexagon of the $(110)_{\text{bcc}}$ planes in comparison to a $(111)_{\text{fcc}}$ plane. As before, the lattice constants have been chosen in order to get the same atomic volume in the two structures. The sum of the squared displacements of the atoms of one hexagon in Fig. 7 is 0.06 in terms of

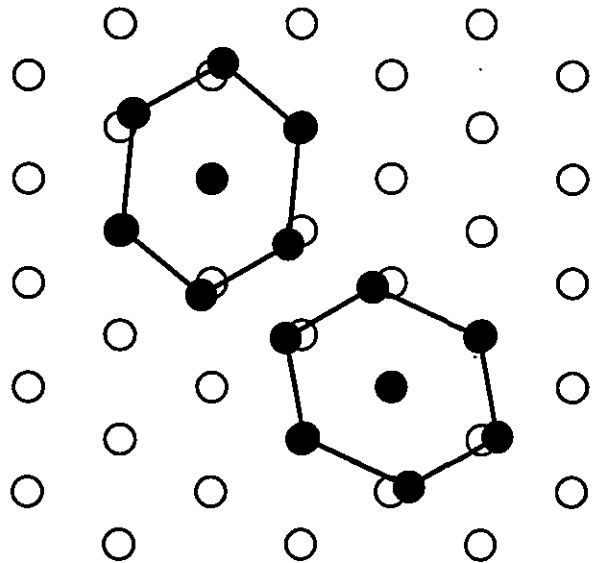


Fig. 7. Formation of $(110)_{\text{bcc}}$ hexagons (full circles) in Kurdjumov-Sachs orientation from a $(111)_{\text{fcc}}$ plane (open circles).

the fcc lattice constant (the sum of the absolute displacements is 0.52 fcc lattice constants). These values are significantly lower than in the case of Fe/Cu(001). Therefore, according to the arguments given above, the stronger tendencies of Fe/Cu(111) to accomplish the structural transformation can be explained by a lower interface energy.

4. Summary and Conclusions

We have done MD simulations of thin films of iron on Cu(001) and Cu(111) substrates using a semiempirical EAM model. In these simulations we were able to reproduce the basic properties of the experimentally observed structural transformation from γ -Fe into α -Fe in such films. In particular, we found a growing tendency of the films to undergo the transformation with increasing film thickness and decreasing temperature. Minor differences between experimental results and our simulations can be explained by the neglect of the growth process during the simulations and the insufficient treatment of magnetism by the EAM model in our calculations.

We have analyzed the local atomic environment of configurations resulting from simulations of Fe/Cu(001). This analysis revealed that actually only a part of the iron atoms transformed into the bcc structure. A visualization of the atomic configuration showed that the amount of α -iron is highest near the surface of the film and decreases in its interior. In these simulations the experimentally observed Pitsch orientation was realized as long as defects (vacancies) were present in the system. During the transformation, stripes of two crystallographically equivalent variants of the bcc structure were formed, which are separated by twinning boundaries. Experimentally, a similar structure has been found in STM investigations.⁷ In contrast to this, simulations of perfect films without vacancies led to different results. In this case the structural transformation was accomplished by a purely distortive Bain transformation and no twin system was formed. This emphasizes the influence of defects on the properties of structural transformations.

Simulations of Fe/Cu(111) showed a significantly reduced stability of the fcc structure in comparison to the simulations of Fe/Cu(001). In these films the bcc structure grew in the Kurdjumov-Sachs orientation and again the formation of a twin sys-

tem was observed. It is rather remarkable that the simulations of thin films on both substrates revealed the experimentally observed orientational relationships.

The different transformation paths realized in our simulations can be explained in a hand-waving manner by considerations of the total displacement of the atoms during the transformation. From this we conclude that especially the energy required by the formation of an interface between α -iron and the substrate is rather crucial for the structural stability of the films. The films remain stable until this interface energy is balanced by the structural energy difference between α - and γ -Fe growing with increasing film thickness and decreasing temperature.

Acknowledgments

We are grateful to Prof. Dr. W. Keune for his critical remarks on the manuscript. This work has been supported by the German Science Council (Deutsche Forschungsgemeinschaft) through the Graduate College "Structure and Dynamics of Heterogeneous Systems."

References

1. L. J. Swartzendruber, V. P. Itkin and C. B. Alcock, in *Phase Diagrams of Binary Nickel Alloys*, ed. P. Nash (ASM International, Materials Park, Ohio, 1991), pp. 110-132.
2. H. Magnan *et al.*, *Phys. Rev. Lett.* **67**, 859 (1991).
3. D. Tian, F. Jona and P. M. Marcus, *Phys. Rev.* **B45**, 11216 (1992).
4. J. Thomassen *et al.*, *Phys. Rev. Lett.* **69**, 3831 (1992).
5. J. Thomassen, B. Feldmann and M. Wuttig, *Surf. Sci.* **264**, 406 (1992).
6. M. Wuttig and J. Thomassen, *Surf. Sci.* **282**, 237 (1993).
7. M. Wuttig *et al.*, *Surf. Sci.* **291**, 14 (1993).
8. D. Li *et al.*, *Phys. Rev. Lett.* **72**, 3112 (1994).
9. R. D. Ellerbrock *et al.*, *Phys. Rev. Lett.* **74**, 3053 (1995).
10. J. Shen *et al.*, *Phys. Rev.* **B56**, 11134 (1997).
11. J. Shen *et al.*, *Phys. Rev. Lett.* **80**, 1980 (1998).
12. S. Müller *et al.*, *Phys. Rev. Lett.* **74**, 765 (1995).
13. W. A. A. Macedo and W. Keune, *Phys. Rev. Lett.* **61**, 475 (1988).
14. M. S. Daw and M. I. Baskes, *Phys. Rev. Lett.* **50**, 1285 (1983).
15. M. S. Daw and M. I. Baskes, *Phys. Rev.* **B29**, 6443 (1984).
16. R. Meyer and P. Entel, *Phys. Rev.* **B57**, 5140 (1998).

17. R. Meyer, Ph.D. thesis (Gerhard-Mercator-Universität, Duisburg, 1998).
18. J. Gui *et al.*, *J. Phys.: Condens. Matter* **6**, 4601 (1994).
19. E. Clementi and C. Roetti, *At. Data Nucl. Data Tables* **14**, 177 (1974).
20. M. P. Allen and D. J. Tildesley, *Computer Simulation of Liquids* (Clarendon, Oxford, 1987).
21. W. G. Hoover, *Phys. Rev.* **A31**, 1695 (1985).
22. M. Parrinello and A. Rahman, *Phys. Rev. Lett.* **45**, 1196 (1980).
23. A. M. Rodriguez, C. Bozzolo and J. Ferrante, *Surf. Sci.* **289**, 100 (1993).
24. W. Keune *et al.*, *J. Appl. Phys.* **79**, 4265 (1996).
25. P. Haasen, *Physikalische Metallkunde* (Springer-Verlag, Berlin, 1974).
26. W. Pitsch, *Philos. Mag.* **4**, 577 (1959).
27. K. Kadau and P. Entel, 1998, to be published.



US006295187B1

(12) **United States Patent**
Pinarbasi

(10) **Patent No.:** **US 6,295,187 B1**
(45) **Date of Patent:** **Sep. 25, 2001**

(54) **SPIN VALVE SENSOR WITH STABLE ANTIPARALLEL PINNED LAYER STRUCTURE EXCHANGE COUPLED TO A NICKEL OXIDE PINNING LAYER**

8-235540 9/1996 (JP) G11B/5/39
8-293108 11/1996 (JP) G11B/5/39
10-32119 2/1998 (JP) G11B/5/39
WO 95/03604 2/1995 (WO) G11B/5/66

OTHER PUBLICATIONS

(75) Inventor: **Mustafa Pinarbasi**, Morgan Hill, CA (US)

(73) Assignee: **International Business Machines Corporation**, Armonk, NY (US)

(*) Notice: Subject to any disclaimer, the term of this patent is extended or adjusted under 35 U.S.C. 154(b) by 0 days.

(21) Appl. No.: **09/343,164**

(22) Filed: **Jun. 29, 1999**

(51) **Int. Cl.**⁷ **G11B 5/30**

(52) **U.S. Cl.** **360/324.11; 360/314**

(58) **Field of Search** **360/324-327**

(56) **References Cited**

U.S. PATENT DOCUMENTS

5,508,866	4/1996	Gill et al.	360/113
5,549,978	8/1996	Iwasaki et al.	428/692
5,563,752	10/1996	Komuro et al.	360/113
5,688,380	11/1997	Koike et al.	204/192.2
5,701,222	12/1997	Gill et al.	360/113
5,701,223	12/1997	Gill et al.	360/113
6,117,569 *	9/2000	Lin	360/113
6,127,053 *	10/2000	Lin	360/113

FOREIGN PATENT DOCUMENTS

5-347013	12/1993	(JP)	G11B/5/39
7-211956	8/1995	(JP)	G11B/5/39
8-127864	5/1996	(JP)	G11B/5/39

Hoshiya et al, "Giant magneoresistance of spin valve films with NiO antiferromagnetic films", *IEEE Translation Journal on Magnetics in Japan*, vol. 9, No. 6, pp 236-241.
 "Spin valves using a bcc-FeCoNi alloy pinned layer", *Institute of Electronics, Information and Communications Engineers*, 1997, vol. 96, No. 486 (MR96 88-94), pp. 45-51.
 Y. Hamakawa et al, "Spin Valve Heads Utilizing Antiferromagnetic NiO Layers", *IEEE Transactions on Magnetics*, vol. 32, No. 1, Jan. 1996, pp. 149-155.
 K. Nakamoto et al, "Design and Read Performance of GMR Heads with NiO", *IEEE Transactions on Magnetics*, vol. 32, No. 5, Sep. 1996, pp. 3374-3379.
 De-Hua Han et al, "NiFe/NiO bilayers with high exchange coupling and low coercive fields", *J. App. Phys.* 81 (8), Part 2, Apr. 15, 1997, pp. 4996-4998.

* cited by examiner

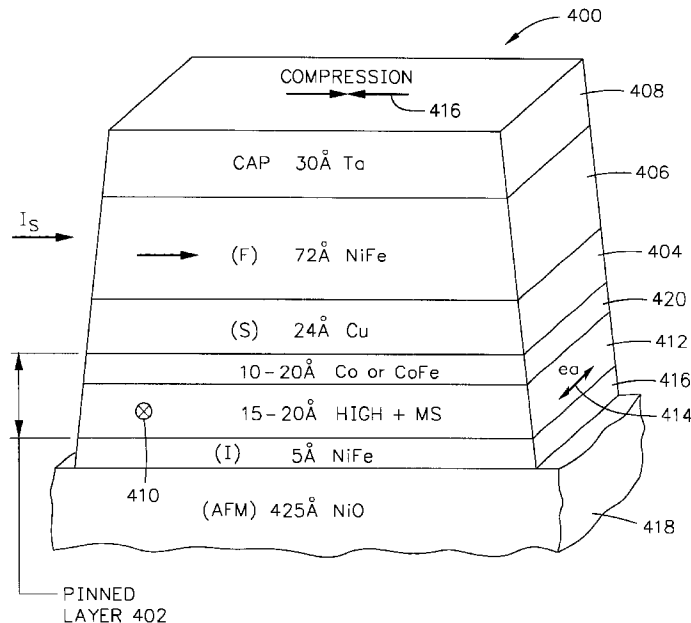
Primary Examiner—A. J. Heinz

(74) *Attorney, Agent, or Firm*—Gray Cary Ware & Freidenrich; Ervin F. Johnston

(57) **ABSTRACT**

A spin valve sensor has a pinned layer structure that has a net positive stress induced uniaxial anisotropy that promotes a pinning of the pinned layer structure in a pinned direction for stabilizing the pinning of the pinned layer structure at high temperatures near to a blocking temperature of a pinning layer which is exchange coupled to the pinned layer.

32 Claims, 9 Drawing Sheets



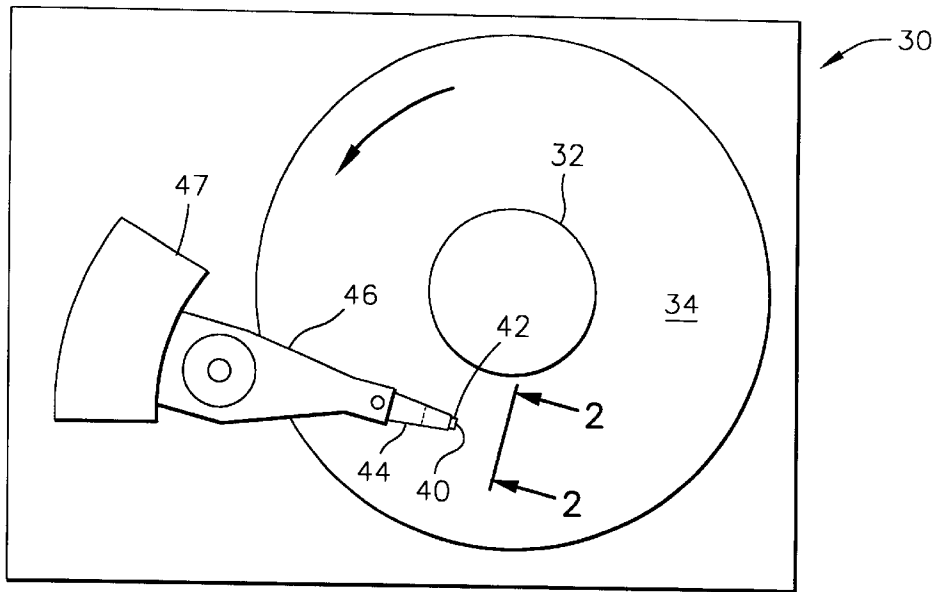


FIG. 1

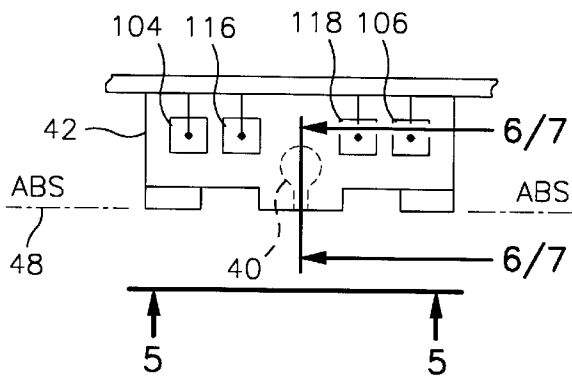


FIG. 2

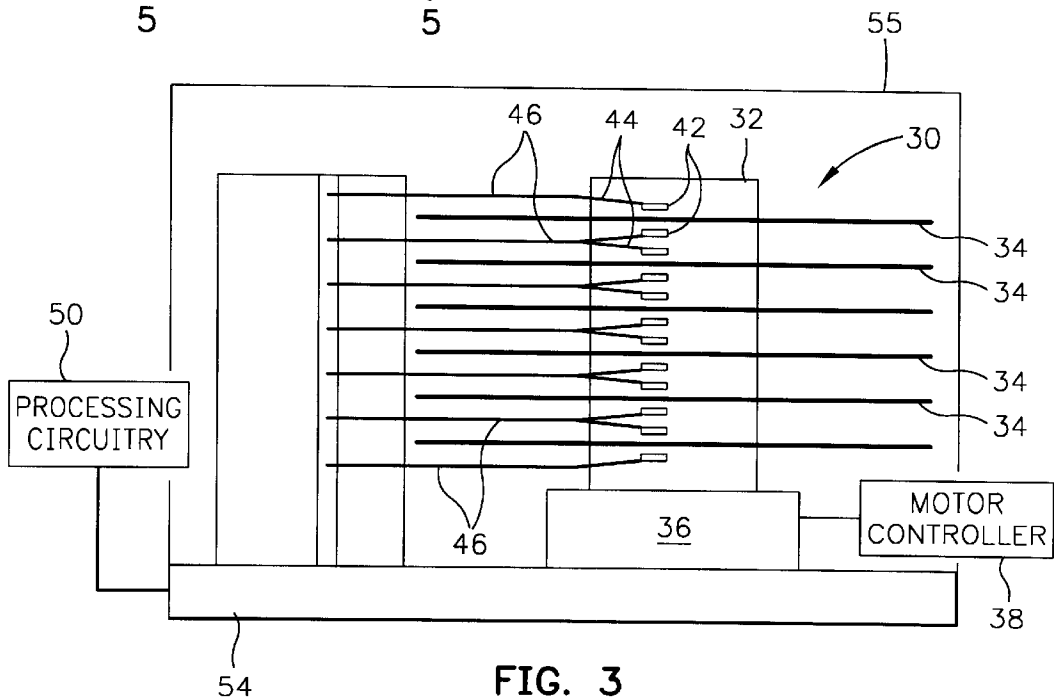
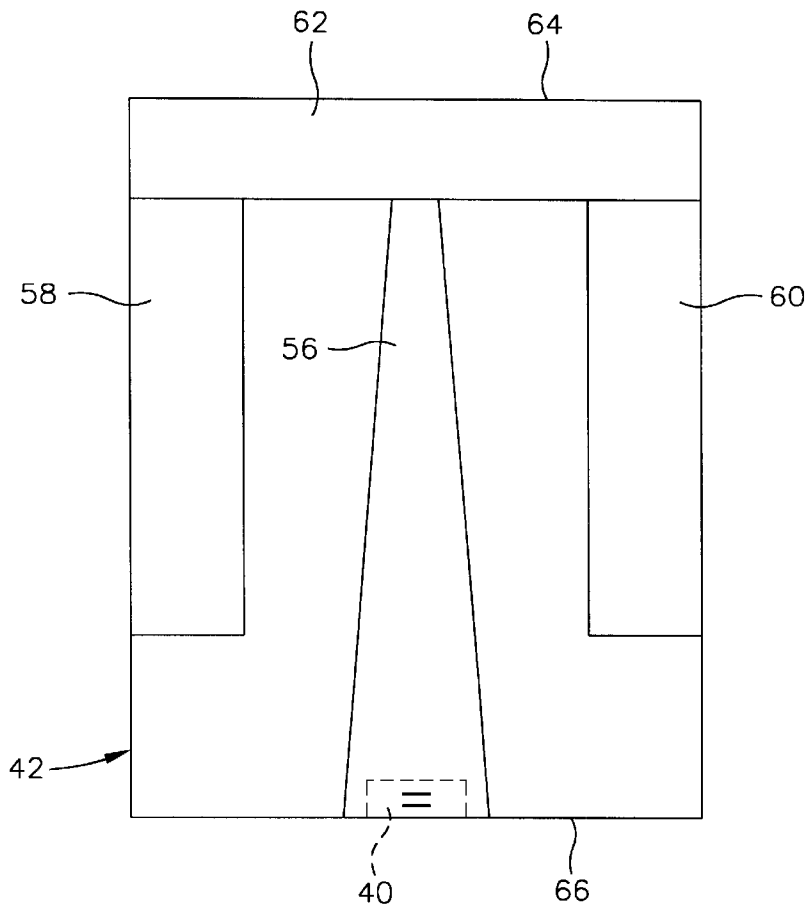
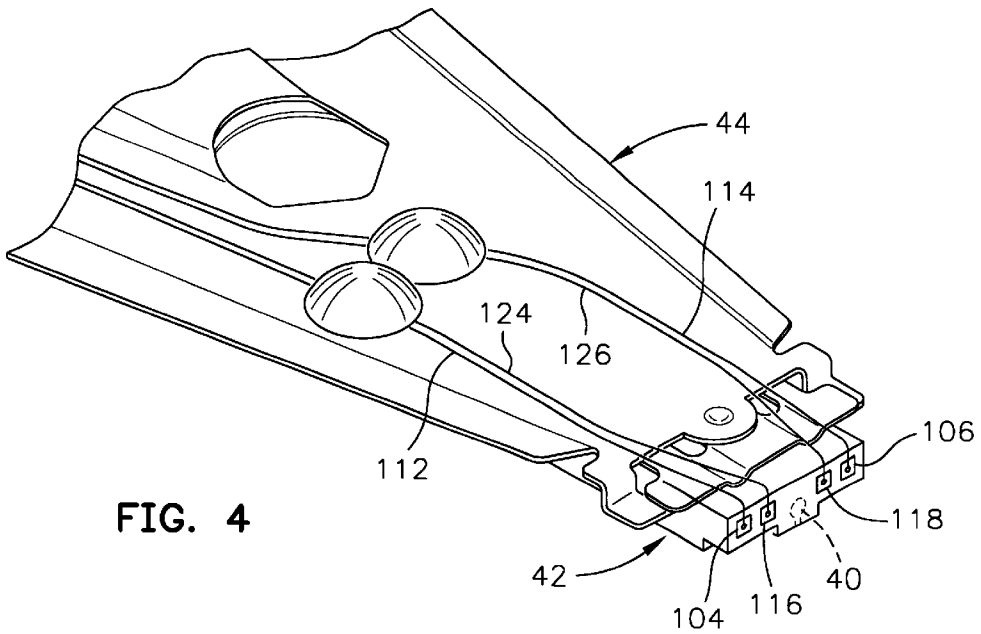


FIG. 3



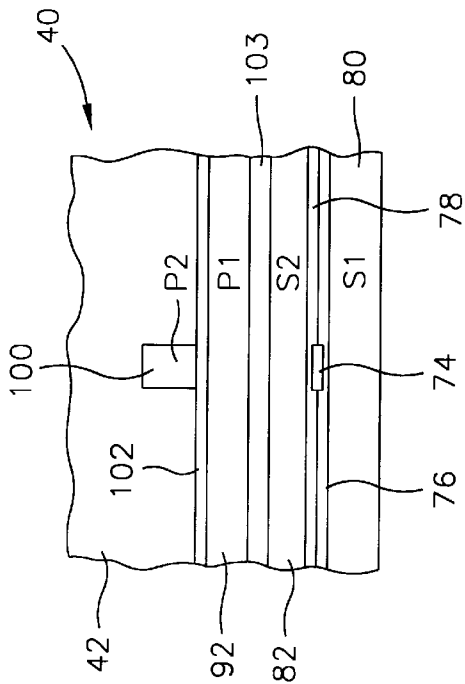


FIG. 8

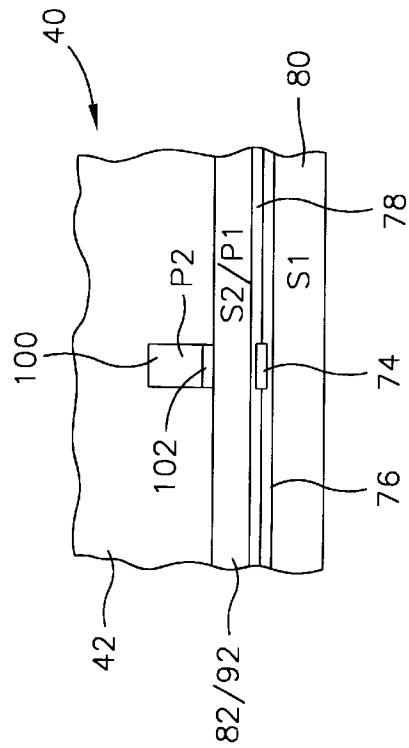


FIG. 9

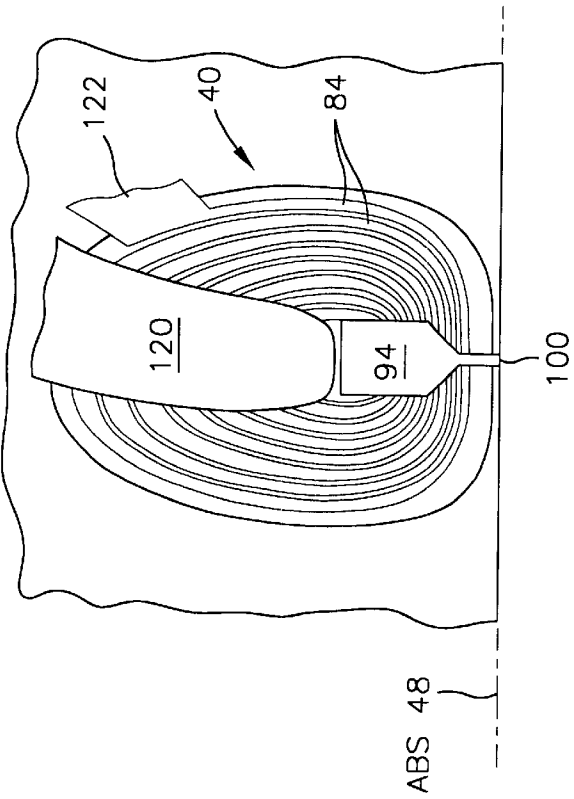


FIG. 10

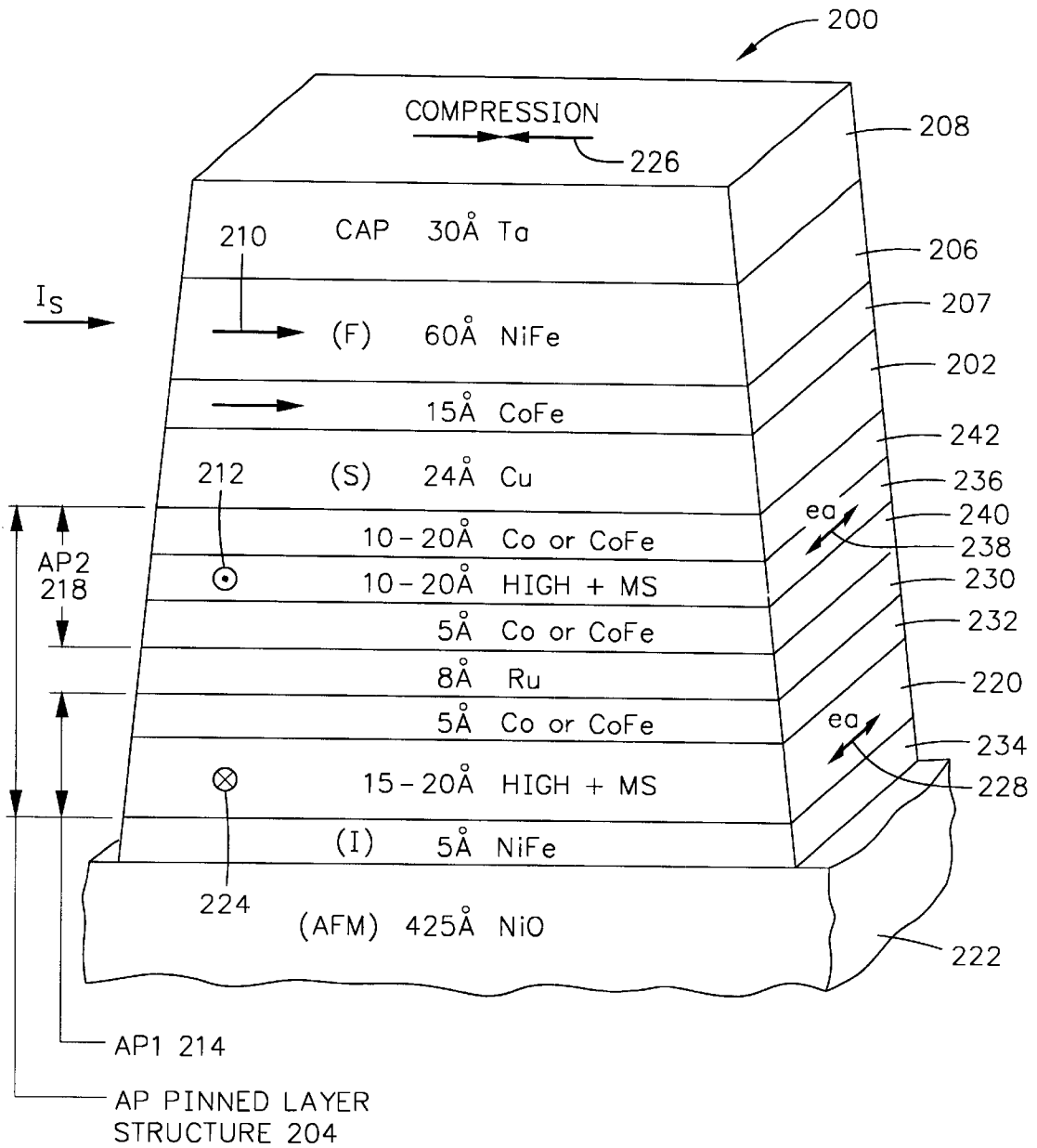


FIG. 12

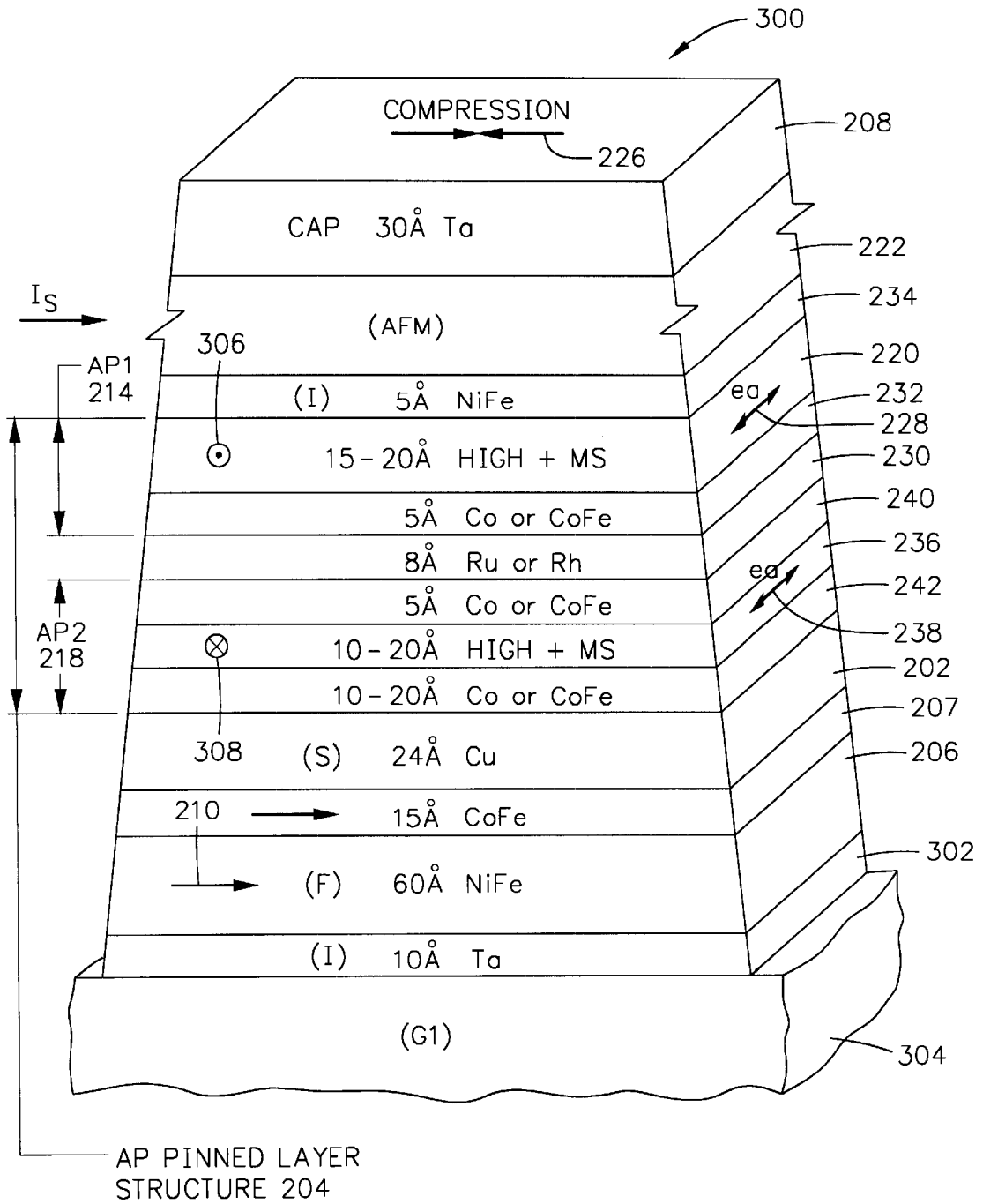


FIG. 13

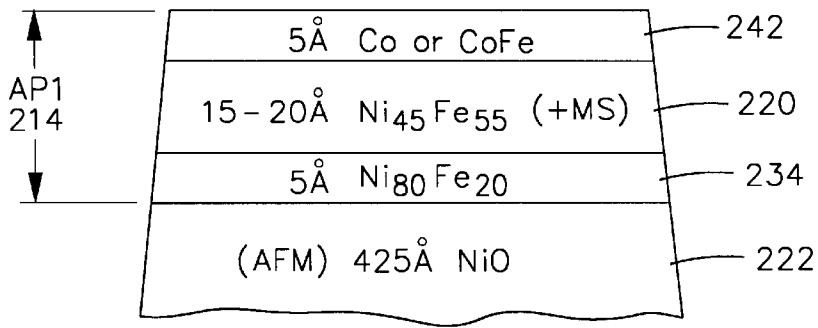


FIG. 14

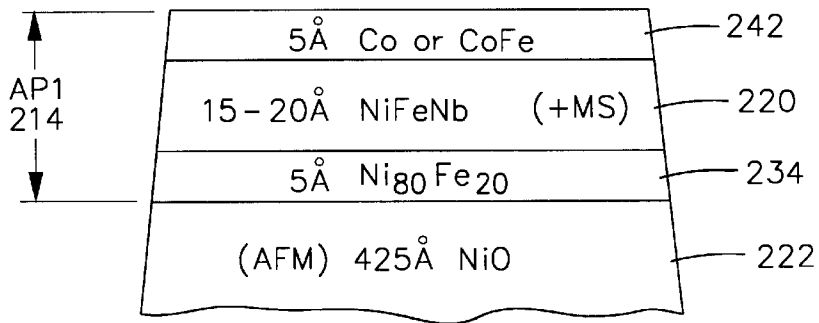


FIG. 15

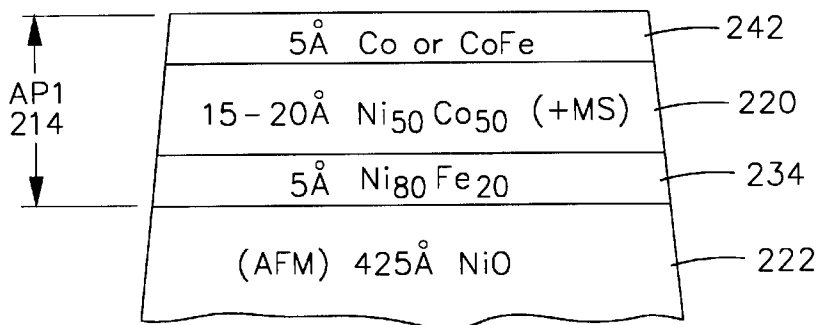
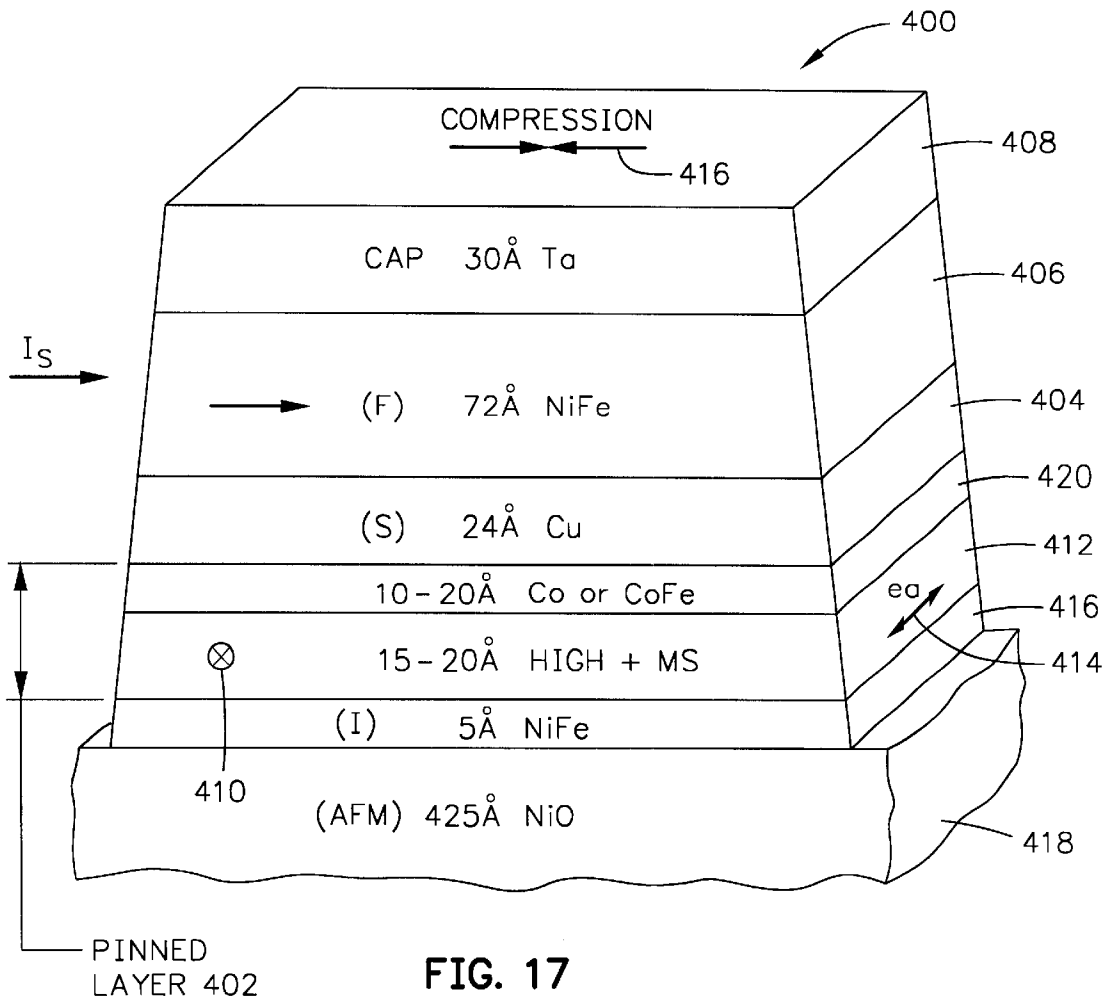


FIG. 16



**SPIN VALVE SENSOR WITH STABLE
ANTIPARALLEL PINNED LAYER
STRUCTURE EXCHANGE COUPLED TO A
NICKEL OXIDE PINNING LAYER**

BACKGROUND OF THE INVENTION

1. Field of the Invention

The present invention relates to a spin valve sensor with a stable antiparallel pinned layer structure exchange coupled to a nickel oxide pinning layer and, more particularly, to an antiparallel pinned layer structure which has at least first and second antiparallel pinned layers wherein at least one of the antiparallel pinned layers includes a thin film that has positive magnetostriction.

2. Description of the Related Art

A high performance read head employs a spin valve sensor for sensing magnetic fields on a moving magnetic medium, such as a rotating magnetic disk or a linearly moving magnetic tape. The sensor includes a nonmagnetic electrically conductive first spacer layer sandwiched between a ferromagnetic pinned layer and a ferromagnetic free layer. An antiferromagnetic pinning layer interfaces the pinned layer for pinning the magnetic moment of the pinned layer 90° to an air bearing surface (ABS) which is an exposed surface of the sensor that faces the magnetic medium. First and second leads are connected to the spin valve sensor for conducting a sense current therethrough. The magnetic moment of the free layer is free to rotate in positive and negative directions from a quiescent or bias point position in response to positive and negative magnetic fields from a moving magnetic medium. The quiescent position is the position of the magnetic moment of the free layer when the sense current is conducted through the sensor without magnetic field signals from a rotating magnetic disk. The quiescent position of the magnetic moment of the free layer is preferably parallel to the ABS. If the quiescent position of the magnetic moment is not parallel to the ABS the positive and negative responses of the free layer will not be equal which results in read signal asymmetry which is discussed in more detail hereinbelow.

The thickness of the spacer layer is chosen so that shunting of the sense current through the sensor and a magnetic coupling between the free and pinned layers are minimized. This thickness is less than the mean free path of electrons conducted through the sensor. With this arrangement, a portion of the conduction electrons are scattered by the interfaces of the spacer layer with the pinned and free layers. When the magnetic moments of the pinned and free layers are parallel with respect to one another scattering is minimal and when their magnetic moments are antiparallel scattering is maximized. An increase in scattering of conduction electrons increases the resistance of the spin valve sensor and a decrease in scattering of the conduction electrons decreases the resistance of the spin valve sensor. Changes in resistance of the spin valve sensor is a function of $\cos \theta$, where θ is the angle between the magnetic moments of the pinned and free layers. This resistance, which changes due to changes in scattering of conduction electrons, is referred to in the art as magnetoresistance (MR). A spin valve sensor has a significantly higher magnetoresistive (MR) coefficient than an anisotropic magnetoresistive (AMR) sensor. For this reason it is sometimes referred to as a giant magnetoresistive (GMR) sensor. Magnetoresistive coefficient is dr/R where dr is the difference in resistance between minimum resistance, where the magnetic moments of the free and pinned layers are parallel, and

maximum resistance, where the magnetic moments of the free and pinned layers are antiparallel, and R is the minimum resistance, where the magnetic moments of the free and pinned layers are parallel.

When a spin valve sensor employs a single pinned layer it is referred to as a simple spin valve. Another type of spin valve sensor is an antiparallel (AP) pinned spin valve sensor. The AP pinned spin valve sensor differs from the simple spin valve sensor in that an AP pinned structure has multiple thin film layers instead of a single pinned layer. The AP pinned structure has an AP coupling layer sandwiched between first and second ferromagnetic pinned layers. The first pinned layer has its magnetic moment oriented in a first direction by exchange coupling to the antiferromagnetic pinning layer. The second pinned layer is immediately adjacent to the spacer layer and is antiparallel coupled to the first pinned layer because of the minimal thickness (in the order of 8 Å) of the AP coupling film. Accordingly, the magnetic moment of the second pinned layer is oriented in a second direction that is antiparallel to the direction of the magnetic moment of the first pinned layer.

The AP pinned structure is preferred over the single pinned layer because the magnetic moments of the first and second pinned layers of the AP pinned structure subtractively combine to provide a net magnetic moment that is less than the magnetic moment of the single pinned layer. The direction of the net moment is determined by the thicker of the first and second pinned layers. A reduced net magnetic moment equates to a reduced demagnetization (demag) field from the AP pinned structure. Since the antiferromagnetic exchange coupling is inversely proportional to the net pinning moment, this increases exchange coupling between the first pinned layer and the pinning layer. The AP pinned spin valve sensor is described in commonly assigned U.S. Pat. No. 5,465,185 to Heim and Parkin which is incorporated by reference herein.

The first and second pinned layers of the AP pinned structure are typically made of cobalt (Co). Unfortunately, cobalt has high coercivity, high magnetostriction and low resistance. When the first and second pinned layers of the AP pinned structure are formed they are sputter deposited in the presence of a magnetic field that is oriented perpendicular to the ABS. This sets the easy axis (e.a.) of the pinned layers perpendicular to the ABS. During a subsequent making of the magnetic head, the AP pinned structure is subjected to magnetic fields that are directed parallel to the ABS. These fields can cause the magnetic moment of the first pinned layer to switch from a desirable first direction perpendicular to the ABS to an undesirable second direction which is not perpendicular to the ABS. The same occurs to the second pinned layer of the AP pinned structure. If the coercivity of the first pinned layer of the AP pinned structure is higher than the exchange coupling between the first pinned layer and the pinning layer the exchange coupling will not return the magnetic moment of the first pinned layer to its original direction. This ruins the read head. This problem can occur during operation of the magnetic head in a disk drive when a magnetic field stronger than the exchange field of the first pinned layer of the AP pinned structure is exerted on the read head.

Efforts continue to increase the MR coefficient (dr/R) of GMR heads. An increase in the MR coefficient equates to higher bit density (bits/square inch of the rotating magnetic disk) read by the read head. When these efforts are undertaken it is important that the coercivity (H_c) of the pinned layer next to the pinning layer not exceed the exchange coupling field therebetween.

SUMMARY OF THE INVENTION

The present invention provides a highly stabilized antiparallel (AP) pinned layer structure which is exchange coupled to a nickel oxide (NiO) pinning layer. At least one of the AP pinned layers includes a thin film composed of a material that has a positive magnetostriction. In an embodiment of the invention, where only one of the AP pinned layers has a thin film composed of a material having positive magnetostriction, the AP pinned layer structure is exchange coupled to the nickel oxide (NiO) pinning layer. With this arrangement the AP pinned layer that is exchange coupled to the nickel oxide (NiO) pinning layer has a stress induced uniaxial anisotropy which is oriented perpendicular to the surface planes of the layers of the spin valve sensor. This uniaxial anisotropy promotes a pinning of the magnetic moment of the AP pinned layer perpendicular to the planes of the layers caused by the exchange coupling of the AP pinned layer to the nickel oxide (NiO) pinning layer. The stress induced uniaxial anisotropy of the AP pinned layer is in the same direction as the orientation of the magnetic moment of the AP pinned layer due to the exchange coupling with the nickel oxide pinning layer. Accordingly, when the pinning strengths of the nickel oxide (NiO) pinning layer is degraded in a magnetic disk drive with operating temperatures as high as 150° C. the stress induced anisotropy, due to the positive magnetostriction of the film in the AP pinned layer exchange coupled to the nickel oxide (NiO) pinning layer, maintains the orientation of the magnetic moment of the AP pinned layer perpendicular to the planes of the layers of the spin valve sensor.

In my investigation I found that when the positive magnetostriction film of the AP pinned layer interfaces the AP coupling layer, which is typically ruthenium (Ru), the performance of the spin valve sensor is degraded. This has been overcome by providing the AP pinned layer with a thin film of cobalt (Co) or cobalt iron (CoFe) between the positive magnetostriction thin film and the ruthenium (Ru) AP coupling layer. I further found that when the positive magnetostriction thin film is a material other than nickel iron (NiFe) the performance of the spin valve sensor is degraded when the positive magnetostriction thin film interfaces the nickel oxide (NiO) pinning layer. This problem has been overcome by providing the AP pinned layer with a nickel iron (NiFe) thin film between the positive magnetostriction thin film and the nickel oxide (NiO) pinning layer.

In a preferred embodiment the second AP pinned layer, which interfaces the spacer layer, also includes a thin film layer that has positive magnetostriction. This further supports pinning of the first AP pinned layer by antiparallel exchange coupling between the first and second AP pinned layers. In the same manner as the first AP pinned layer the second AP pinned layer may include a thin film of cobalt (Co) or cobalt iron (CoFe) between the positive magnetostriction thin film and the AP coupling layer of ruthenium (Ru). I have further enhanced the performance of the spin valve sensor by providing the second AP pinned layer with a third thin film which distinguishes it from the first AP pinned layer. The second AP pinned layer may be provided with a thin film of cobalt (Co) or cobalt iron (CoFe) between the positive magnetostriction thin film and the copper (Cu) spacer layer. The preferred AP pinned layer structure includes all of the thin films, as described hereinabove, exchange coupled to a nickel oxide (NiO) pinning layer. However, in a broad aspect of the invention only one of the AP pinned layers has a positive magnetostriction thin film, with or without the other thin films, exchange coupled to

pinning layers which may be composed of antiferromagnetic materials other than nickel oxide (NiO). The above arrangement may be applied to either a top or a bottom spin valve sensor wherein the pinning layer is at the bottom or at the top respectively of the spin valve sensor. Further, the present invention applies to a single pinned layer structure which includes a positive magnetostriction thin film and a thin film of cobalt (Co) or cobalt iron (CoFe) located between the positive magnetostriction thin film and the copper (Cu) spacer layer. This single pinned layer structure may further include a thin film of nickel iron (NiFe) between the positive magnetostriction thin film and the nickel oxide (NiO) pinning layer when the positive magnetostriction thin film is composed of a material other than nickel iron (NiFe).

An object of the present invention is to provide an antiparallel (AP) pinned layer structure which has a net positive stress induced uniaxial anisotropy that supplements a pinning field between the pinned layer structure and a pinning layer.

Another object is to provide a highly stable antiparallel pinned layer structure that is exchange coupled to a nickel oxide (NiO) pinning layer during operating temperatures of the AP pinned layer structure in a magnetic disk drive.

A further object is to provide one or both of the AP pinned layers of an AP pinned layer structure with a thin film composed of a positive magnetostriction material.

Other objects and attendant advantages of the invention will be appreciated upon reading the following description taken together with the accompanying drawings.

BRIEF DESCRIPTION OF THE DRAWINGS

FIG. 1 is a plan view of an exemplary magnetic disk drive;

FIG. 2 is an end view of a slider with a magnetic head of the disk drive as seen in plane 2—2;

FIG. 3 is an elevation view of the magnetic disk drive wherein multiple disks and magnetic heads are employed;

FIG. 4 is an isometric illustration of an exemplary suspension system for supporting the slider and magnetic head;

FIG. 5 is an ABS view of the magnetic head taken along plane 5—5 of FIG. 2;

FIG. 6 is a partial view of the slider and a piggyback magnetic head as seen in plane 6—6 of FIG. 2;

FIG. 7 is a partial view of the slider and a merged magnetic head as seen in plane 7—7 of FIG. 2;

FIG. 8 is a partial ABS view of the slider taken along plane 8—8 of FIG. 6 to show the read and write elements of the piggyback magnetic head;

FIG. 9 is a partial ABS view of the slider taken along plane 9—9 of FIG. 7 to show the read and write elements of the merged magnetic head;

FIG. 10 is a view taken along plane 10—10 of FIGS. 6 or 7 with all material above the coil layer and leads removed;

FIG. 11 is an isometric ABS illustration of a read head which employs an AP pinned spin valve (SV) sensor;

FIG. 12 is an ABS illustration of the present AP pinned structure in a bottom spin valve sensor;

FIG. 13 is an ABS illustration of the present AP pinned layer structure in a top spin valve sensor;

FIG. 14 is an ABS illustration of the first AP pinned layer with a positive magnetostriction thin film of $\text{Ni}_{45}\text{Fe}_{55}$;

FIG. 15 is an ABS illustration of the first AP pinned layer with a positive magnetostriction thin film composed of nickel iron niobium (NiFeNb);

FIG. 16 is an ABS illustration of a first AP pinned layer with a positive magnetostriction thin film composed of nickel cobalt ($\text{Ni}_{50}\text{Co}_{50}$); and

FIG. 17 is an ABS illustration of a single pinned layer structure having a positive magnetostriction thin film in a spin valve sensor.

DESCRIPTION OF THE PREFERRED EMBODIMENTS

MAGNETIC DISK DRIVE

Referring now to the drawings wherein like reference numerals designate like or similar parts throughout the several views, FIGS. 1–3 illustrate a magnetic disk drive 30. The drive 30 includes a spindle motor 32 that supports and rotates a magnetic disk 34. The spindle 32 is rotated by a motor 36 that is controlled by a motor controller 38. A slider 42 with a combined read and write magnetic head 40 is supported by a suspension 44 and actuator arm 46 which is selectively rotatably positioned by an actuator 47. A plurality of disks, sliders and suspensions may be employed in a large capacity direct access storage device (DASD) as shown in FIG. 3. The suspension 44 and actuator arm 46 position the slider 42 so that the magnetic head 40 is in a transducing relationship with a surface of the magnetic disk 34. When the disk 34 is rotated by the motor 36 the slider is supported on a thin (typically, $0.05\ \mu\text{m}$) cushion of air (air bearing) between the surface of the disk 34 and the air bearing surface (ABS) 48. The magnetic head 40 may then be employed for writing information to multiple circular tracks on the surface of the disk 34, as well as for reading information therefrom. Processing circuitry 50 exchanges signals, representing such information, with the head 40, provides motor drive signals for rotating the magnetic disk 34, and provides control signals to the actuator 47 for moving the slider to various tracks. In FIG. 4 the slider 42 is shown mounted to a suspension 44. The components described hereinabove may be mounted on a frame 54 of a housing, as shown in FIG. 3.

FIG. 5 is an ABS view of the slider 42 and the magnetic head 40. The slider has a center rail 56 that supports the magnetic head 40, and side rails 58 and 60. The rails 56, 58 and 60 extend from a cross rail 62. With respect to rotation of the magnetic disk 34, the cross rail 62 is at a leading edge 64 of the slider and the magnetic head 40 is at a trailing edge 66 of the slider.

FIG. 6 is a side cross-sectional elevation view of a piggyback magnetic head 40, which includes a write head portion 70 and a read head portion 72, the read head portion employing a spin valve sensor 74 of the present invention. FIG. 8 is an ABS view of FIG. 6. The spin valve sensor 74 is sandwiched between nonmagnetic electrically insulative first and second read gap layers 76 and 78, and the read gap layers are sandwiched between ferromagnetic first and second shield layers 80 and 82. In response to external magnetic fields, the resistance of the spin valve sensor 74 changes. A sense current I_s conducted through the sensor causes these resistance changes to be manifested as potential changes. These potential changes are then processed as readback signals by the processing circuitry 50 shown in FIG. 3.

The write head portion 70 of the magnetic head 40 includes a coil layer 84 sandwiched between first and second insulation layers 86 and 88. A third insulation layer 90 may be employed for planarizing the head to eliminate ripples in the second insulation layer caused by the coil layer 84. The first, second and third insulation layers are referred to in the

art as an “insulation stack”. The coil layer 84 and the first, second and third insulation layers 86, 88 and 90 are sandwiched between first and second pole piece layers 92 and 94. The first and second pole piece layers 92 and 94 are magnetically coupled at a back gap 96 and have first and second pole tips 98 and 100 which are separated by a write gap layer 102 at the ABS. An insulation layer 103 is located between the second shield layer 82 and the first pole piece layer 92. Since the second shield layer 82 and the first pole piece layer 92 are separate layers this head is known as a piggyback head. As shown in FIGS. 2 and 4, first and second solder connections 104 and 106 connect leads from the spin valve sensor 74 to leads 112 and 114 on the suspension 44, and third and fourth solder connections 116 and 118 connect leads 120 and 122 from the coil 84 (see FIG. 8) to leads 124 and 126 on the suspension.

FIGS. 7 and 9 are the same as FIGS. 6 and 8 except the second shield layer 82 and the first pole piece layer 92 are a common layer. This type of head is known as a merged magnetic head. The insulation layer 103 of the piggyback head in FIGS. 6 and 8 is omitted.

FIG. 11 is an isometric ABS illustration of the read head 72 shown in FIGS. 6 or 8. The read head 72 includes the present spin valve sensor 130 which is located on an antiferromagnetic (AFM) pinning layer 132. A ferromagnetic pinned layer in the spin valve sensor 130, which is to be described hereinafter, has a magnetic moment that is pinned by the magnetic spins of the pinning layer 132. The AFM pinning layer may be $425\ \text{\AA}$ of nickel oxide (NiO). First and second hard bias and lead layers 134 and 136 are connected to first and second side edges 138 and 140 of the spin valve sensor. This connection is known in the art as a contiguous junction and is fully described in commonly assigned U.S. Pat. No. 5,018,037 which is incorporated by reference herein. The first hard bias and lead layers 134 include a first hard bias layer 140 and a first lead layer 142 and the second hard bias and lead layers 136 include a second hard bias layer 144 and a second lead layer 146. The hard bias layers 140 and 144 cause magnetic fields to extend longitudinally through the spin valve sensor 130 for stabilizing the magnetic domains therein. The AFM pinning layer 132, the spin valve sensor 130 and the first and second hard bias and lead layers 134 and 136 are located between nonmagnetic electrically insulative first and second read gap layers 148 and 150. The first and second read gap layers 148 and 150 are, in turn, located between ferromagnetic first and second shield layers 152 and 154.

THE PRESENT INVENTION

FIG. 12 shows an ABS illustration of a preferred embodiment 200 of the present spin valve sensor. The spin valve sensor 200 includes a spacer layer (S) 202 which is located between an antiparallel (AP) pinned layer structure 204 and a free layer structure (F) which may include films 206 and 207. On top of the free layer 206 is a cap layer 208 for protecting the free layer from subsequent formations of layers of the read head. The free layer structure 206 and 207 has a magnetic moment 210 which is directed parallel to the ABS in a quiescent state (no signal field), either from right to left or from left to right, as shown in FIG. 12. The AP pinned layer structure 204 has a magnetic moment 212 which is pinned perpendicular to the ABS, either away from the ABS or toward the ABS, as shown in FIG. 12. When a signal field from a track of a rotating magnetic disk rotates the magnetic moment 210 upwardly the magnetic moments 210 and 212 become more antiparallel, which increases the resistance of the spin valve sensor and when the signal field

from the track of a rotating magnetic disk rotates the magnetic moment **210** downwardly the magnetic moments **210** and **212** become more parallel, which decreases the resistance of the spin valve sensor. In a sense current I_s circuit these resistance changes are manifested as potential changes which are processed as playback signals by the processing circuitry shown in FIG. 3.

The AP pinned layer structure **204** may include first and second AP pinned layers (AP1) and (AP2) **214** and **218**. The first AP pinned layer **214** includes a first thin film **220** which is composed of a material that has a positive magnetostriction (+MS). The first AP pinned layer **214** is exchange coupled to an antiferromagnetic pinning layer **222**, which is composed of nickel oxide, which pins a magnetic moment **224** of the positive magnetostriction first thin film **220** perpendicular to and away from the ABS, as shown in FIG. 12.

In prior art AP pinned layers, which do not employ a positive magnetostriction thin film **220**, the pinning of the magnetic moment **224** is not stable when the read sensor reaches operating temperatures as high as 150° C. in a magnetic disk drive. While a blocking temperature of the nickel oxide (NiO) pinning layer **222** is 215°–225° C., there is a blocking temperature distribution where magnetic spins of the pinning layer are free to rotate below the blocking temperature. Blocking temperature is the temperature at which all of the magnetic spins of the pinned layer are no longer pinned by the pinning layer. Unfortunately, there is a percentage of the blocking temperature distribution that is at and below 150° C. which means that a percentage of the magnetic spins of the pinning layer are free to rotate at these temperatures. This causes the pinning strengths between the pinning layer **222** and the first AP pinned layer **214** to be degraded allowing extraneous fields to relocate the magnetic moment **224** in an orientation that is not perpendicular to the ABS. If the coercivity (H_C) of the first AP pinned layer **214** is greater than the pinning strength, the pinning layer **222** will not have sufficient pinning strength to bring the magnetic moment **224** back to its perpendicular orientation, as shown in FIG. 12.

By providing the first AP pinned layer **214** with the positive magnetostriction thin film **220** the first AP pinned layer **214** has a stress induced uniaxial anisotropy which supports the pinning of the magnetic moment **224** in its orientation shown in FIG. 12. This is made possible due to the fact that after lapping the magnetic head structure the layers of the spin valve sensor **200** are in compression parallel to the ABS. This is exemplified at **226** for the top cap layer **226** and is the same for the layers therebelow, including the AP pinned layer structure **204**. Because of the compression, the positive magnetostriction of the thin film **220** causes the easy axis **228** of the positive magnetostriction thin film **220** to be perpendicular to the ABS. Accordingly, when the pinning layer **222** pins the magnetic moment **224** perpendicular to and away from the ABS there is a stress induced uniaxial anisotropy which is oriented in the same direction. If the pinning layer **222** pins the thin film layer **220** perpendicular to and toward the ABS the stress induced anisotropy would be in the same direction, namely perpendicular to and toward the ABS. The stress induced uniaxial anisotropy finds its orientation when the magnetic spins of the pinning layer **222** are reset by applying a magnetic field to the first AP pinned layer which orients the magnetic moment of the thin film **220** perpendicular to and away from the ABS, as shown in FIG. 12.

The AP pinned layer structure **214**, **224** includes an antiparallel (AP) coupling layer **230** which is located

between the first and second AP pinned layers **214** and **218**. I found that when the positive magnetostriction thin film **220** interfaces the AP coupling layer **230**, which is typically composed of ruthenium (Ru), that the performance of the spin valve sensor is degraded. I have overcome this problem by providing a thin film of cobalt (Co) or cobalt iron (CoFe) between the positive magnetostriction thin film **220** and the AP coupling layer **230**. Further, I found that when the positive magnetostriction layer **220** interfaces the nickel oxide (NiO) pinning layer **222** that the performance of the spin valve sensor is degraded. I have overcome this problem by providing the first AP pinned layer **214** with a nickel iron (NiFe) thin film **234** which is located between the positive magnetostriction thin film **220** and the pinning layer **222**.

In a preferred embodiment the second AP pinned layer **218** also includes a positive magnetostriction thin film **236**. Because of the positive magnetostriction of the thin film **236** this thin film also has an easy axis **238** which is oriented perpendicular to the ABS. By antiparallel coupling between the first and second AP pinned layers **214** and **218** the magnetic moment **212** of the positive magnetostriction thin film **236** is oriented perpendicular to toward the ABS, as shown in FIG. 12. This causes a stress induced uniaxial anisotropy which is oriented in the same direction for supporting the orientation of the magnetic moment **212** perpendicular to and toward the ABS. It should be noted that because of antiparallel coupling between the first and second AP pinned layers **214** and **218** the stress induced uniaxial anisotropy of the second AP pinned layer **218** will additionally support the orientation of the magnetic moment **224** of the positive magnetostriction film **220** perpendicular to and away from the ABS. This is particularly important when the spin valve sensor reaches operating temperatures of the disk drive which reduces the pinning strength between the nickel oxide (NiO) pinning layer **222** and the positive magnetostriction thin film **220**. Accordingly, the present AP pinned layer structure **224** is highly stabilized by employing a positive magnetostriction thin film in each of the first and second AP pinned layers **214** and **218**.

For the same reason as explained for the first AP pinned layer **214** a thin film of cobalt (Co) or cobalt iron (CoFe) **240** is provided between the positive magnetostriction thin film **236** and the AP coupling layer **230** for improving the performance of the spin valve sensor. In a preferred embodiment the second AP pinned layer **218** includes a third thin film which differs from the thin film **234** employed in the first AP pinned layer **214**. The thin film **242** in the second AP pinned layer is located between the positive magnetostriction thin film **236** and the copper (Cu) spacer layer **202**. I found that the thin film **242** further increases the performance of the spin valve sensor. In a preferred embodiment the AP pinned layer **204** includes all of the thin films as described hereinabove.

Preferred thicknesses and materials for the layers and thin films are 425 Å of nickel oxide (NiO) for the pinning layer **222**, 5 Å of nickel iron (NiFe) for the thin film **234**, 15 Å to 20 Å of a positive magnetostriction material for the thin film **220**, 5 Å of cobalt (Co) or cobalt iron (CoFe) for the thin film **232**, 8 Å of ruthenium (Ru) for the AP coupling layer **230**, 5 Å of cobalt (Co) or cobalt iron (CoFe), for the thin film **240** 10–20 Å of a positive magnetostriction material for the thin film **236**, 10–20 Å of cobalt (Co) or cobalt iron (CoFe) for the thin film **242**, 24 Å of copper (Cu) for the spacer layer **202**, 60 Å of nickel iron (NiFe) for the free layer film **206** and 15 Å of cobalt iron (CoFe) for the free layer film **207** and 30 Å of tantalum (Ta) for the cap **208**. It should be understood that the magnetic moments of the thin films **234**

and 232 will be oriented in the same direction as the magnetic moment 224, and that the magnetic moments of the thin films 240 and 242 will be oriented in the same direction as the magnetic moment 212. The thickness of the first AP pinned layer 214 may be greater or less than the thickness of the second AP pinned layer 218. It should be noted that the pinning layer 222 is below the other layers of the spin valve sensor. This means that the layers of the spin valve sensor are formed on top of and after the formation of the pinning layer 222. This type of spin valve sensor is known in the art as a bottom spin valve sensor since the pinning layer is located at the bottom of the sensor.

FIG. 13 shows an ABS illustration of another preferred embodiment 300 of the present invention which is the same as the embodiment 200 shown in FIG. 12, except the AP pinned layer structure 204 is turned upside down, the spacer layer 202 and the free layer structure 206 and 207 are located below the AP pinned layer structure 204, a seed layer, such as a tantalum (Ta) layer 302 10 Å–30 Å thick, is provided between the free layer 206 and 207 and a first gap layer (G1) 304 and an antiferromagnetic (AFM) pinning layer 222, which may be nickel oxide (NiO), is located above the AP pinned layer structure 204. A further difference is that the magnetic moment 306 of the first AP pinned layer is perpendicular to and toward the ABS and the magnetic moment 308 of the second AP pinned layer is perpendicular and away from the ABS, as shown in FIG. 13. Because of the compression 226 the easy axis 228 and 238 of the positive magnetostriction thin films will be oriented perpendicular to the ABS so that when the magnetic spins of the pinning layer 222 are oriented perpendicular to and toward the ABS the positive magnetostriction thin films 220 will be a stress induced uniaxial anisotropy supporting the magnetic moment 306 in a direction perpendicular to and toward the ABS and the positive magnetostriction thin film 236 will have a stress induced uniaxial anisotropy that supports the orientation of the magnetic moment 308 in a direction perpendicular to and away from the ABS. The pinning layer 222 may be composed of an antiferromagnetic material other than nickel oxide (NiO), such as alpha iron oxide ($\alpha\text{Fe}_2\text{O}_3$), nickel manganese (NiMn), iron manganese (FeMn), platinum manganese (PtMn) or iridium manganese (IrMn). In a preferred embodiment, however, the pinning layer 222 is nickel oxide (NiO). Since the pinning layer 222 is located at the top of the spin valve sensor in FIG. 13, this type of spin valve sensor is known in the art as a top spin valve sensor.

Various thin film layers for the first AP pinned layer 214 in either of the spin valves 200 or 300 in FIGS. 12 and 13 are shown in FIGS. 14, 15 and 16. In each of the embodiments shown in FIGS. 14, 15 and 16 a thin film layer of nickel iron ($\text{Ni}_{80}\text{Fe}_{20}$) 234 5 Å thick is employed between the positive magnetostriction thin film 220 and the nickel oxide (NiO) pinning layer 222. Further, in each of the embodiments shown in FIGS. 14, 15 and 16 a thin film of cobalt (Co) or cobalt iron (CoFe) is employed between the positive magnetostriction thin film 220 and the AP coupling layer 230 of ruthenium (Ru). The difference between the embodiments in FIGS. 14, 15 and 16 is the material used for the positive magnetostriction thin film 220. In the embodiment shown in FIG. 14 the positive magnetostriction thin film 220 is 15 Å to 20 Å of nickel iron ($\text{Ni}_{45}\text{Fe}_{55}$), the positive magnetostriction 220 in the embodiment in FIG. 15 is 15 Å to 20 Å of nickel iron niobium (NiFeNb) and the positive magnetostriction thin film 220 in FIG. 16 is 15 Å to 20 Å of nickel cobalt ($\text{Ni}_{50}\text{Co}_{50}$). Each of these materials for the thin film 220 has a positive magnetostriction. The nickel

iron ($\text{Ni}_{45}\text{Fe}_{55}$) has a magnetostriction of $+5 \times 10^{-5}$, the nickel iron niobium (NiFeNb) has a magnetostriction of $+4 \times 10^{-5}$ and the nickel cobalt ($\text{Ni}_{50}\text{Co}_{50}$) has a magnetostriction of $+1-10 \times 10^{-5}$. As a comparison, nickel iron ($\text{Ni}_{80}\text{Fe}_{20}$) has substantially zero magnetostriction. In regard to the second AP pinned layer 218 in either of the embodiments 200 or 300 in FIGS. 12 and 13, the materials of the thin films may be identical as that shown for the first AP pinned layer 214 in FIGS. 14, 15 and 16, except the thin film of cobalt (Co) or cobalt iron (CoFe) 242 shown in FIGS. 12 and 13 is substituted for the nickel iron ($\text{Ni}_{80}\text{Fe}_{20}$) thin film 234 in FIGS. 14, 15 and 16.

It has been found that when the positive magnetostriction layer 220 interfaces the ruthenium (Ru) AP coupling layer 230 the strength of the antiparallel coupling between the first and second AP pinned layers 214 and 218 is degraded. I found that when the positive magnetostriction thin film 220 is cobalt iron (CoFe) it has a high coercivity (H_C) when it interfaces the nickel oxide (NiO) pinning layer 222. This coercivity (H_C) can easily exceed the pinning strength of the pinning layer 222 so that during operating temperatures the magnetic moment 224 of the thin film 220 can be switched from its orientation shown in FIGS. 12 and 13 and remain at the switched position even after termination of the operating temperature because the coercivity (H_C) of the thin film 220 exceeds the pinning strength of the pinning layer 222. However, if the material of the thin film 220 is nickel iron ($\text{Ni}_{45}\text{Fe}_{55}$) it can interface the nickel oxide (NiO) pinning layer 222 which obviates the need for the nickel iron (NiFe) thin film 234.

FIG. 17 is an ABS illustration of another embodiment 400 of the spin valve sensor. This spin valve sensor differs from the embodiments 200 and 300 in that the pinned layer structure 402 is a single pinned layer structure instead of an AP pinned layer structure. A spacer layer 404 is located between the pinned layer structure 402 and the free layer 406. A cap layer 408 is located on the free layer 406 for its protection from subsequent processing steps. The AP pinned layer 402 has a magnetic moment 410 which is pinned perpendicular to and toward the ABS or away from the ABS, as shown in FIG. 17. The sense current I_S is directed from left to right so as to support the pinning of the magnetic moment 410 in the direction shown.

The pinned layer structure 402 includes a positive magnetostriction (+MS) thin film 412 which has an easy axis 414 oriented perpendicular to the ABS because of the compression 416 which is manifested in the pinned layer structure 402. The pinned layer structure 402 includes a thin film 416 of nickel iron (NiFe) between the positive magnetostriction thin film 412 and a nickel oxide (NiO) pinning layer 418. I found this thin film 416 to be necessary when the positive magnetostriction thin film 412 is cobalt iron (CoFe) so as to reduce its coercivity (H_C) below the pinning strength of the pinning layer 418, as discussed hereinabove. Further, I have provided a thin film 420 of cobalt (Co) or cobalt iron (CoFe) between the positive magnetostriction thin film 412 and the copper (Cu) spacer layer 404 for enhancing the performance of the spin valve sensor. The thicknesses of the layers and thin films of the embodiment 400 are the same as the equivalent layers in the embodiments 200 and 300.

Clearly, other embodiments and modifications of this invention will occur readily to those of ordinary skill in the art in view of these teachings. Therefore, this invention is to be limited only by following claims, which include all such embodiments and modifications when viewed in conjunction with the above specification and accompanying drawings.

I claim:

1. A magnetic read head having an air bearing surface (ABS) comprising:
 - a spin valve sensor that includes:
 - a ferromagnetic free layer structure having a magnetic moment that is free to rotate from a first direction in response to signal fields from a moving magnetic medium;
 - a ferromagnetic antiparallel (AP) pinned layer structure;
 - an antiferromagnetic (AFM) pinning layer exchange coupled to the AP pinned layer structure for pinning a magnetic moment of the AP pinned layer structure in a second direction;
 - a nonmagnetic conductive spacer layer located between the free layer structure and the AP pinned layer structure;
 - the (AP) pinned layer structure including:
 - first and second antiparallel (AP) pinned layers;
 - an antiparallel (AP) coupling layer between the first and second AP pinned layers;
 - the first AP pinned layers including a first pinned film that has a positive magnetostriction and a second pinned film that is composed of cobalt (Co) or cobalt iron (CoFe); and
 - the second pinned film being located between and interfacing each of the first pinned film and the AP coupling layer.
2. A magnetic read head as claimed in claim 1 including:
 - nonmagnetic conductive first and second lead layers electrically connected to the spin valve sensor;
 - nonmagnetic nonconductive first and second read gap layers;
 - the spin valve sensor and the first and second lead layers being located between the first and second read gap layers; and
 - ferromagnetic first and second shield layers; and
 - the first and second read gap layers being located between the first and second shield layers.
3. A magnetic read head as claimed in claim 2 wherein the pinning layer is nickel oxide (NiO), the first pinned film is Ni₄₅Fe₅₅ and the first pinned film is interfaces the pinning layer.
4. A magnetic read as claimed in claim 2 including:
 - the pinning layer being nickel oxide (NiO); and
 - the first AP pinned layer including a third film of nickel iron which is located between and interfaces each of the pinning layer and the first pinned film.
5. A magnetic read head as claimed in claim 4 wherein the first pinned film is nickel iron niobium (NiFeNb).
6. A magnetic read head as claimed in claim 4 wherein the first pinned film is nickel cobalt (Ni₅₀Co₅₀).
7. A magnetic read head as claimed in claim 4 wherein the second AP pinned layer has a first pinned film with a positive magnetostriction and a second pinned film of cobalt (Co) or cobalt iron (CoFe) which is located between and interfaces the first pinned film and the spacer layer.
8. A magnetic read head as claimed in claim 7 wherein the first pinned film of the second AP pinned layer is nickel iron (Ni₄₅Fe₅₅).
9. A magnetic read head as claimed in claim 7 wherein the first pinned film of the second AP pinned layer is nickel iron niobium (NiFeNb).
10. A magnetic read head as claimed in claim 7 wherein the first pinned film of the second AP pinned layer is nickel cobalt Ni₅₀Co₅₀.

11. A magnetic read head as claimed in claim 7 including:
 - the second AP pinned layer including a third pinned film composed of cobalt (Co) or cobalt iron (CoFe); and
 - the third film of being located between and interfacing each of the AP coupling layer and the first pinned film of the second AP pinned layer.
12. A magnetic head assembly having a read head and a write head and an air bearing surface (ABS) comprising:
 - the write head including:
 - first and second pole piece layers;
 - each of the first and second pole piece layers having a yoke portion located between a pole tip portion and a back gap portion;
 - a nonmagnetic write gap layer located between the pole tip portions of the first and second pole piece layers;
 - an insulation stack with at least one coil layer embedded therein located between the yoke portions of the first and second pole piece layers; and
 - the first and second pole piece layers being connected at their back gaps portions; and
 - the read head including:
 - a spin valve sensor;
 - first and second lead layers electrically connected to the spin valve sensor;
 - nonmagnetic nonconductive first and second read gap layers;
 - the spin valve sensor and the first and second lead layers being located between the first and second read gap layers;
 - the spin valve sensor including:
 - a ferromagnetic free layer structure having a magnetic moment that is free to rotate from a first direction in response to signal fields from a moving magnetic medium;
 - a ferromagnetic antiparallel (AP) pinned layer structure;
 - an antiferromagnetic (AFM) pinning layer exchange coupled to the AP pinned layer structure for pinning a magnetic moment of the AP pinned layer structure in a second direction;
 - a nonmagnetic conductive spacer layer located between the free layer structure and the AP pinned layer structure;
 - the (AP) pinned layer structure including:
 - first and second antiparallel (AP) pinned layers;
 - an antiparallel (AP) coupling layer between the first and second AP pinned layers; and
 - the first AP pinned layers including a first pinned film that has a positive magnetostriction and a second pinned film that is composed of cobalt (Co) or cobalt iron (CoFe); and
 - the second pinned film being located between and interfacing each of the first pinned film and the AP coupling layer.
13. A magnetic head assembly as claimed in claim 12 including:
 - the read head further including:
 - a ferromagnetic second shield layer;
 - a nonmagnetic electrically insulative separation layer; and
 - the separation layer being located between the second shield layer and the first pole piece layer.
14. A magnetic head assembly as claimed in claim 12 including:
 - the pinning layer being nickel oxide (NiO); and
 - the first AP pinned layer including a third film of nickel iron which is located between and interfaces each of the pinning layer and the first pinned film.

13

15. A magnetic head assembly as claimed in claim 12 wherein the second AP pinned layer has a first pinned film with a positive magnetostriction and a second pinned film of cobalt (Co) or cobalt iron (CoFe) which is located between and interfaces the first pinned film and the spacer layer.

16. A magnetic head assembly as claimed in claim 15 including:
 the second AP pinned layer including a third pinned film composed of cobalt (Co) or cobalt iron (CoFe); and
 the third film of the second AP pinned layer being located between and interfacing each of the AP coupling layer and the first pinned film of the second AP pinned layer.

17. A magnetic head assembly as claimed in claim 16 including:
 the pinning, layer being nickel oxide (NiO); and
 the first AP pinned layer including a third film of nickel iron which is located between and interfaces each of the pinning layer and the first pinned film.

18. A magnetic head assembly as claimed in claim 17 wherein the first pinned film of each of the first and second AP pinned layers is nickel iron niobium (NiFeNb).

19. A magnetic head assembly as claimed in claim 17 wherein the first pinned film of each of the first and second AP pinned layers is nickel cobalt (NiCo).

20. A magnetic disk drive having at least one slider that has an air bearing surface (ABS), the slider supporting at least one magnetic head assembly that includes a read head and a write head, the disk drive comprising:
 the write head including:
 first and second pole piece layers;
 each of the first and second pole piece layers having a yoke portion located between a pole tip portion and a back gap portion;
 a nonmagnetic write gap layer located between the pole tip portions of the first and second pole piece layers;
 an insulation stack with at least one coil layer embedded therein located between the yoke portions of the first and second pole piece layers; and
 the first and second pole piece layers being connected at their back gaps portions; and
 the read head having a spin valve sensor that includes:
 a ferromagnetic free layer structure having a magnetic moment that is free to rotate from a first direction in response to signal fields from a moving magnetic medium;
 a ferromagnetic antiparallel (AP) pinned layer structure;
 an antiferromagnetic (AFM) pinning layer exchange coupled to the AP pinned layer structure for pinning a magnetic moment of the AP pinned layer structure in a second direction;
 a nonmagnetic conductive spacer layer located between the free layer structure and the AP pinned layer structure;
 the (AP) pinned layer structure including:
 first and second antiparallel (AP) pinned layers;
 an antiparallel (AP) coupling layer between the first and second AP pinned layers;
 the first AP pinned layers including a first pinned film that has a positive magnetostriction and a second pinned film that is composed of cobalt (Co) or cobalt iron (CoFe); and
 the second pinned film being located between and interfacing each of the first pinned film and the AP coupling layer;
 the read head further including:

14

nonmagnetic conductive first and second lead layers electrically connected to the spin valve sensor;
 nonmagnetic nonconductive first and second read gap layers;
 the spin valve sensor and the first and second lead layers being located between the first and second read gap layers;
 a ferromagnetic first shield layer; and
 the first and second read gap layers being located between the first shield layer and the first pole piece layer; and
 a housing;
 a magnetic disk rotatably supported in the housing;
 a support mounted in the housing for supporting the magnetic head assembly with its ABS facing the magnetic disk so that the magnetic head assembly is in a transducing relationship with the magnetic disk;
 a spindle motor for rotating the magnetic disk;
 an actuator connected to the support for moving the magnetic head assembly to multiple positions with respect to said magnetic disk; and
 a processor connected to the magnetic head assembly to the means for rotating the magnetic disk and to the positioning means for exchanging signals with the magnetic head assembly, for controlling movement of the magnetic disk and for controlling the position of the magnetic head assembly.

21. A magnetic disk drive as claimed in claim 20 including:
 the read head further including:
 a ferromagnetic second shield layer;
 a nonmagnetic electrically insulative separation layer; and
 the separation layer being located between the second shield layer the first pole piece layer.

22. A magnetic disk drive as claimed in claim 20 wherein the pinning layer is nickel oxide (NiO), the first film is nickel iron (Ni₄₅Fe₅₅) and the first pinned film interfaces the pinning layer.

23. A magnetic disk drive as claimed in claim 20 including:
 the pinning layer being nickel oxide (NiO); and
 the first AP pinned layer including a third film of nickel iron which is located between and interfaces each of the pinning, layer and the first pinned film.

24. A magnetic disk drive as claimed in claim 23 wherein the second AP pinned layer has a first pinned film with a positive magnetostriction and a second pinned film of cobalt (Co) or cobalt iron (CoFe) which is located between and interfaces the first pinned film and the spacer layer.

25. A magnetic disk drive as claimed in claim 4 including:
 the second AP pinned layers including a third pinned film composed of cobalt (Co) or cobalt iron (CoFe); and
 the third film of the second AP pinned layer being located between and interfacing each of the AP coupling layer and the first pinned film of the second AP pinned layer.

26. A magnetic disk drive as claimed in claim 25 wherein the first pinned film of each of the first and second AP pinned layers is nickel iron niobium (NiFeNb).

27. A magnetic disk drive as claimed in claim 26 wherein the first pinned film of each of the first and second AP pinned layers is nickel cobalt (NiCo).

15

28. A magnetic read head having an air bearing surface (ABS) comprising:

- a spin valve sensor that includes:
 - a ferromagnetic free layer structure having a magnetic moment that is free to rotate from a first direction in response to signal fields from a moving magnetic medium;
 - a ferromagnetic pinned layer structure;
 - an antiferromagnetic (AFM) pinning layer exchange coupled to the pinned layer structure for pinning a magnetic moment of the pinned layer structure in a second direction;
 - a nonmagnetic conductive spacer layer located between the free layer structure and the pinned layer structure; and
 - the first pinned film having a positive magnetostriction and the second pinned film being cobalt (Co) or cobalt iron (CoFe) and being located between the first pinned film and spacer layer.

16

29. A magnetic read head as claimed in claim 28 including:

- nonmagnetic conductive first and second lead layers electrically connected to the spin valve sensor;
- nonmagnetic nonconductive first and second read gap layers;
- the spin valve sensor and the first and second lead layers being located between the first and second read gap layers; and
- ferromagnetic first and second shield layers; and the first and second read gap layers being located between the first and second shield layers.

30. A magnetic read head as claimed in claim 29 wherein the first pinned film is substantially nickel iron (Ni₄₅Fe₅₅).

31. A magnetic read head as claimed in claim 29 wherein the first pinned film is nickel iron niobium (NiFeNb).

32. A magnetic read head as claimed in claim 29 wherein the first pinned film is substantially nickel cobalt (Ni₅₀Co₅₀).

* * * * *

Fabrication of patterned ferromagnetic shape memory thin films

P. Álvarez-Alonso^{1,a}, A. Pérez-Checa¹, I.R. Aseguinolaza¹, J. Alonso^{2,3},
A.V. Svalov¹, V.A. Chernenko^{3,4}, and J.M. Barandiarán³

¹Departamento de Electricidad y Electrónica, UPV/EHU, Leioa 48940, Spain

²Department of Physics, University of South Florida, Tampa, FL 33647 USA

³BCMaterials & University of Basque Country, UPV/EHU, Bilbao 48080, Spain

⁴Ikerbasque, Basque Foundation of Science, Bilbao 48011, Spain

^apablo.alvarez@ehu.es

Keywords: Ni-Mn-Ga Antidots, Martensitic Transformation, Silicon Substrate, Patterning

Abstract. We report two possible routes of fabrication of large surfaces of ferromagnetic shape memory antidots with tunable pore size and center-to-center distances. By using the drop coating method, we have prepared a large area of 2D arrays (typically 1cm²) of polystyrene spheres (PS) (1.4±0.1µm diameter) on a Si substrate. We have used reactive ion etching with a gas mixture of O₂ (12sccm) and Ar (5sccm) to reduce the diameter of the PS spheres whereby controlling the size of pores. The film deposition was performed on a substrate heated at 500°C (route 1) and at room temperature with subsequent annealing in a furnace at 500°C for 4 hours (route 2). Route 1 proved to be promising but more work is needed to optimize it. The antidots of Ni-Mn-Ga obtained along route 2 are ferromagnetic with a Curie temperature ~100°C, and a spread martensitic transformation (between -100°C and -30°C).

Introduction

Ferromagnetic shape memory alloy (FSMA) thin films have been the subject of intense research because of the interesting underlying physics and high potential for applications [1]. FSMAs exhibit a magnetic-field-activated giant recoverable strain of about 10% together with pronounced mechanical/electrical/magnetic/caloric properties, making them very suitable for the use in sensing/actuating devices [2-4]. When in thin film form, these properties can be affected by several parameters, including the composition, internal stress, thermal treatment, morphology and thickness of the thin films [5,6].

It is also well known that a material will exhibit a different behaviour when reduced to the nanoscale, a fact that has opened new opportunities in the field of sensors and actuators. For example, free-standing nanofabricated thin films of Ni-Mn-Ga FSMAs have attracted great interest due to their actuation capabilities related to the thermoelastic and magnetomechanical coupling effects [7-9]. In this sense, the abilities of micro- and nano-fabrication of FSMAs and downscaling of their functional properties are crucial for implementation in devices like microelectromechanical systems (MEMS). In general, two different approaches have been developed to fabricate micro/nanostructured materials: "top-down" [e.g., reactive ion etching (RIE)] and "bottom-up" (e.g., film sputter deposition). A particularly interesting technique to fabricate these materials is the Sphere Lithography, which combines characteristics of both approaches to improve the quality of the patterned structures. This technique is based on a two-step process [10]: a) the fabrication of a periodic array of the self-assembled polystyrene (PS) spheres on the substrate, which acts as a mask for b) the deposition of the material of interest.

In this work, we present two procedures based on the sphere lithography to fabricate antidot-patterned thin films of Ni-Mn-Ga.

Experimental Procedure

Previous studies have shown that the deposition temperature is a determining factor to achieve the appropriate structural and magnetic order of Ni-Mn-Ga films [4]. Due to the degradation of the spheres above 70°C, we propose two routes to fabricate Ni-Mn-Ga patterned films that overcome the temperature limitation. A sketch of both procedures is shown in Fig.1(a). The routes start with two common steps: (a) the formation of a template by depositing a single layer of PS spheres ($1.3\pm 0.1\mu\text{m}$ diameter, see inset in Fig.1(b), obtained by dispersion polymerization [11]), on the surface of a Si wafer using the drop-coating method [12]; and (b) reduction of the PS spheres [$0.9\pm 0.1\mu\text{m}$ diameter, see inset in Fig.1(c)] by a RIE process, working under the conditions presented in Table 1.

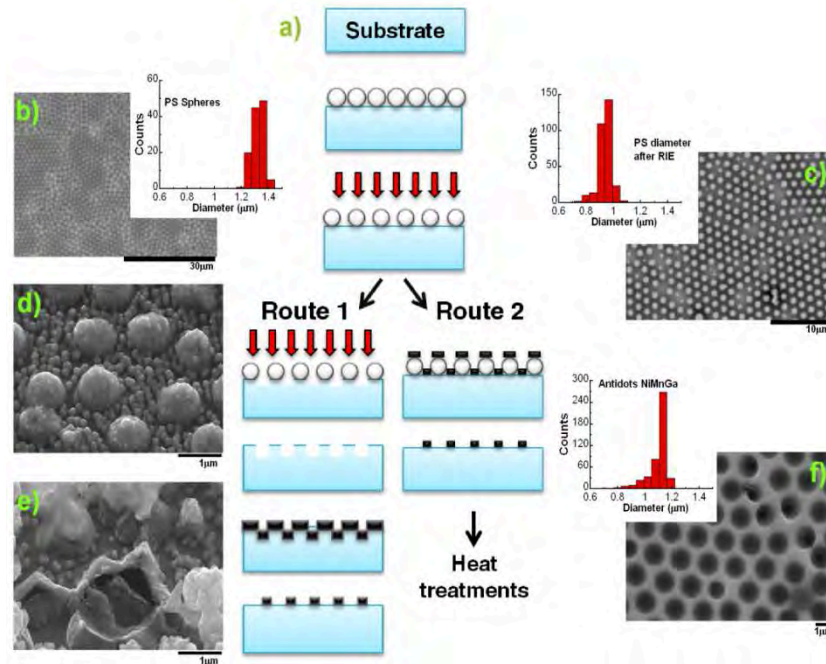


Figure 1. a) Scheme of the two routes used to fabricate Ni-Mn-Ga antidots. Red arrows denote the RIE treatment, Ni-Mn-Ga film is sketched by black color. SEM micrograph of the PS spheres (b), PS spheres after RIE (c), Si pillars covered by Ni-Mn-Ga (d), collapse of the pillars after KOH etch (e), and antidot-patterned Ni-Mn-Ga film obtained by route 2 (f). Insets: histograms for the diameters of the PS spheres before and after RIE, and of the Ni-Mn-Ga antidots.

Table 1. Conditions for the reactive ion etching of the different layers.

	Gas flow (sccm)	ICP/RF power (W)	Pressure (Torr)	Temperature (°C)	Time (min)
PS spheres	O ₂ :12/Ar:5	0/100	0.1	20	3
SiO ₂	SF ₆ :30	150/150	0.1	10	0.3
Si	CHF ₃ :10	0/50	0.02	10	15

To avoid a heat-induced degradation of PS, route 1 uses the Si wafer as a sacrificial layer. Thus, the following steps are taken: (1c) without removing the spheres, we fabricate Si dots by a selective etching of the wafer by RIE (see conditions in Table 1); (1d) then the PS spheres are removed; and (1e) Ni-Mn-Ga is deposited at 500°C by DC magnetron sputtering (Pfeiffer vacuum classic 500 station), using the parameters shown in Table 2. Finally, to remove the Si dots, the samples were (1f) subjected to a wet etching with a solution of 20% KOH at different temperatures, between 60 and 100°C, during 1 to 10min.

On the other hand, route 2 comprises: (2c) a deposition of Ni-Mn-Ga alloy at room temperature under the conditions summarized in Table 2; and (2d) a removal of the PS spheres with Tetrahydrofuran. Due to the low crystallinity of the as-deposited samples, they show neither a martensitic transformation nor a ferro-to-paramagnetic transition, and hence, the samples must be annealed at 500°C during 4h under vacuum (10^{-5} Torr) after deposition. In addition to the patterned samples, continuous 500nm thick Ni-Mn-Ga films have been deposited onto non-patterned substrates using the deposition conditions and heat treatments of route 2 to contrast their properties with the patterned analogs.

Table 2. Parameters of the sputter deposition of Ni-Mn-Ga thin films in both procedures.

Route	Distance Target-Substrate (cm)	RF power (W)	Pressure (Torr)	Temperature (°C)	Time (min)
1	9	150	$2.0 \cdot 10^{-2}$	500	5
2	9	150	$2.0 \cdot 10^{-2}$	20	10

The structural and compositional characterization of the samples was carried out by a scanning electron microscopy (SEM) (Hitachi TM 3000) and energy dispersive X-ray spectroscopy. An atomic force microscope (Nanotec DSP Classic) was used to determine the films surface profile. The temperature dependences of the magnetization $M(T)$ and resistivity were measured by a vibrating sample magnetometer and four-probe method, respectively.

Results

The deposition of a 250nm-thick Ni-Mn-Ga film by route 1 led to an additional sidewall deposition alongside the Si dots [see Fig.1(d)], hindering their elimination by wet etching –only a few percent of the Si pillars were eliminated, provoking the collapse of the Ni-Mn-Ga layer, as shown in Fig. 1(e). This issue was attributed to an excessive Ni-Mn-Ga/Si dot thickness ratio and could be further overcome by the optimization of the film thickness. An antidot-patterned $\text{Ni}_{50}\text{Mn}_{27}\text{Ga}_{23}$ (at.%) thin film was successfully obtained through route 2, as demonstrated by SEM in Fig.1(f). The antidots present a narrow diameter distribution with a mean value of around $1.1 \pm 0.1 \mu\text{m}$ [see inset in Fig.1(f)] and they are arranged in hexagonal-type close packing forming coherent domains of about $15 \mu\text{m}$ of length. The dots have a height of about 500nm and diameter of around $1 \mu\text{m}$.

The results of the magnetic and electric measurements are shown in Fig. 2 for the previously cited patterned film and two continuous films deposited on unpatterned substrates at 500°C ($\text{Ni}_{48}\text{Mn}_{32}\text{Ga}_{20}$) and at 20°C with subsequent post-annealing ($\text{Ni}_{50}\text{Mn}_{27}\text{Ga}_{23}$). The continuous film deposited at high temperature displays a Curie temperature [defined as the inflexion point of the $M(T)$ curve] at $\sim 100^\circ\text{C}$ with a sharp magnetization drop, evidencing a high atomic ordering. It also exhibits the martensitic transformation in a broad interval between -50°C and 50°C , which could be a result of a wide stress distribution in the film. The continuous film deposited at room temperature and annealed at 500°C presents a Curie temperature of about 50°C , far below the expected from its composition ($\sim 100^\circ\text{C}$), while the martensitic transformation does not appear in the studied temperature interval. The reason of those features could be the partial crystal lattice disorder that remains from the room temperature deposition, even after heat treatment [4]. In the patterned film, the Curie temperature appears at about 100°C , although a coexistence of the ordered and less-ordered phases could be inferred from the multiple magnetization drops from 25°C to 100°C . A hint of the martensitic transformation is manifested below -30°C . The value of the Curie temperature and the occurrence of the martensitic transformation indicate that, in this case, the $L2_1$ atomic ordering degree is much higher than in the continuous film. The diffusion assisted higher atomic ordering during annealing in this case could be promoted by the enhanced amount and mobility of crystal defects due to the antidot boundaries.

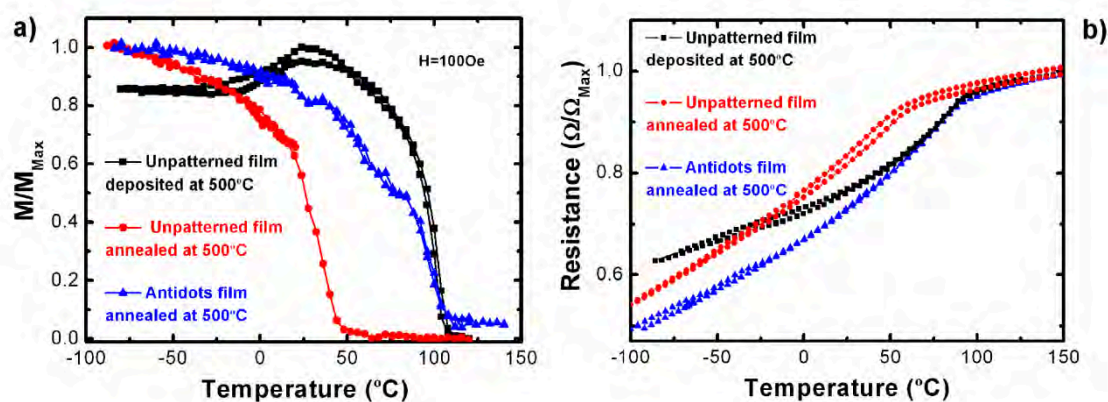


Figure 2. a) Normalized magnetization at $H=100\text{Oe}$ and b) normalized electrical resistance as a function of temperature, evidencing the Curie and martensitic transformation temperatures.

Summary

Two ways for Ni-Mn-Ga thin film micropatterning have been developed by using self-assembled polystyrene spheres and reactive ion etching. The process allows tailoring the dimensions of the pattern, giving rise to different properties of the FSMA film. The patterned films have shown functional features like ferromagnetism and martensitic transformation, making them interesting for microdevices. The lattice ordering is incomplete in thin films deposited at room temperature with subsequent annealing. Further efforts will be focused on the elaboration of a route in which high-temperature deposition would be employed using the sacrificial layer method.

Acknowledgement

We are grateful to the UPV/EHU Química Macromolecular group and the SGIker team, especially to Dr. I. Orue for technical help. The financial support from the Spanish Ministry MINECO is acknowledged (project MAT2011-28217-C02-02). Javier Alonso acknowledges the financial support provided through a postdoctoral fellowship from Basque Government.

References

- [1] D.C. Dunand and P. Müllner: *Adv. Mater.* Vol. 23 (2011), p 216005D.
- [2] D. Auernhammer et. al: *Smart Mater. Struct.* Vol. 18 (2009), p. 104016.
- [3] M. Chmielus et. al: *Nat. Mater.* Vol. 8 (2009), p. 863–866.
- [4] A. Planes et. al: *J. Phys. Condens. Matter.* Vol. 21 (2009), p. 233201.
- [5] I.R. Aseguinolaza et. al: *J. Mater. Sci.* Vol. 47 (2012), p. 3658–3662.
- [6] V.A. Chernenko et. al: *Mater. Trans.* Vol. 47 (2006), p. 619.
- [7] M. Kohl et. al: *Mater. Sci. Eng. A.* Vol. 438–440 (2006), p. 940–943.
- [8] C. Lay et. al: *Proceedings of the 13th IEEE International Conference on Nanotechnology*, Beijing, China, August 5-8 (2013), p. 954-957.
- [9] N. Aubry et. al: *Proc. Natl. Acad. Sci.* Vol. 105 (2008), p. 3711–3714.
- [10] P. Colson et. al: *J. Nanomater.* Vol. 2013 (2013), p. 948510.
- [11] J. Lee et. al: *J. Colloid Interface Sci.* Vol. 298 (2006), p. 663–671.
- [12] J. Rybczynski et. al: *Colloids Surf. Physicochem. Eng. Asp.* Vol. 219 (2003), p. 1–6.

Proceedings of the 4th International Conference on Materials and Applications for Sensors and Transducers

10.4028/www.scientific.net/KEM.644

Fabrication of Patterned Ferromagnetic Shape Memory Thin Films

10.4028/www.scientific.net/KEM.644.219

DOI References

- [1] D.C. Dunand and P. Müllner: Adv. Mater. Vol. 23 (2011), p 216005D.
<http://dx.doi.org/10.1002/adma.201002753>
- [2] D. Auernhammer et. al: Smart Mater. Struct. Vol. 18 (2009), p.104016.
<http://dx.doi.org/10.1088/0964-1726/18/10/104016>
- [3] M. Chmielus et. al: Nat. Mater. Vol. 8 (2009), pp.863-866.
<http://dx.doi.org/10.1038/nmat2527>
- [4] A. Planes et. al: J. Phys. Condens. Matter. Vol. 21 (2009), p.233201.
<http://dx.doi.org/10.1088/0953-8984/21/23/233201>
- [5] I.R. Aseguinolaza et. al: J. Mater. Sci. Vol. 47 (2012), pp.3658-3662.
<http://dx.doi.org/10.1007/s10853-011-6212-2>
- [6] V.A. Chernenko et. al: Mater. Trans. Vol. 47 (2006), p.619.
<http://dx.doi.org/10.2320/matertrans.47.619>
- [9] N. Aubry et. al: Proc. Natl. Acad. Sci. Vol. 105 (2008), pp.3711-3714.
<http://dx.doi.org/10.1073/pnas.0712392105>
- [11] J. Lee et. al: J. Colloid Interface Sci. Vol. 298 (2006), pp.663-671.
<http://dx.doi.org/10.1016/j.jcis.2006.01.001>
- [12] J. Rybczynski et. al: Colloids Surf. Physicochem. Eng. Asp. Vol. 219 (2003), pp.1-6.
[http://dx.doi.org/10.1016/S0927-7757\(03\)00011-6](http://dx.doi.org/10.1016/S0927-7757(03)00011-6)

Improvements are driven by you.

You can send us feedback or request assistance by emailing onlineservice@springer.com or visiting www.springer.com/springermaterials

SpringerMaterials is continuously improving...

More info



Search



Menu

- [Home](#)
- [Contact us](#)

More search tools

- [Search by elements](#)
- [Search by structure](#)

Inorganic Solid Phases

Fe₆₀Co₄₀ (Fe_{0.7}Co_{0.3} ht) Crystal Structure

Download Data CIF

- **Content available to subscribers**
- To view content, please [Log in](#) or contact your [Springer representative](#)

General Information

- **Phase Label(s):** Fe_{0.7}Co_{0.3} ht
- **Structure Class(es):** b.c.c. atom arrangement
- **Classification by Properties:** ferromagnet FM, hard magnet, metal
- **Mineral Name(s):** –
- **Pearson Symbol:** cI2
- **Space Group:** 229

- **Phase Prototype:** W
- **Measurement Detail(s):** Debye-Scherrer film (determination of cell and structural parameters), X-rays, Mo K α (determination of cell and structural parameters), T = 298 K (determination of cell and structural parameters)
- **Phase Class(es):** –
- **Compound Class(es):** intermetallic
- **Interpretation Detail(s):** cell parameters determined and type with fixed coordinates assigned; composition dependence studied
- **Sample Detail(s):** powder (determination of cell and structural parameters)

Substance Summary

- **Standard Formula:** Fe_{0.6}Co_{0.4}
- **Alphabetic Formula:** Co_{0.4}Fe_{0.6}
- **Published Formula:** Fe₆₀Co₄₀
- **Refined Formula:** Co_{0.40}Fe_{0.60}
- **Wyckoff Sequence:** 229,a
- **Z Formula Units:** 2
- **Density:** $\rho = 8.09 \text{ Mg}\cdot\text{m}^{-3}$

Cite this page

- [Citation](#)

3D Interactive Structure

- **Content available to subscribers**
- To view content, please [Log in](#) or contact your [Springer representative](#)

Crystallographic Data

Cell Parameters

Cell Parameters	Published Data	Unit Cell	Standardized I Niggli
Space Group	—	—	—
a	—	—	—
b	—	—	—
c	—	—	—
α	—	—	—
β	—	—	—
γ	—	—	—
a/b	—	—	—
b/c	—	—	—

c/a

- **Content available to subscribers**
- To view content, please [Log in](#) or contact your [Springer representative](#)



Showing 1 to 10 of 11 entries

Atom Coordinates

Standardized

Site	Element	Wyckoff Symbol	Symmetry	X	Y	Z	Occupation
—	—	—	—	—	—	—	—

- **Content available to subscribers**
- To view content, please [Log in](#) or contact your [Springer representative](#)



Showing 1 to 1 of 1 entries

Published

Site	Element	Wyckoff Symbol	Symmetry	X	Y	Z
—	—	—	—	—	—	—

- **Content available to subscribers**
- To view content, please [Log in](#) or contact your [Springer representative](#)



Showing 1 to 1 of 1 entries

Experimental Details

- **Content available to subscribers**
- To view content, please [Log in](#) or contact your [Springer representative](#)

Reference

- **Content available to subscribers**
- To view content, please [Log in](#) or contact your [Springer representative](#)

About this content

- **Database name**

LINUS PAULING FILE Multinaries Edition – 2012

- **Dataset ID**

sd_0555891

- **Copyright**

©Springer & Material Phases Data System (MPDS), Switzerland & National Institute for Materials Science (NIMS), Japan, 2014

- **Chief Editor**

Pierre Villars, Material Phases Data System (MPDS), CH-6354 Vitznau, Switzerland

villars.mpds@bluewin.ch

- **Credits**



SpringerMaterials Release 2014.

Data generated pre-2002: © Springer & MPDS & NIMS; post-2001: © Springer & MPDS

All Rights Reserved. Version 2014.09.

Project Coordinator: Shuichi Iwata

Section-Editor: Karin Cenzual (Crystal Structures)

Cite this content

Pierre Villars, Material Phases Data System (MPDS), CH-6354 Vitznau, Switzerland (ed.)
SpringerMaterials Fe60Co40 (Fe0.7Co0.3 ht) Crystal Structure
http://materials.springer.com/isp/crystallographic/docs/sd_0555891 sd_0555891 (Springer-Verlag
GmbH, Heidelberg, © 2014) Accessed: 10-09-2015

Citation copied
sd_0555891

Other sites

- [Springer.com](http://www.springer.com)
- [SpringerLink](http://www.springerlink.com)
- [SpringerProtocols](http://www.springerprotocols.com)

Help & contacts

- [Contact us](#)
- [Imprint](#)

Legal

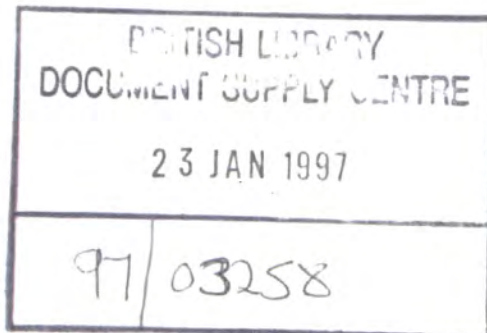
© Springer, part of Springer Science+Business Media

[Privacy policy, disclaimer, general terms & conditions](#)

Not logged in unaffiliated 204.130.0.8

THIRD EDITION

PRINCIPLES OF MATERIALS SCIENCE AND ENGINEERING



William F. Smith

Professor of Engineering
University of Central Florida

McGraw-Hill, Inc.

New York St. Louis San Francisco Auckland Bogotá
Caracas Lisbon London Madrid
Mexico City Milan Montreal New Delhi
San Juan Singapore Sydney Tokyo Toronto

PRINCIPLES OF MATERIALS SCIENCE AND ENGINEERING

Copyright © 1996, 1990, 1986 by McGraw-Hill, Inc. All rights reserved. Printed in the United States of America. Except as permitted under the United States Copyright Act of 1976, no part of this publication may be reproduced or distributed in any form or by any means, or stored in a data base or retrieval system, without the prior written permission of the publisher.

This book is printed on acid-free paper.

1 2 3 4 5 6 7 8 9 0 DOC DOC 9 0 9 8 7 6 5

ISBN 0-07-059241-1

This book was set in Cheltenham Light by York Graphic Services, Inc.

The editors were B. J. Clark and Jack Maisel.

the production supervisor was Denise L. Puryear.

The cover was designed by Jo Jones.

R. R. Donnelley & Sons Company was printer and binder.

On the Cover:

Polymer-matrix composite tube being filament-braided with aramid fibers and an epoxy matrix. Computerized braiding machines fabricate these tubes for critical applications in the medical, electrical, automotive, and aerospace industries. (Courtesy of Polygon Company, Walkerton, Ind.)

Library of Congress Cataloging-in-Publication Data

Smith, William Fortune. (date).

Principles of materials science and engineering / William F. Smith.—3d ed.

p. cm.—(McGraw-Hill series in materials science and engineering)

Includes bibliographical references (p.) and index.

ISBN 0-07-059241-1

I. Materials. I. Title. II. Series.

TA403.S596 1996

620.1'1—dc20

94-48015

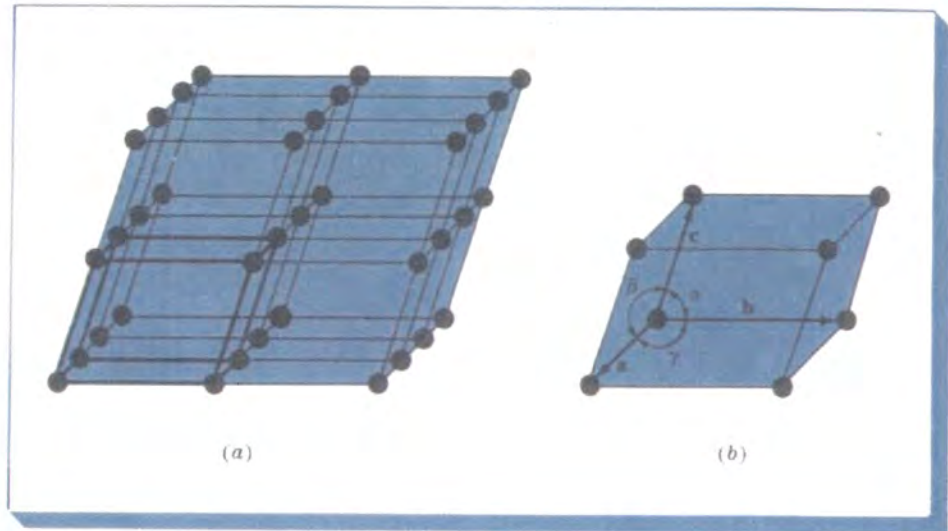
Crystal Structures and Crystal Geometry

3.1 THE SPACE LATTICE AND UNIT CELLS

The physical structure of solid materials of engineering importance depends mainly on the arrangements of the atoms, ions, or molecules which make up the solid and the bonding forces between them. If the atoms or ions of a solid are arranged in a pattern that repeats itself in three dimensions, they form a solid which is said to have a *crystal structure* and is referred to as a *crystalline solid* or *crystalline material*. Examples of crystalline materials are metals, alloys, and some ceramic materials.

Atomic arrangements in crystalline solids can be described by referring the atoms to the points of intersection of a network of lines in three dimensions. Such a network is called a *space lattice* (Fig. 3.1a) and can be described as an infinite three-dimensional array of points. Each point in the space lattice has identical surroundings. In an ideal crystal the grouping of lattice points about any given point are identical with the grouping about any other lattice point in the crystal lattice. Each space lattice can thus be described by specifying the atom positions in a repeating *unit cell*, such as the one heavily

FIGURE 3.1 (a) Space lattice of ideal crystalline solid. (b) Unit cell showing lattice constants.



outlined in Fig. 3.1a. The size and shape of the unit cell can be described by three lattice vectors \mathbf{a} , \mathbf{b} , and \mathbf{c} , originating from one corner of the unit cell (Fig. 3.1b). The axial lengths a , b , and c and the interaxial angles α , β , and γ are the *lattice constants* of the unit cell.

3.2 CRYSTAL SYSTEMS AND BRAVAIS LATTICES

By assigning specific values for axial lengths and interaxial angles, unit cells of different types can be constructed. Crystallographers have shown that only seven different types of unit cells are necessary to create all point lattices. These crystal systems are listed in Table 3.1.

Many of the seven crystal systems have variations of the basic unit cell. A. J. Bravais¹ showed that 14 standard unit cells could describe all possible lattice networks. These Bravais lattices are illustrated in Fig. 3.2. There are four basic types of unit cells: (1) simple, (2) body-centered, (3) face-centered, and (4) base-centered.

In the cubic system there are three types of unit cells: simple cubic, body-centered cubic, and face-centered cubic. In the orthorhombic system all four types are represented. In the tetragonal system there are only two: simple and body-centered. The face-centered tetragonal unit cell appears to be missing but can be constructed from four body-centered tetragonal unit cells. The

¹August Bravais (1811–1863) French crystallographer who derived the 14 possible arrangements of points in space

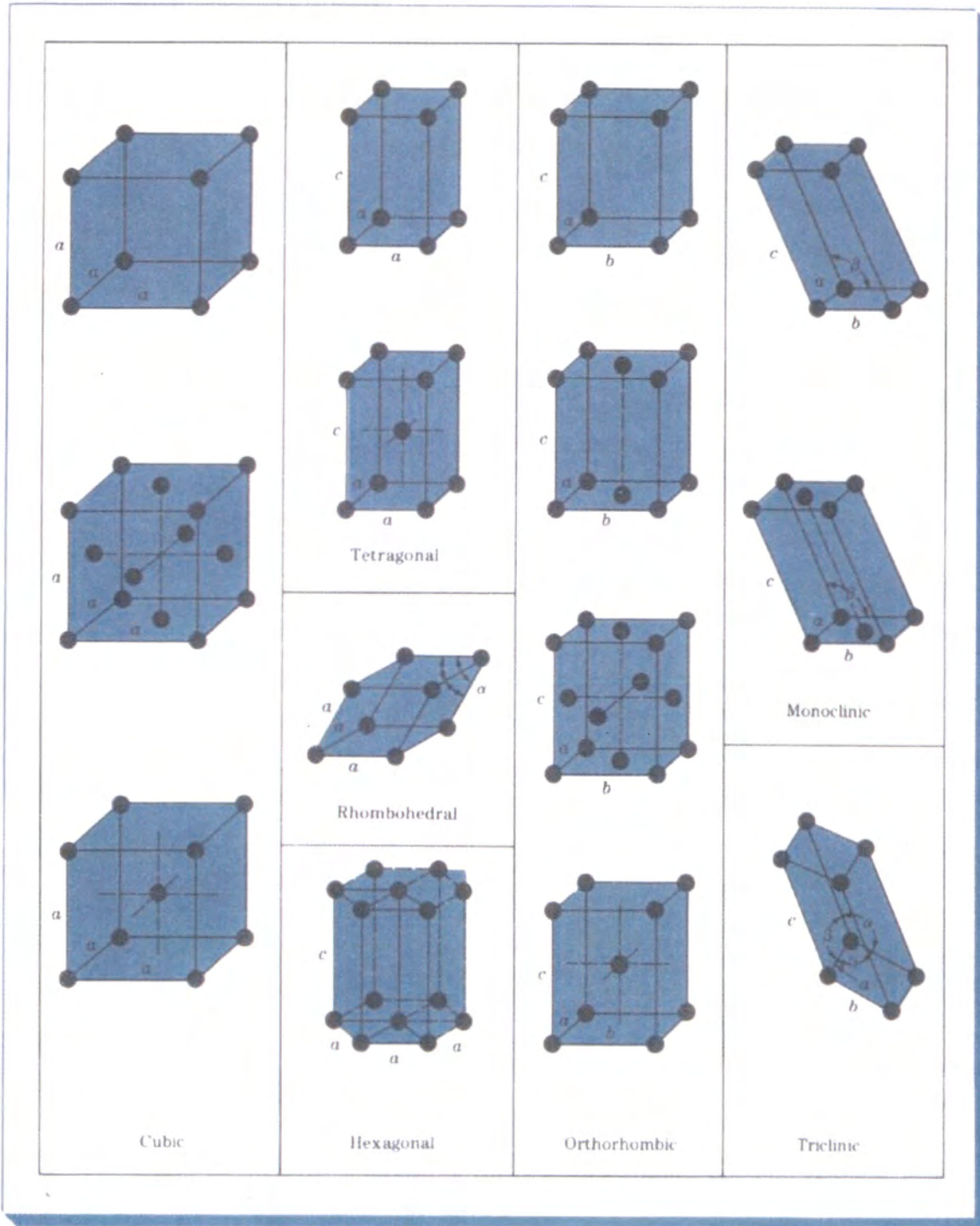


FIGURE 3.2 The 14 Bravais conventional unit cells grouped according to crystal system. The dots indicate lattice points that, when located on faces or at corners, are shared by other identical lattice unit cells. (After W. G. Moffatt, G. W. Pearsall, and J. Wulff, "The Structure and Properties of Materials," vol. 1: "Structure," Wiley, 1964, p. 47.)

TABLE 3.1 Classification of Space Lattices by Crystal System

Crystal system	Axial lengths and interaxial angles	Space lattice
Cubic	Three equal axes at right angles $a = b = c, \alpha = \beta = \gamma = 90^\circ$	Simple cubic Body-centered cubic Face-centered cubic
Tetragonal	Three axes at right angles, two equal $a = b \neq c, \alpha = \beta = \gamma = 90^\circ$	Simple tetragonal Body-centered tetragonal
Orthorhombic	Three unequal axes at right angles $a \neq b \neq c, \alpha = \beta = \gamma = 90^\circ$	Simple orthorhombic Body-centered orthorhombic Base-centered orthorhombic Face-centered orthorhombic
Rhombohedral	Three equal axes, equally inclined $a = b = c, \alpha = \beta = \gamma \neq 90^\circ$	Simple rhombohedral
Hexagonal	Two equal axes at 120° , third axis at right angles $a = b \neq c, \alpha = \beta = 90^\circ, \gamma = 120^\circ$	Simple hexagonal
Monoclinic	Three unequal axes, one pair not at right angles $a \neq b \neq c, \alpha = \gamma = 90^\circ \neq \beta$	Simple monoclinic Base-centered monoclinic
Triclinic	Three unequal axes, unequally inclined and none at right angles $a \neq b \neq c, \alpha \neq \beta \neq \gamma \neq 90^\circ$	Simple triclinic

monoclinic system has simple and base-centered unit cells, and the rhombohedral, hexagonal, and triclinic systems have only one simple type of unit cell.

3.3 PRINCIPAL METALLIC CRYSTAL STRUCTURES

In this chapter the principal crystal structures of elemental metals will be discussed in detail. In Chap. 10 the principal ionic and covalent crystal structures which occur in ceramic materials will be treated.

Most elemental metals (about 90 percent) crystallize upon solidification into three densely packed crystal structures: *body-centered cubic (BCC)* (Fig. 3.3a), *face-centered cubic (FCC)* (Fig. 3.3b) and *hexagonal close packed (HCP)* (Fig. 3.3c). The HCP structure is a denser modification of the simple hexagonal crystal structure shown in Fig. 3.2. Most metals crystallize in these dense-packed structures because energy is released as the atoms come closer together and bond more tightly with each other. Thus, the densely packed structures are in lower and more stable energy arrangements.

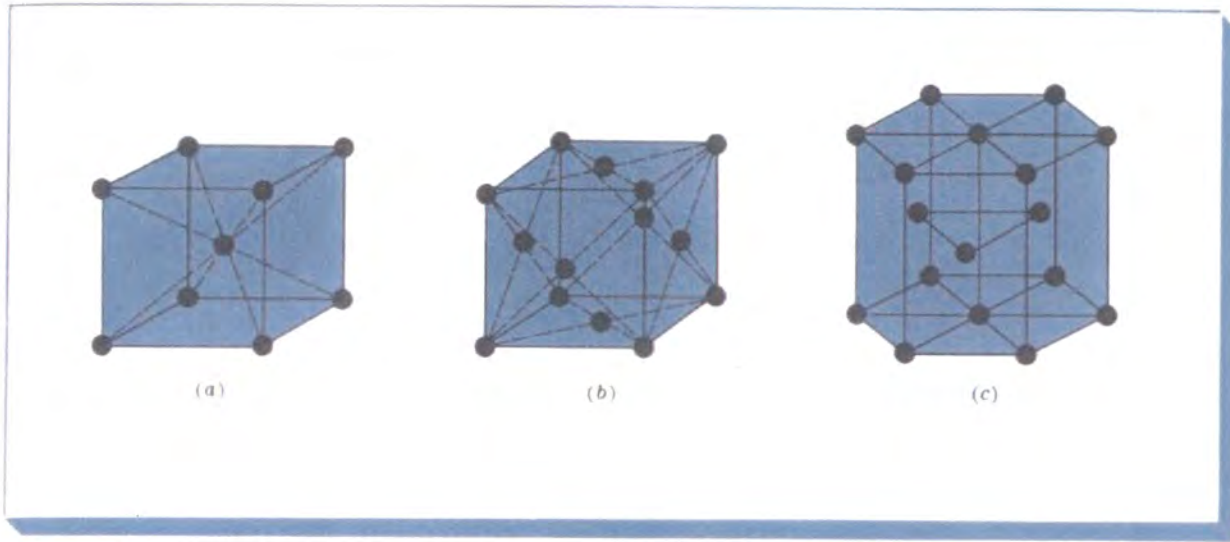


FIGURE 3.3 Principal metal crystal structure unit cells: (a) body-centered cubic, (b) face-centered cubic, (c) hexagonal close-packed.

The extremely small size of the unit cells of crystalline metals which are shown in Fig. 3.3 should be emphasized. The cube side of the unit cell of body-centered cubic iron, for example, at room temperature is equal to 0.287×10^{-9} m, or 0.287 nanometer (nm).¹ Therefore, if unit cells of pure iron are lined up side by side, in 1 mm there will be

$$1 \text{ mm} \times \frac{1 \text{ unit cell}}{0.287 \text{ nm} \times 10^{-6} \text{ mm/nm}} = 3.48 \times 10^6 \text{ unit cells!}$$

Let us now examine in detail the arrangement of the atoms in the three principal crystal structure unit cells. Although an approximation, we shall consider atoms in these crystal structures to be hard spheres. The distance between the atoms (interatomic distance) in crystal structures can be determined experimentally by x-ray diffraction analysis.² For example, the interatomic distance between two aluminum atoms in a piece of pure aluminum at 20°C is 0.2862 nm. The radius of the aluminum atom in the aluminum metal is assumed to be half the interatomic distance, or 0.143 nm. The atomic radii of selected metals are listed in Tables 3.2 to 3.4.

Body-Centered Cubic (BCC) Crystal Structure

First, consider the atomic-site unit cell for the BCC crystal structure shown in Fig. 3.4a. In this unit cell the solid spheres represent the centers where atoms are located and clearly indicate their relative positions. If we represent the

¹1 nanometer = 10^{-9} meter

²Some of the principles of x-ray diffraction analysis will be studied in Sec. 3.11

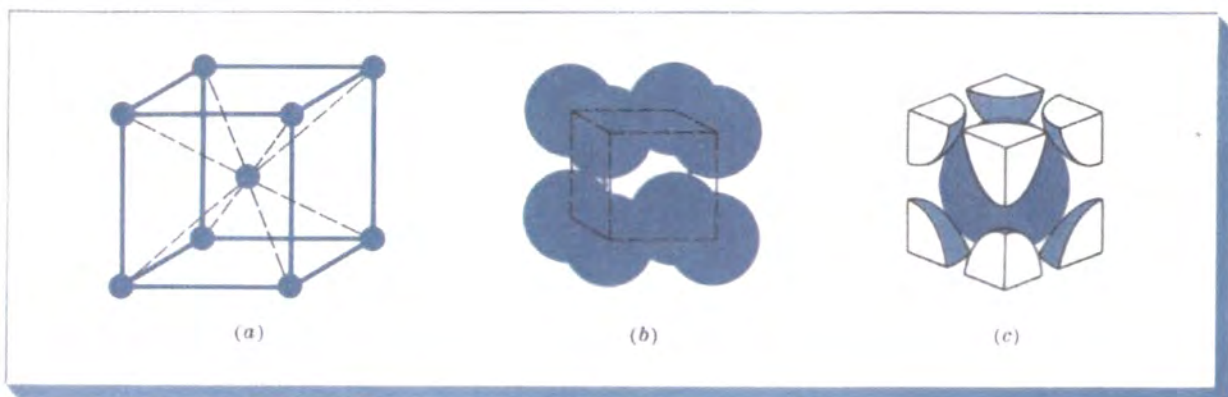


FIGURE 3.4 BCC unit cells: (a) atomic-site unit cell, (b) hard-sphere unit cell, and (c) isolated unit cell.

atoms in this cell as hard spheres, then the unit cell appears as shown in Fig. 3.4b. In this unit cell we see that the central atom is surrounded by eight nearest neighbors and is said to have a coordination number of 8.

If we isolate a single hard-sphere unit cell, we obtain the model shown in Fig. 3.4c. Each of these cells has the equivalent of two atoms per unit cell. One complete atom is located at the center of the unit cell, and an eighth of a sphere is located at each corner of the cell, making the equivalent of another atom. Thus there is a total of 1 (at the center) $+ 8 \times \frac{1}{8}$ (at the corners) $= 2$

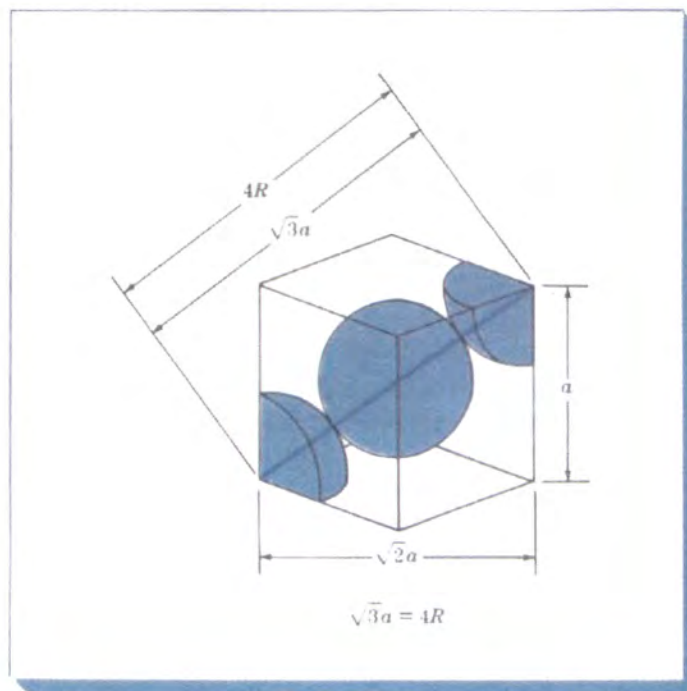


FIGURE 3.5 BCC unit cell showing relationship between the lattice constant a and the atomic radius R

atoms per unit cell. The atoms in the BCC unit cell contact each other across the cube diagonal, as indicated in Fig. 3.5, so that the relationship between the length of the cube side a and the atomic radius R is

$$\sqrt{3}a = 4R \quad \text{or} \quad a = \frac{4R}{\sqrt{3}} \quad (3.1)$$

Example Problem 3.1

Iron at 20°C is BCC with atoms of atomic radius 0.124 nm. Calculate the lattice constant a for the cube edge of the iron unit cell.

Solution:

From Fig. 3.5 it is seen that the atoms in the BCC unit cell touch across the cube diagonals. Thus, if a is the length of the cube edge, then

$$\sqrt{3}a = 4R \quad (3.1)$$

where R is the radius of the iron atom. Therefore

$$a = \frac{4R}{\sqrt{3}} = \frac{4(0.124 \text{ nm})}{\sqrt{3}} = 0.2864 \text{ nm} \blacktriangleleft$$

TABLE 3.2 Selected Metals Which Have the BCC Crystal Structure at Room Temperature (20°C) and Their Lattice Constants and Atomic Radii

Metal	Lattice constant a , nm	Atomic radius R ,* nm
Chromium	0.289	0.125
Iron	0.287	0.124
Molybdenum	0.315	0.136
Potassium	0.533	0.231
Sodium	0.429	0.186
Tantalum	0.330	0.143
Tungsten	0.316	0.137
Vanadium	0.304	0.132

* Calculated from lattice constants by using Eq. (3.1), $R = \sqrt{3}a/4$.

If the atoms in the BCC unit cell are considered to be spherical, an atomic packing factor (APF) can be calculated by using the equation

$$\text{Atomic packing factor (APF)} = \frac{\text{volume of atoms in unit cell}}{\text{volume of unit cell}} \quad (3.2)$$

Using this equation, the APF for the BCC unit cell (Fig. 3.3a) is calculated to be 68 percent (see Example Problem 3.2). That is, 68 percent of the volume of the BCC unit cell is occupied by atoms and the remaining 32 percent is empty space. The BCC crystal structure is *not* a close-packed structure since the atoms could be packed closer together. Many metals such as iron, chromium, tungsten, molybdenum, and vanadium have the BCC crystal structure at room temperature. Table 3.2 lists the lattice constants and atomic radii of selected BCC metals.

Example Problem 3.2

Calculate the atomic packing factor (APF) for the BCC unit cell, assuming the atoms to be hard spheres.

Solution:

$$\text{APF} = \frac{\text{volume of atoms in BCC unit cell}}{\text{volume of BCC unit cell}} \quad (3.2)$$

Since there are two atoms per BCC unit cell, the volume of atoms in the unit cell of radius R is

$$V_{\text{atoms}} = (2)\left(\frac{4}{3}\pi R^3\right) = 8.373R^3$$

The volume of the BCC unit cell is

$$V_{\text{unit cell}} = a^3$$

where a is the lattice constant. The relationship between a and R is obtained from Fig. 3.5, which shows that the atoms in the BCC unit cell touch each other across the cubic diagonal. Thus

$$\sqrt{3}a = 4R \quad \text{or} \quad a = \frac{4R}{\sqrt{3}} \quad (3.1)$$

Thus

$$V_{\text{unit cell}} = a^3 = 12.32R^3$$

The atomic packing factor for the BCC unit cell is, therefore,

$$\text{APF} = \frac{V_{\text{atoms/unit cell}}}{V_{\text{unit cell}}} = \frac{8.373R^3}{12.32R^3} = 0.68 \blacktriangleleft$$

Face-Centered Cubic (FCC) Crystal Structure

Consider next the FCC lattice-point unit cell of Fig. 3.6*a*. In this unit cell there is one lattice point at each corner of the cube and one at the center of each cube face. The hard-sphere model of Fig. 3.6*b* indicates that the atoms in the FCC crystal structure are packed as close together as possible. The APF for this close-packed structure is 0.74 as compared to 0.68 for the BCC structure which is not close-packed.

The FCC unit cell as shown in Fig. 3.6*c* has the equivalent of four atoms per unit cell. The eight corner octants account for one atom ($8 \times \frac{1}{8} = 1$), and the six half-atoms on the cube faces contribute another three atoms, making a total of four atoms per unit cell. The atoms in the FCC unit cell contact each other across the cubic face diagonal, as indicated in Fig. 3.7, so that the relationship between the length of the cube side a and the atomic radius R is

$$\sqrt{2}a = 4R \quad \text{or} \quad a = \frac{4R}{\sqrt{2}} \quad (3.3)$$

The APF for the FCC crystal structure is 0.74, which is greater than the 0.68 factor for the BCC structure. The APF of 0.74 is for the closest packing possible of "spherical atoms." Many metals such as aluminum, copper, lead, nickel, and iron at elevated temperatures (912 to 1394°C) crystallize with the FCC crystal structure. Table 3.3 lists the lattice constants and atomic radii for some selected FCC metals.

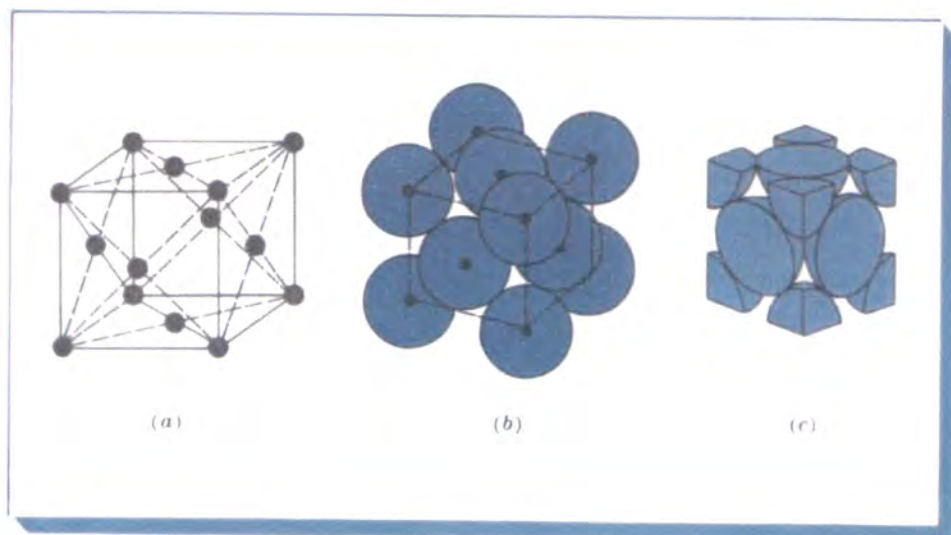


FIGURE 3.6 FCC unit cells: (a) atomic-site unit cell, (b) hard-sphere unit cell, and (c) isolated unit cell.

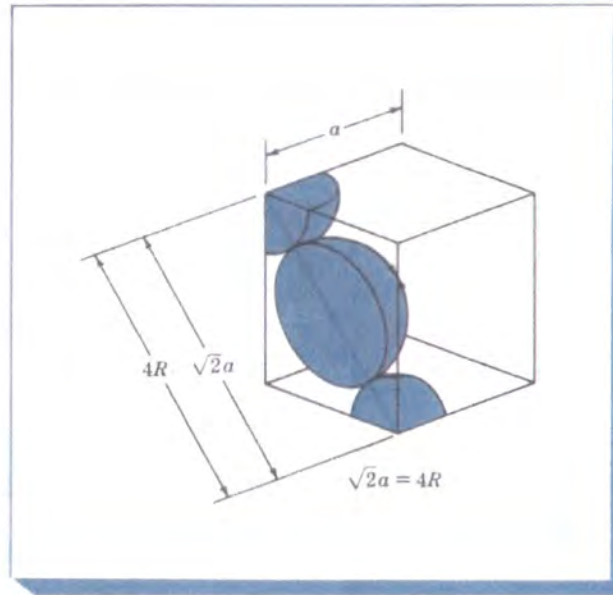


FIGURE 3.7 FCC unit cell showing relationship between the lattice constant a and atomic radius R . Since the atoms touch across the face diagonals $\sqrt{2}a = 4R$.

TABLE 3.3 Selected Metals Which Have the FCC Crystal Structure at Room Temperature (20°C) and Their Lattice Constants and Atomic Radii

Metal	Lattice constant a , nm	Atomic radius R ,* nm
Aluminum	0.405	0.143
Copper	0.3615	0.128
Gold	0.408	0.144
Lead	0.495	0.175
Nickel	0.352	0.125
Platinum	0.393	0.139
Silver	0.409	0.144

* Calculated from lattice constants by using Eq. (3.3), $R = \sqrt{2}a/4$

Hexagonal Close-Packed (HCP) Crystal Structure

The third common metallic crystal structure is the HCP structure shown in Fig. 3.8. Metals do not crystallize into the simple hexagonal crystal structure shown in Fig. 3.2 because the APF is too low. The atoms can attain a lower energy and a more stable condition by forming the HCP structure of Fig. 3.8. The APF of the HCP crystal structure is 0.74, the same as that for the FCC crystal structure since in both structures the atoms are packed as tightly as possible. In both

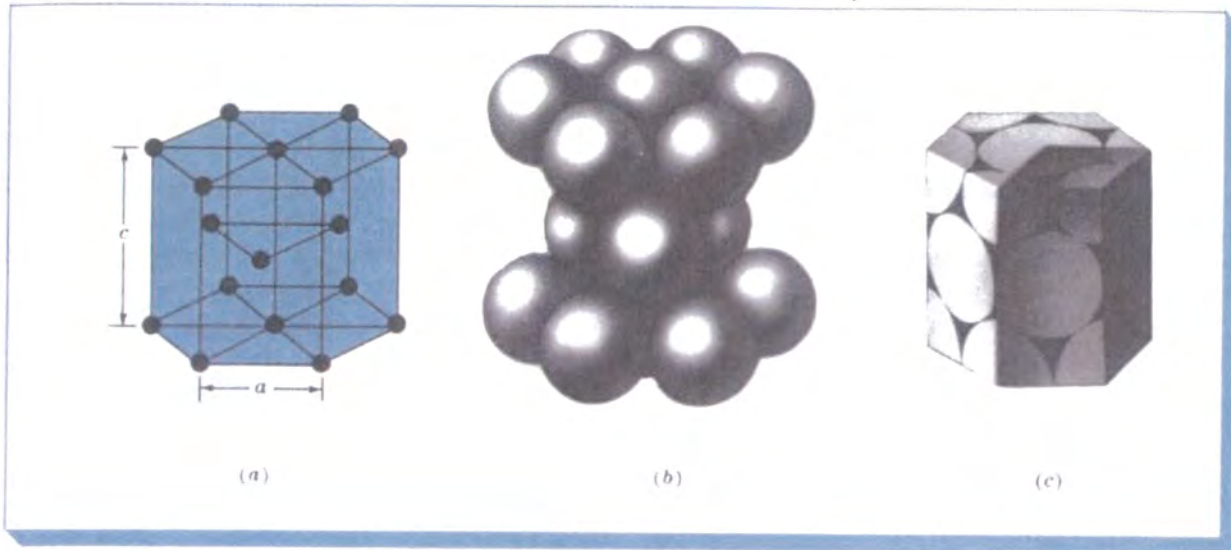


FIGURE 3.8 HCP unit cells. (a) atomic-site unit cell, (b) hard-sphere unit cell, and (c) isolated unit cell. [(b) and (c) After F. M. Miller, "Chemistry: Structure and Dynamics," McGraw-Hill, 1984, p. 296.]

the HCP and FCC crystal structures each atom is surrounded by 12 other atoms, and thus both structures have a coordination number of 12. The differences in the atomic packing in FCC and HCP crystal structures will be discussed in Sec. 3.8.

The isolated HCP unit cell is shown in Fig. 3.8c and has the equivalent of six atoms per unit cell. Three atoms form a triangle in the middle layer, as indicated by the atomic sites in Fig. 3.8a. There are six $\frac{1}{6}$ -atom sections on both the top and bottom layers, making an equivalent of two more atoms ($2 \times 6 \times \frac{1}{6} = 2$). Finally, there is one-half an atom in the center of both the

TABLE 3.4 Selected Metals Which Have the HCP Crystal Structure at Room Temperature (20°C) and Their Lattice Constants, Atomic Radii, and c/a Ratios

Metal	Lattice constants, nm		Atomic radius R, nm	c/a ratio	% deviation from ideality
	a	c			
Cadmium	0.2973	0.5618	0.149	1.890	+15.7
Zinc	0.2665	0.4947	0.133	1.856	+13.6
Ideal HCP				1.633	0
Magnesium	0.3209	0.5209	0.160	1.623	-0.66
Cobalt	0.2507	0.4069	0.125	1.623	-0.66
Zirconium	0.3231	0.5148	0.160	1.593	-2.45
Titanium	0.2950	0.4683	0.147	1.587	-2.81
Beryllium	0.2286	0.3584	0.113	1.568	-3.98

top and bottom layers, making the equivalent of one more atom. The total number of atoms in the HCP crystal structure unit cell is thus $3 + 2 + 1 = 6$.

The ratio of the height c of the hexagonal prism of the HCP crystal structure to its basal side a is called the c/a ratio (Fig. 3.8a). The c/a ratio for an ideal HCP crystal structure consisting of uniform spheres packed as tightly together as possible is 1.633. Table 3.4 on page 79 lists some important HCP metals and their c/a ratios. Of the metals listed, cadmium and zinc have c/a ratios higher than ideality, which indicates that the atoms in these structures are slightly elongated along the c axis of the HCP unit cell. The metals magnesium, cobalt, zirconium, titanium, and beryllium have c/a ratios less than the ideal ratio. Therefore, in these metals the atoms are slightly compressed in the direction along the c axis. Thus, for the HCP metals listed in Table 3.4 there is a certain amount of deviation from the ideal hard-sphere model.

Example Problem 3.3

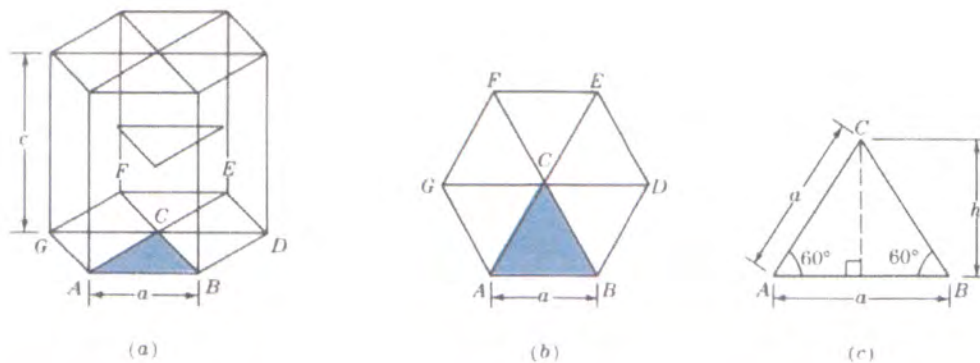
Calculate the volume of the zinc crystal structure unit cell by using the following data: pure zinc has the HCP crystal structure with lattice constants $a = 0.2665$ nm and $c = 0.4947$ nm.

Solution:

FIGURE 3.9 Diagrams for calculating the volume of an HCP unit cell (a) HCP unit cell. (b) Base of HCP unit cell. (c) Triangle ABC removed from base of unit cell.

The volume of the zinc HCP unit cell can be obtained by determining the area of the base of the unit cell and then multiplying this by its height (Fig. 3.9).

The area of the base of the unit cell is area $ABDEFG$ of Fig. 3.9a and b. This total area consists of the areas of six equilateral triangles of area ABC of Fig. 3.9c.



$$\begin{aligned} \text{Area of triangle } ABC &= \frac{1}{2}(\text{base})(\text{height}) \\ &= \frac{1}{2}(a)(a \sin 60^\circ) = \frac{1}{2}a^2 \sin 60^\circ \end{aligned}$$

From Fig. 3.9b,

$$\begin{aligned} \text{Total area of HCP base} &= (6)\left(\frac{1}{2}a^2 \sin 60^\circ\right) \\ &= 3a^2 \sin 60^\circ \end{aligned}$$

From Fig. 3.9a,

$$\begin{aligned} \text{Volume of zinc HCP unit cell} &= (3a^2 \sin 60^\circ)(c) \\ &= (3)(0.2665 \text{ nm})^2(0.8660)(0.4947 \text{ nm}) \\ &= 0.0913 \text{ nm}^3 \blacktriangleleft \end{aligned}$$

3.4 ATOM POSITIONS IN CUBIC UNIT CELLS

To locate atom positions in cubic unit cells, we use rectangular x , y , and z axes. In crystallography the positive x axis is usually the direction coming out of the paper, the positive y axis is the direction to the right of the paper, and the positive z axis is the direction to the top (Fig. 3.10). Negative directions are opposite to those just described.

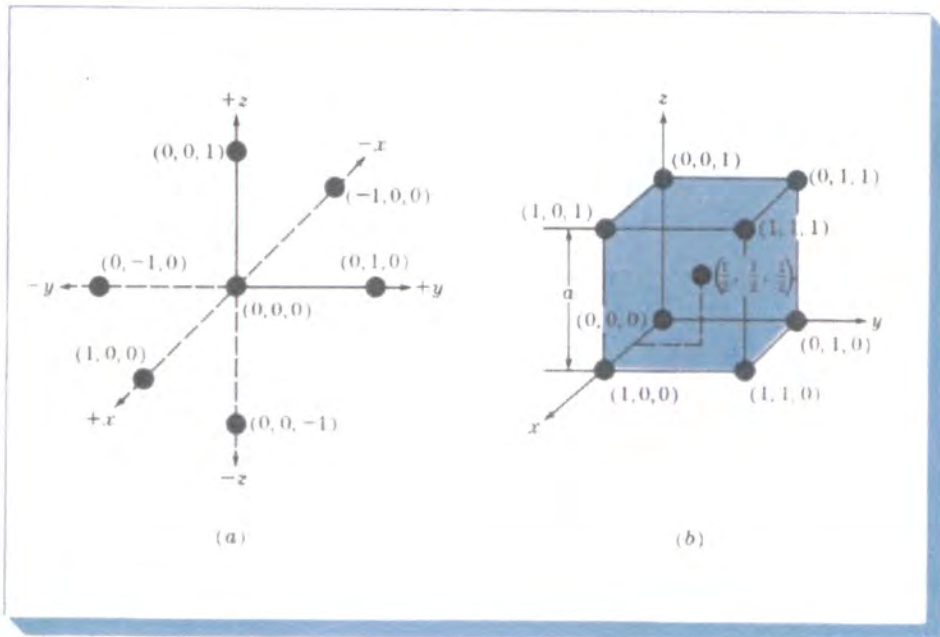


FIGURE 3.10 (a) Rectangular x , y , and z axes for locating atom positions in cubic unit cells. (b) Atom positions in a BCC unit cell.

Atom positions in unit cells are located by using unit distances along the x , y , and z axes, as indicated in Fig. 3.10a. For example, the position coordinates for the atoms in the BCC unit cell are shown in Fig. 3.10b. The atom positions for the eight corner atoms of the BCC unit cell are

$$\begin{array}{cccc} (0, 0, 0) & (1, 0, 0) & (0, 1, 0) & (0, 0, 1) \\ (1, 1, 1) & (1, 1, 0) & (1, 0, 1) & (0, 1, 1) \end{array}$$

The center atom in the BCC unit cell has the position coordinates $(\frac{1}{2}, \frac{1}{2}, \frac{1}{2})$. For simplicity sometimes only two atom positions in the BCC unit cell are specified which are $(0, 0, 0)$ and $(\frac{1}{2}, \frac{1}{2}, \frac{1}{2})$. The remaining atom positions of the BCC unit cell are assumed to be understood. In the same way the atom positions in the FCC unit cell can be located.

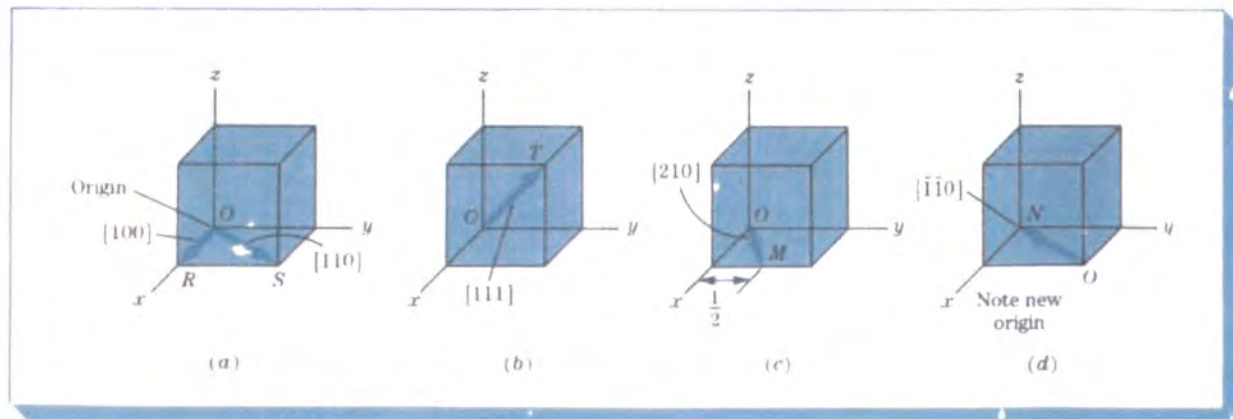
3.5 DIRECTIONS IN CUBIC UNIT CELLS

Frequently it is necessary to refer to specific directions in crystal lattices. This is especially important for metals and alloys that have properties which vary with crystallographic orientation. For cubic crystals the crystallographic direction indices are the vector components of the direction resolved along each of the coordinate axes and reduced to the smallest integers.

To diagrammatically indicate a direction in a cubic unit cell, we draw a direction vector from an origin which is usually a corner of the cubic cell until it emerges from the cube surface (Fig. 3.11). The position coordinates of the unit cell where the direction vector emerges from the cube surface after being converted to integers are the direction indices. The direction indices are enclosed by square brackets with no separating commas.

For example, the position coordinates of the direction vector OR in Fig.

FIGURE 3.11 Some directions in cubic unit cells



3.11a where it emerges from the cube surface are $(1, 0, 0)$, and so the direction indices for the direction vector OR are $[100]$. The position coordinates of the direction vector OS (Fig. 3.11a) are $(1, 1, 0)$, and so the direction indices for OS are $[110]$. The position coordinates for the direction vector OT (Fig. 3.11b) are $(1, 1, 1)$, and so the direction indices of OT are $[111]$.

The position coordinates of the direction vector OM (Fig. 3.11c) are $(1, \frac{1}{2}, 0)$, and since the direction vectors must be integers, these position coordinates must be multiplied by 2 to obtain integers. Thus, the direction indices of OM become $2(1, \frac{1}{2}, 0) = [210]$. The position coordinates of the vector ON (Fig. 3.11d) are $(-1, -1, 0)$. A negative direction index is written with a bar over the index. Thus, the direction indices for the vector ON are $[\bar{1}\bar{1}0]$. Note that to draw the direction ON inside the cube the origin of the direction vector had to be moved to the front lower-right corner of the unit cube (Fig. 3.11d). Further examples of cubic direction vectors are given in Example Problem 3.4.

The letters u, v, w are used in a general sense for the direction indices in the $x, y,$ and z directions, respectively, and are written as $[uvw]$. It is also important to note that *all parallel direction vectors have the same direction indices*.

Directions are said to be *crystallographically equivalent* if the atom spacing along each direction is the same. For example, the following cubic edge directions are crystallographic equivalent directions:

$$[100], [010], [001], [0\bar{1}0], [00\bar{1}], [\bar{1}00] = \langle 100 \rangle$$

Equivalent directions are called *indices of a family or form*. The notation $\langle 100 \rangle$ is used to indicate cubic edge directions collectively. Other directions of a form are the cubic body diagonals $\langle 111 \rangle$ and the cubic face diagonals $\langle 110 \rangle$.

Example Problem 3.4

Draw the following direction vectors in cubic unit cells.

- (a) $[100]$ and $[110]$ (b) $[112]$ (c) $[\bar{1}10]$ (d) $[\bar{3}2\bar{1}]$

Solution:

- (a) The position coordinates for the $[100]$ direction are $(1, 0, 0)$ (Fig. 3.12a). The position coordinates for the $[110]$ direction are $(1, 1, 0)$ (Fig. 3.12a).
- (b) The position coordinates for the $[112]$ direction are obtained by dividing the direction indices by 2 so that they will lie within the unit cube. Thus they are $(\frac{1}{2}, \frac{1}{2}, 1)$ (Fig. 3.12b).
- (c) The position coordinates for the $[\bar{1}10]$ direction are $(-1, 1, 0)$ (Fig. 3.12c). Note that the origin for the direction vector must be moved to the lower left front corner of the cube.

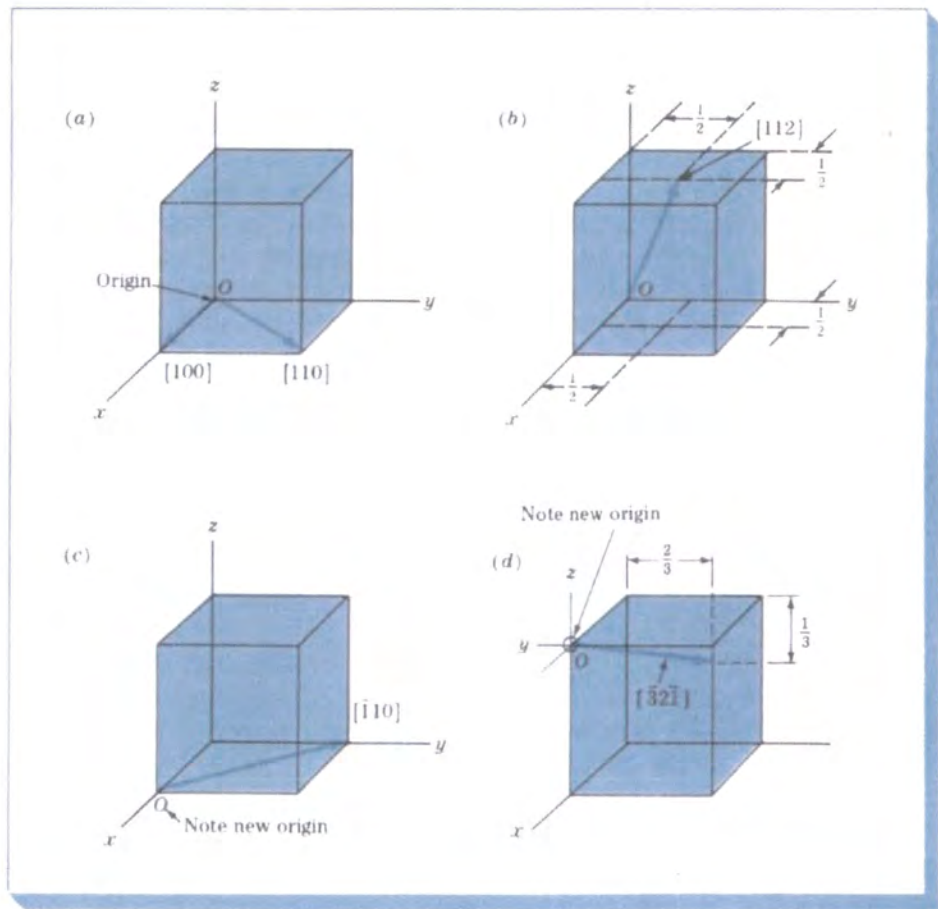


FIGURE 3.12 Direction vectors in cubic unit cells.

(d) The position coordinates for the $[\bar{3}2\bar{1}]$ direction are obtained by first dividing all the indices by 3, the largest index. This gives $-1, \frac{2}{3}, -\frac{1}{3}$ for the position coordinates of the exit point of the direction $[\bar{3}2\bar{1}]$ which are shown in Fig. 3.12d.

Example Problem 3.5

Determine the direction indices of the cubic direction shown in Fig. EP3.5a.

Solution:

Parallel directions have the same direction indices, and so we move the direction vector in a parallel manner until its tail reaches the nearest corner of the cube, still keeping the vector within the cube. Thus, in this case, the upper left front corner becomes the new origin for the direction vector (Fig. EP3.5b). We can now determine the position coordinates where the direction vector leaves the unit cube. These are $x = -1, y =$

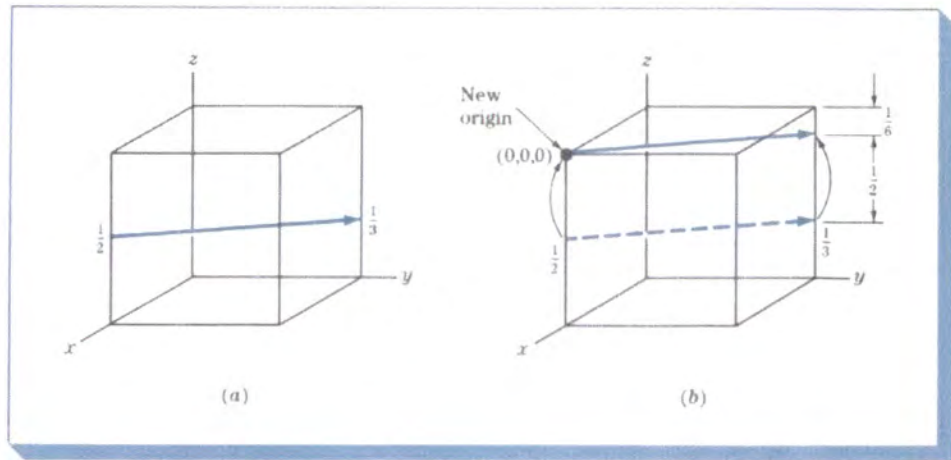


FIGURE EP3.5

+1, and $z = -\frac{1}{3}$. The position coordinates of the direction where it leaves the unit cube are thus $(-1, +1, -\frac{1}{3})$. The direction indices for this direction are, after clearing the fraction $3x$, $(-1, +1, -\frac{1}{3})$, or $[\bar{1}1\bar{1}]$.

Example Problem 3.6

Determine the direction indices of the cubic direction between the position coordinates $(\frac{3}{4}, 0, \frac{1}{4})$ and $(\frac{1}{4}, \frac{1}{2}, \frac{1}{2})$.

Solution:

First we locate the origin and termination points of the direction vector in a unit cube, as shown in Fig. EP3.6. The fraction vector components for this direction are

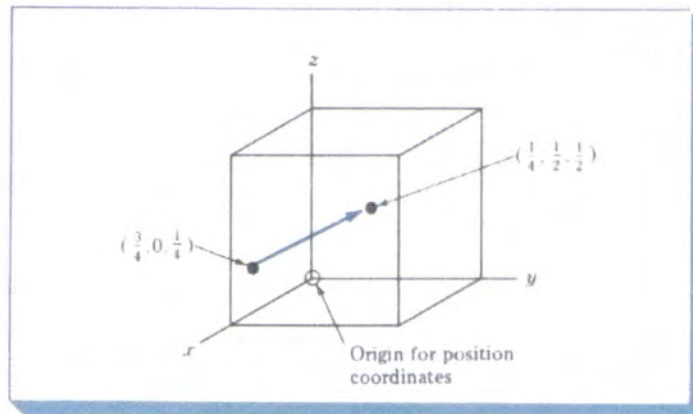


FIGURE EP3.6

$$x = -\left(\frac{3}{4} - \frac{1}{4}\right) = -\frac{1}{2}$$

$$y = \left(\frac{1}{2} - 0\right) = \frac{1}{2}$$

$$z = \left(\frac{1}{2} - \frac{1}{4}\right) = \frac{1}{4}$$

Thus, the vector direction has fractional vector components of $-\frac{1}{2}, \frac{1}{2}, \frac{1}{4}$. The direction indices will be in the same ratio as their fractional components. By multiplying the fraction vector components by 4, we obtain $[\bar{2}21]$ for the direction indices of this vector direction.

3.6 MILLER INDICES FOR CRYSTALLOGRAPHIC PLANES IN CUBIC UNIT CELLS

Sometimes it is necessary to refer to specific lattice planes of atoms within a crystal structure, or it may be of interest to know the crystallographic orientation of a plane or group of planes in a crystal lattice. To identify crystal planes in cubic crystal structures, the *Miller¹ notation system* is used. The *Miller indices of a crystal plane* are defined as the *reciprocals of the fractional intercepts (with fractions cleared) which the plane makes with the crystallographic x, y, and z axes of the three nonparallel edges of the cubic unit cell*. The cube edges of the unit cell represent unit lengths, and the intercepts of the lattice planes are measured in terms of these unit lengths.

The procedure for determining the Miller indices for a cubic crystal plane is as follows:

1. Choose a plane that does *not* pass through the origin at (0, 0, 0).
2. Determine the intercepts of the plane in terms of the crystallographic x, y, and z axes for a unit cube. These intercepts may be fractions.
3. Form the reciprocals of these intercepts.
4. Clear fractions and determine the *smallest* set of whole numbers which are in the same ratio as the intercepts. These whole numbers are the Miller indices of the crystallographic plane and are enclosed in parentheses without the use of commas. The notation (hkl) is used to indicate Miller indices in a general sense, where h, k, and l are the Miller indices of a cubic crystal plane for the x, y, and z axes, respectively.

Figure 3.13 shows three of the most important crystallographic planes of cubic crystal structures. Let us first consider the shaded crystal plane in Fig. 3.13a, which has the intercepts 1, ∞ , ∞ for the x, y, and z axes, respectively.

¹William Hallows Miller (1801–1880) English crystallographer who published a "Treatise on Crystallography" in 1839, using crystallographic reference axes which were parallel to the crystal edges and using reciprocal indices

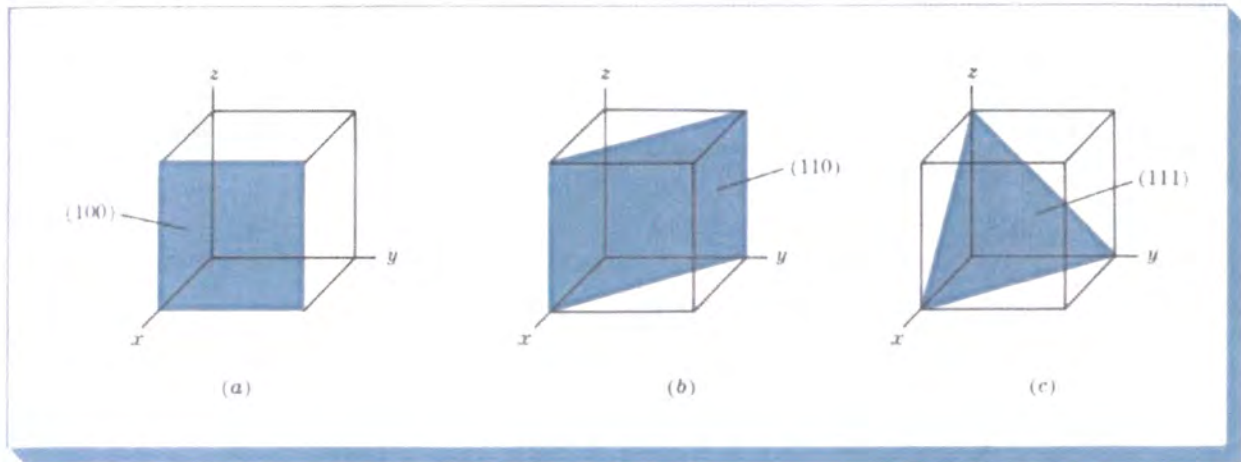


FIGURE 3.13 Miller indices of some important cubic crystal planes. (a) (100), (b) (110), and (c) (111).

We take the reciprocals of these intercepts to obtain the Miller indices, which are therefore 1, 0, 0. Since these numbers do not involve fractions, the Miller indices for this plane are (100), which is read as the one-zero-zero plane. Next let us consider the second plane shown in Fig. 3.13b. The intercepts of this plane are 1, 1, ∞ . Since the reciprocals of these numbers are 1, 1, 0, which do not involve fractions, the Miller indices of this plane are (110). Finally, the third plane (Fig. 3.13c) has the intercepts 1, 1, 1, which give the Miller indices (111) for this plane.

Consider now the cubic crystal plane shown in Fig. 3.14 which has the intercepts $\frac{1}{3}$, $\frac{2}{3}$, 1. The reciprocals of these intercepts are 3, $\frac{3}{2}$, 1. Since fractional

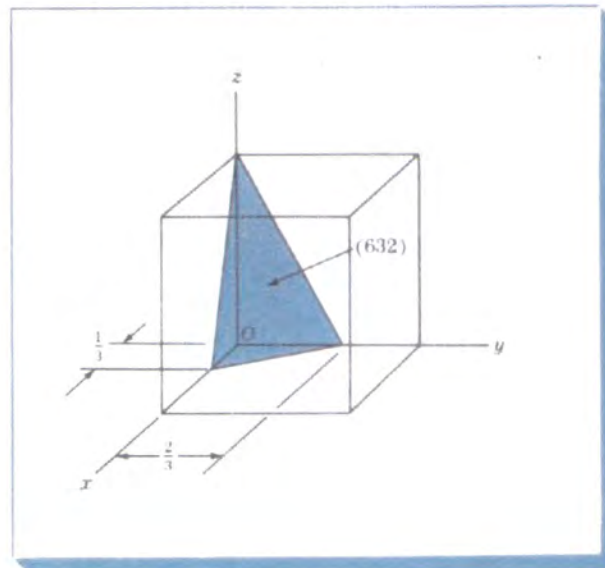


FIGURE 3.14 Cubic crystal plane (632) which has fractional intercepts.

intercepts are not allowed, these fractional intercepts must be multiplied by 2 to clear the $\frac{1}{2}$ fraction. Thus, the reciprocal intercepts become 6, 3, 2 and the Miller indices are (632). Further examples of cubic crystal planes are shown in Example Problem 3.7.

If the crystal plane being considered passes through the origin so that one or more intercepts are zero, the plane must be moved to an equivalent position in the same unit cell and the plane must remain parallel to the original plane. This is possible because all equispaced parallel planes are indicated by the same Miller indices.

If sets of equivalent lattice planes are related by the symmetry of the crystal system, they are called *planes of a family or form*, and the indices of one plane of the family are enclosed in braces as $\{hkl\}$ to represent the indices of a family of symmetrical planes. For example, the Miller indices of the cubic surface planes (100), (010), and (001) are designated collectively as a family or form by the notation $\{100\}$.

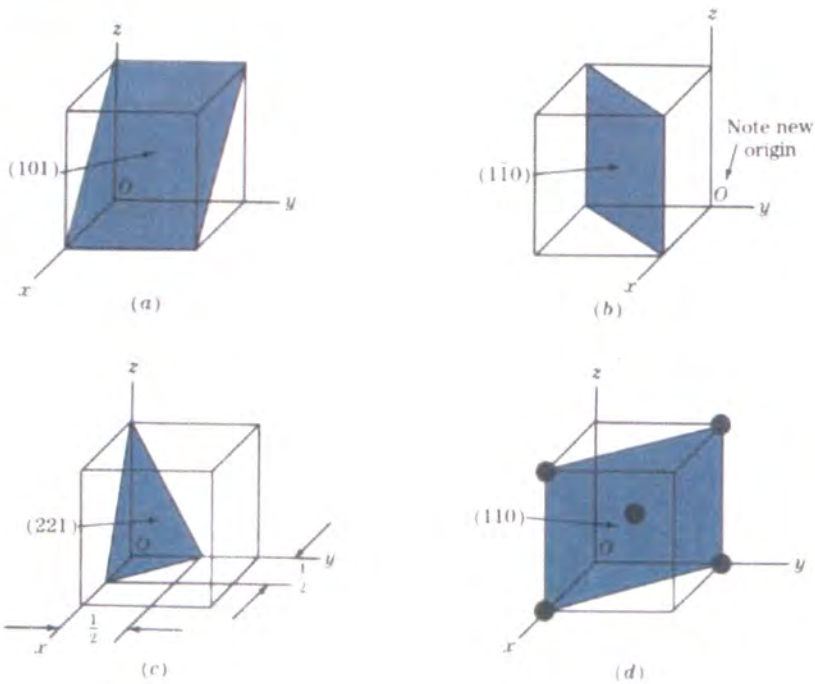
Example Problem 3.7

Draw the following crystallographic planes in cubic unit cells:

(a) (101) (b) $(1\bar{1}0)$ (c) (221)

(d) Draw a (110) plane in a BCC atomic-site unit cell, and list the position coordinates of the atoms whose centers are intersected by this plane.

Solutions:



- (a) First determine the reciprocals of the Miller indices of the (101) plane. These are $1, \infty, 1$. The (101) plane must pass through a unit cube at intercepts $x = 1$ and $z = 1$ and be parallel to the y axis.
- (b) First determine the reciprocals of the Miller indices of the $(1\bar{1}0)$ plane. These are $1, -1, \infty$. The $(1\bar{1}0)$ plane must pass through a unit cube at intercepts $x = 1$ and $y = -1$ and be parallel to the z axis. Note that the origin of axes must be moved to the lower right back side of the cube.
- (c) First determine the reciprocals of the Miller indices of the (221) plane. These are $\frac{1}{2}, \frac{1}{2}, 1$. The (221) plane must pass through a unit cube at intercepts $x = \frac{1}{2}, y = \frac{1}{2}$, and $z = 1$.
- (d) Atom positions whose centers are intersected by the (110) plane are $(1, 0, 0), (0, 1, 0), (1, 0, 1), (0, 1, 1)$, and $(\frac{1}{2}, \frac{1}{2}, \frac{1}{2})$. These positions are indicated by the solid circles.

An important relationship for the cubic system, and *only the cubic system*, is that the direction indices of a direction *perpendicular* to a crystal plane are the same as the Miller indices of that plane. For example, the [100] direction is perpendicular to the (100) crystal plane.

In cubic crystal structures the *interplanar spacing* between two closest parallel planes with the same Miller indices is designated d_{hkl} , where h, k , and l are the Miller indices of the planes. This spacing represents the distance from a selected origin containing one plane and another parallel plane with the

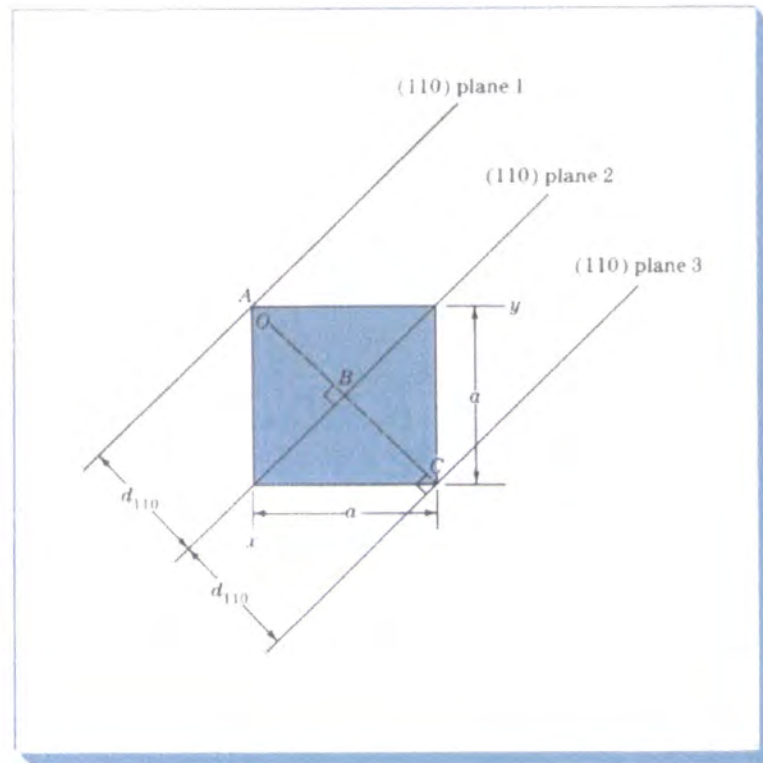


FIGURE 3.15 Top view of cubic unit cell showing the distance between (110) crystal planes, d_{110} .

same indices which is closest to it. For example, the distance between (110) planes 1 and 2, d_{110} , in Fig. 3.15 on page 89 is AB . Also, the distance between (110) planes 2 and 3 is d_{110} and is length BC in Fig. 3.15. From simple geometry, it can be shown that for cubic crystal structures

$$d_{hkl} = \frac{a}{\sqrt{h^2 + k^2 + l^2}} \quad (3.4)$$

where d_{hkl} = interplanar spacing between parallel closest planes with Miller indices h , k , and l

a = lattice constant (edge of unit cube)

h, k, l = Miller indices of cubic planes being considered

Example Problem 3.8

Determine the Miller indices of the cubic crystallographic plane shown in Fig. EP3.8a.

Solution:

First, transpose the plane parallel to the z axis $\frac{1}{4}$ unit to the right along the y axis as shown in Fig. EP3.8b so that the plane intersects the x axis at a unit distance from the new origin located at the lower-right back corner of the cube. The new intercepts of the transposed plane with the coordinate axes are now $(+1, -\frac{1}{2}, \infty)$. Next, we take the reciprocals of these intercepts to give $(1, -\frac{1}{2}, 0)$. Finally, we clear the $\frac{1}{2}$ fraction to obtain $(5\bar{1}20)$ for the Miller indices of this plane

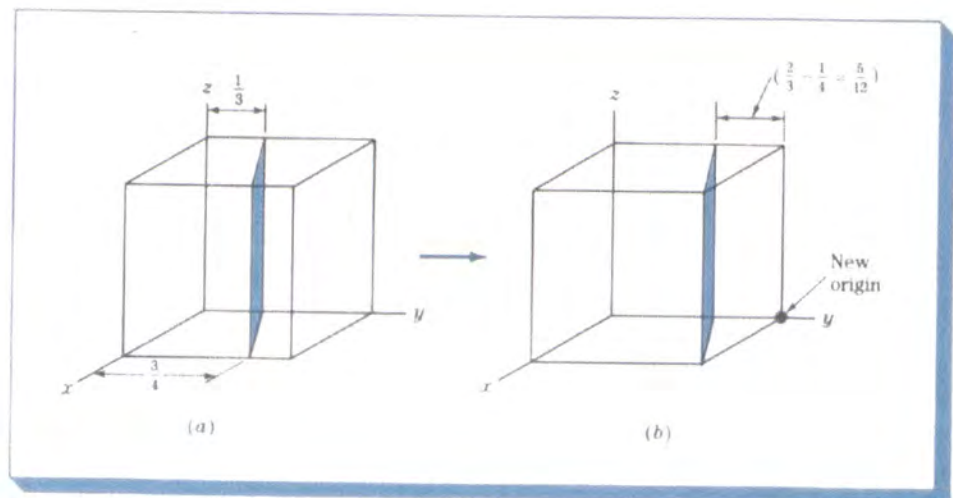


FIGURE EP3.8

Example Problem 3.9

Determine the Miller indices of the cubic crystal plane which intersects the position coordinates $(1, \frac{1}{4}, 0)$, $(1, 1, \frac{1}{2})$, $(\frac{3}{4}, 1, \frac{1}{4})$, and all coordinate axes.

Solution:

First, we locate the three position coordinates as indicated in Fig. EP3.9 at A , B , and C . Next, we join A and B and extend AB to D and then join A and C . Finally, we join A to C to complete plane ACD . The origin for this plane in the cube can be chosen at E , which gives axial intercepts for plane ACD at $x = -\frac{1}{2}$, $y = -\frac{1}{4}$, and $z = \frac{1}{2}$. The reciprocals of these axial intercepts are -2 , $-\frac{1}{4}$, and 2 . Multiplying these intercepts by 3 clears the fraction, giving Miller indices for the plane of $(\bar{6}\bar{4}6)$.

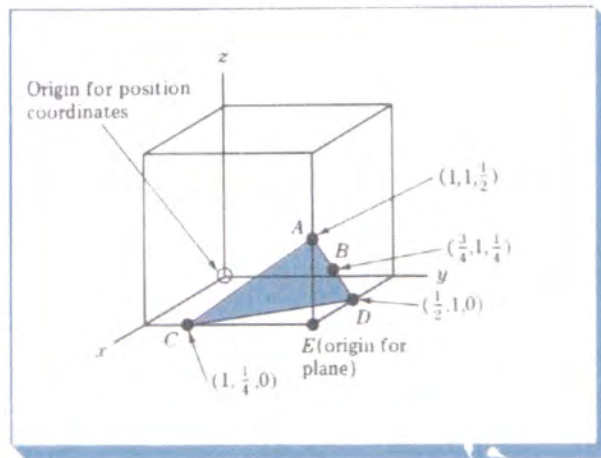


FIGURE EP3.9

Example Problem 3.10

Copper has an FCC crystal structure and a unit cell with a lattice constant of 0.361 nm. What is its interplanar spacing d_{220} ?

Solution:

$$d_{hkl} = \frac{a}{\sqrt{h^2 + k^2 + l^2}} = \frac{0.361 \text{ nm}}{\sqrt{(2)^2 + (2)^2 + (0)^2}} = 0.128 \text{ nm} \blacktriangleleft$$

3.7 CRYSTALLOGRAPHIC PLANES AND DIRECTIONS IN HEXAGONAL UNIT CELLS

Indices for Crystal Planes in HCP Unit Cells

Crystal planes in HCP unit cells are commonly identified by using four indices instead of three. The HCP crystal plane indices, called *Miller-Bravais indices*, are denoted by the letters h , k , i , and l and are enclosed in parentheses as $(hkil)$. These four-digit hexagonal indices are based on a coordinate system with four axes, as shown in Fig. 3.16 in an HCP unit cell. There are three basal axes, a_1 , a_2 , and a_3 , which make 120° with each other. The fourth axis or c axis is the vertical axis located at the center of the unit cell. The a unit of measurement along the a_1 , a_2 , and a_3 axes is the distance between the atoms along these axes and is indicated in Fig. 3.16. The unit of measurement along the c axis is the height of the unit cell. The reciprocals of the intercepts that a crystal plane makes with the a_1 , a_2 , and a_3 axes give the h , k , and i indices, while the reciprocal of the intercept with the c axis gives the l index.

Basal planes The basal planes of the HCP unit cell are very important planes for this unit cell and are indicated in Fig. 3.17a. Since the basal plane on the top of the HCP unit cell in Fig. 3.17a is parallel to the a_1 , a_2 , and a_3 axes, the intercepts of this plane with these axes will all be infinite. Thus, $a_1 = \infty$, $a_2 = \infty$, and $a_3 = \infty$. The c axis, however, is unity since the top basal plane intersects the c axis at unit distance. Taking the reciprocals of these intercepts gives the Miller-Bravais indices for the HCP basal plane. Thus $h = 0$, $k = 0$, $i = 0$, and $l = 1$. The HCP basal plane is, therefore, a zero-zero-zero-one or (0001) plane.

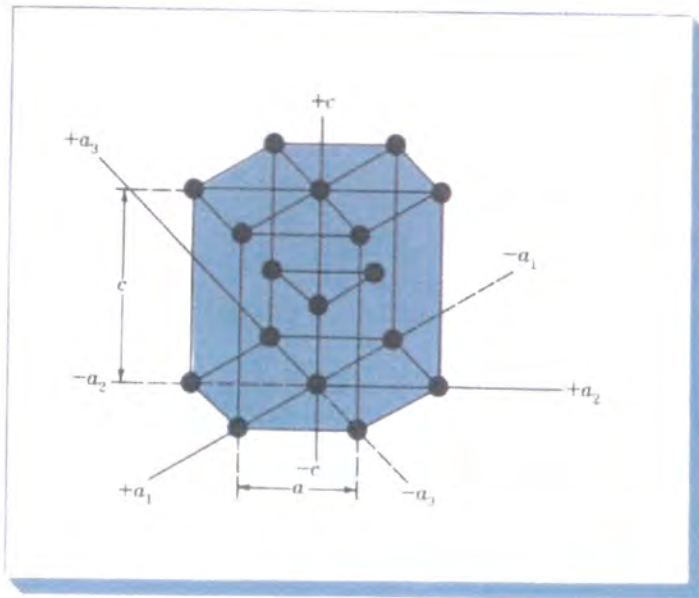


FIGURE 3.16 The four coordinate axes (a_1 , a_2 , a_3 , and c) of the HCP crystal structure unit cell

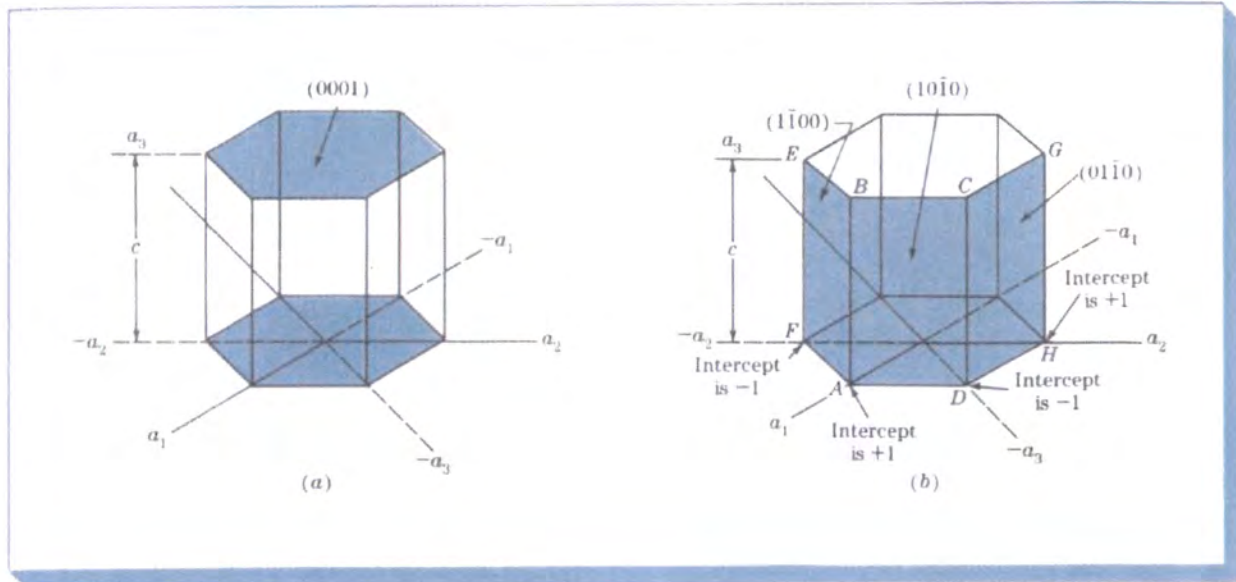


FIGURE 3.17 Miller-Bravais indices of hexagonal crystal planes: (a) basal planes, and (b) prism planes.

Prism planes Using the same method, the intercepts of the front prism plane (ABCD) of Fig. 3.17b are $a_1 = +1$, $a_2 = \infty$, $a_3 = -1$, and $c = \infty$. Taking the reciprocals of these intercepts gives $h = 1$, $k = 0$, $i = -1$, and $l = 0$, or the $(10\bar{1}0)$ plane. Similarly, the ABEF prism plane of Fig. 3.17b has the indices $(1\bar{1}00)$ and the DCGH plane the indices $(01\bar{1}0)$. All HCP prism planes can be identified collectively as the $\{10\bar{1}0\}$ family of planes.

Sometimes HCP planes are identified only by three indices (hkl) since $h + k = -i$. However, the $(hkil)$ indices are used more commonly because they reveal the hexagonal symmetry of the HCP unit cell.

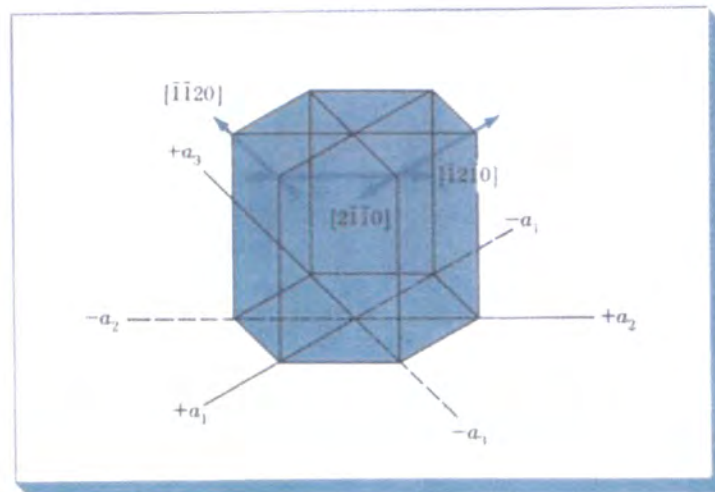


FIGURE 3.18 Some important directions in HCP unit cells.

Direction Indices in HCP Unit Cells

Directions in HCP unit cells are also usually indicated by four indices $u, v, t,$ and w enclosed by square brackets as $[uv\bar{t}w]$. The $u, v,$ and t indices are lattice vectors in the $a_1, a_2,$ and a_3 directions, respectively (Fig. 3.16), and the w index is a lattice vector in the c direction. To maintain uniformity for both HCP indices for planes and directions, it has been agreed that $u + v = -t$ for directions also, leading to a cumbersome method of designating directions whose method of determination is beyond the scope of this book. Some of the important directions in HCP unit cells are indicated in Fig. 3.18.

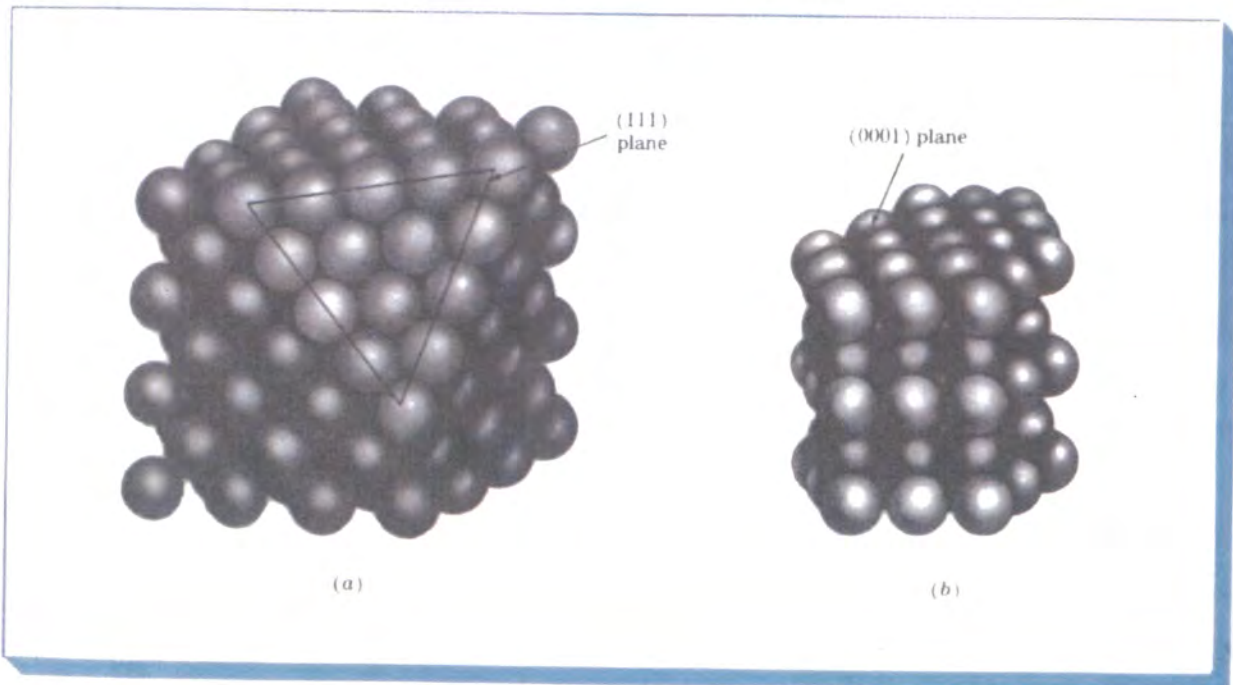
3.8 COMPARISON OF FCC, HCP, AND BCC CRYSTAL STRUCTURES

Face-Centered Cubic and Hexagonal Close-Packed Crystal Structures

As previously pointed out, both the HCP and FCC crystal structures are close-packed structures. That is, their atoms which are considered approximate "spheres" are packed together as closely as possible so that an atomic packing factor of 0.74 is attained.¹ The (111) planes of the FCC crystal structure shown

¹As pointed out in Sec. 3.3, the atoms in the HCP structure deviate to varying degrees from ideality. In some HCP metals the atoms are elongated along the c axis, and in other cases they are compressed along the c axis (see Table 3.4)

FIGURE 3.19 Comparison of the (a) FCC crystal structure showing the close-packed (111) planes, and (b) the HCP crystal structure showing the close-packed (0001) planes. (After W. G. Moffatt, G. W. Pearsall, and J. Wulff, "The Structure and Properties of Materials," vol. 1, "Structure," Wiley, 1964, p. 51.)



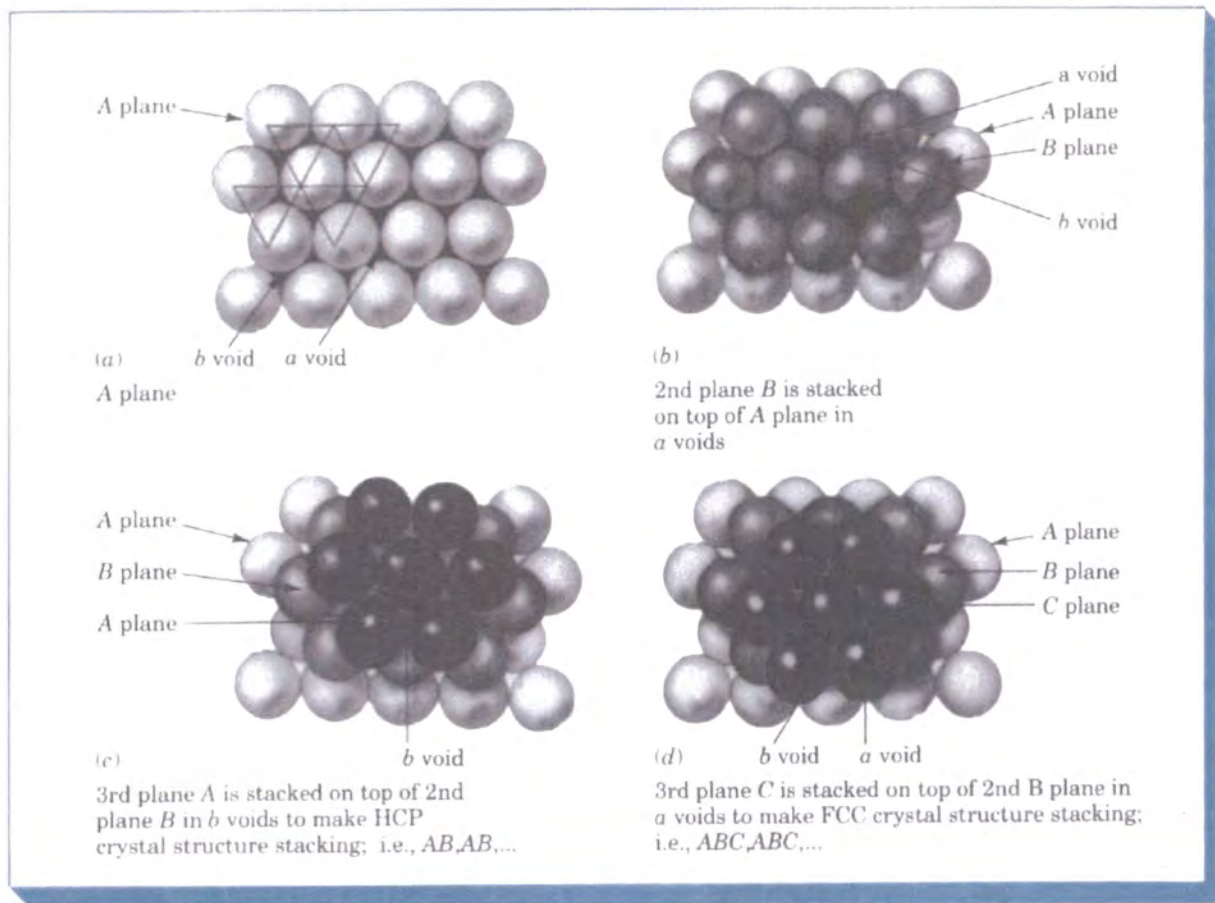


FIGURE 3.20 Formation of HCP and FCC crystal structures by changing the stacking of close-packed planes of atoms. (a) A plane containing a - and b -type voids between the atoms. (b) B plane is stacked on top of A plane in a voids. (c) Third plane: Another A plane is stacked on top of the b voids of B plane to make HCP crystal structure stacking: i.e., $ABAB, \dots$. (d) Third plane (alternate): a C plane is stacked on the a voids of B plane to make an FCC stacked crystal structure: $ABCABC, \dots$

in Fig. 3.19a have the identical packing arrangement as the (0001) planes of the HCP crystal structure shown in Fig. 3.19b. However, the three-dimensional FCC and HCP crystal structures are not identical because there is a difference in the stacking arrangement of their atomic planes, which can best be described by considering the stacking of hard spheres representing atoms. As a useful analogy, one can imagine the stacking of planes of equal-sized marbles on top of each other, minimizing the space between the marbles.

Consider first a plane of close-packed atoms designated the A plane, as shown in Fig. 3.20a. Note that there are two different types of empty spaces or voids between the atoms. The voids pointing to the top of the page are designated a voids and those pointing to the bottom of the page, b voids. A second plane of atoms can be placed over the a or b voids and the same three-dimensional structure will be produced. Let us place plane B over the a voids,

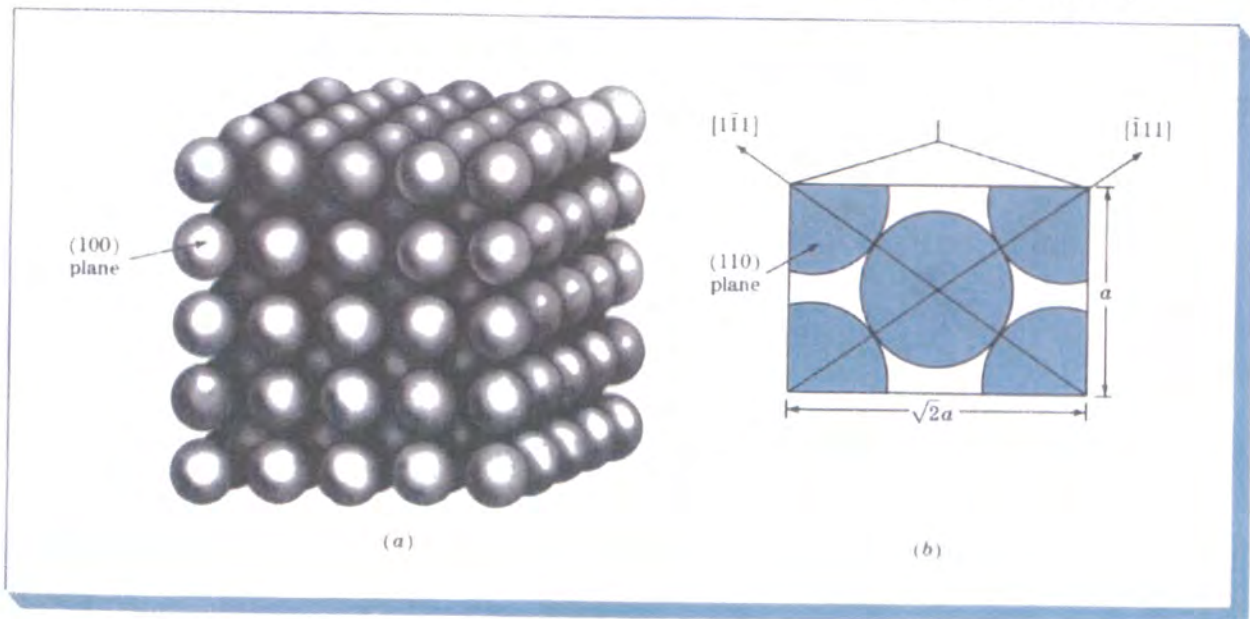
as shown in Fig. 3.20*b*. Now if a third plane of atoms is placed over plane *B* to form a close-packed structure, it is possible to form two different close-packed structures. One possibility is to place the atoms of the third plane in the *b* voids of the *B* plane. Then the atoms of this third plane will lie directly over those of the *A* plane and thus can be designated another *A* plane (Fig. 3.20*c*). If subsequent planes of atoms are placed in this same alternating stacking arrangement, then the stacking sequence of the three-dimensional structure produced can be denoted by *ABABAB*... Such a stacking sequence leads to the HCP crystal structure (Fig. 3.19*b*).

The second possibility for forming a simple close-packed structure is to place the third plane in the *a* voids of plane *B* (Fig. 3.20*d*). This third plane is designated the *C* plane since its atoms lie neither directly above those of the *B* plane nor of the *A* plane. The stacking sequence in this close-packed structure is thus designated *ABCABCABC*... and leads to the FCC structure shown in Fig. 3.19*a*.

**Body-Centered
Cubic Crystal
Structure**

The BCC structure is not a close-packed structure and hence does not have close-packed planes like the {111} planes in the FCC structure and the {0001} planes in the HCP structure. The most densely packed planes in the BCC structure are the {110} family of planes of which the (110) plane is shown in Fig. 3.21*b*. The atoms, however, in the BCC structure do have close-packed directions along the cube diagonals, which are the <111> directions.

FIGURE 3.21 BCC crystal structure showing (a) the (100) plane and (b) a section of the (110) plane. Note that this is not a close-packed structure but that diagonals are close-packed directions. [(a) After W. G. Moffatt, G. W. Pearsall, and J. Wulff, "The Structure and Properties of Materials," vol. I: "Structure," Wiley, 1964, p. 51.]



3.9 VOLUME, PLANAR, AND LINEAR DENSITY UNIT-CELL CALCULATIONS

Volume Density Using the hard-sphere atomic model for the crystal structure unit cell of a metal and a value for the atomic radius of the metal obtained from x-ray diffraction analysis, a value for the volume density of a metal can be obtained by using the equation

$$\text{Volume density of metal} = \rho_v = \frac{\text{mass/unit cell}}{\text{volume/unit cell}} \quad (3.5)$$

In Example Problem 3.11 a value of 8.98 Mg/m^3 (8.98 g/cm^3) is obtained for the density of copper. The handbook experimental value for the density of copper is 8.96 Mg/m^3 (8.96 g/cm^3). The slightly lower density of the experimental value could be attributed to the absence of atoms at some atomic sites (vacancies), line defects, and mismatch where grains meet (grain boundaries). These crystalline defects are discussed in Chap. 4. Another cause of the discrepancy could also be due to the atoms not being perfect spheres.

Example Problem 3.11

Copper has an FCC crystal structure and an atomic radius of 0.1278 nm . Assuming the atoms to be hard spheres which touch each other along the face diagonals of the FCC unit cell as shown in Fig. 3.7, calculate a theoretical value for the density of copper in megagrams per cubic meter. The atomic mass of copper is 63.54 g/mol .

Solution:

For the FCC unit cell, $\sqrt{2}a = 4R$, where a is the lattice constant of the unit cell and R is the atomic radius of the copper atom. Thus

$$a = \frac{4R}{\sqrt{2}} = \frac{(4)(0.1278 \text{ nm})}{\sqrt{2}} = 0.361 \text{ nm}$$

$$\text{Volume density of copper} = \rho_v = \frac{\text{mass/unit cell}}{\text{volume/unit cell}} \quad (3.5)$$

In the FCC unit cell there are four atoms/unit cell. Each copper atom has a mass of $(63.54 \text{ g/mol})/(6.02 \times 10^{23} \text{ atoms/mol})$. Thus the mass m of Cu atoms in the FCC unit cell is

$$m = \frac{(4 \text{ atoms})(63.54 \text{ g/mol})}{6.02 \times 10^{23} \text{ atoms/mol}} \left(\frac{10^{-6} \text{ Mg}}{\text{g}} \right) = 4.22 \times 10^{-28} \text{ Mg}$$

The volume V of the Cu unit cell is

$$V = a^3 = \left(0.361 \text{ nm} \times \frac{10^{-9} \text{ m}}{\text{nm}}\right)^3 = 4.70 \times 10^{-29} \text{ m}^3$$

Thus the density of copper is

$$\rho_c = \frac{m}{V} = \frac{4.22 \times 10^{-28} \text{ Mg}}{4.70 \times 10^{-29} \text{ m}^3} = 8.98 \text{ Mg/m}^3 \quad (8.98 \text{ g/cm}^3) \blacktriangleleft$$

Planar Atomic Density

Sometimes it is important to determine the atomic densities on various crystal planes. To do this a quantity called the *planar atomic density* is calculated by using the relationship

$$\begin{aligned} \text{Planar atomic density} &= \rho_p \\ &= \frac{\text{equiv. no. of atoms whose centers are intersected by selected area}}{\text{selected area}} \end{aligned} \quad (3.6)$$

For convenience the area of a plane which intersects a unit cell is usually used in these calculations, as shown, for example, in Fig. 3.22 for the (110) plane in a BCC unit cell. In order for an atom area to be counted in this calculation, the plane of interest must intersect the center of an atom. In Example Problem 3.12 the (110) plane intersects the centers of five atoms, but the equivalent of only two atoms is counted since only one-quarter of each of the four corner atoms is included in the area inside the unit cell. Figure 3.22A shows area occupied by atoms on a planar section of an (111) plane in the FCC lattice.

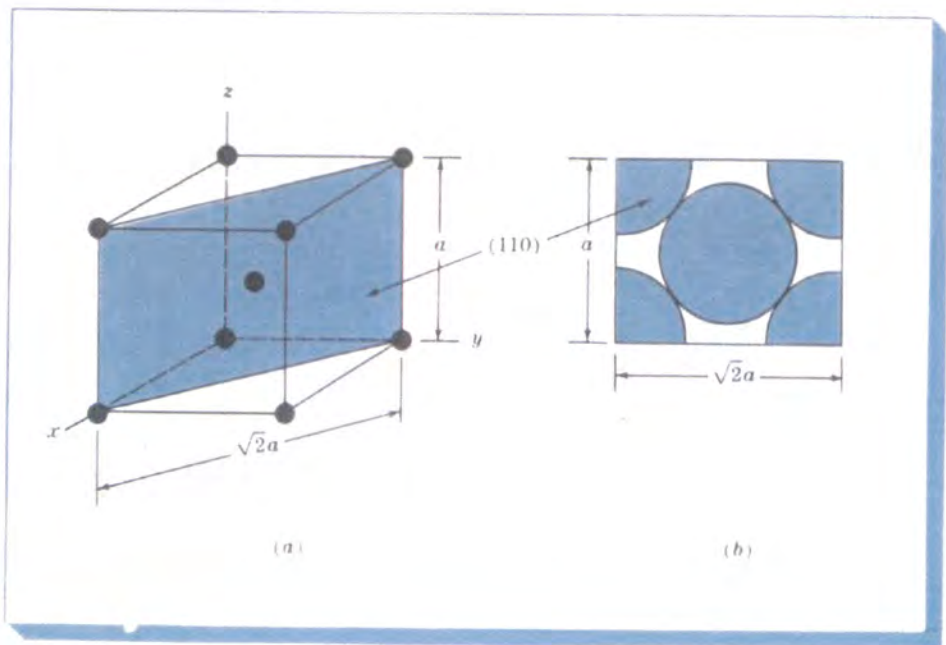


FIGURE 3.22 (a) A BCC atomic-site unit cell showing a shaded (110) plane. (b) Areas of atoms in BCC unit cell cut by the (110) plane.

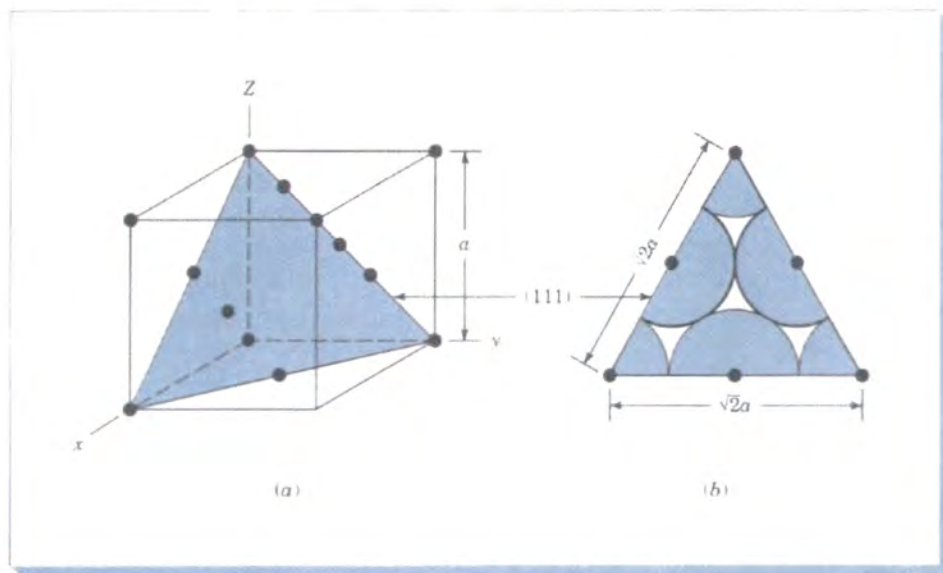


FIGURE 3.22A (a) An FCC atomic-site unit cell showing a shaded (111) plane. (b) Areas of atoms in FCC unit cell cut by the (111) plane.

Example Problem 3.12

Calculate the planar atomic density ρ_p on the (110) plane of the α iron BCC lattice in atoms per square millimeter. The lattice constant of α iron is 0.287 nm.

Solution:

$$\rho_p = \frac{\text{equiv. no. of atoms whose centers are intersected by selected area}}{\text{selected area}} \quad (3.6)$$

The equivalent number of atoms intersected by the (110) plane in terms of the surface area inside the BCC unit cell is shown in Fig. 3.22 and is

$$1 \text{ atom at center} + 4 \times \frac{1}{4} \text{ atoms at four corners of plane} = 2 \text{ atoms}$$

The area intersected by the (110) plane inside the unit cell (selected area) is

$$(\sqrt{2}a)(a) = \sqrt{2}a^2$$

Thus the planar atomic density is

$$\begin{aligned} \rho_p &= \frac{2 \text{ atoms}}{\sqrt{2}(0.287 \text{ nm})^2} = \frac{17.2 \text{ atoms}}{\text{nm}^2} \\ &= \frac{17.2 \text{ atoms}}{\text{nm}^2} \times \frac{10^{12} \text{ nm}^2}{\text{mm}^2} \\ &= 1.72 \times 10^{13} \text{ atoms/mm}^2 \quad \blacktriangleleft \end{aligned}$$

Linear Atomic Density

Sometimes it is important to determine the atomic densities in various directions in crystal structures. To do this a quantity called the *linear atomic density* is calculated by using the relationship

$$\begin{aligned} \text{Linear atomic density} &= \rho_l \\ &= \frac{\text{no. of atomic diam. intersected by selected length of line in direction of interest}}{\text{selected length of line}} \end{aligned} \quad (3.7)$$

Example Problem 3.13 shows how the linear atomic density can be calculated in the [110] direction in a pure copper crystal lattice.

Example Problem 3.13

Calculate the linear atomic density ρ_l in the [110] direction in the copper crystal lattice in atoms per millimeter. Copper is FCC and has a lattice constant of 0.361 nm.

Solution:

The atoms whose centers the [110] direction intersects are shown in Fig. 3.23. We shall select the length of the line to be the length of the face diagonal of the FCC unit cell, which is $\sqrt{2}a$. The number of atomic diameters intersected by this length of line are $\frac{1}{2} + 1 + \frac{1}{2} = 2$ atoms. Thus using Eq. (3.7), the linear atomic density is

$$\begin{aligned} \rho_l &= \frac{2 \text{ atoms}}{\sqrt{2}a} = \frac{2 \text{ atoms}}{\sqrt{2}(0.361 \text{ nm})} = \frac{3.92 \text{ atoms}}{\text{nm}} \\ &= \frac{3.92 \text{ atoms}}{\text{nm}} \times \frac{10^6 \text{ nm}}{\text{mm}} \\ &= 3.92 \times 10^6 \text{ atoms/mm} \quad \blacktriangleleft \end{aligned}$$

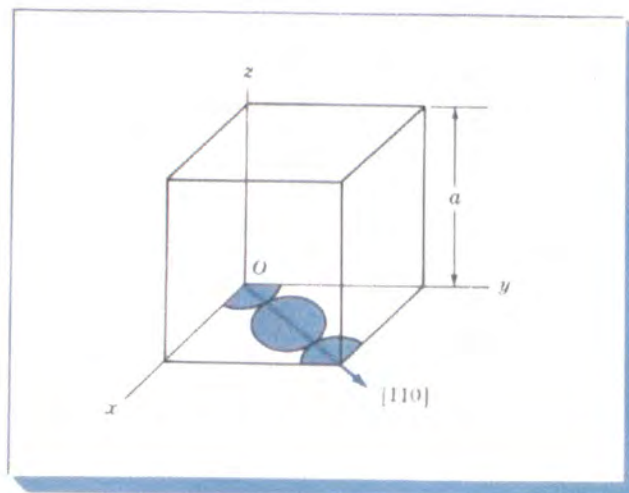


FIGURE 3.23 Diagram for calculating the atomic linear density in the [110] direction in an FCC unit cell.

3.10 POLYMORPHISM OR ALLOTROPY

Many elements and compounds exist in more than one crystalline form under different conditions of temperature and pressure. This phenomenon is termed *polymorphism*, or *allotropy*. Many industrially important metals such as iron, titanium, and cobalt undergo allotropic transformations at elevated temperatures at atmospheric pressure. Table 3.5 lists some selected metals which show allotropic transformations and the structure changes which occur.

Iron exists in both BCC and FCC crystal structures over the temperature range from room temperature to its melting point at 1539°C, as shown in Fig. 3.24. Alpha (α) iron exists from -273 to 912°C and has the BCC crystal structure.

TABLE 3.5 Allotropic Crystalline Forms of Some Metals

Metal	Crystal structure at room temperature	At other temperatures
Ca	FCC	BCC (>447°C)
Co	HCP	FCC (>427°C)
Hf	HCP	BCC (>1742°C)
Fe	BCC	FCC (912–1394°C) BCC (>1394°C)
Li	BCC	HCP (< -193°C)
Na	BCC	HCP (< -233°C)
Ti	HCP	BCC (>234°C)
Ti	HCP	BCC (>883°C)
Y	HCP	BCC (>1481°C)
Zr	HCP	BCC (>872°C)

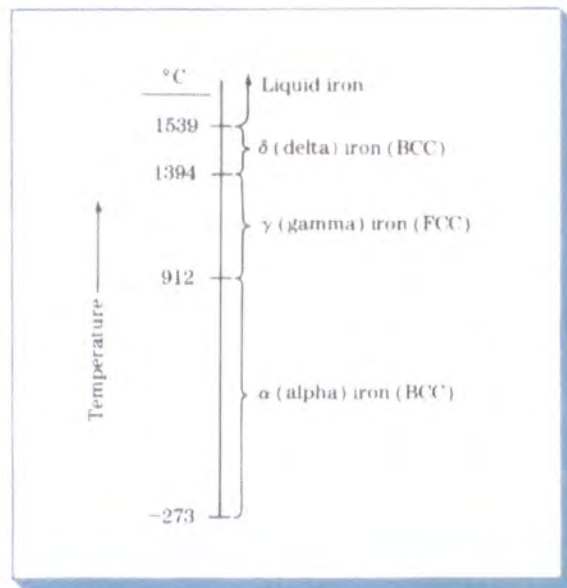


FIGURE 3.24 Allotropic crystalline forms of iron over temperature ranges at atmospheric pressure.

Gamma (γ) iron exists from 912 to 1394°C and has the FCC crystal structure. Delta (δ) iron exists from 1394 to 1539°C, which is the melting point of iron. The crystal structure of δ iron is also BCC but with a larger lattice constant than α iron.

Example Problem 3.14

Calculate the theoretical volume change accompanying a polymorphic transformation in a pure metal from the FCC to BCC crystal structure. Assume the hard-sphere atomic model and that there is no change in atomic volume before and after the transformation.

Solution:

In the FCC crystal structure unit cell, the atoms are in contact along the face diagonal of the unit cell, as shown in Fig. 3.7. Hence

$$\sqrt{2}a = 4R \quad \text{or} \quad a = \frac{4R}{\sqrt{2}} \quad (3.3)$$

In the BCC crystal structure unit cell, the atoms are in contact along the body diagonal of the unit cell as shown in Fig. 3.5. Hence

$$\sqrt{3}a = 4R \quad \text{or} \quad a = \frac{4R}{\sqrt{3}} \quad (3.1)$$

The volume per atom for the FCC crystal lattice, since it has four atoms per unit cell, is

$$V_{\text{FCC}} = \frac{a^3}{4} = \left(\frac{4R}{\sqrt{2}}\right)^3 \left(\frac{1}{4}\right) = 5.66R^3$$

The volume per atom for the BCC crystal lattice, since it has two atoms per unit cell, is

$$V_{\text{BCC}} = \frac{a^3}{2} = \left(\frac{4R}{\sqrt{3}}\right)^3 \left(\frac{1}{2}\right) = 6.16R^3$$

The change in volume associated with the transformation from the FCC to BCC crystal structure, assuming no change in atomic radius, is

$$\begin{aligned} \frac{\Delta V}{V_{\text{FCC}}} &= \frac{V_{\text{BCC}} - V_{\text{FCC}}}{V_{\text{FCC}}} \\ &= \left(\frac{6.16R^3 - 5.66R^3}{5.66R^3}\right) 100\% = +8.8\% \quad \blacktriangleleft \end{aligned}$$

3.11 CRYSTAL STRUCTURE ANALYSIS

Our present knowledge of crystal structures has been obtained mainly by x-ray diffraction techniques which utilize x-rays about the same wavelength as the distance between crystal lattice planes. However, before discussing the manner in which x-rays are diffracted in crystals, let us consider how x-rays are produced for experimental purposes.

X-Ray Sources

X-rays used for diffraction are electromagnetic waves with wavelengths in the range 0.05 to 0.25 nm (0.5 to 2.5 Å). By comparison the wavelength of visible light is of the order of 600 nm (6000 Å). In order to produce x-rays for diffraction purposes, a voltage of about 35 kV is necessary and is applied between a cathode and an anode target metal, both of which are contained in a vacuum, as shown in Fig. 3.25. When the tungsten filament of the cathode is heated, electrons are released by thermionic emission and accelerated through the vacuum by the large voltage difference between the cathode and anode, thereby gaining kinetic energy. When the electrons strike the target metal (e.g., molybdenum), x-rays are given off. However, most of the kinetic energy (about 98 percent) is converted into heat, so the target metal must be cooled externally.

FIGURE 3.25 Schematic diagram of the cross section of a sealed-off filament x-ray tube. (After B. D. Cullity, "Elements of X-Ray Diffraction," 2d ed., Addison-Wesley, 1978, p. 23.)

The x-ray spectrum emitted at 35 kV using a molybdenum target is shown in Fig. 3.26. The spectrum shows continuous x-ray radiation in the wavelength range from about 0.2 to 1.4 Å (0.02 to 0.14 nm) and two spikes of characteristic radiation which are designated the K_{α} and K_{β} lines. The wavelengths of the K_{α} and K_{β} lines are characteristic for an element. For molybdenum, the K_{α} line occurs at a wavelength of about 0.7 Å (0.07 nm). The origin of the characteristic

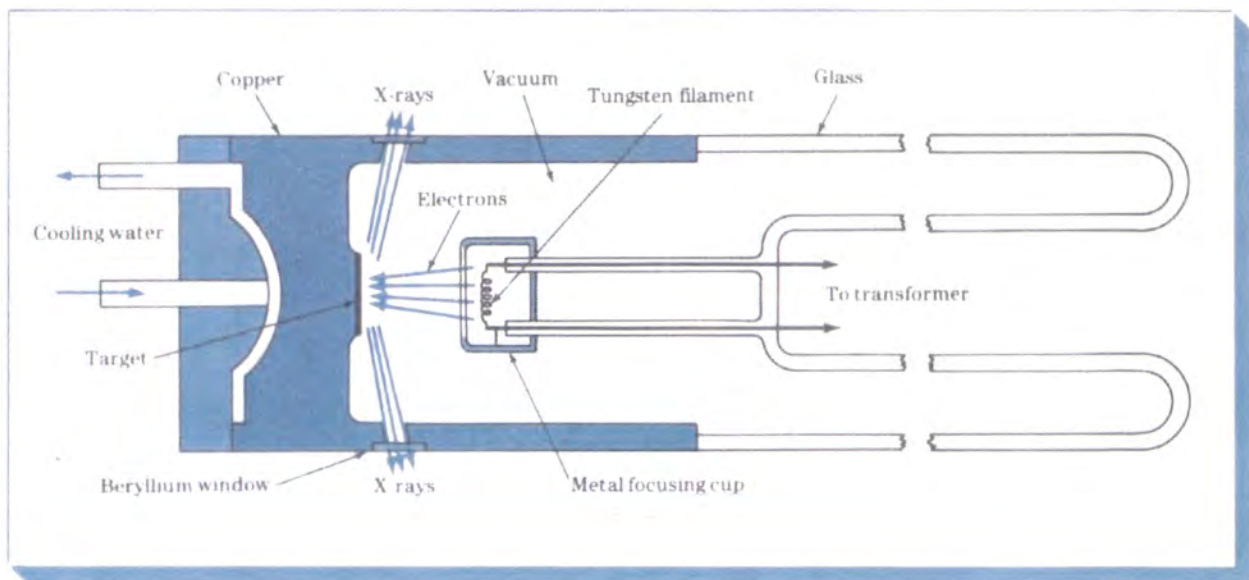
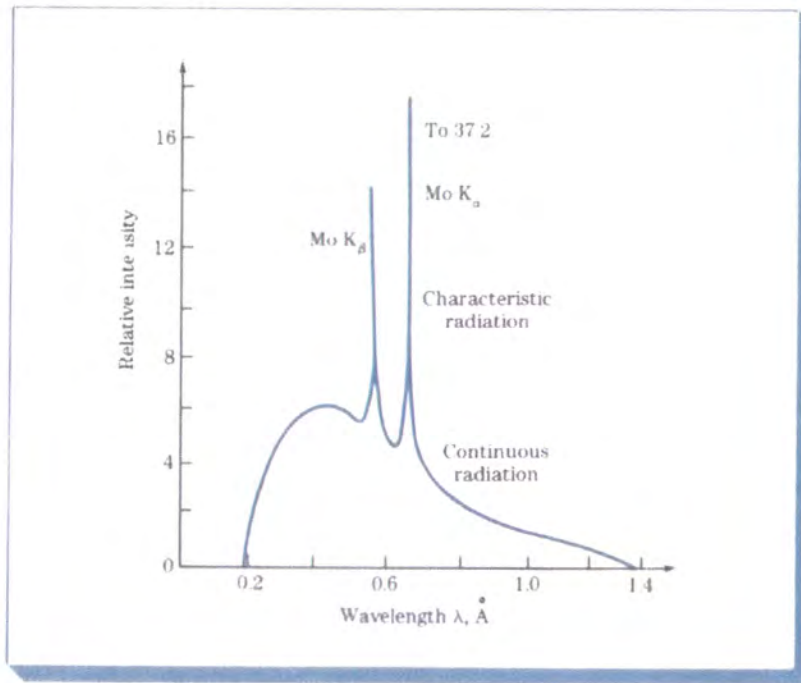
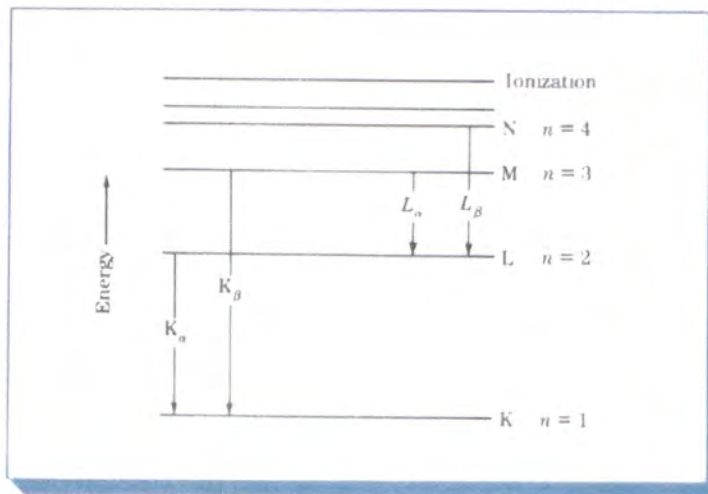


FIGURE 3.26 X-ray emission spectrum produced when molybdenum metal is used as the target metal in an x-ray tube operating at 35 kV.



radiation is explained as follows. First, K electrons (electrons in the $n = 1$ shell) are knocked out of the atom by highly energetic electrons bombarding the target, leaving excited atoms. Next, some electrons in higher shells (that is, $n = 2$ or 3) drop down to lower energy levels to replace the lost K electrons, emitting energy of a characteristic wavelength. The transition of electrons from

FIGURE 3.27 Energy levels of electrons in molybdenum showing the origin of K_{α} and K_{β} radiation.



the L ($n = 2$) shell to the K ($n = 1$) shell creates energy of the wavelength of the K_{α} line, as indicated in Fig. 3.27.

X-Ray Diffraction

Since the wavelengths of some x-rays are about equal to the distance between planes of atoms in crystalline solids, reinforced diffraction peaks of radiation of varying intensities can be produced when a beam of x-rays strikes a crystalline solid. However, before considering the application of x-ray diffraction techniques to crystal structure analysis, let us examine the geometric conditions necessary to produce diffracted or reinforced beams of reflected x-rays.

Consider a monochromatic (single-wavelength) beam of x-rays to be incident on a crystal, as shown in Fig. 3.28. For simplification let us allow the crystal planes of atomic scattering centers to be replaced by crystal planes which act as mirrors in reflecting the incident x-ray beam. In Fig. 3.28 the horizontal lines represent a set of parallel crystal planes with Miller indices (hkl). When an incident beam of monochromatic x-rays of wavelength λ strikes this set of planes at an angle such that the wave patterns of the beam leaving the various planes are *not in phase*, *no reinforced beam will be produced* (Fig. 3.28a). Thus destructive interference occurs. If the reflected wave patterns of the beam leaving the various planes are in phase, then reinforcement of the beam or constructive interference occurs (Fig. 3.28b).

Let us now consider incident x-rays 1 and 2 as indicated in Fig. 3.28c. For these rays to be in phase, the extra distance of travel of ray 2 is equal to $MP + PN$, which must be an integral number of wavelengths λ . Thus

$$n\lambda = MP + PN \quad (3.8)$$

where $n = 1, 2, 3, \dots$ and is called the *order of the diffraction*. Since both MP and PN equal $d_{hkl} \sin \theta$, where d_{hkl} is the interplanar spacing of the crystal planes of indices (hkl), the condition for constructive interference (i.e., the production of a diffraction peak of intense radiation) must be

$$n\lambda = 2d_{hkl} \sin \theta \quad (3.9)$$

This equation, known as *Bragg's law*,¹ gives the relationship among the angular positions of the reinforced diffracted beams in terms of the wavelength λ of the incoming x-ray radiation and of the interplanar spacings d_{hkl} of the crystal planes. In most cases, the first order of diffraction where $n = 1$ is used, and so for this case Bragg's law takes the form

$$\lambda = 2d_{hkl} \sin \theta \quad (3.10)$$

¹William Henry Bragg (1862-1942) English physicist who worked in x-ray crystallography

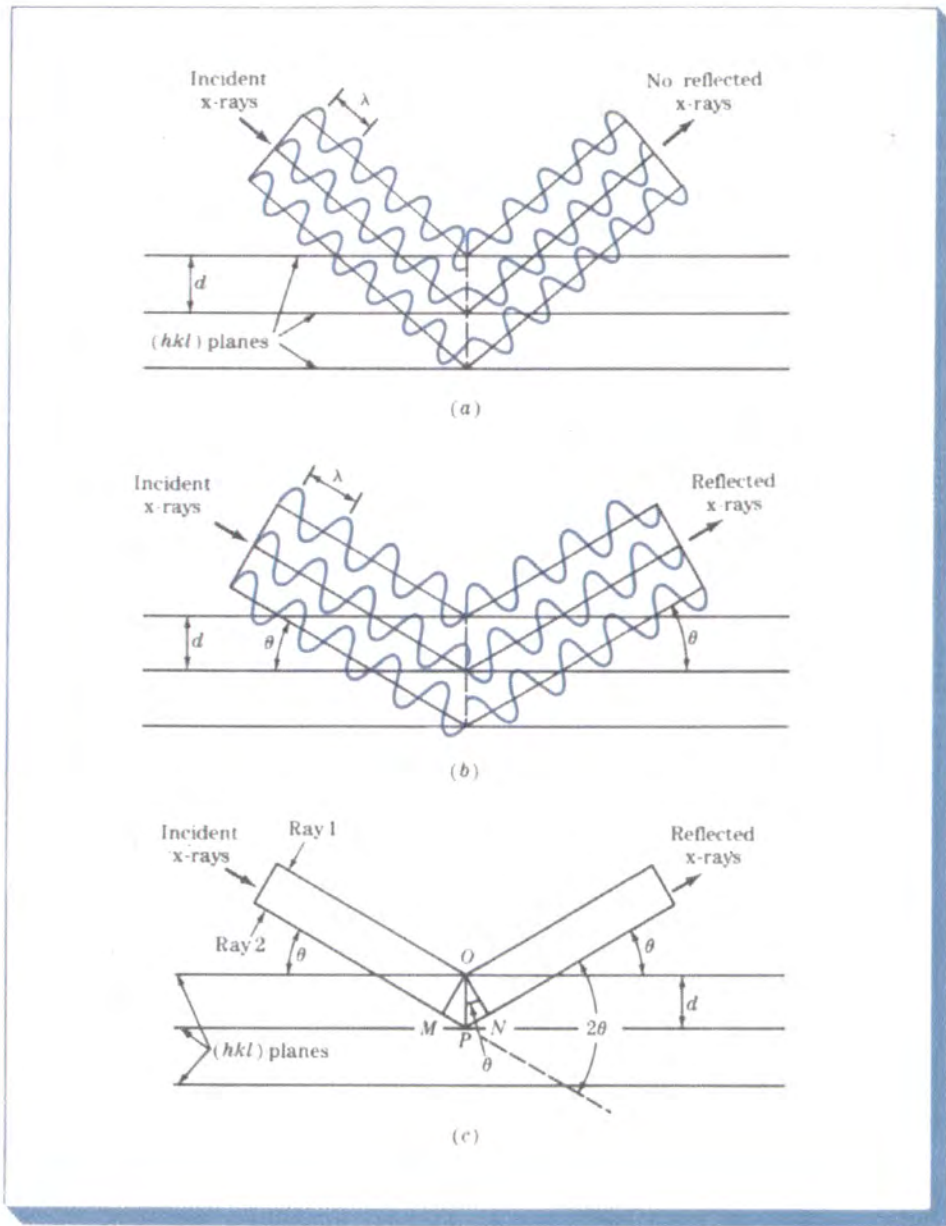


FIGURE 3.28 The reflection of an x-ray beam by the (hkl) planes of a crystal. (a) No reflected beam is produced at an arbitrary angle of incidence. (b) At the Bragg angle θ , the reflected rays are in phase and reinforce one another. (c) Similar to (b) except that the wave representation has been omitted. (After A. G. Guy and J. J. Hren, "Elements of Physical Metallurgy," 3d ed., Addison-Wesley, 1974, p. 201.)

Example Problem 3.15

A sample of BCC iron was placed in an x-ray diffractometer using incoming x-rays with a wavelength $\lambda = 0.1541$ nm. Diffraction from the $\{110\}$ planes was obtained at $2\theta = 44.704^\circ$. Calculate a value for the lattice constant a of BCC iron. (Assume first-order diffraction with $n = 1$.)

Solution:

$$\begin{aligned}
 2\theta &= 44.704^\circ & \theta &= 22.35^\circ \\
 \lambda &= 2d_{hkl} \sin \theta & & (3.10) \\
 d_{110} &= \frac{\lambda}{2 \sin \theta} = \frac{0.1541 \text{ nm}}{2(\sin 22.35^\circ)} \\
 &= \frac{0.1541 \text{ nm}}{2(0.3803)} = 0.2026 \text{ nm}
 \end{aligned}$$

Rearranging Eq. (3.4) gives

$$a = d_{hkl} \sqrt{h^2 + k^2 + l^2}$$

Thus

$$\begin{aligned}
 a(\text{Fe}) &= d_{110} \sqrt{1^2 + 1^2 + 0^2} \\
 &= (0.2026 \text{ nm})(1.414) = 0.287 \text{ nm} \blacktriangleleft
 \end{aligned}$$

**X-Ray Diffraction
Analysis of Crystal
Structures**

The powder method of x-ray diffraction analysis The most commonly used x-ray diffraction technique is the *powder method*. In this technique a powdered specimen is utilized so that there will be a random orientation of many crystals to ensure that some of the particles will be oriented in the x-ray beam to satisfy the diffraction conditions of Bragg's law. Modern x-ray crystal analysis uses an x-ray diffractometer which has a radiation counter to detect the angle and intensity of the diffracted beam (Fig. 3.29). A recorder automatically plots the intensity of the diffracted beam as the counter moves on a goniometer¹ circle (Fig. 3.30) which is in synchronization with the specimen over a range of 2θ values. Figure 3.31 shows an x-ray diffraction recorder chart for the intensity of the diffracted beam vs. the diffraction angles 2θ for a powdered pure-metal specimen. In this way both the angles of the diffracted beams and their intensities can be recorded at one time. Sometimes a powder camera with an enclosed filmstrip is used instead of the diffractometer, but this method is much slower and in most cases less convenient.

¹A goniometer is an instrument for measuring angles

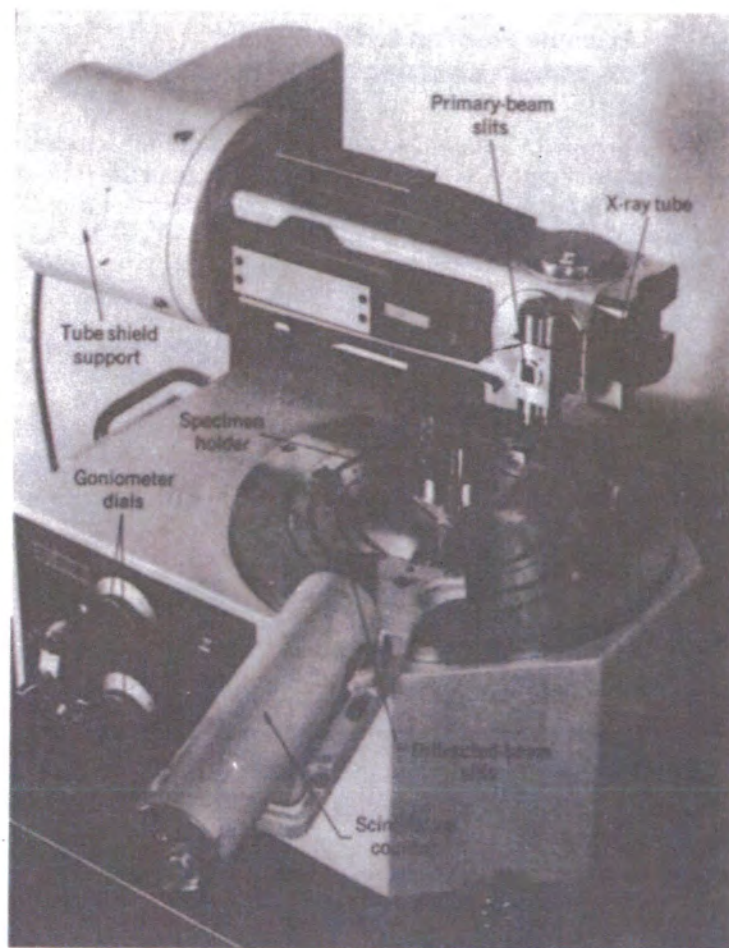


FIGURE 3.29 An x-ray diffractometer (with x-radiation shields removed). (Phillips Electronic Instruments, Inc.)

Diffraction conditions for cubic unit cells X-ray diffraction techniques enable the structures of crystalline solids to be determined. The interpretation of x-ray diffraction data for most crystalline substances is complex and beyond the scope of this book, and so only the simple case of diffraction in pure cubic metals will be considered. The analysis of x-ray diffraction data for cubic unit cells can be simplified by combining Eq. (3.4),

$$d_{hkl} = \frac{a}{\sqrt{h^2 + k^2 + l^2}}$$

with the Bragg equation $\lambda = 2d \sin \theta$, giving

$$\lambda = \frac{2a \sin \theta}{\sqrt{h^2 + k^2 + l^2}} \quad (3.11)$$

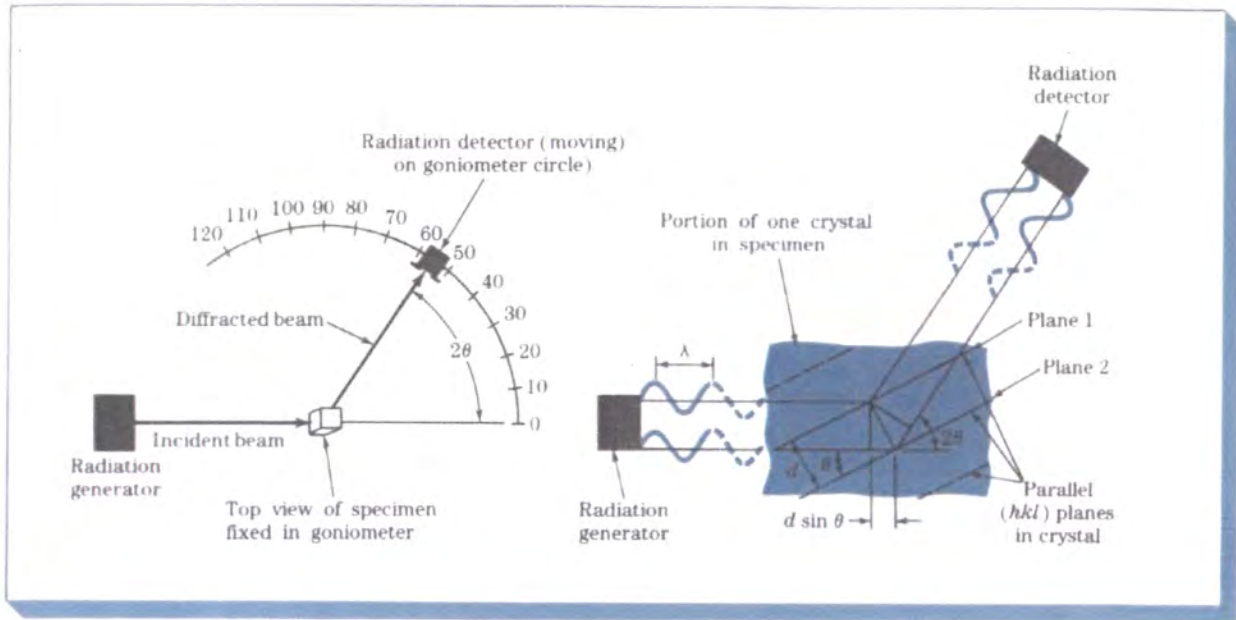
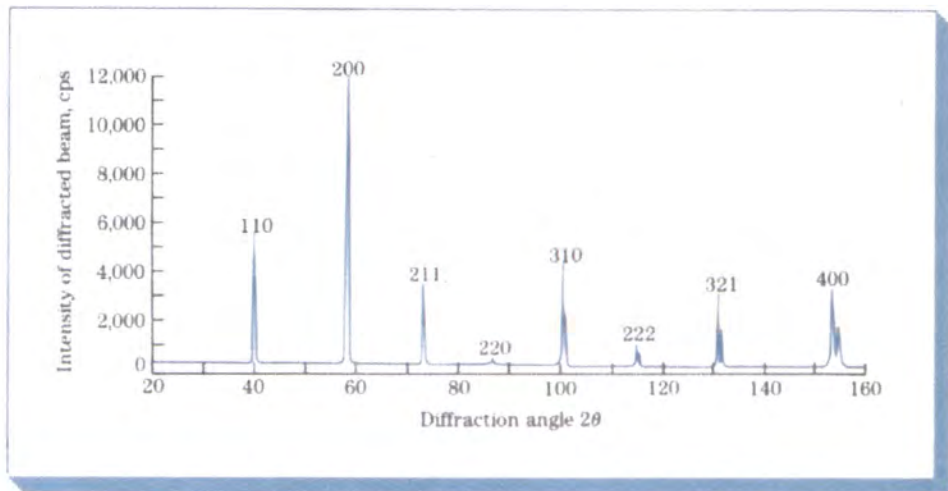


FIGURE 3.30 Schematic illustration of the diffractometer method of crystal analysis and of the conditions necessary for diffraction. (After A. G. Guy, "Essentials of Materials Science," McGraw-Hill, 1976.)

FIGURE 3.31 Record of the diffraction angles for a tungsten sample obtained by the use of a diffractometer with copper radiation. (After A. G. Guy and J. J. Hren, "Elements of Physical Metallurgy," 3d ed., Addison-Wesley, 1974, p. 208.)



This equation can be used along with x-ray diffraction data to determine if a cubic crystal structure is body-centered or face-centered cubic. The rest of this subsection will describe how this is done.

To use Eq. (3.11) for diffraction analysis, we must know which crystal planes are the diffracting planes for each type of crystal structure. For the

simple cubic lattice, reflections from all (hkl) planes are possible. However, for the BCC structure diffraction occurs only on planes whose Miller indices when added together $(h + k + l)$ total to an even number (Table 3.6). Thus, for the BCC crystal structure the principal diffracting planes are $\{110\}$, $\{200\}$, $\{211\}$, etc., which are listed in Table 3.7. In the case of the FCC crystal structure, the principal diffracting planes are those whose Miller indices are either all even or all odd (zero is considered even). Thus, for the FCC crystal structure the diffracting planes are $\{111\}$, $\{200\}$, $\{220\}$, etc., which are listed in Table 3.7.

Interpreting experimental x-ray diffraction data for metals with cubic crystal structures We can use x-ray diffractometer data to determine crystal structures. A simple case to illustrate how this analysis can be used is to distinguish between the BCC and FCC crystal structures of a cubic metal. Let us assume that we have a metal which has either a BCC or an FCC crystal structure and that we are able to identify the principal diffracting planes and their corresponding 2θ values, as indicated for the metal tungsten in Fig. 3.31.

TABLE 3.6 Rules for Determining the Diffracting (hkl) Planes in Cubic Crystals

Bravais lattice	Reflections present	Reflections absent
BCC	$(h + k + l) = \text{even}$	$(h + k + l) = \text{odd}$
FCC	(h, k, l) all odd or all even	(h, k, l) not all odd or all even

TABLE 3.7 Miller Indices of the Diffracting Planes for BCC and FCC Lattices

Cubic planes (hkl)	$h^2 + k^2 + l^2$	Sum $\Sigma(h^2 + k^2 + l^2)$	Cubic diffracting planes (hkl)	
			FCC	BCC
{100}	$1^2 + 0^2 + 0^2$	1		
{110}	$1^2 + 1^2 + 0^2$	2		110
{111}	$1^2 + 1^2 + 1^2$	3	111	
{200}	$2^2 + 0^2 + 0^2$	4	200	200
{210}	$2^2 + 1^2 + 0^2$	5		
{211}	$2^2 + 1^2 + 1^2$	6		211
...		7		
{220}	$2^2 + 2^2 + 0^2$	8	220	220
{221}	$2^2 + 2^2 + 1^2$	9		
{310}	$3^2 + 1^2 + 0^2$	10		310

By squaring both sides of Eq. (3.11) and solving for $\sin^2 \theta$, we obtain

$$\sin^2 \theta = \frac{\lambda^2(h^2 + k^2 + l^2)}{4a^2} \quad (3.12)$$

From x-ray diffraction data we can obtain experimental values of 2θ for a series of principal diffracting $\{hkl\}$ planes. Since the wavelength of the incoming radiation and the lattice constant a are both constants, we can eliminate these quantities by forming the ratio of two $\sin^2 \theta$ values as

$$\frac{\sin^2 \theta_A}{\sin^2 \theta_B} = \frac{h_A^2 + k_A^2 + l_A^2}{h_B^2 + k_B^2 + l_B^2} \quad (3.13)$$

where θ_A and θ_B are two diffracting angles associated with the principal diffracting planes $\{h_A k_A l_A\}$ and $\{h_B k_B l_B\}$, respectively.

Using Eq. (3.13) and the Miller indices of the first two sets of principal diffracting planes listed in Table 3.7 for BCC and FCC crystal structures, we can determine values for the $\sin^2 \theta$ ratios for both BCC and FCC structures.

For the BCC crystal structure the first two sets of principal diffracting planes are the $\{110\}$ and $\{200\}$ planes (Table 3.7). Substitution of the Miller $\{hkl\}$ indices of these planes into Eq. (3.13) gives

$$\frac{\sin^2 \theta_A}{\sin^2 \theta_B} = \frac{1^2 + 1^2 + 0^2}{2^2 + 0^2 + 0^2} = 0.5 \quad (3.14)$$

Thus, if the crystal structure of the unknown cubic metal is BCC, the ratio of the $\sin^2 \theta$ values which correspond to the first two principal diffracting planes will be 0.5.

For the FCC crystal structure the first two sets of principal diffracting planes are the $\{111\}$ and $\{200\}$ planes (Table 3.7). Substitution of the Miller $\{hkl\}$ indices of these planes into Eq. (3.13) gives

$$\frac{\sin^2 \theta_A}{\sin^2 \theta_B} = \frac{1^2 + 1^2 + 1^2}{2^2 + 0^2 + 0^2} = 0.75 \quad (3.15)$$

Thus, if the crystal structure of the unknown cubic metal is FCC, the ratio of the $\sin^2 \theta$ values which correspond to the first two principal diffracting planes will be 0.75.

Example Problem 3.16 uses Eq. (3.13) and experimental x-ray diffraction data for the 2θ values for the principal diffracting planes to determine whether an unknown cubic metal is BCC or FCC. X-ray diffraction analysis is usually much more complicated than Example Problem 3.16, but the principles used are the same. Both experimental and theoretical x-ray diffraction analysis has been and continues to be used for the determination of the crystal structure of materials.

Example Problem 3.16

An x-ray diffractometer recorder chart for an element which has either the BCC or the FCC crystal structure shows diffraction peaks at the following 2θ angles: 40, 58, 73, 86.8, 100.4, and 114.7. The wavelength of the incoming x-ray used was 0.154 nm.

- Determine the cubic structure of the element.
- Determine the lattice constant of the element.
- Identify the element.

Solution:

- Determination of the crystal structure of the element.* First, the $\sin^2 \theta$ values are calculated from the 2θ diffraction angles.

2θ , deg	θ , deg	$\sin \theta$	$\sin^2 \theta$
40	20	0.3420	0.1170
58	29	0.4848	0.2350
73	36.5	0.5948	0.3538
86.8	43.4	0.6871	0.4721
100.4	50.2	0.7683	0.5903
114.7	57.35	0.8420	0.7090

Next the ratio of the $\sin^2 \theta$ values of the first and second angles is calculated:

$$\frac{\sin^2 \theta}{\sin^2 \theta} = \frac{0.117}{0.235} = 0.498 \approx 0.5$$

The crystal structure is BCC since this ratio is ≈ 0.5 . If the ratio had been ≈ 0.75 , the structure would have been FCC.

- Determination of the lattice constant.* Rearranging Eq. (3.12) and solving for a^2 gives

$$a^2 = \frac{\lambda^2 h^2 + k^2 + l^2}{4 \sin^2 \theta} \quad (3.16)$$

or

$$a = \frac{\lambda}{2} \sqrt{\frac{h^2 + k^2 + l^2}{\sin^2 \theta}} \quad (3.17)$$

Substituting into Eq. (3.17) $h = 1$, $k = 1$, and $l = 0$ for the h, k, l Miller indices of the first set of principal diffracting planes for the BCC crystal structure, which are the $\{110\}$ planes, the corresponding value for $\sin^2 \theta$, which is 0.117, and 0.154 nm for λ , the incoming radiation, gives

$$a = \frac{0.154 \text{ nm}}{2} \sqrt{\frac{1^2 + 1^2 + 0^2}{0.117}} = 0.318 \text{ nm} \blacktriangleleft$$

- (c) *Identification of the element.* The element is tungsten since this element has a lattice constant of 0.316 nm and is BCC.

SUMMARY

Atomic arrangements in crystalline solids can be described by a network of lines called a *space lattice*. Each space lattice can be described by specifying the atom positions in a repeating *unit cell*. There are seven crystal systems based on the geometry of the axial lengths and interaxial angles of the unit cells. These seven systems have a total of 14 sublattices (unit cells) based on the internal arrangements of atomic sites within the unit cells.

In metals the most common crystal structure unit cells are: *body-centered cubic* (BCC), *face-centered cubic* (FCC), and *hexagonal close-packed* (HCP) (which is a dense variation of the simple hexagonal structure).

Crystal directions in cubic crystals are the vector components of the directions resolved along each of the component axes and reduced to smallest integers. They are indicated as $[uvw]$. Families of directions are indexed by the direction indices enclosed by pointed brackets as $\langle uvw \rangle$. *Crystal planes* in cubic crystals are indexed by the reciprocals of the axial intercepts of the plane (followed by the elimination of fractions) as (hkl) . Cubic crystal planes of a form (family) are indexed with braces as $\{hkl\}$. Crystal planes in hexagonal crystals are commonly indexed by four indices h , k , i , and l enclosed in parentheses as $(hkil)$. These indices are the reciprocals of the intercepts of the plane on the a_1 , a_2 , a_3 , and c axes of the hexagonal crystal structure unit cell. Crystal directions in hexagonal crystals are the vector components of the direction resolved along each of the four coordinate axes and reduced to smallest integers as $[uvtw]$.

Using the hard-sphere model for atoms, calculations can be made for the volume, planar, and linear density of atoms in unit cells. Planes in which atoms are packed as tightly as possible are called *close-packed planes*, and directions in which atoms are in closest contact are called *close-packed directions*. Atomic packing factors for different crystal structures can also be determined by assuming the hard-sphere atomic model. Some metals have different crystal structures at different ranges of temperature and pressure, a phenomenon called *polymorphism*.

Crystal structures of crystalline solids can be determined by using x-ray diffraction analysis techniques. X-rays are diffracted in crystals when the *Bragg's law* ($n\lambda = 2d \sin \theta$) conditions are satisfied. By using the x-ray diffractometer and the *powder method*, the crystal structure of many crystalline solids can be determined.

DEFINITIONS

Sec. 3.1

Crystal: a solid composed of atoms, ions, or molecules arranged in a pattern that is repeated in three dimensions.

Crystal structure: a regular three-dimensional pattern of atoms or ions in space.

Space lattice: a three-dimensional array of points each of which has identical surroundings.

Lattice point: one point in an array in which all the points have identical surroundings.

Unit cell: a convenient repeating unit of a space lattice. The axial lengths and axial angles are the lattice constants of the unit cell.

Sec. 3.3

Body-centered cubic (BCC) unit cell: a unit cell with an atomic packing arrangement in which one atom is in contact with eight identical atoms located at the corners of an imaginary cube.

Face-centered cubic (FCC) unit cell: a unit cell with an atomic packing arrangement in which 12 atoms surround a central atom. The stacking sequence of layers of close-packed planes in the FCC crystal structure is *ABCABC*. . . .

Hexagonal close-packed (HCP) unit cell: a unit cell with an atomic packing arrangement in which 12 atoms surround a central identical atom. The stacking sequence of layers of close-packed planes in the HCP crystal structure is *ABABAB*. . . .

Atomic packing factor (APF): the volume of atoms in a selected unit cell divided by the volume of the unit cell.

Sec. 3.5

Indices of direction in a cubic crystal: a direction in a cubic unit cell is indicated by a vector drawn from the origin at one point in a unit cell through the surface of the unit cell; the position coordinates (*x*, *y*, and *z*) of the vector where it leaves the surface of the unit cell (with fractions cleared) are the indices of direction. These indices, designated *u*, *v*, and *w* are enclosed in brackets as [*uvw*]. Negative indices are indicated by a bar over the index.

Sec. 3.6

Indices for cubic crystal planes (Miller indices): the reciprocals of the intercepts (with fractions cleared) of a crystal plane with the *x*, *y*, and *z* axes of a unit cube are called the Miller indices of that plane. They are designated *h*, *k*, and *l* for the *x*, *y*, and *z* axes, respectively, and are enclosed in parentheses as (*hkl*). Note that the selected crystal plane must *not* pass through the origin of the *x*, *y*, and *z* axes.

Sec. 3.9

Volume density ρ_v : mass per unit volume; this quantity is usually expressed in Mg/m³ or g/cm³.

Planar density ρ_p : the equivalent number of atoms whose centers are intersected by a selected area divided by the selected area.

Linear density ρ_l : the number of atoms whose centers lie on a specific direction on a specific length of line in a unit cube.

Sec. 3.10

Polymorphism (as pertains to metals): the ability of a metal to exist in two or more crystal structures. For example, iron can have a BCC or an FCC crystal structure, depending on the temperature.

PROBLEMS

- 3.1.1 Define a crystalline solid.
- 3.1.2 Define a crystal structure. Give examples of materials which have crystal structures.
- 3.1.3 Define a space lattice.
- 3.1.4 Define a unit cell of a space lattice. What lattice constants define a unit cell?
- 3.2.1 What are the 14 Bravais unit cells?
- 3.3.1 What are the three most common metal crystal structures? List five metals which have each of these crystal structures.
- 3.3.2 How many atoms per unit cell are there in the BCC crystal structure?
- 3.3.3 What is the coordination number for the atoms in the BCC crystal structure?
- 3.3.4 What is the relationship between the length of the side a of the BCC unit cell and the radius of its atoms?
- 3.3.5 Potassium at 20°C is BCC and has an atomic radius of 0.238 nm. Calculate a value for its lattice constant a in nanometers.
- 3.3.6 Tungsten at 20°C is BCC and has an atomic radius of 0.141 nm. Calculate a value for its lattice constant a in nanometers.
- 3.3.7 Tantalum at 20°C is BCC and has a lattice constant of 0.33026 nm. Calculate a value for the atomic radius of a tungsten atom in nanometers.
- 3.3.8 Barium at 20°C is BCC and has a lattice constant of 0.5019 nm. Calculate a value for the atomic radius of a chromium atom in nanometers.
- 3.3.9 How many atoms per unit cell are there in the FCC crystal structure?
- 3.3.10 What is the coordination number for the atoms in the FCC crystal structure?
- 3.3.11 Copper is FCC and has a lattice constant of 0.3615 nm. Calculate a value for the atomic radius of a copper atom in nanometers.
- 3.3.12 Calcium is FCC and has a lattice constant of 0.5582 nm. Calculate a value for the atomic radius of an aluminum atom in nanometers.
- 3.3.13 Iridium is FCC and has an atomic radius of 0.135 nm. Calculate a value for its lattice constant a in nanometers.
- 3.3.14 Aluminum is FCC and has an atomic radius of 0.143 nm. Calculate a value for its lattice constant a in nanometers.
- 3.3.15 Calculate the atomic packing factor for the FCC structure.
- 3.3.16 How many atoms per unit cell are there in the HCP crystal structure?
- 3.3.17 What is the coordination number for the atoms in the HCP crystal structure?
- 3.3.18 What is the ideal c/a ratio for HCP metals?
- 3.3.19 Of the following HCP metals, which have higher or lower c/a ratios than the ideal ratio: Zr, Ti, Zn, Mg, Co, Cd, and Be?
- 3.3.20 Calculate the volume in cubic nanometers of the beryllium crystal structure unit cell. Beryllium is HCP at 20°C with $a = 0.22856$ nm and $c = 0.35832$ nm.
- 3.3.21 Magnesium at 20°C is HCP. The height c of its unit cell is 0.52105 nm and its c/a ratio is 1.623. Calculate a value for its lattice constant a in nanometers.

- 3.3.22 Cadmium at 20°C is HCP. Using a value of 0.148 nm for the atomic radius of cadmium atoms, calculate a value for its unit-cell volume. Assume a packing factor of 0.74.
- 3.4.1 How are atomic positions located in cubic unit cells?
- 3.4.2 List the atom positions for the eight corner and six face-centered atoms of the FCC unit cell.
- 3.5.1 How are the indices for a crystallographic direction in a cubic unit cell determined?
- 3.5.2 Draw the following directions in a BCC unit cell and list the position coordinates of the atoms whose centers are intersected by the direction vector:
 (a) $[100]$ (b) $[110]$ (c) $[111]$
- 3.5.3 Draw direction vectors in unit cubes for the following cubic directions:
 (a) $[1\bar{1}\bar{1}]$ (b) $[1\bar{1}0]$ (c) $[\bar{1}2\bar{1}1]$ (d) $[\bar{1}\bar{1}3]$
- 3.5.4 Draw direction vectors in unit cubes for the following cubic directions:
 (a) $[1\bar{2}\bar{1}]$ (d) $[20\bar{1}]$ (g) $[\bar{2}21]$ (j) $[20\bar{3}]$
 (b) $[21\bar{2}]$ (e) $[10\bar{2}]$ (h) $[\bar{3}23]$ (k) $[\bar{1}\bar{2}\bar{2}]$
 (c) $[\bar{3}\bar{2}1]$ (f) $[2\bar{3}3]$ (i) $[1\bar{2}3]$ (l) $[\bar{2}\bar{2}3]$
- 3.5.5 What are the indices of the directions shown in the unit cubes of Fig. P3.5.5?

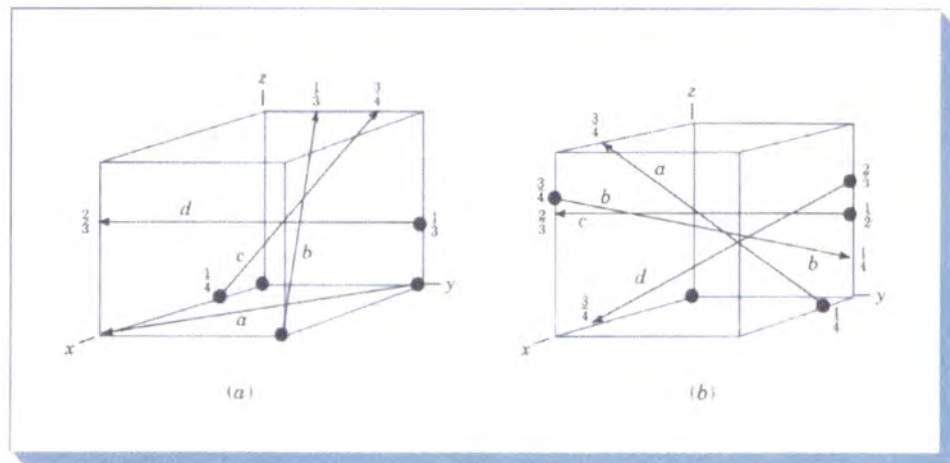


FIGURE P3.5.5

- 3.5.6 A direction vector passes through a unit cube from the $(\frac{1}{4}, 0, \frac{1}{4})$ to the $(\frac{1}{4}, \frac{3}{4}, 1)$ positions. What are its direction indices?
- 3.5.7 A direction vector passes through a unit cube from the $(\frac{1}{4}, \frac{3}{4}, 0)$ to the $(\frac{1}{2}, \frac{1}{2}, 0)$ positions. What are its direction indices?
- 3.5.8 What are the crystallographic directions of a family or form? What generalized notation is used to indicate them?
- 3.5.9 What are the directions of the $\langle 100 \rangle$ family or form for a unit cube?
- 3.5.10 What are the directions of the $\langle 111 \rangle$ family or form for a unit cube?
- 3.5.11 What $\langle 110 \rangle$ -type directions lie on the (111) plane of a cubic unit cell?
- 3.5.12 What $\langle 111 \rangle$ -type directions lie on the (110) plane of a cubic unit cell?
- 3.6.1 How are the Miller indices for a crystallographic plane in a cubic unit cell determined? What generalized notation is used to indicate them?

- 3.6.2 Draw in unit cubes the crystal planes which have the following Miller indices:
 (a) $(2\bar{1}3)$ (d) $(3\bar{3}1)$ (g) $(1\bar{2}0)$ (j) $(1\bar{2}\bar{2})$
 (b) $(2\bar{1}\bar{2})$ (e) $(\bar{3}1\bar{2})$ (h) $(2\bar{3}\bar{2})$ (k) $(1\bar{3}3)$
 (c) $(\bar{3}\bar{2}1)$ (f) $(20\bar{3})$ (i) $(\bar{3}3\bar{2})$ (l) $(\bar{2}\bar{2}3)$
- 3.6.3 What are the Miller indices of the cubic crystallographic planes shown in Fig. P3.6.3?
- 3.6.4 What is the notation used to indicate a family or form of cubic crystallographic planes?
- 3.6.5 What are the $\{100\}$ family of planes of the cubic system?
- 3.6.6 Draw the following crystallographic planes in a BCC unit cell and list the position of the atoms whose centers are intersected by each of the planes:
 (a) (100) (b) (110) (c) (111)
- 3.6.7 Draw the following crystallographic planes in an FCC unit cell and list the position coordinates of the atoms whose centers are intersected by each of the planes:
 (a) (100) (b) (110) (c) (111)

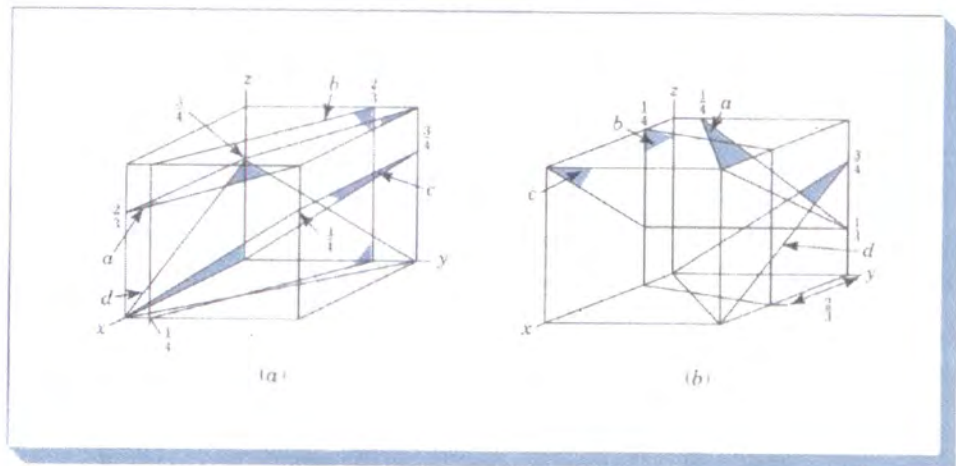


FIGURE P3.6.3

- 3.6.8 A cubic plane has the following axial intercepts: $a = \frac{1}{3}$, $b = -\frac{2}{3}$, $c = \frac{1}{3}$. What are the Miller indices of this plane?
- 3.6.9 A cubic plane has the following axial intercepts: $a = -\frac{1}{2}$, $b = \frac{1}{2}$, $c = \frac{2}{3}$. What are the Miller indices of this plane?
- 3.6.10 A cubic plane has the following axial intercepts: $a = 1$, $b = \frac{2}{3}$, $c = -\frac{1}{2}$. What are the Miller indices of this plane?
- 3.6.11 Determine the Miller indices of the cubic crystal plane which intersects the following position coordinates: $(1, 0, 0)$; $(1, \frac{1}{2}, \frac{1}{4})$; $(\frac{1}{2}, \frac{1}{2}, 0)$
- 3.6.12 Determine the Miller indices of the cubic crystal plane which intersects the following position coordinates: $(\frac{1}{2}, 0, \frac{1}{2})$; $(0, 0, 1)$; $(1, 1, 1)$
- 3.6.13 Determine the Miller indices of the cubic crystal plane which intersects the following position coordinates: $(1, \frac{1}{2}, 1)$; $(\frac{1}{2}, 0, \frac{3}{4})$; $(1, 0, \frac{1}{2})$
- 3.6.14 Determine the Miller indices of the cubic crystal plane which intersects the following position coordinates: $(0, 0, \frac{1}{2})$; $(1, 0, 0)$; $(\frac{1}{2}, \frac{1}{2}, 0)$

- 3.6.15 Nickel is FCC and has a lattice constant of 0.35236 nm. Calculate the following interplanar spacings in nm.
 (a) d_{111} (b) d_{200} (c) d_{220}
- 3.6.16 Molybdenum is BCC and has a lattice constant of 0.31468 nm. Calculate the following interplanar spacings in nm.
 (a) d_{110} (b) d_{220} (c) d_{310}
- 3.6.17 The d_{321} interplanar spacing in a BCC metal is 0.084165 nm. (a) What is its lattice constant "a"? (b) What is the atomic radius of the metal? (c) What could this metal be based on its lattice constant "a"?
- 3.6.18 The d_{222} interplanar spacing in an FCC metal is 0.11327 nm. (a) What is its lattice constant "a"? (b) What is the atomic radius of the metal? (c) What could this metal be based on its lattice constant "a"?
- 3.7.1 How are crystallographic planes indicated in HCP unit cells?
- 3.7.2 What notation is used to describe HCP crystal planes?
- 3.7.3 Draw the hexagonal crystal planes whose Miller-Bravais indices are:
 (a) $(10\bar{1}1)$ (d) $(12\bar{1}2)$ (g) $(\bar{1}2\bar{1}2)$ (j) $(\bar{1}100)$
 (b) $(01\bar{1}1)$ (e) $(2\bar{1}\bar{1}1)$ (h) $(2\bar{2}00)$ (k) $(\bar{2}111)$
 (c) $(\bar{1}2\bar{1}0)$ (f) $(1\bar{1}01)$ (i) $(10\bar{1}2)$ (l) (1012)
- 3.7.4 Determine the Miller-Bravais indices of the hexagonal crystal planes in Fig. P3.7.4.

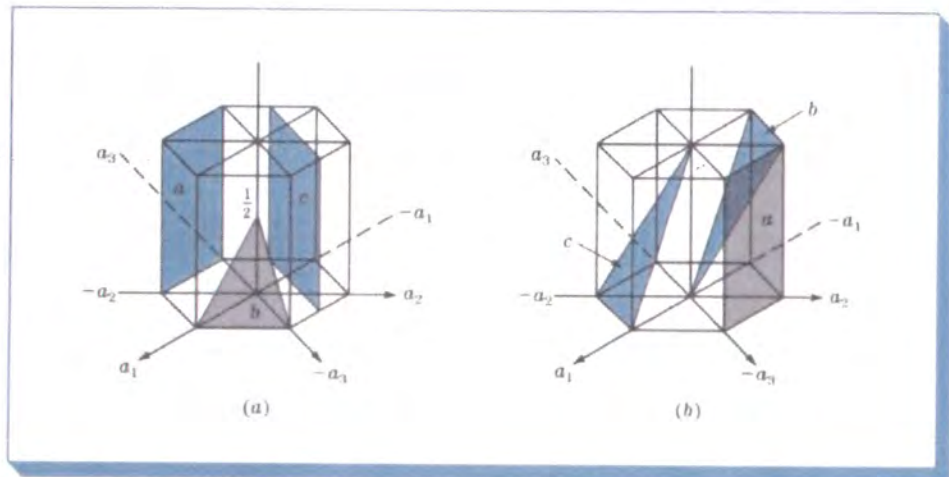


FIGURE P3.7.4

- 3.8.1 What is the difference in the stacking arrangement of close-packed planes in (a) the HCP crystal structure and (b) the FCC crystal structure?
- 3.8.2 What are the densest-packed planes in (a) the FCC structure and (b) the HCP structure?
- 3.8.3 What are the closest-packed directions in (a) the FCC structure and (b) the HCP structure?
- 3.9.1 The lattice constant for BCC niobium at 20°C is 0.33007 nm, and its density is 8.60 g/cm³. Calculate a value for its atomic mass.
- 3.9.2 Calculate a value for the density of FCC silver in grams per cubic centimeters from its lattice constant a of 0.40856 nm and its atomic mass of 107.87 g/mol.

- 3.9.3 Calculate the planar atomic density in atoms per square millimeter for the following crystal planes in BCC tungsten, which has a lattice constant of 0.31648 nm: (a) (100), (b) (110), (c) (111).
- 3.9.4 Calculate the planar atomic density in atoms per square millimeter for the following crystal planes in FCC nickel, which has a lattice constant of 0.35236 nm: (a) (100), (b) (110), (c) (111).
- 3.9.5 Calculate the planar atomic density in atoms per square millimeter for the (0001) plane in HCP cobalt, which has an a constant of 0.2506 nm and a c constant of 0.4069 nm.
- 3.9.6 Calculate the linear atomic density in atoms per millimeter for the following directions in BCC tantalum, which has a lattice constant of 0.33026 nm: (a) [100], (b) [110], (c) [111].
- 3.9.7 Calculate the linear atomic density in atoms per millimeter for the following directions in FCC platinum, which has a lattice constant of 0.39239 nm: (a) [100], (b) [110], (c) [111].
- 3.10.1 What is polymorphism with respect to metals?
- 3.10.2 Titanium goes through a polymorphic change from BCC to HCP crystal structure upon cooling through 882°C. Calculate the percentage change in volume when the crystal structure changes from BCC to HCP. The lattice constant a of the BCC unit cell at 882°C is 0.332 nm, and the HCP unit cell has $a = 0.2950$ nm and $c = 0.4683$ nm.
- 3.10.3 Pure iron goes through a polymorphic change from BCC to FCC upon heating through 912°C. Calculate the volume change associated with the change in crystal structure from BCC to FCC if at 912°C the BCC unit cell has a lattice constant $a = 0.293$ nm and the FCC unit cell $a = 0.363$ nm.
- 3.11.1 What are x-rays, and how are they produced?
- 3.11.2 Draw a schematic diagram of an x-ray tube used for x-ray diffraction, and indicate on it the path of the electrons and x-rays.
- 3.11.3 What is the characteristic x-ray radiation? What is its origin?
- 3.11.4 Distinguish between destructive interference and constructive interference of reflected x-ray beams through crystals.
- 3.11.5 Derive Bragg's law by using the simple case of incident x-ray beams being diffracted by parallel planes in a crystal.
- 3.11.6 A sample of BCC metal was placed in an x-ray diffractometer using x-rays with a wavelength of $\lambda = 0.1541$ nm. Diffraction from the {310} planes was obtained at $2\theta = 101.502^\circ$. Calculate a value for the lattice constant a for this BCC elemental metal. (Assume first-order diffraction, $n = 1$.)
- 3.11.7 X-rays of an unknown wavelength are diffracted by a nickel sample. The 2θ angle was 102.072° for the {220} planes. What is the wavelength of the x-rays used? (The lattice constant of nickel = 0.352236 nm; assume first-order diffraction, $n = 1$.)
- *3.11.8 An x-ray diffractometer recorder chart for an element which has either the BCC or the FCC crystal structure showed diffraction peaks at the following 2θ angles: 38.184° , 44.392° , 64.576° , and 77.547° . (Wavelength of the incoming radiation was 0.154056 nm.)
- (a) Determine the crystal structure of the element.
- (b) Determine the lattice constant of the element.
- (c) Identify the element.

- *3.11.9 An x-ray diffractometer recorder chart for an element which has either the BCC or the FCC crystal structure showed diffraction peaks at the following 2θ angles: 25.062° , 35.698° , 44.116° , and 51.405° . (Wavelength λ of the incoming radiation was 0.154056 nm.)
- Determine the crystal structure of the element
 - Determine the lattice constant of the element.
 - Identify the element.
- *3.11.10 An x-ray diffractometer recorder chart for an element which has either the BCC or the FCC crystal structure showed diffraction peaks at the following 2θ angles: 38.116° , 44.277° , 64.426° , and 77.472° . (Wavelength of the incoming radiation was 0.154056 nm.)
- Determine the crystal structure of the element.
 - Determine the lattice constant of the element.
 - Identify the element.
- *3.11.11 An x-ray diffractometer recorder chart for an element which has either the BCC or the FCC crystal structure showed diffraction peaks at the following 2θ angles: 40.113° , 46.659° , 68.080° , and 82.090° . (Wavelength λ of the incoming radiation was 0.154056 nm.)
- Determine the crystal structure of the element.
 - Determine the lattice constant of the element.
 - Identify the element.

*Data from International Centre for Diffraction Data

METALS HANDBOOK

8th Edition

VOL. 8

Metallography, Structures and Phase Diagrams

*prepared under direction of the
ASM HANDBOOK COMMITTEE*

Taylor Lyman, Editor (deceased 8 March 1973)
Howard E. Boyer, Managing Editor
William J. Carnes, Chief Copy Editor
Margaret W. Chevalier, Chief Illustrator

Senior Editors:
Edward A. Durand and Paul M. Unterweiser

Associate Editors:
Hugh Baker, Philip D. Harvey and
Helen Lawton Waldorf

Assistant Editors:
Helen V. Bukovics, Craig W. Kirkpatrick
and Jack W. Kothera



AMERICAN SOCIETY FOR METALS

Metals Park, Ohio 44073

Copyright © 1973

BY THE

AMERICAN SOCIETY FOR METALS

All rights reserved

No part of this book may be reproduced, stored in a retrieval system, or transmitted, in any form or by any means, electronic, mechanical, photocopying, recording, or otherwise, without the prior written permission of the publisher.

First printing, September 1973

Nothing contained in the Metals Handbook is to be construed as a grant of any right of manufacture, sale, or use in connection with any method, process, apparatus, product, or composition, whether or not covered by letters patent or registered trade mark, nor as a defense against liability for the infringement of letters patent or registered trade mark.

Library of Congress Catalog Card Number: 27-12046

PRINTED IN THE UNITED STATES OF AMERICA

CONSTITUTION OF BINARY ALLOYS

By DONALD T. HAWKINS and RALPH HULTGREN*

CONTENTS

Introduction	251
Phase Diagrams of Binary Alloy Systems	252
Notes and References for Binary Phase Diagrams	339

Introduction

THIS SECTION presents phase diagrams for 434 binary alloy systems, selected to serve the largest number of industrial metallurgists. Many of the diagrams were provided by contributors familiar experimentally with the systems; the remainder were selected by the authors from the literature. The contributor's name or initials appear at the lower left of each diagram. Contributors other than the authors are listed at the bottom of this page.

The phase diagrams are in the alphabetical order of the chemical symbols of the components. The symbol for the more important component is on the left side of the diagram. Intermetallic

phases are designated by consecutive Greek letters, left to right, except for phases having other generally accepted designations, such as the sigma phase. Terminal solid solutions are identified by the symbol for the element, in parentheses, instead of by Greek letters.

The diagrams are plotted in weight percentages; however, atomic percentage is shown at the top of each diagram. Temperature is plotted in degrees Centigrade; degrees Fahrenheit are also indicated. All temperatures were corrected to the 1968 International Practical Temperature Scale.[†] Known temperatures are indicated in Centigrade with a degree sign; known compositions, by numbers (usually with no per cent signs). All constructions agree with the general laws of phase equilibria. Many regions are shown in detail on an enlarged scale.

Dashed lines on the diagrams signify doubt as to the position of the line in question. A dotted line signifies the Curie and Néel magnetic transformation

temperatures. Notes and references for each alloy system in the diagrams, as well as for 18 systems for which no diagrams are shown, are presented in the section that begins on page 339. Crystal structures of intermediate phases of many systems are tabulated with the notes, and are collated into the table that begins on page 243. Crystal structures of the elements are given in the table on page 242.

Melting points and transformation temperatures of the pure elements are in accordance with the tables on the back endpapers in this volume.

Many diagrams here were adopted from those published by M. Hansen, and in the supplements by R. P. Elliott and F. A. Shunk (see general references 3, 4 and 5 in the list on page 339).

We are grateful to the contributors of diagrams and data, to Stephen S. Vogt and David K. Mullin, who assisted with plotting and calculations, and to Leo Brewer, who provided some of the references and crystal structures.

*Dr. Hawkins is Information Scientist, Bell Laboratories, Murray Hill, N. J. (formerly, Research Metallurgist, Lawrence Berkeley Laboratory, University of California). Dr. Hultgren is Professor Emeritus—Metallurgy, Dept. of Materials Science and Engineering, Lawrence Berkeley Laboratory, University of California.

[†]For a discussion of the 1948 and 1968 temperature scales, see T. B. Douglas, *J Res Nat Bur Std*, Vol 73A (1969), p 451-470.

Contributors of Phase Diagrams for Binary Alloy Systems

HALLE ABRAMS, Research Engineer, Alloy Development Section, Homer Research Laboratories, Bethlehem Steel Corp.; DAVID G. ALEXANDER, Assistant Metallurgist, Ames Laboratory USAEC, Iowa State University; DENNIS BISHOP, Research Engineer, Metals Research Laboratories, Olin Corp.; BRUCE L. BRAMFITT, Research Engineer, Homer Research Laboratories, Bethlehem Steel Corp.; W. G. BUGDEN, Investigator, Johnson, Matthey & Co., Ltd.; R. N. CARON, Research Metallurgist, Metals Research Laboratories, Olin Corp.

Y. AUSTIN CHANG, Professor and Chairman, Materials Dept., College of Engineering and Applied Sciences, University of Wisconsin—Milwaukee; J. C. CHASTON, Consulting Metallurgist; JOHN CHIPMAN, Professor Emeritus, Massachusetts Institute of Technology; S. L. COULING, Senior Technical Advisor, Battelle—Columbus Laboratories; JACK CRANE, Section Chief, Physical Metallurgy, Olin Corp.; A. S. DARLING, Research Consultant, Johnson, Matthey & Co., Ltd.

CARL DiMARTINI, Superintendent, Physical Metallurgy, Central Research Laboratories, American Smelting & Refining Co.; FINLEY H. ELLINGER, Metallurgist, Los Alamos Scientific Laboratory; SAM FRIEDMAN, Research Metallurgist, Metals Research Laboratories, Olin Corp.; J. I. GOLDSTEIN, Associate Professor, Dept. of Metallurgy and Materials Science, Lehigh University; M. ILEGEMS, Technical Staff, Bell Laboratories; ROBERT E. JOHNSON, Senior Process Engineer, Engineering Center, Kennecott Copper Corp.

HERBERT H. KELLOGG, Stanley-Thompson Professor of Chemical Metallurgy, Henry Krumb School of Mines, Columbia University; A. G. KNAPTON, Senior Metallurgist, Johnson, Matthey & Co., Ltd.; AVINASH D. KULKARNI, Staff Scientist, Chase Brass and Copper Co.; RICHARD D. LANAM, Engineer-Specialist, Metals Research Laboratories, Olin Corp.; A. R. MARDER, Supervisor, Research Dept., Homer Research Laboratory, Bethlehem Steel Corp.; HAROLD MARGOLIN, Professor of Metallurgical Engineering, Dept. of Metallurgy and Materials Sciences, New York University; DANIEL J. MAYKUTH, Director, Cobalt Information Center, Bat-

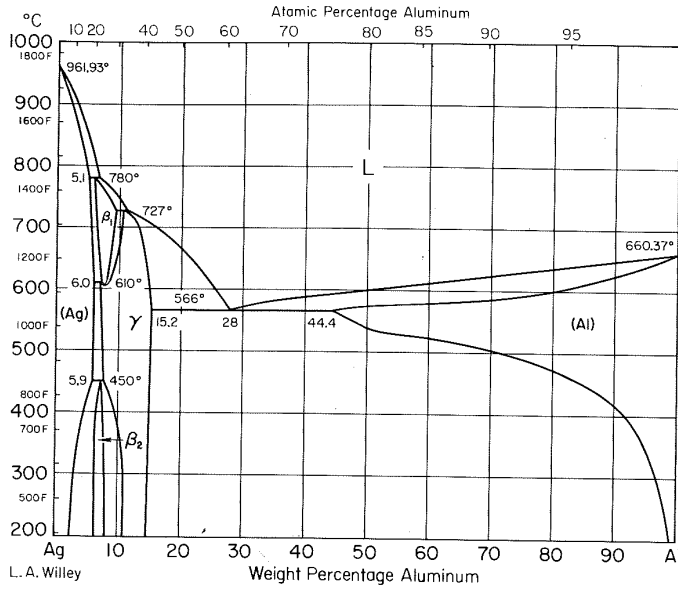
telle—Columbus Laboratories; E. C. OREN, Engineer, Homer Research Laboratories, Bethlehem Steel Corp.; MORTON B. PANISH, Technical Staff, Bell Laboratories; M. VIKRAM RAO, Research Associate, Dept. of Materials Science and Engineering, Stanford University; F. N. RHINES, Professor and Chairman, Dept. of Materials Science and Engineering, University of Florida; MALCOLM J. ROBERTS, Research Supervisor, Homer Research Laboratories, Bethlehem Steel Corp.; PRADEEP K. ROHATGI, Research Engineer, Homer Research Laboratories, Bethlehem Steel Corp.

ROBERT C. RUHL, Director of Engineering, Chase Brass and Copper Co.; G. L. SELMAN, Department Manager, Metallurgical Research, Johnson, Matthey & Co., Ltd.; EUGENE SHAPIRO, Group Supervisor, Metals Research Laboratories, Olin Corp.; STANLEY SHAPIRO, Metal Structures Group Supervisor, Metals Research Laboratories, Olin Corp.; SUDHIR K. SHARMA, Research Engineer, Homer Research Laboratories, Bethlehem Steel Corp.; WALTER SHOWAK, Supervisor, Applications Research, Research Dept., New Jersey Zinc Co. (Gulf+Western).

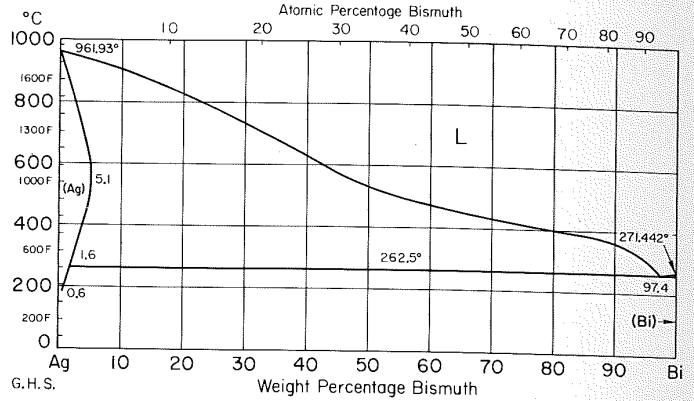
JAMES W. SIMPSON, Research Scientist, Applications Research Div., Research Dept., New Jersey Zinc Co. (Gulf+Western); GEORGE H. SISTARE, Metallurgical Consultant, Technical Laboratory, Handy & Harman; WARREN F. SMITH, JR., Metallurgist, Olin Corp.; CHARLES E. SOHL, Patent Associate, Metals Research Laboratories, Olin Corp.

E. T. STEPHENSON, Research Engineer, Homer Research Laboratories, Bethlehem Steel Corp.; EDMUND K. STORMS, Staff Member, Los Alamos Scientific Laboratory; THEODORE E. TOROK, Research Engineer, Homer Research Laboratories, Bethlehem Steel Corp.; PHILIP A. TUCKER, Group Leader, Mound Laboratory, Monsanto Research Corp.; DEREK TYLER, Supervisor, Process Sciences Group, Metals Research Laboratories, Olin Corp.; RICHARD M. WATERSTRAT, Research Associate, American Dental Assn. Research Unit, National Bureau of Standards; LOWELL A. WILLEY (retired), Alcoa Research Laboratories; L. R. WOODYATT, Research Engineer, Homer Research Laboratories, Bethlehem Steel Corp.; CARL A. ZAPFFE, Consulting Metallurgist.

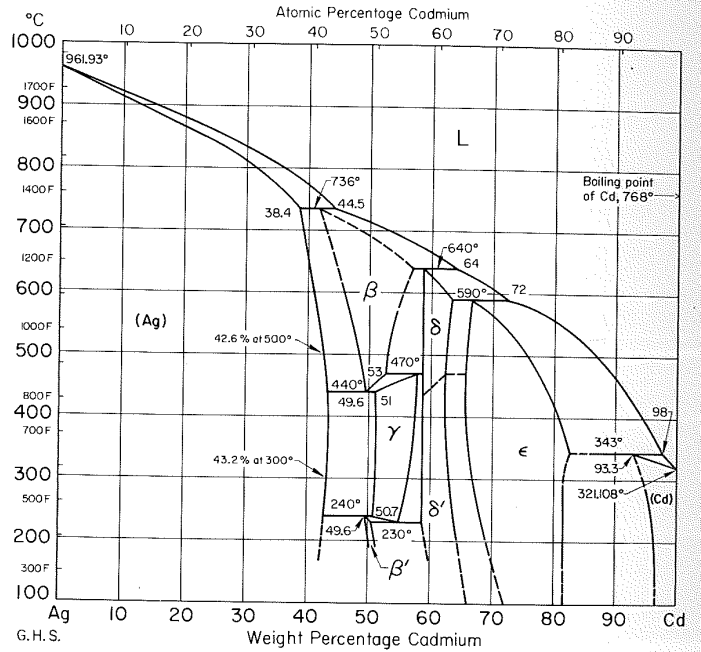
Ag-Al Silver-Aluminum



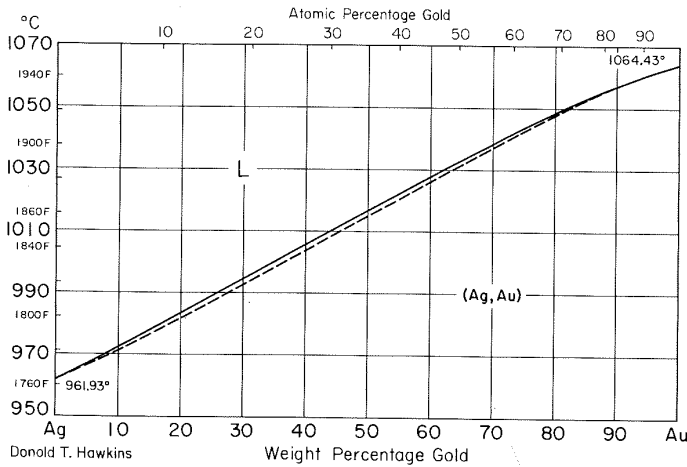
Ag-Bi Silver-Bismuth



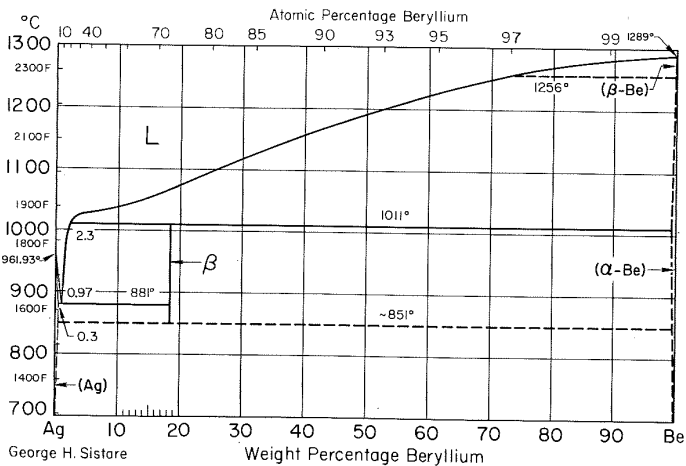
Ag-Cd Silver-Cadmium



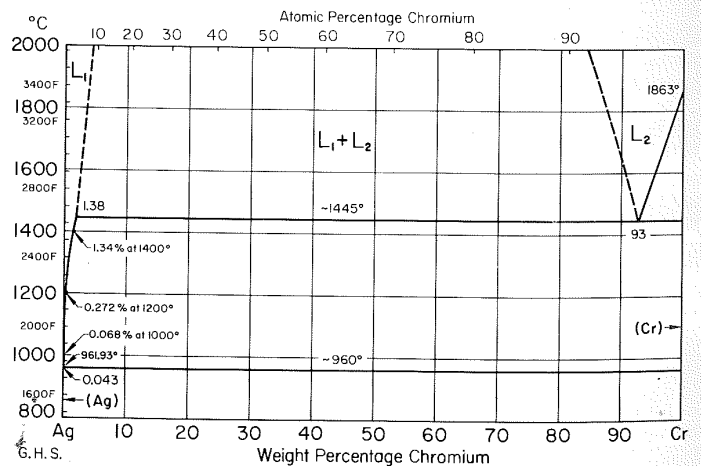
Ag-Au Silver-Gold



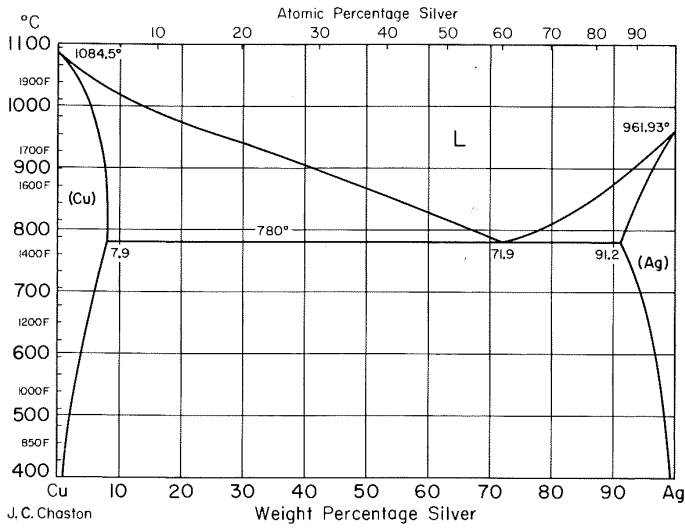
Ag-Be Silver-Beryllium



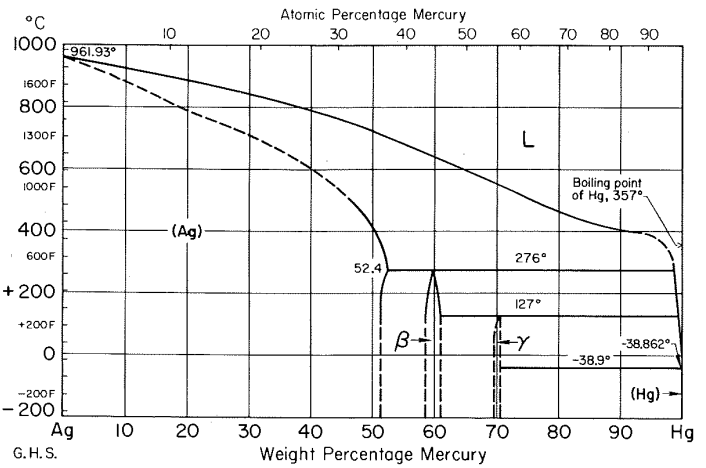
Ag-Cr Silver-Chromium



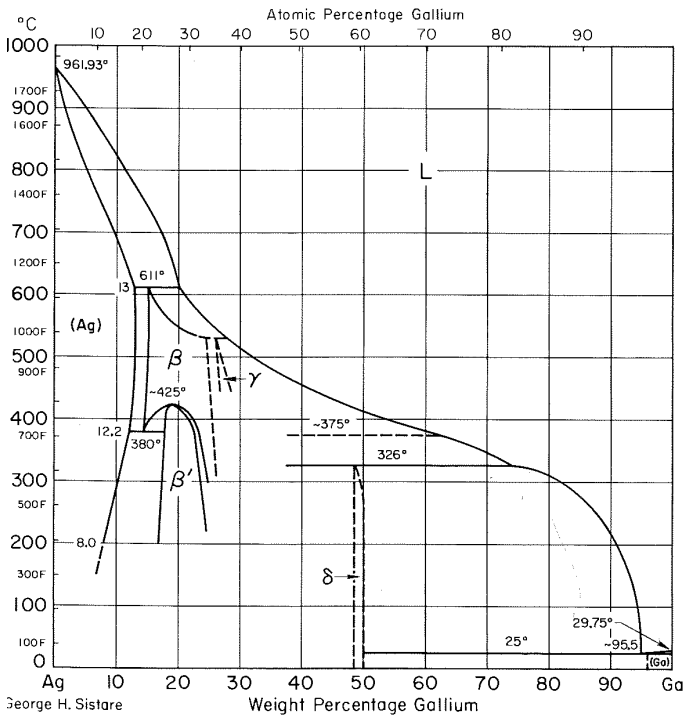
Ag-Cu Silver-Copper



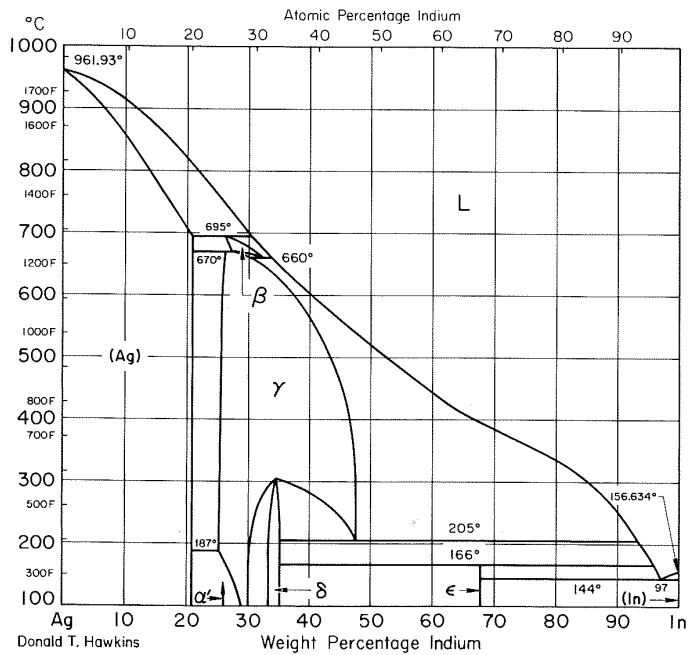
Ag-Hg Silver-Mercury



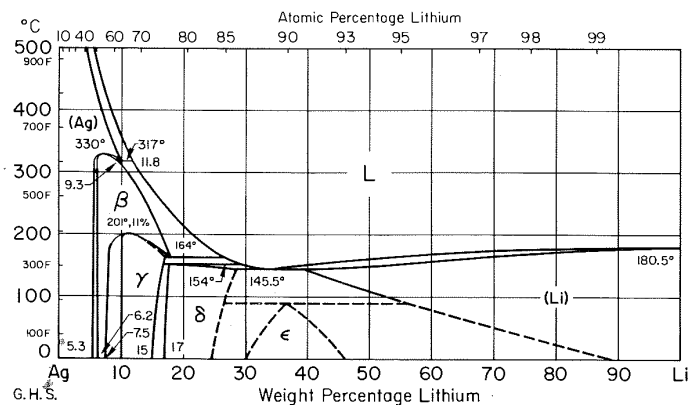
Ag-Ga Silver-Gallium



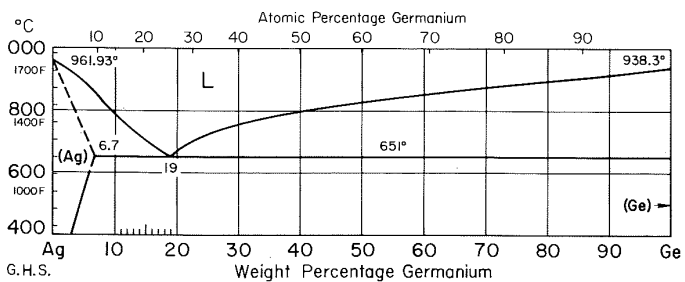
Ag-In Silver-Indium



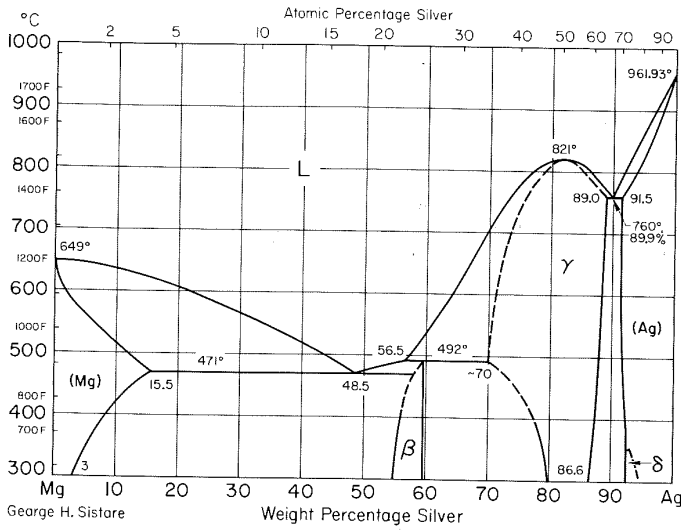
Ag-Li Silver-Lithium



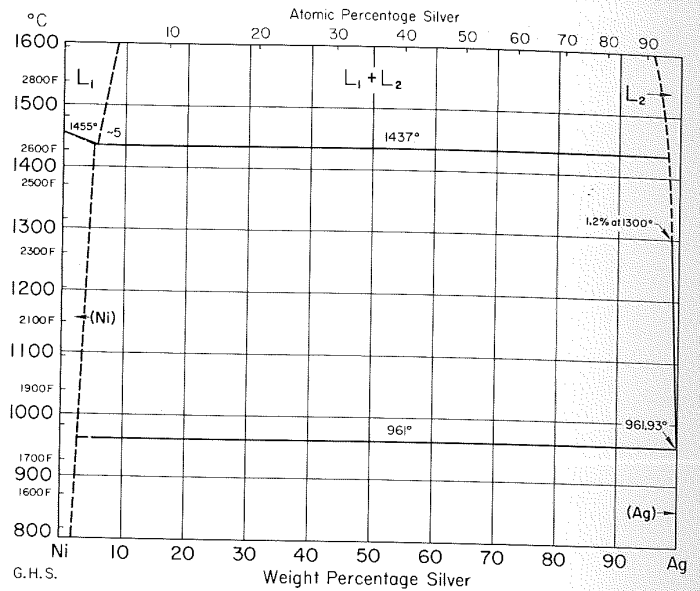
Ag-Ge Silver-Germanium



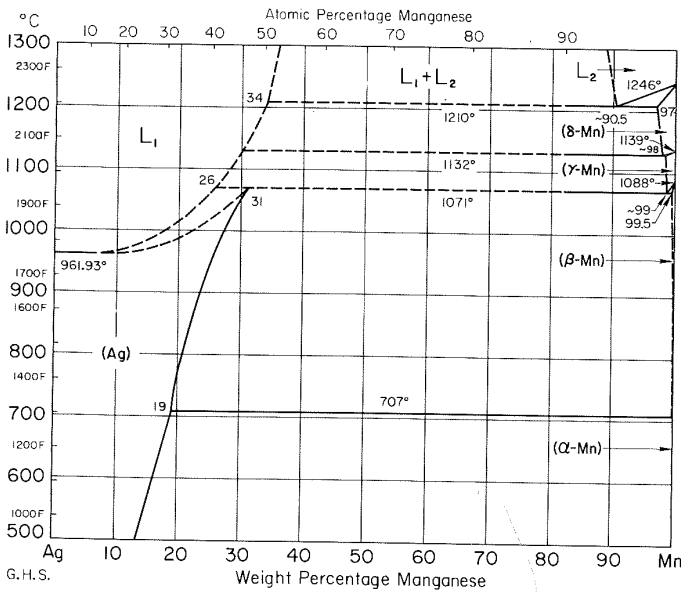
Ag-Mg Silver-Magnesium



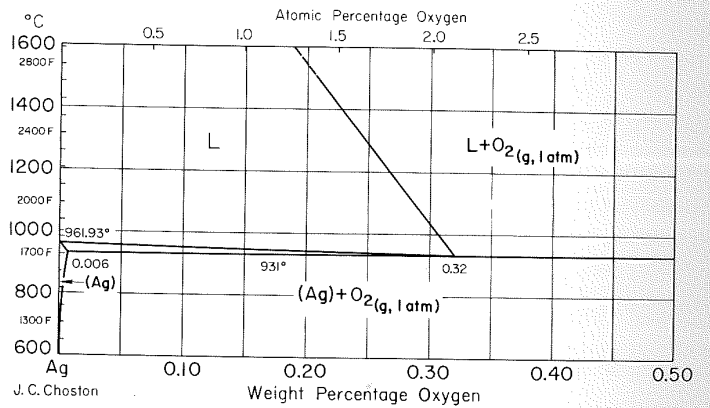
Ag-Ni Silver-Nickel



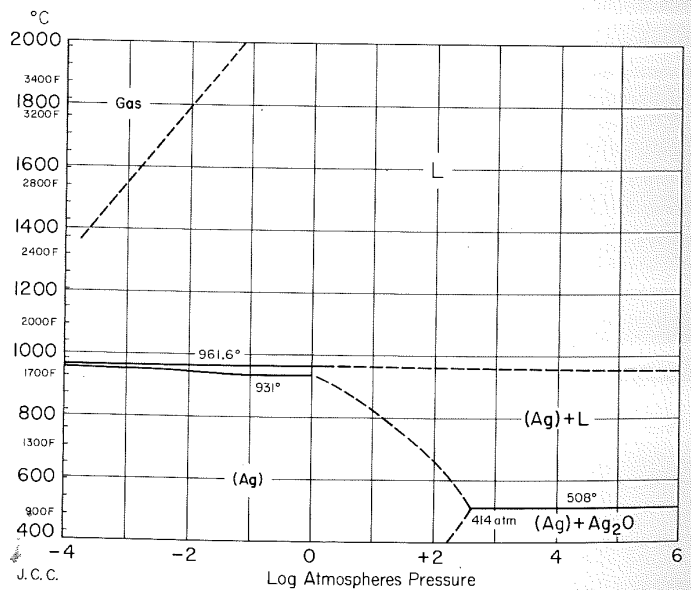
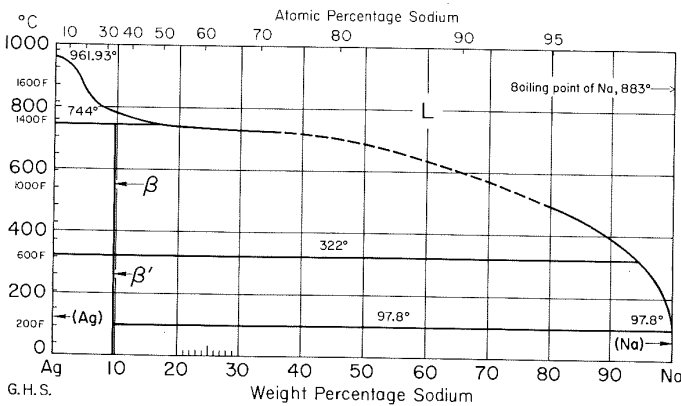
Ag-Mn Silver-Manganese



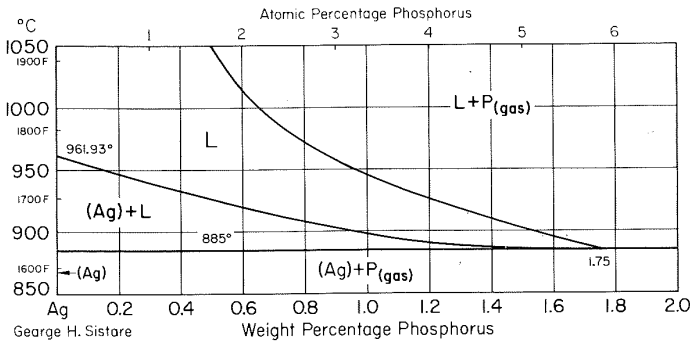
Ag-O Silver-Oxygen



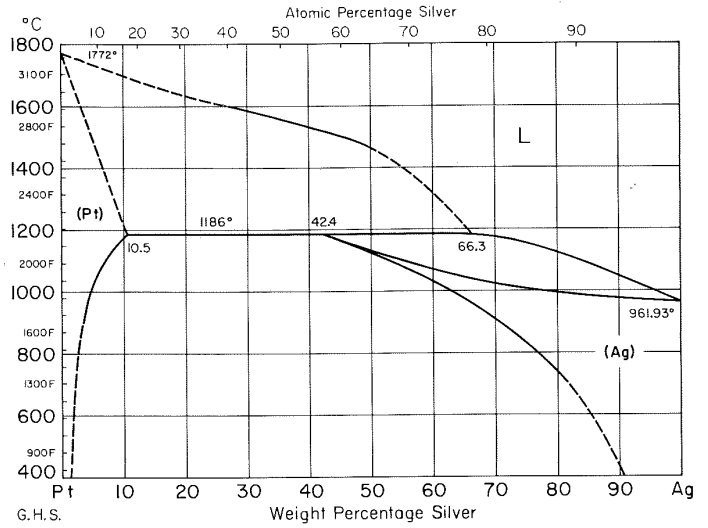
Ag-Na Silver-Sodium



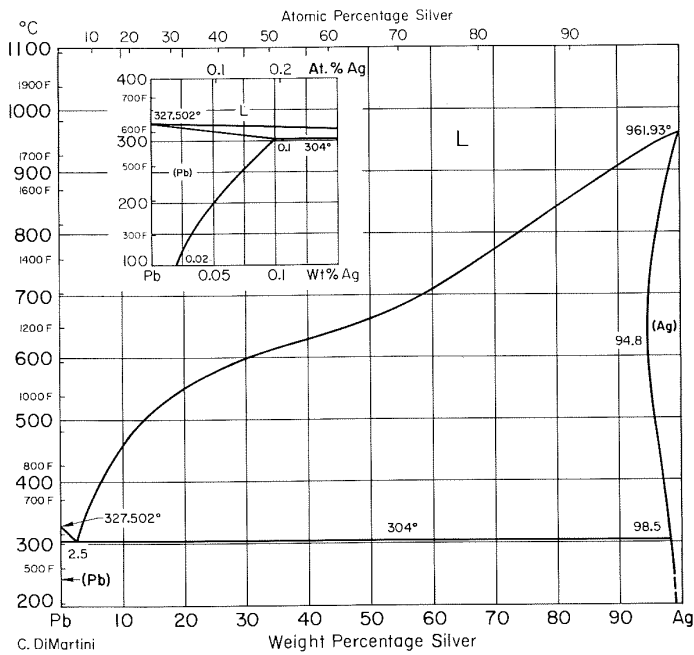
Ag-P Silver-Phosphorus



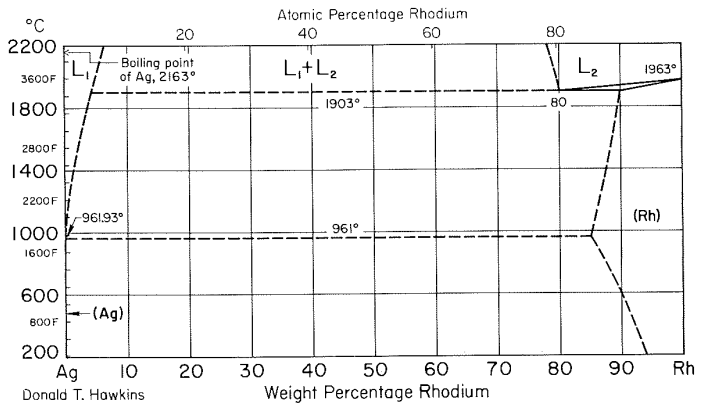
Ag-Pt Silver-Platinum



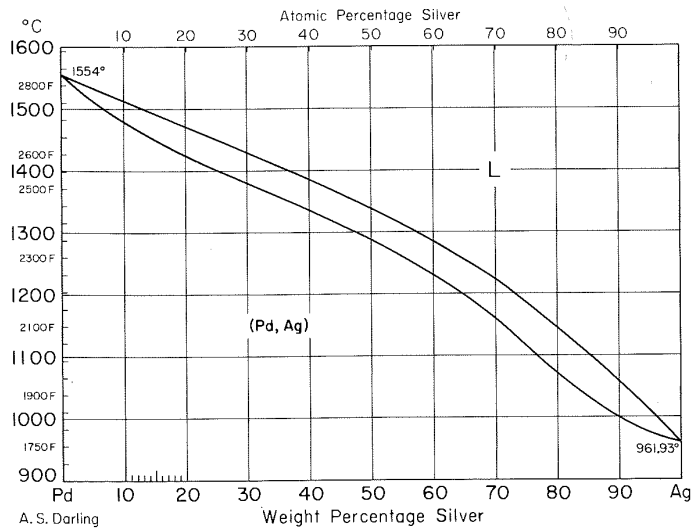
Ag-Pb Silver-Lead



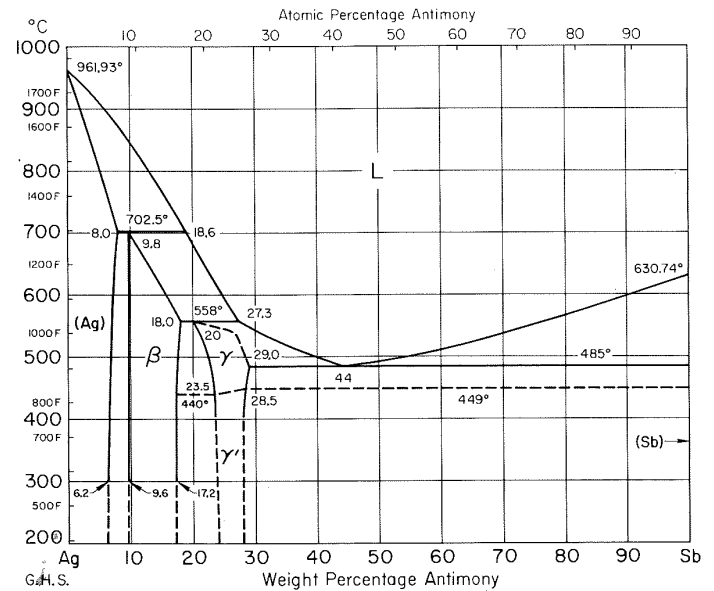
Ag-Rh Silver-Rhodium



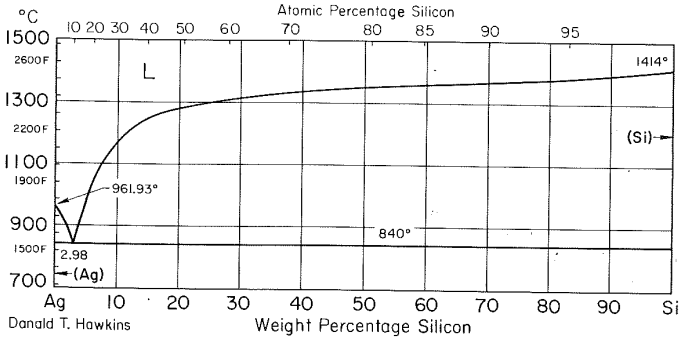
Ag-Pd Silver-Palladium



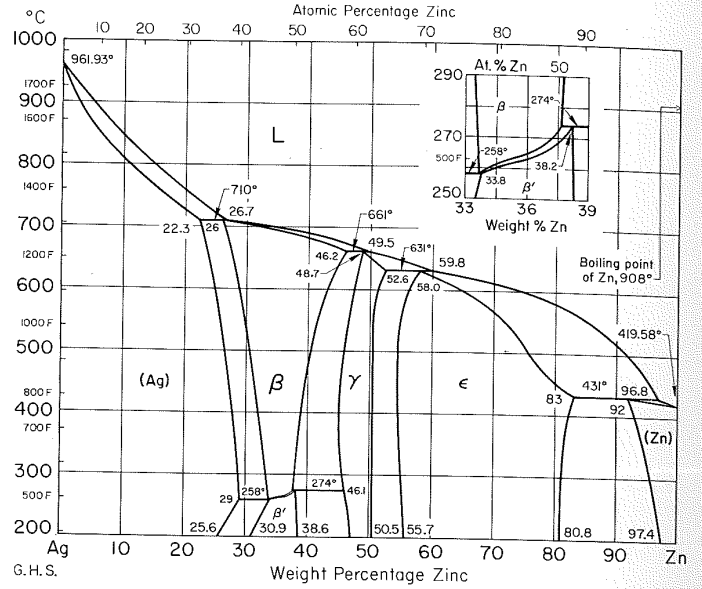
Ag-Sb Silver-Antimony



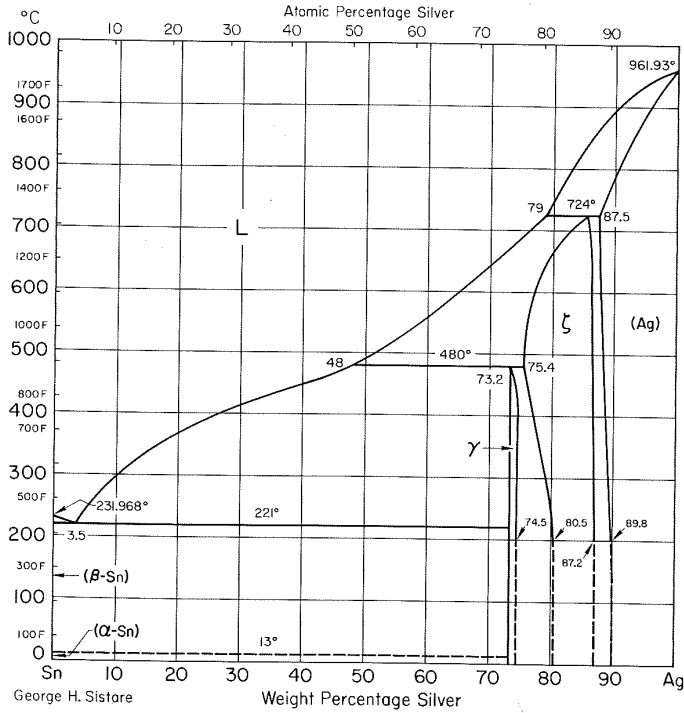
Ag-Si Silver-Silicon



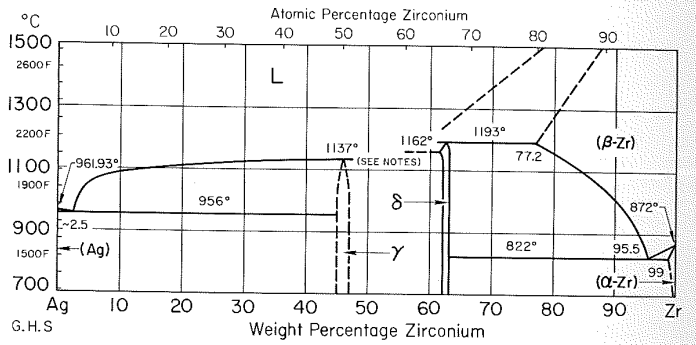
Ag-Zn Silver-Zinc



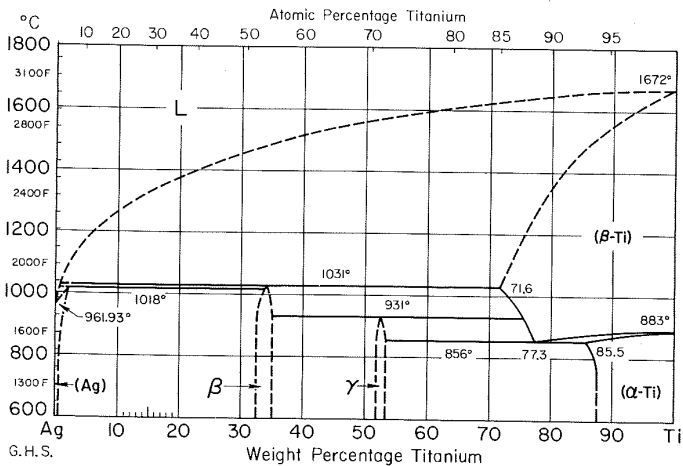
Ag-Sn Silver-Tin



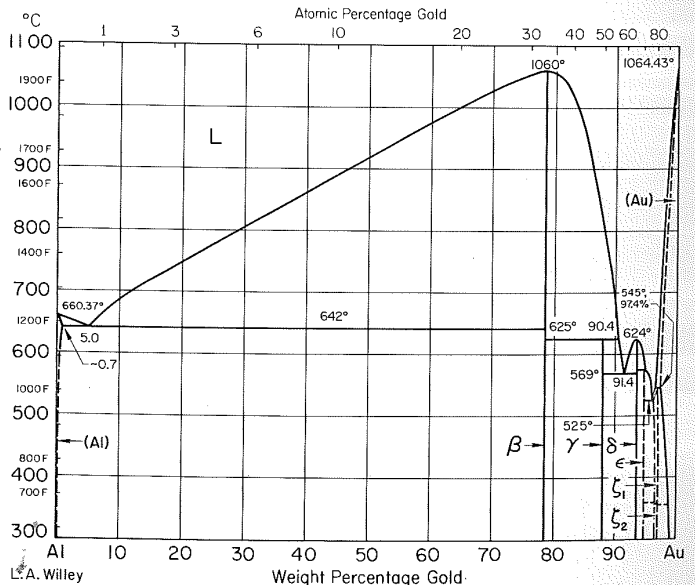
Ag-Zr Silver-Zirconium



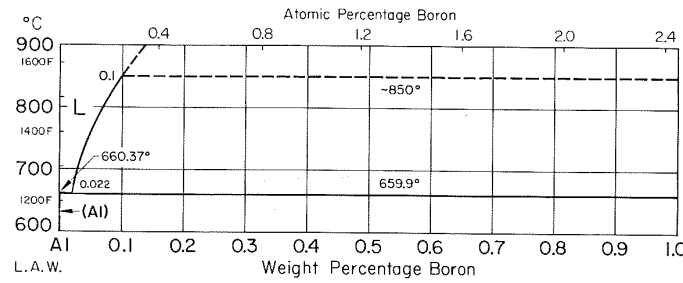
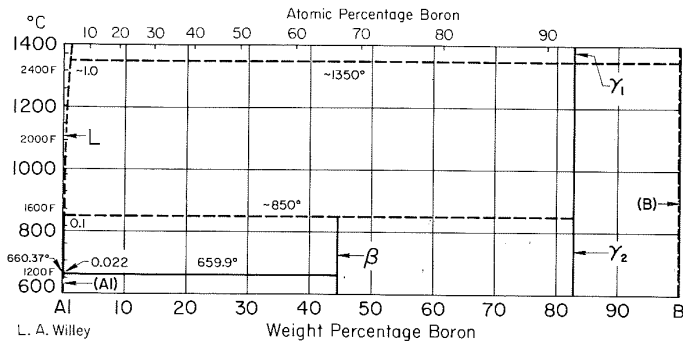
Ag-Ti Silver-Titanium



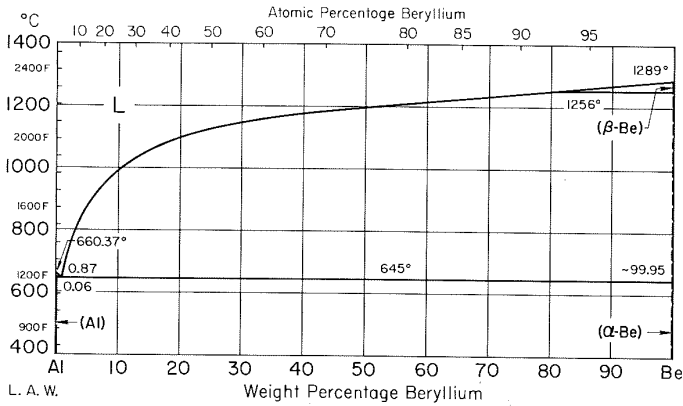
Al-Au Aluminum-Gold



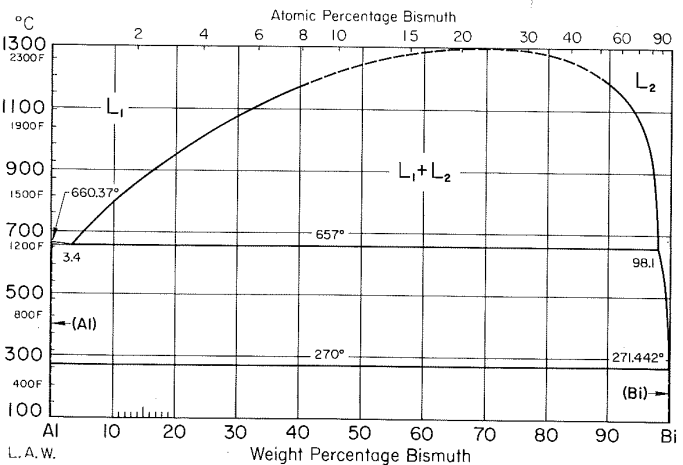
Al-B Aluminum-Boron



Al-Be Aluminum-Beryllium



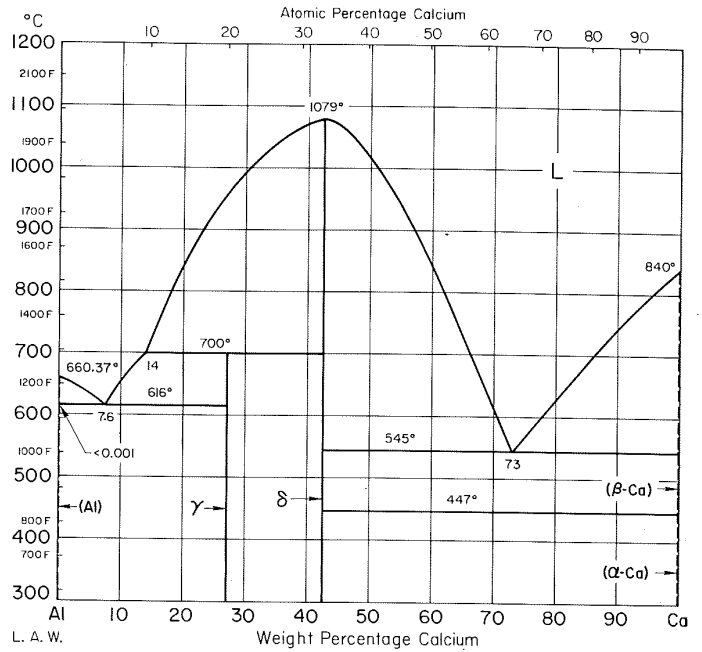
Al-Bi Aluminum-Bismuth



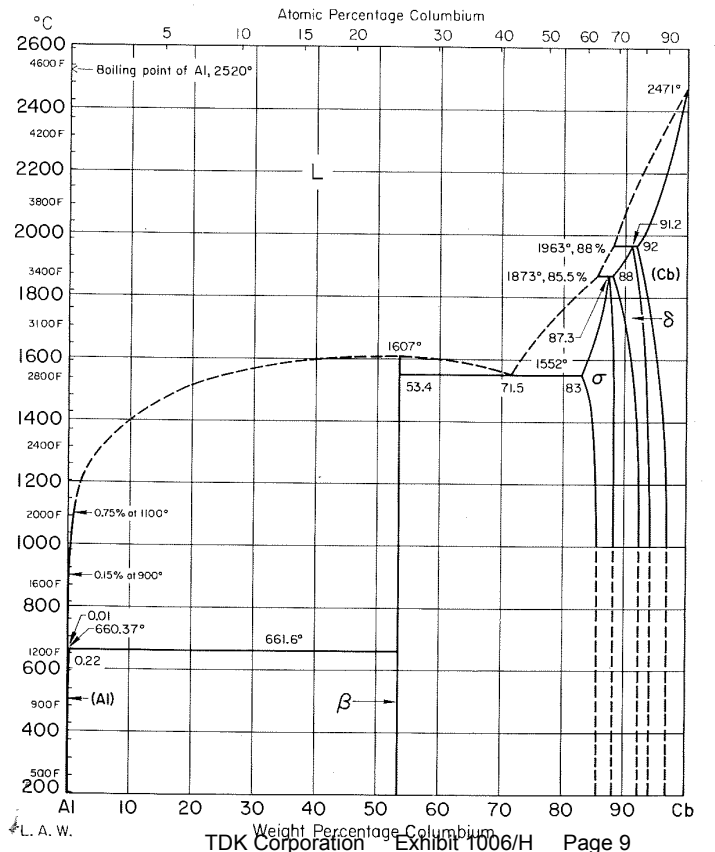
Al-C Aluminum-Carbon

See Notes.

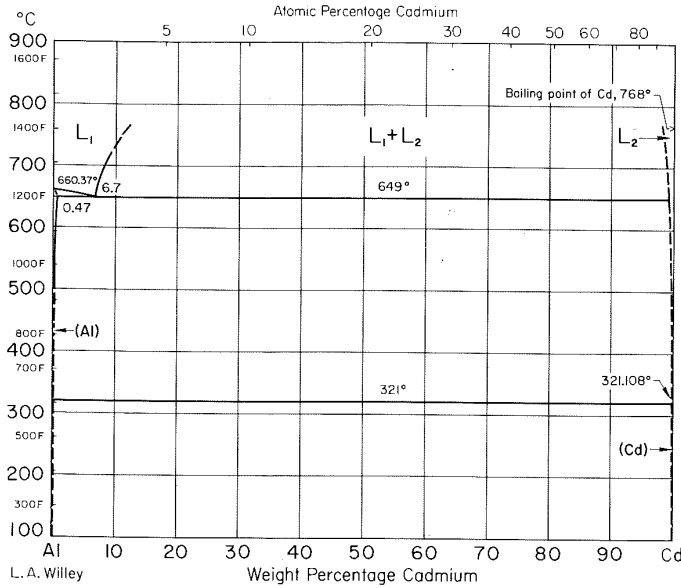
Al-Ca Aluminum-Calcium



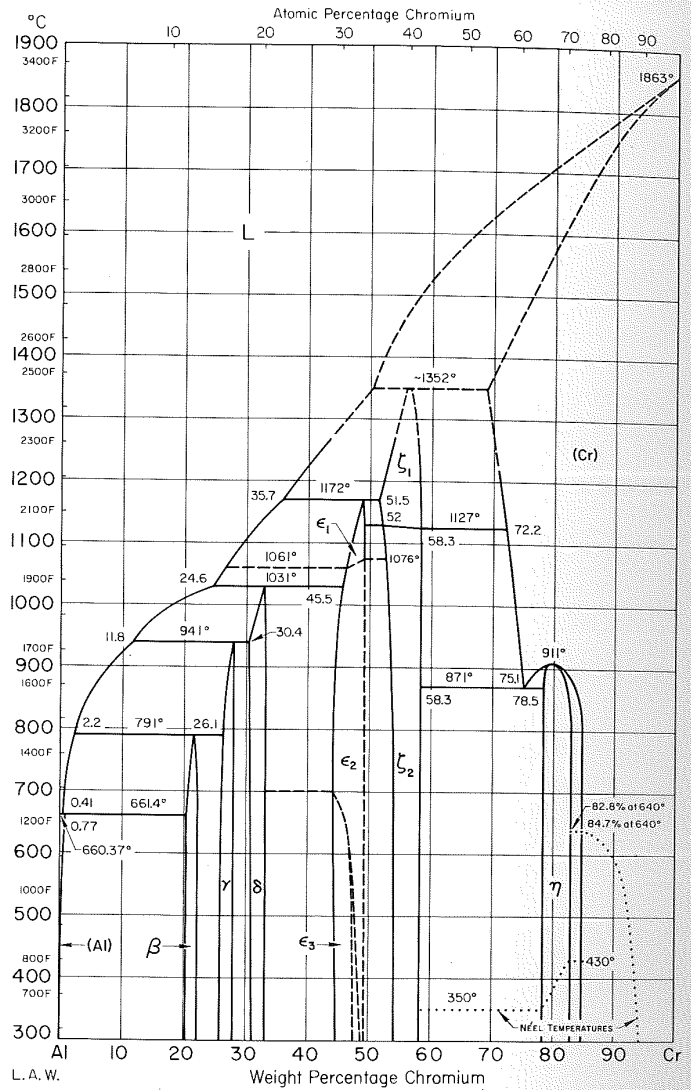
Al-Cb Aluminum-Columbium



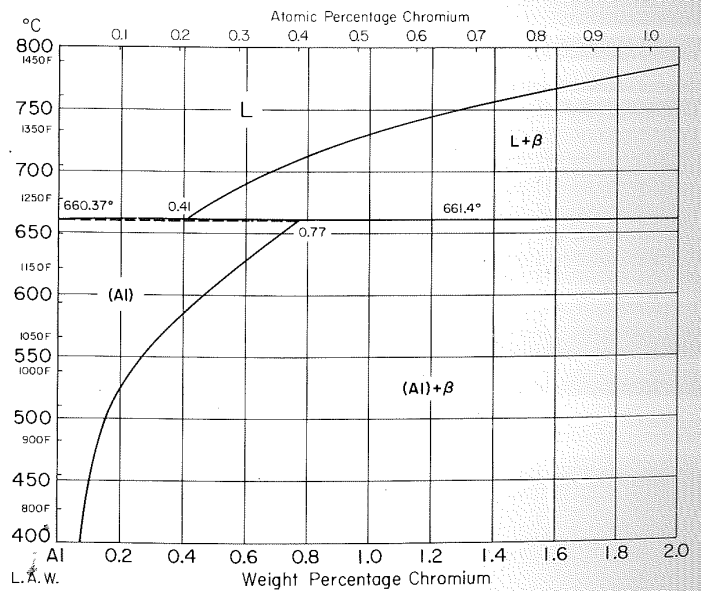
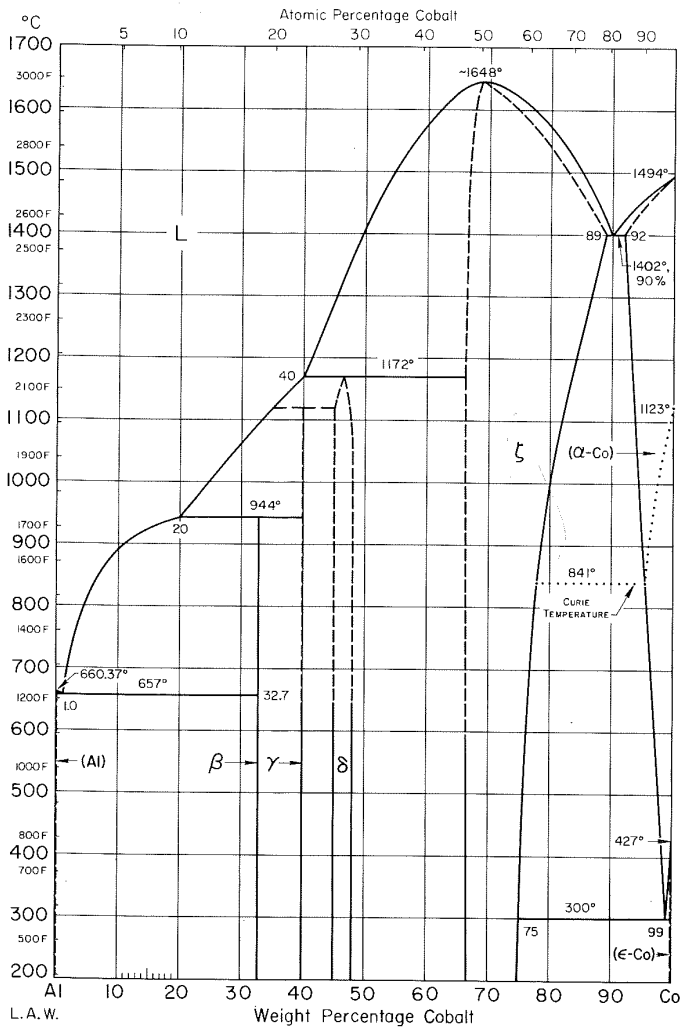
Al-Cd Aluminum-Cadmium



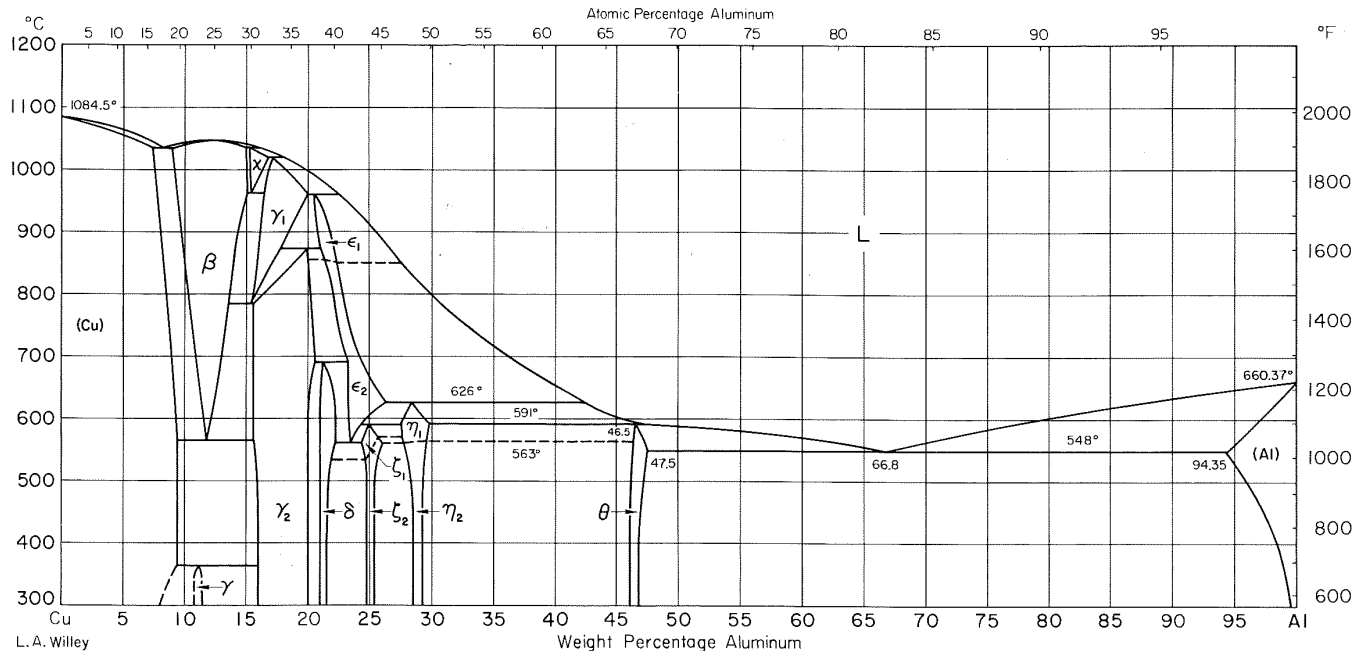
Al-Cr Aluminum-Chromium



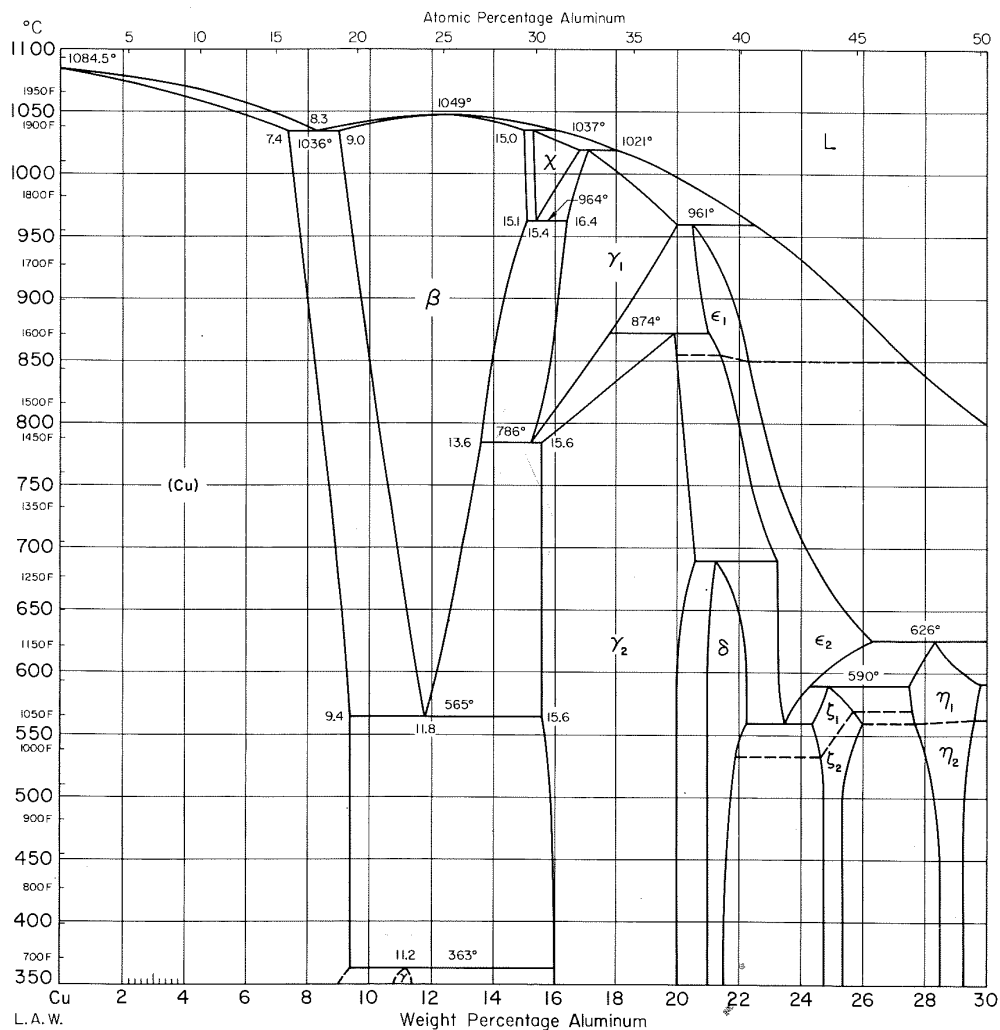
Al-Co Aluminum-Cobalt



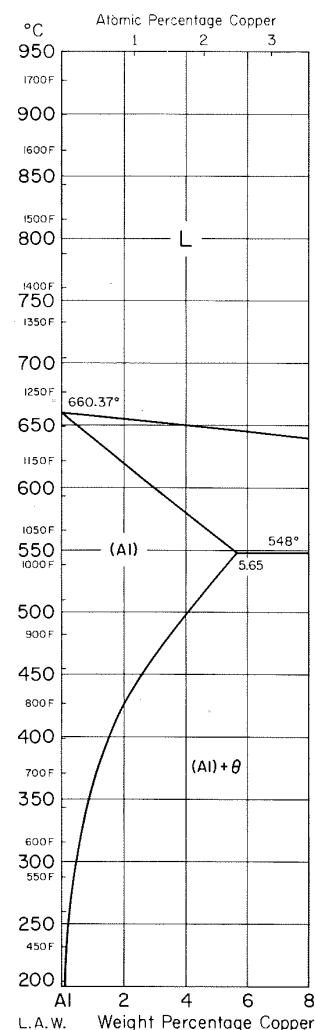
Al-Cu Aluminum-Copper



L. A. Willey

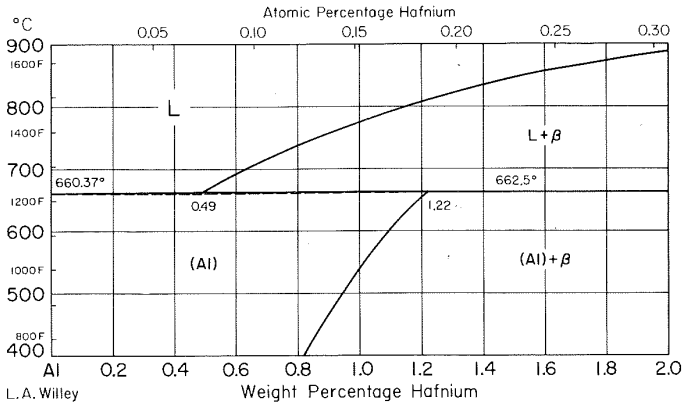


L. A. W.

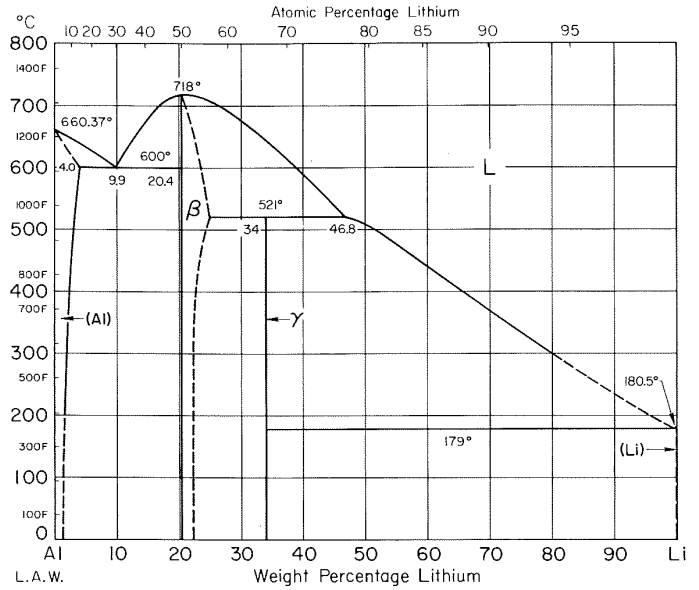


L. A. W.

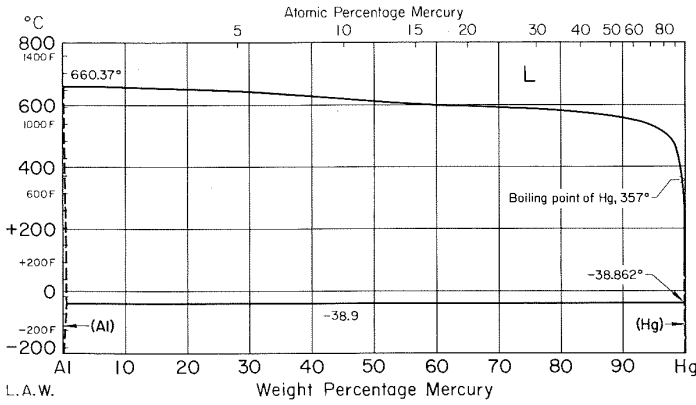
Al-Hf Aluminum-Hafnium



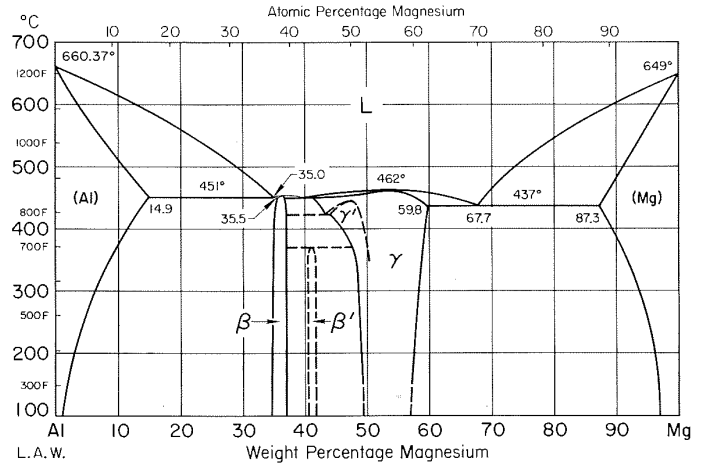
Al-Li Aluminum-Lithium



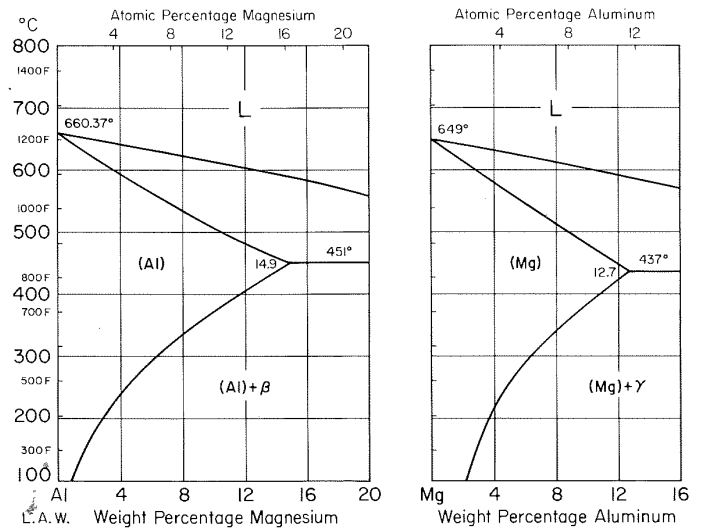
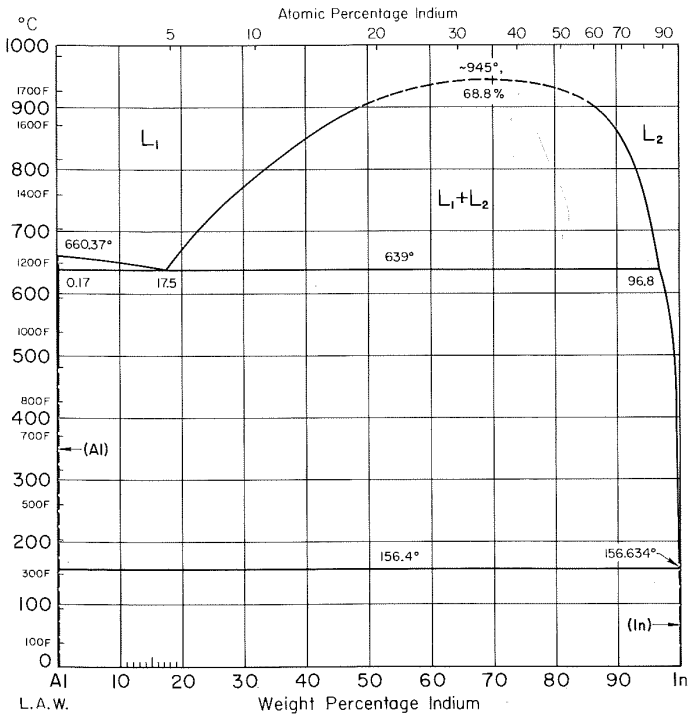
Al-Hg Aluminum-Mercury



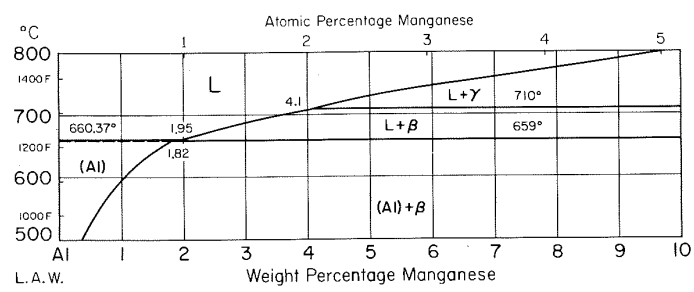
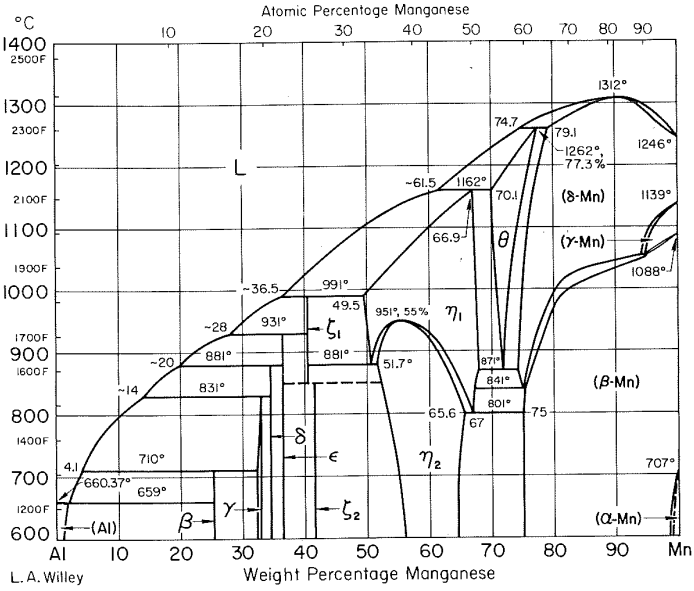
Al-Mg Aluminum-Magnesium



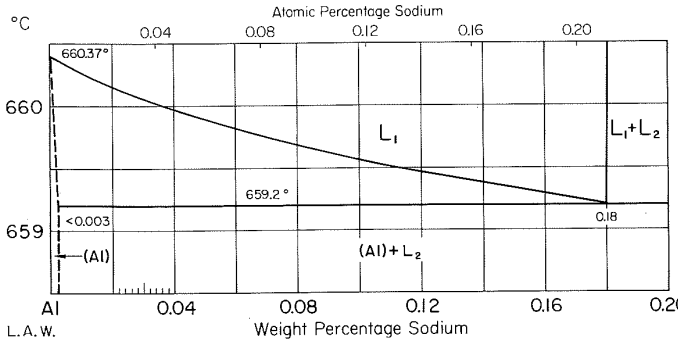
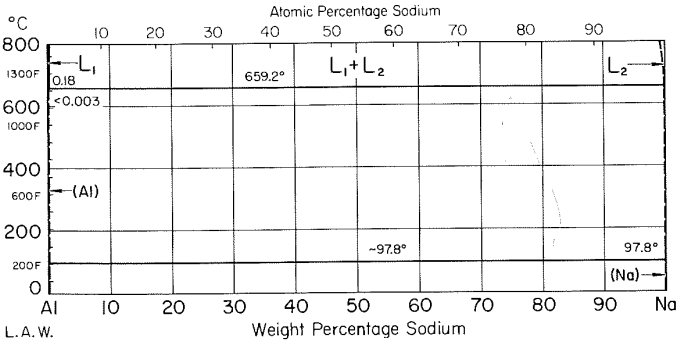
Al-In Aluminum-Indium



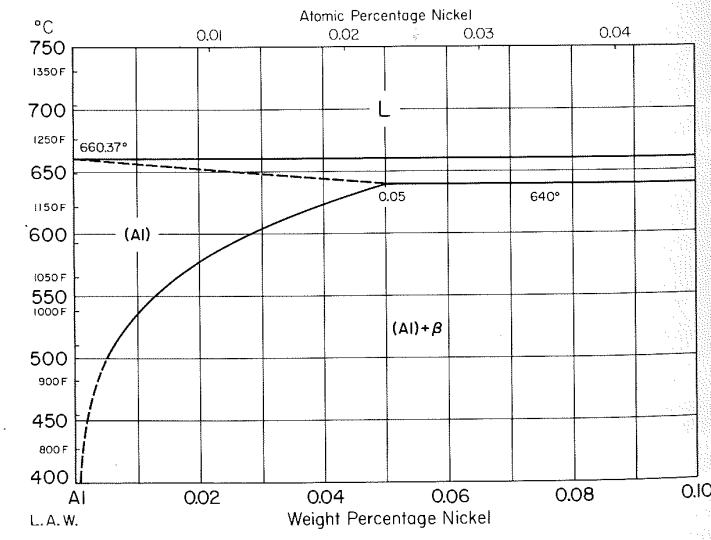
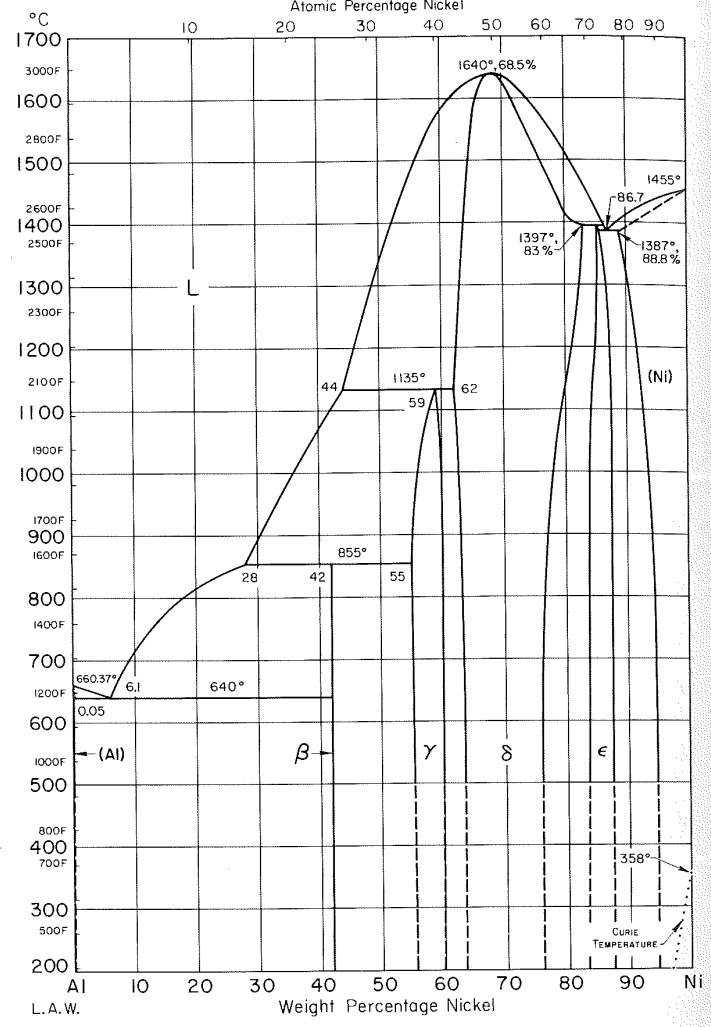
Al-Mn Aluminum-Manganese



Al-Na Aluminum-Sodium



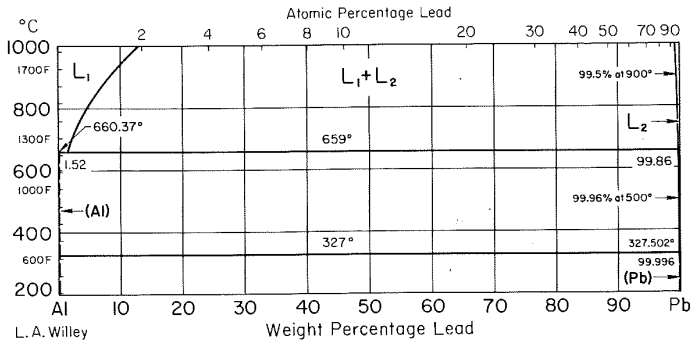
Al-Ni Aluminum-Nickel



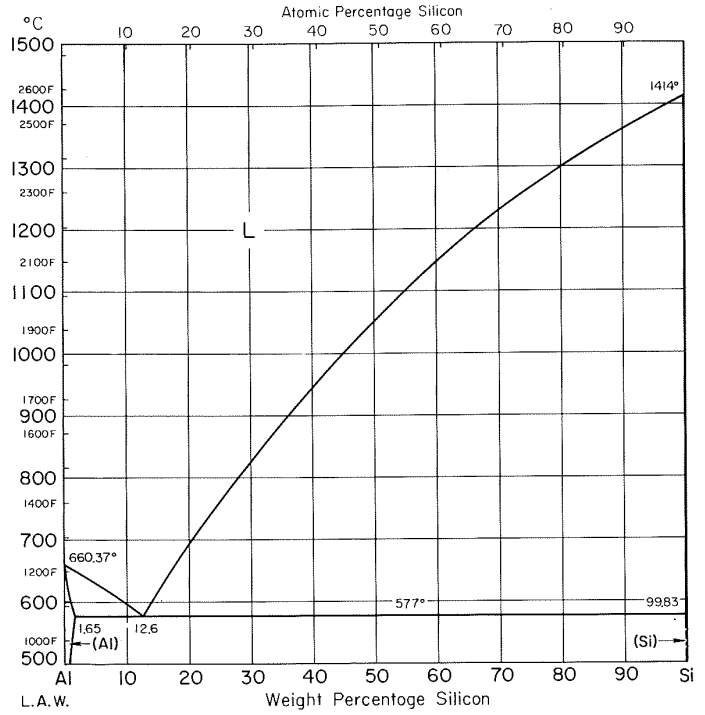
Al-O Aluminum-Oxygen

See Notes.

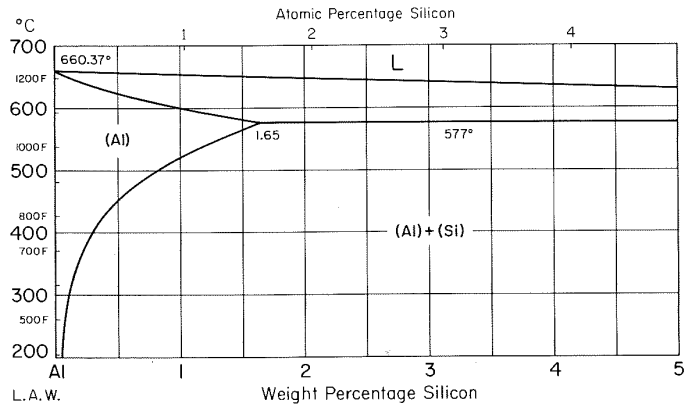
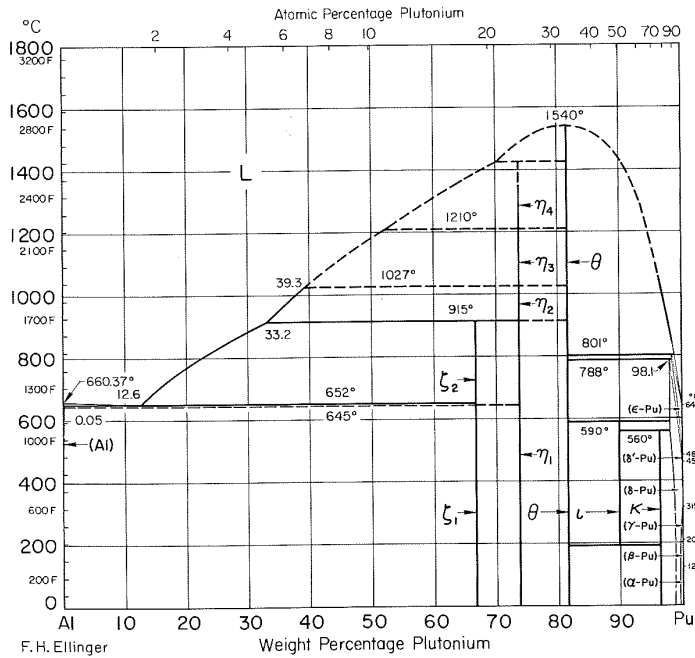
Al-Pb Aluminum-Lead



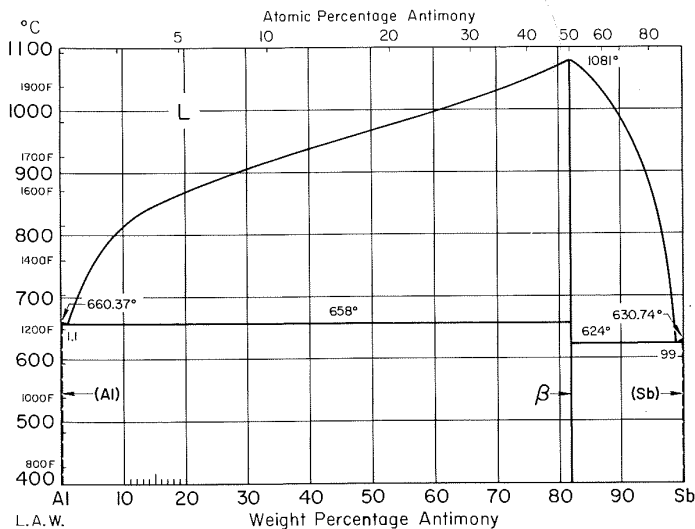
Al-Si Aluminum-Silicon



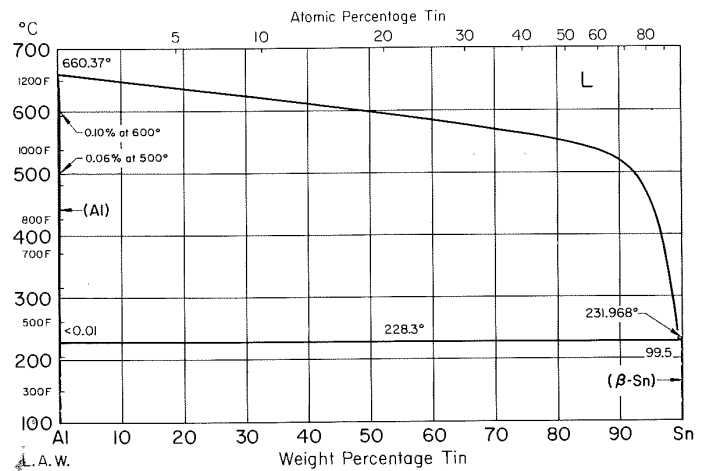
Al-Pu Aluminum-Plutonium



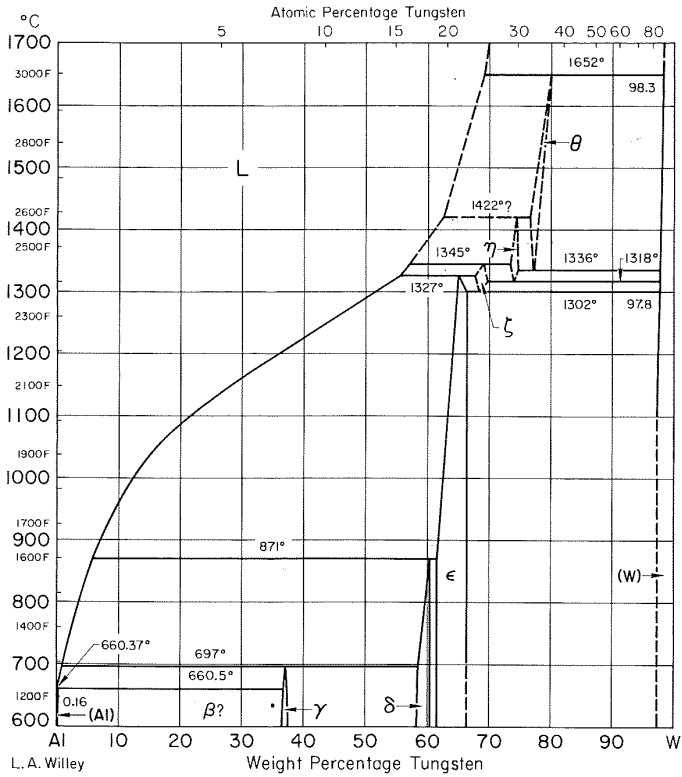
Al-Sb Aluminum-Antimony



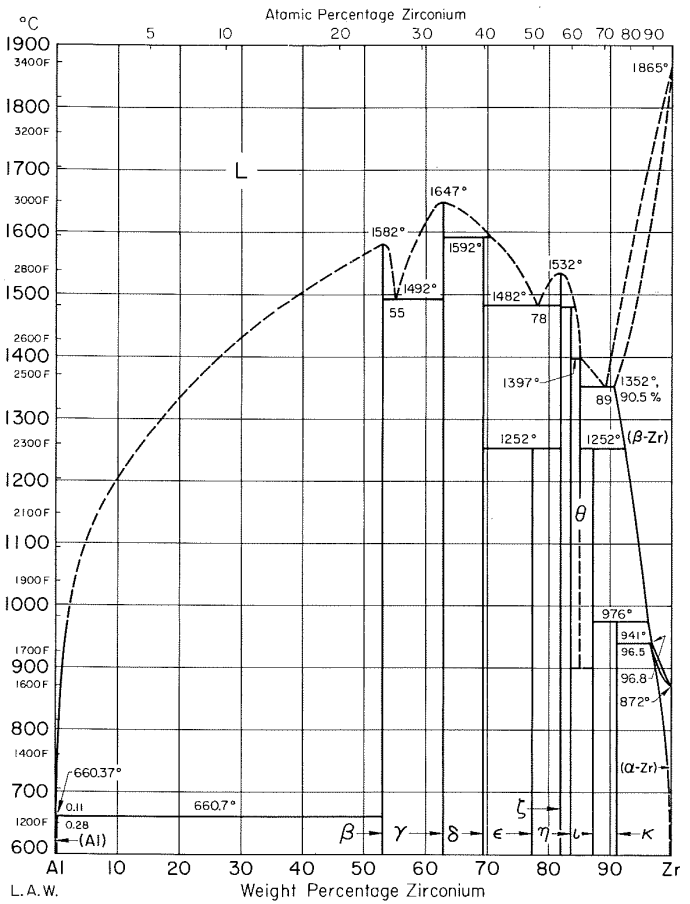
Al-Sn Aluminum-Tin



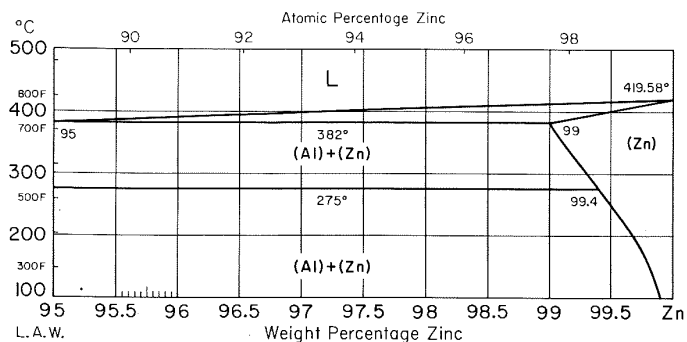
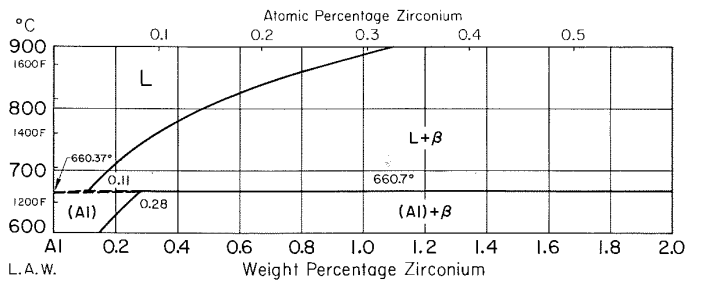
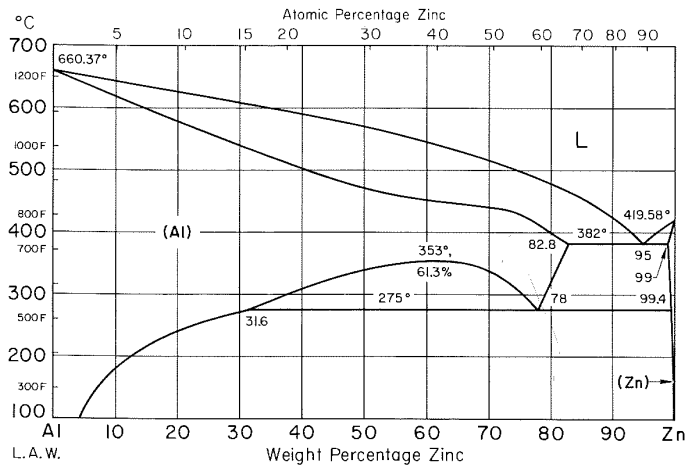
Al-W Aluminum-Tungsten



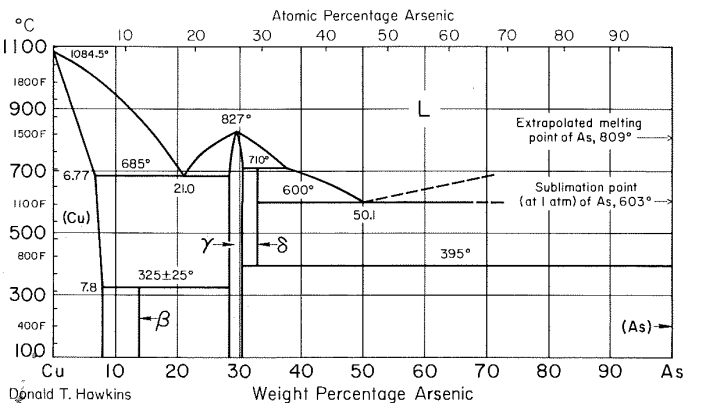
Al-Zr Aluminum-Zirconium



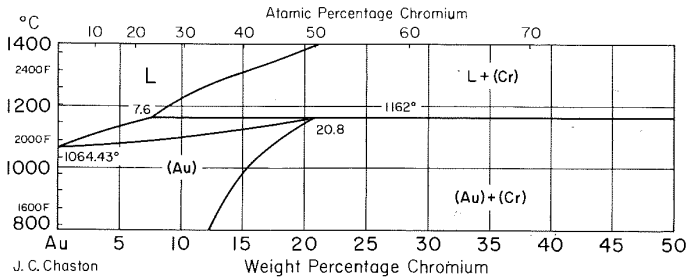
Al-Zn Aluminum-Zinc



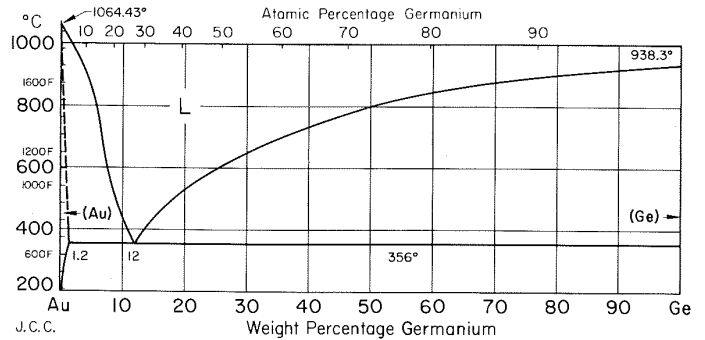
As-Cu Arsenic-Copper



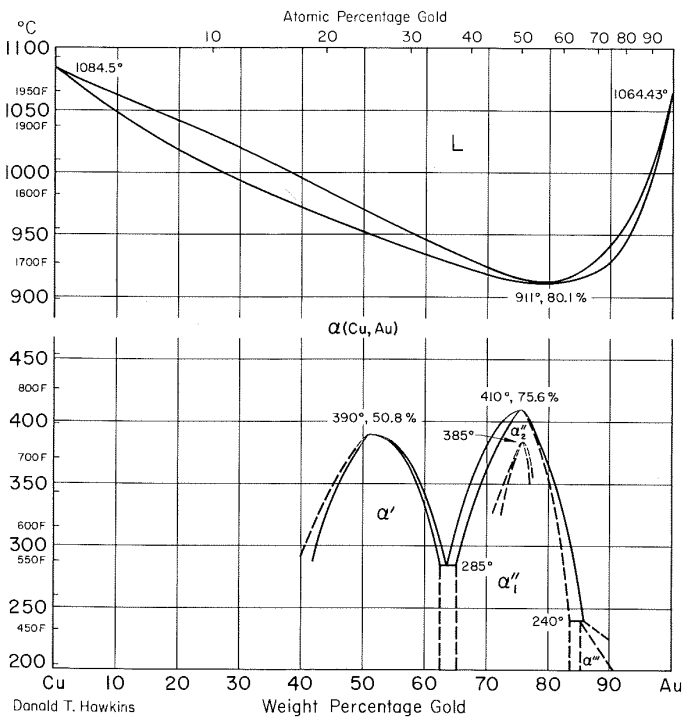
Au-Cr Gold-Chromium



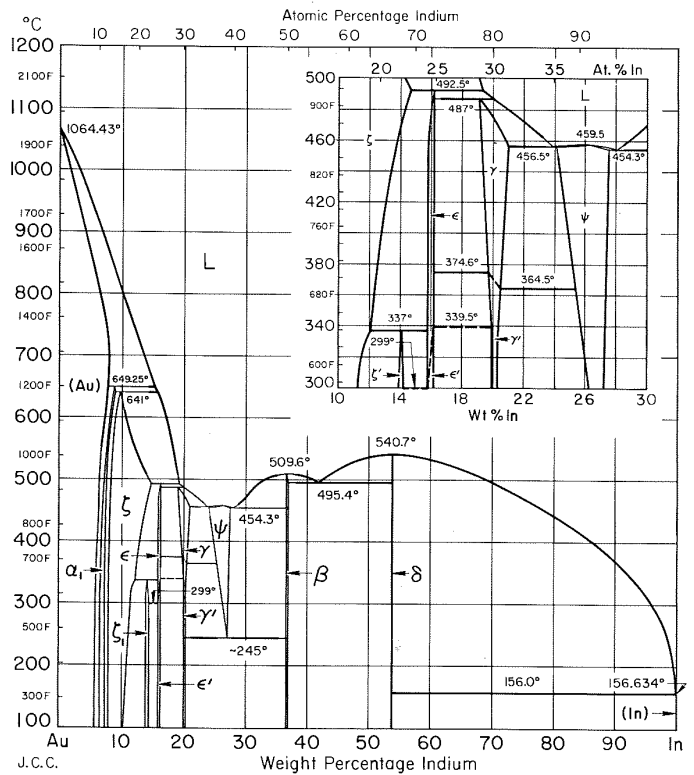
Au-Ge Gold-Germanium



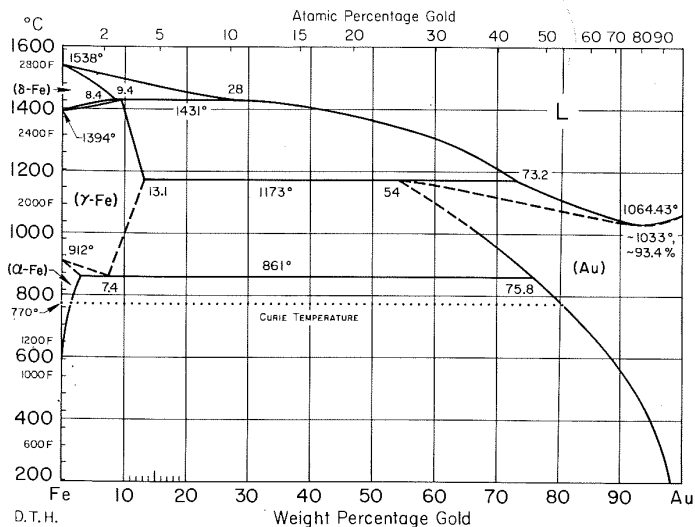
Au-Cu Gold-Copper



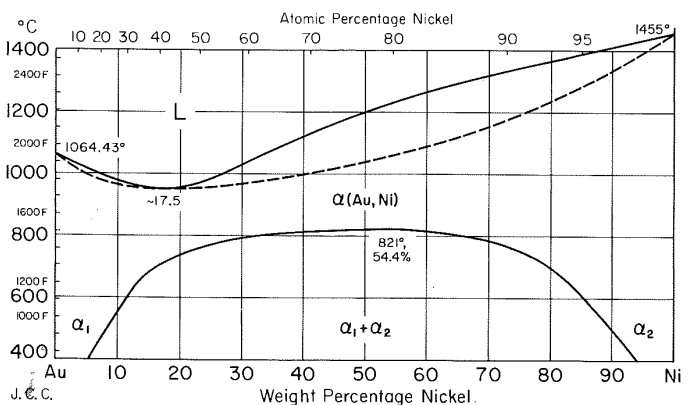
Au-In Gold-Indium



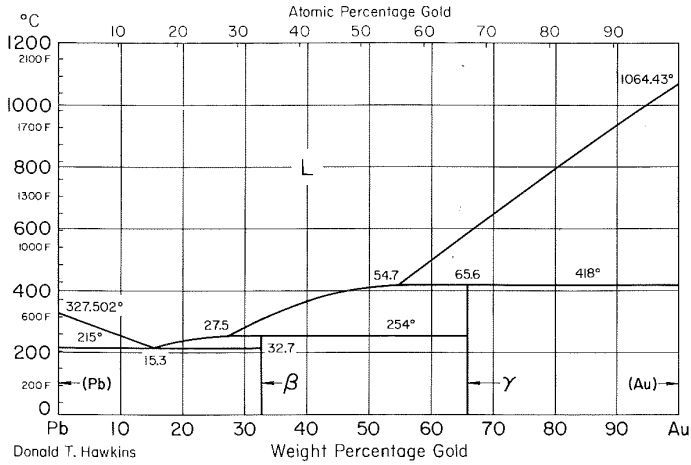
Au-Fe Gold-Iron



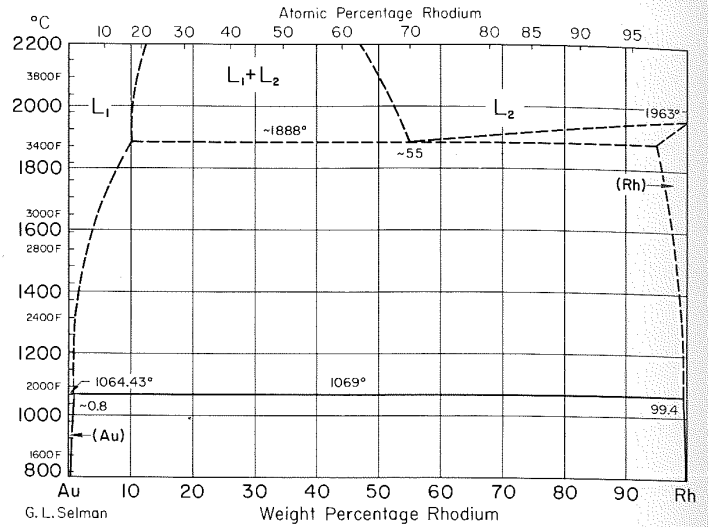
Au-Ni Gold-Nickel



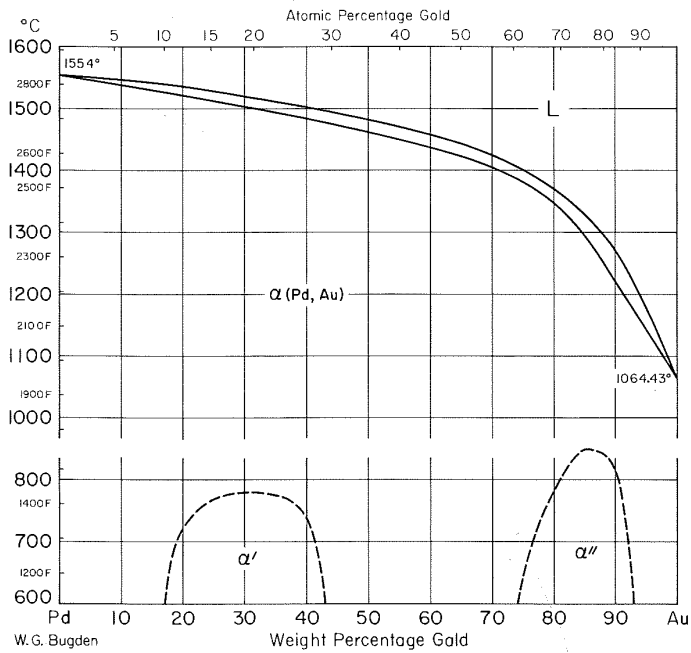
Au-Pb Gold-Lead



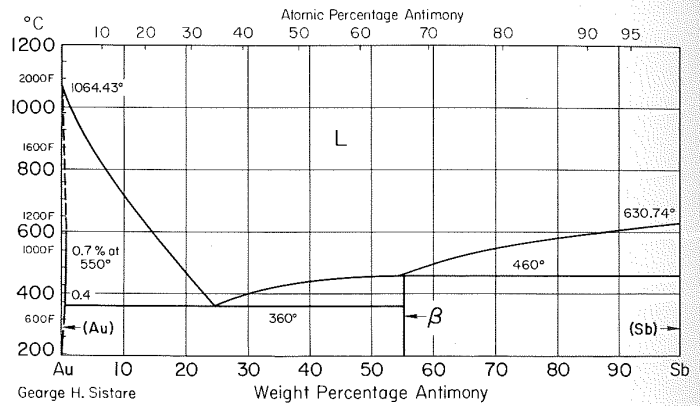
Au-Rh Gold-Rhodium



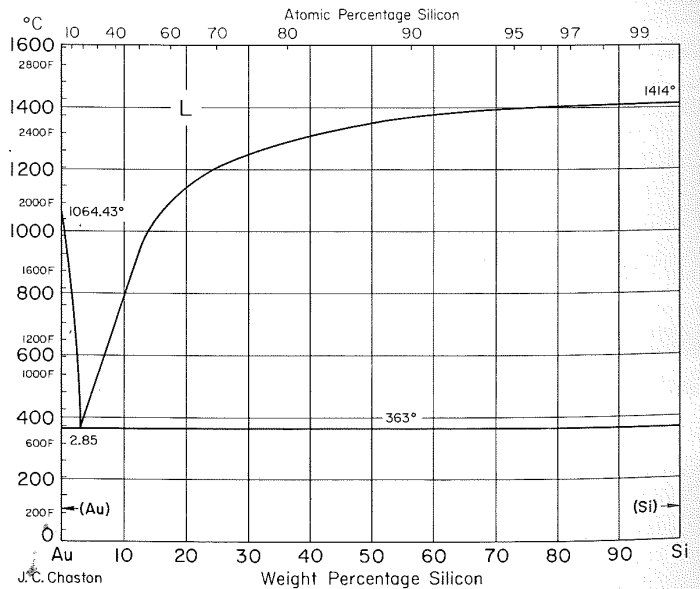
Au-Pd Gold-Palladium



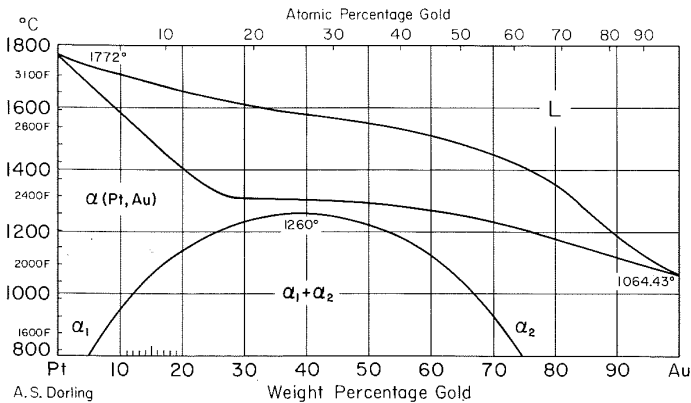
Au-Sb Gold-Antimony



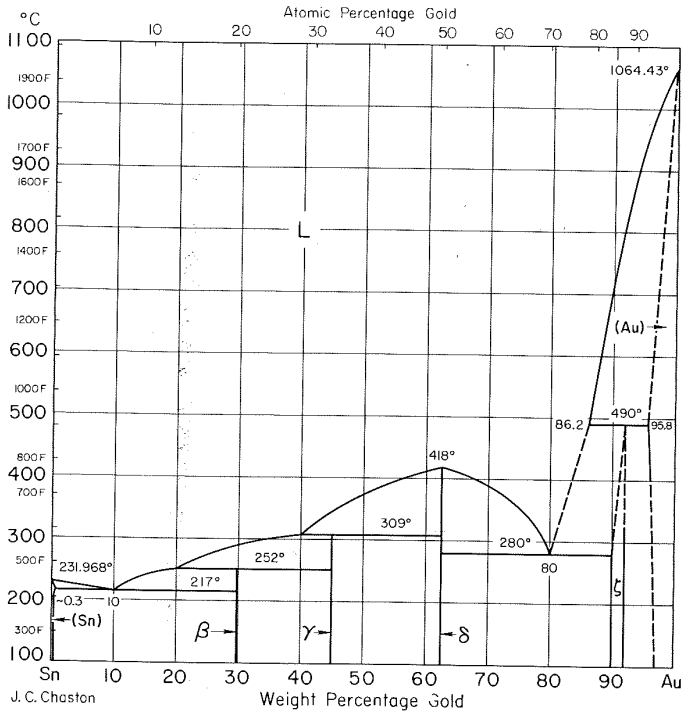
Au-Si Gold-Silicon



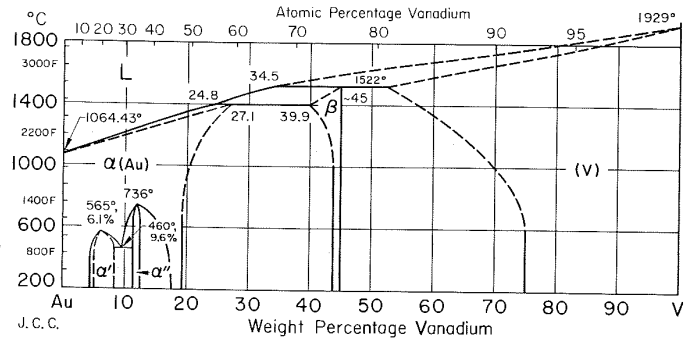
Au-Pt Gold-Platinum



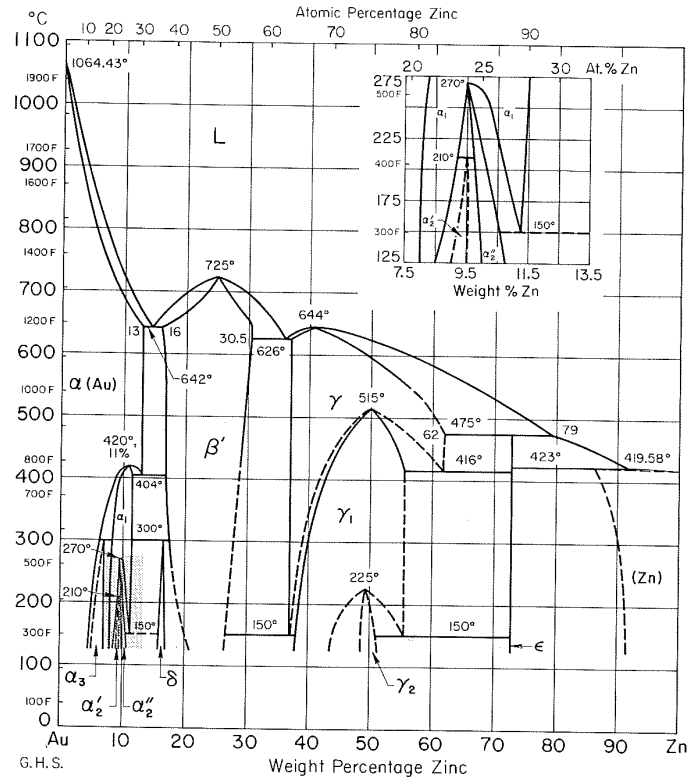
Au-Sn Gold-Tin



Au-V Gold-Vanadium



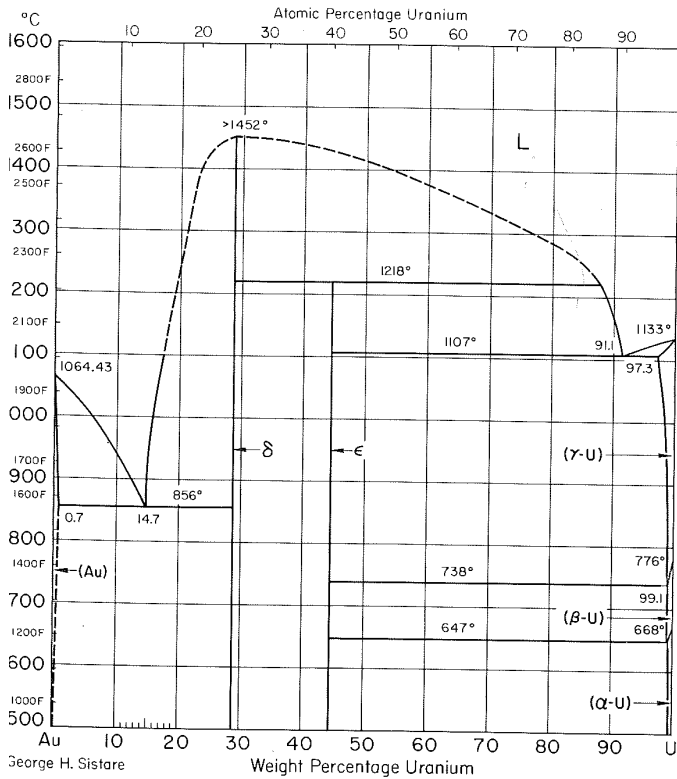
Au-Zn Gold-Zinc



Au-Ti Gold-Titanium

See Notes.

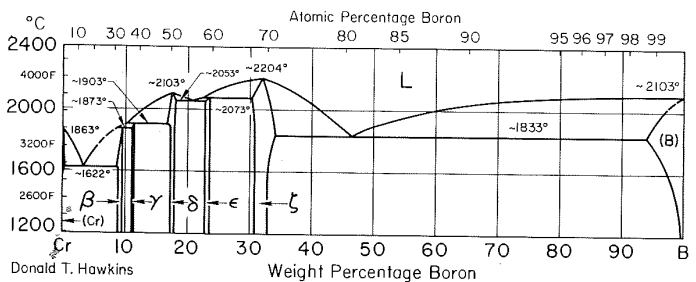
Au-U Gold-Uranium



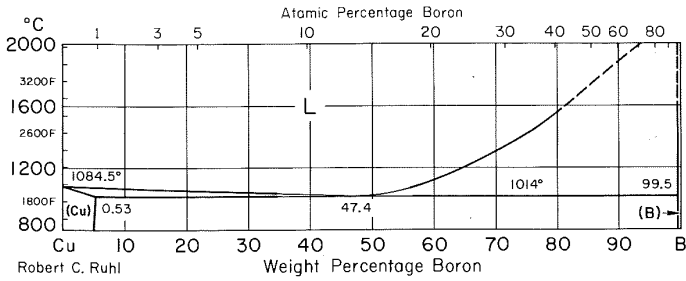
Au-Zr Gold-Zirconium

See Notes.

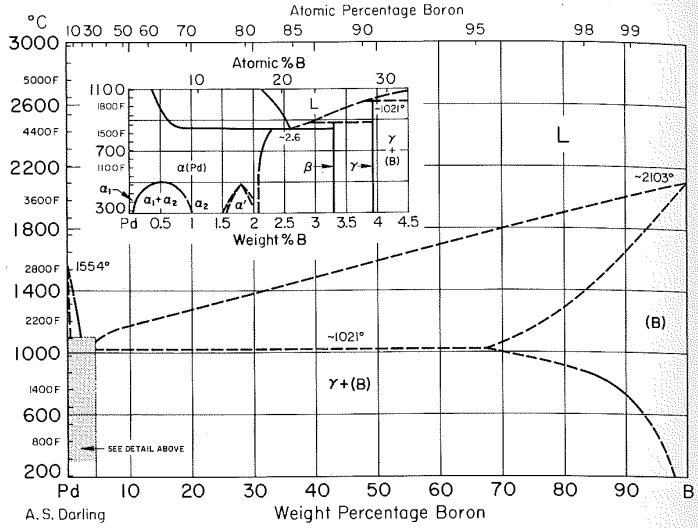
B-Cr Boron-Chromium



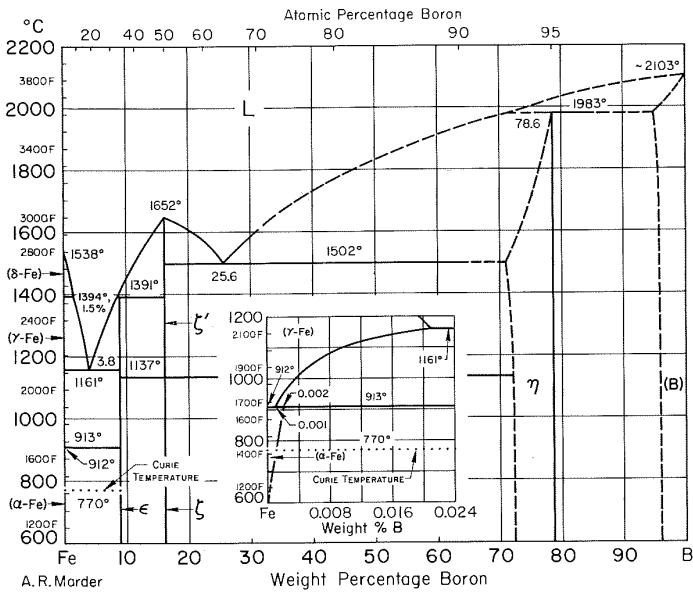
B-Cu Boron-Copper



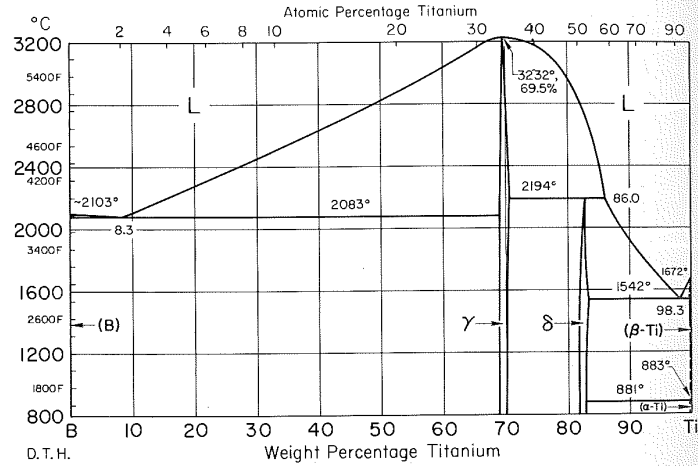
B-Pd Boron-Palladium



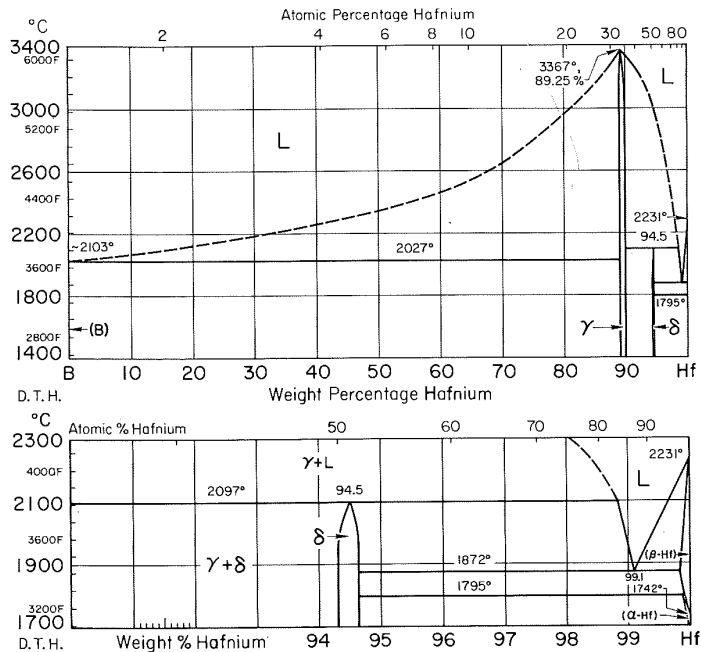
B-Fe Boron-Iron



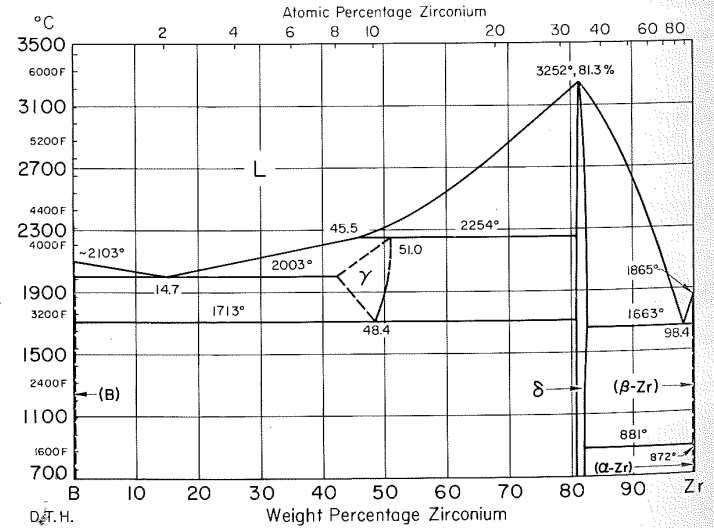
B-Ti Boron-Titanium



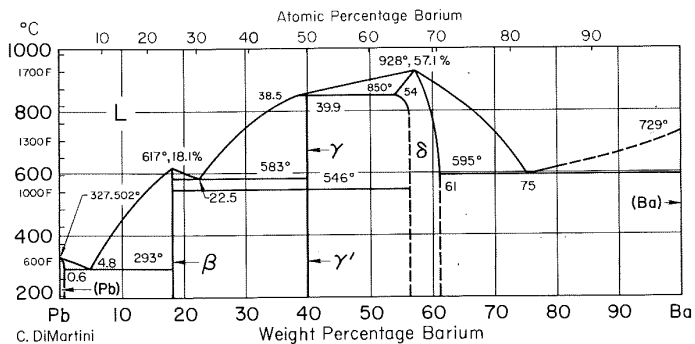
B-Hf Boron-Hafnium



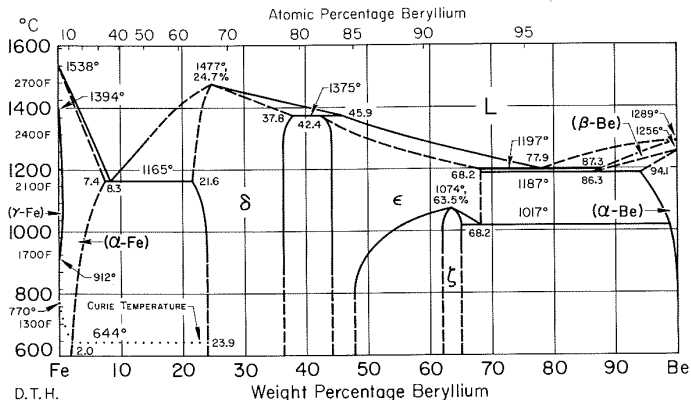
B-Zr Boron-Zirconium



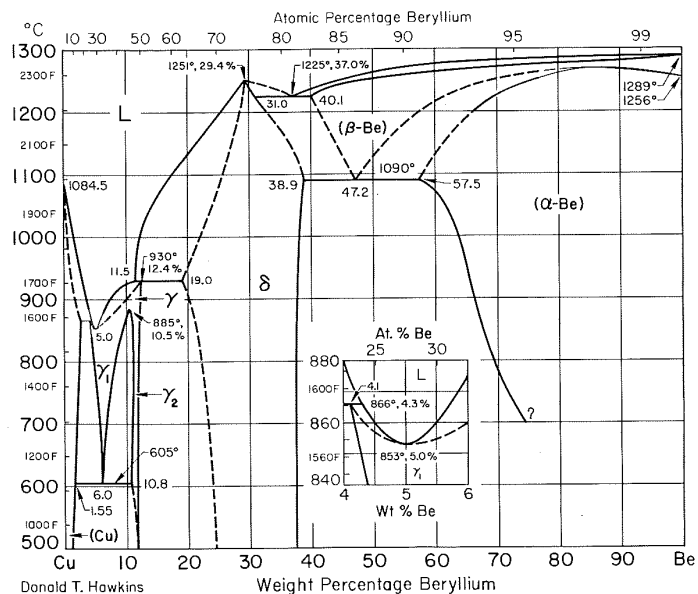
Ba-Pb Barium-Lead



Be-Fe Beryllium-Iron



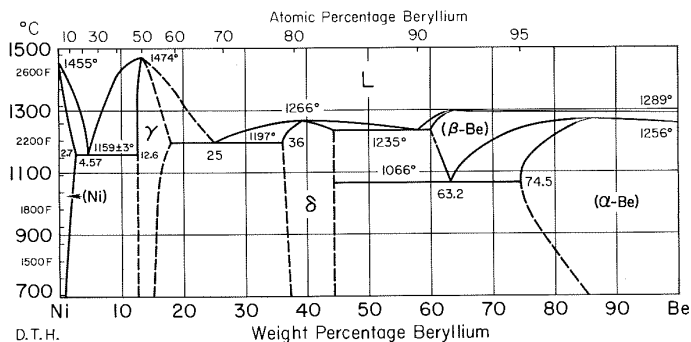
Be-Cu Beryllium-Copper



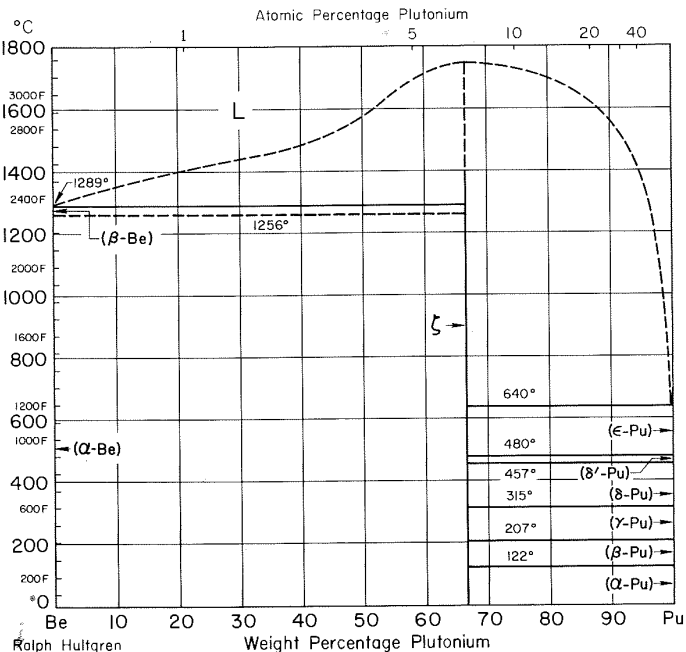
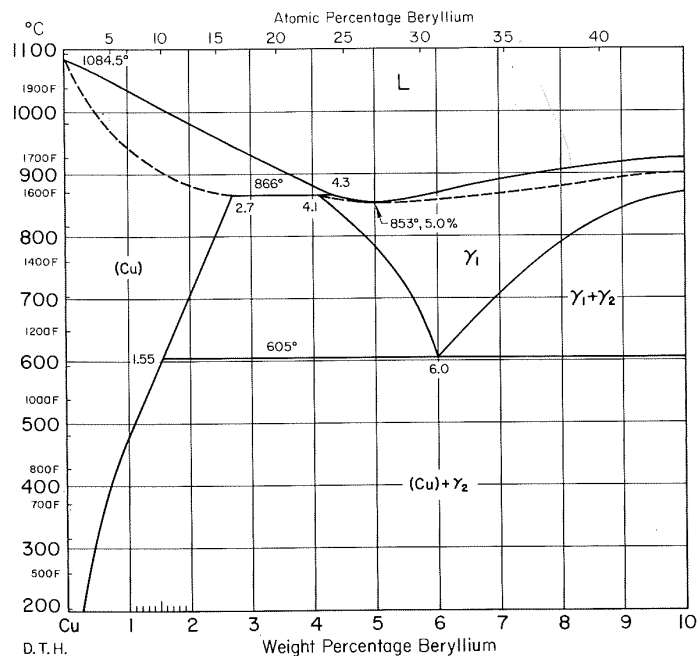
Be-Hf Beryllium-Hafnium

See Notes.

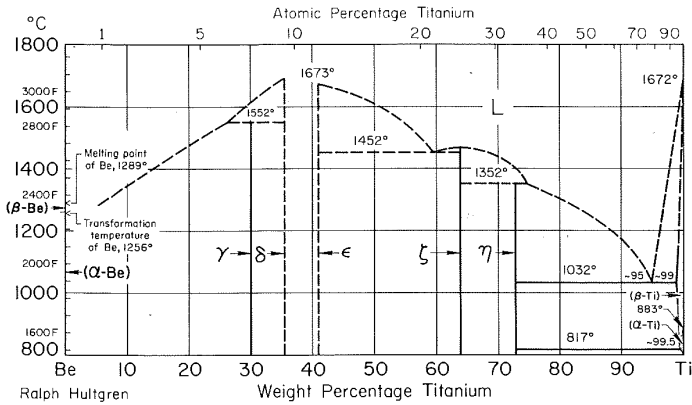
Be-Ni Beryllium-Nickel



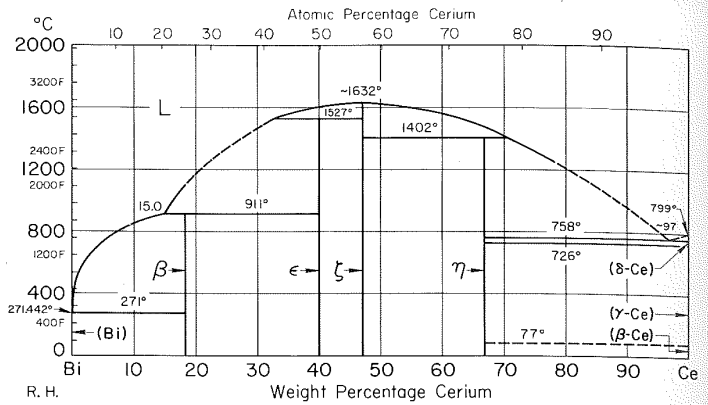
Be-Pu Beryllium-Plutonium



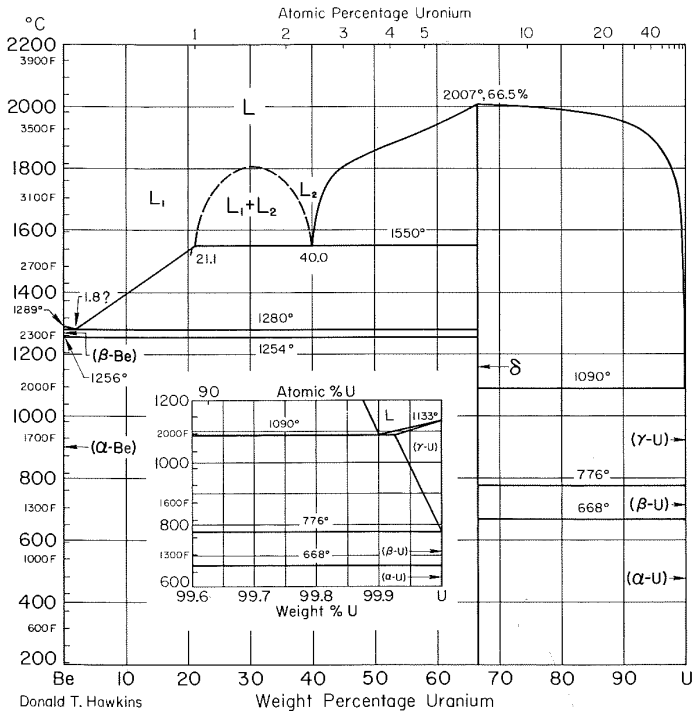
Be-Ti Beryllium-Titanium



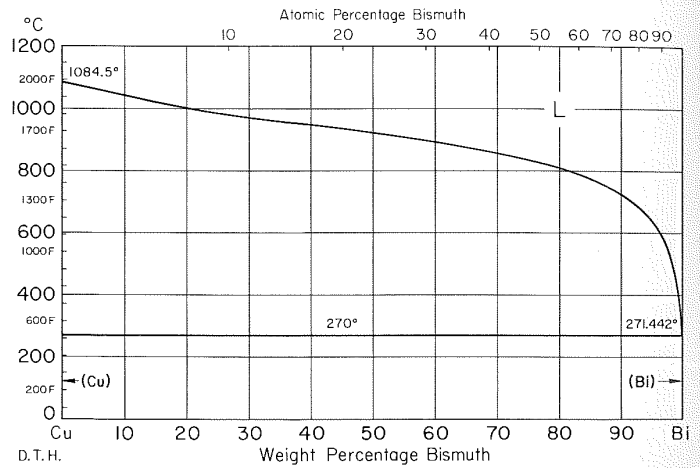
Bi-Ce Bismuth-Cerium



Be-U Beryllium-Uranium



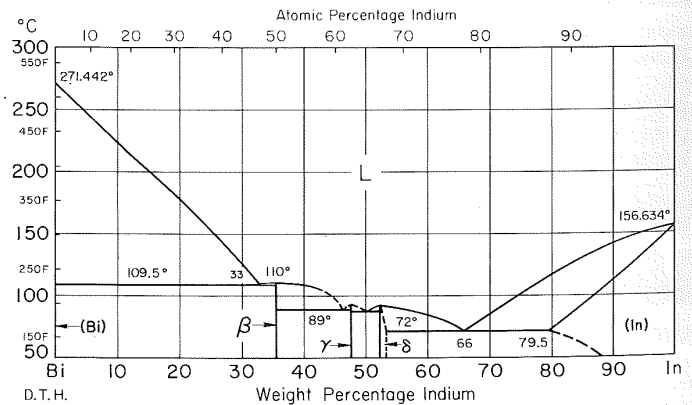
Bi-Cu Bismuth-Copper



Bi-Fe Bismuth-Iron

See Notes.

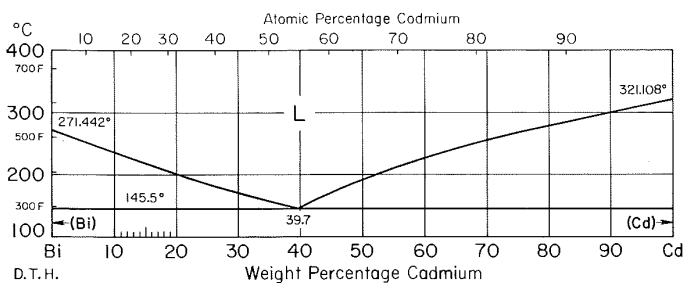
Bi-In Bismuth-Indium



Be-Zr Beryllium-Zirconium

See Notes.

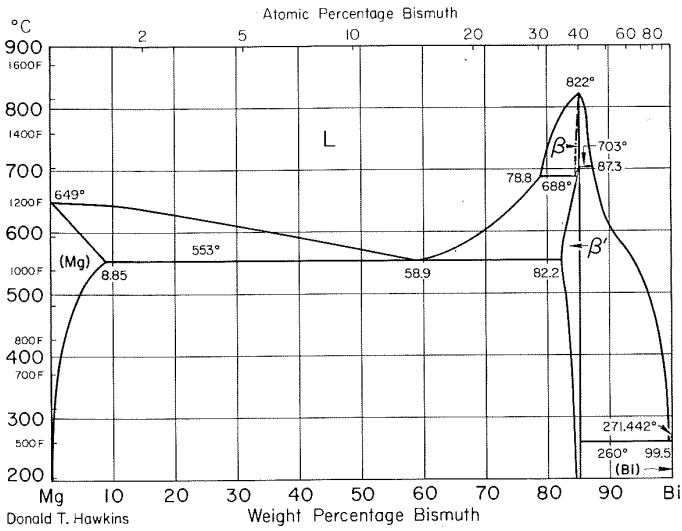
Bi-Cd Bismuth-Cadmium



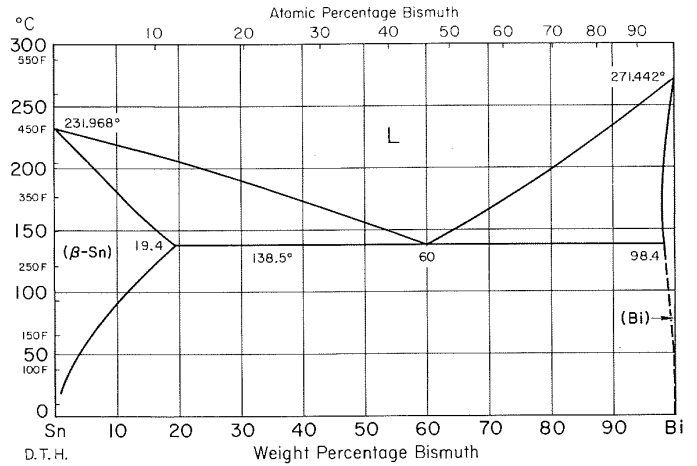
Bi-Li Bismuth-Lithium

See Notes.

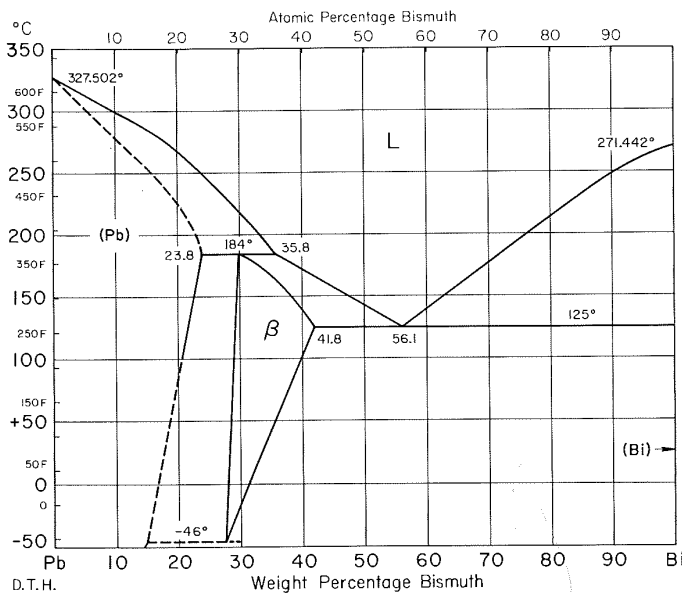
Bi-Mg Bismuth-Magnesium



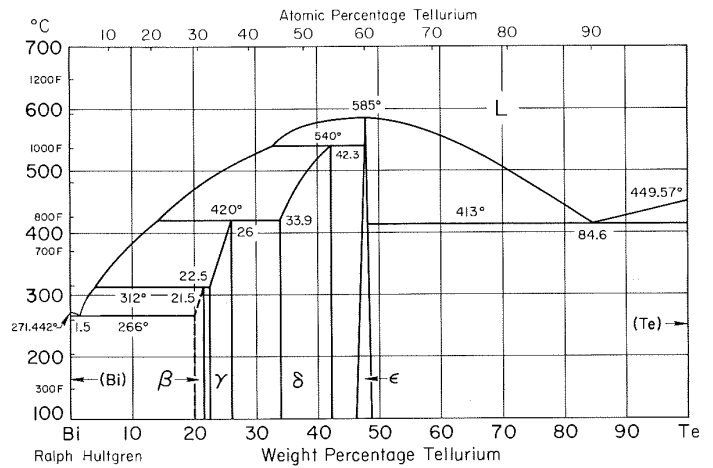
Bi-Sn Bismuth-Tin



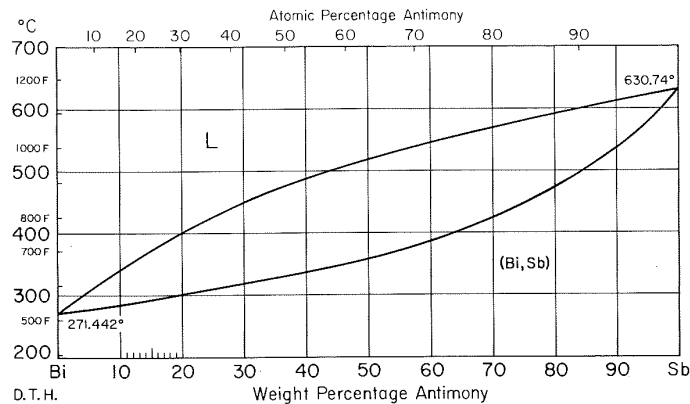
Bi-Pb Bismuth-Lead



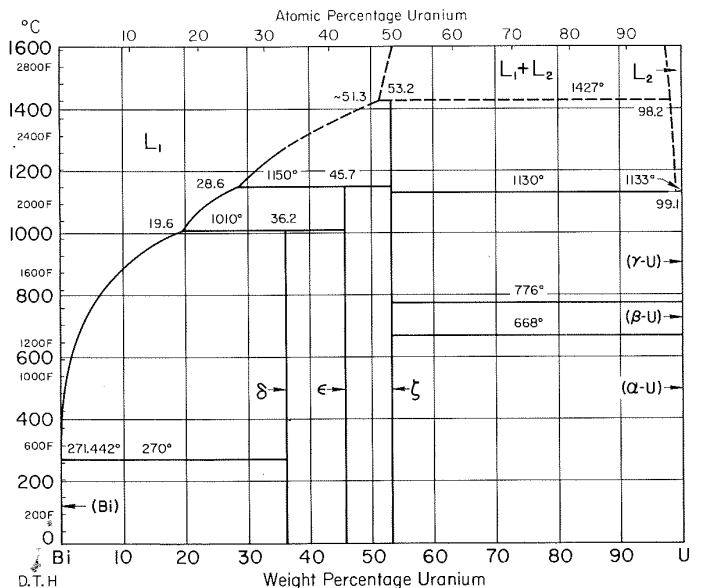
Bi-Te Bismuth-Tellurium



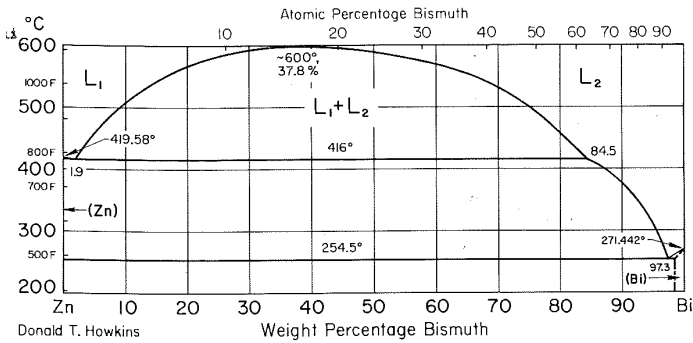
Bi-Sb Bismuth-Antimony



Bi-U Bismuth-Uranium

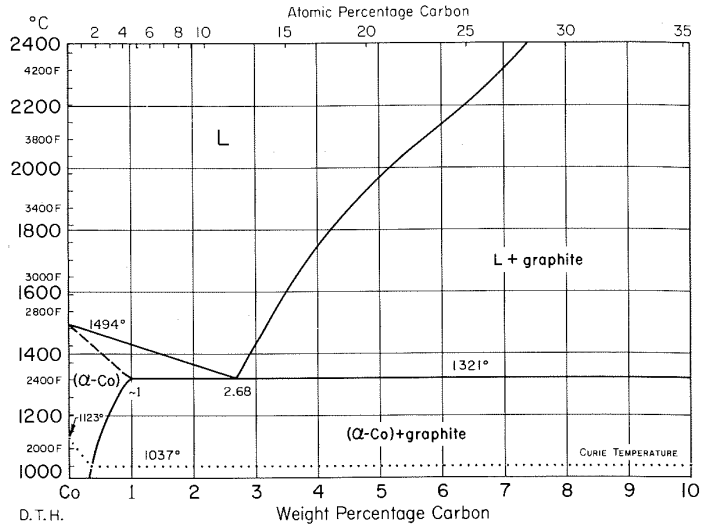


Bi-Zn Bismuth-Zinc



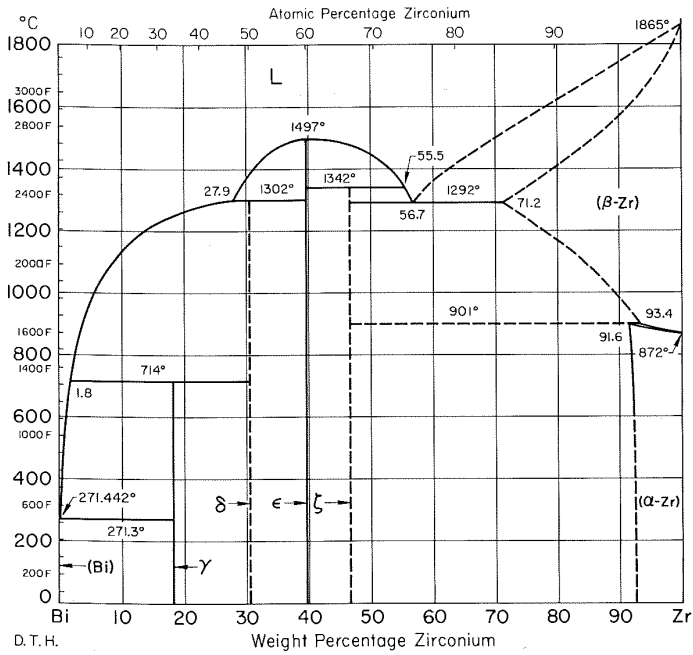
Donald T. Hawkins

C-Co Carbon-Cobalt



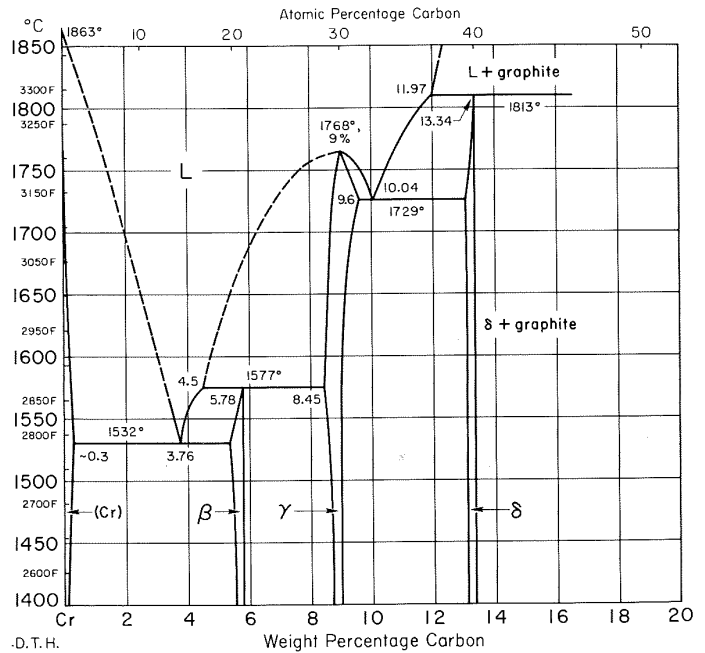
D.T.H.

Bi-Zr Bismuth-Zirconium



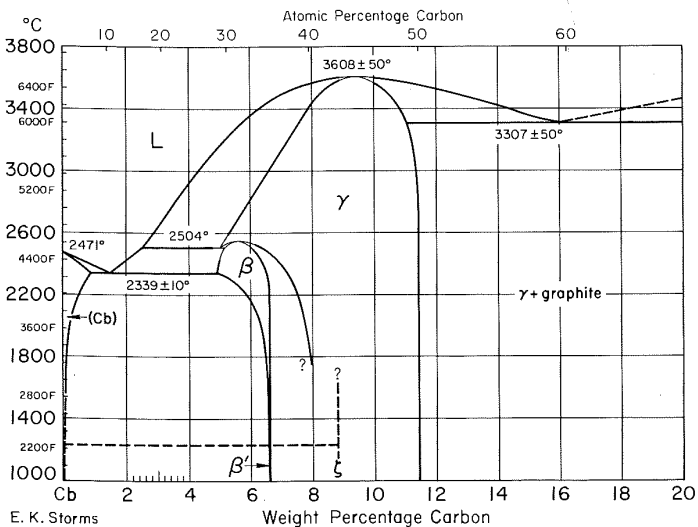
D.T.H.

C-Cr Carbon-Chromium



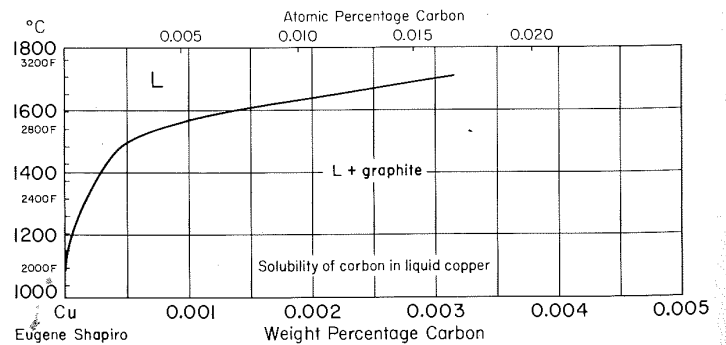
D.T.H.

C-Cb Carbon-Columbium



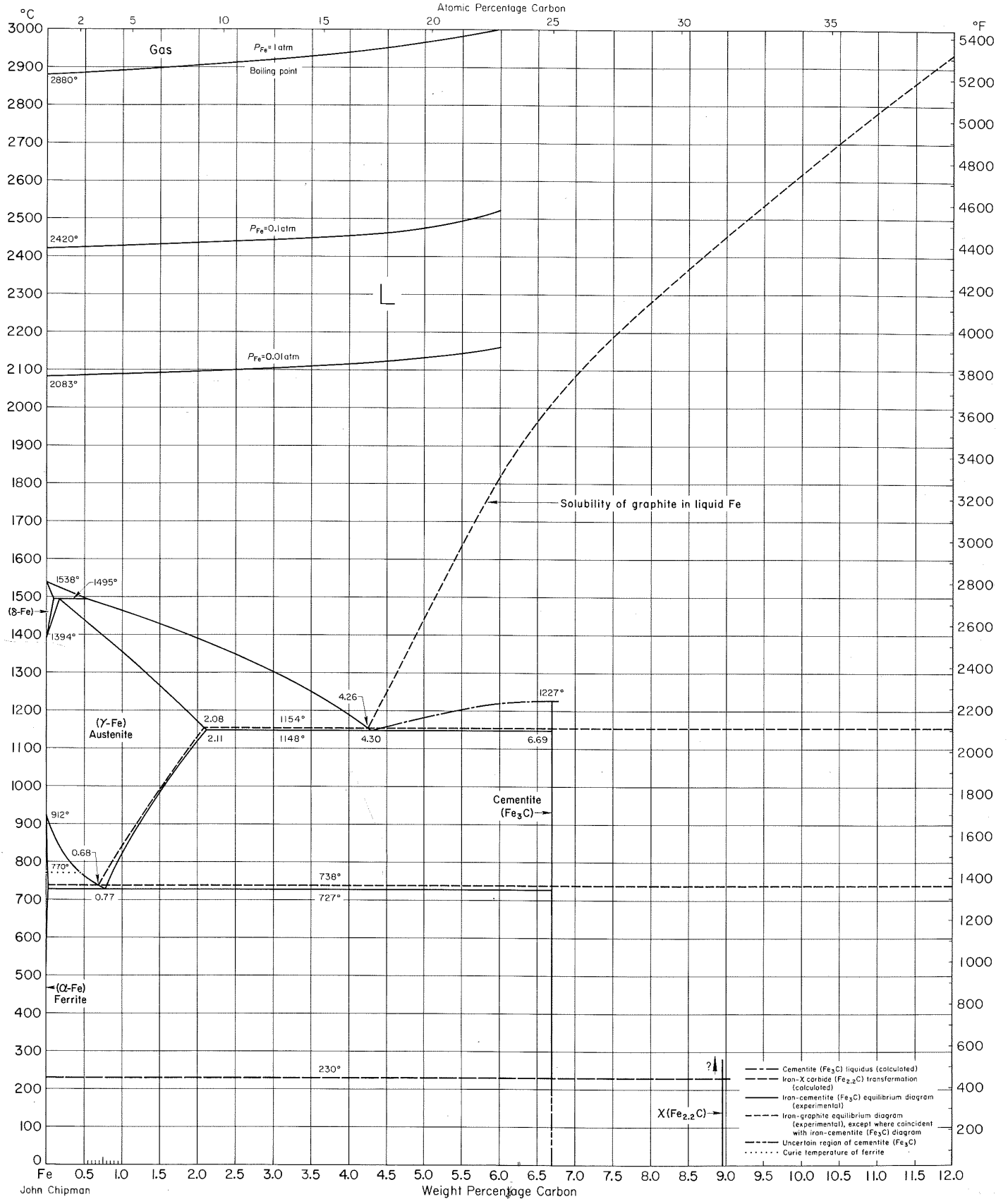
E. K. Storms

C-Cu Carbon-Copper

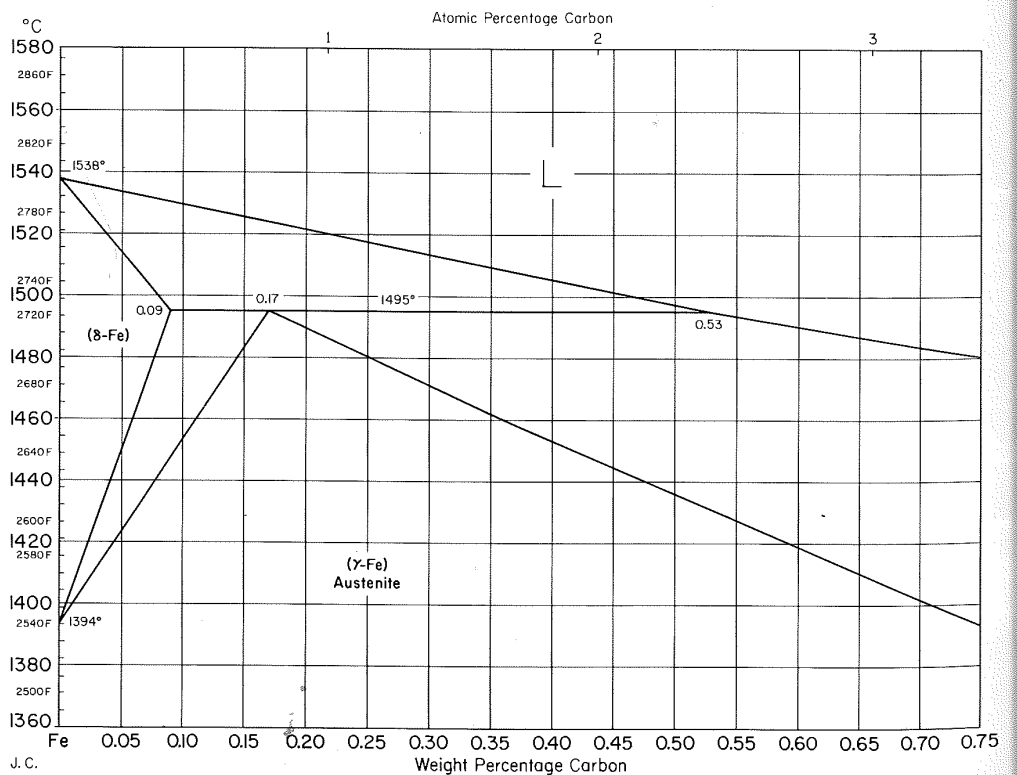
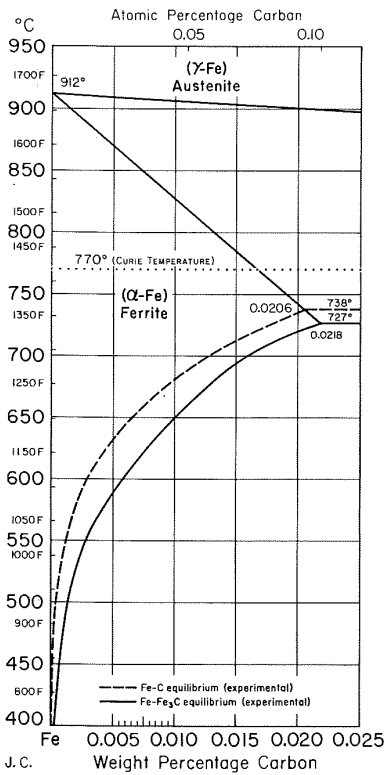
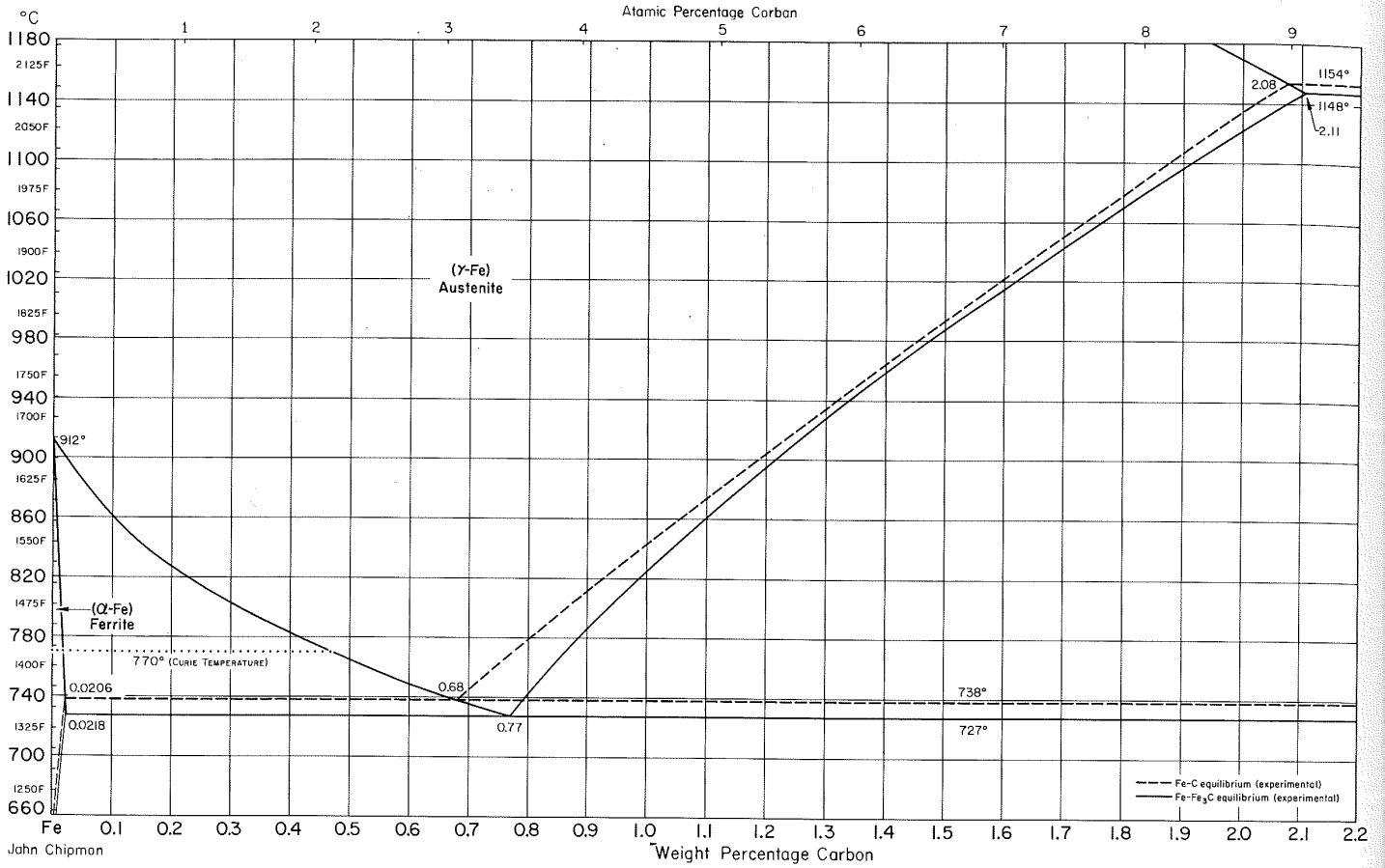


Eugene Shapiro

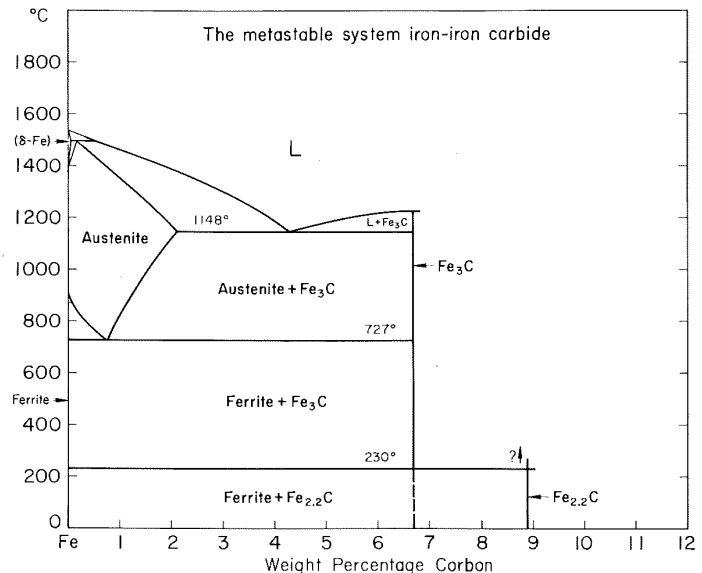
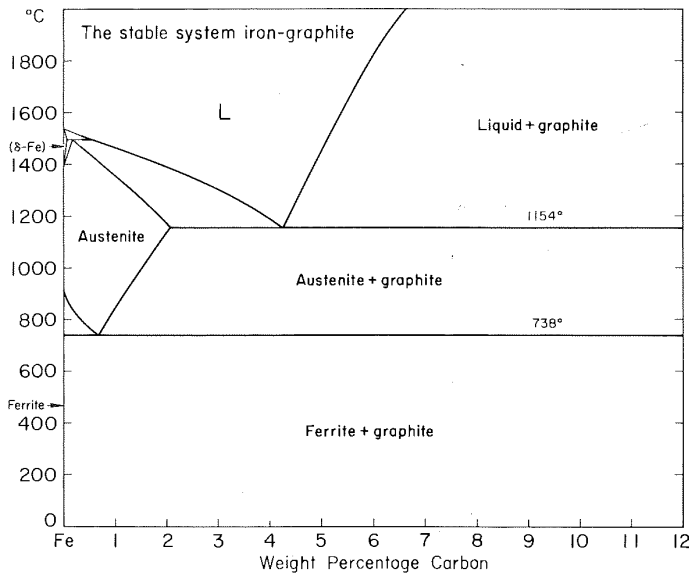
C-Fe Carbon-Iron



C-Fe Carbon-Iron



Two-phase fields involving graphite or iron carbide



C-Fe (Carbon-Iron)

By JOHN CHIPMAN

The diagrams and tables are from a review by Chipman (1). Many iron carbides have been reported, but only those that have been studied under stable or metastable equilibrium conditions are considered here.

The major lines of the diagrams are based on direct observations and are drawn to conform to the known thermodynamic properties of iron, from Orr and Chipman (2), and to experimentally determined activity coefficients. Lines showing composition-temperature relations at several pressures were calculated from (a) the known vapor pressure of liquid iron, from Hultgren *et al* (3); and (b) the activity of iron in liquid-iron-plus-carbon solution, from Chipman (1) and Syu *et al* (4). The liquidus curve for cementite (Fe₃C) has never been observed but was calculated by Chipman (1, 5) from the free energy of cementite and from that of the equilibrium liquid as extrapolated into the metastable range below the graphite liquidus.

Crystal-structure data are given in the notes for the C-Fe system, on page 350 in this volume.

The Austenite Field. The properties and boundary lines of the face-centered cubic austenite (γ -Fe) solid-solution area are well known. The activity of carbon as a function of temperature and composition has been determined by many observers, chiefly through studies of the equilibria: C (in Fe) + 2H₂ = CH₄ and C (in Fe) + CO₂ = 2CO. The earlier investigations of the latter reaction, by Dünwald and Wagner (6) and by Smith (7), are in agreement with the more recent work of Scheil *et al* (8) — except at the highest carbon concentrations — and of Ban-ya *et al* (9). Studies of the former reaction have been subject to errors, especially at low carbon levels, because of the reaction of methane with residual gas impurities. These errors may have caused the differences observed by Smith (7) between activity coefficients determined by the two equilibria. Studies based on the latter reaction were subject to similar but generally smaller errors, which increased with increasing temperature and carbon content.

The solubility of graphite in austenite (γ -Fe) was calculated from the data on activity of carbon in austenite, using the equations presented by Chipman (1). These solubility values are in rather good agreement with the direct measurements of Wells (10) and of Gurry (11) and with a downward extrapolation of the solidus line of Benz and Elliott (12) to the eutectic temperature. Average values of these three determinations are listed in Table 1.

The (γ -Fe)-Liquid Equilibrium. The austenite solidus line of Benz and Elliott and a portion of the austenite liquidus line of Buckley and Hume-Rothery (13) are shown in the diagram. The solidus line was given a slight inflection with downward curvature near its lower end to conform to the data of Ban-ya

Table 1. Solubility of Graphite and Cementite in γ -Fe (Austenite)

Temperature		Graphite		Cementite	
C	F	C:Fe(a)	C, wt %	C:Fe(a)	C, wt %
727(b)	1341	0.0320	0.68	0.0356	0.77
738(c)	1360	0.0408	0.87	0.0442	0.94
800	1472	0.0561	1.19	0.0580	1.22
900	1652	0.0725	1.53	0.0730	1.55
1000	1832	0.0896	1.89	0.0910	1.92
1100	2012	0.0990	2.08	0.1000	2.11
1148(d)	2098
1154(e)	2109

(a) Ratio of number of carbon atoms to number of iron atoms. (b) Cementite eutectoid. (c) Graphite eutectoid. (d) Cementite eutectic. (e) Graphite eutectic.

Table 2. Solid-Liquid Equilibria for γ -Fe

Temperature		γ -Fe Solidus		Liquidus	
C	F	C:Fe(a)	C, wt %	C:Fe(a)	C, wt %
1148(b)	2098	0.1000	2.11	0.2092	4.30
1154(c)	2109	0.0900	2.08	0.2072	4.26
1200	2192	0.0877	1.85	0.1906	3.93
1250	2282	0.0718	1.59	0.1689	3.50
1300	2372	0.0613	1.30	0.1450	3.02
1350	2462	0.0475	1.01	0.1179	2.47
1400	2552	0.0333	0.71	0.0891	1.88
1450	2642	0.0196	0.42	0.0570	1.21
1495(d)	2723	0.0079	0.17	0.0248	0.53
1527(e)	2781	0.0000	0.00	0.0000	0.00
1538(f)	2800

(a) Ratio of number of carbon atoms to number of iron atoms. (b) Cementite eutectic. (c) Graphite eutectic. (d) Peritectic. (e) Metastable melting point of γ -Fe. (f) Melting point of δ -Fe.

et al. Both lines are superior in accuracy to those of earlier investigators and are supported by data of Adcock (14). When the liquidus and solidus lines are extended, as shown by Chipman (1), they intersect at the metastable melting point of γ -Fe (1527 C; 2781 F) as calculated by Orr and Chipman. Values from the curves in their entirety are listed in Table 2.

The Liquid Phase. The best data on the activity of carbon in liquid Fe-C alloys were determined by Richardson and Dennis (15) at 1560, 1660 and 1760 C (2840, 3020 and 3200 F), using the equilibrium: C (in Fe) + CO₂ = 2CO. For lower temperatures, Chipman (1) used the activity of carbon in austenite at points along the solidus to determine the activity coefficient in the liquid for compositions along the liquidus.

The solubility of graphite in liquid iron has been measured by many investigators. Up to 1800 C (3272 F), excellent agreement is found among Ruer and Biren (16), Chipman *et al* (17) and Kitchener *et al* (18). Data for temperatures up to 2500 C (4532 F) were reported by Ruer and Biren, for up to 2875 C (5207 F) by Cahill *et al* (19), and for 2050 to 2375 C (3722 to 4307 F) by Vertman *et al* (20). Interpolated data and estimates of probable accuracy are given in Table 3. The

Table 3. Solubility of Graphite in Liquid Iron

Temperature C		C, wt %	Temperature F		C, wt %
1154	2109		4.26 ± 0.02	2100	
1200	2192	4.37	2200	3992	7.56 ± 0.3
1300	2372	4.63	2300	4172	8.10
1400	2552	4.88	2400	4352	8.68
1500	2732	5.14	2500	4532	9.28 ± 0.4
1600	2912	5.40 ± 0.03	2600	4712	9.87
1700	3092	5.66	2700	4892	10.50
1800	3272	5.94 ± 0.05	2800	5072	11.12
1900	3452	6.26 ± 0.10	2900	5252	11.75 ± 0.5
2000	3632	6.63 ± 0.10			

Table 4. Solubility of Graphite, Fe₃C and Fe_{2.2}C in α -Fe (Ferrite)

Temperature C		Solubility, ppm			Temperature F		Solubility, ppm		
		Graph- ite(a)	Fe ₃ C(b)	Fe _{2.2} C(c)			Graph- ite(a)	Fe ₃ C(b)	Fe _{2.2} C(c)
738	1360	206	500	932	4.3	13	...
727	1341	...	218	...	450	842	1.35	5.7	...
700	1292	127	160	...	400	752	0.37	2.3	...
650	1202	63	102	...	350	662	0.081	0.75	1.3
600	1112	28	57	...	300	572	0.013	0.21	0.30
550	1022	11.7	28	...	250	482	...	0.045	0.050
					200	392	...	0.007	0.0055

(a) Data derived from equation in Chipman (1). (b) Calculated from observed value at 727 C (1341 F) and free energy of formation. (c) From free energy of formation.

selected eutectic at 1154 C (2109 F) and 4.24 to 4.28 wt % C has been confirmed by Ruth and Turpin (21).

The δ Phase and Peritectic. The δ -Fe region is shown on the diagram with the peritectic at 1495 C (2723 F), as recommended by Buckley and Hume-Rothery. The liquidus of δ -Fe phase is shown as a straight line from the melting point to 0.53 wt % C at the peritectic. The compositions of the peritectic are: δ -Fe, 0.09 wt % C; γ -Fe, 0.17 wt % C; liquid, 0.53 wt % C. Compositions of δ -Fe and liquid at the peritectic are averages of several published values that have been selected to agree with the heat effects at 1394 C (2541 F), and at the melting point, from Orr and Chipman, and with the activity of iron in the δ -Fe and liquid solutions from Chipman (5) and Syu *et al.*

The α - γ Equilibrium. The (γ -Fe)-(α -Fe + γ -Fe) phase boundary is based almost entirely on the data of Mehl and Wells (22), corrected by 1 C (1.8 F) at the pure iron end with negligible correction at the eutectoid end. The intersections of Chipman's solubility lines (1) place the Fe-graphite eutectoid at 738 C (1360 F) and 0.68 wt % C, and the Fe-cementite eutectoid at 727 C (1341 F) and 0.77 wt % C. The latter temperature agrees with Smith and Darken (23) and is 4 C (7 F) higher than that of Mehl and Wells.

The (α -Fe)-(α -Fe + γ -Fe) phase boundary, which is based on data at 800 and 750 C (1472 and 1382 F) by Smith (7), is extrapolated to 0.0206 and 0.0218 wt % C at the graphite and cementite eutectoid temperatures.

Solubility of Graphite in α -Fe. The activity of carbon in body-centered-cubic α -Fe was determined by Smith (7, 24) and Swartz (25) at 590 to 800 C (1094 to 1472 F). The activity in body-centered-cubic δ -Fe at the peritectic temperature (1495 C; 2723 F) is known from the activity in the γ -Fe and liquid phases. These activity data, and the activity of carbon at the peritectic temperature, were used to calculate the values for the solubility of graphite in α -Fe that are given in Table 4.

The Iron Carbides. Numerous carbides of iron are reported, ranging in composition from FeC to Fe₃C. Only two of these have been studied under metastable equilibrium conditions, and it is only for these two that thermodynamic data are available.

Cementite, sometimes called θ carbide, is usually assigned the formula Fe₃C, but its exact conformance to the stoichiometric composition has not been proved. A slight iron deficiency above 800 C (1472 F) was suggested by Benz *et al.* (26). Several observers have reported variations in composition and in the lattice parameter.

The existence of Fe₂C was suggested by Glud *et al.* (27). An x-ray diffraction pattern by Hofmann and Groll (28) for iron carburized at temperatures below 400 C (752 F) showed an unknown carbide and Fe₃C; in iron carburized above 400 C (752 F), only Fe₃C was found. Experiments using a hydrogen-reduction method for determination of carbide and free carbon contents showed that when iron was carburized with CO at 225 C (437 F), the product contained 9.7 wt % C, the carbon content of Fe₂C. At higher temperatures, a mixture of Fe₂C and Fe₃C was formed; at 400 C (752 F) and above, only Fe₃C was formed. The x-ray diffraction pattern for the new carbide

was determined by Hägg (29). This carbide is frequently called Hägg or χ carbide and has a slightly variable composition approximating Fe_{2.2}C.

The solubilities of Fe₃C and Fe_{2.2}C in α -Fe (ferrite) are given in Table 4.

Cementite (θ Carbide). The (γ -Fe)-(γ -Fe + cementite) phase boundary is from Ban-ya *et al.*, and is based on the direct measurements of solubility by Smith (30) and on the CO-CO₂ equilibrium measurements by Scheil *et al.* The Fe₃C liquidus line and the melting point (1227 C; 2241 F) were calculated by Chipman (1). Values from the phase boundary are listed in Table 1.

The solubility of cementite in α -Fe (ferrite) was calculated from the free energy of formation of cementite as determined by the gas-solid equilibrium studies of Scheil *et al.* Within the temperature range shown in the diagram, the result is in fair agreement with studies by Swartz of the solubility of stress-free cementite using internal-friction methods.

Hägg (χ) Carbide. The carbide prepared by Browning *et al.* (31) by treatment of hydrogen-reduced iron with butane at 275 C (527 F) was identified by its diffraction pattern as the same as that prepared by Hägg at 225 C (437 F). Both observers found that this carbide was converted to Fe₃C by heating to 500 C (932 F). The structure was listed as orthorhombic with the added notation that a monoclinic or triclinic structure was not excluded. Recent studies show a monoclinic structure isotypic with Mn₅C₂. The χ carbide is represented by the formula Fe_{2.2}C (or Fe₅C₂) and has a Curie temperature of 247 C (477 F).

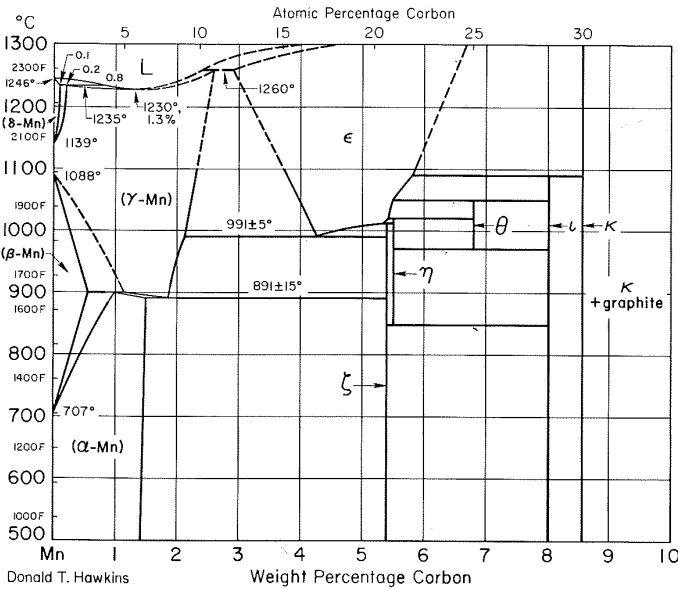
The transformation indicated on the diagram at 230 C (446 F) is uncertain but is based on observations of gas equilibria with the respective carbides by Browning *et al.* Below a temperature estimated at 230 to 350 C (446 to 662 F), χ carbide is more stable than cementite.

The ϵ carbide occurs as a transition phase in the tempering and aging of steel. It has not been isolated, and its thermodynamic properties are unknown. Hofer (32) described it as close-packed hexagonal with a Curie temperature of 370 C (698 F) and a variable composition—commonly about Fe_{2.4}C.

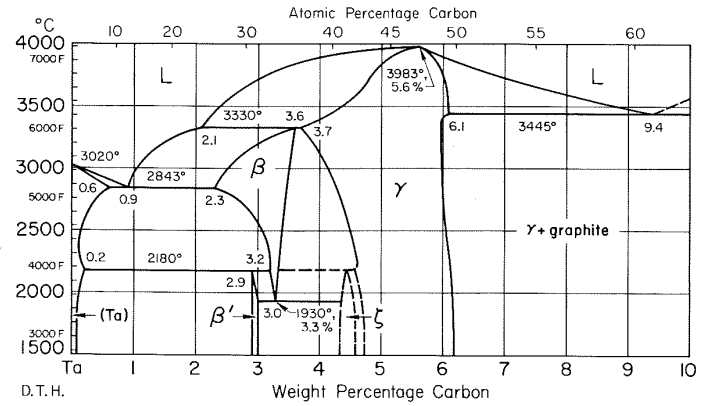
References

1. J. Chipman, *Met Trans*, Vol 3, 1972, p 55-64
2. R. L. Orr and J. Chipman, *Trans Met Soc AIME*, Vol 239, 1967, p 630-633
3. R. Hultgren, P. D. Desai, D. T. Hawkins, M. Gleiser and K. K. Kelley, "Selected Values of The Thermodynamic Properties of Binary Alloys", American Society for Metals, 1973
4. T. Syu, A. V. Polyakov and A. M. Samarin, *Izv Vyssh Ucheb Zaved Chern Met*, No. 11, 1959, p 3-12
5. J. Chipman, *Met Trans*, Vol 1, 1970, p 2163-2168
6. H. Dünwald and C. Wagner, *Z Anorg Allgem Chem*, Vol 199, 1931, p 321-346
7. R. P. Smith, *J Am Chem Soc*, Vol 68, 1946, p 1163-1175
8. E. Scheil, T. Schmidt and J. Wünnig, *Arch Eisenhuettenw*, Vol 32, 1961, p 251-260
9. S. Ban-ya, J. F. Elliott and J. Chipman, *Met Trans*, Vol 1, 1970, p 1313-1320
10. C. Wells, *Trans Am Soc Met*, Vol 26, 1938, p 289-344
11. R. W. Gurry, *Trans AIME*, Vol 150, 1942, p 147-153
12. M. G. Benz and J. F. Elliott, *Trans Met Soc AIME*, Vol 221, 1961, p 323-331 and p 888
13. R. A. Buckley and W. Hume-Rothery, *J Iron Steel Inst*, Vol 196, 1960, p 403-406; Vol 200, 1962, p 142-143
14. F. Adcock, *J Iron Steel Inst*, Vol 135, 1937, p 281-287
15. F. D. Richardson and W. E. Dennis, *Trans Faraday Soc*, Vol 49, 1953, p 171-180
16. R. Ruer, J. Biren, *Z Anorg Allgem Chem*, Vol 113, 1920, p 98-112
17. J. Chipman, R. M. Alfred, L. W. Gott, R. B. Small, D. M. Wilson, C. N. Thomson, D. L. Guernsey and J. C. Fulton, *Trans Am Soc Met*, Vol 44, p 1215-1230
18. J. A. Kitchener, J. O'M. Bockris and D. A. Spratt, *Trans Faraday Soc*, Vol 48, 1952, p 608-617
19. J. A. Cahill, A. D. Kirshenbaum and A. V. Grosse, *Trans Am Soc Met*, Vol 57, 1964, p 417-426
20. A. A. Vertman, V. K. Grigorovich, N. A. Nedumov and A. M. Samarin, *Dokl Akad Nauk SSSR*, Vol 159, 1964, p 121-124
21. J. C. Ruth and M. Turpin, *C R Acad Sci Paris*, Vol 265, 1967, p 786-788
22. R. F. Mehl and C. Wells, *Trans AIME*, Vol 125, 1937, p 429-469
23. R. P. Smith and L. S. Darken, *Trans AIME*, Vol 215, 1959, p 727-728
24. R. P. Smith, *Trans Met Soc AIME*, Vol 224, 1962, p 105-111
25. J. C. Swartz, *Trans Met Soc AIME*, Vol 239, 1967, p 68-75; Vol 245, 1969, p 1083-1092
26. R. Benz, J. F. Elliott and J. Chipman, *Met Trans*, Vol 1, 1973
27. W. Glud, K. V. Otto and H. Ritter, *Ber Ges Kohlentech*, Vol 3, 1929, p 40
28. U. Hofmann, E. Groll, *Z Anorg Allgem Chem*, Vol 191, 1930, p 914
29. G. Hägg, *Z Kristallogr*, Vol 89, 1934, p 92
30. R. P. Smith, *Trans Met Soc AIME*, Vol 215, 1959, p 954-957
31. L. C. Browning, T. W. DeWitt and P. H. Emmett, *J Am Chem Soc*, Vol 72, 1950, p 4211-4217
32. L. J. E. Hofer, *U S Bur Mines Bull*, No 631, 1966

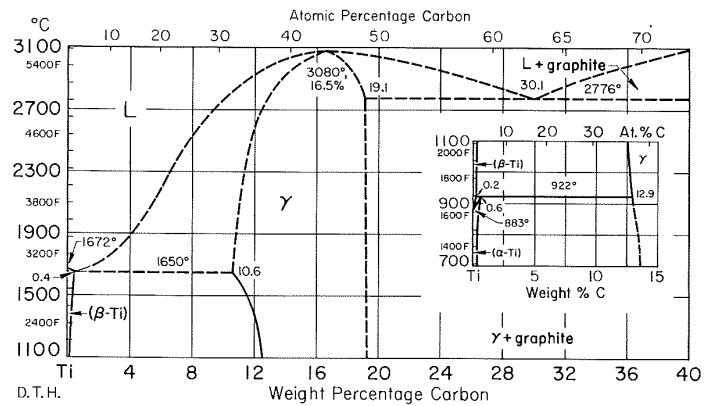
C-Mn Carbon-Manganese



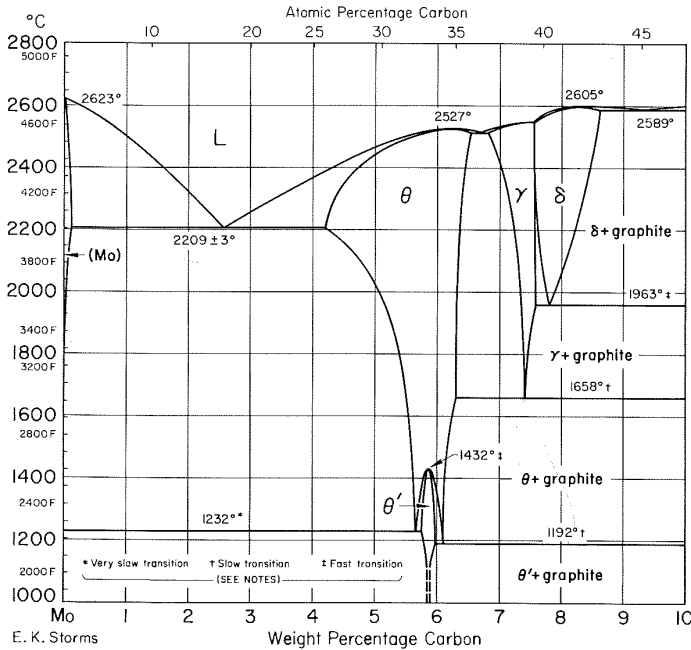
C-Ta Carbon-Tantalum



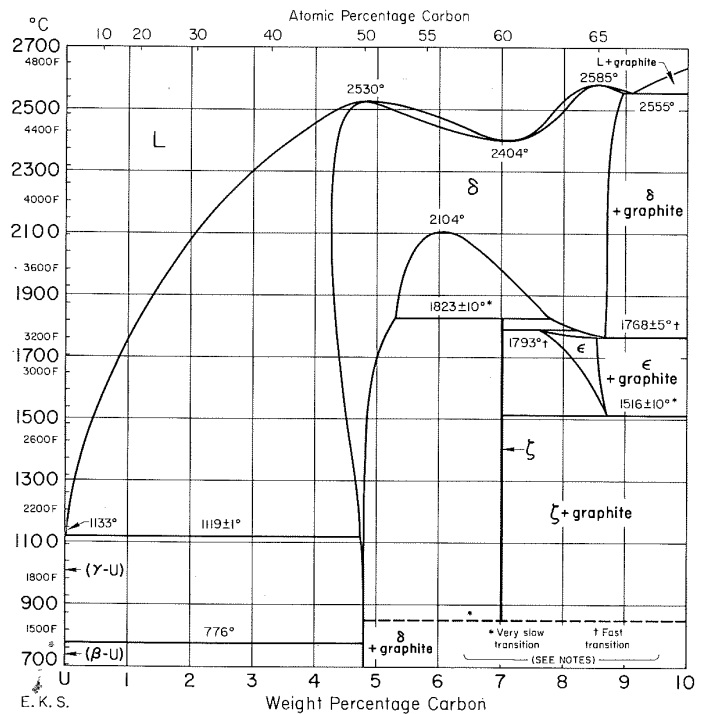
C-Ti Carbon-Titanium



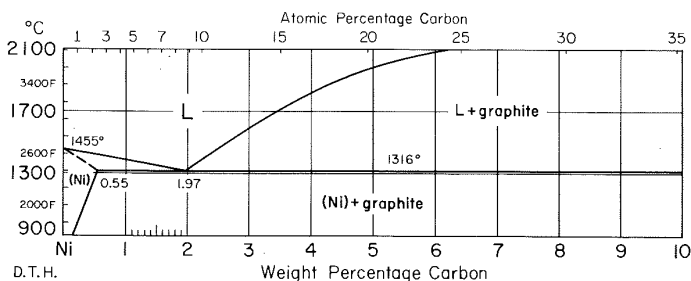
C-Mo Carbon-Molybdenum



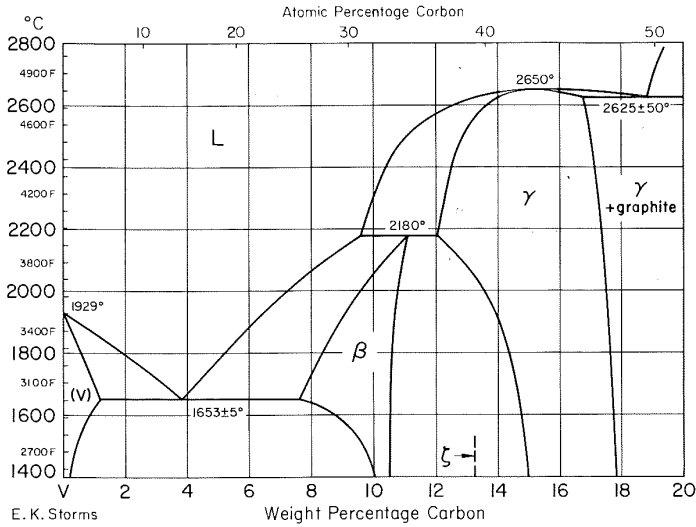
C-U Carbon-Uranium



C-Ni Carbon Nickel

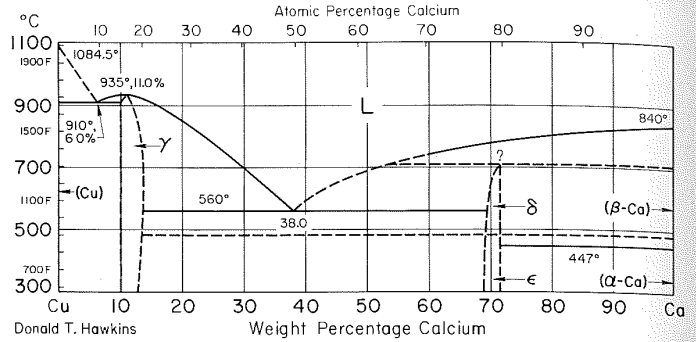


C-V Carbon-Vanadium



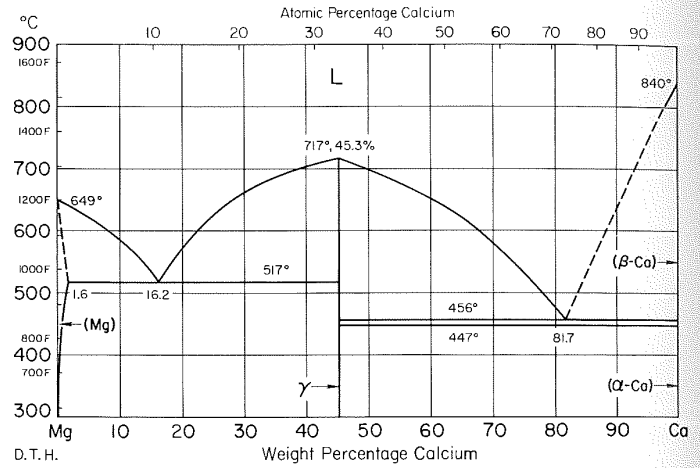
E. K. Storms

Ca-Cu Calcium-Copper



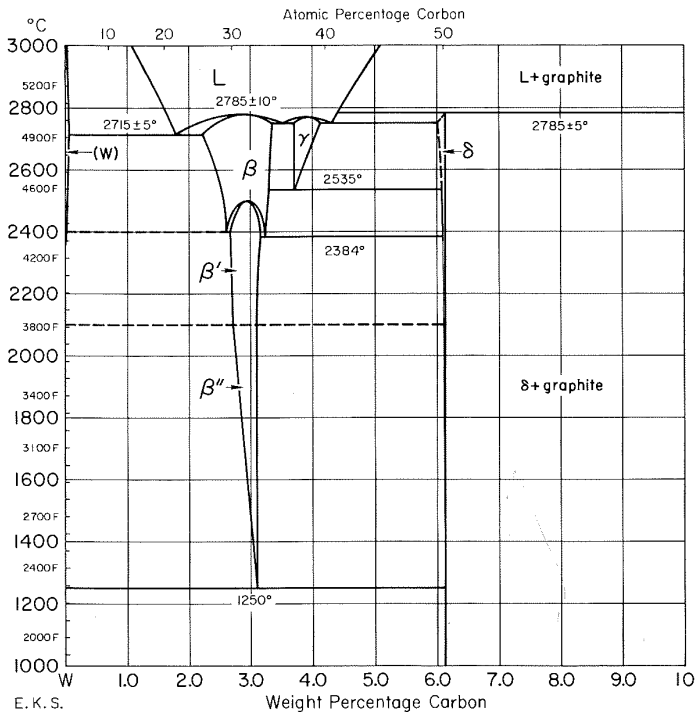
Donald T. Hawkins

Ca-Mg Calcium-Magnesium



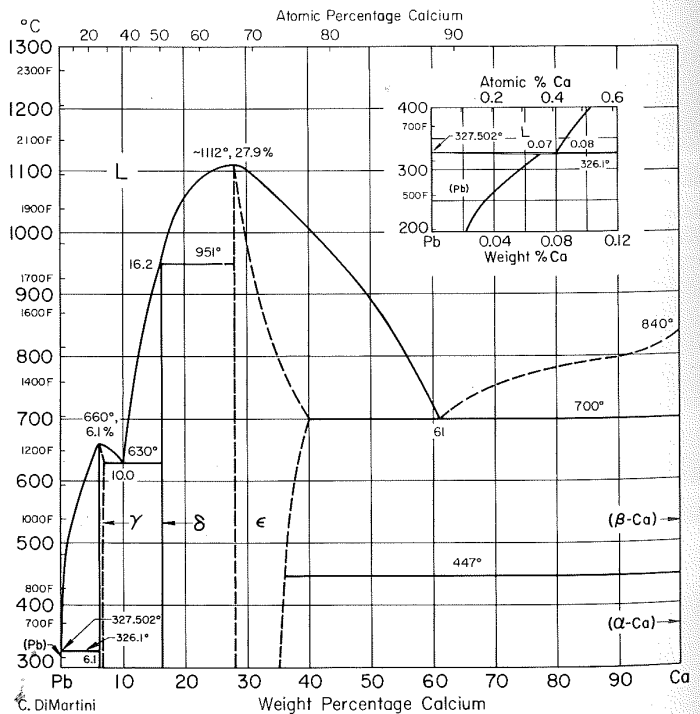
D. T. H.

C-W Carbon-Tungsten



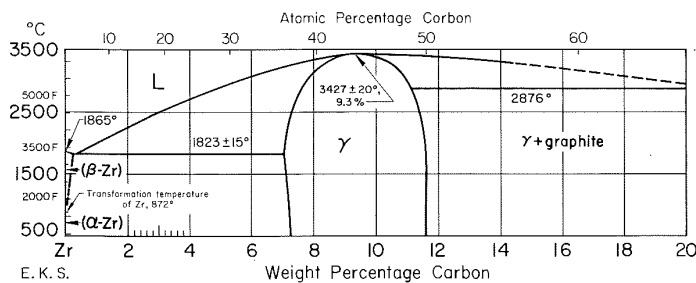
E. K. S.

Ca-Pb Calcium-Lead



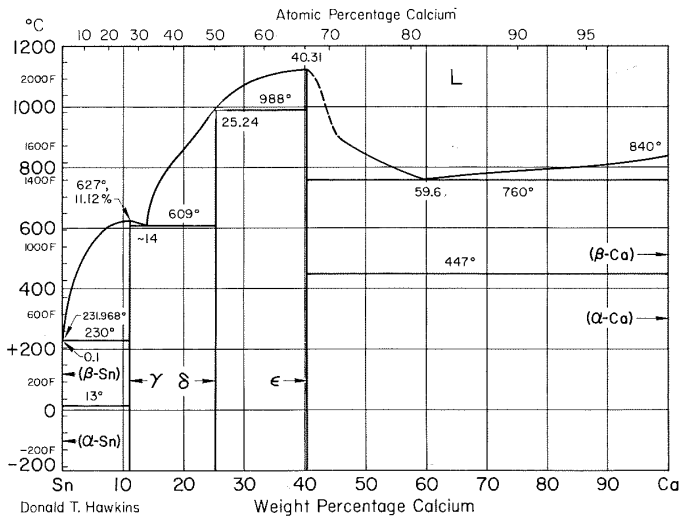
C. DiMartini

C-Zr Carbon-Zirconium

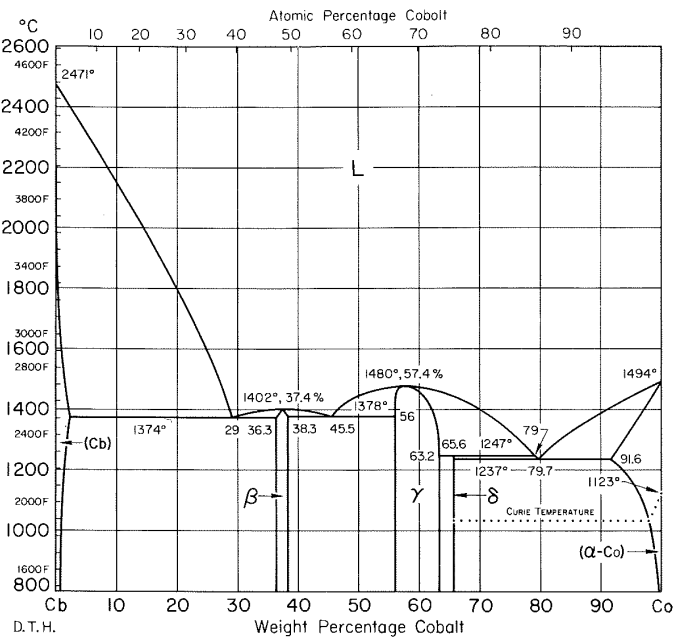


E. K. S.

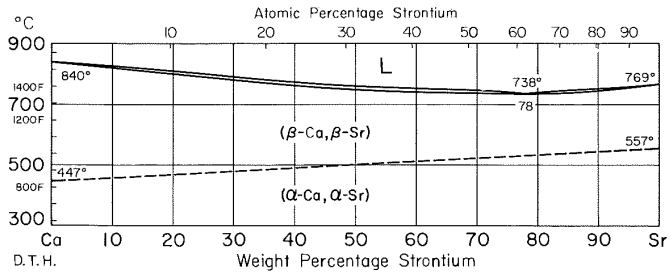
Ca-Sn Calcium-Tin



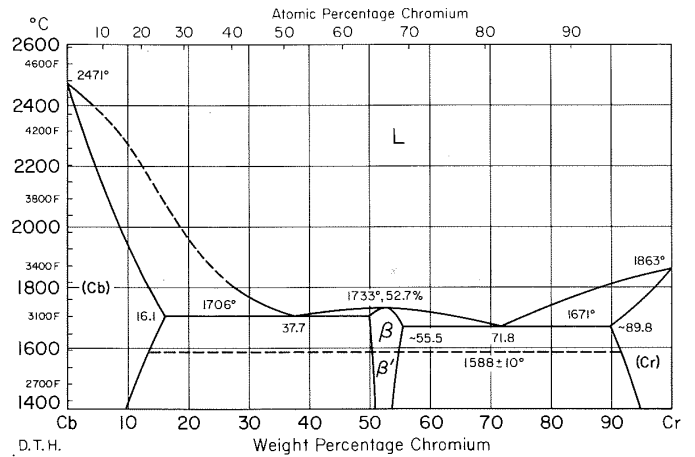
Cb-Co Columbiuim-Cobalt



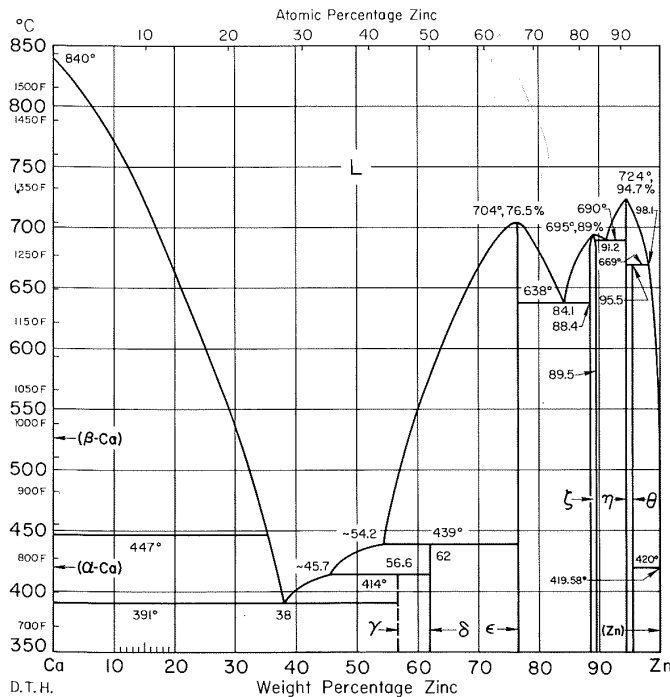
Ca-Sr Calcium-Strontium



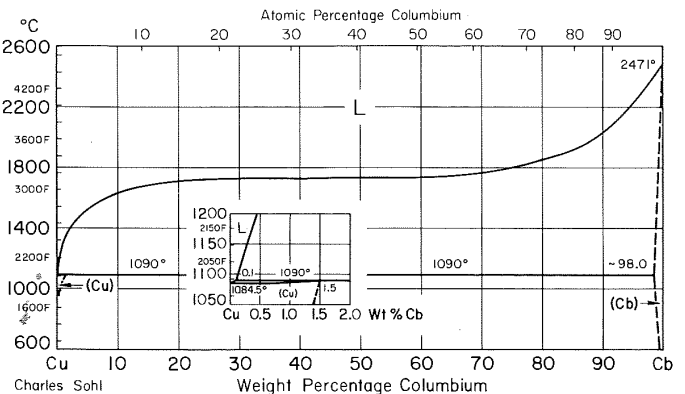
Cb-Cr Columbiuim-Chromium



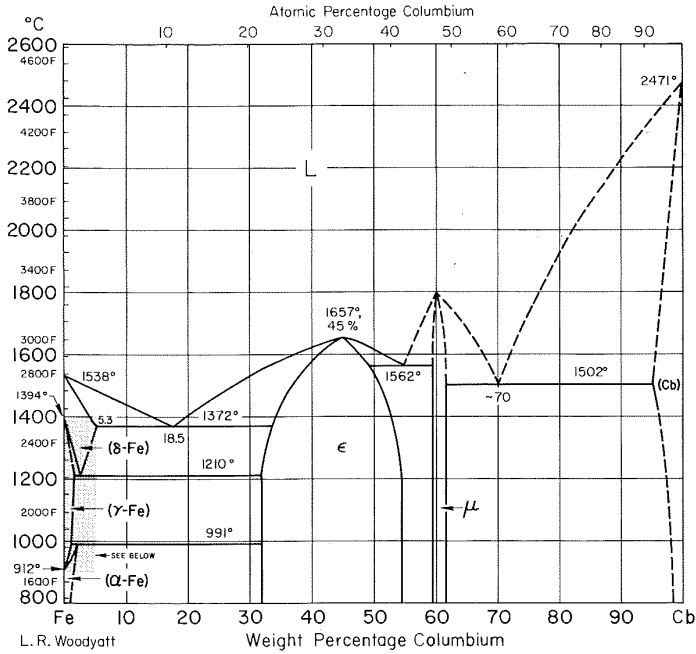
Ca-Zn Calcium-Zinc



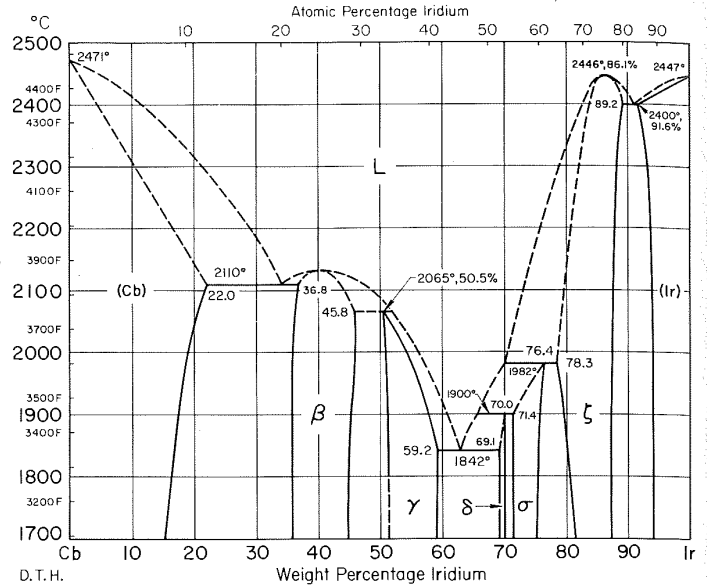
Cb-Cu Columbiuim-Copper



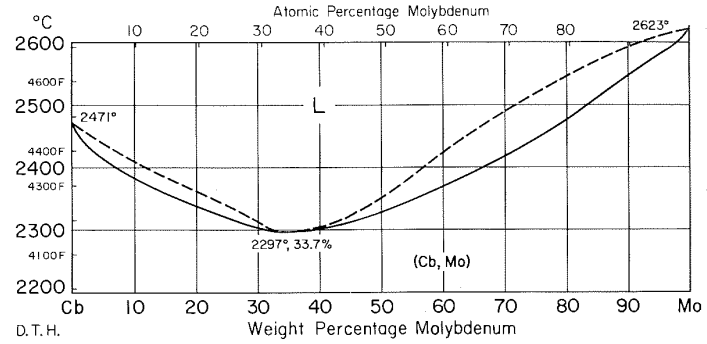
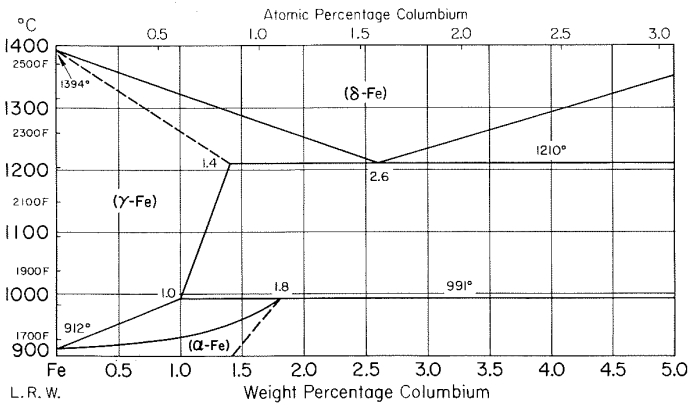
Cb-Fe Columbian-Iron



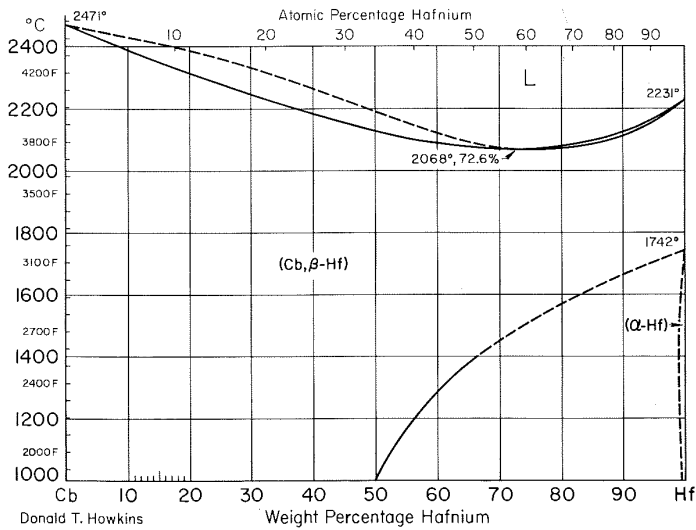
Cb-Ir Columbian-Iridium



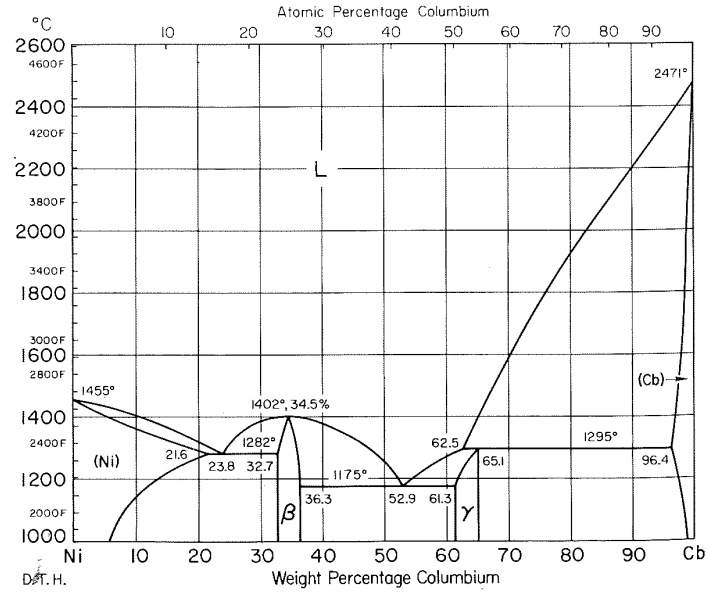
Cb-Mo Columbian-Molybdenum



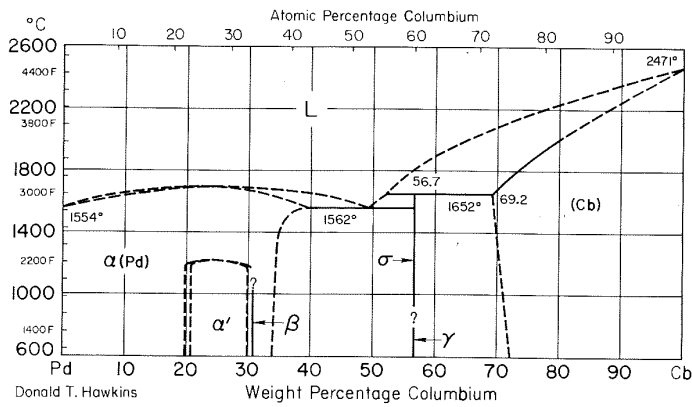
Cb-Hf Columbian-Hafnium



Cb-Ni Columbian-Nickel

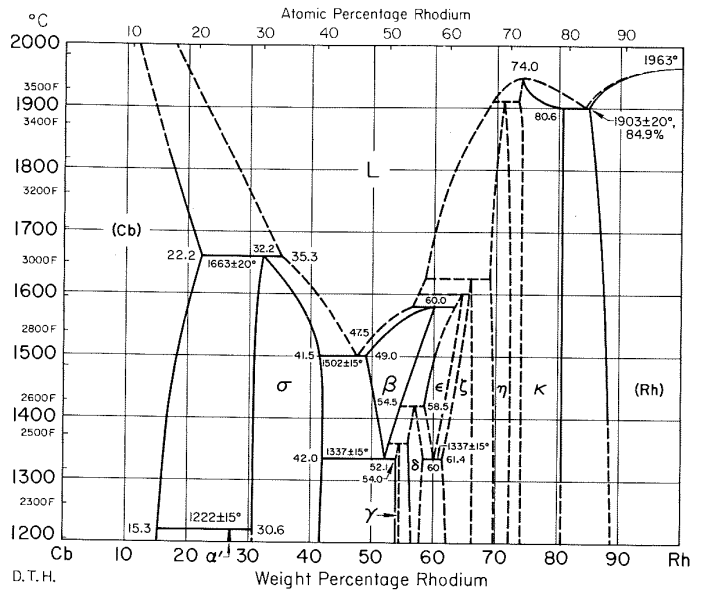


Cb-Pd Columbium-Palladium



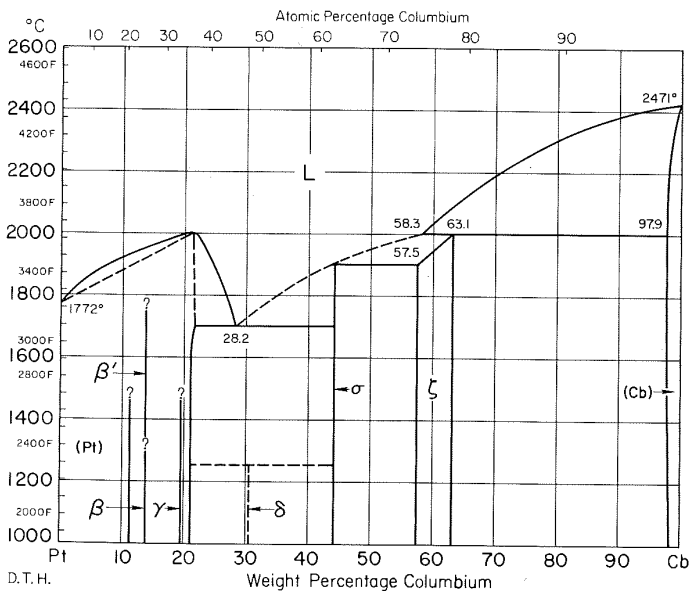
Donald T. Hawkins

Cb-Rh Columbium-Rhodium



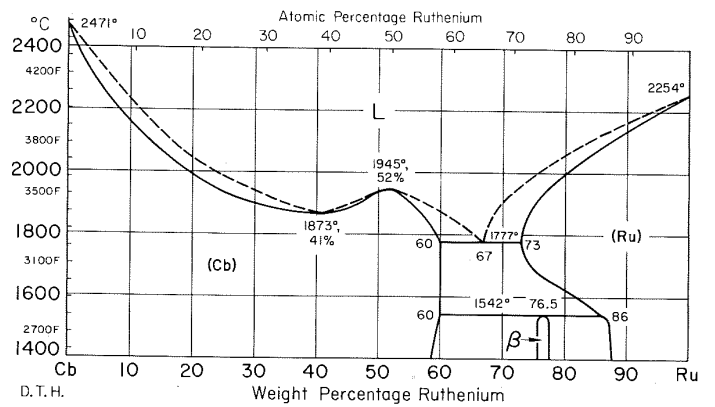
D.T.H.

Cb-Pt Columbium-Platinum



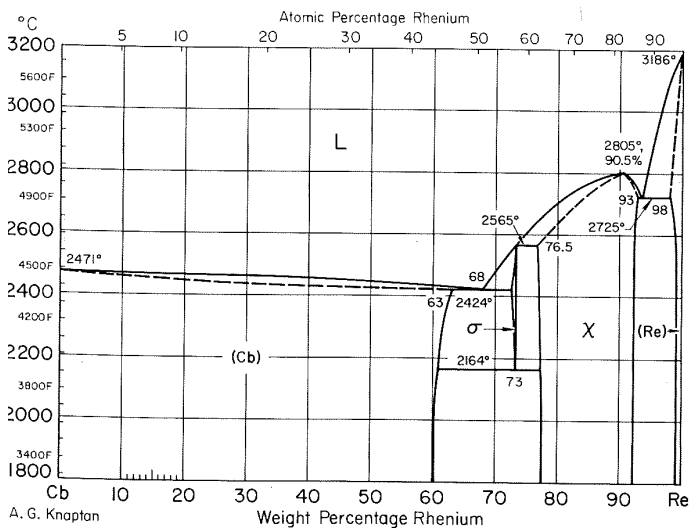
D.T.H.

Cb-Ru Columbium-Ruthenium



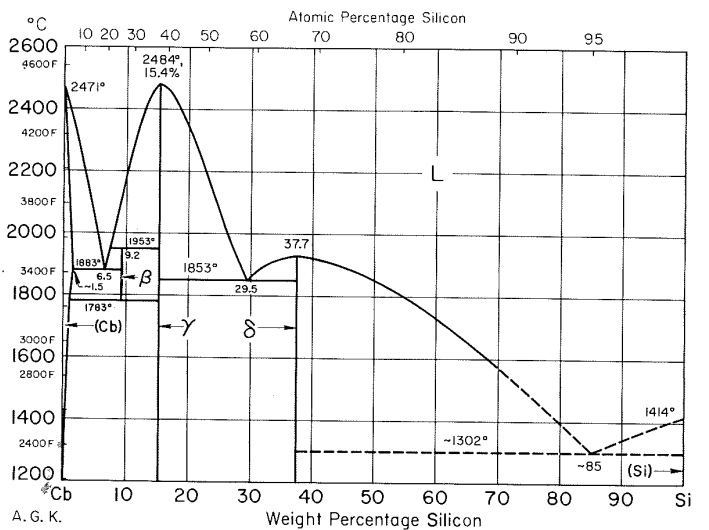
D.T.H.

Cb-Re Columbium-Rhenium



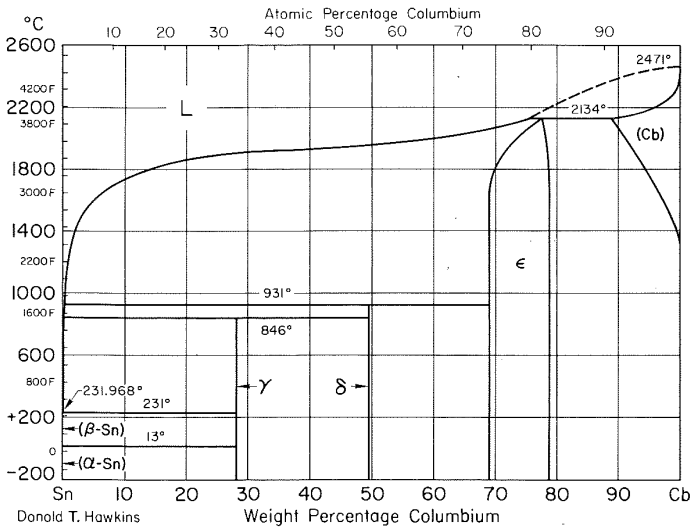
A. G. Knapton

Cb-Si Columbium-Silicon

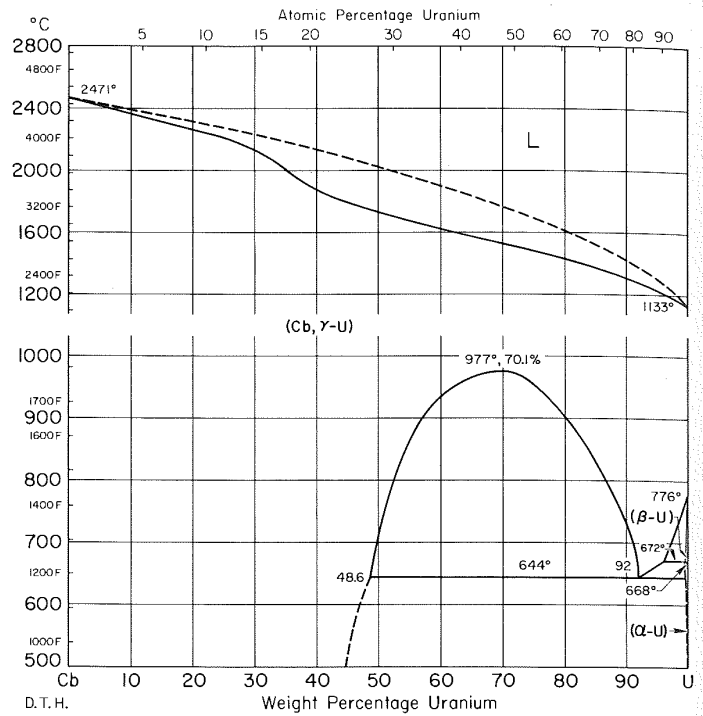


A. G. K.

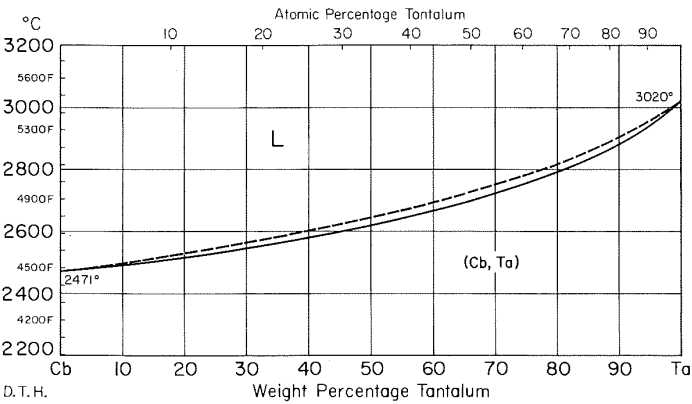
Cb-Sn Columbium-Tin



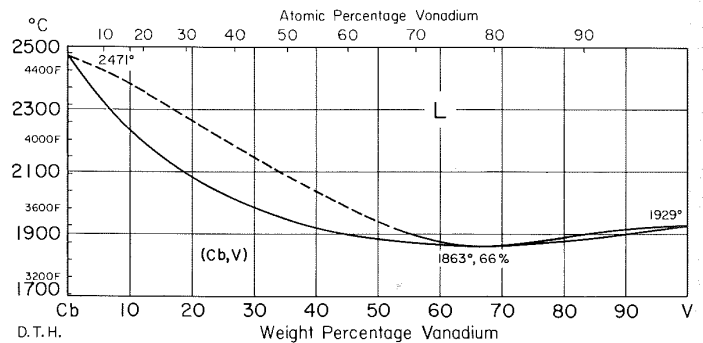
Cb-U Columbium-Uranium



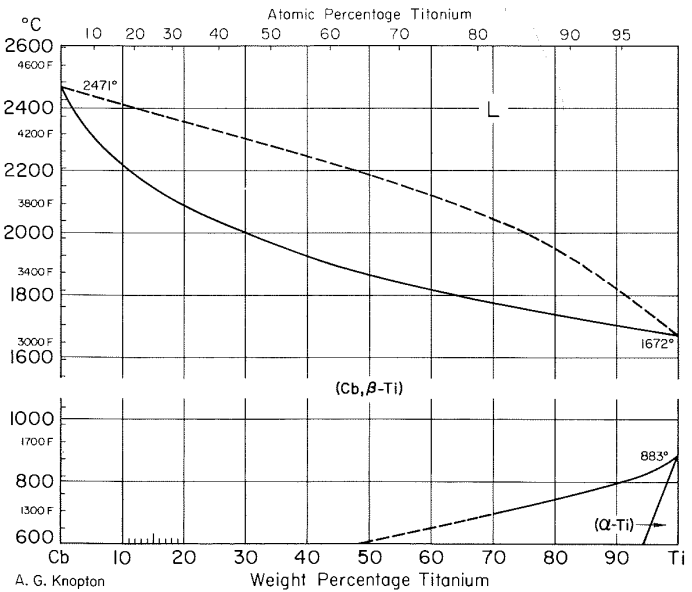
Cb-Ta Columbium-Tantalum



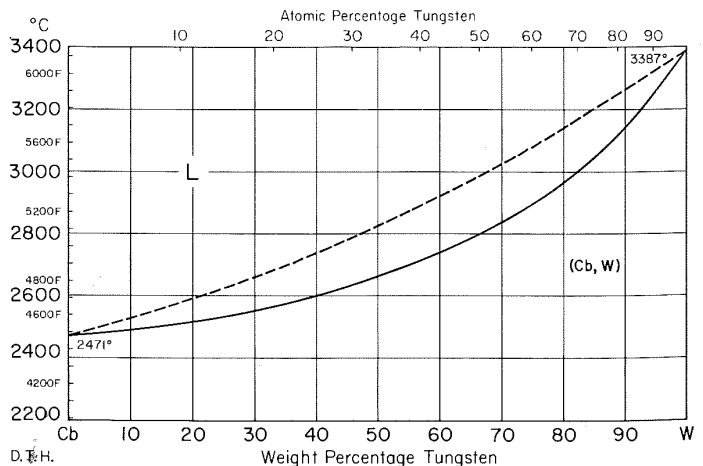
Cb-V Columbium-Vanadium



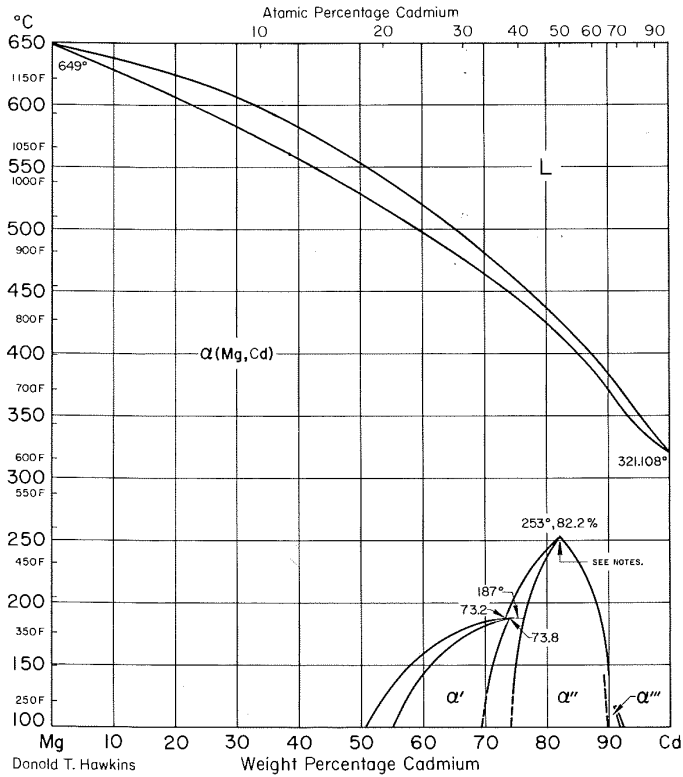
Cb-Ti Columbium-Titanium



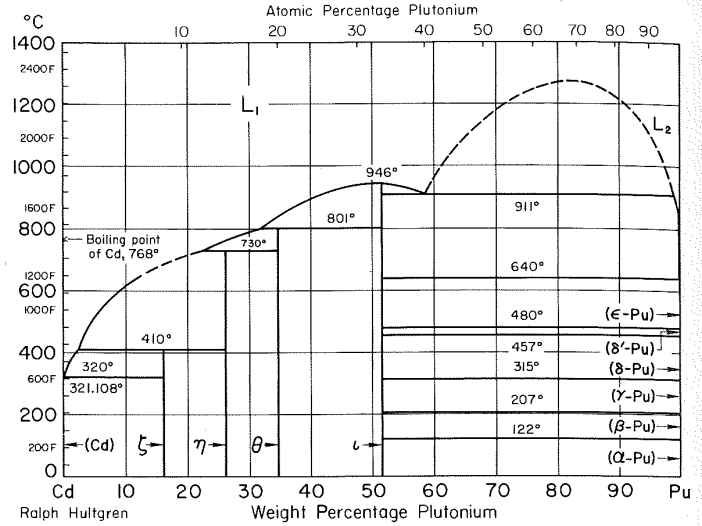
Cb-W Columbium-Tungsten



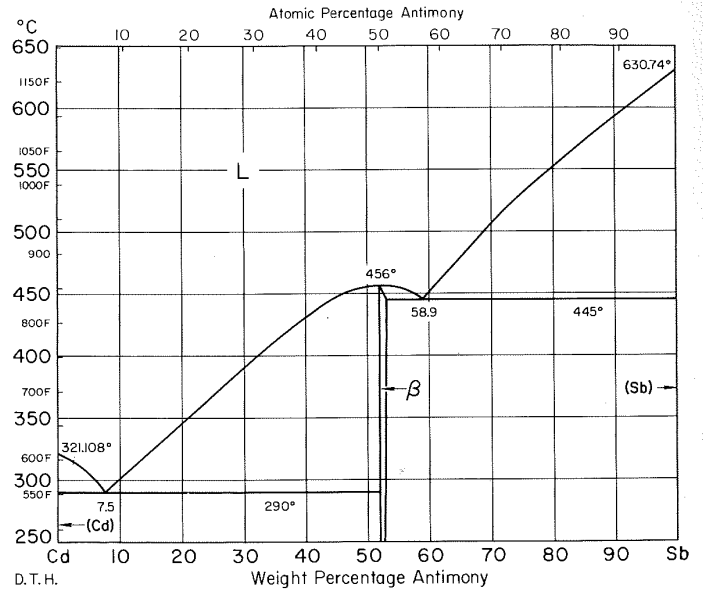
Cd-Mg Cadmium-Magnesium



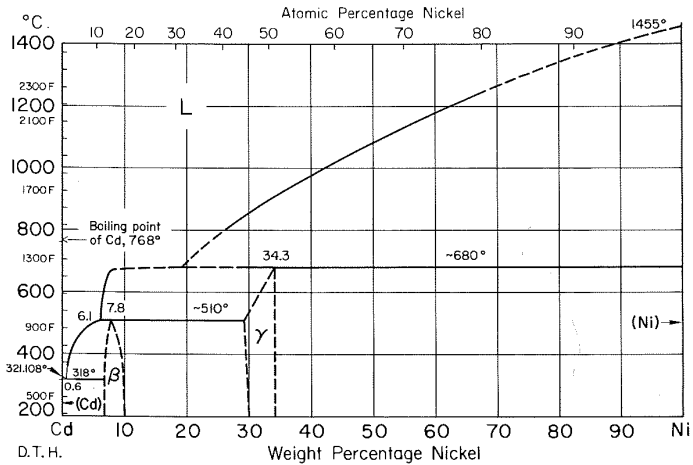
Cd-Pu Cadmium-Plutonium



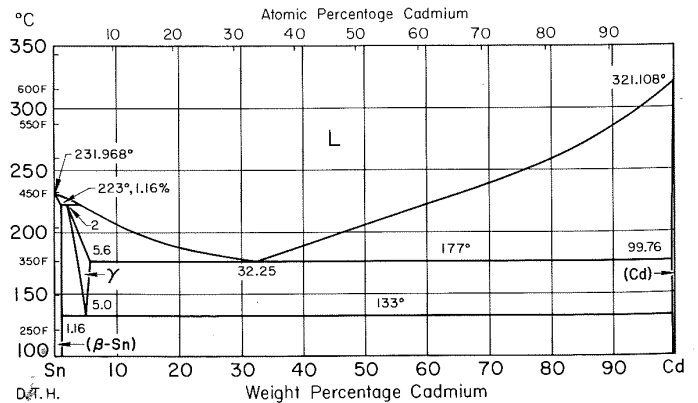
Cd-Sb Cadmium-Antimony



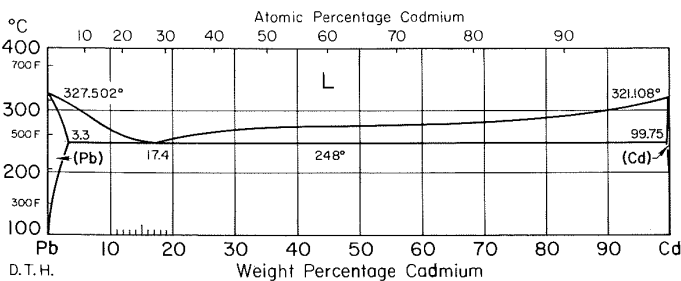
Cd-Ni Cadmium-Nickel



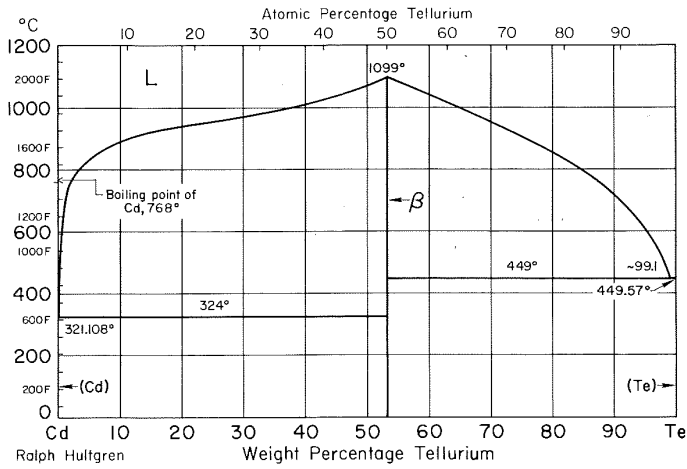
Cd-Sn Cadmium-Tin



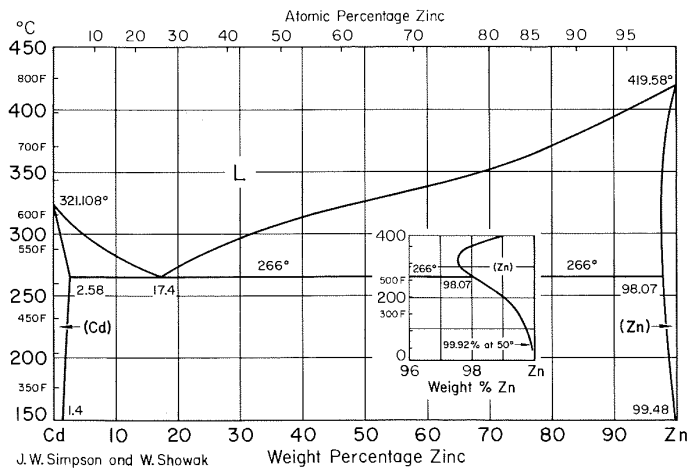
Cd-Pb Cadmium-Lead



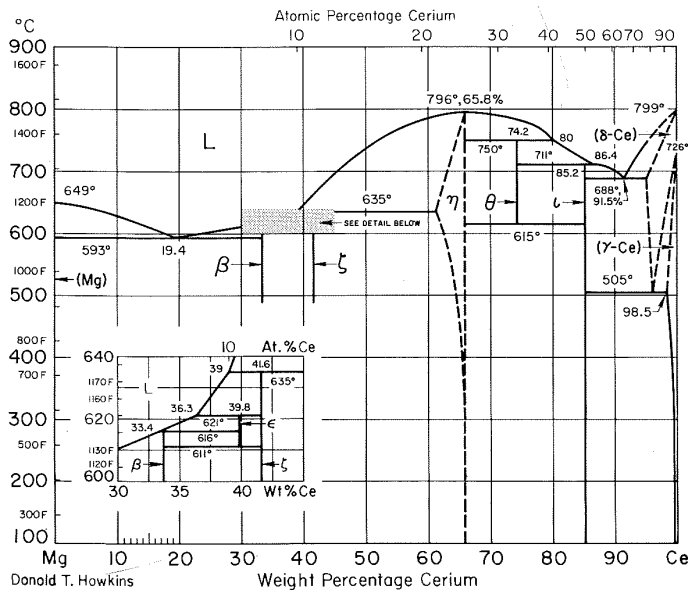
Cd-Te Cadmium-Tellurium



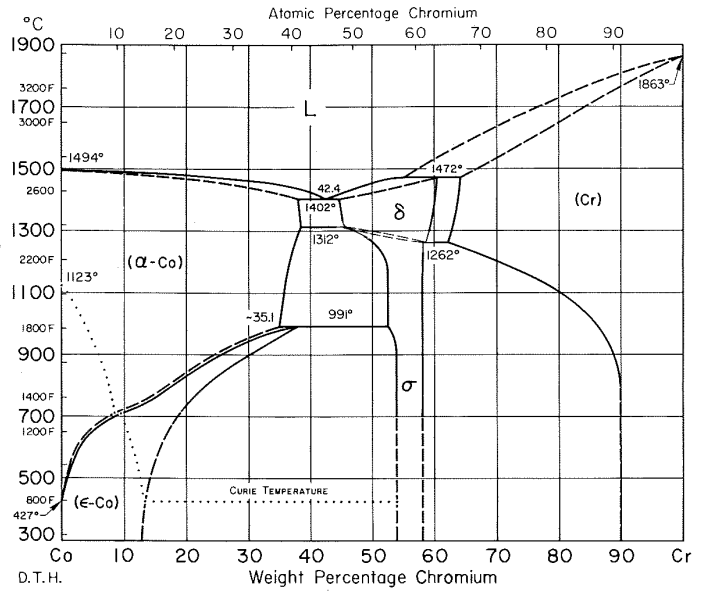
Cd-Zn Cadmium-Zinc



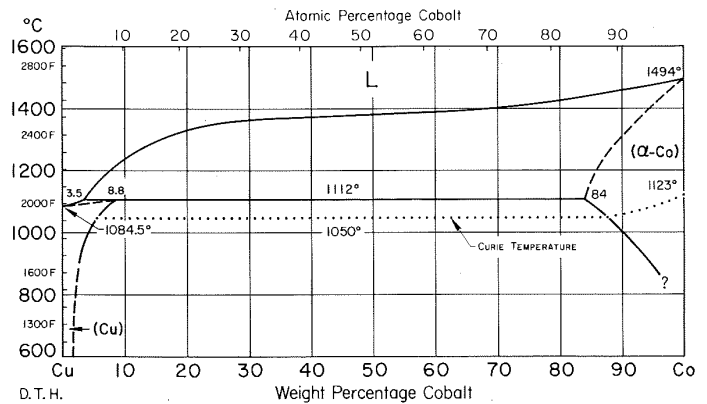
Ce-Mg Cerium-Magnesium



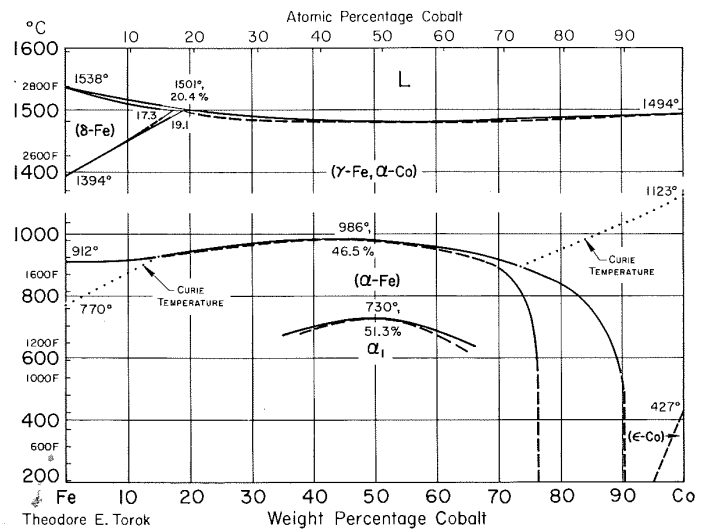
Co-Cr Cobalt-Chromium



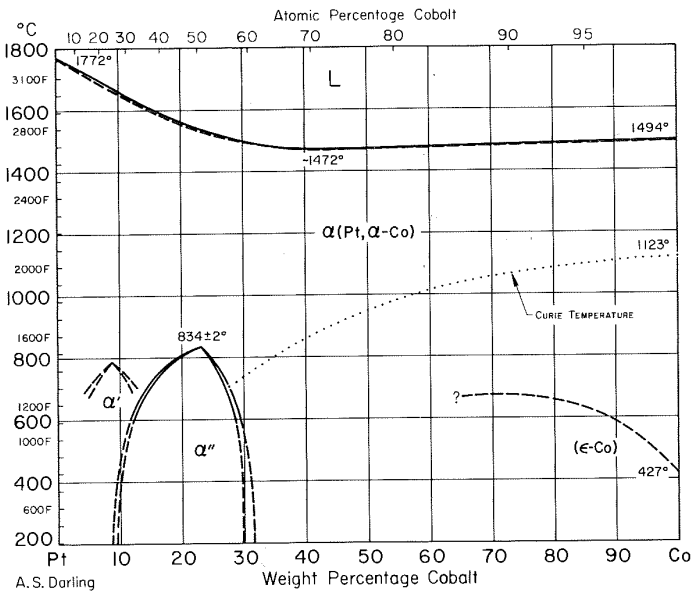
Co-Cu Cobalt-Copper



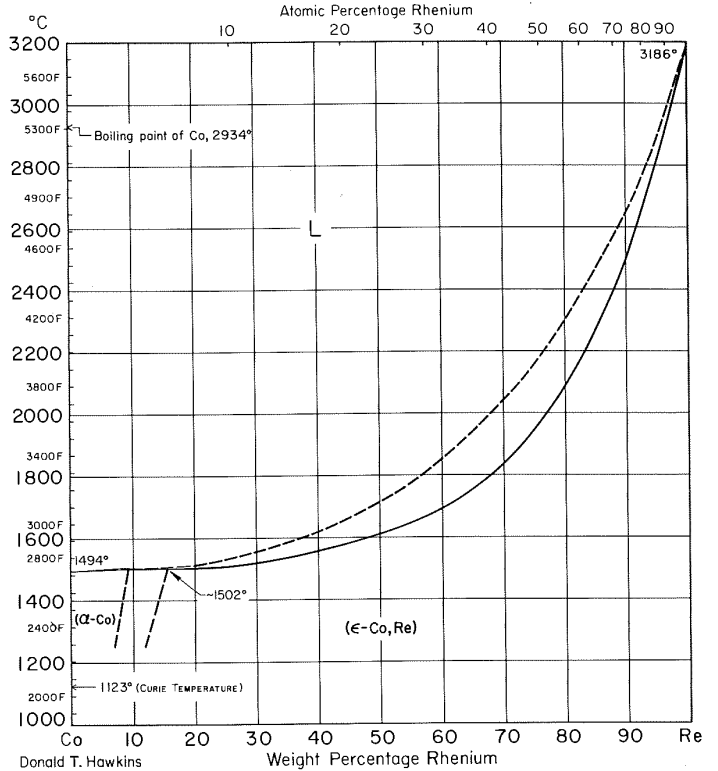
Co-Fe Cobalt-Iron



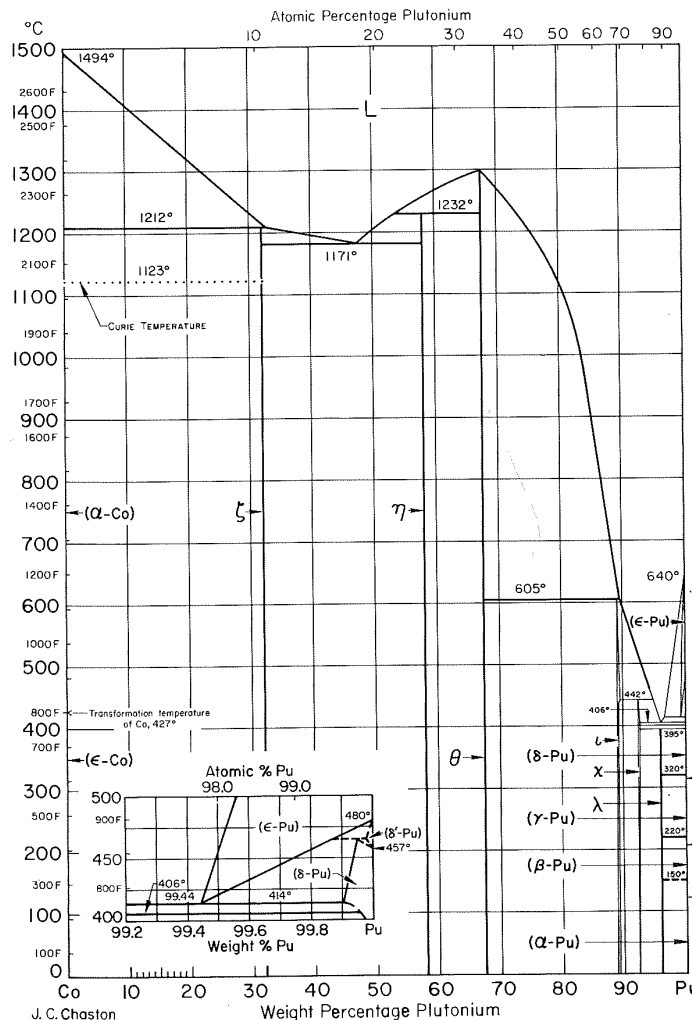
Co-Pt Cobalt-Platinum



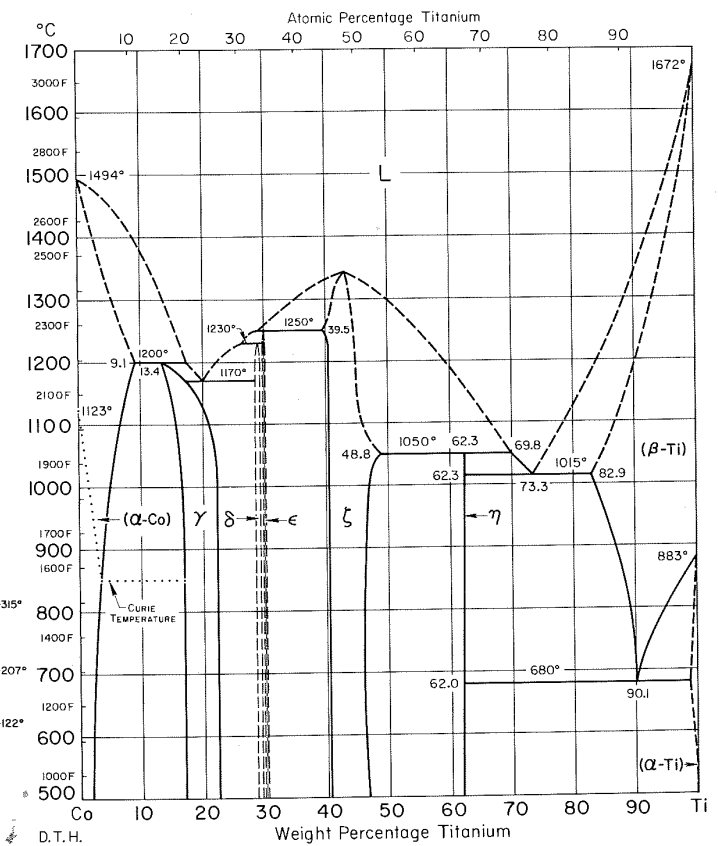
Co-Re Cobalt-Rhenium



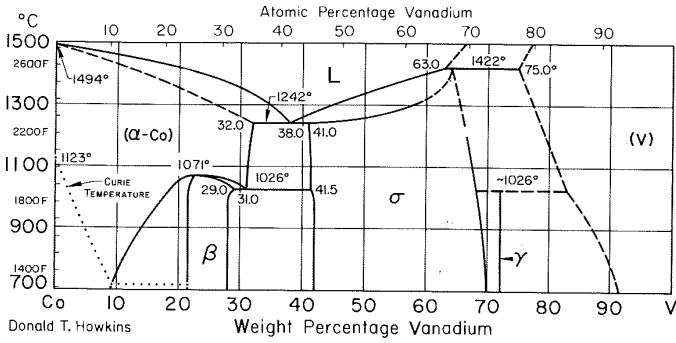
Co-Pu Cobalt-Plutonium



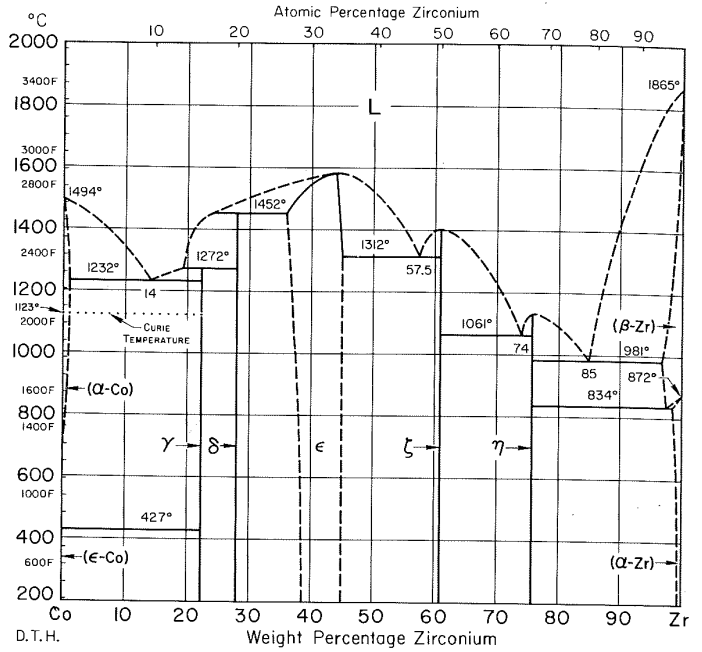
Co-Ti Cobalt-Titanium



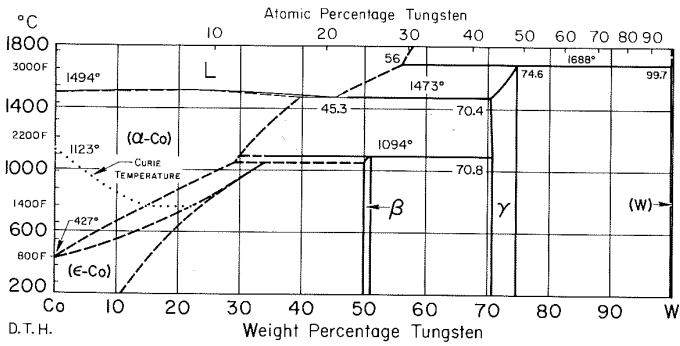
Co-V Cobalt-Vanadium



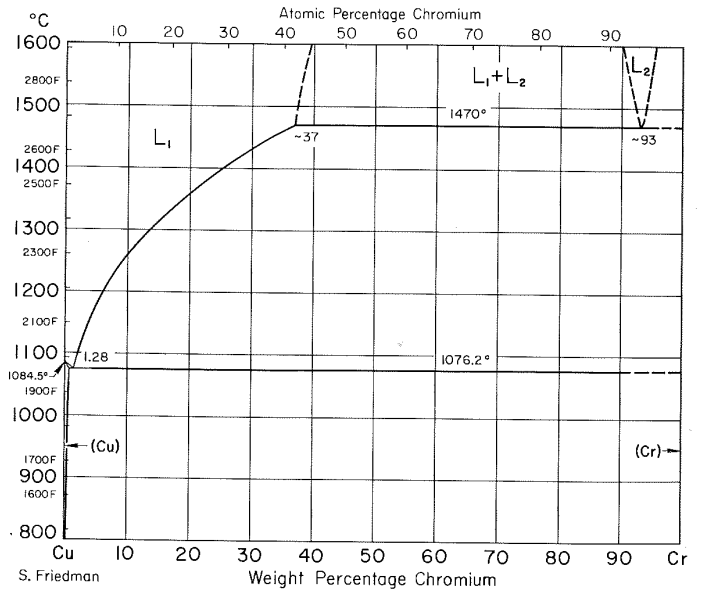
Co-Zr Cobalt-Zirconium



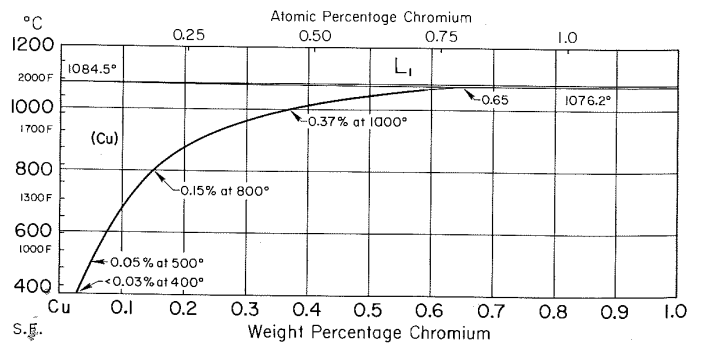
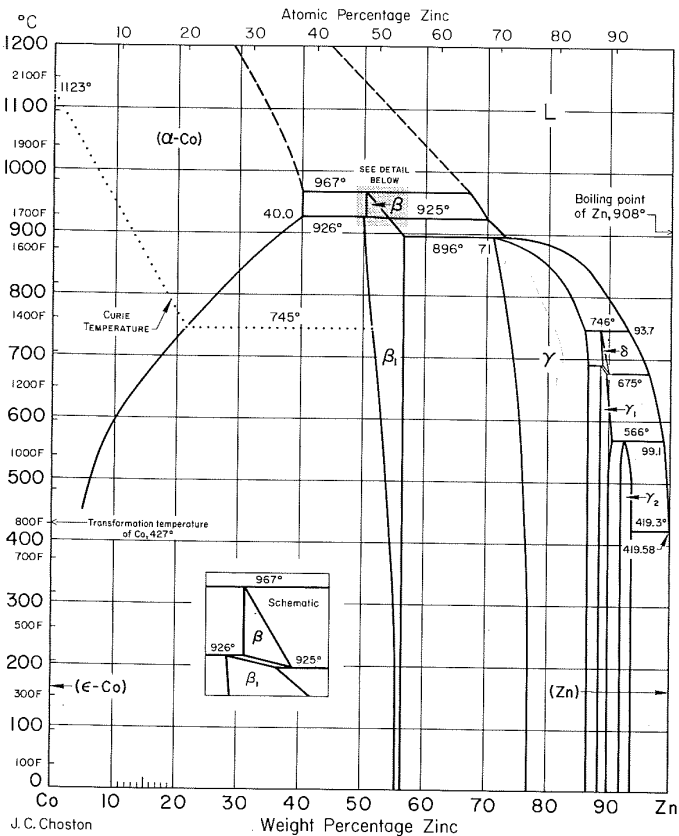
Co-W Cobalt-Tungsten



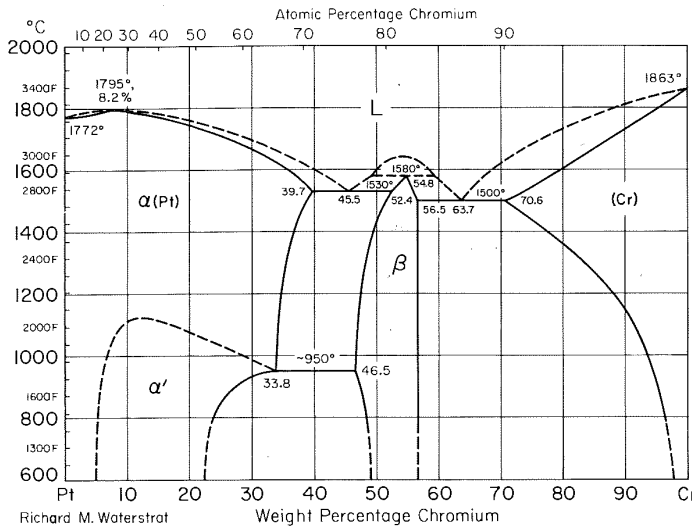
Cr-Cu Chromium-Copper



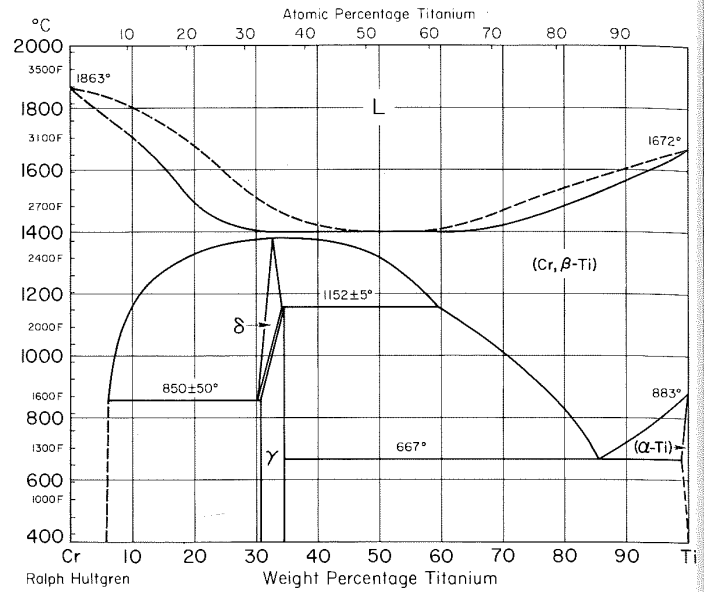
Co-Zn Cobalt-Zinc



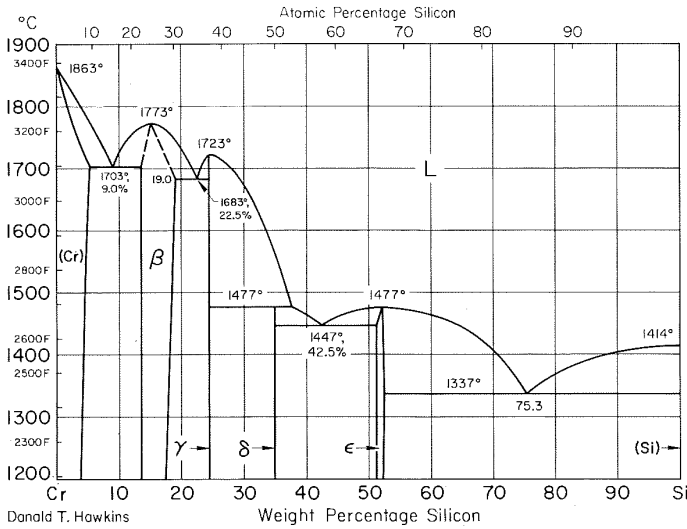
Cr-Pt Chromium-Platinum



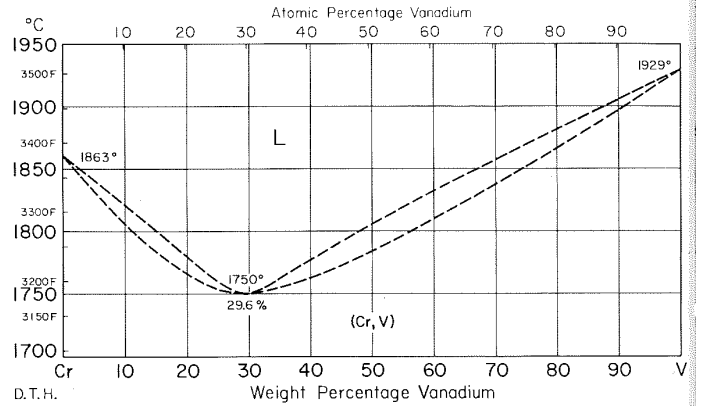
Cr-Ti Chromium-Titanium



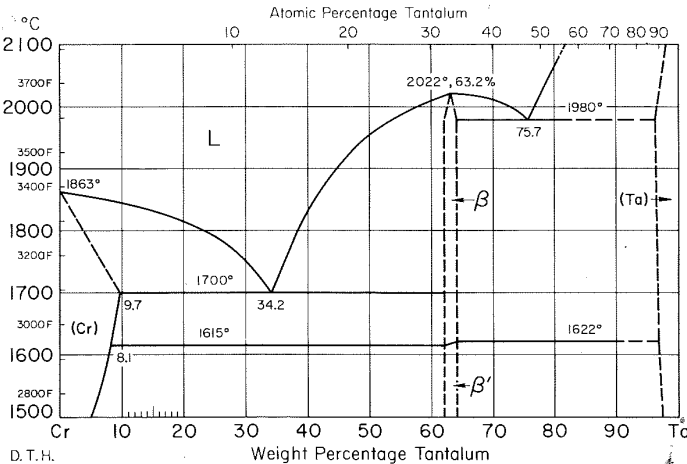
Cr-Si Chromium-Silicon



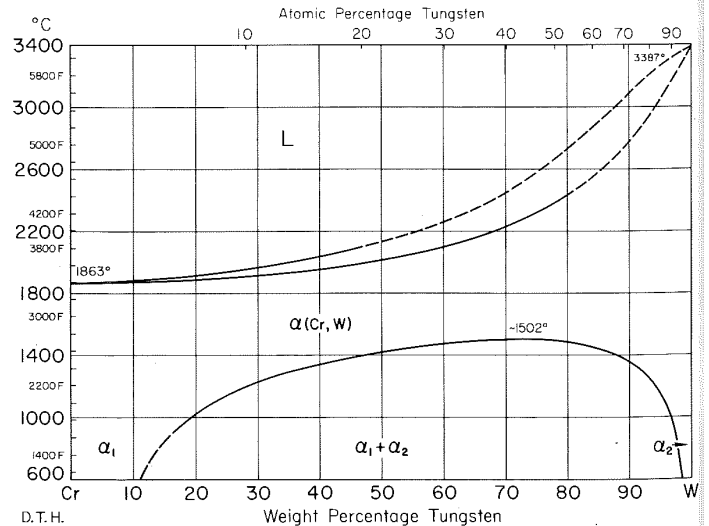
Cr-V Chromium-Vanadium



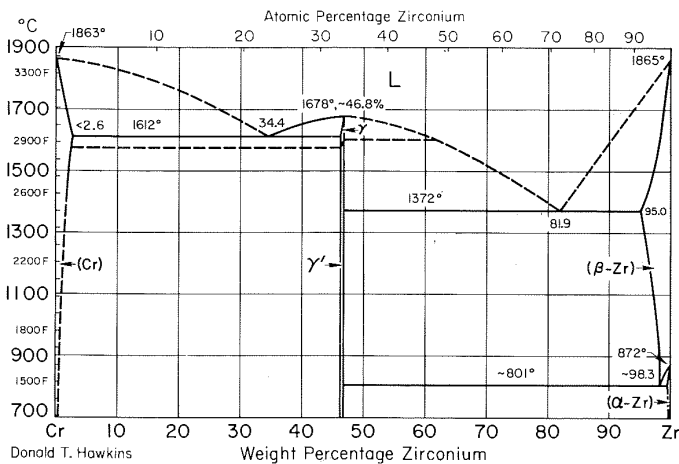
Cr-Ta Chromium-Tantalum



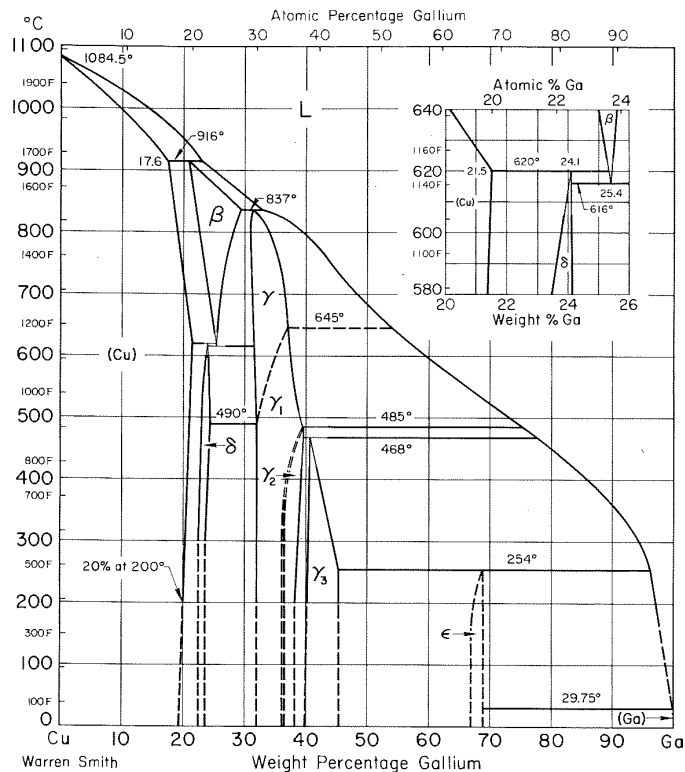
Cr-W Chromium-Tungsten



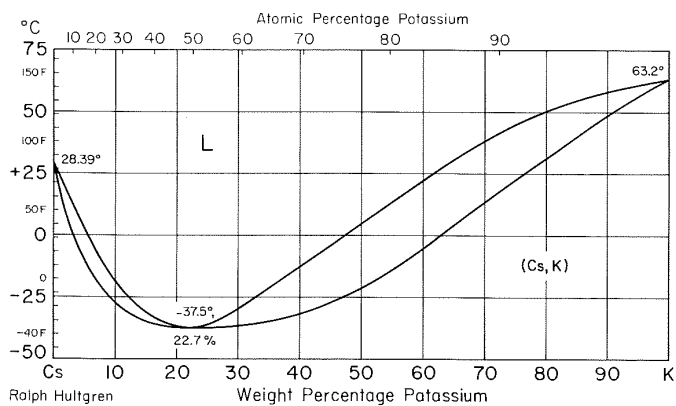
Cr-Zr Chromium-Zirconium



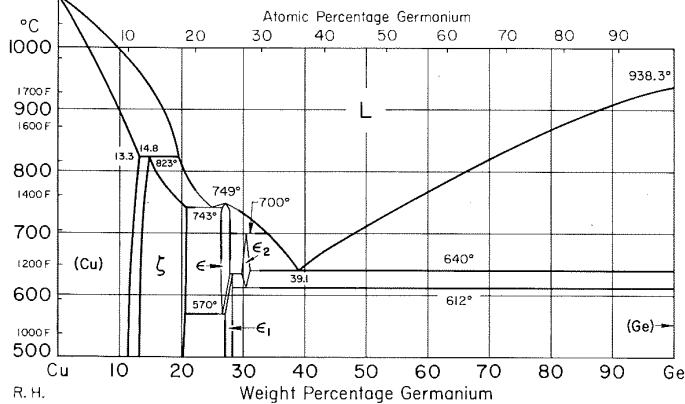
Cu-Ga Copper-Gallium



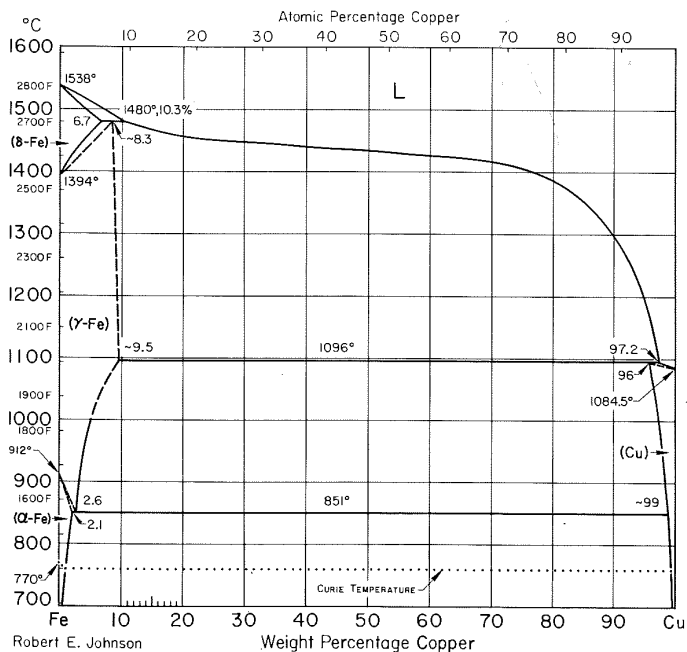
Cs-K Cesium-Potassium



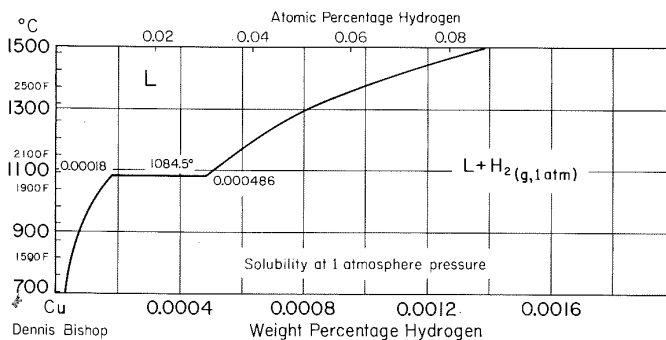
Cu-Ge Copper-Germanium



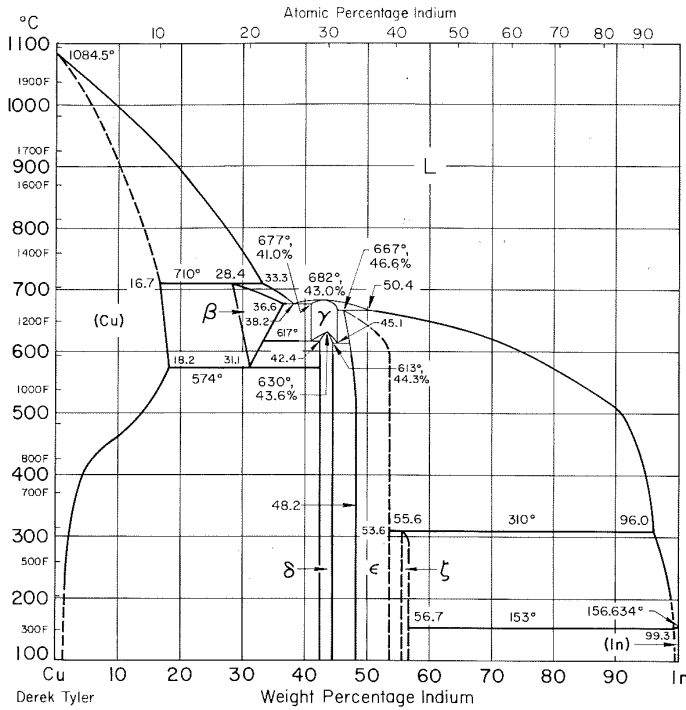
Cu-Fe Copper-Iron



Cu-H Copper-Hydrogen

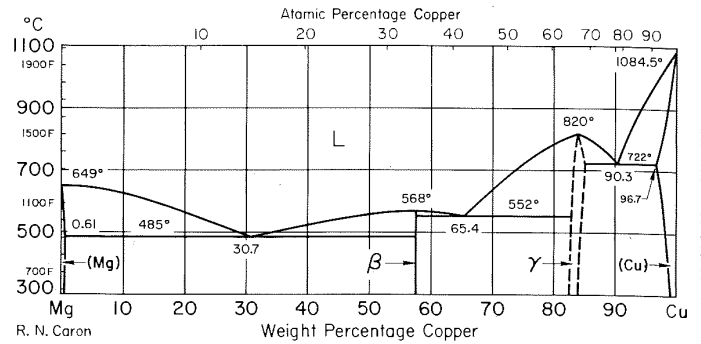


Cu-In Copper-Indium



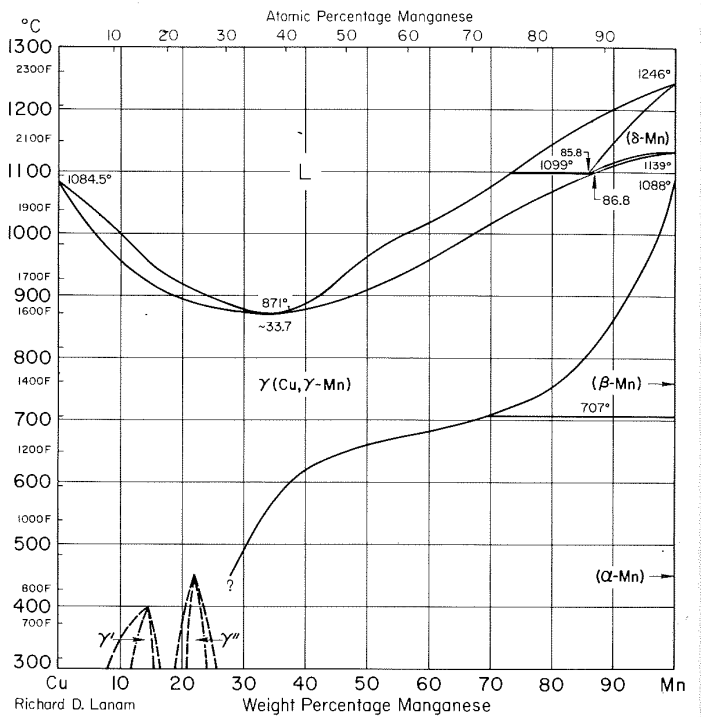
Derek Tyler

Cu-Mg Copper-Magnesium



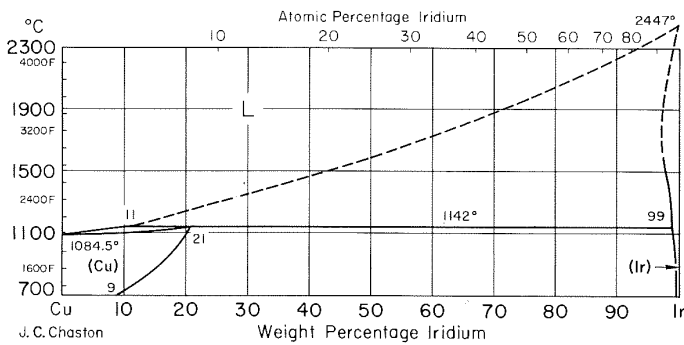
R. N. Caron

Cu-Mn Copper-Manganese



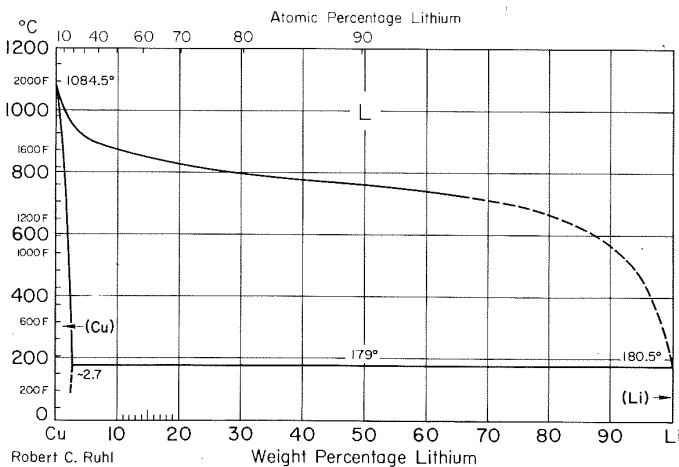
Richard D. Lanam

Cu-Ir Copper-Iridium



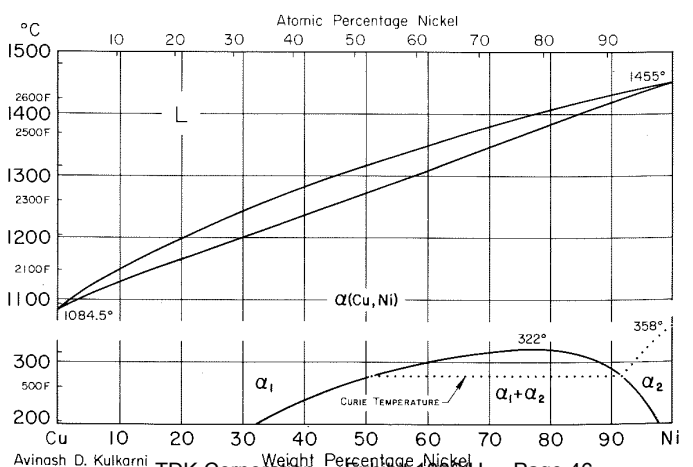
J. C. Chaston

Cu-Li Copper-Lithium



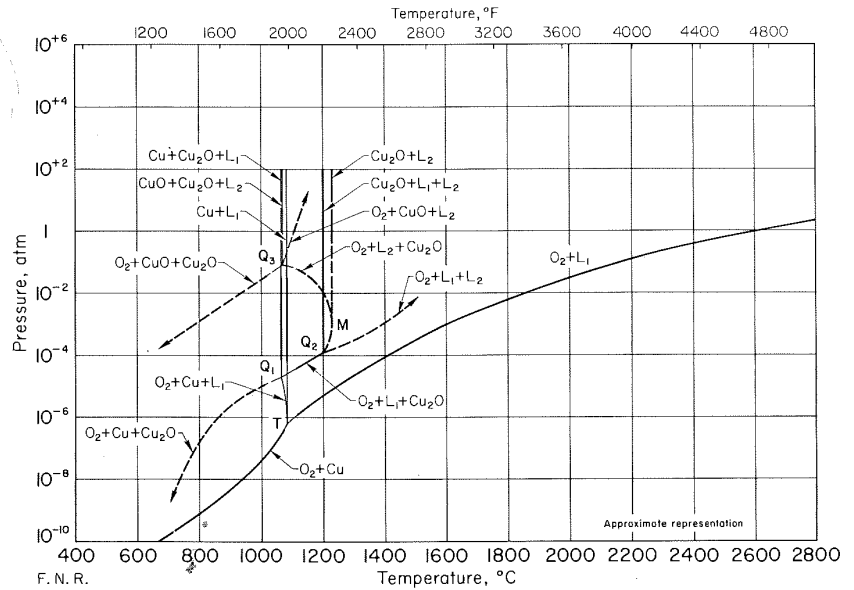
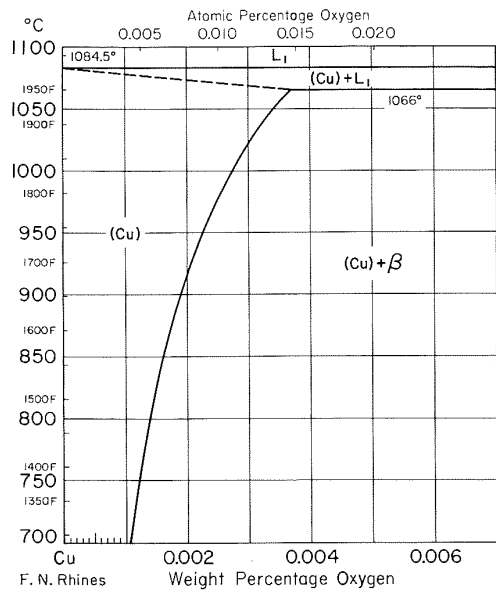
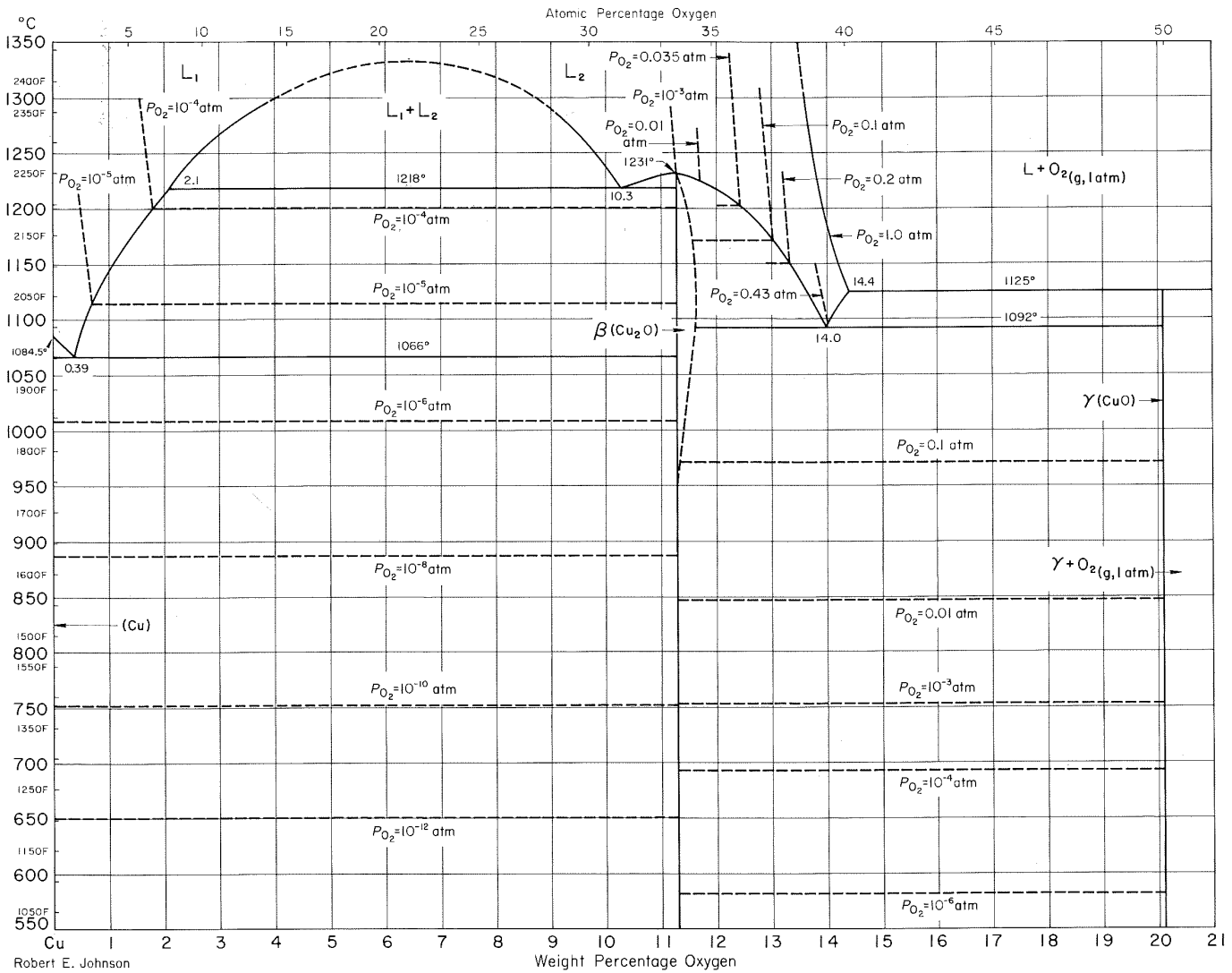
Robert C. Ruhl

Cu-Ni Copper-Nickel

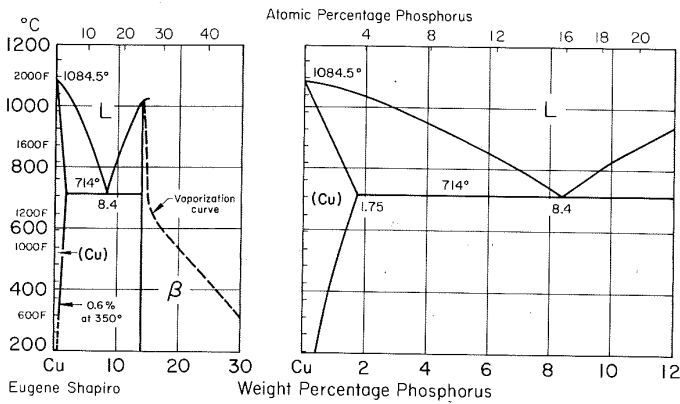


Avinash D. Kulkarni

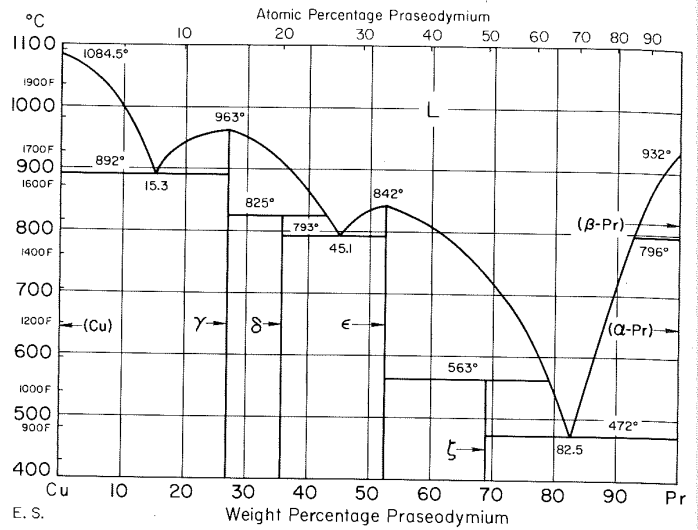
Cu-O Copper-Oxygen



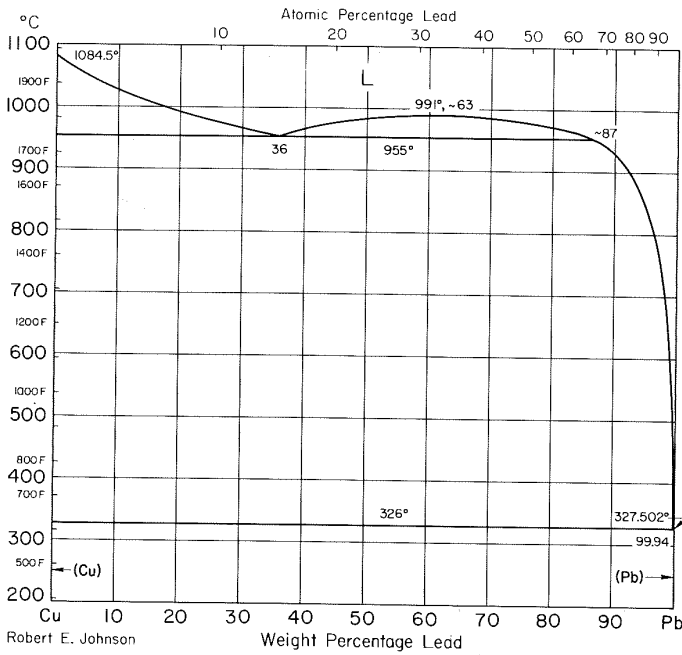
Cu-P Copper-Phosphorus



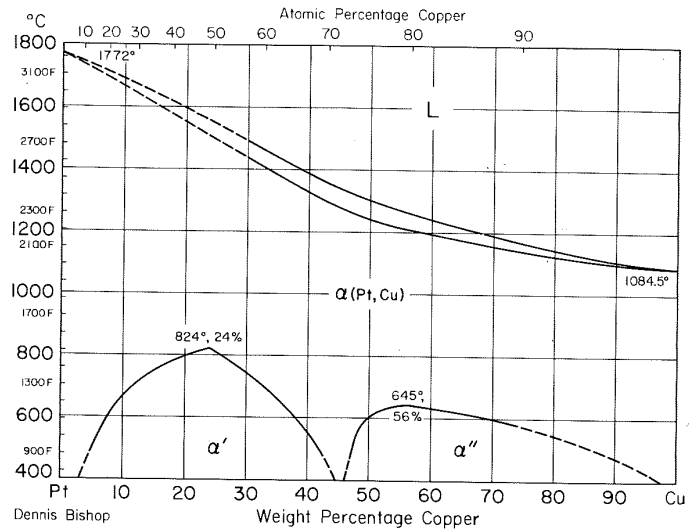
Cu-Pr Copper-Praseodymium



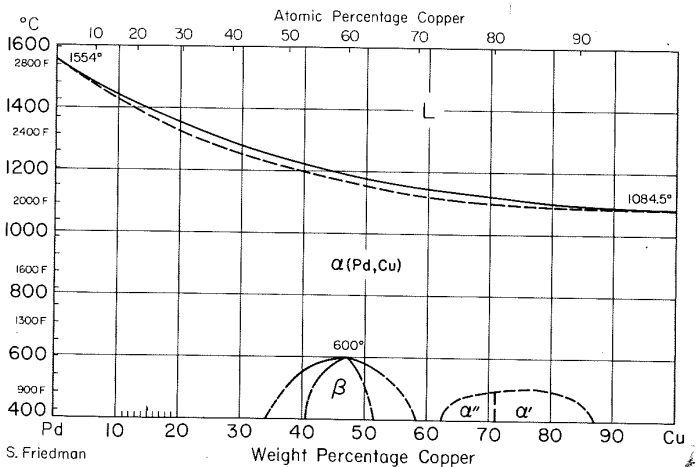
Cu-Pb Copper-Lead



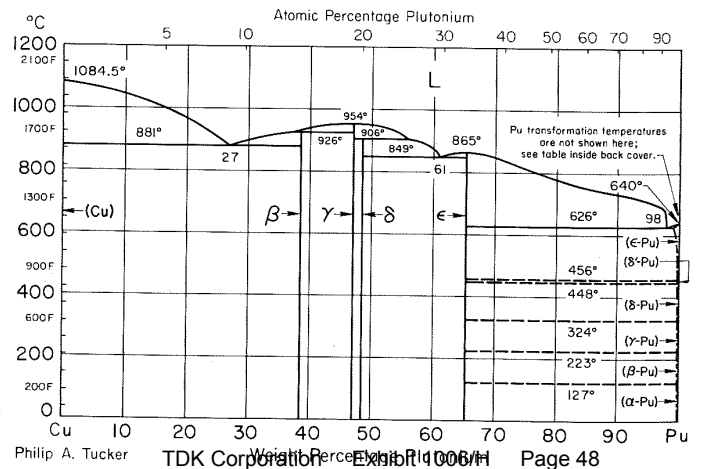
Cu-Pt Copper-Platinum



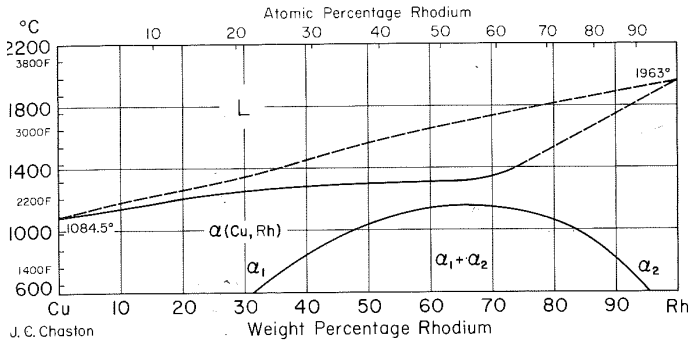
Cu-Pd Copper-Palladium



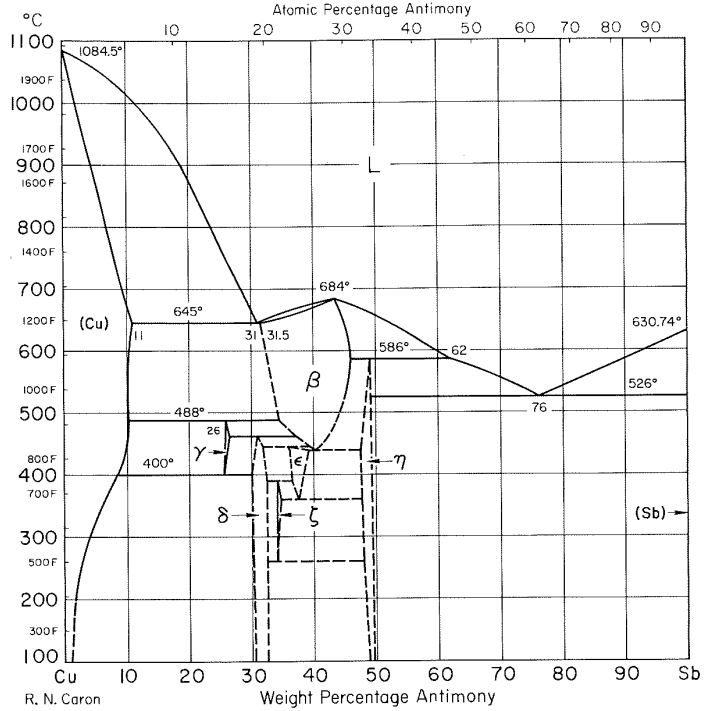
Cu-Pu Copper-Plutonium



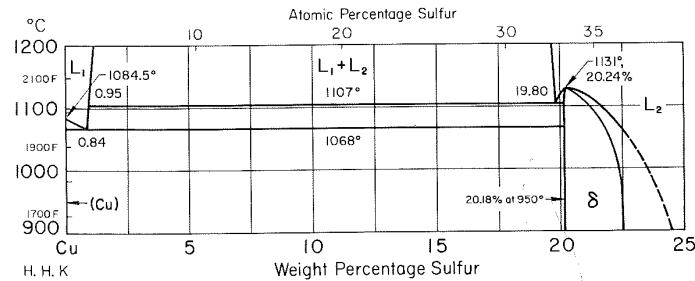
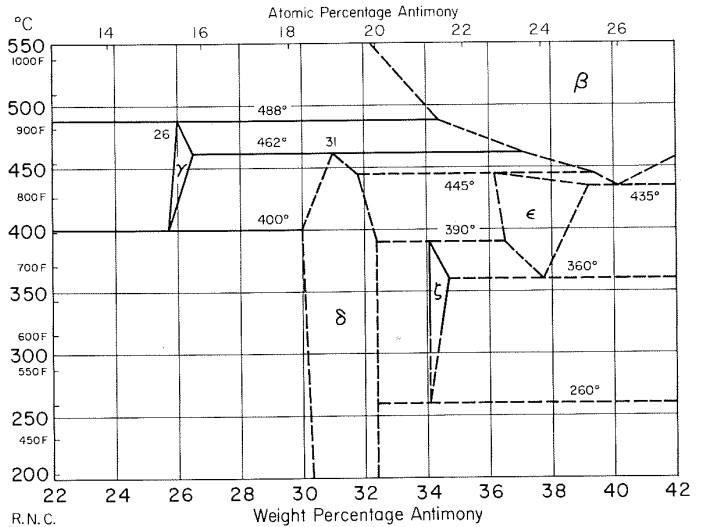
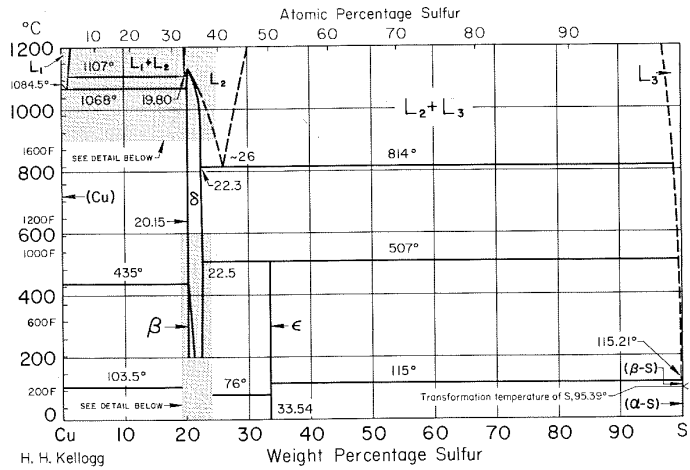
Cu-Rh Copper-Rhodium



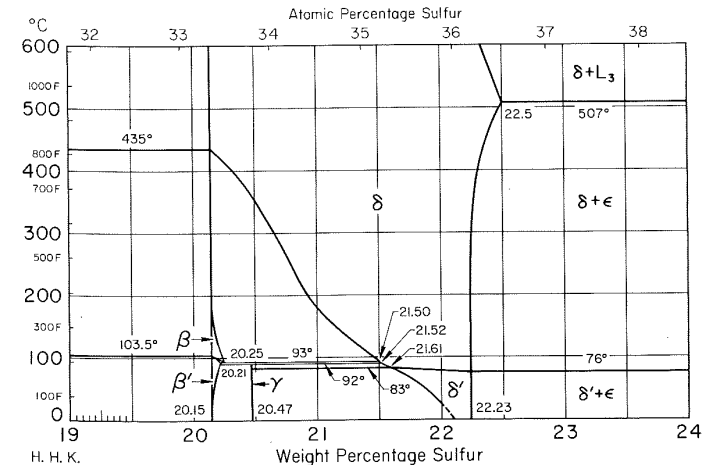
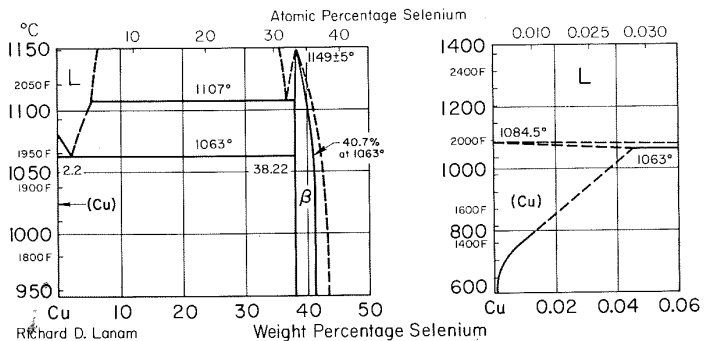
Cu-Sb Copper-Antimony



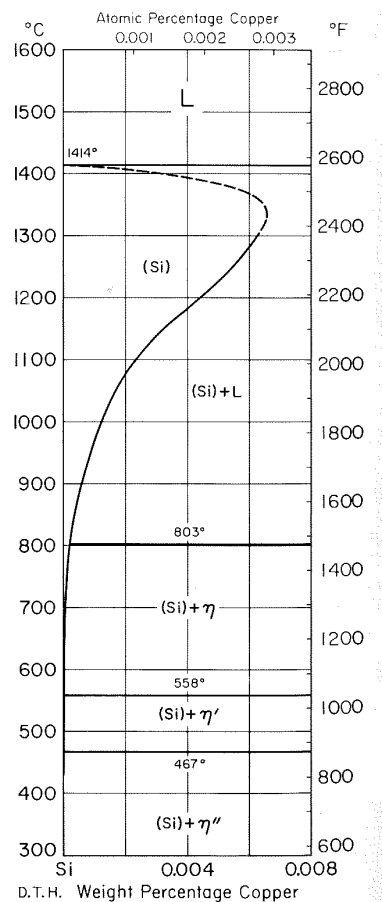
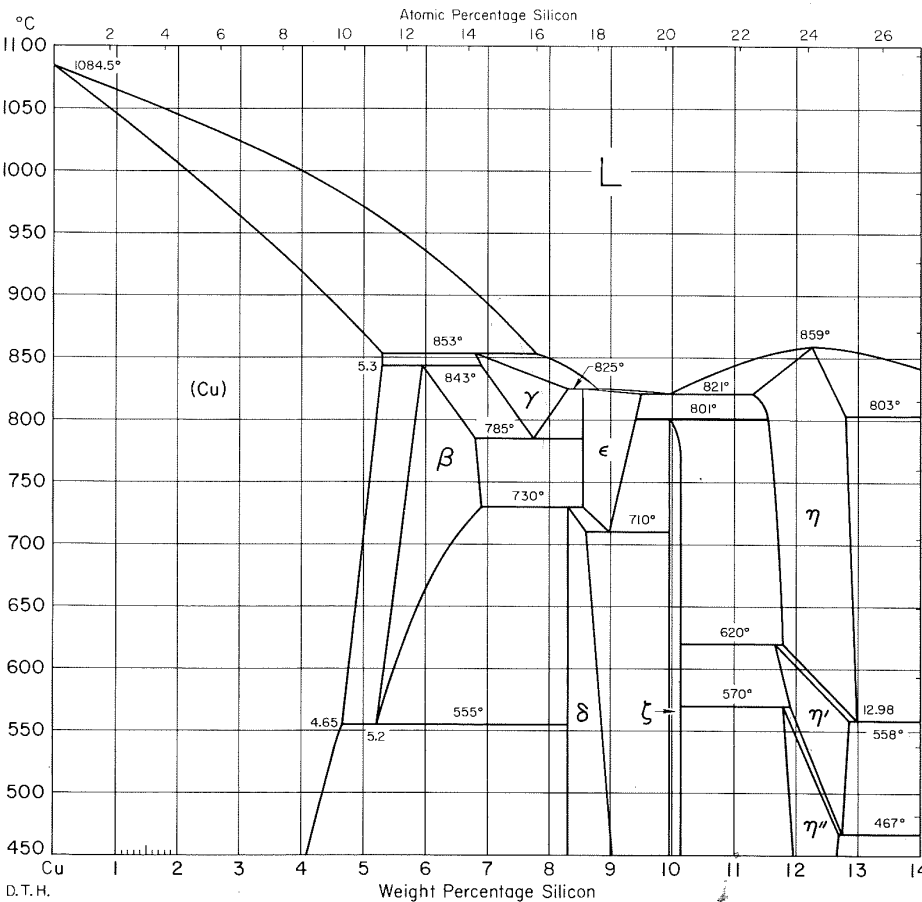
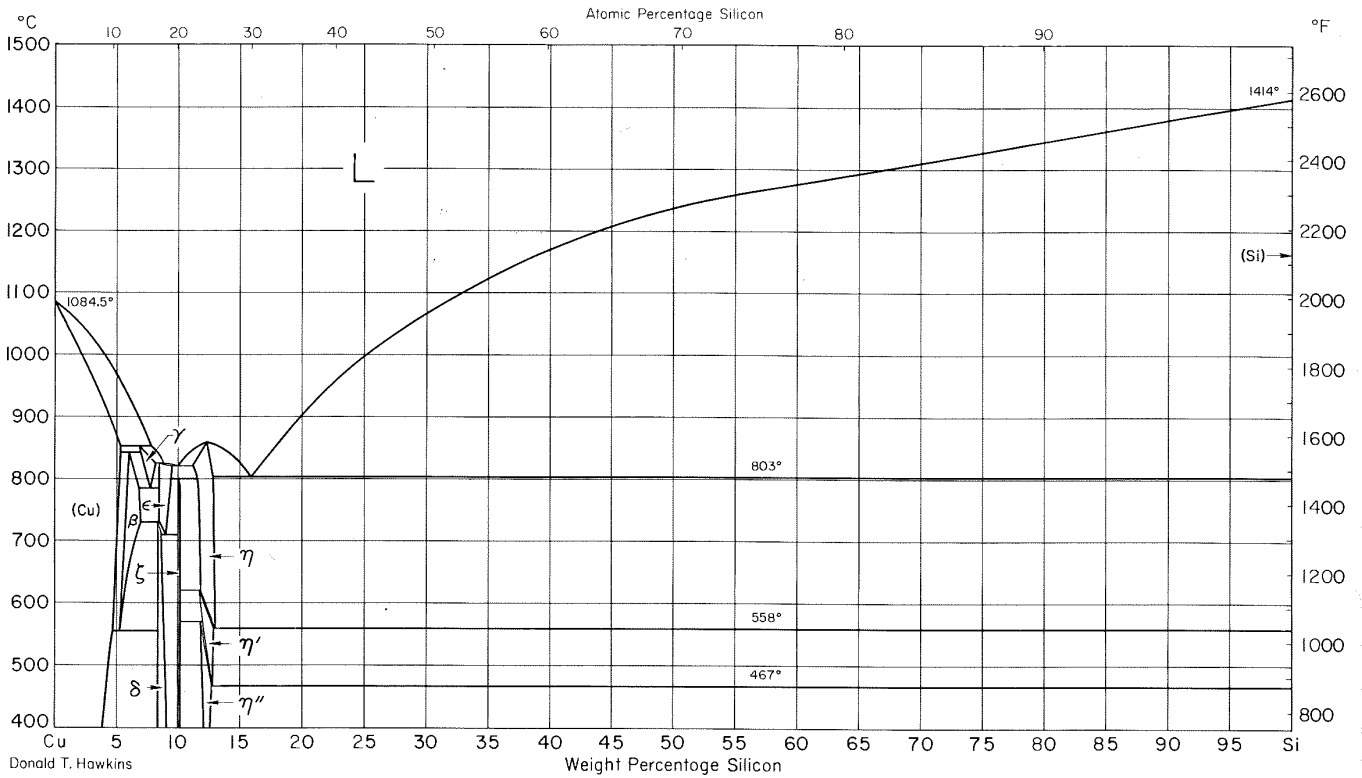
Cu-S Copper-Sulfur



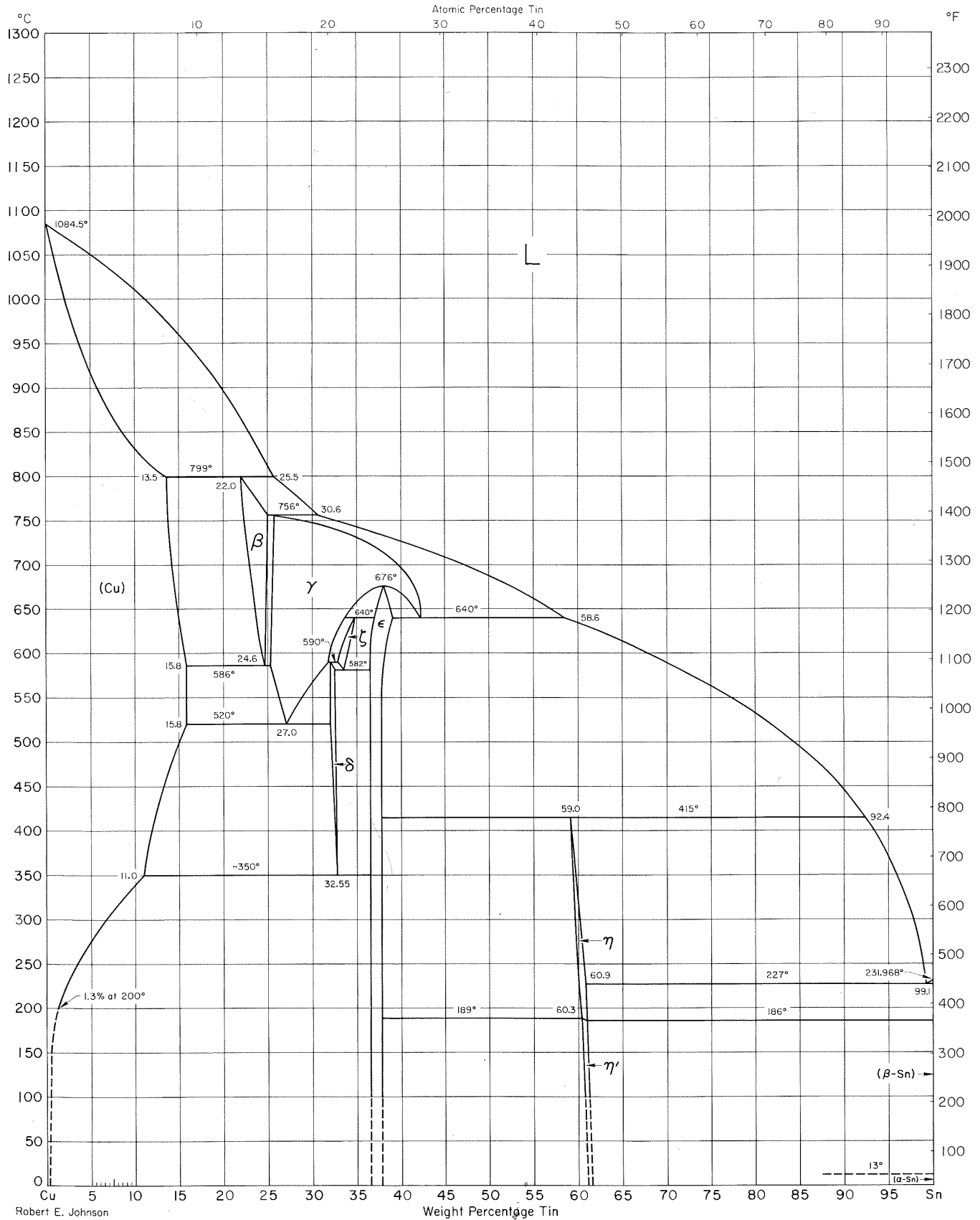
Cu-Se Copper-Selenium



Cu-Si Copper-Silicon



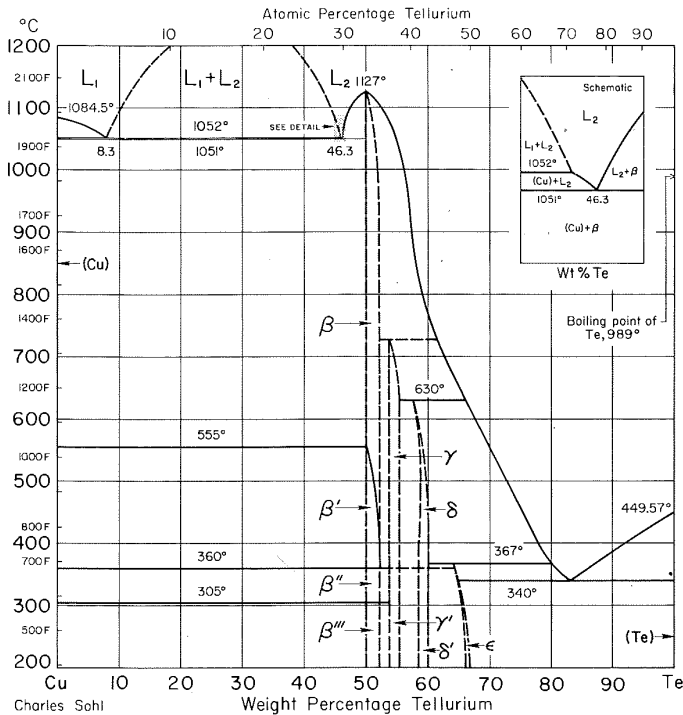
Cu-Sn Copper-Tin



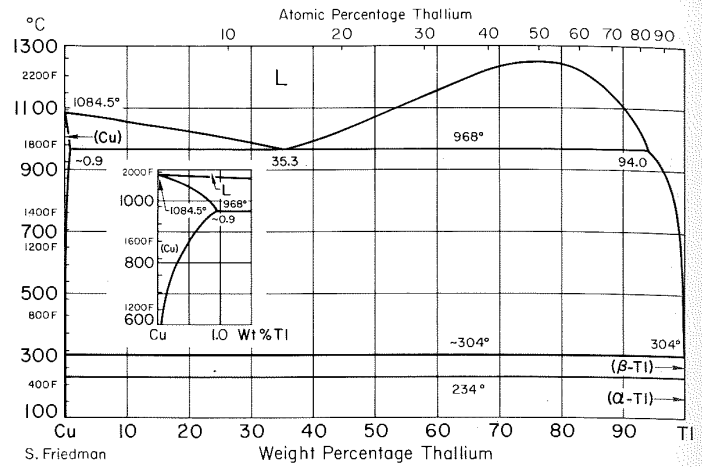
Robert E. Johnson

Weight Percentage Tin

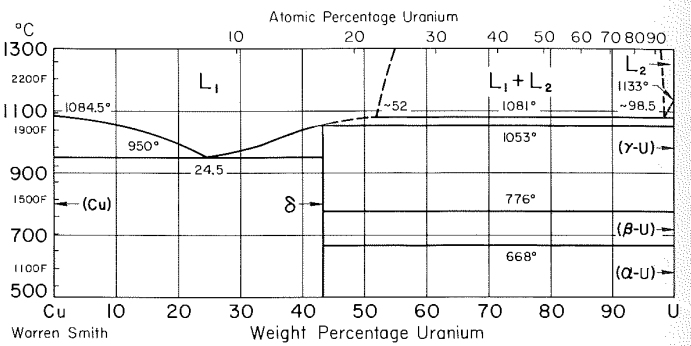
Cu-Te Copper-Tellurium



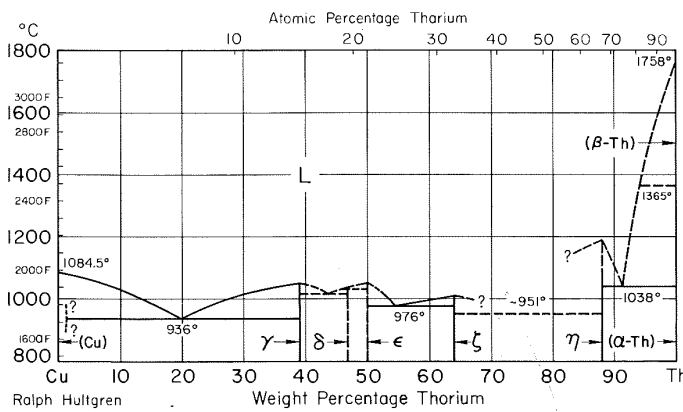
Cu-Tl Copper-Thallium



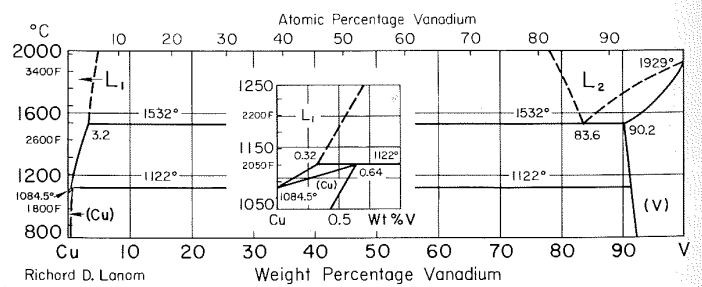
Cu-U Copper-Uranium



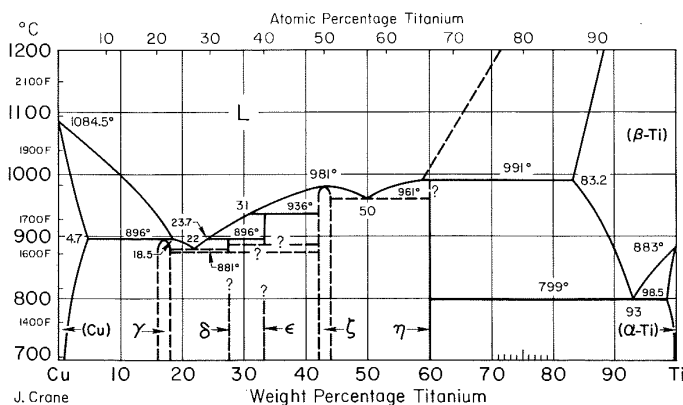
Cu-Th Copper-Thorium



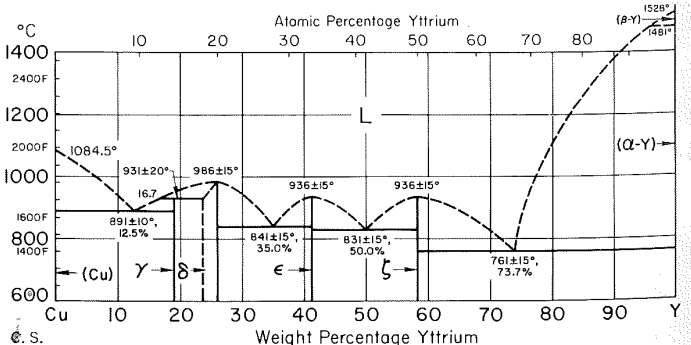
Cu-V Copper-Vanadium



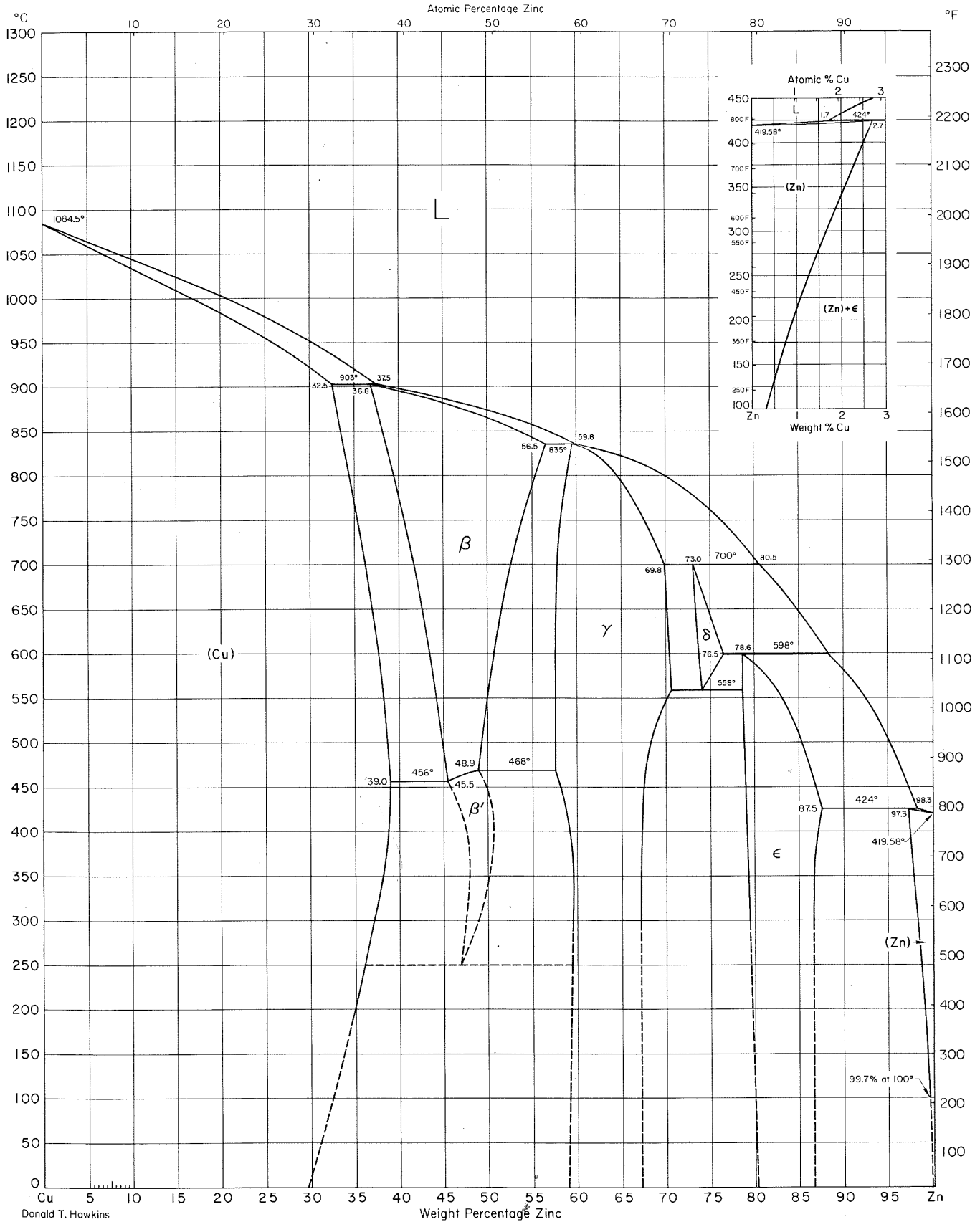
Cu-Ti Copper-Titanium



Cu-Y Copper-Yttrium

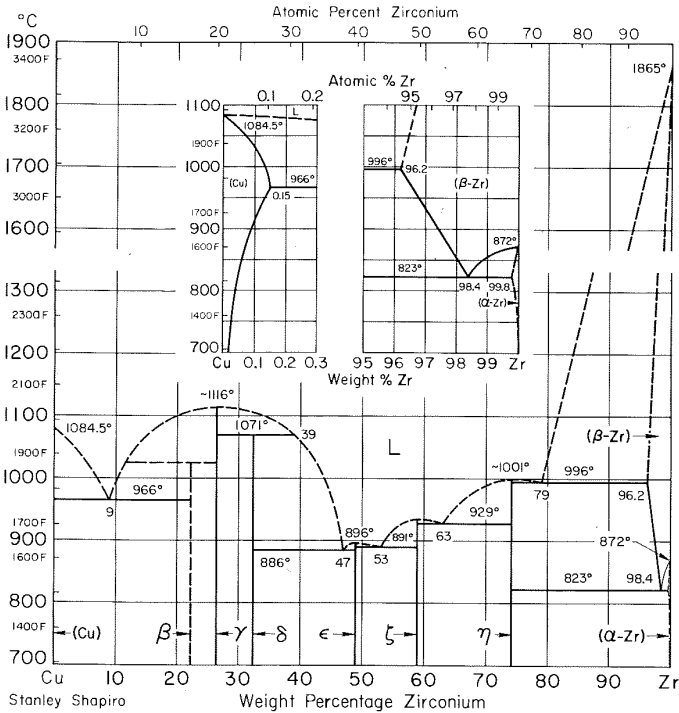


Cu-Zn Copper-Zinc

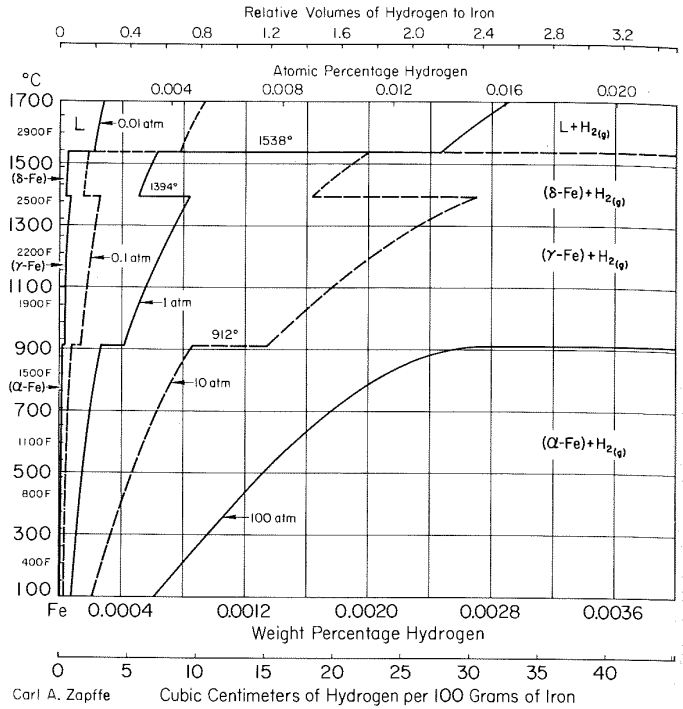


Donald T. Hawkins

Cu-Zr Copper-Zirconium



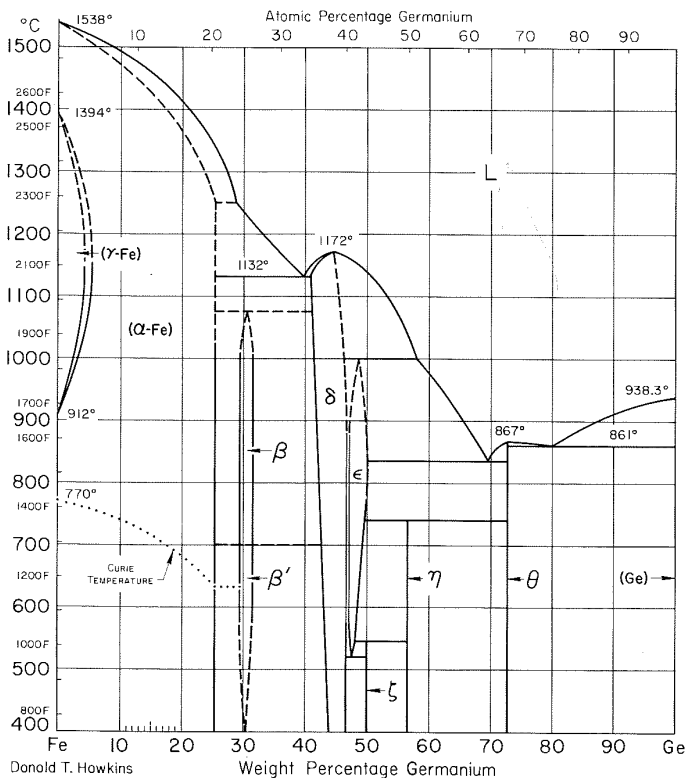
Fe-H Iron-Hydrogen



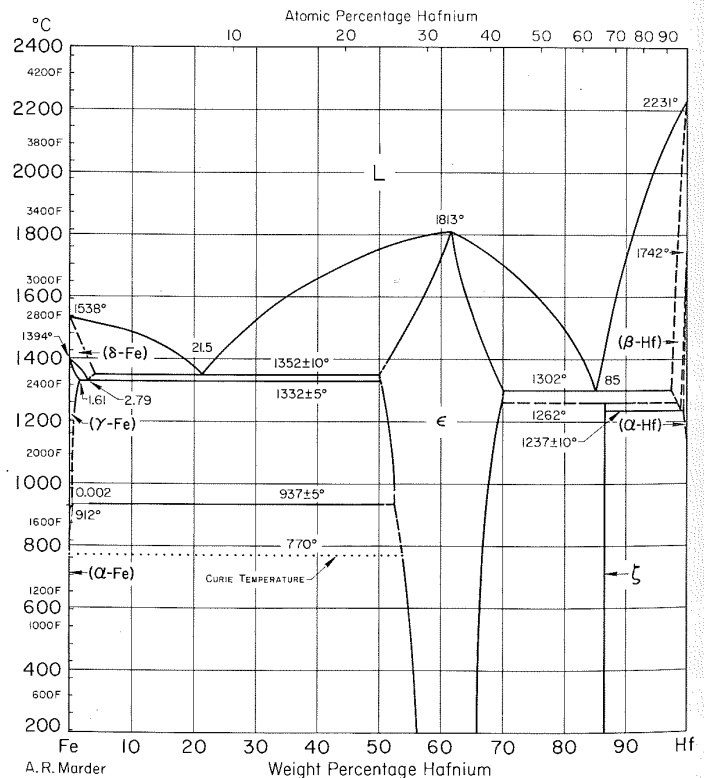
Fe-C Iron-Carbon

See "C-Fe Carbon-Iron".

Fe-Ge Iron-Germanium



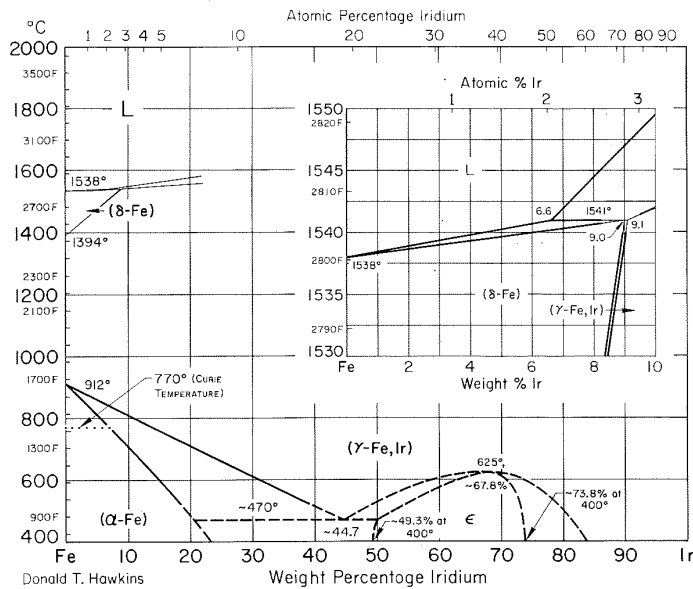
Fe-Hf Iron-Hafnium



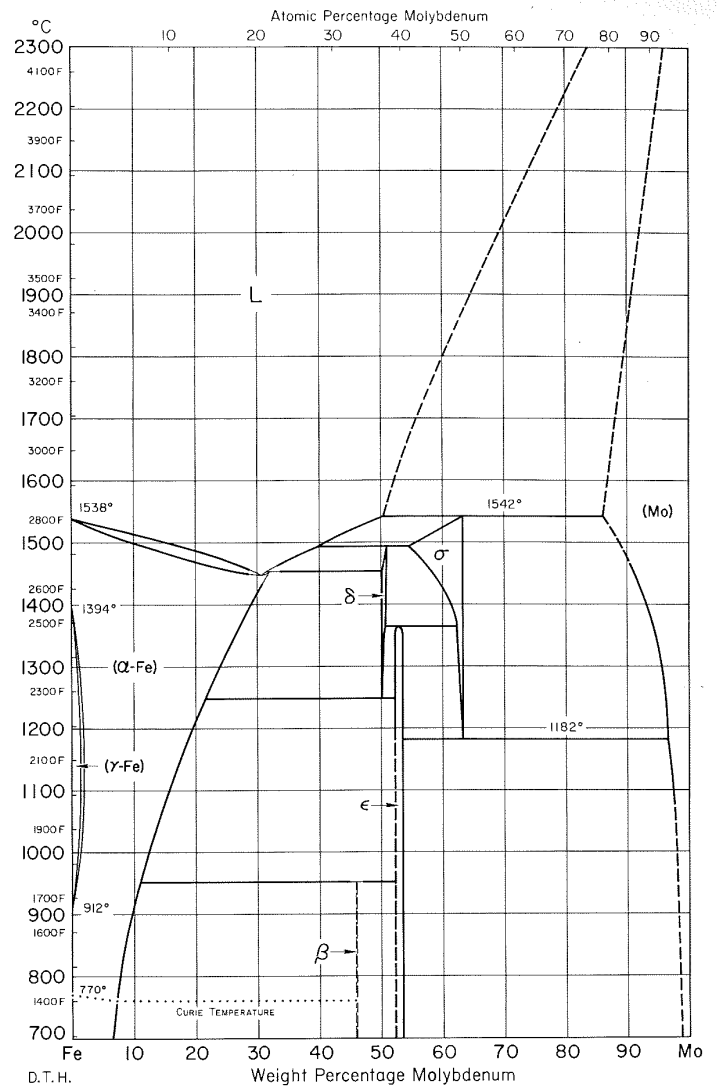
Fe-Hg Iron-Mercury

See Notes.

Fe-Ir Iron-Iridium



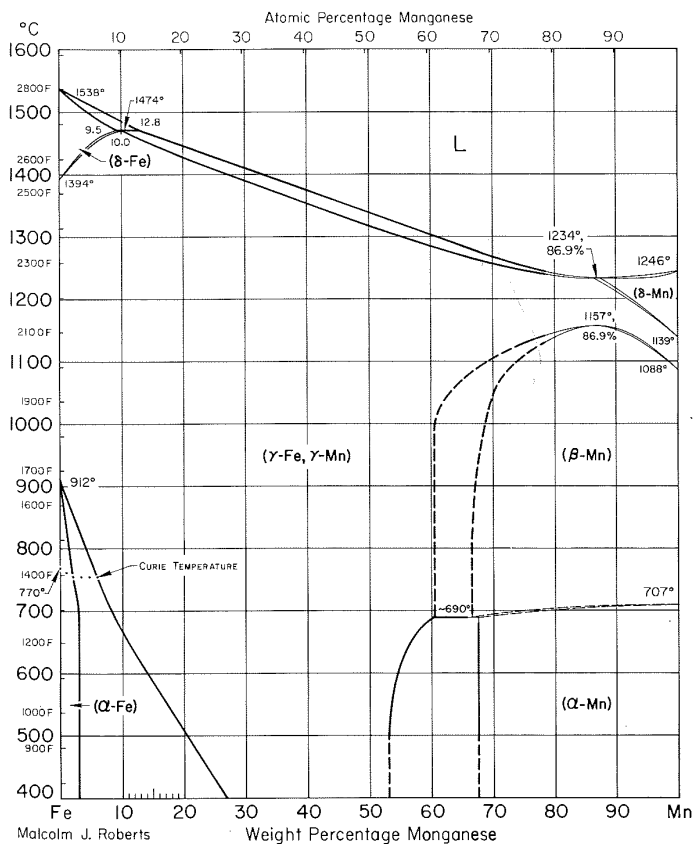
Fe-Mo Iron-Molybdenum



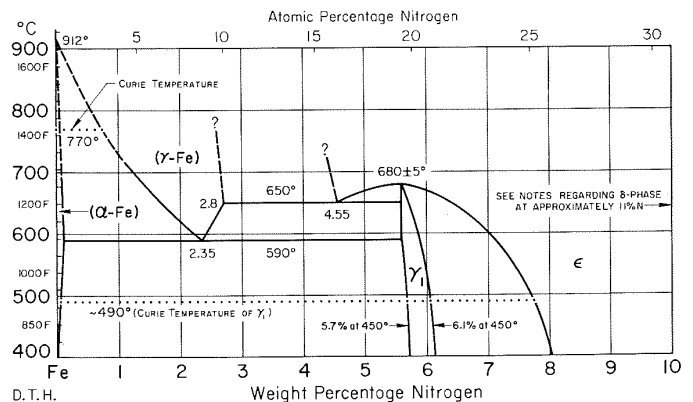
- Fe-K Iron-Potassium
- Fe-Li Iron-Lithium
- Fe-Mg Iron-Magnesium

See Notes.

Fe-Mn Iron-Manganese



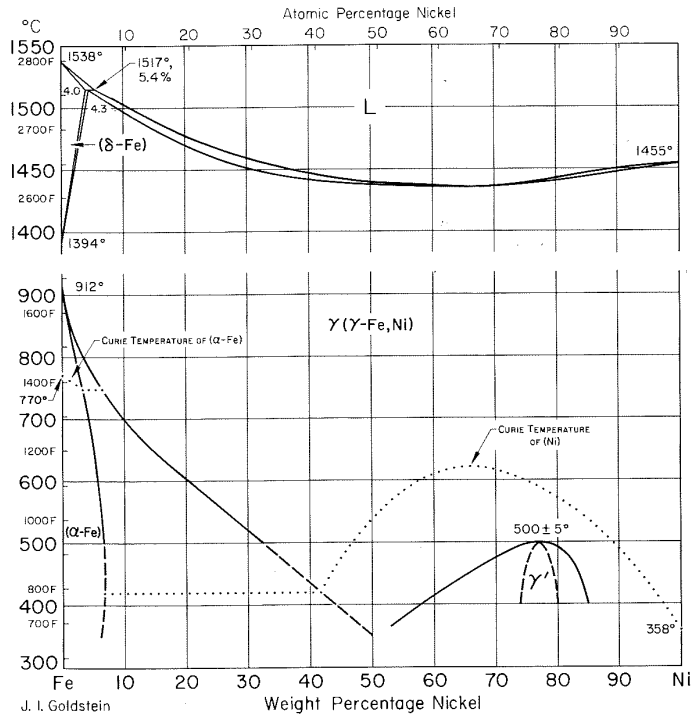
Fe-N Iron-Nitrogen



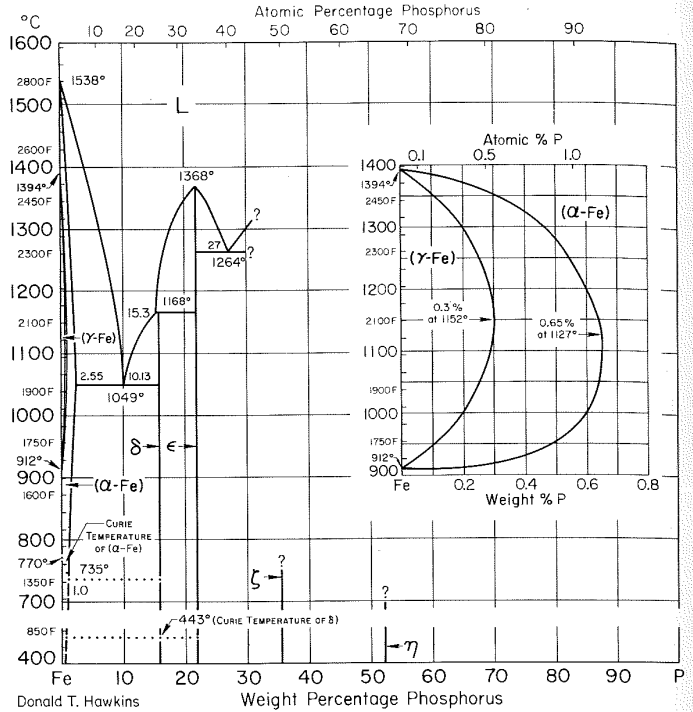
Fe-Na Iron-Sodium

See Notes.

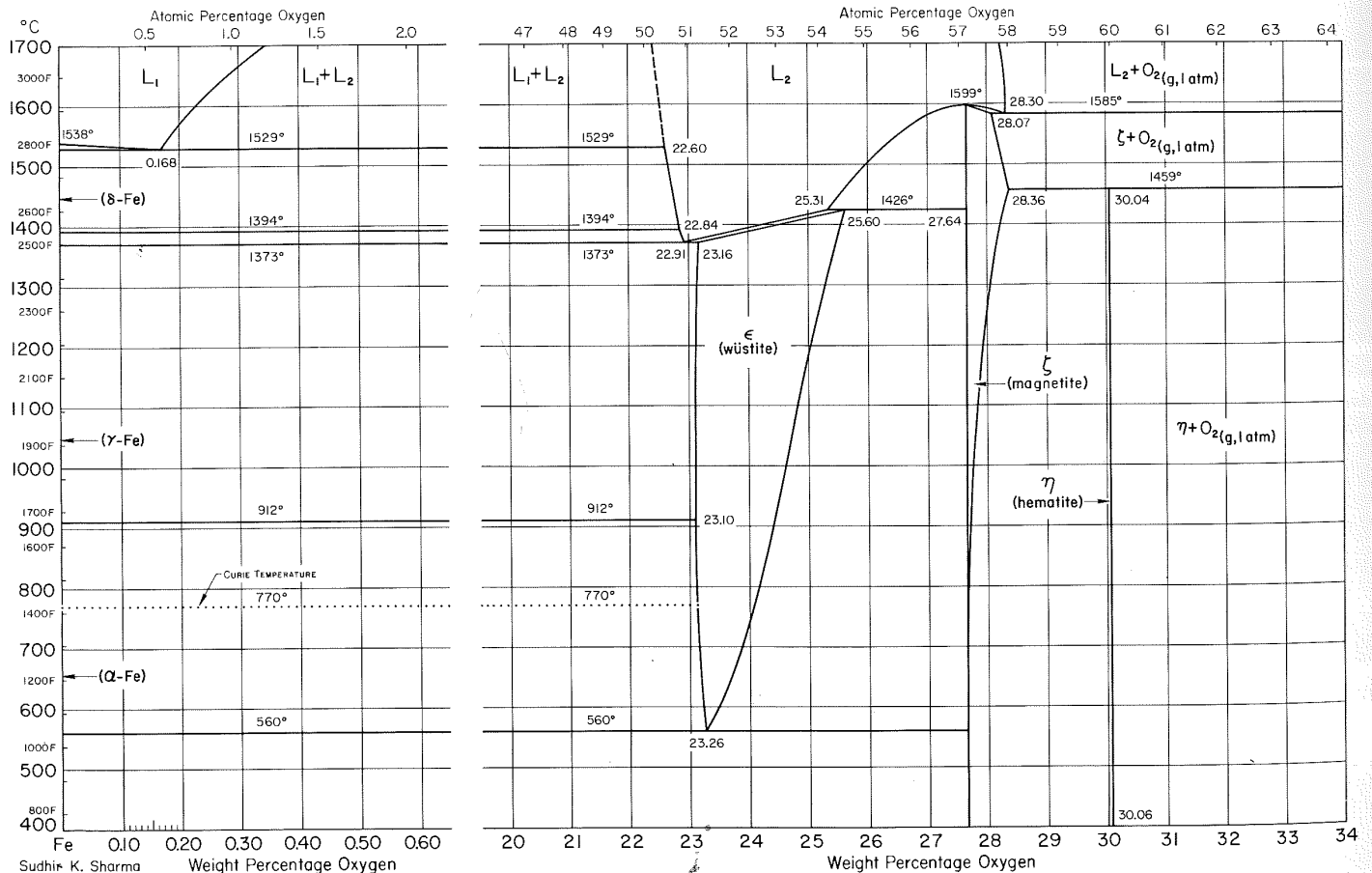
Fe-Ni Iron-Nickel



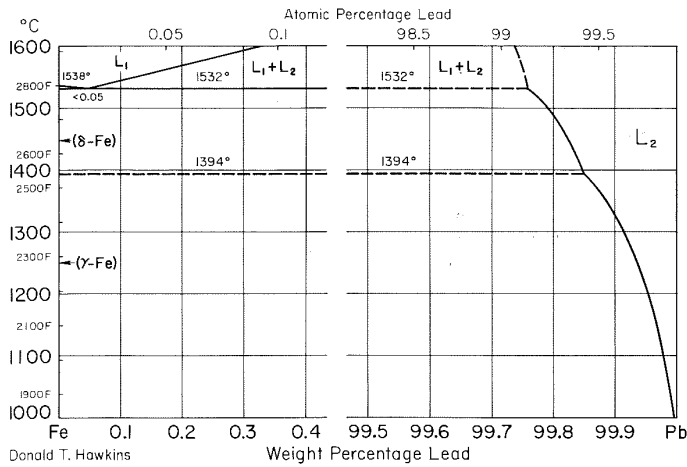
Fe-P Iron-Phosphorus



Fe-O Iron-Oxygen

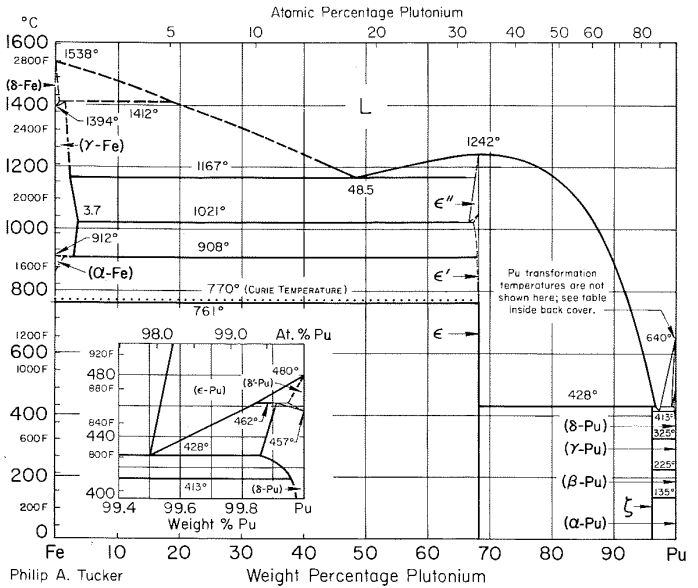


Fe-Pb Iron-Lead



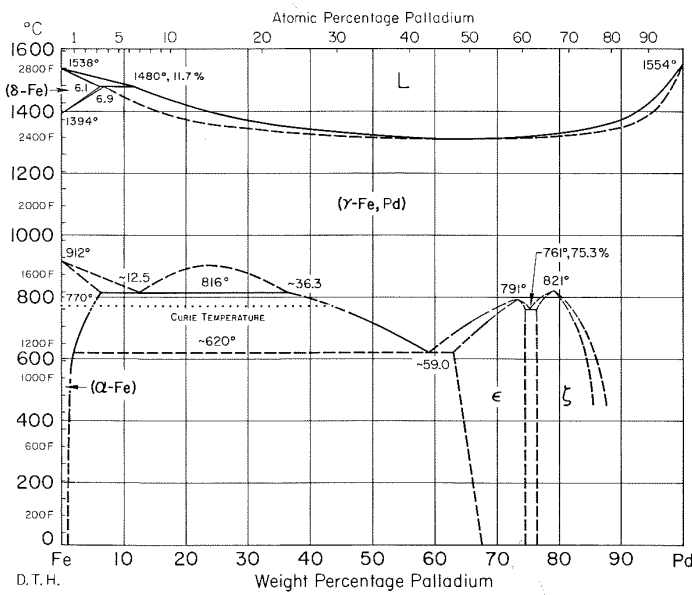
Donald T. Hawkins

Fe-Pu Iron-Plutonium



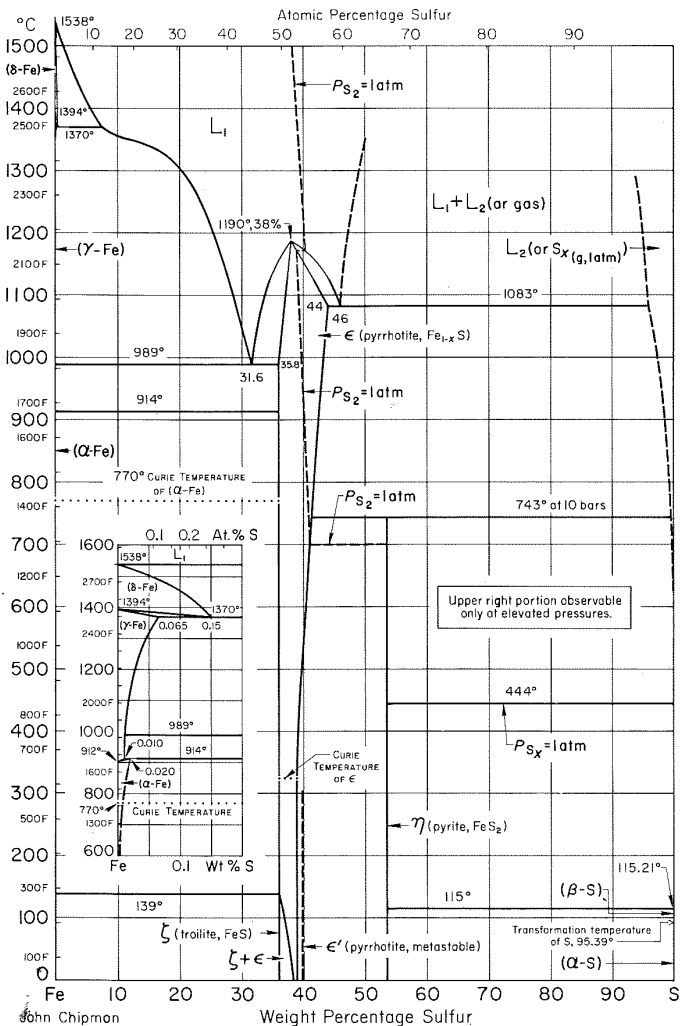
Philip A. Tucker

Fe-Pd Iron-Palladium



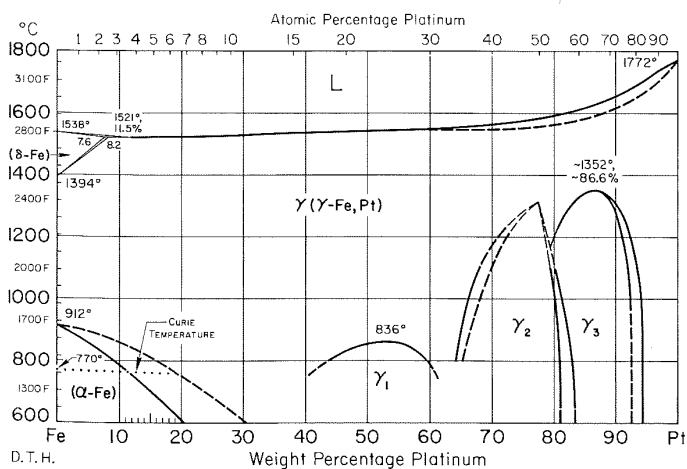
D. T. H.

Fe-S Iron-Sulfur



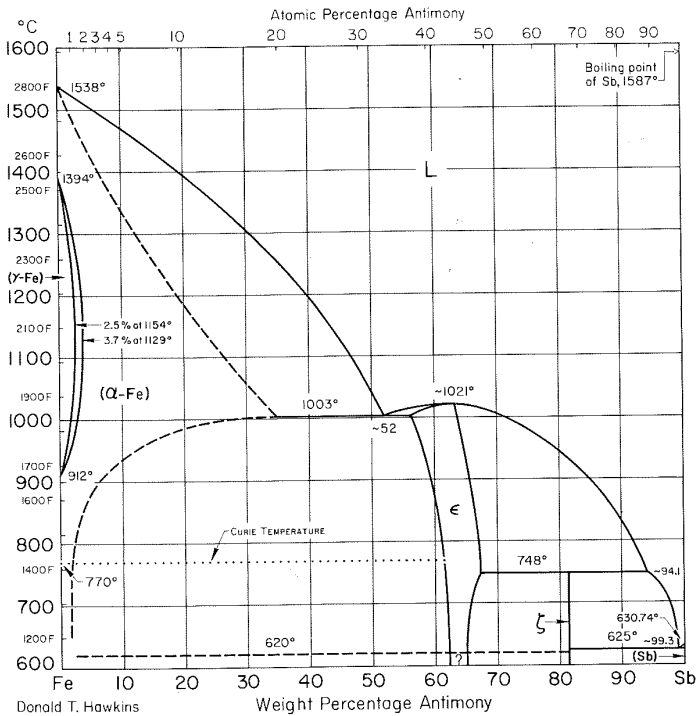
John Chipman

Fe-Pt Iron-Platinum

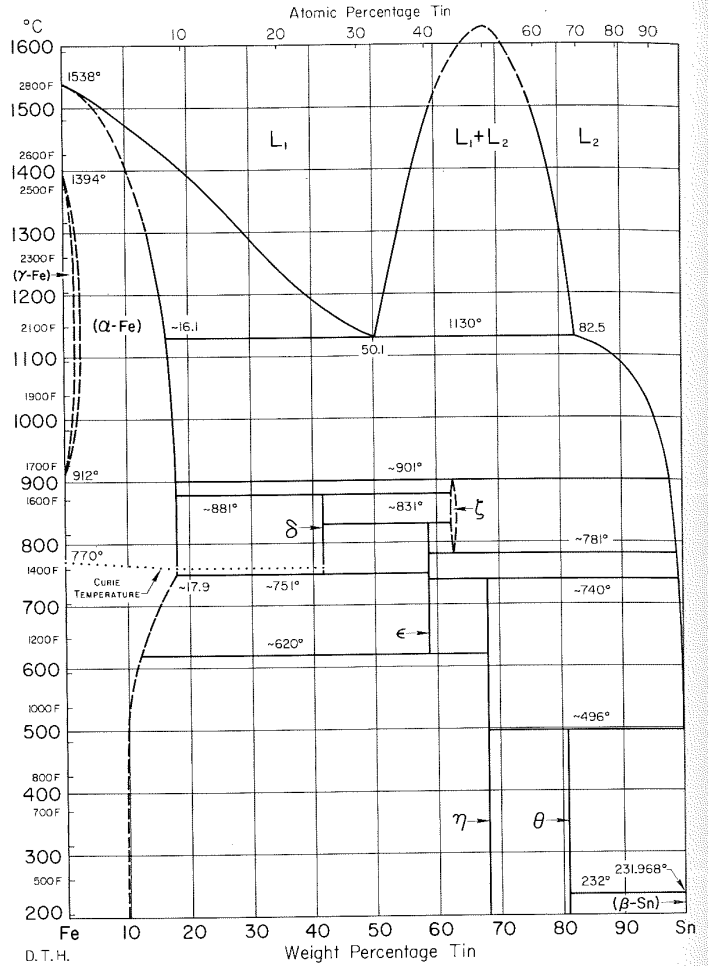


D. T. H.

Fe-Sb Iron-Antimony



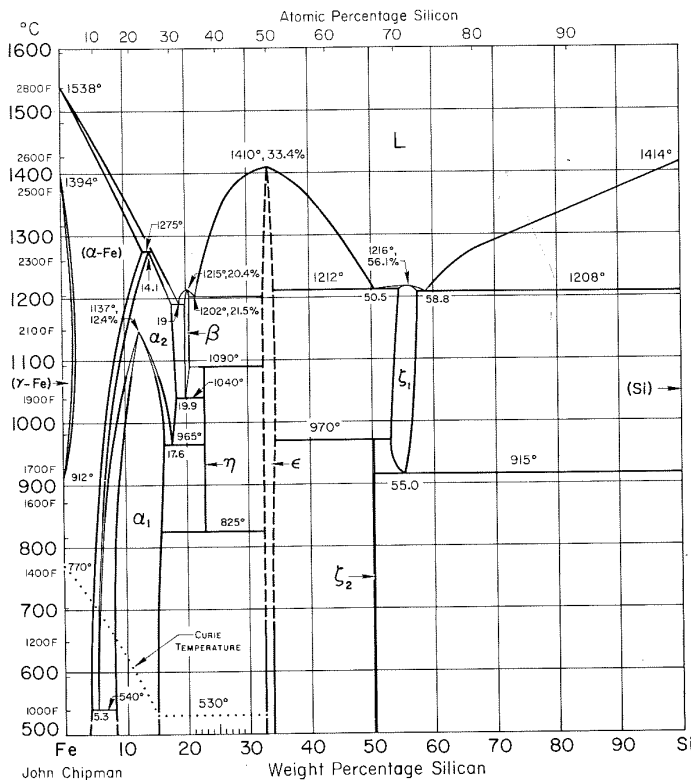
Fe-Sn Iron-Tin



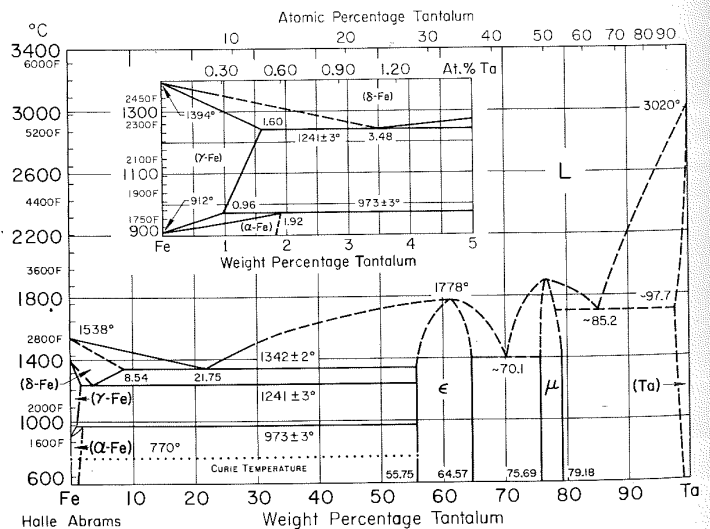
Fe-Se Iron-Selenium

See Notes.

Fe-Si Iron-Silicon



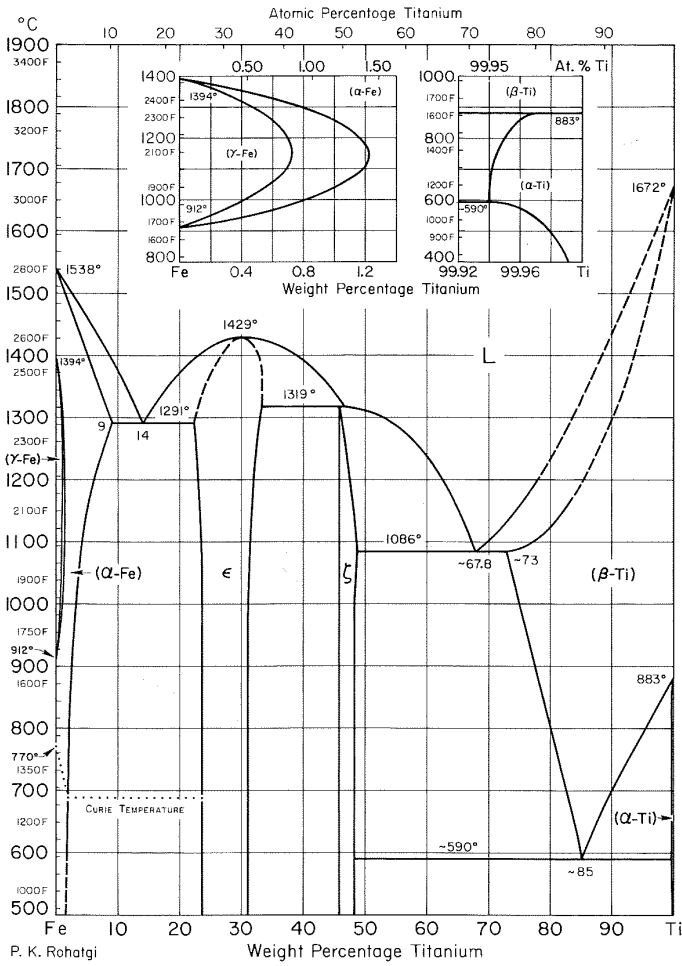
Fe-Ta Iron-Tantalum



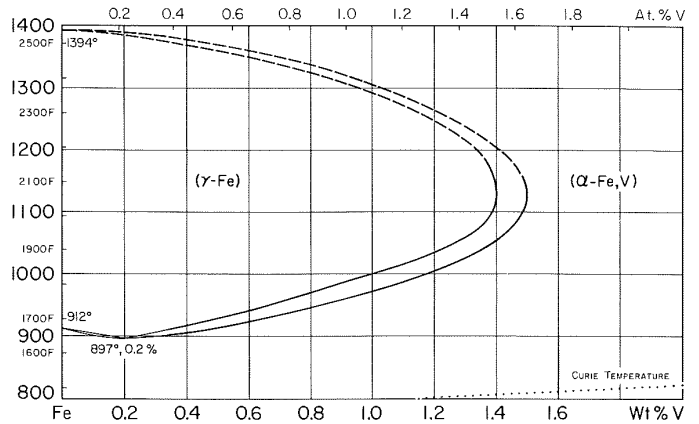
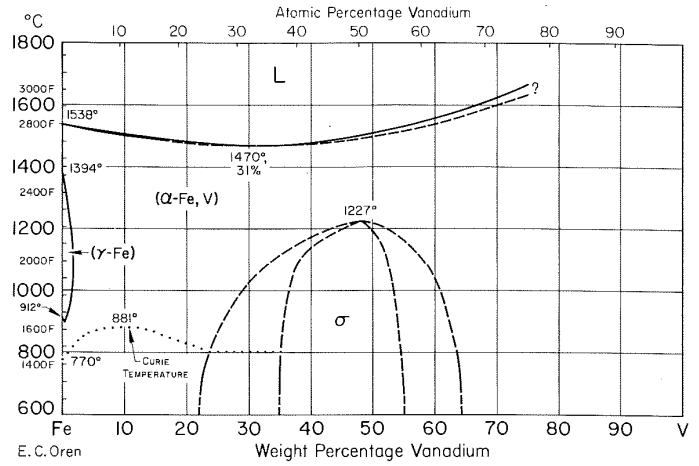
Fe-Te Iron-Tellurium

See Notes.

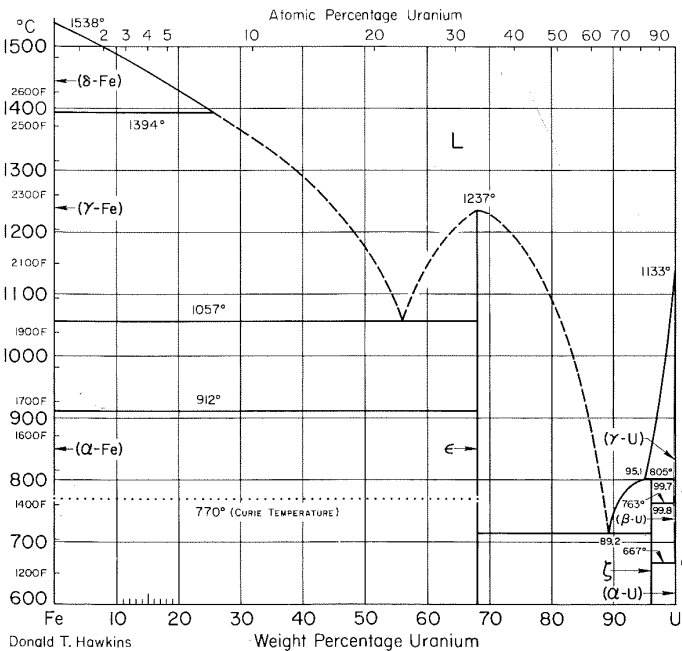
Fe-Ti Iron-Titanium



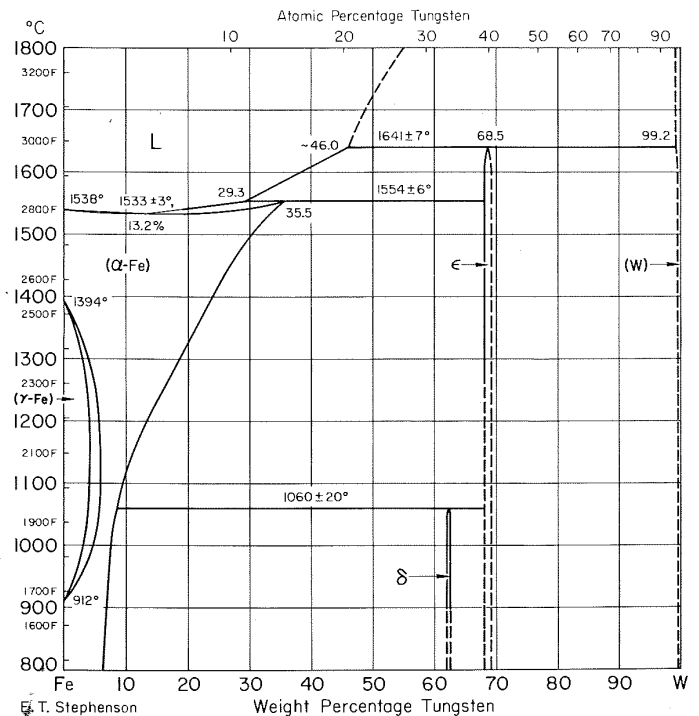
Fe-V Iron-Vanadium



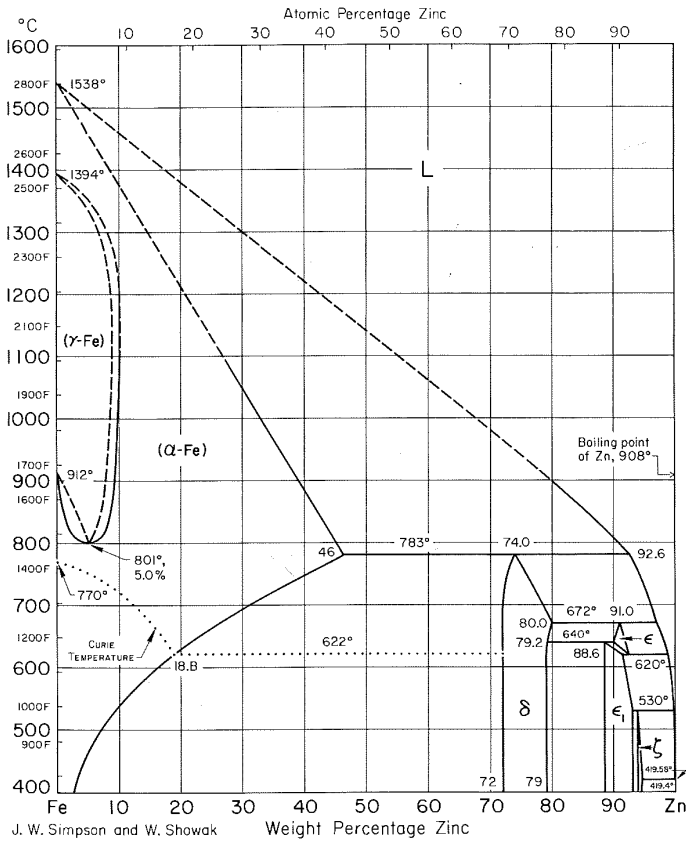
Fe-U Iron-Uranium



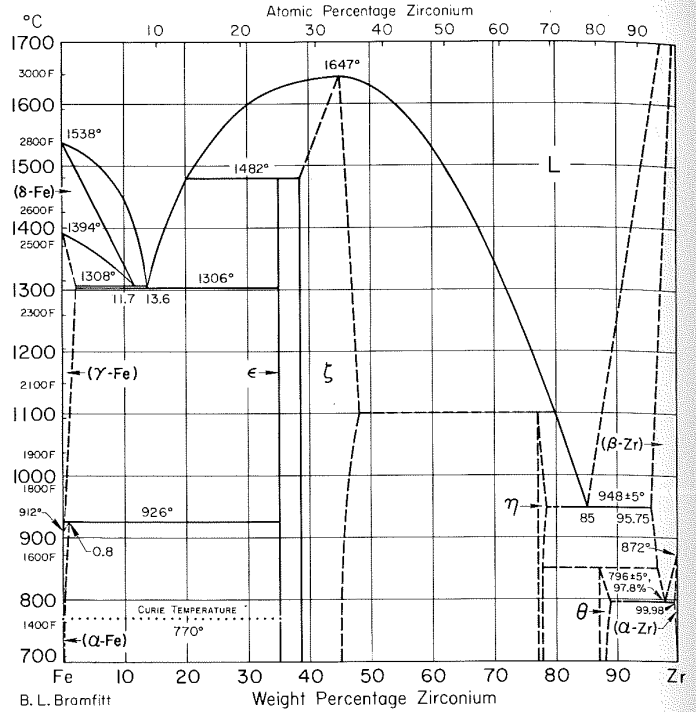
Fe-W Iron-Tungsten



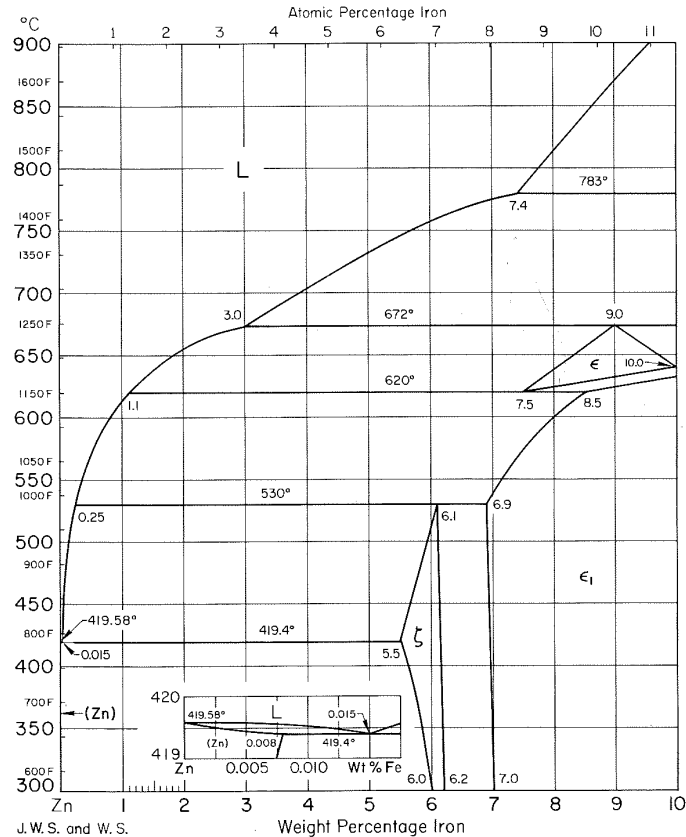
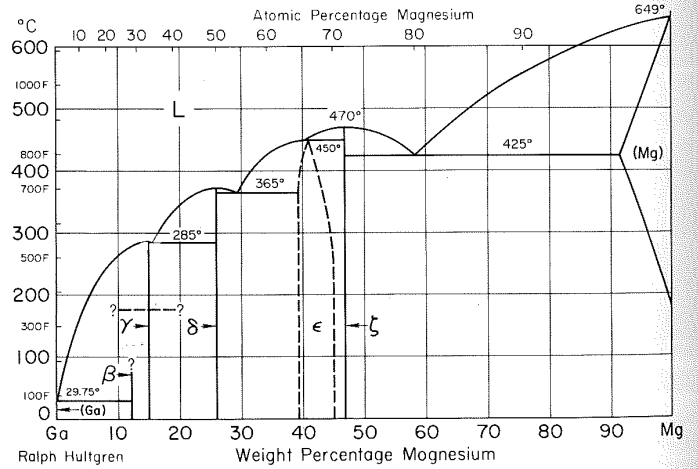
Fe-Zn Iron-Zinc



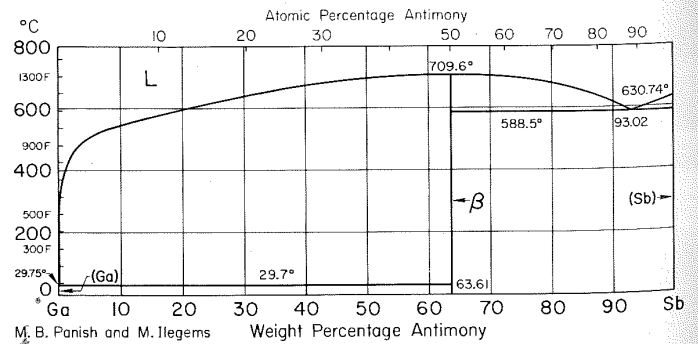
Fe-Zr Iron-Zirconium



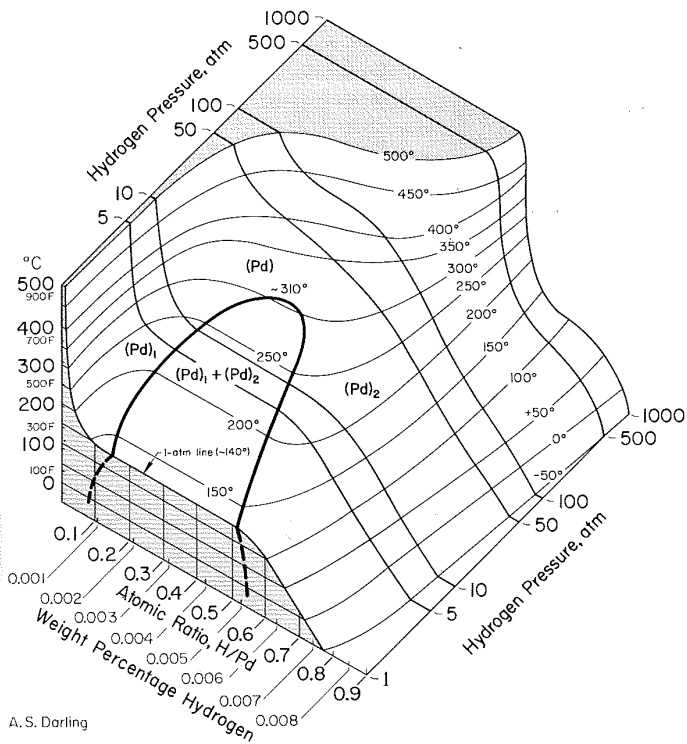
Ga-Mg Gallium-Magnesium



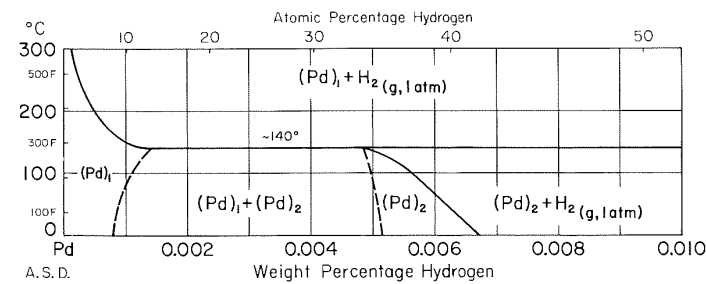
Ga-Sb Gallium-Antimony



H-Pd Hydrogen-Palladium

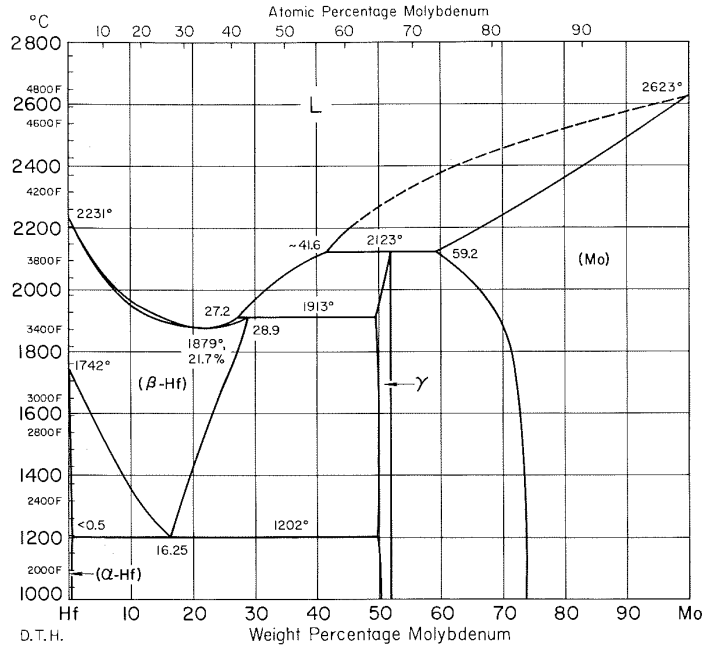


A. S. Darling

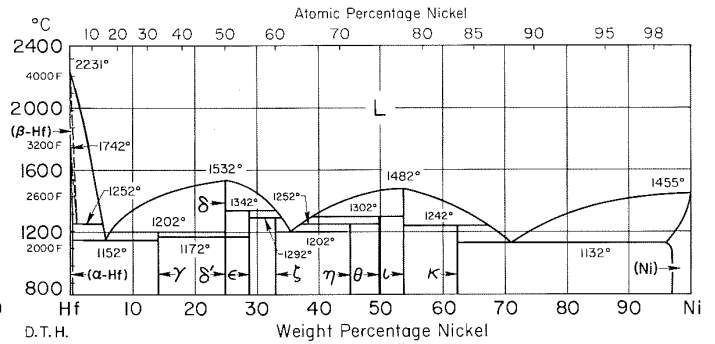


A. S. D.

Hf-Mo Hafnium-Molybdenum

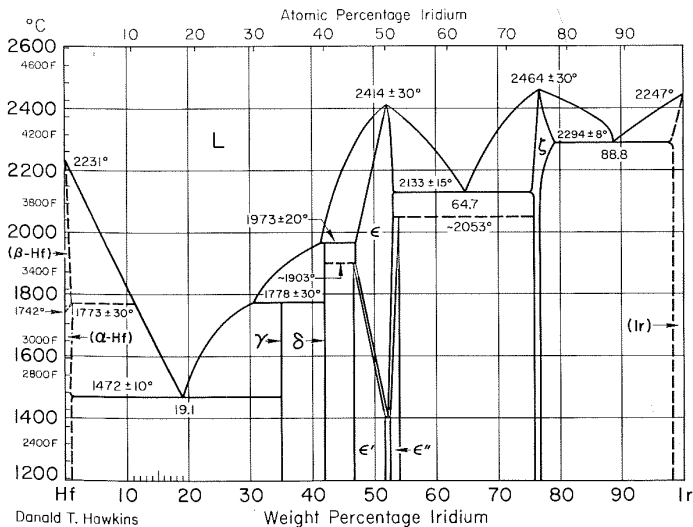


Hf-Ni Hafnium-Nickel



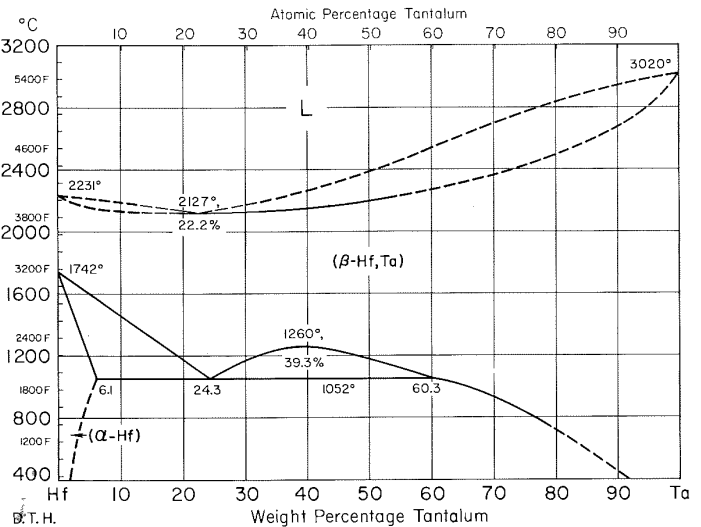
D. T. H.

Hf-Ir Hafnium-Iridium



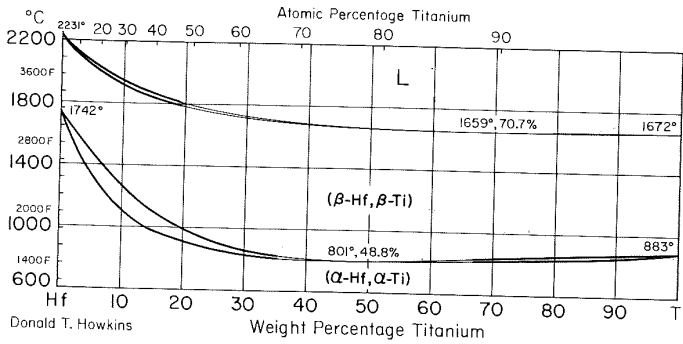
Danald T. Hawkins

Hf-Ta Hafnium-Tantalum

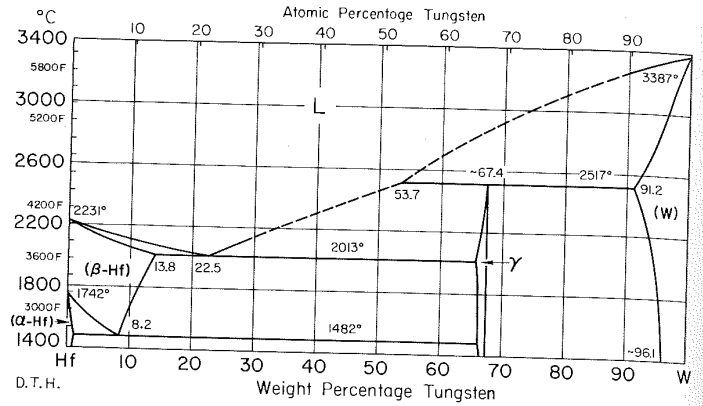


D. T. H.

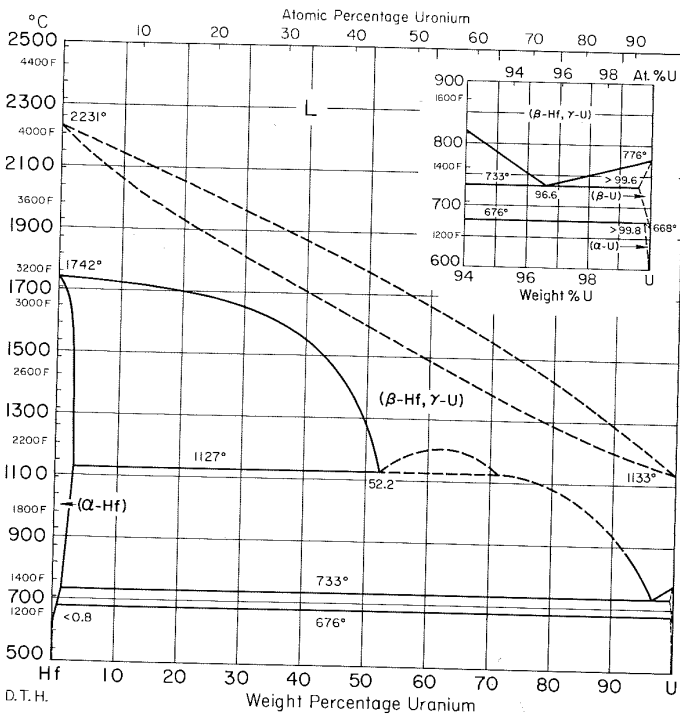
Hf-Ti Hafnium-Titanium



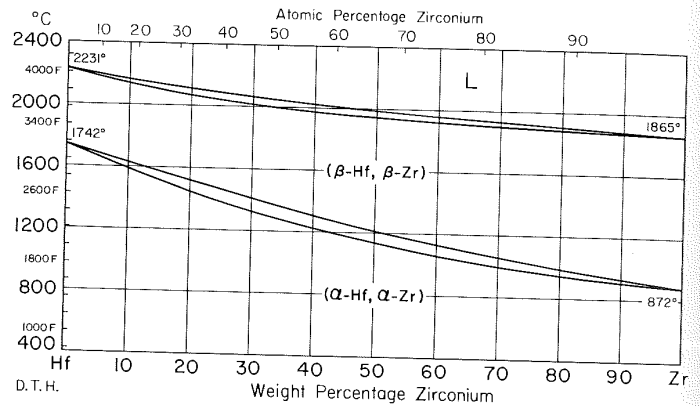
Hf-W Hafnium-Tungsten



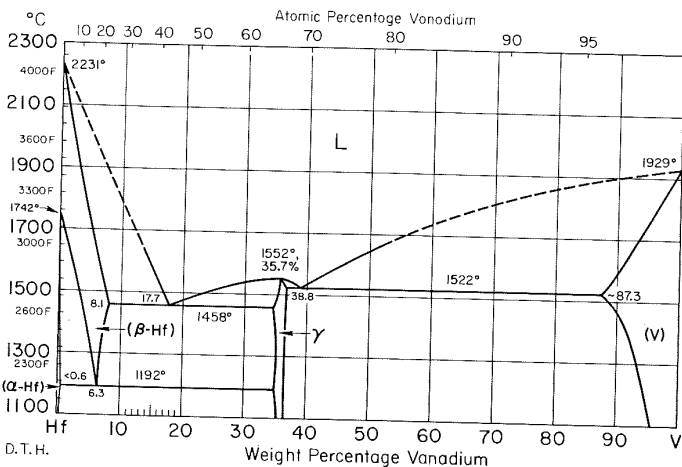
Hf-U Hafnium-Uranium



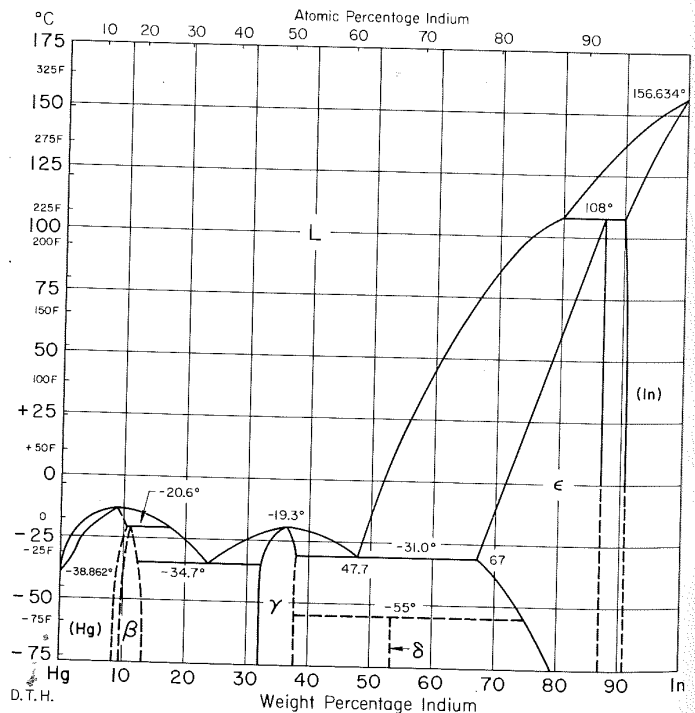
Hf-Zr Hafnium-Zirconium



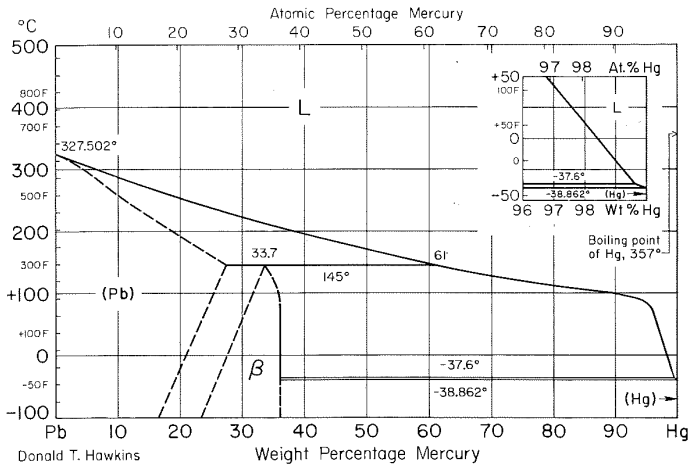
Hf-V Hafnium-Vanadium



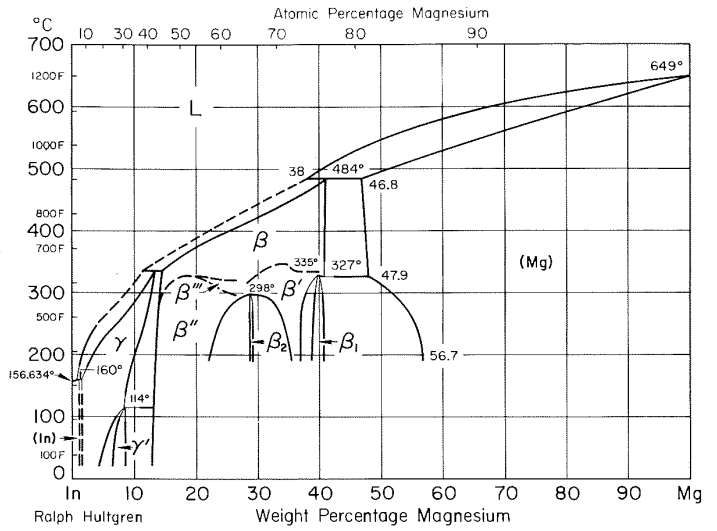
Hg-In Mercury-Indium



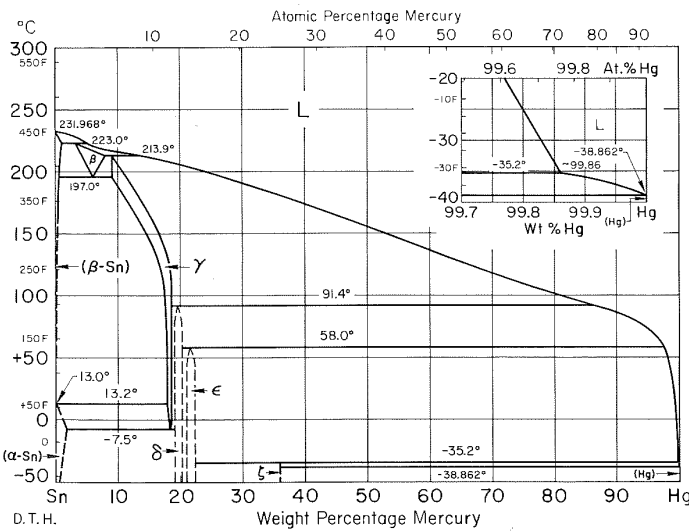
Hg-Pb Mercury-Lead



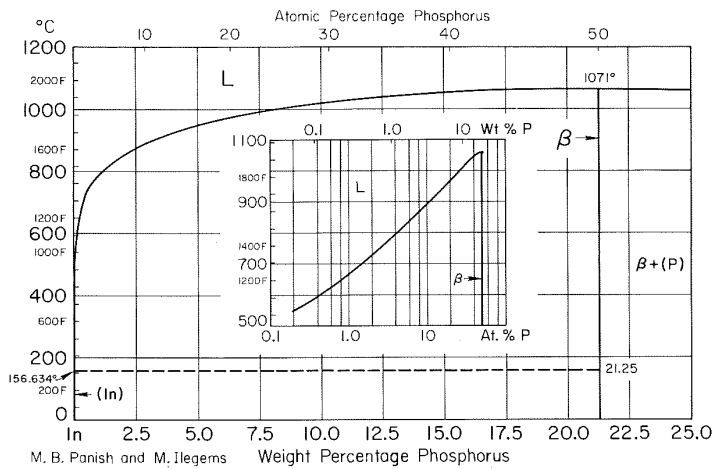
In-Mg Indium-Magnesium



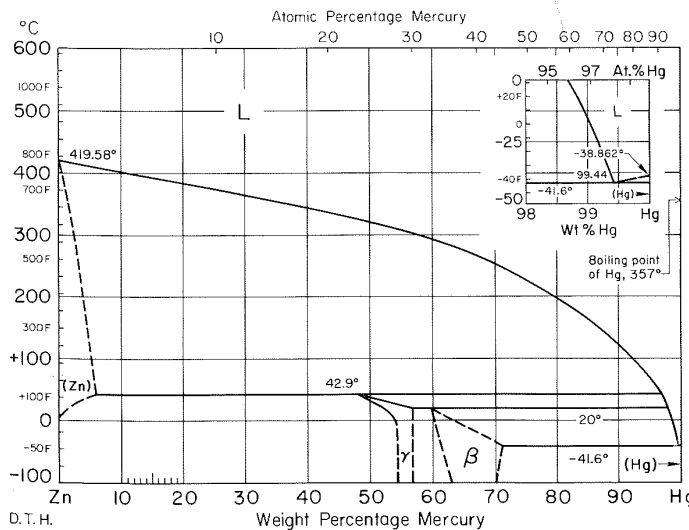
Hg-Sn Mercury-Tin



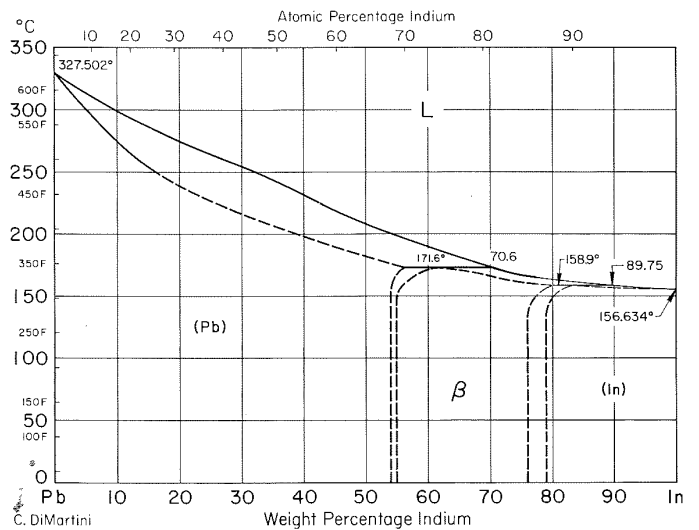
In-P Indium-Phosphorus



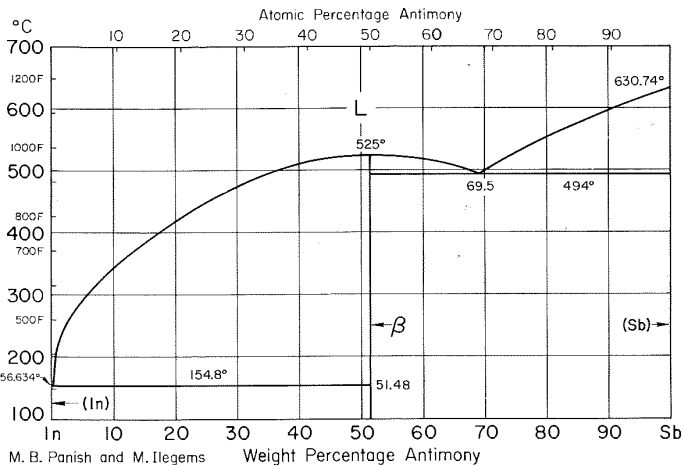
Hg-Zn Mercury-Zinc



In-Pb Indium-Lead

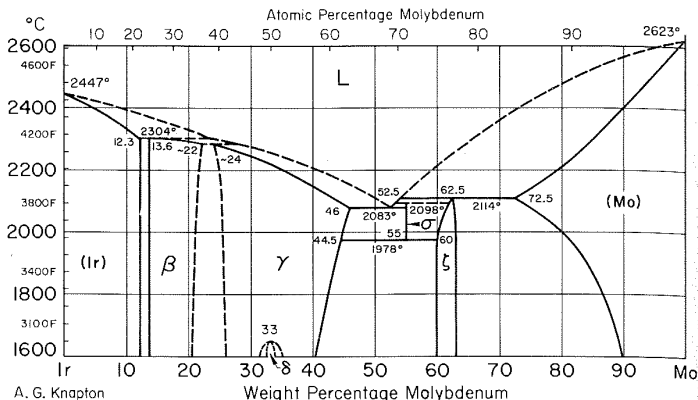


In-Sb Indium-Antimony



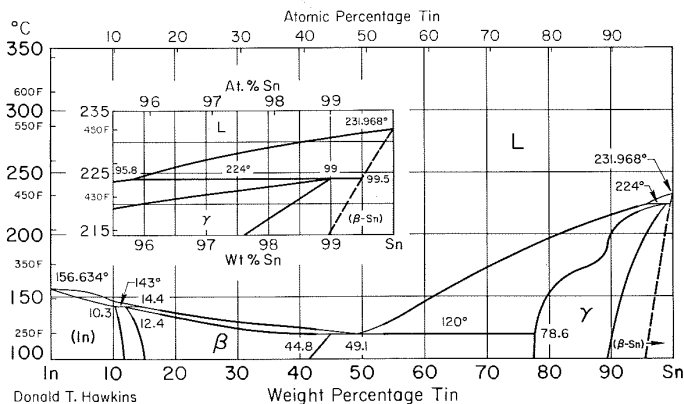
M. B. Panish and M. Illegems

Ir-Mo Iridium-Molybdenum



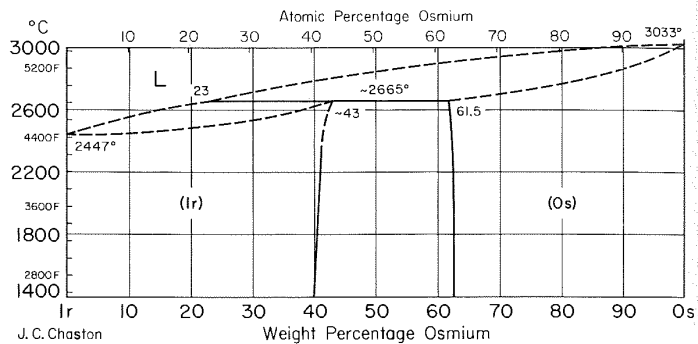
A. G. Knapton

In-Sn Indium-Tin



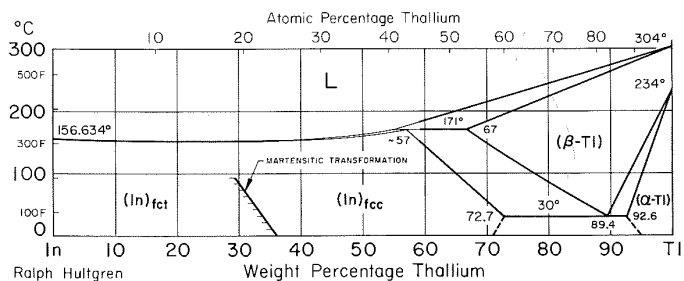
Donald T. Hawkins

Ir-Os Iridium-Osmium



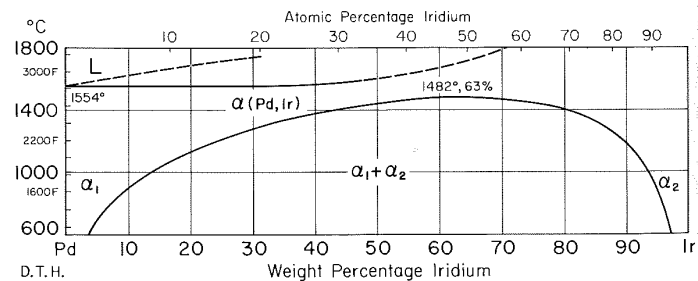
J. C. Chaston

In-Tl Indium-Thallium



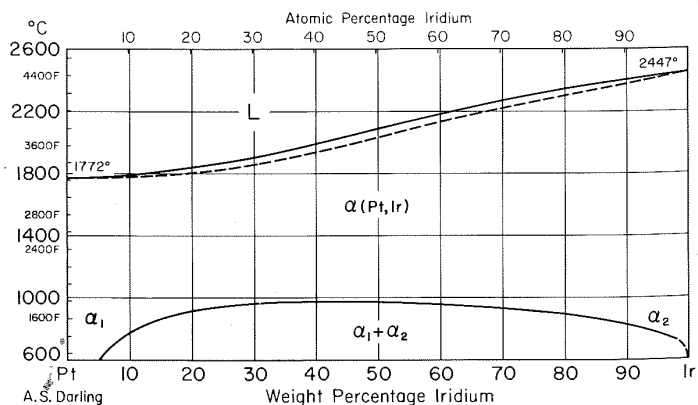
Ralph Hultgren

Ir-Pd Iridium-Palladium



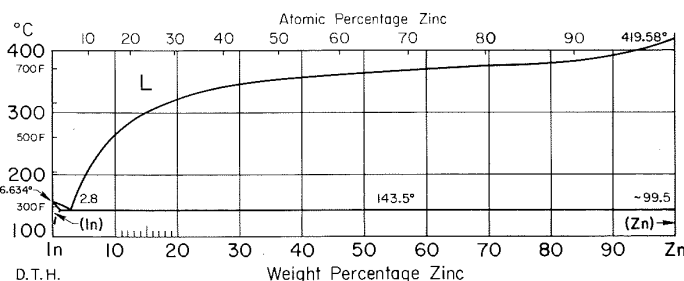
D.T.H.

Ir-Pt Iridium-Platinum



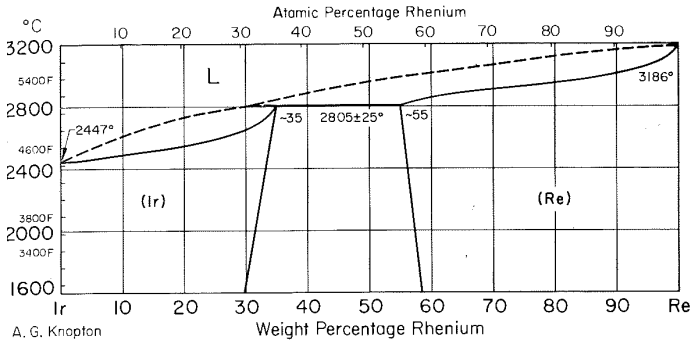
A.S. Darling

In-Zn Indium-Zinc



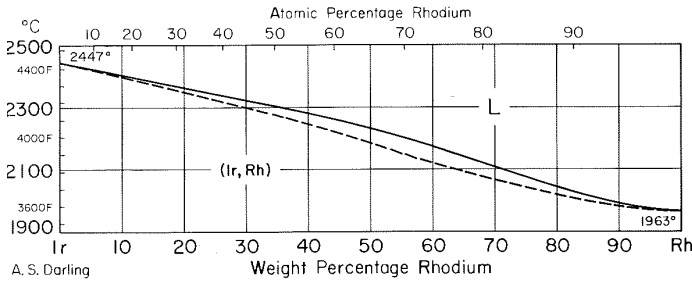
D.T.H.

Ir-Re Iridium-Rhenium



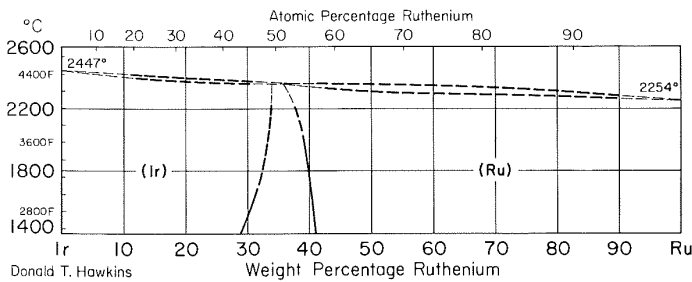
A. G. Kopton

Ir-Rh Iridium-Rhodium



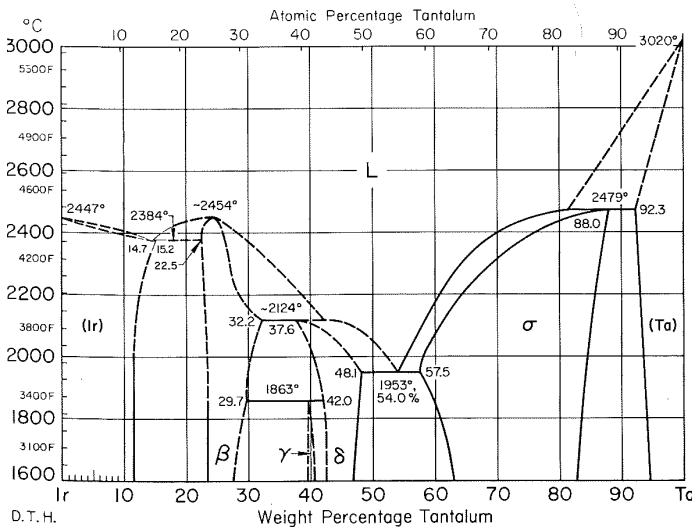
A. S. Darling

Ir-Ru Iridium-Ruthenium



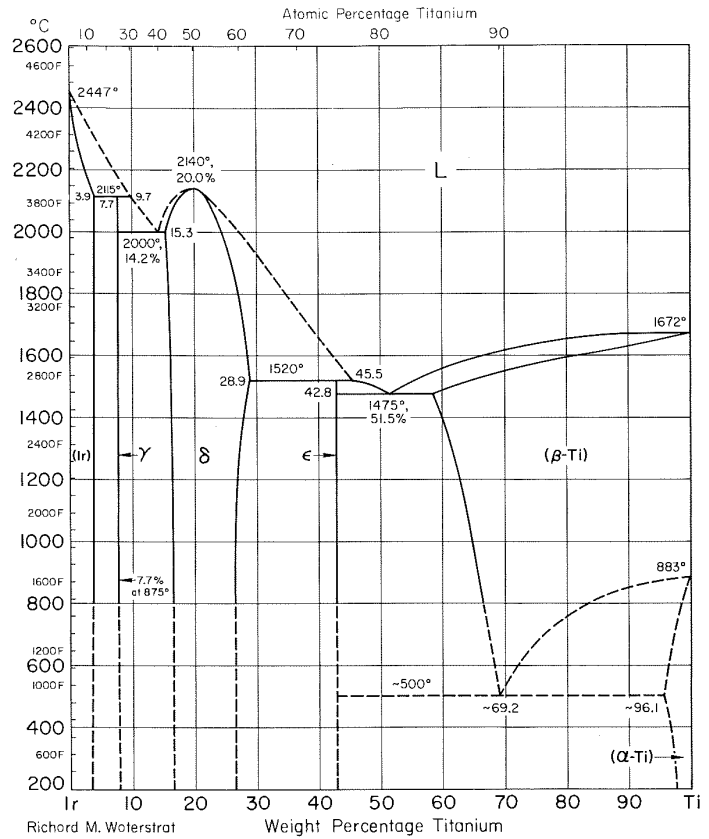
Donald T. Hawkins

Ir-Ta Iridium-Tantalum



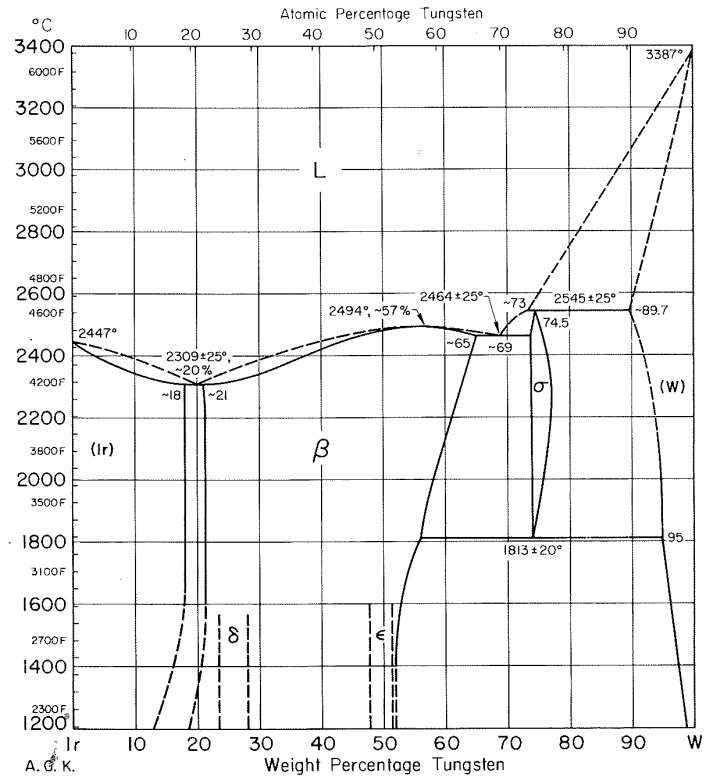
D. T. H.

Ir-Ti Iridium-Titanium



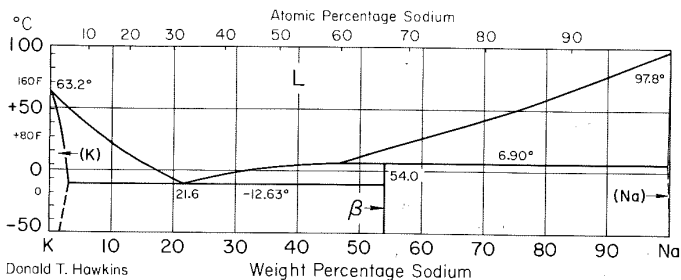
Richard M. Woterstrat

Ir-W Iridium-Tungsten

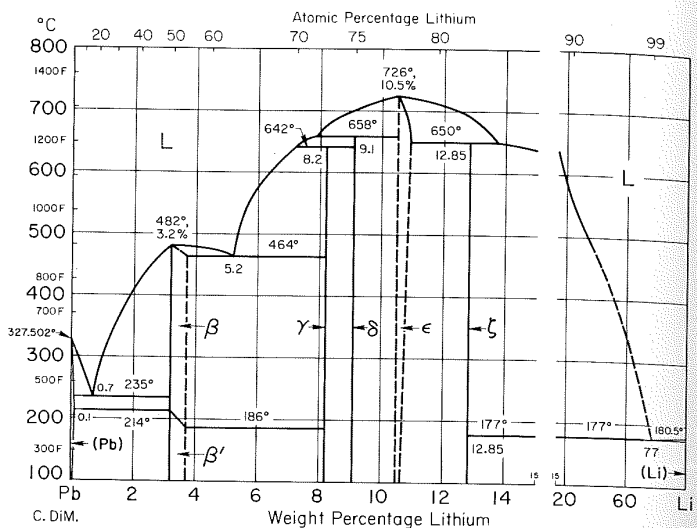


A. G. K.

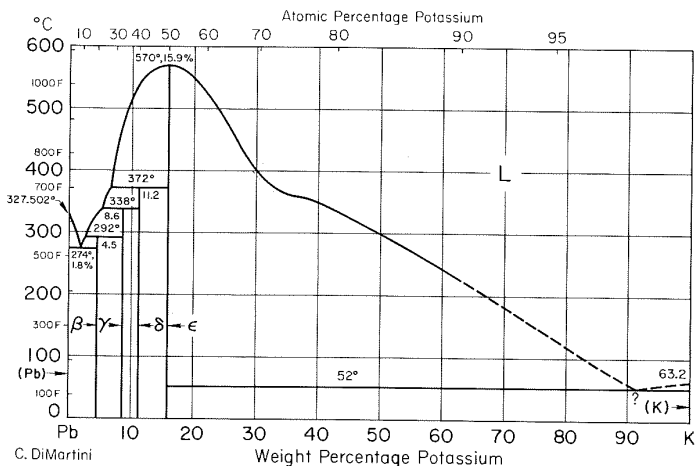
K-Na Potassium-Sodium



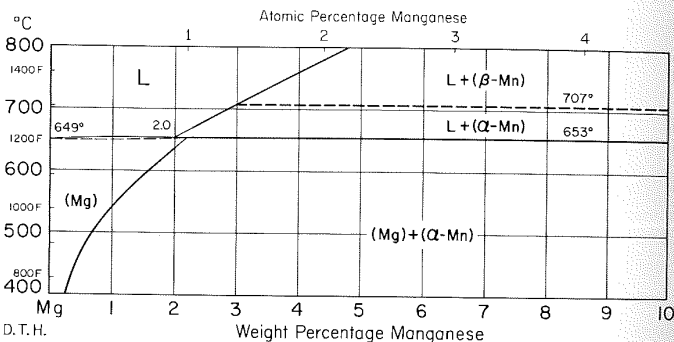
Li-Pb Lithium-Lead



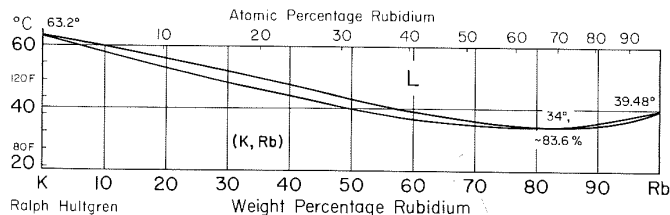
K-Pb Potassium-Lead



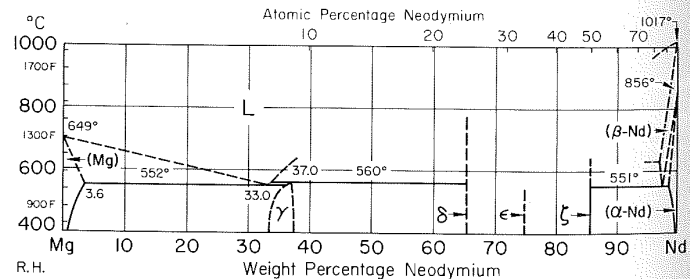
Mg-Mn Magnesium-Manganese



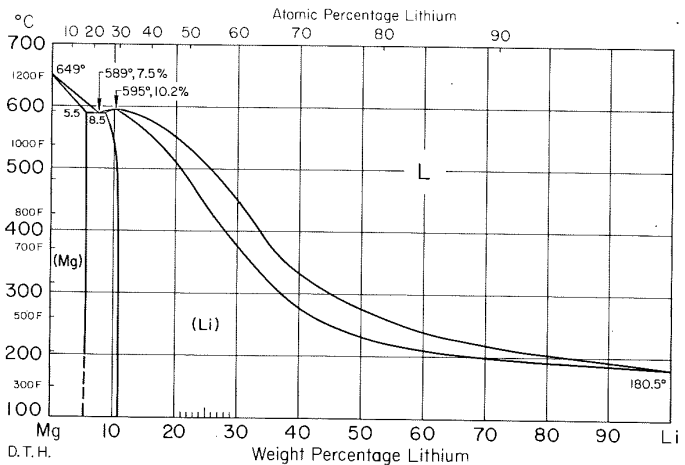
K-Rb Potassium-Rubidium



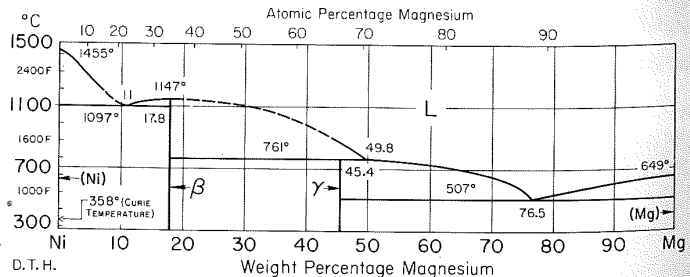
Mg-Nd Magnesium-Neodymium



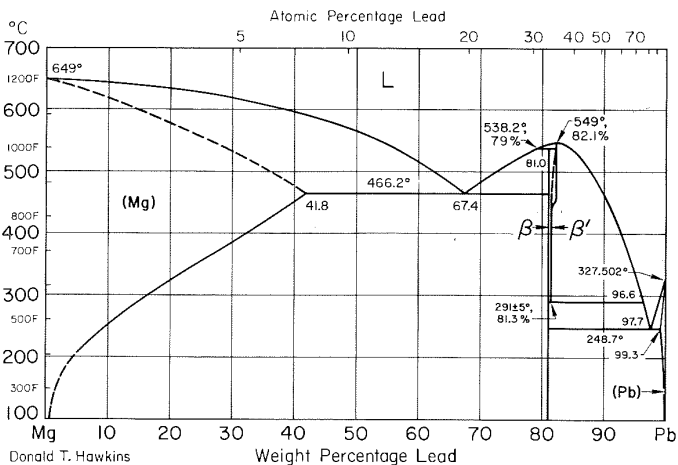
Li-Mg Lithium-Magnesium



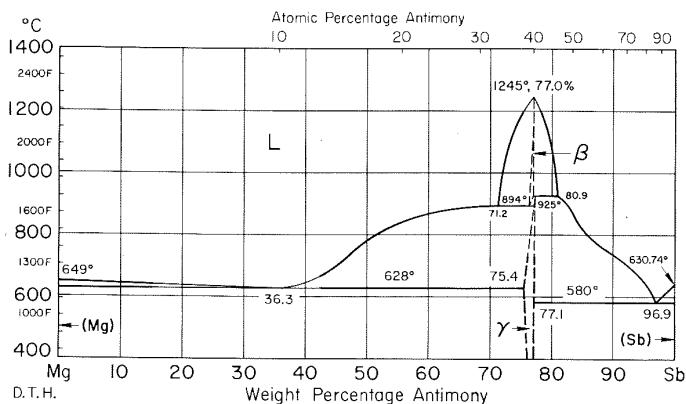
Mg-Ni Magnesium-Nickel



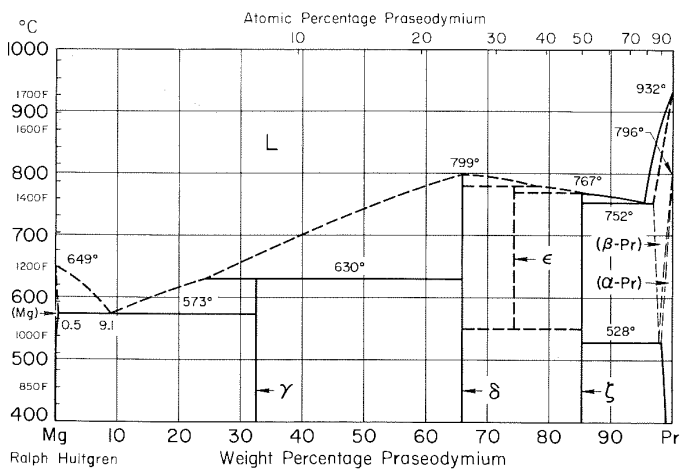
Mg-Pb Magnesium-Lead



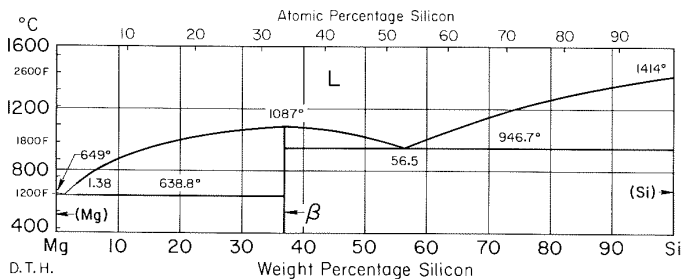
Mg-Sb Magnesium-Antimony



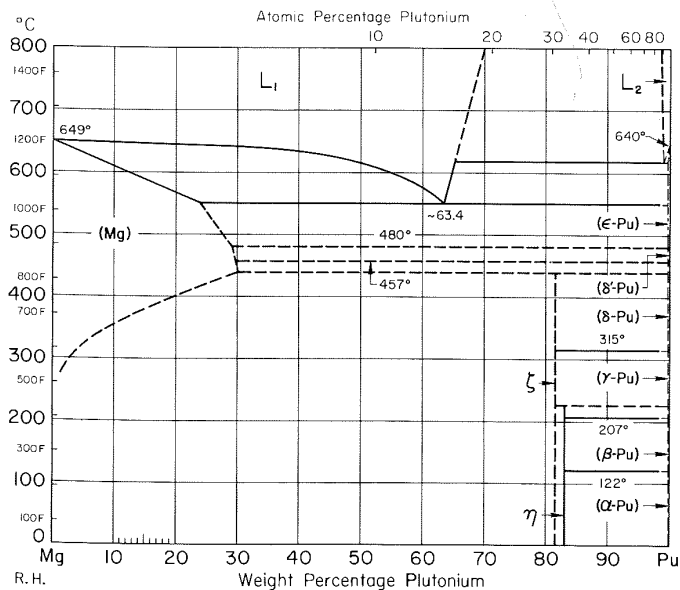
Mg-Pr Magnesium-Praseodymium



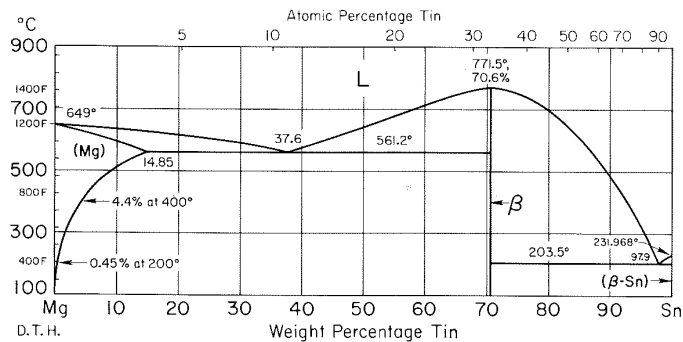
Mg-Si Magnesium-Silicon



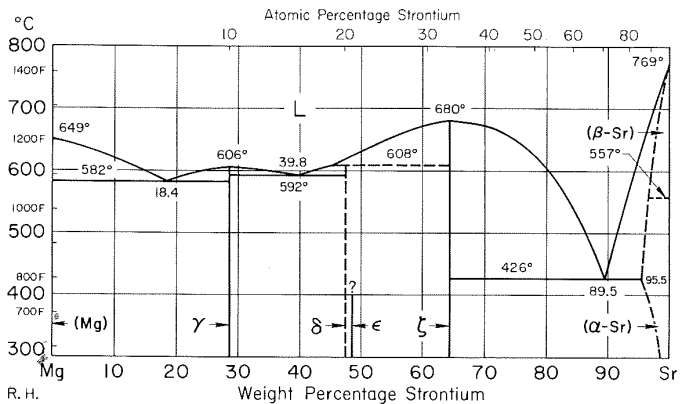
Mg-Pu Magnesium-Plutonium



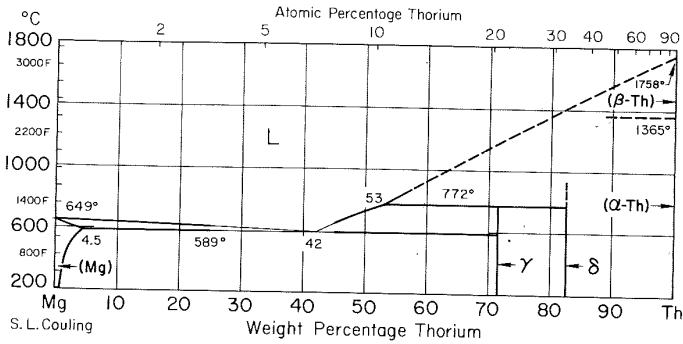
Mg-Sn Magnesium-Tin



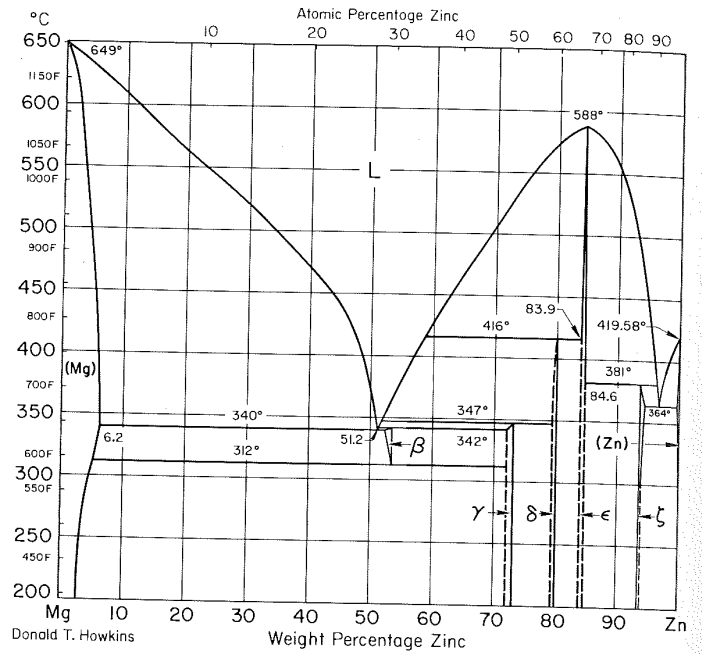
Mg-Sr Magnesium-Strontium



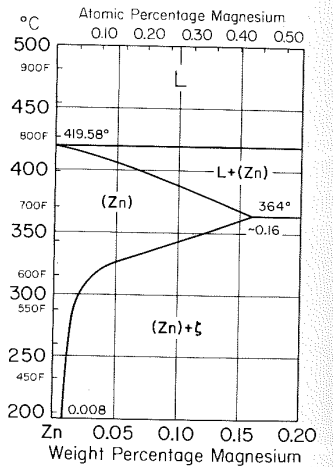
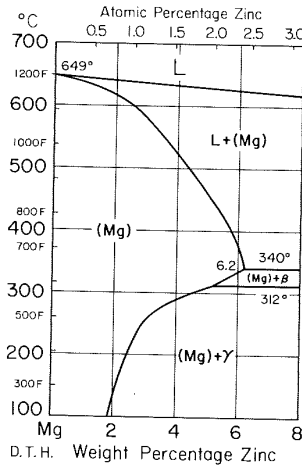
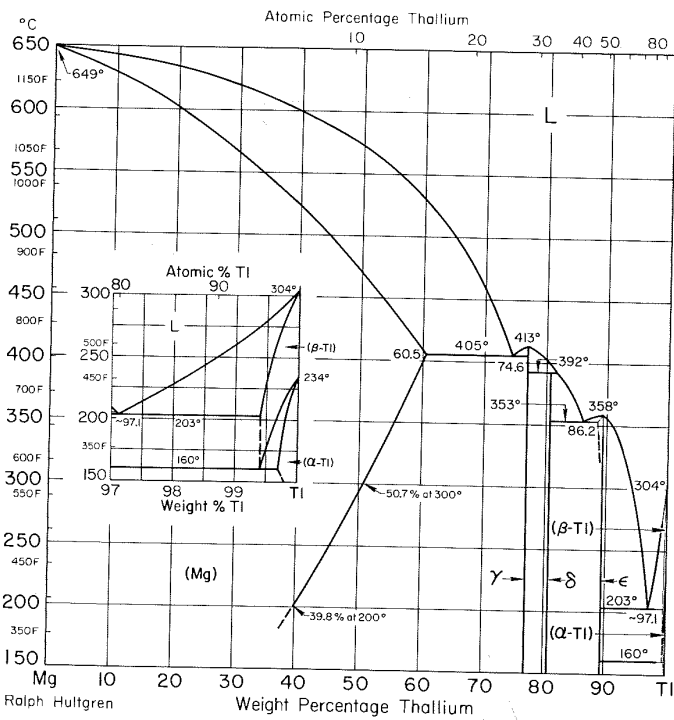
Mg-Th Magnesium-Thorium



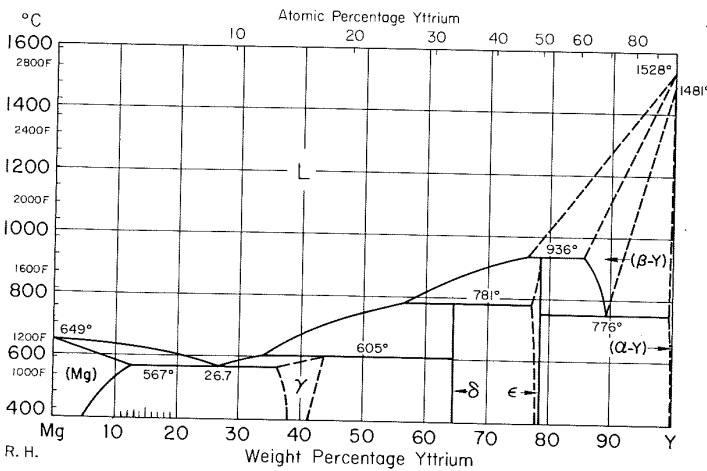
Mg-Zn Magnesium-Zinc



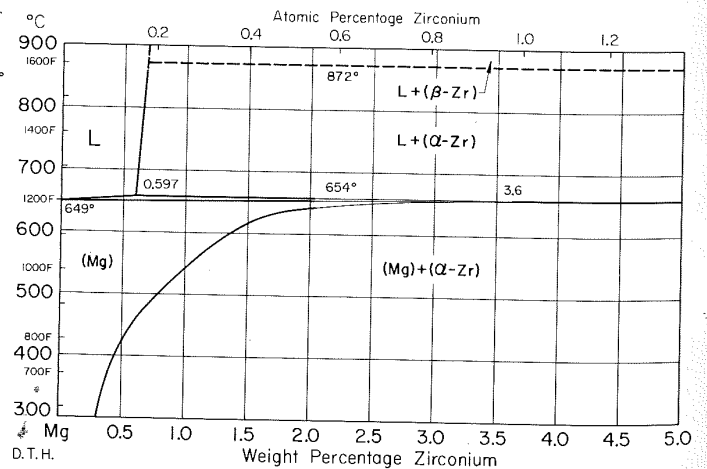
Mg-Tl Magnesium-Thallium



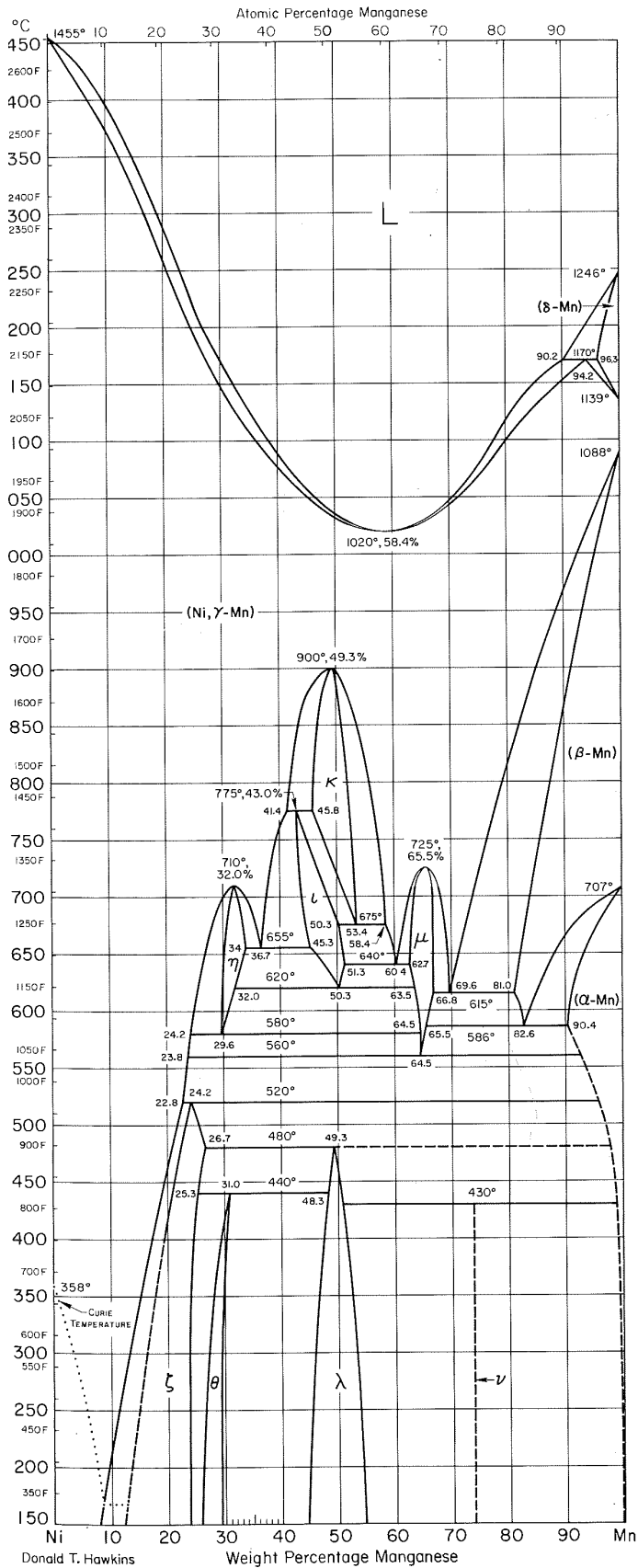
Mg-Y Magnesium-Yttrium



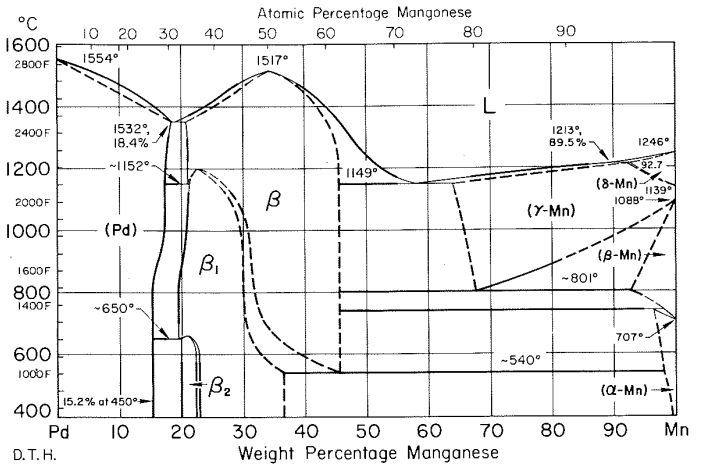
Mg-Zr Magnesium-Zirconium



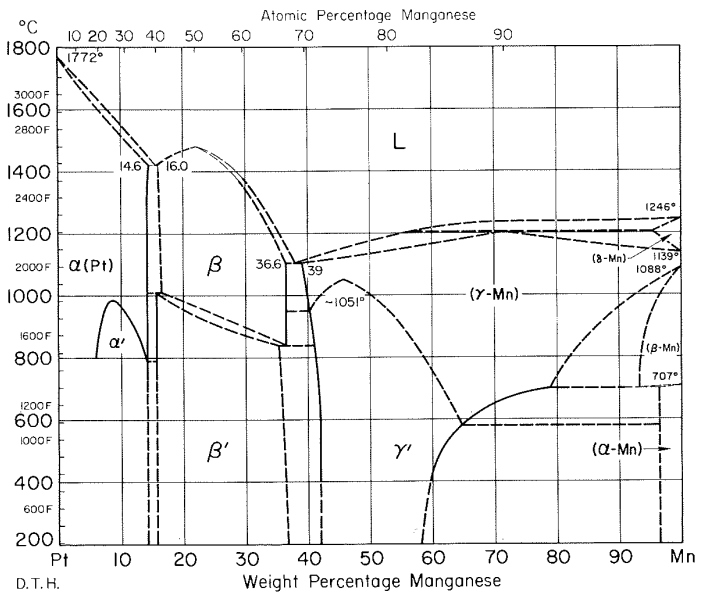
Mn-Ni Manganese-Nickel



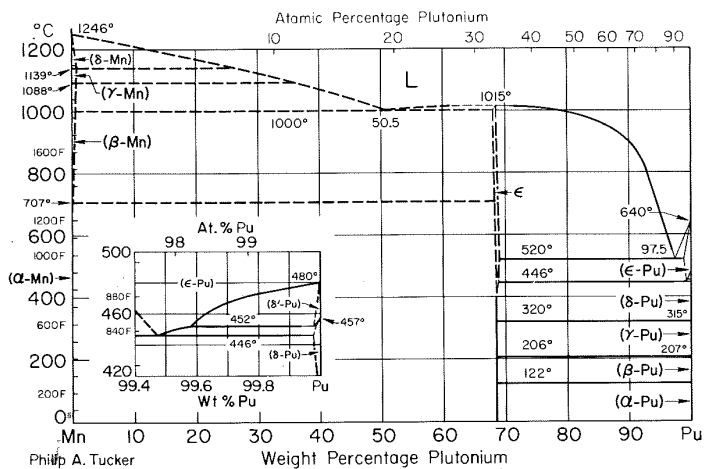
Mn-Pd Manganese-Palladium



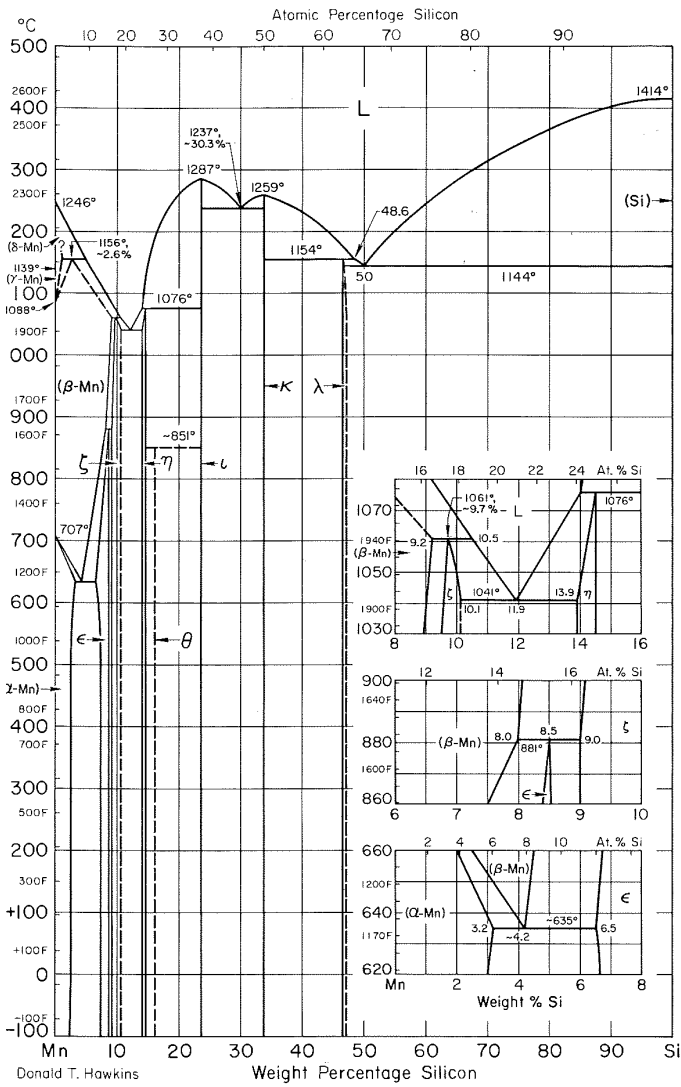
Mn-Pt Manganese-Platinum



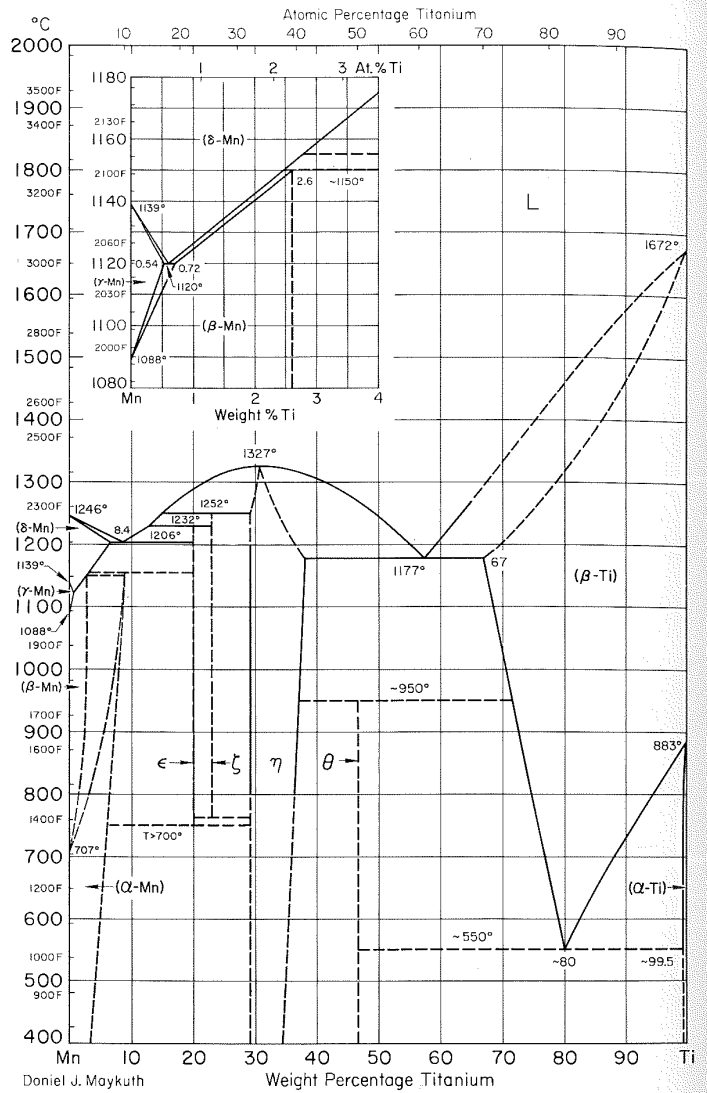
Mn-Pu Manganese-Plutonium



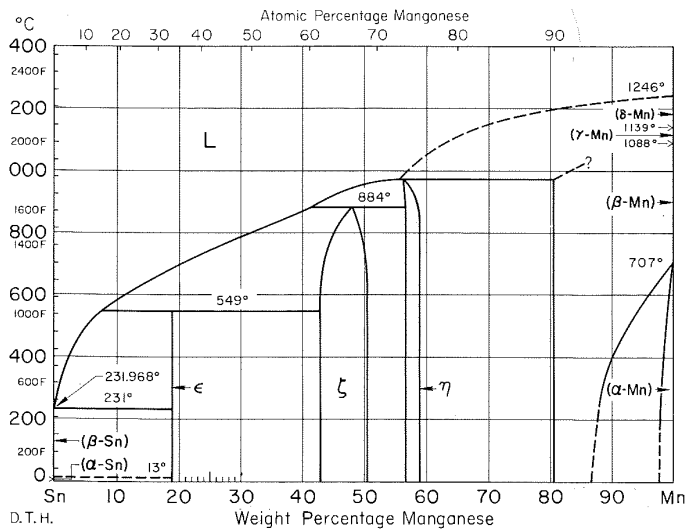
Mn-Si Manganese-Silicon



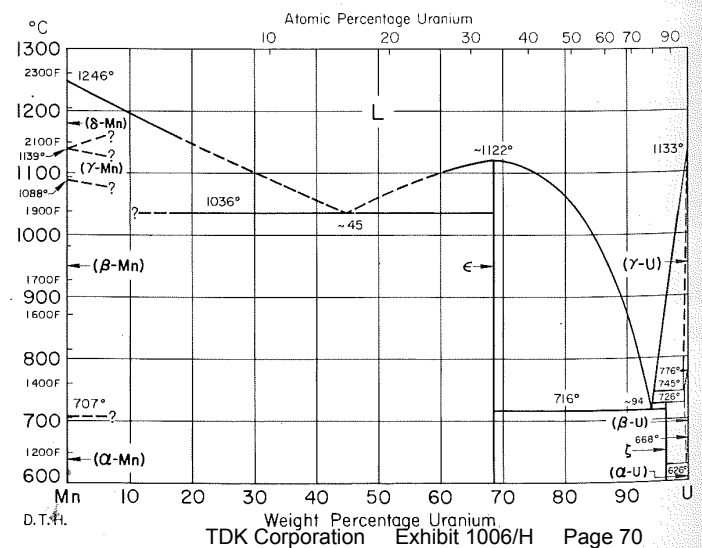
Mn-Ti Manganese-Titanium



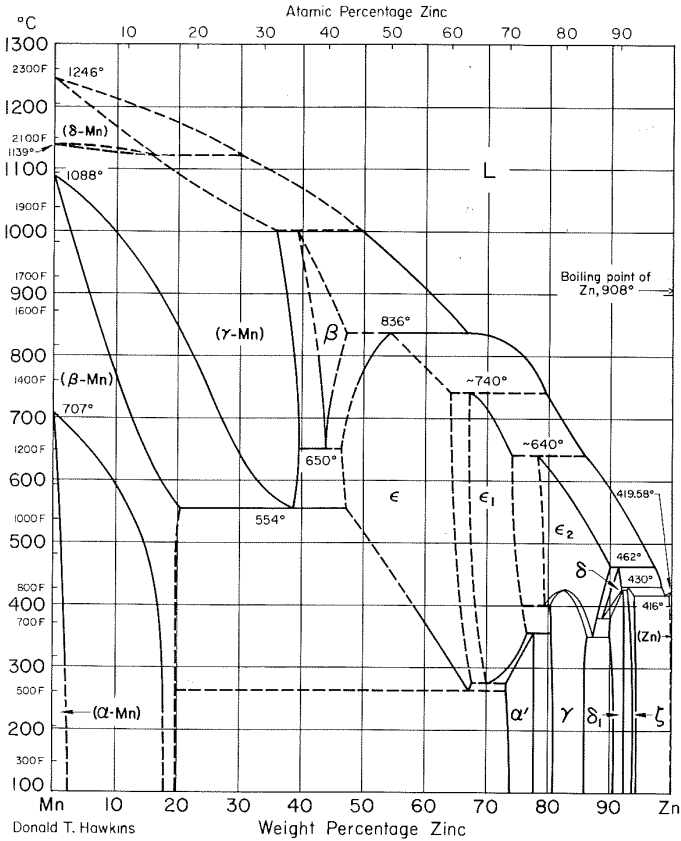
Mn-Sn Manganese-Tin



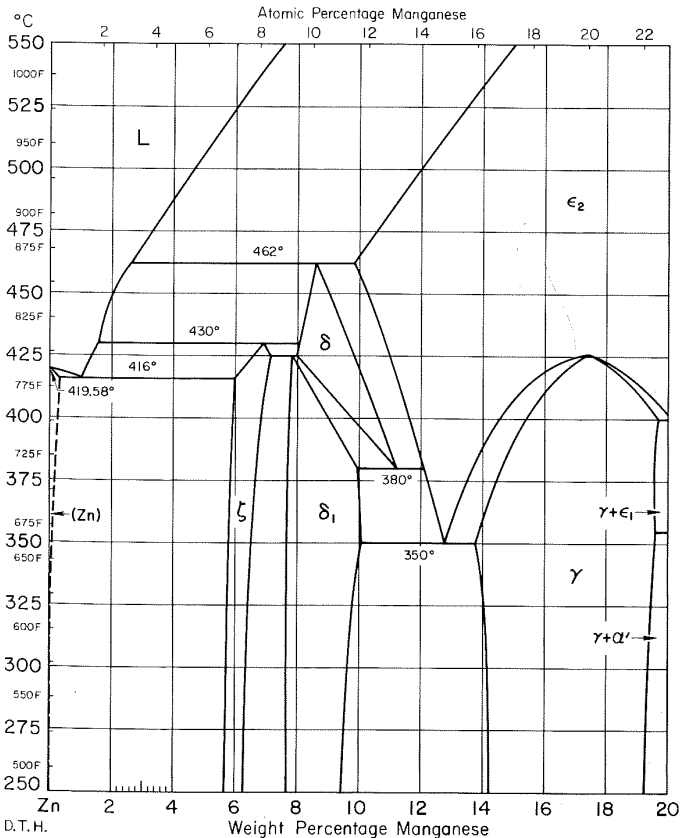
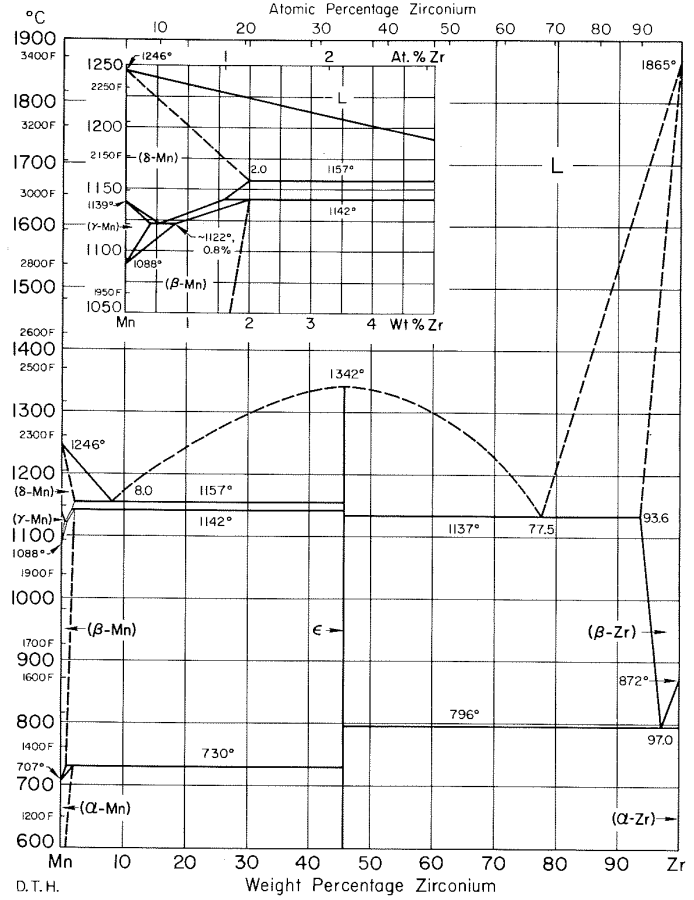
Mn-U Manganese-Uranium



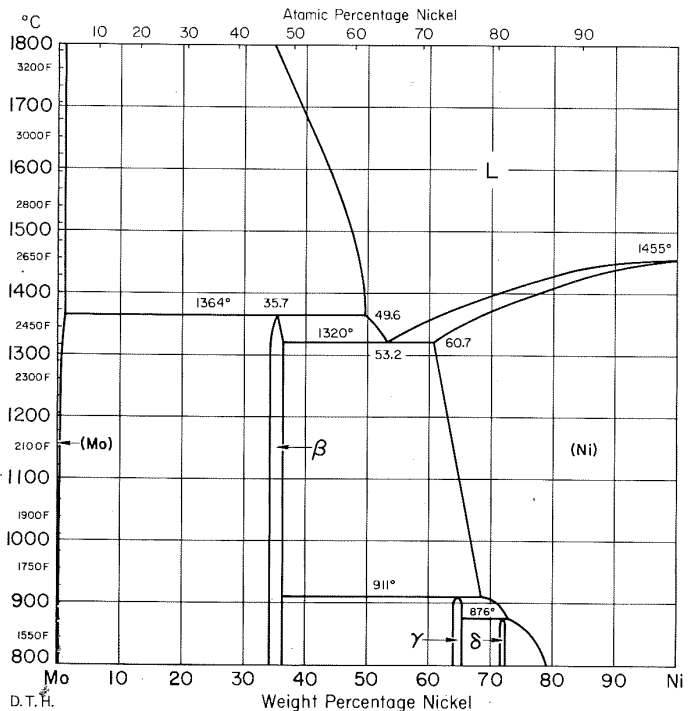
Mn-Zn Manganese-Zinc



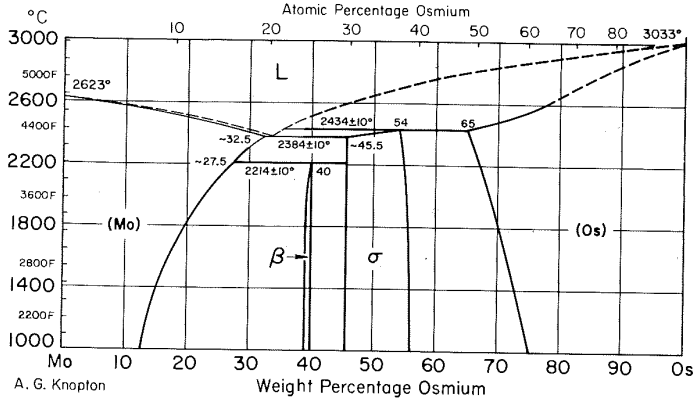
Mn-Zr Manganese-Zirconium



Mo-Ni Molybdenum-Nickel

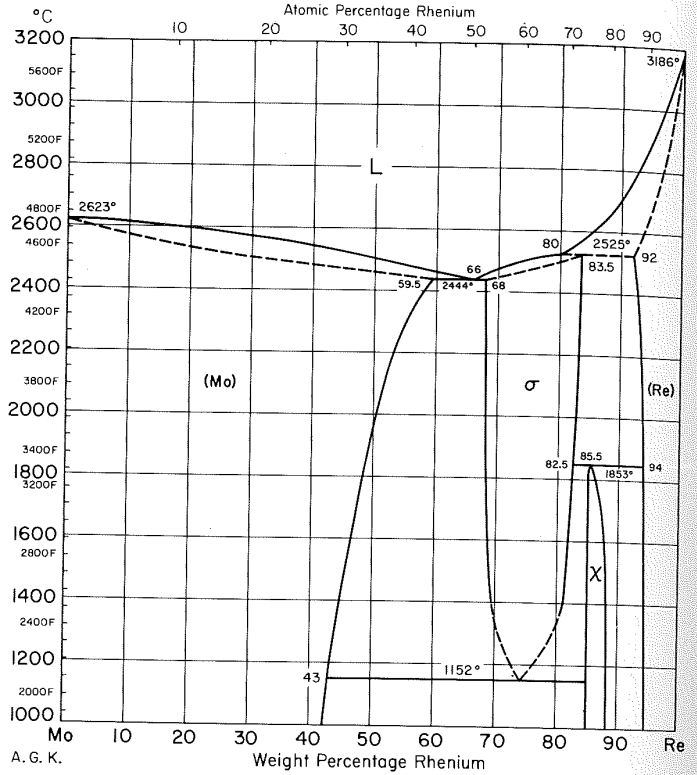


Mo-Os Molybdenum-Osmium



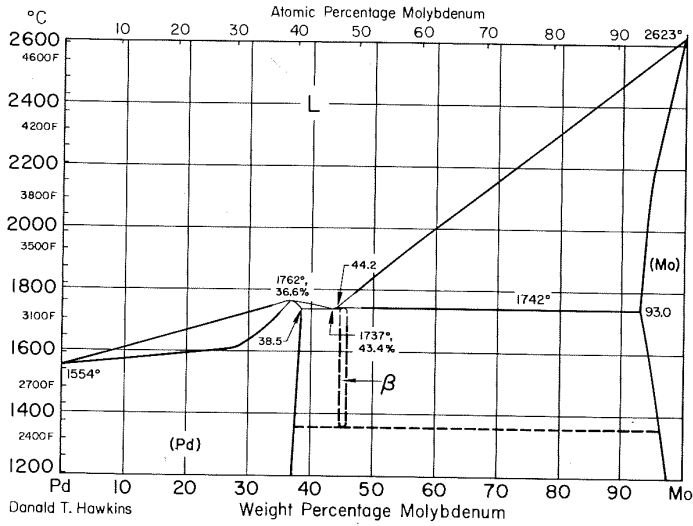
A. G. Knopfon

Mo-Re Molybdenum-Rhenium



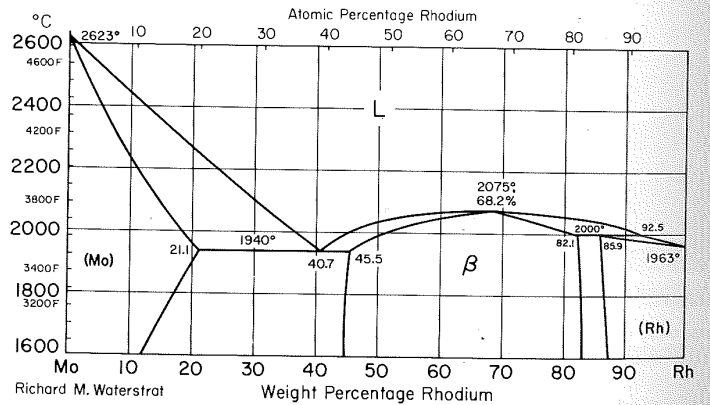
A. G. K.

Mo-Pd Molybdenum-Palladium



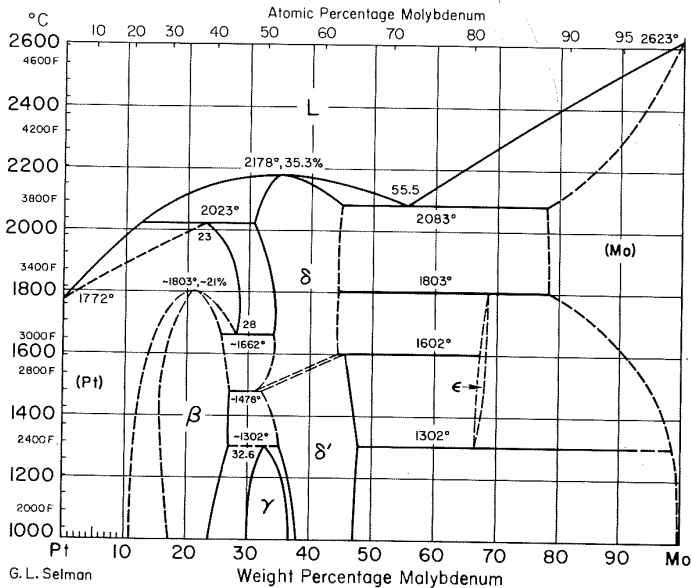
Donald T. Hawkins

Mo-Rh Molybdenum-Rhodium



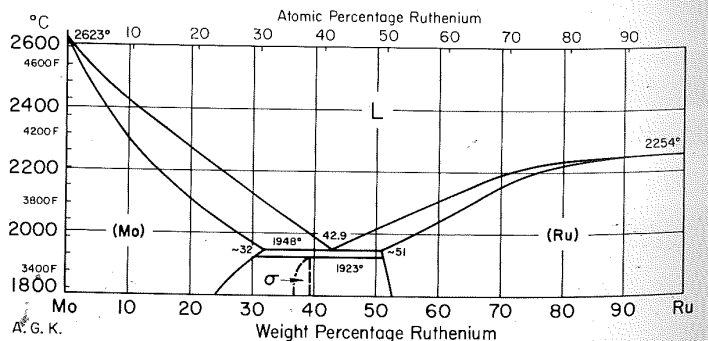
Richard M. Waterstrat

Mo-Pt Molybdenum-Platinum



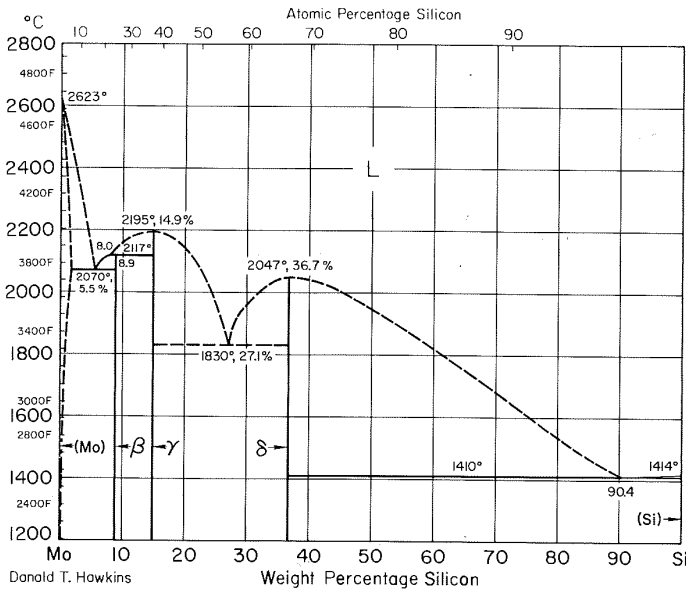
G. L. Selman

Mo-Ru Molybdenum-Ruthenium

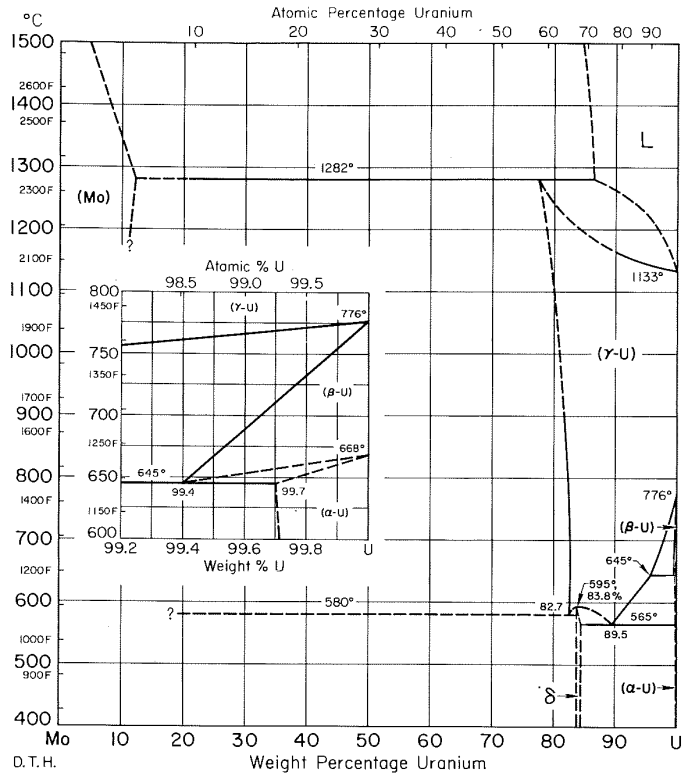


A. G. K.

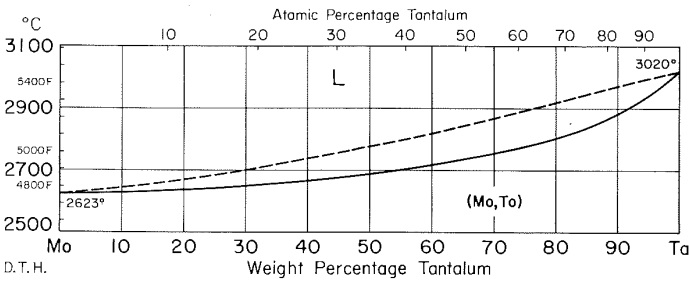
Mo-Si Molybdenum-Silicon



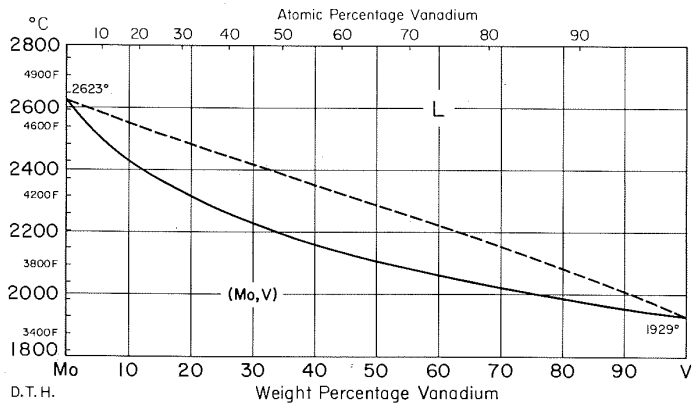
Mo-U Molybdenum-Uranium



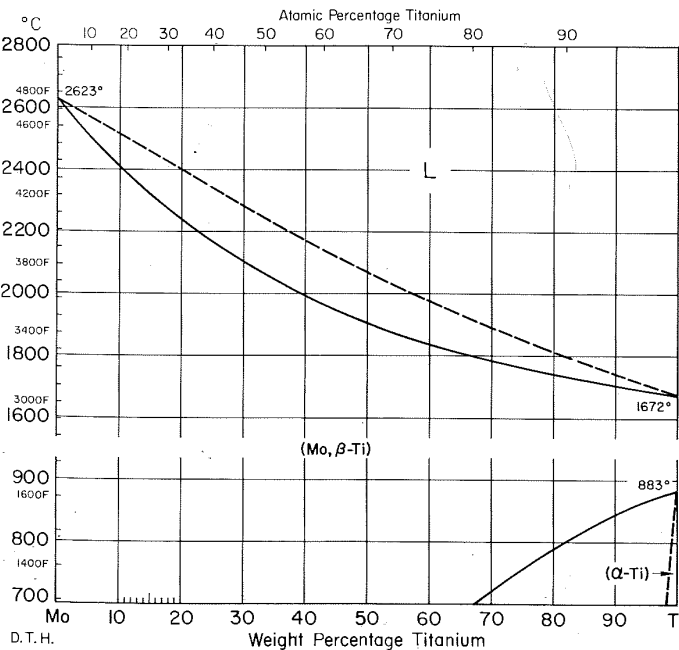
Mo-Ta Molybdenum-Tantalum



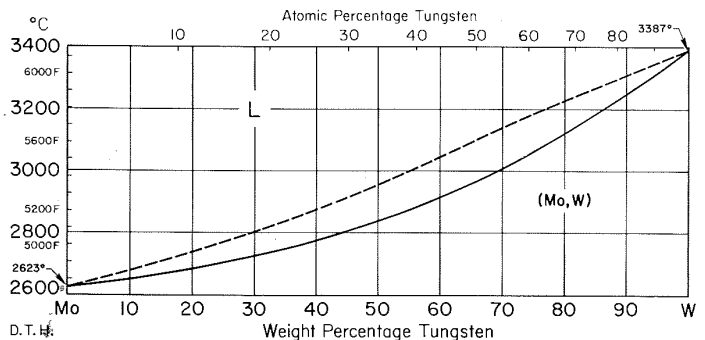
Mo-V Molybdenum-Vanadium



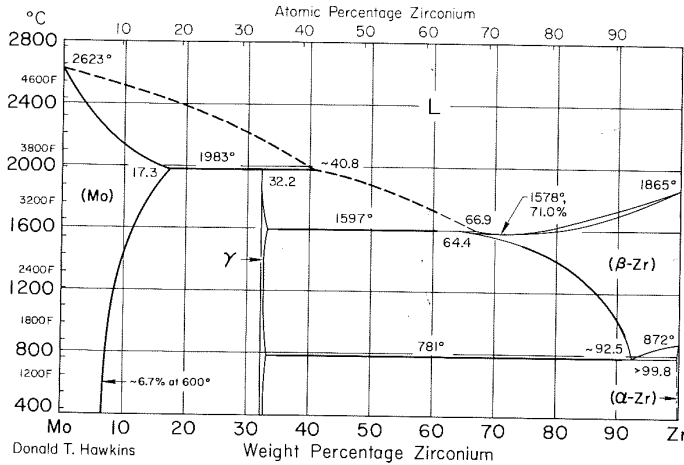
Mo-Ti Molybdenum-Titanium



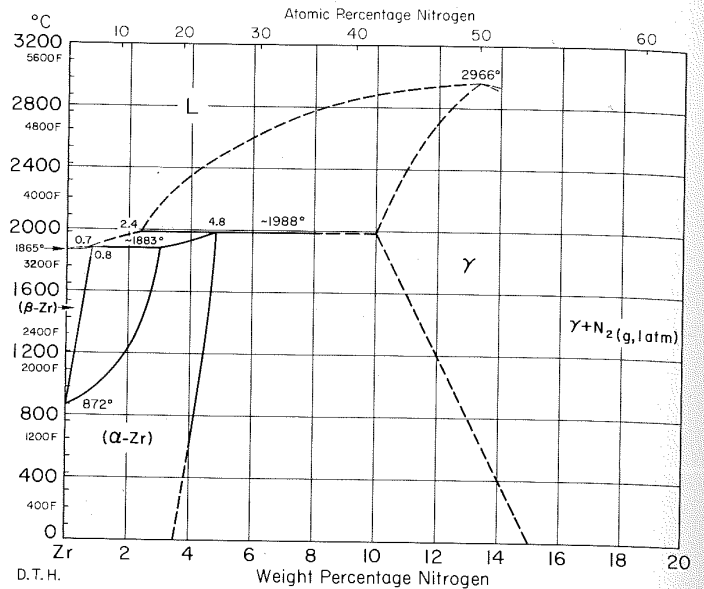
Mo-W Molybdenum-Tungsten



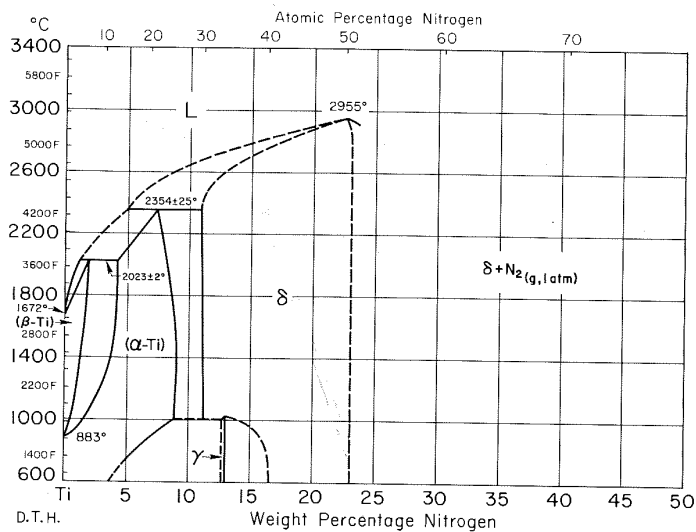
Mo-Zr Molybdenum-Zirconium



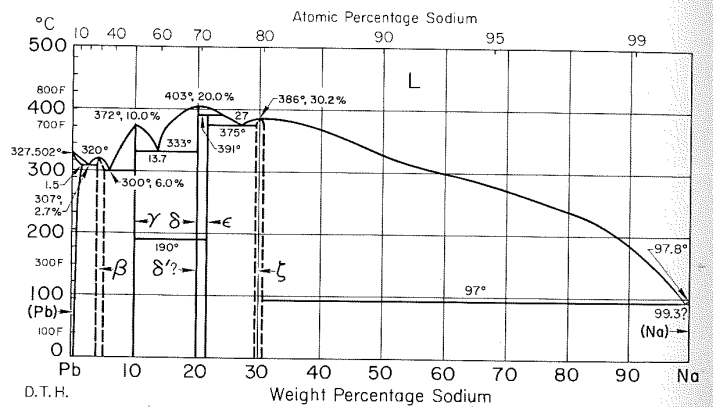
N-Zr Nitrogen-Zirconium



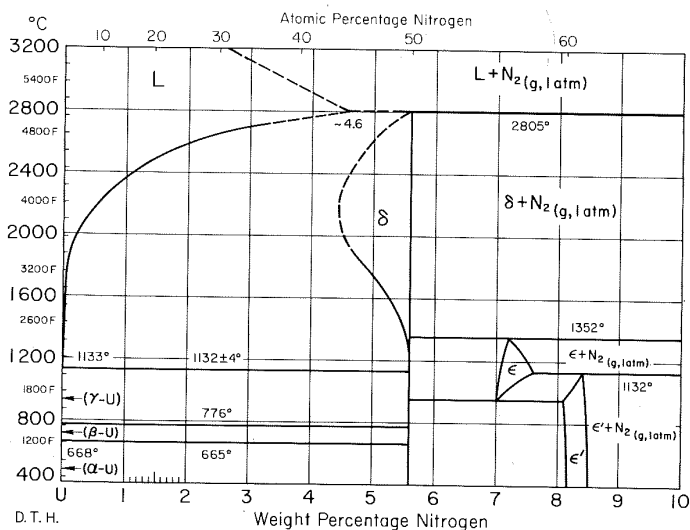
N-Ti Nitrogen-Titanium



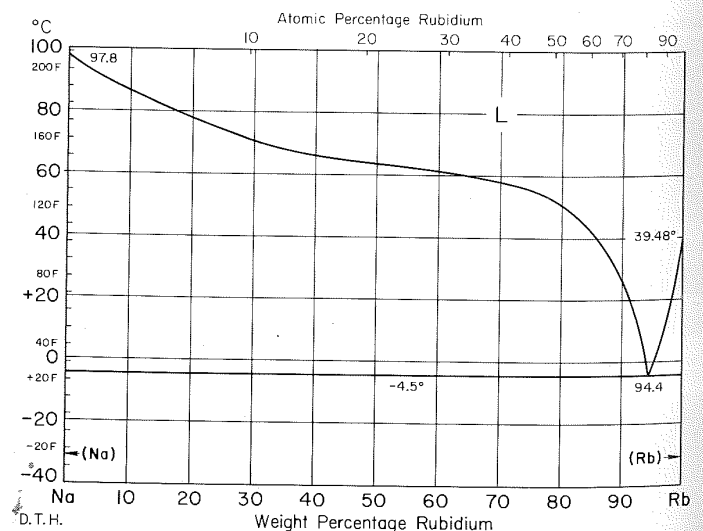
Na-Pb Sodium-Lead



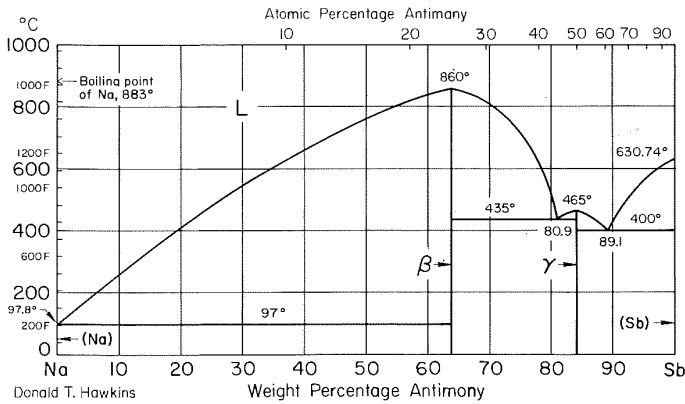
N-U Nitrogen-Uranium



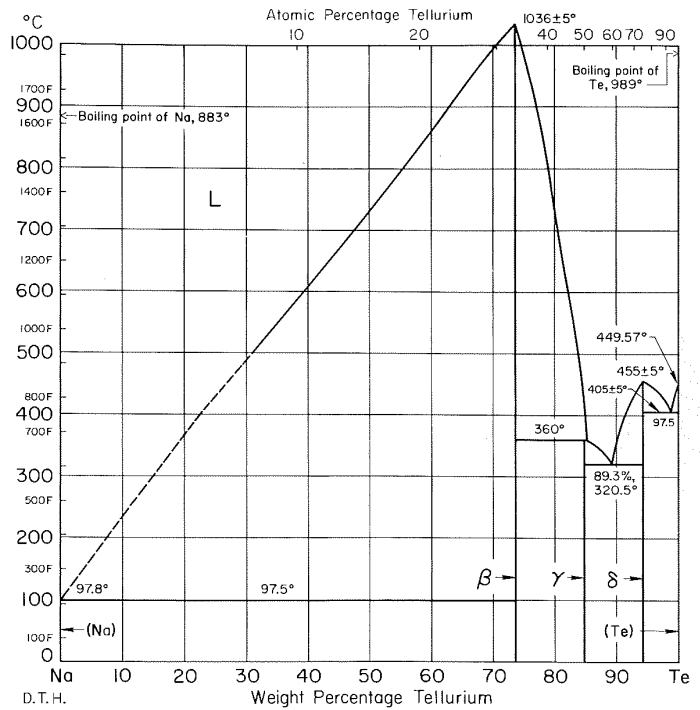
Na-Rb Sodium-Rubidium



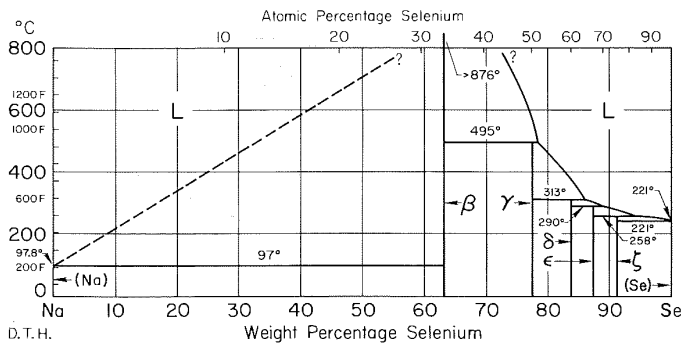
Na-Sb Sodium-Antimony



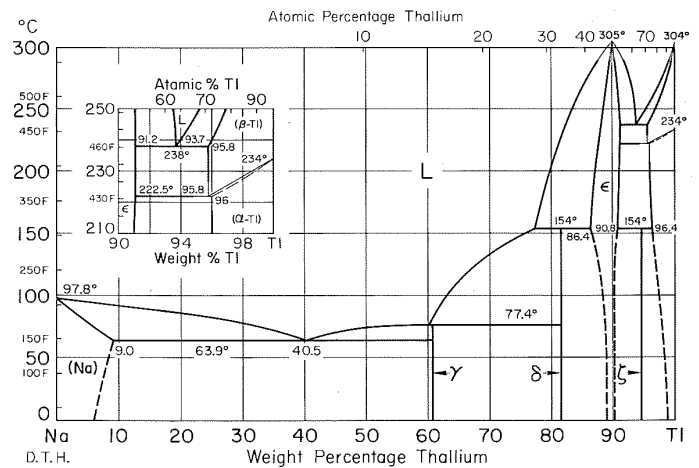
Na-Te Sodium-Tellurium



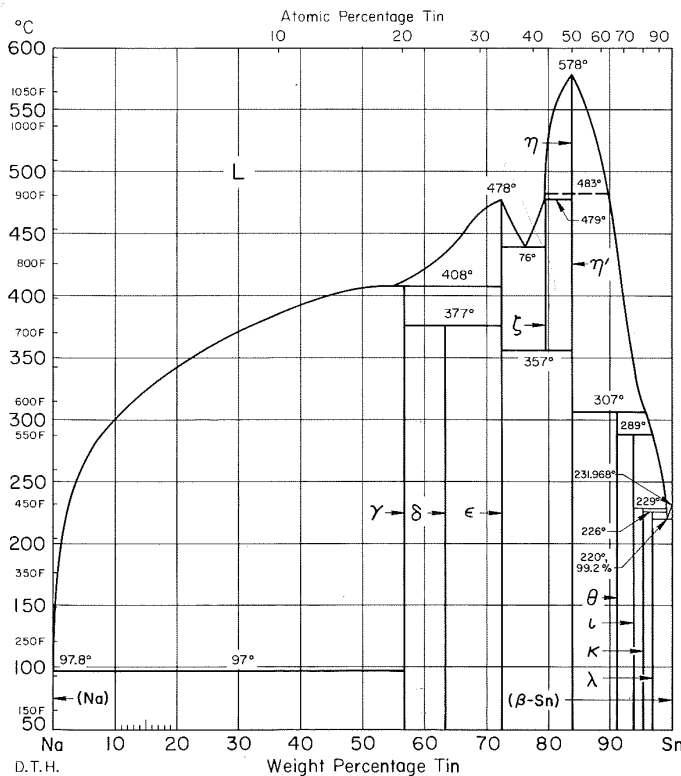
Na-Se Sodium-Selenium



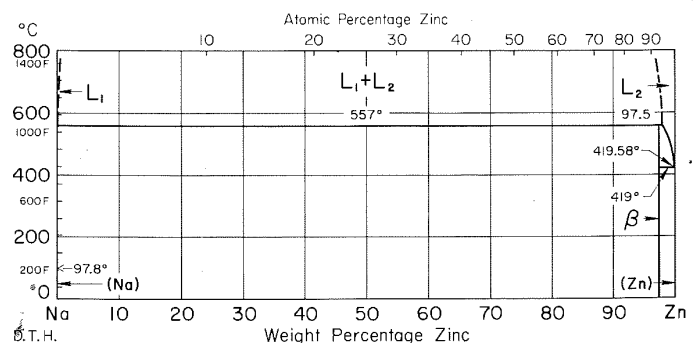
Na-Tl Sodium-Thallium



Na-Sn Sodium-Tin



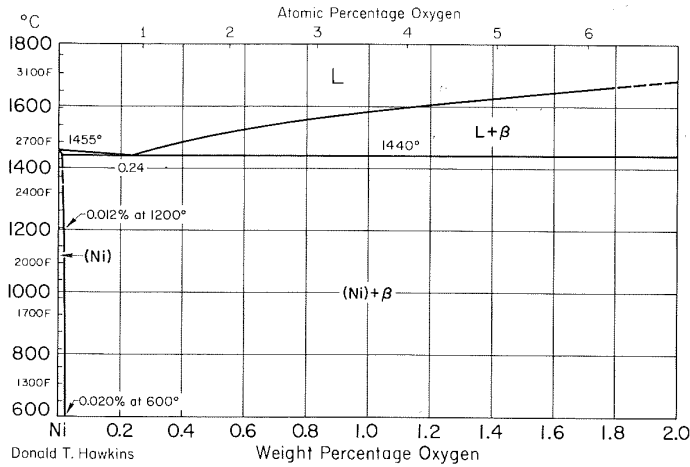
Na-Zn Sodium-Zinc



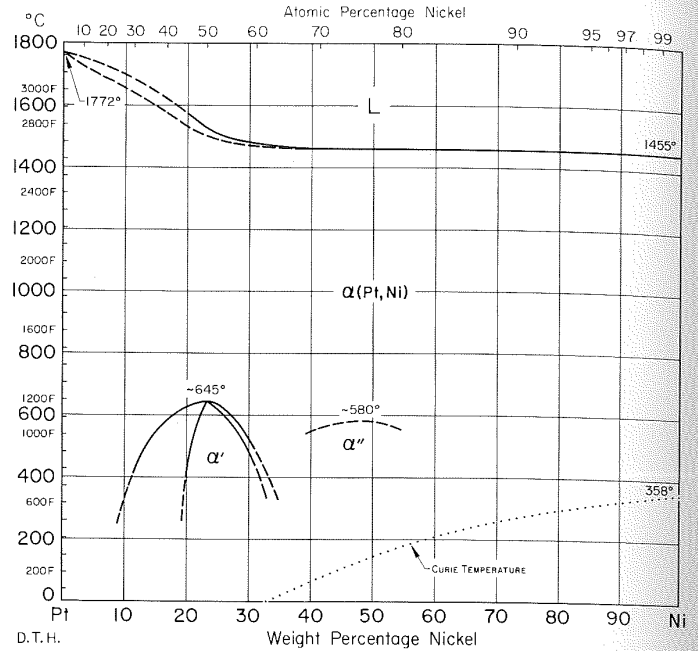
Nb systems

See Cb

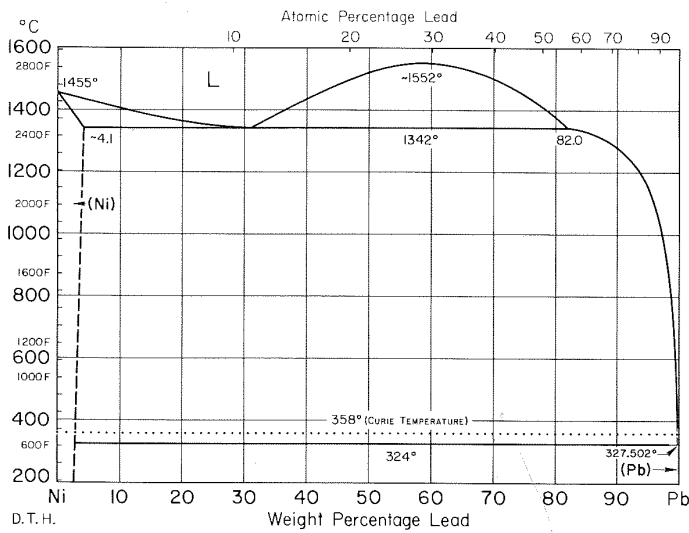
Ni-O Nickel-Oxygen



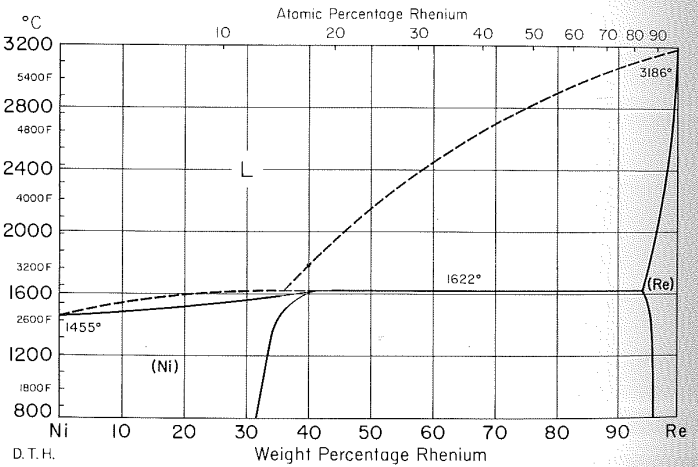
Ni-Pt Nickel-Platinum



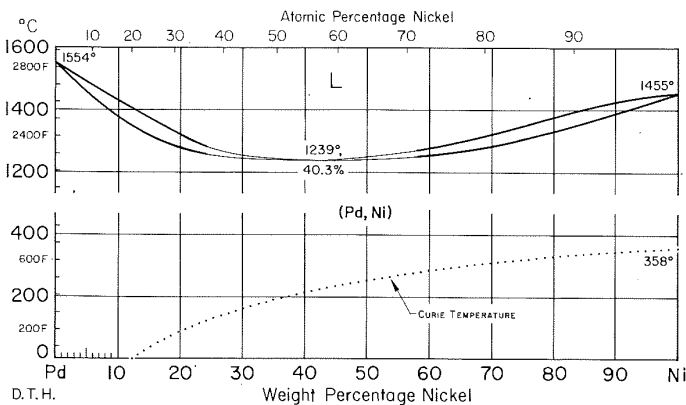
Ni-Pb Nickel-Lead



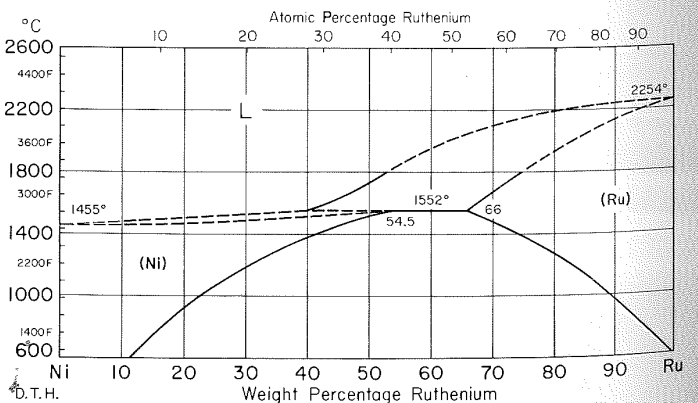
Ni-Re Nickel-Rhenium



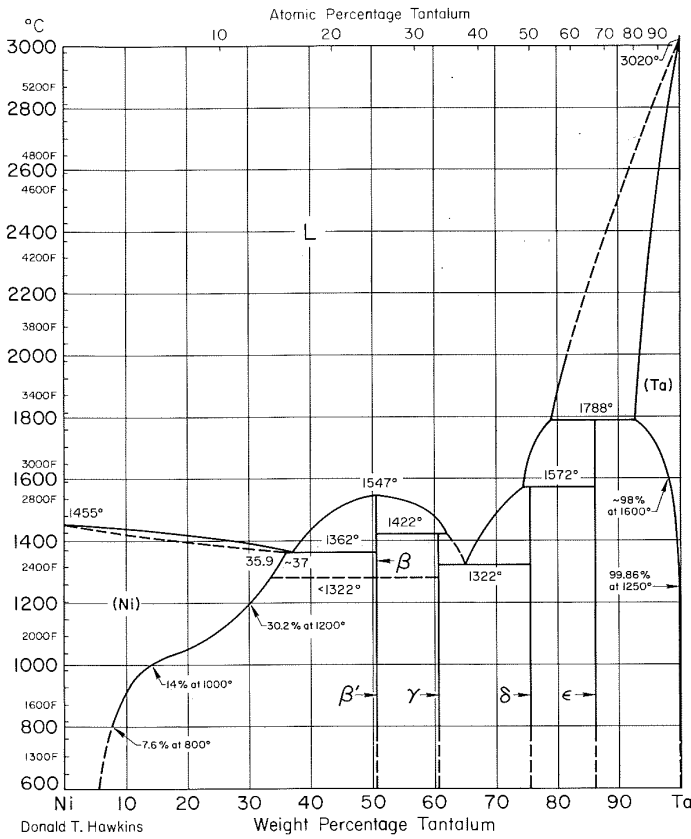
Ni-Pd Nickel-Palladium



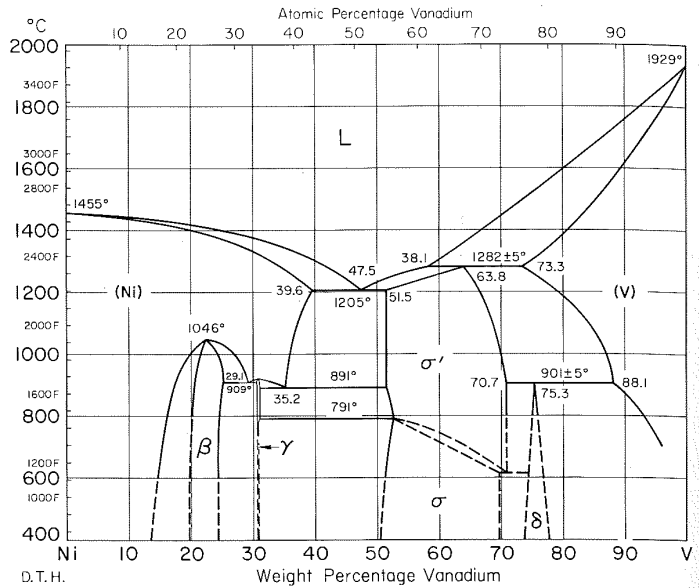
Ni-Ru Nickel-Ruthenium



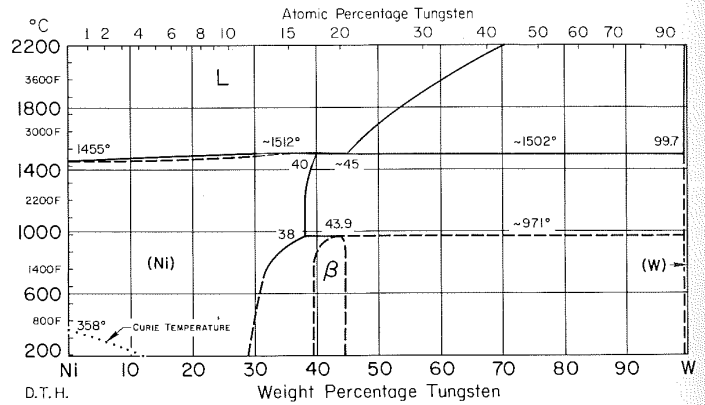
Ni-Ta Nickel-Tantalum



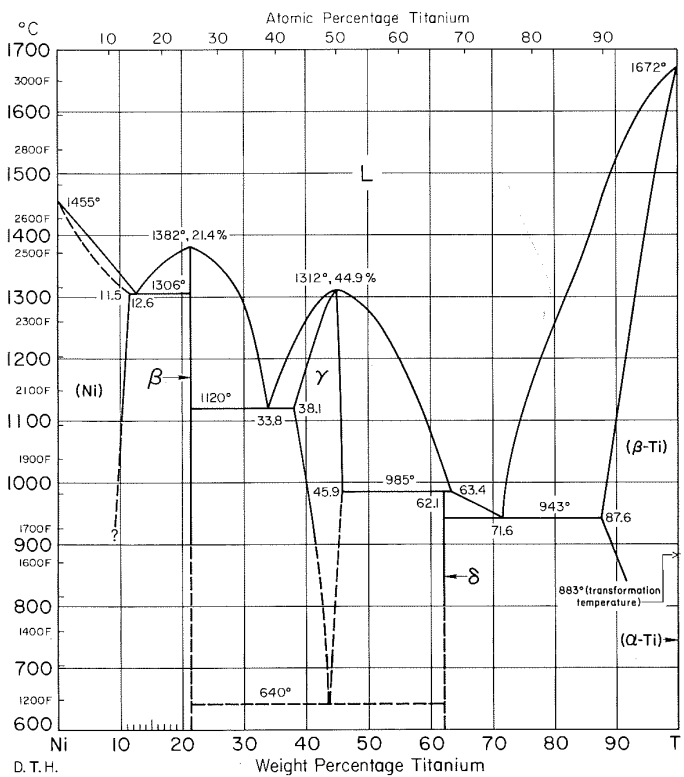
Ni-V Nickel-Vanadium



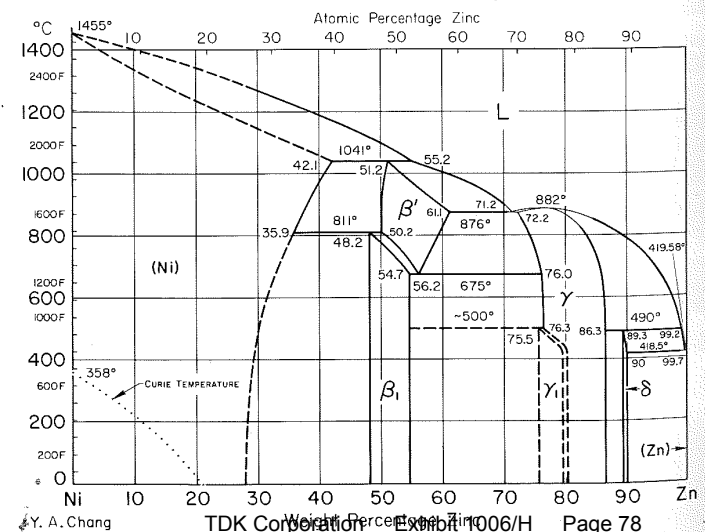
Ni-W Nickel-Tungsten



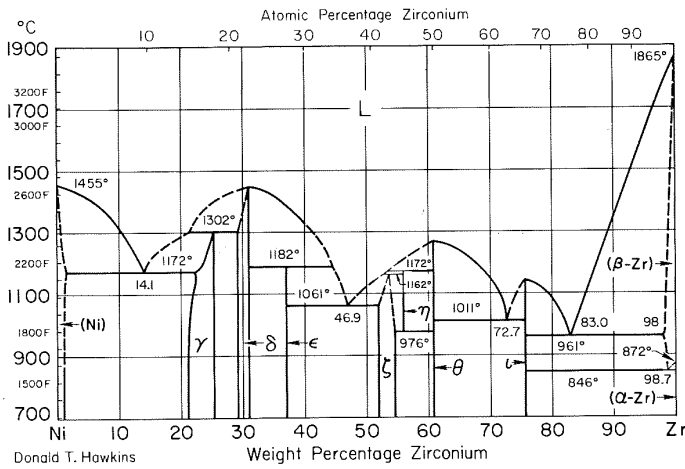
Ni-Ti Nickel-Titanium



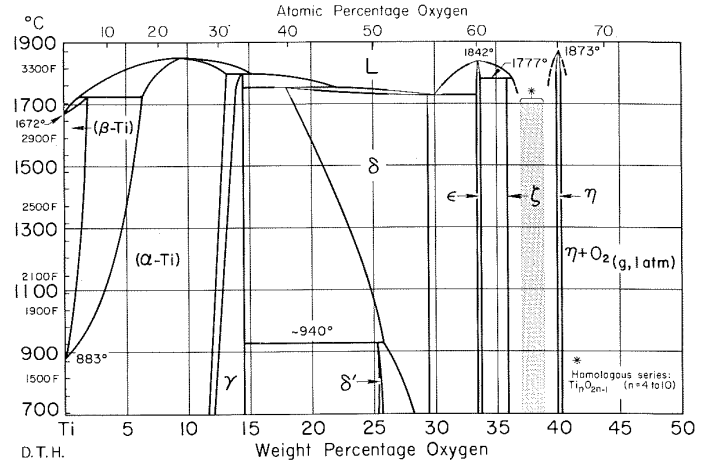
Ni-Zn Nickel-Zinc



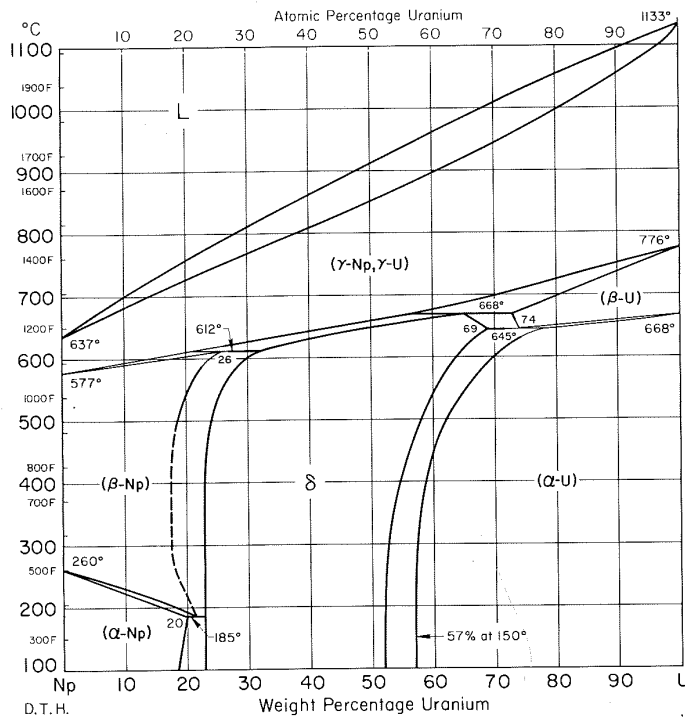
Ni-Zr Nickel-Zirconium



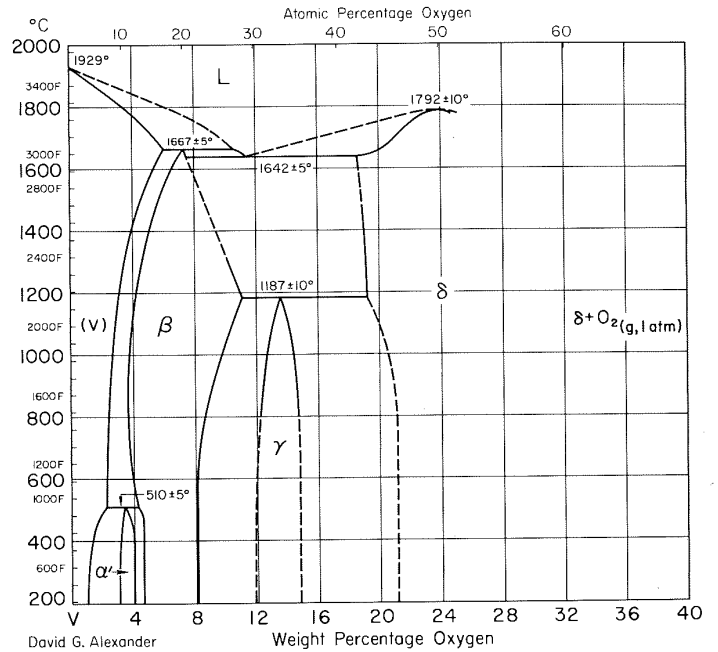
O-Ti Oxygen-Titanium



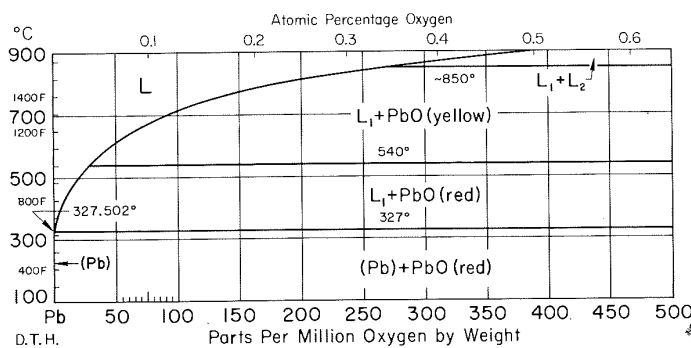
Np-U Neptunium-Uranium



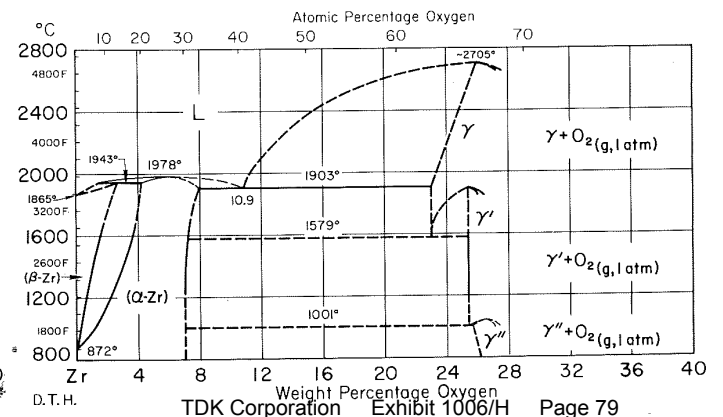
O-V Oxygen-Vanadium



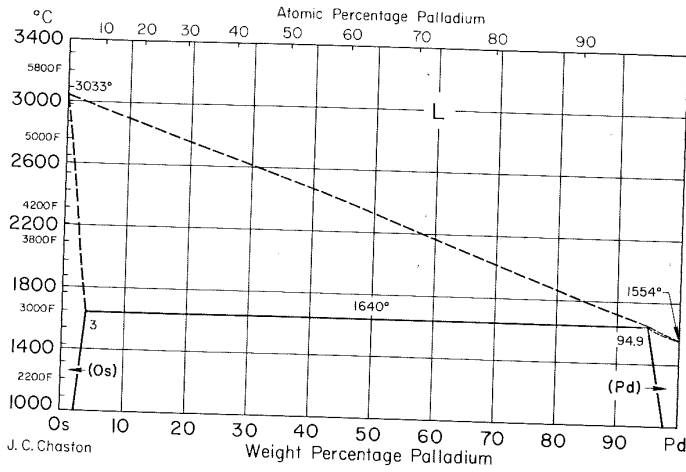
O-Pb Oxygen-Lead



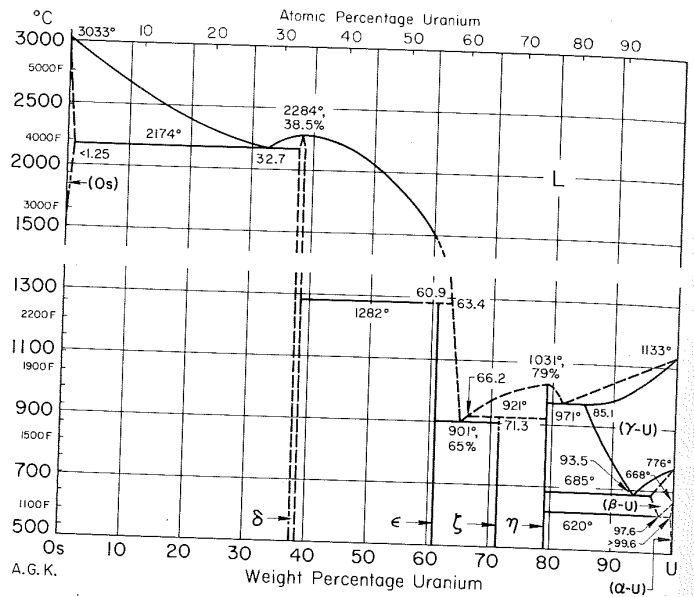
O-Zr Oxygen-Zirconium



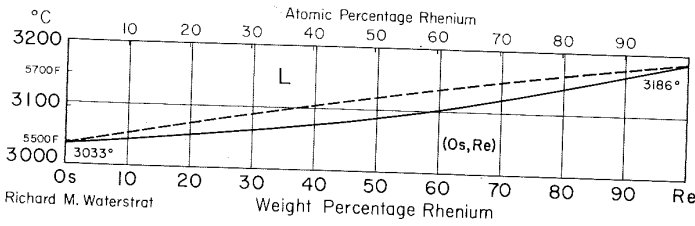
Os-Pd Osmium-Palladium



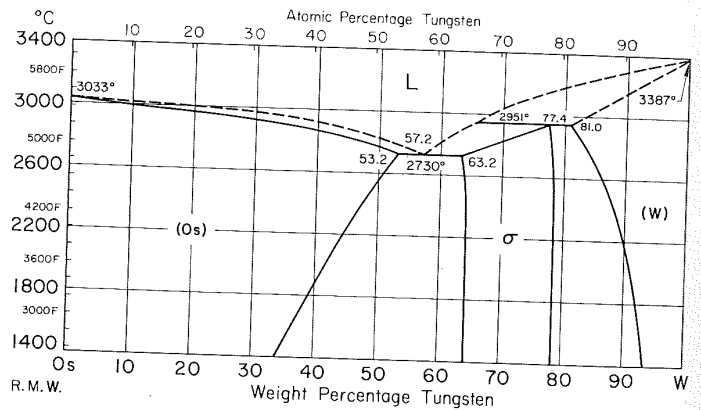
Os-U Osmium-Uranium



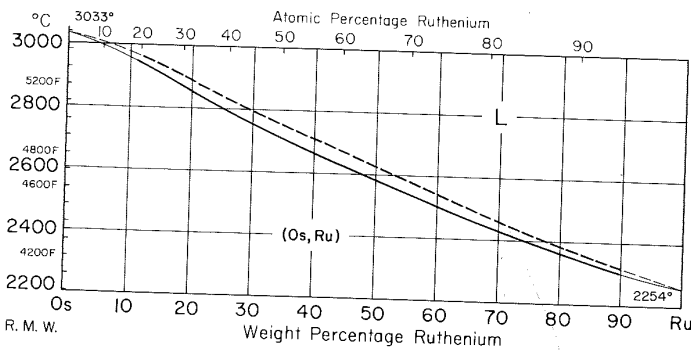
Os-Re Osmium-Rhenium



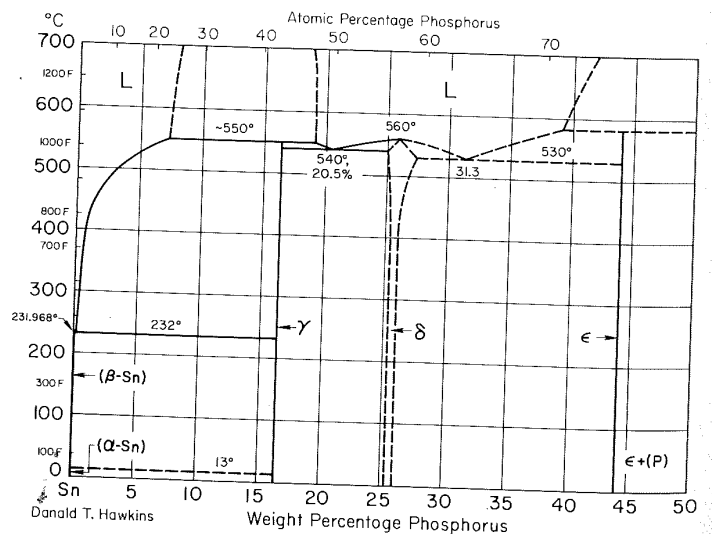
Os-W Osmium-Tungsten



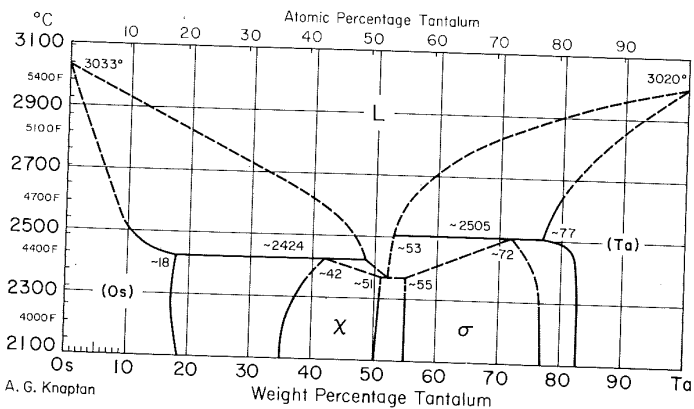
Os-Ru Osmium-Ruthenium



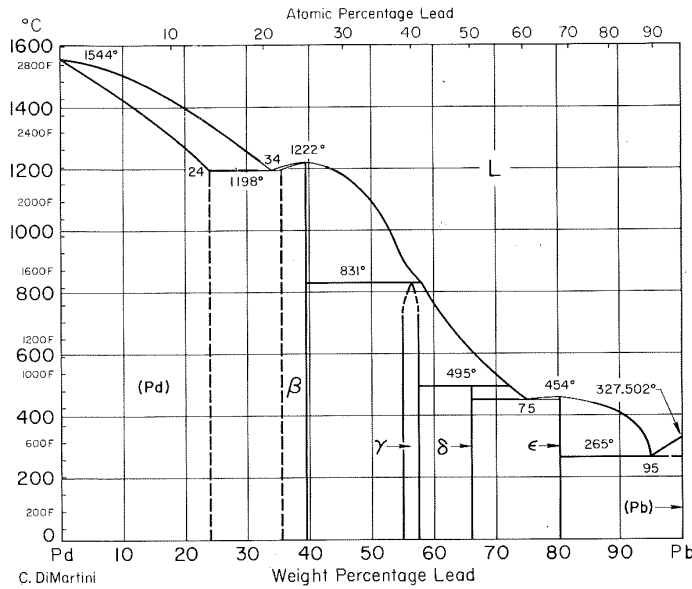
P-Sn Phosphorus-Tin



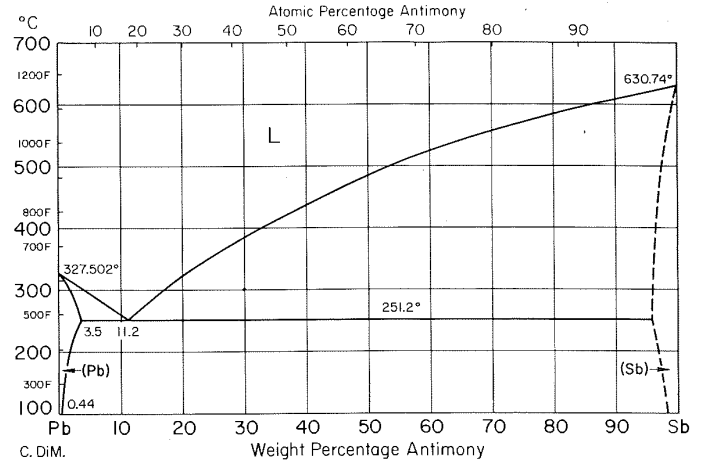
Os-Ta Osmium-Tantalum



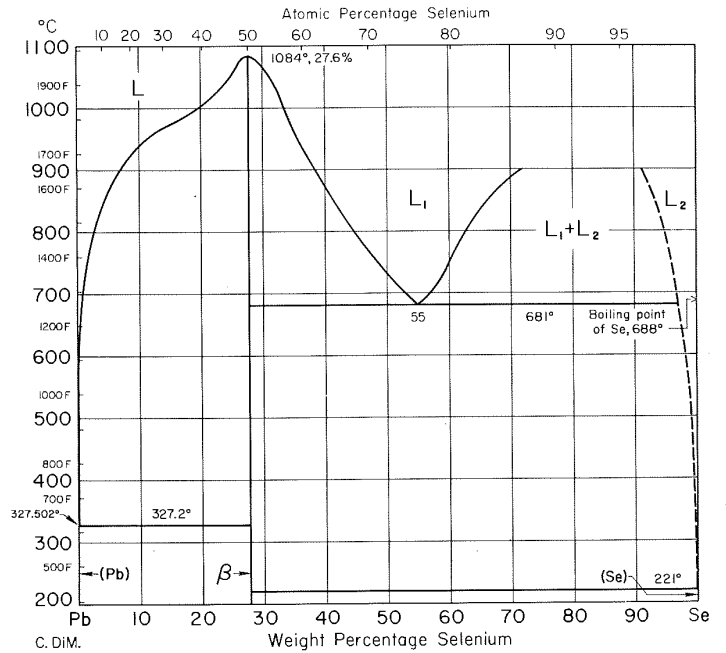
Pb-Pd Lead-Palladium



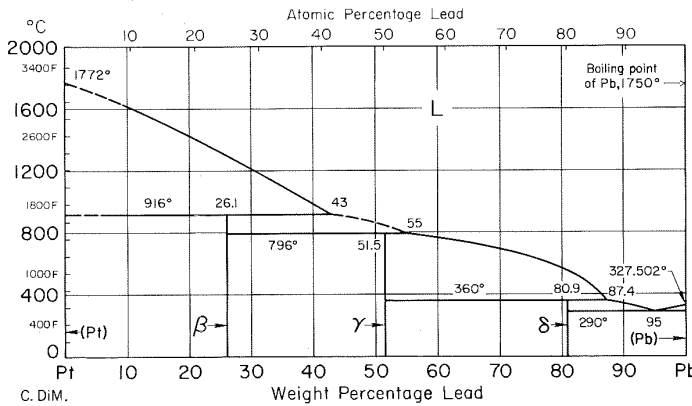
Pb-Sb Lead-Antimony



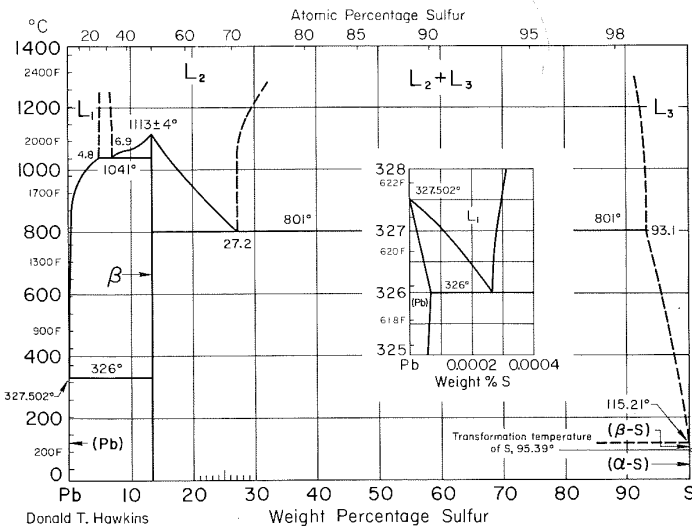
Pb-Se Lead-Selenium



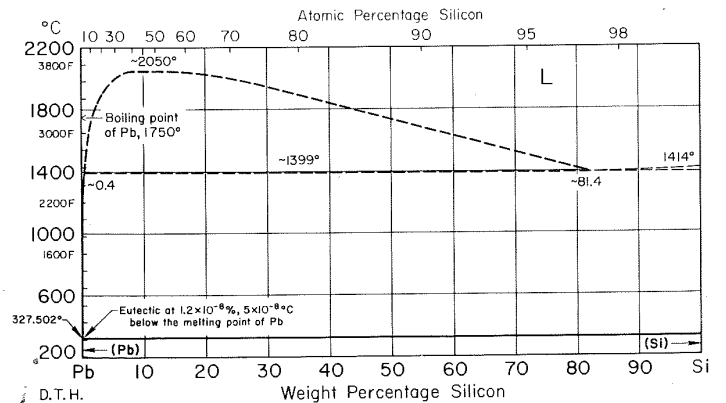
Pb-Pt Lead-Platinum



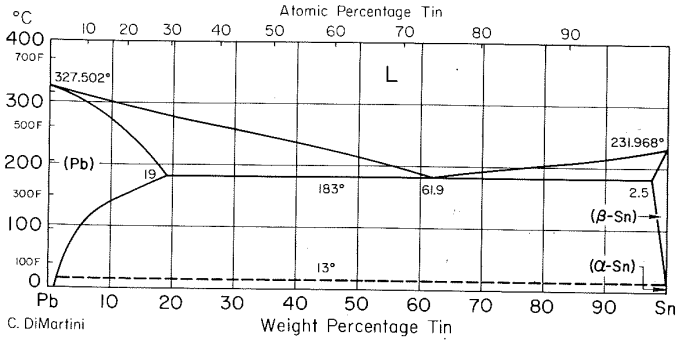
Pb-S Lead-Sulfur



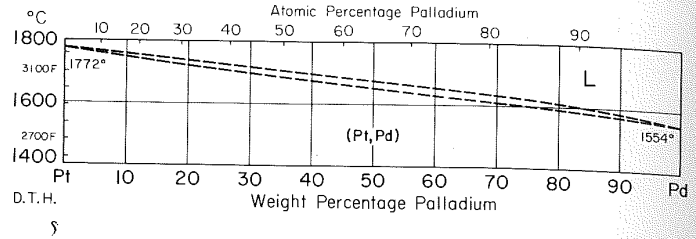
Pb-Si Lead-Silicon



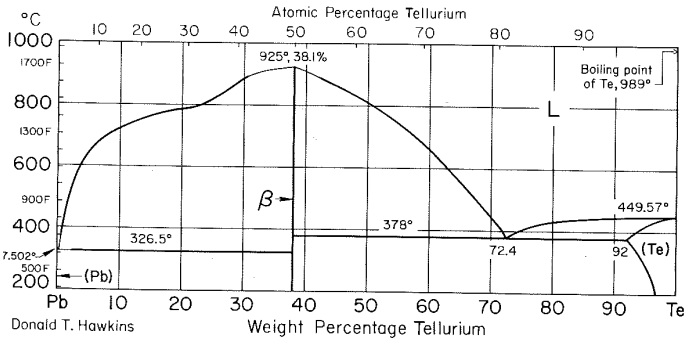
Pb-Sn Lead-Tin



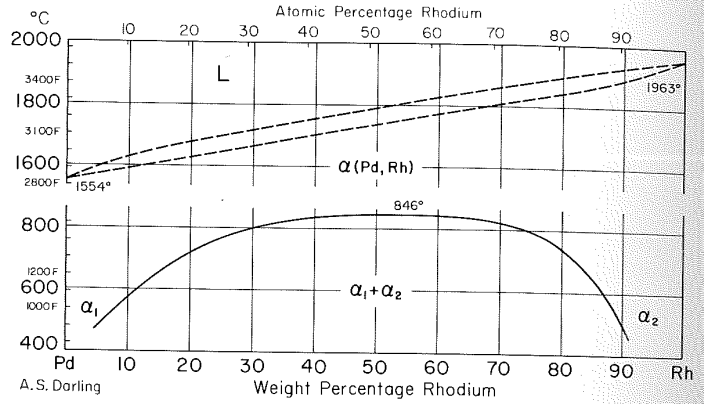
Pd-Pt Palladium-Platinum



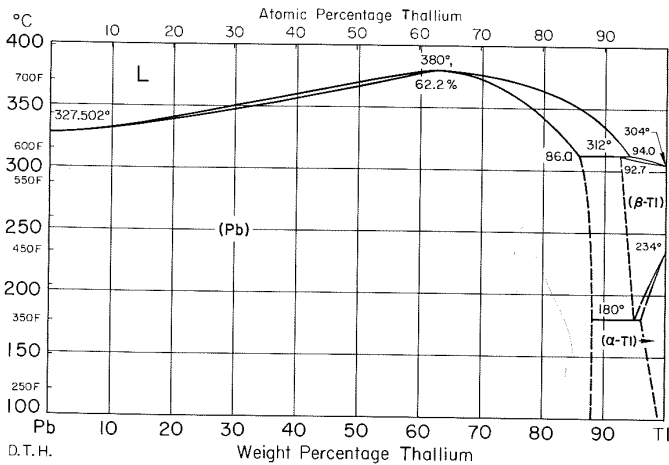
Pb-Te Lead-Tellurium



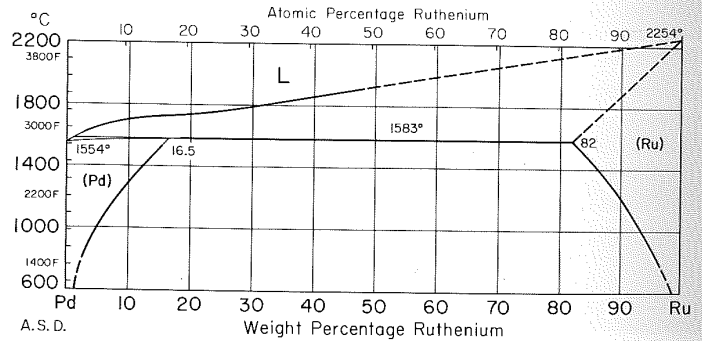
Pd-Rh Palladium-Rhodium



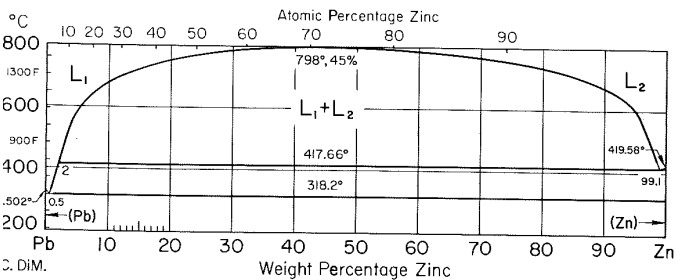
Pb-Tl Lead-Thallium



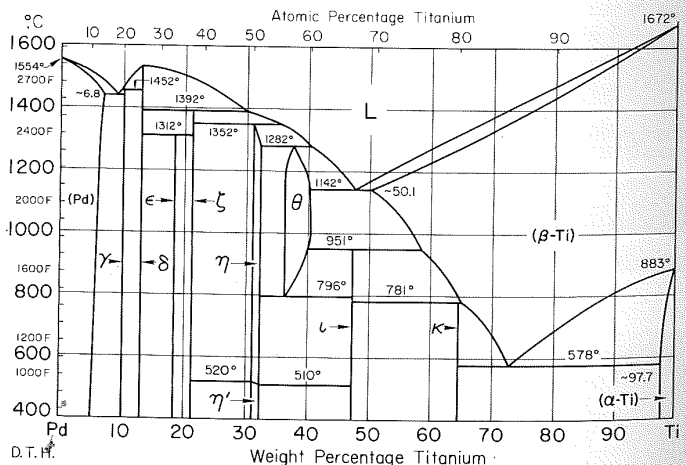
Pd-Ru Palladium-Ruthenium



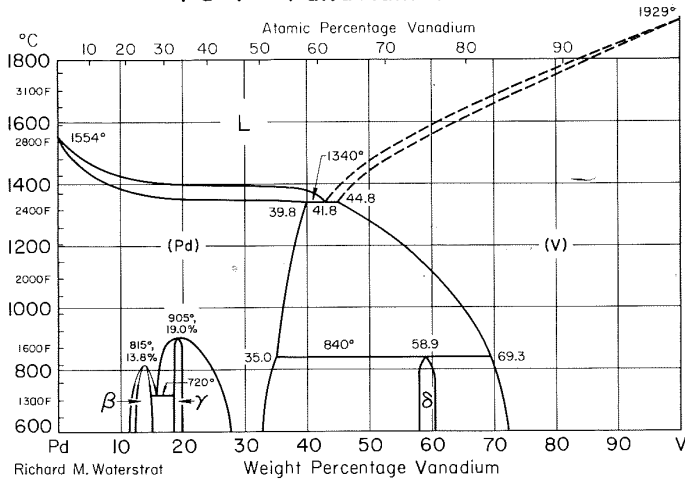
Pb-Zn Lead-Zinc



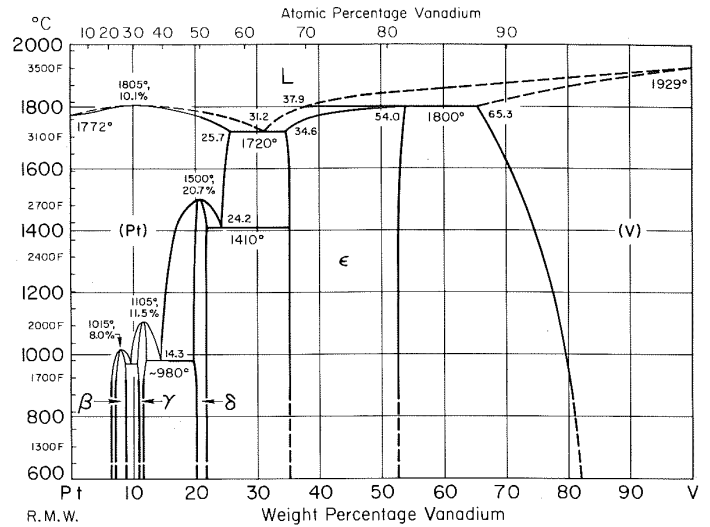
Pd-Ti Palladium-Titanium



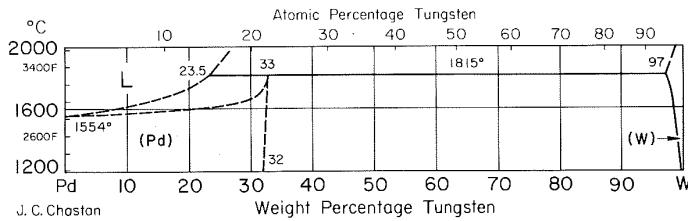
Pd-V Palladium-Vanadium



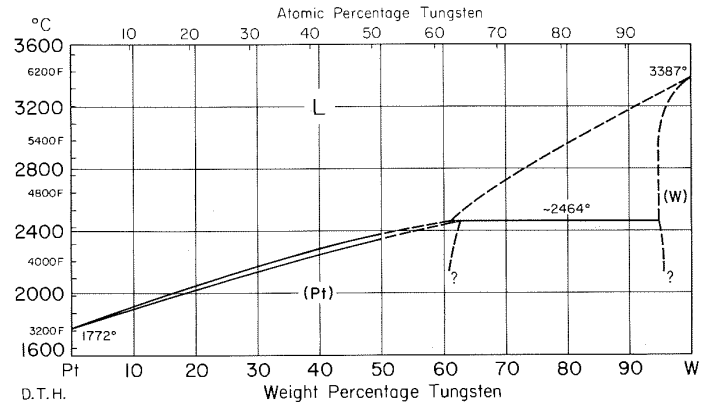
Pt-V Platinum-Vanadium



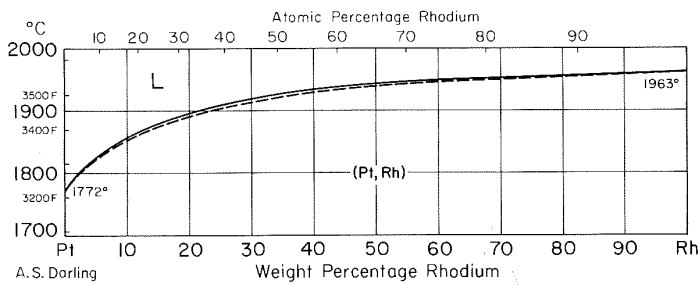
Pd-W Palladium-Tungsten



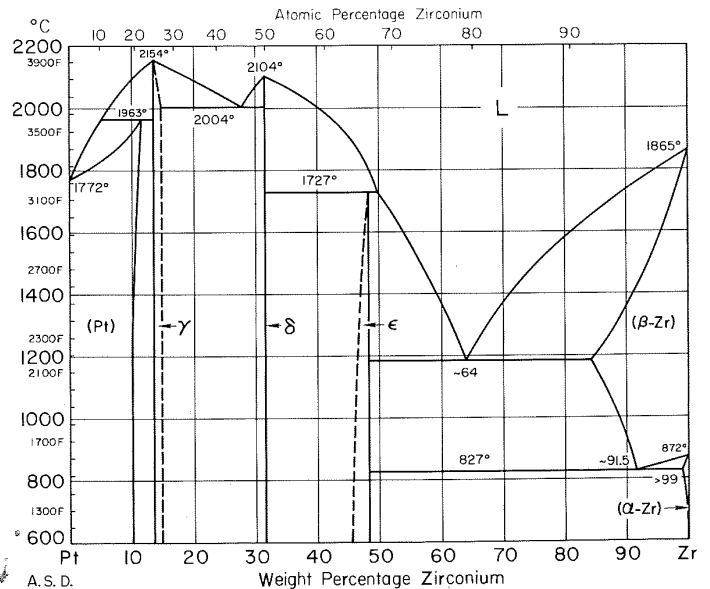
Pt-W Platinum-Tungsten



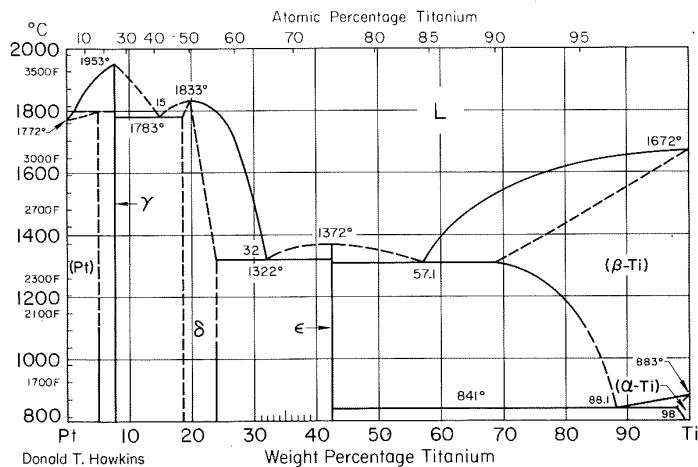
Pt-Rh Platinum-Rhodium



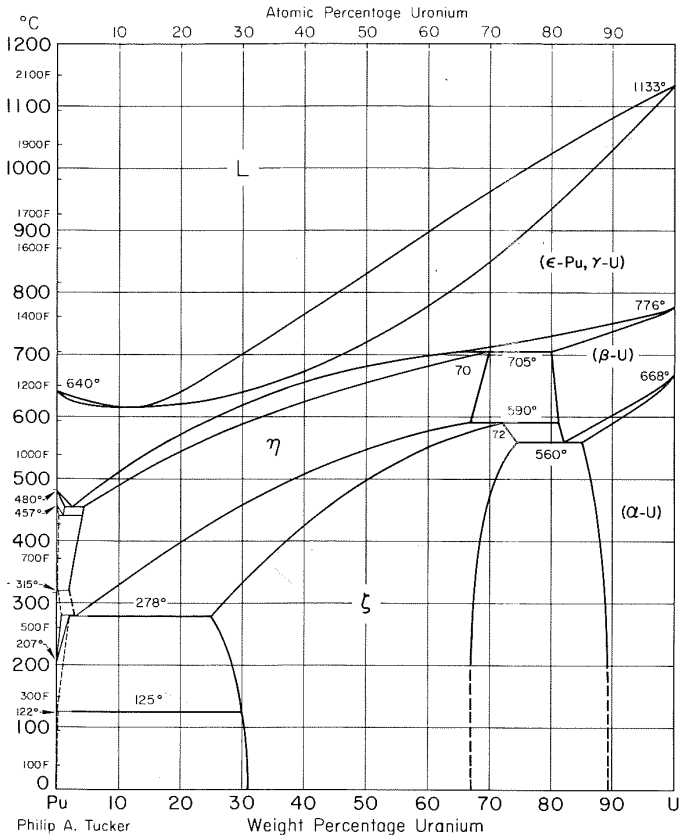
Pt-Zr Platinum-Zirconium



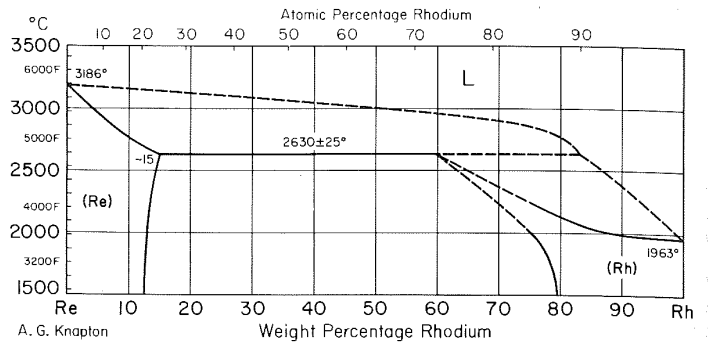
Pt-Ti Platinum-Titanium



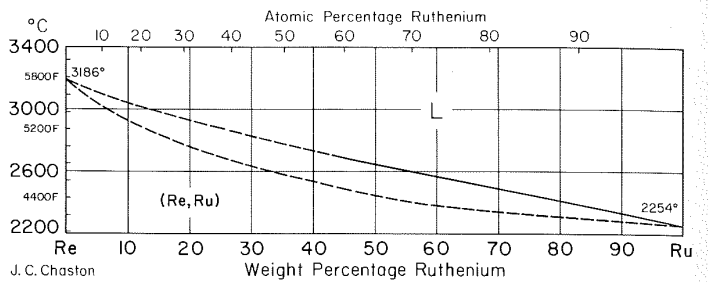
Pu-U Plutonium-Uranium



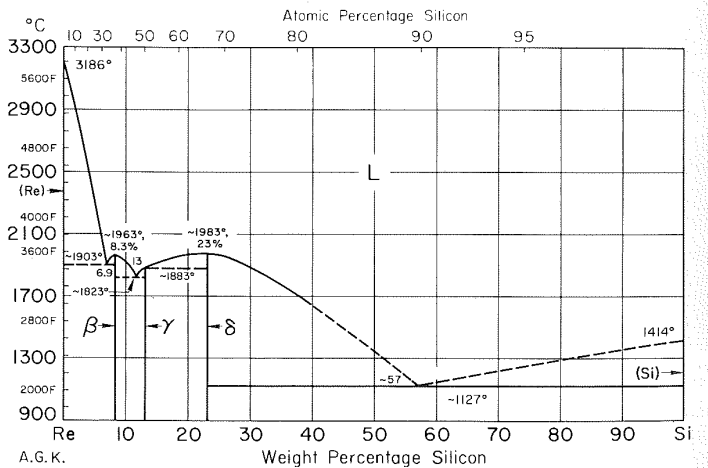
Re-Rh Rhenium-Rhodium



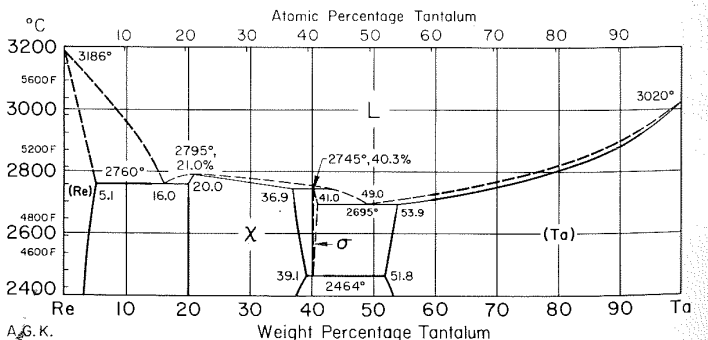
Re-Ru Rhenium-Ruthenium



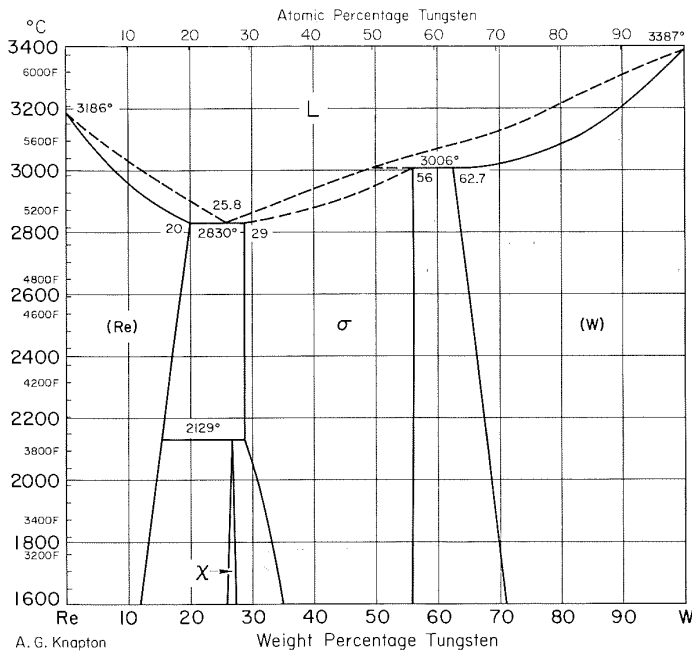
Re-Si Rhenium-Silicon



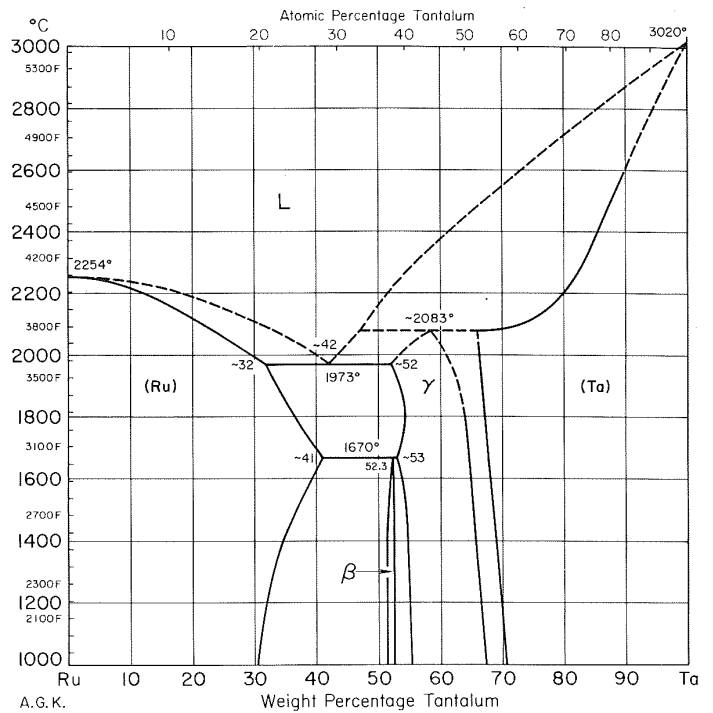
Re-Ta Rhenium-Tantalum



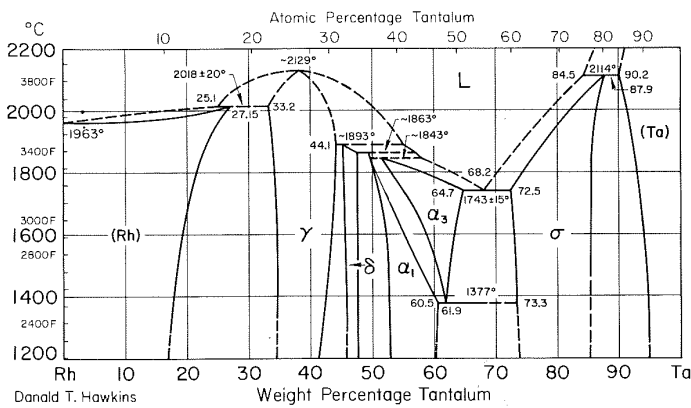
Re-W Rhenium-Tungsten



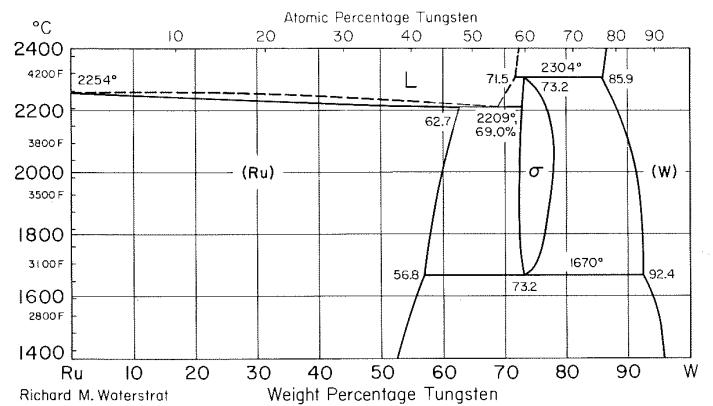
Ru-Ta Ruthenium-Tantalum



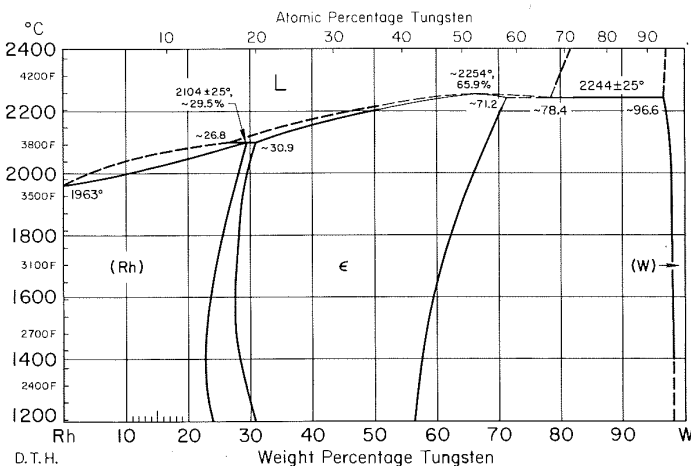
Rh-Ta Rhodium-Tantalum



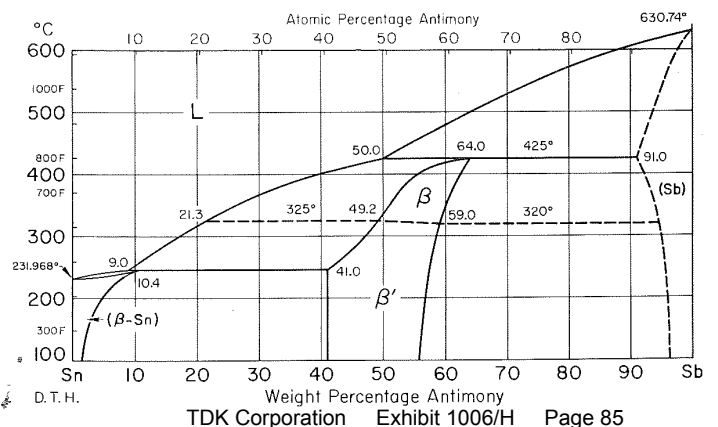
Ru-W Ruthenium-Tungsten



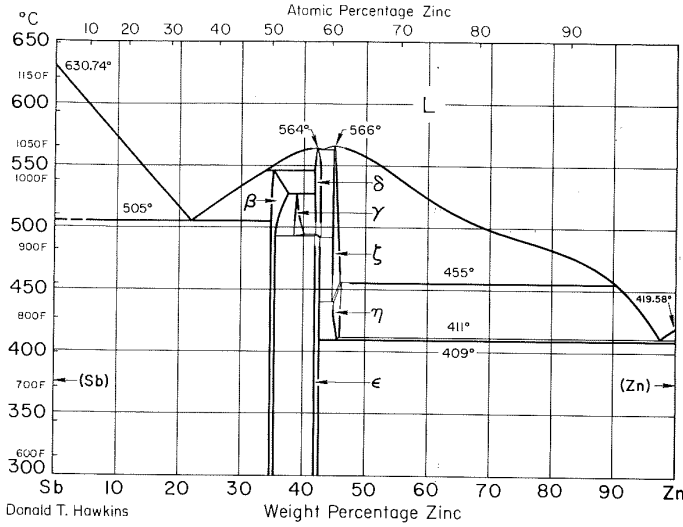
Rh-W Rhodium-Tungsten



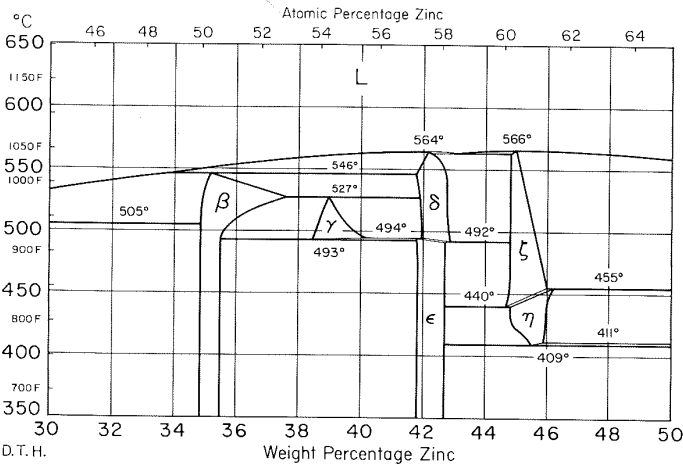
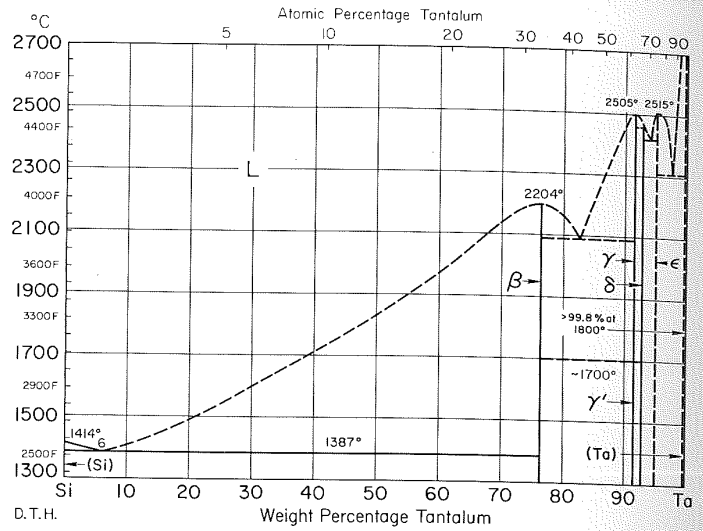
Sb-Sn Antimony-Tin



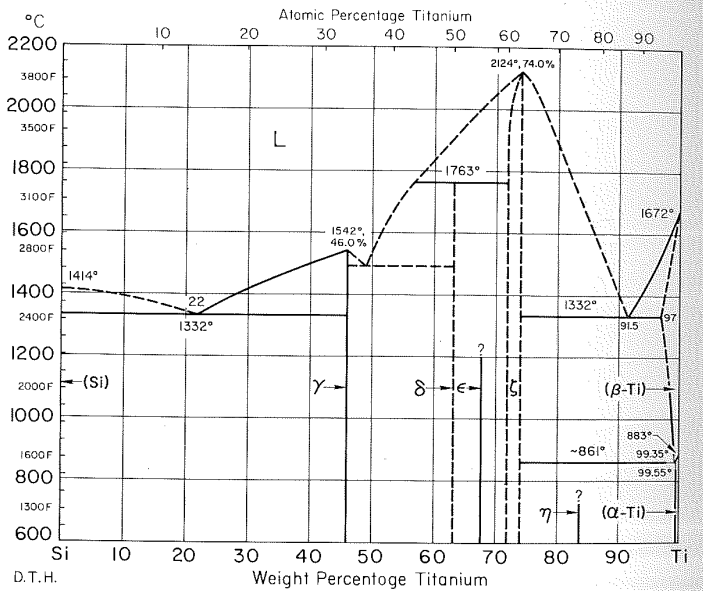
Sb-Zn Antimony-Zinc



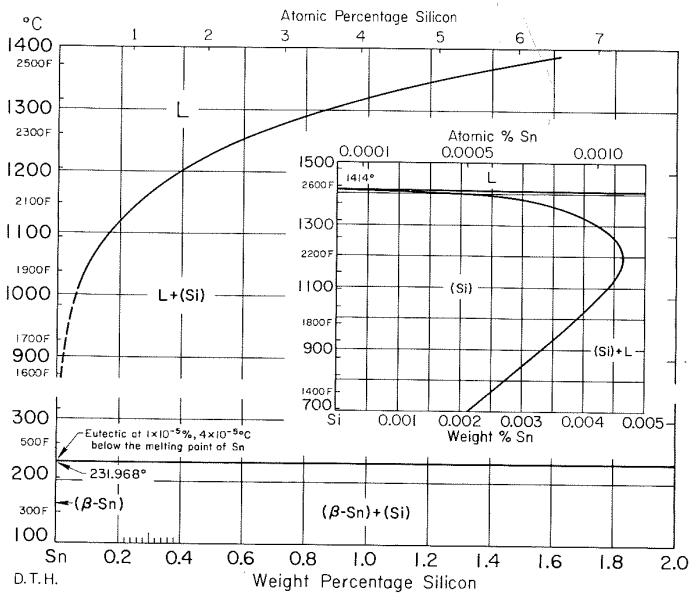
Si-Ta Silicon-Tantalum



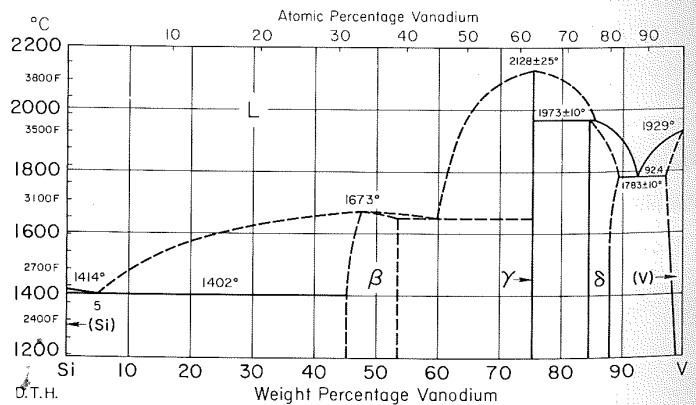
Si-Ti Silicon-Titanium



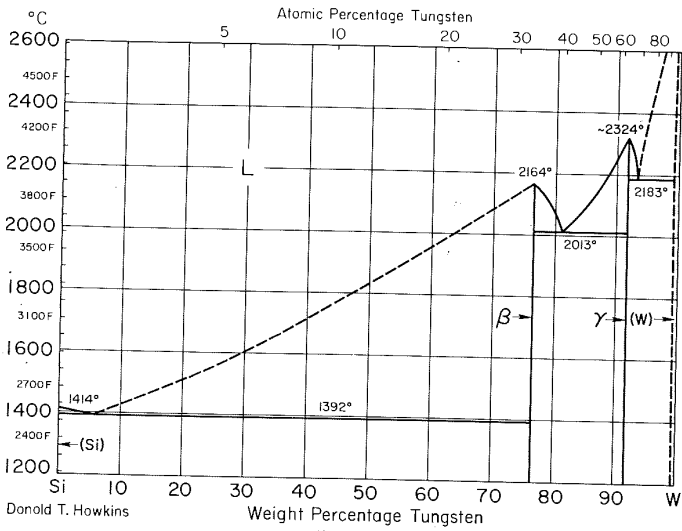
Si-Sn Silicon-Tin



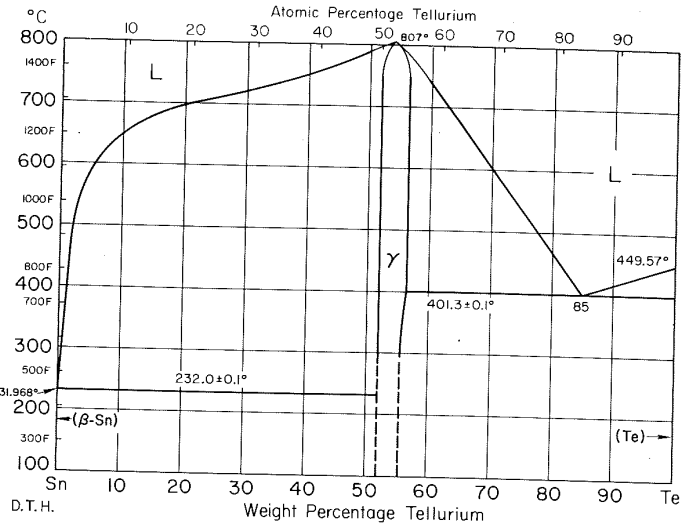
Si-V Silicon-Vanadium



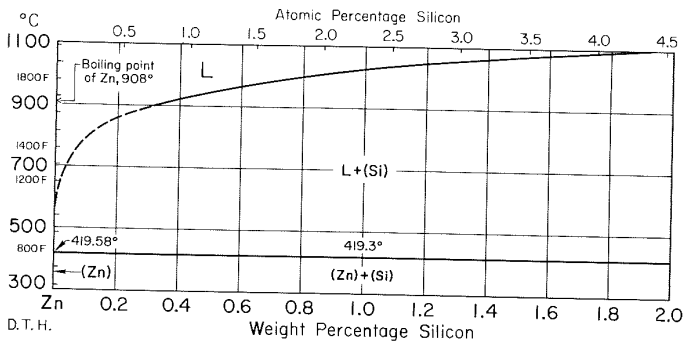
Si-W Silicon-Tungsten



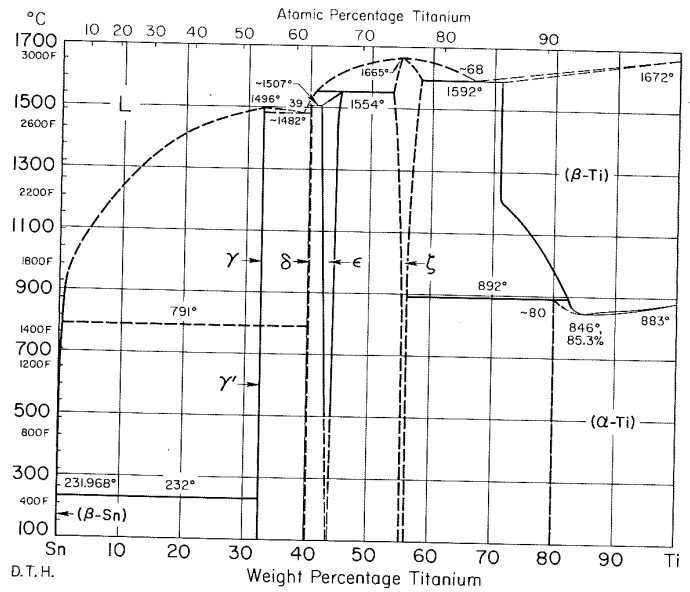
Sn-Te Tin-Tellurium



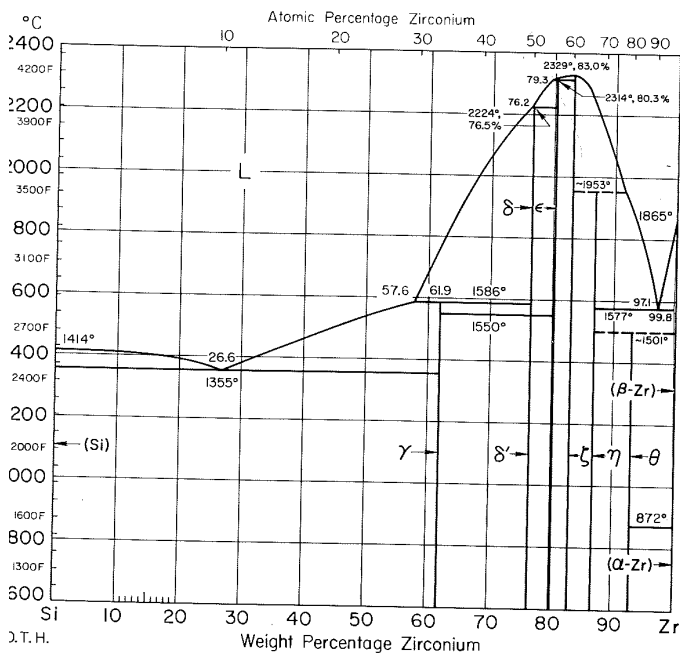
Si-Zn Silicon-Zinc



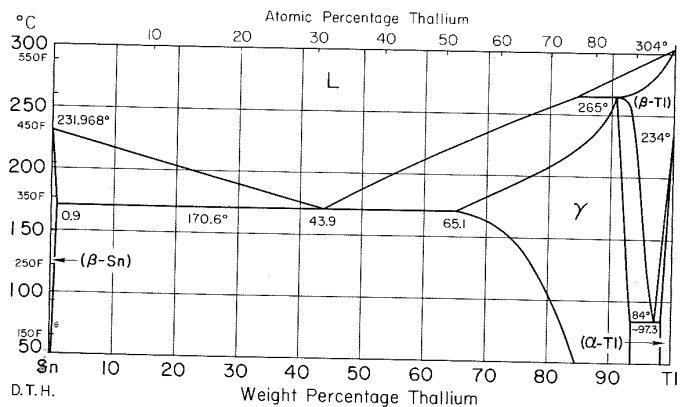
Sn-Ti Tin-Titanium



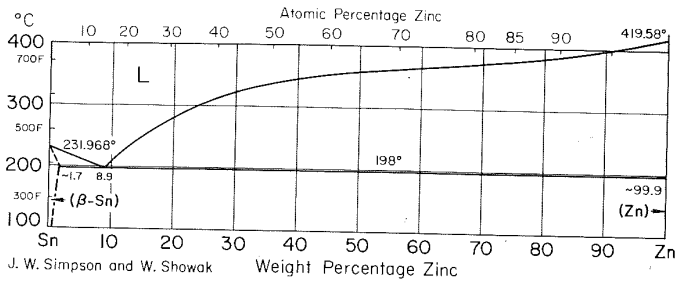
Si-Zr Silicon-Zirconium



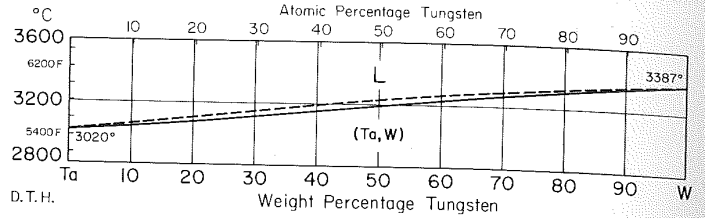
Sn-Tl Tin-Thallium



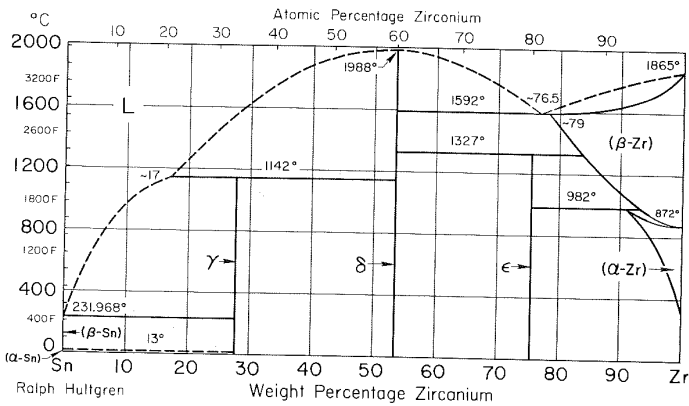
Sn-Zn Tin-Zinc



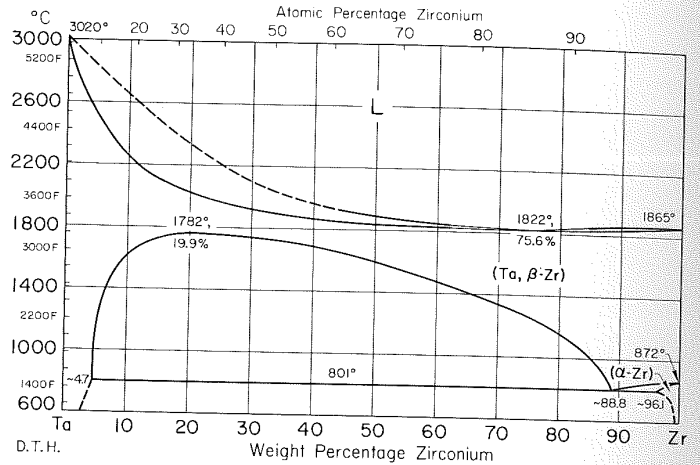
Ta-W Tantalum-Tungsten



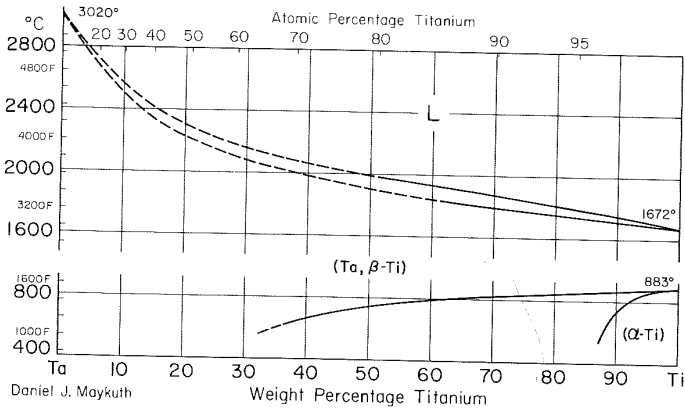
Sn-Zr Tin-Zirconium



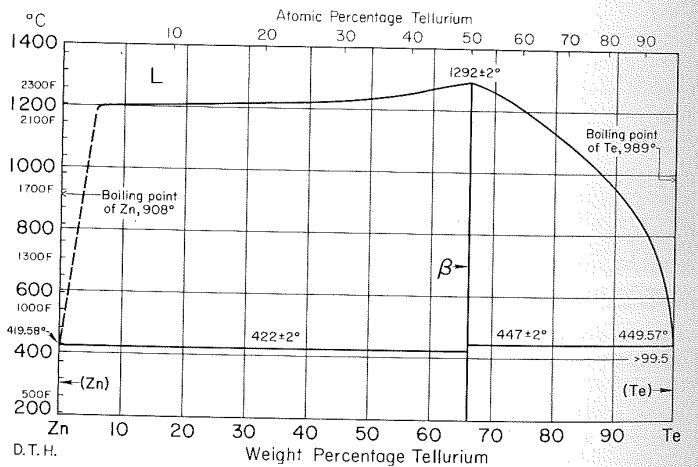
Ta-Zr Tantalum-Zirconium



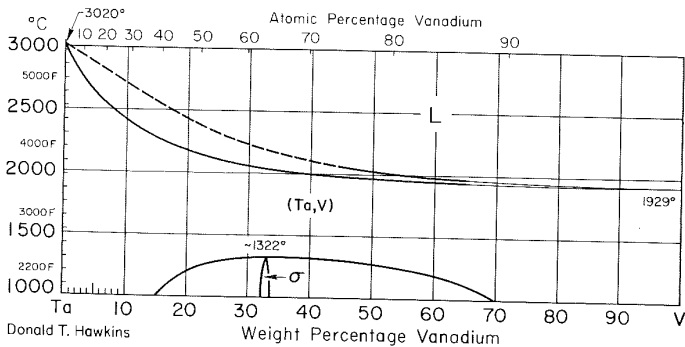
Ta-Ti Tantalum-Titanium



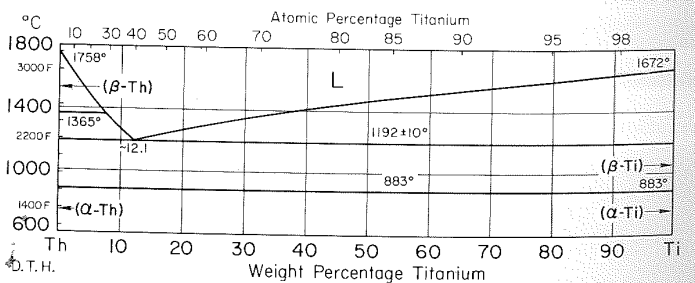
Te-Zn Tellurium-Zinc



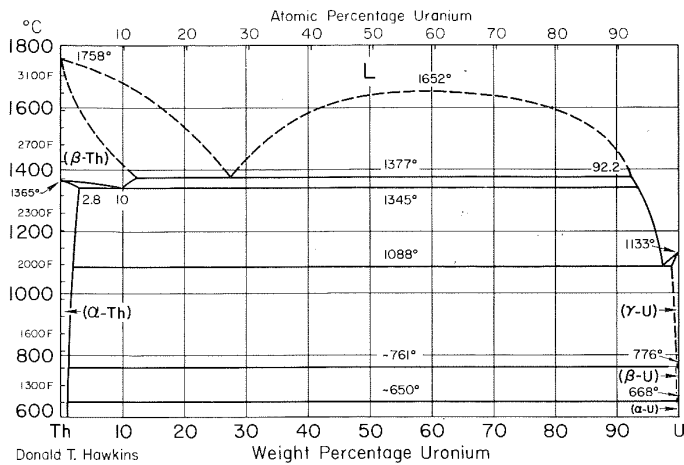
Ta-V Tantalum-Vanadium



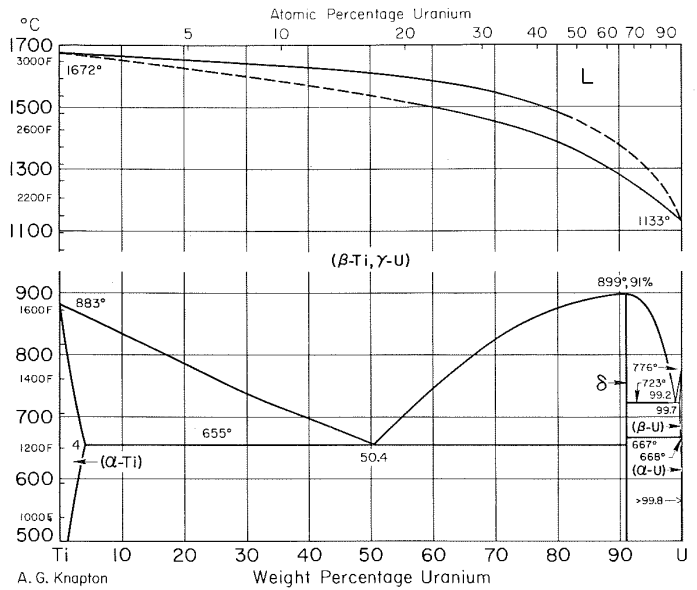
Th-Ti Thorium-Titanium



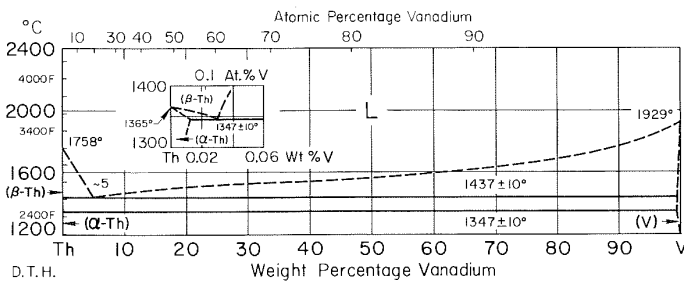
Th-U Thorium-Uranium



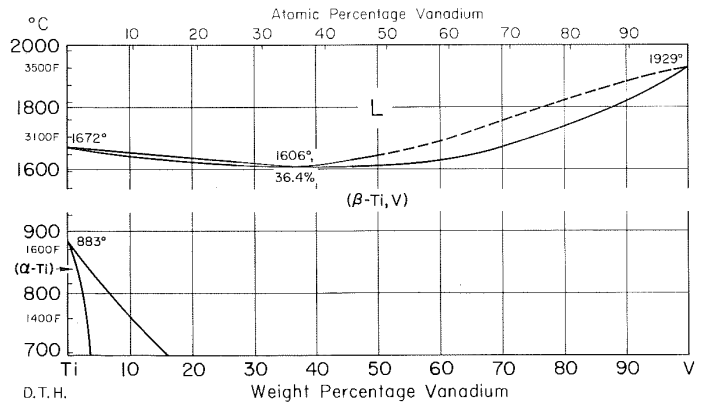
Ti-U Titanium-Uranium



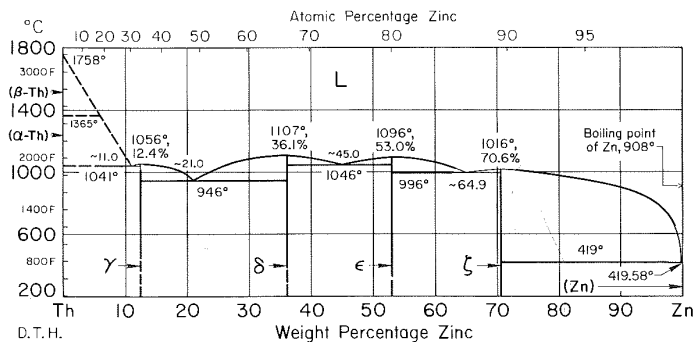
Th-V Thorium-Vanadium



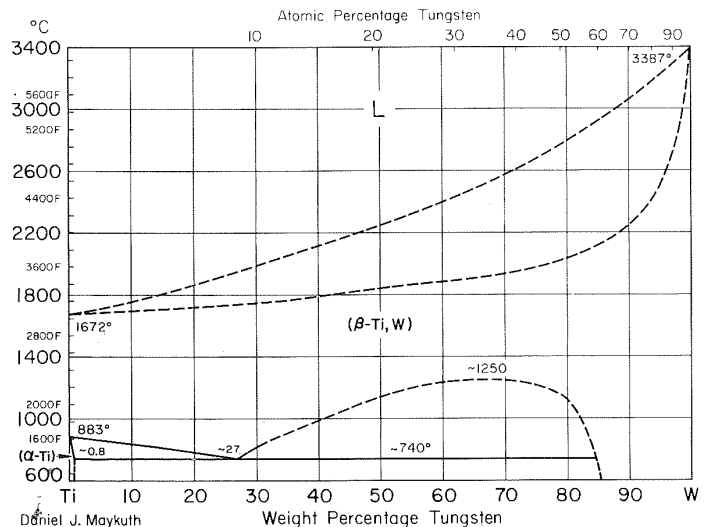
Ti-V Titanium-Vanadium



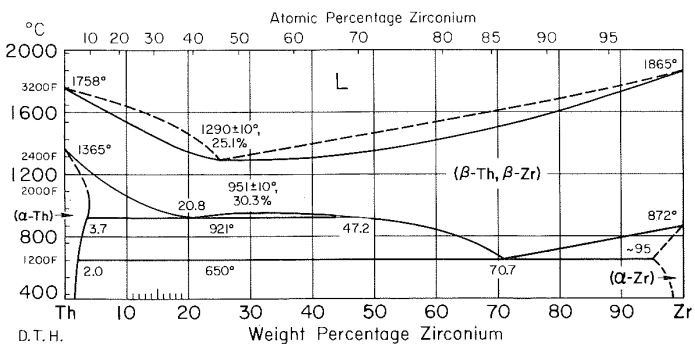
Th-Zn Thorium-Zinc



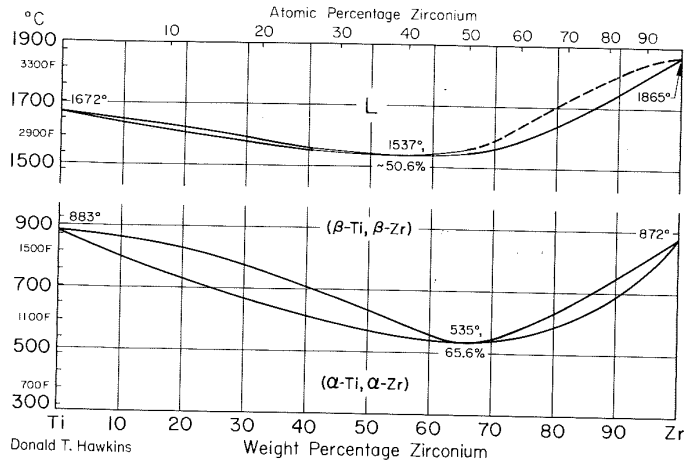
Ti-W Titanium-Tungsten



Th-Zr Thorium-Zirconium

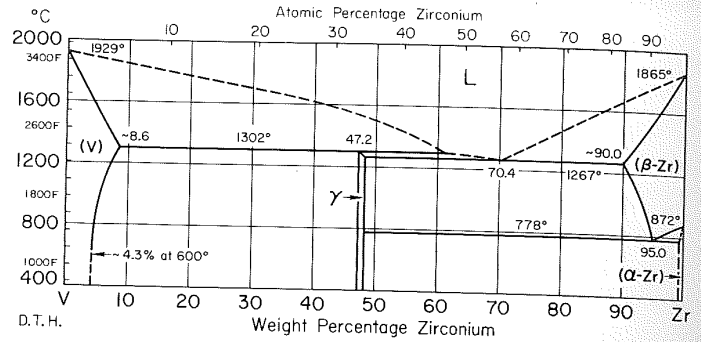


Ti-Zr Titanium-Zirconium



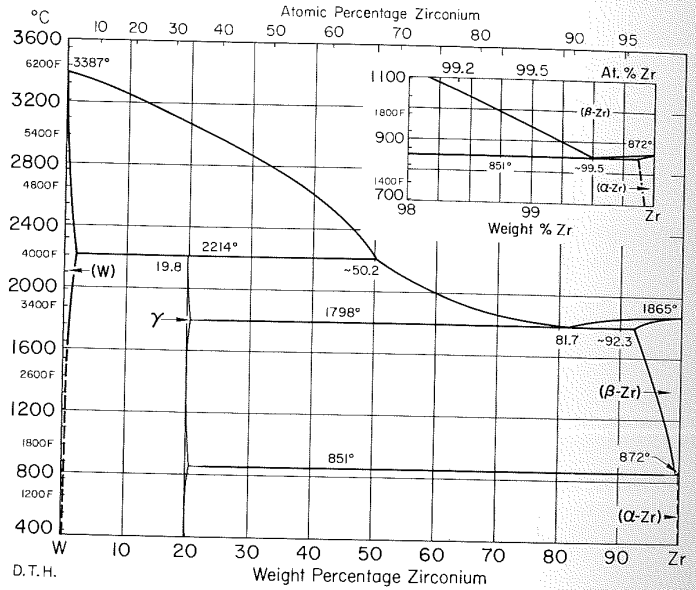
Donald T. Hawkins

V-Zr Vanadium-Zirconium



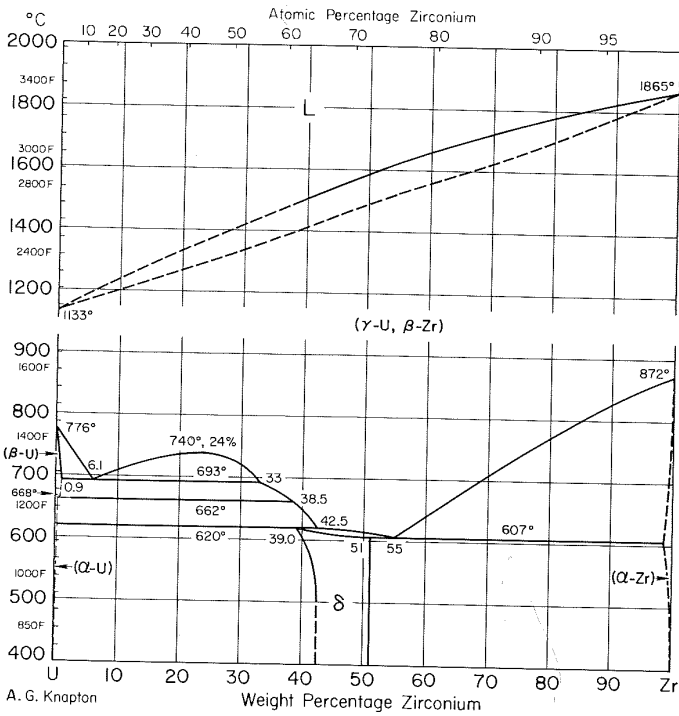
D.T.H.

W-Zr Tungsten-Zirconium



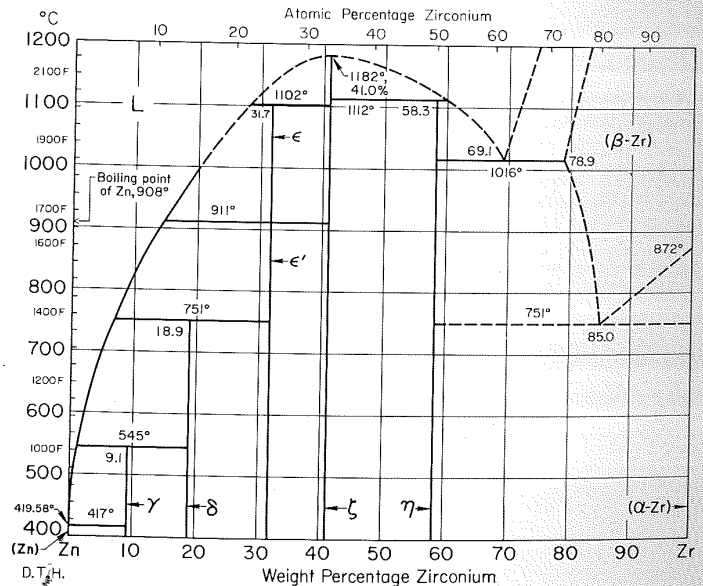
D.T.H.

U-Zr Uranium-Zirconium



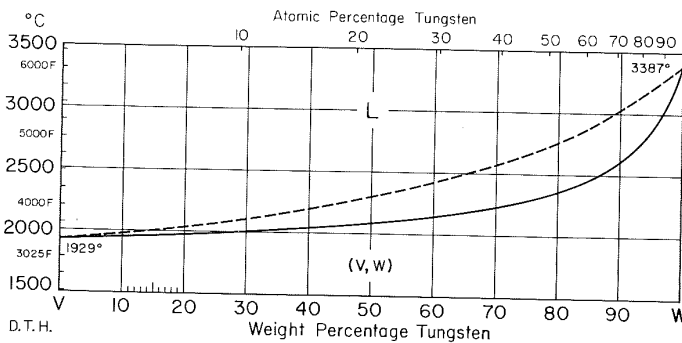
A. G. Knapton

Zn-Zr Zinc-Zirconium



D.T.H.

V-W Vanadium-Tungsten



D.T.H.

Section II: Phase Diagram Evaluations

The Fe-Ni (Iron-Nickel) System

By *L.J. Swartzendruber*
National Institute of Standards and Technology
V.P. Itkin
University of Toronto
and
C.B. Alcock
University of Notre Dame

Equilibrium Diagram

The equilibrium phases of the Fe-Ni system are: (1) the liquid, L; (2) the bcc, high-temperature (δ Fe) solid solution; (3) the fcc (γ Fe,Ni) solid solution; (4) the bcc, low-temperature (α Fe) solid solution; and (5) the FeNi₃ intermetallic compound, which forms by a first-order order-disorder transformation below 517 °C and has an extended range of homogeneity.

Early systematic efforts to construct a phase diagram for Fe-Ni were made by [1899Osm], [05Gue], [10Heg], and [10Rue]. Evaluated phase diagrams for the Fe-Ni system were given previously by [38Mar], [Hansen], [Shunk], and [82Kub]. The present assessed Fe-Ni equilibrium diagram is shown in Fig. 1.

Liquidus and Solidus

The liquidus and solidus for Fe-rich alloys up to about 12 at.% Ni were measured by [57Hel] using thermal analysis. [23Han] measured the liquidus and solidus over the entire range of composition. Measurements were also made by [05Gue], [25Kas], [31Ben], [37Jen], [25Vog], [27Vog] and [28Vog]. The data are summarized in Table 1. According to [23Han], the minimum in the liquidus curve is located at 1438 °C (temperatures quoted throughout were converted to IPTS-68) and about 67 at.% Ni. According to [37Jen], the minimum is between 1422 and 1427 °C. Based on a least-squares fit taking into account both the measured boundaries and available thermodynamic data (see Thermodynamics), we find the most probable location for the minimum to be 1440 °C and 66.0 at.% Ni, in good agreement with [23Han].

[64Hum] calculated the Fe-rich liquidus/solidus based on an ideal-solution model. This procedure gives too large a separation between the liquidus and solidus when extended to Ni-rich alloys. The liquidus and solidus separations of Fig. 1 are based primarily on those predicted by the measured thermodynamic parameters in the liquid and fcc phases, with the assessed boundary location giving greatest weight to the measurements of the liquidus. These boundaries are close to the predictions of [85Tom], which were based on thermodynamic parameters measured using mass spectrometry. They are shown on an expanded scale in Fig. 2.

Phase Boundaries

Measurements of the (α Fe/ δ Fe) phase boundaries were made by [20Han], [23Han], [25Kas], and [57Hel]. Comparisons with thermodynamic measurements (see below) and with liquidus and solidus measurements indicate a narrow two-phase (α Fe) + (δ Fe) region and a narrow peritectic reaction—L + (δ Fe) \leftrightarrow (γ Fe,Ni) at

1514 \pm 2 °C and 3.5, 4.9, and 4.2 \pm 0.5 at.% Ni, respectively. Measured values are listed in Table 1 and compared with the equilibrium diagram in Fig. 3.

(α Fe)/(γ Fe,Ni) Phase Boundaries

Due to the sluggishness of the (γ Fe,Ni) \rightarrow (α Fe) and (α Fe) \rightarrow (γ Fe,Ni) phase transformations below 800 °C, the (α Fe)/(γ Fe,Ni) equilibrium boundaries are difficult to determine (see Metastable Phases). [36Jet], [39Owe], [41Owe], and [49Owe] used powder X-ray diffraction (XRD) techniques down to 300 °C. [65Gol] used electron microprobe techniques to measure concentration profiles on samples equilibrated at temperatures as low as 500 °C. [80Rom] used a scanning transmission electron microscope (STEM) on samples equilibrated between 670 and 300 °C. These results, along with those of [69Sta], demonstrated clearly the retrograde solubility of Ni in (α Fe). The data of [49Owe], [49Jon], [65Gol], and [80Rom] agree fairly well at 500 °C and above. The boundaries shown in Fig. 1 were constructed using these data, giving greatest weight to the results of [80Rom]. Numerical values determined by the various investigators are given in Table 2. Figure 3 shows the assessed boundaries and compares them with the experimental data. Enthalpies of the (α Fe) \rightarrow (γ Fe,Ni) transformation were measured by [26Kaw], [36Sam], [37Koe], [40Zui], [59Sch], and [67Hil].

FeNi₃

Evidence for ordered FeNi₃ was obtained first by [32Dah], [33Dah], [36Dah], [39Kus], and [39Lee] using XRD. Because of the nearly equal X-ray scattering factors for Fe and Ni, the ordering is difficult to observe with X-rays (see [38Haw]). The results of [39Lee] were confirmed by [39Haw], also with X-rays. Variations in the magnetic properties, electrical resistance, and hardness with heat treatment of alloys showing FeNi₃ order were investigated by [32Dah], [33Dah], and [36Dah]. Based on X-ray and electron microscope observation of annealed thin films and on the results of [52Hun], [63Heu] concluded that the (γ Fe,Ni) phase decomposes eutectoidally to (α Fe) and FeNi₃ at 345 °C and 52 at.% Ni, a conclusion that still appears valid. (The existence of a eutectoid near this same point based on the magnetic transition had been postulated earlier; see [21Mer].)

The critical behavior of the temperature derivative of the resistivity around the FeNi₃ composition was investigated by [82Ore]. No anomaly in the resistivity was found at the order-disorder temperature, but one was found at the Curie temperature. The phase diagram in the composition range 69 to 77 at.% Ni and in the temperature range around 510 °C was studied in considerable detail by [80Van] and [81Van] using Mössbauer spectroscopy. They ex-

plained a 15 °C hysteresis zone between ordus and disordus as a magnetic effect. [81Lef] investigated the local atomic arrangement in FeNi₃ using neutron diffuse scattering and a single crystal quenched from four different temperatures. [72Cal] found that the order-disorder transformation of FeNi₃ is not second order and observed a two-phase zone of 5 or 6 °C for alloys between 71 and 75 at.% Ni. On the basis of a calorimetric study, [52lid] and

[54lid] concluded that short-range order forms in FeNi₃ before long-range order is observable by other methods.

The ordering behavior of FeNi₃ was also investigated by [37Kal], [39Haw], [39Kay], [40Nix], [48Kal], [50Jos], [53Rhi], [53Gei], [57Lya], [57Vit], [58Kus], [62Kac], [63Dav], [63Tre], [65Gon], [72Cal], [73Cal], [75Bil], [75Leb], [77Hut], [79Des], and

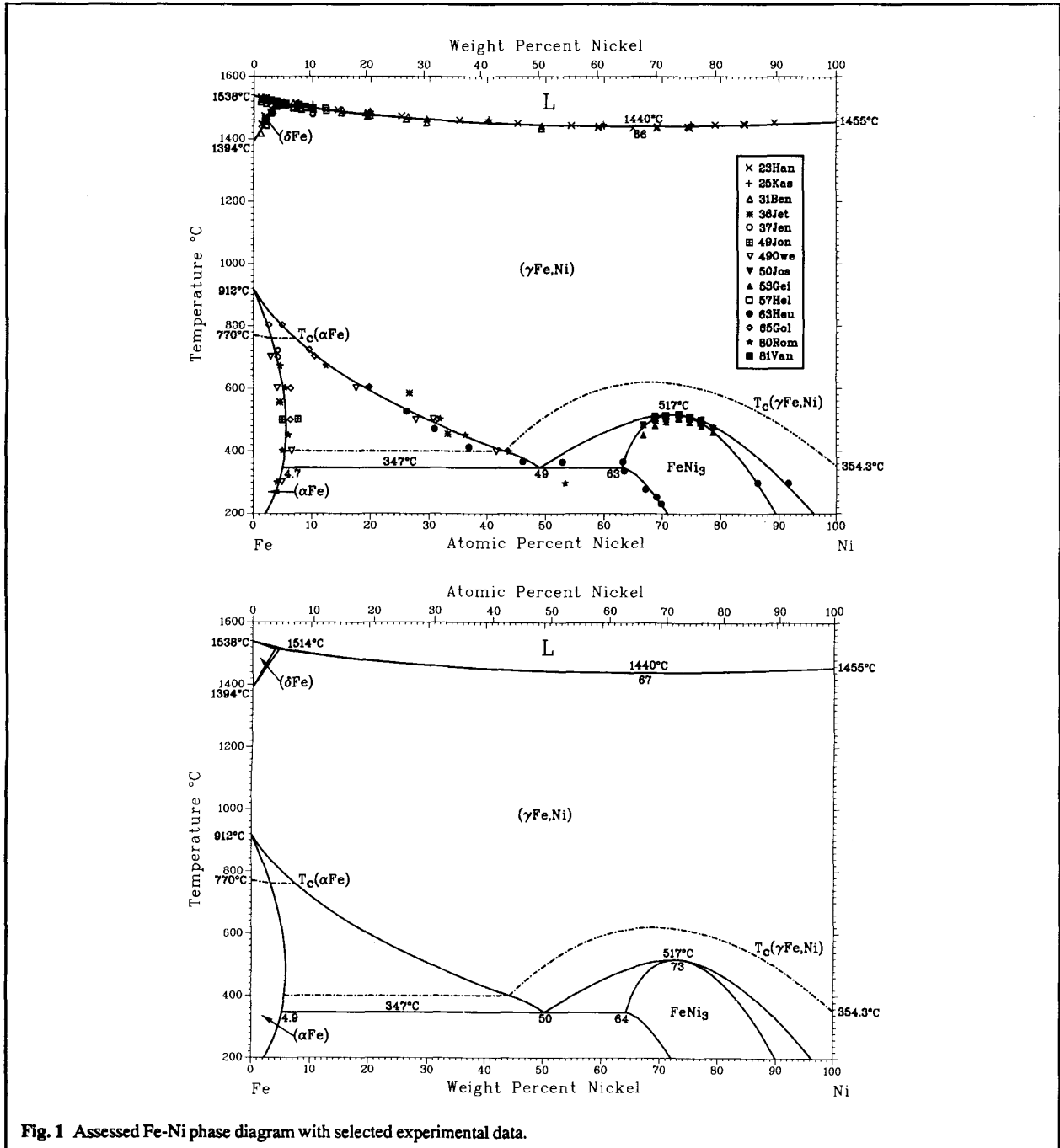


Fig. 1 Assessed Fe-Ni phase diagram with selected experimental data.

Section II: Phase Diagram Evaluations

Table 1 High-Temperature Phase Boundary Data for Fe-Ni Alloys

Composition, at. % Ni	Liquidus	Solidus	Temperature, °C	
			(δ Fe)/(δ Fe) + (γ Fe,Ni)	(δ Fe) + (γ Fe,Ni)/(γ Fe,Ni)
From [10Rue]				
0	1538
9.6	1515
19.2	1488
29.0	1472
38.8	1452
48.8	1448
58.8	1443
68.9	1441
79.2	1446
100	1455
From [23Han]				
1.1	1532	...	1447	...
2.0	1530	...	1471	...
2.9	1523	...	1497	...
3.7	1521	...	1504	...
5.1	1506
5.8	1506
8.0	1501
10.0	1496
14.6	1493
24.7	1474
34.8	1460
45.1	1449
54.6	1443
59.3	1442	1437
65.1	1439	1435
66.7	1439
69.3	1439	1434
74.5	1440	1436
79.2	1445
84.2	1447
89.1	1453
From [25Kas]				
1.3	1532	1526	1454	...
2.0	1530	1520	1470	...
5.0	1518
7.5	1516	1510	1512	...
10.0	1510	1504
20.0	1488	1488	1484	...
40.0	1463	1456
60.0	1447	1441
80.0	1448	1443
From [31Ben]				
1.1	1526	1519	1417	...
2.1	1526	1512	1443	...
3.0	1523	...	1490	...
3.9	1518	1507
6.6	1514	1499
7.1	1511	1497
7.8	1507	1497
8.0	1509	1493
10.0	1504	1485
14.9	1492	1483
19.5	1477	1472
19.9	1483	1475
25.7	1472	1462
29.3	1464	1451
49.2	1441	1432

(continued)

Note: All results corrected to IPTS-68 and to agree with 1538 °C as the melting temperature of pure Fe and 1455 °C as the melting temperature of pure Ni.

Table 1 High-Temperature Phase Boundary Data for Fe-Ni Alloys (continued)

Composition, at. % Ni	Liquidus	Solidus	Temperature, °C	
			(δ Fe)/(δ Fe) + (γ Fe,Ni)	(δ Fe) + (γ Fe,Ni)/(γ Fe,Ni)
From [37Jen]				
10.0.....	...	1479
20.0.....	...	1458
30.0.....	...	1447
40.0.....	...	1441
50.0.....	...	1440
60.0.....	...	1439
70.0.....	...	1418
80.0.....	...	1423
90.0.....	...	1438
From [57Hel]				
1.84.....	1528	1526	1455	1462
2.79.....	1524	1520	1484	1483
3.76.....	1520	1514	1503	1506.5
4.62.....	1516	1511.5	1514	...
5.72.....	1513.5	1510
7.61.....	1508.5	1503.5
8.95.....	1502.5	1598.5
12.23.....	1497	1491

Note: All results corrected to IPTS-68 and to agree with 1538 °C as the melting temperature of pure Fe and 1455 °C as the melting temperature of pure Ni.

[84Lef]. Experimental values reported by various investigators are listed in Table 3 and compared in Fig. 4.

Metastable Phases

At low temperature (under about 800 °C), the (α Fe) + (γ Fe,Ni) field is relatively broad, and attainment of equilibrium involves considerable diffusion. Diffusion rates at these lower temperatures are low; consequently, very long times are required to establish equilibrium, and normal conditions favor a diffusionless (or martensitic) transformation. This transformation exhibits considerable hysteresis. In early work, [20Han] used metallography to determine two sets of boundaries for the (α Fe) + (γ Fe,Ni) two-phase region—one on heating, and one on cooling. The (γ Fe,Ni)/(α Fe) + (γ Fe,Ni) boundary determined in this way agrees closely with that determined by thermal analysis (the (α Fe)/(α Fe) + (γ Fe,Ni) boundary is not detected by thermal analysis). [20Han] also concluded that the (α Fe) \rightarrow (γ Fe,Ni) transformation is accelerated by the presence of impurities.

From a practical standpoint, a diagram giving the details of this irreversible transformation is often of more importance than one giving the equilibrium boundaries in this region. Figure 5 exhibits experimental transformation measurements of [25Pes], [27Hon], [49Jon], and [56Kau] and compares them with the equilibrium boundaries. In this figure, the supersaturated bcc phase that results from the diffusionless transformation is denoted α_2 . The solid lines are estimates of A_s , M_s , A_f , and M_f , where A_s and M_s are the so-called austenite and martensite start temperatures (10 vol.% of the alloy having transformed), and A_f and M_f are the so-called austenite and martensite finish temperatures (90 vol.% of the alloy having transformed). These lines are valid only over a range of cooling and heating temperatures between approximately 2 and 150 °C/min. The uncertainties in the estimated A_s , A_f , M_s , and

M_f temperatures are large, but decrease as the Ni concentration decreases.

In the α_2 or (γ Fe,Ni) field, the alloy will be all (γ Fe,Ni) if it is being cooled from the (γ Fe,Ni) field or all α_2 if it is being heated from the α_2 field. Because the transformation from (γ Fe,Ni) to α_2 is diffusionless, it can occur at very low temperatures for alloys with greater than 30 at. % Ni. [56Kau] reported the M_s temperature of (–223 °C) (50 K) for a 33 at. % Ni alloy. In addition, the M_s temperatures of various steels are known [54Mey, 48Fis, 74Ume, 63Yeo, 82Bro1] to change with the temperature at which they are austenized. That this change is due to the effect of austenizing temperature on grain size was shown by [51Mac] and [74Ume]. For an Fe-31 at. % Ni alloy, [74Ume] found that the M_s temperature varied between 200 and 230 °C as the grain size varied between 5 and 70 μ m. Impurities and internal stresses also have an important effect on the transformation temperatures [e.g. 82Rod].

The diffusionless character of the $\alpha_2 \rightarrow$ (γ Fe,Ni) transformation was shown clearly by [32Sch]. [34Deh] reported that the transformed alloy is bcc, and is not tetragonal as is Fe-C martensite, with the microstructural similarity of the two martensites being due to the similar way in which they transform from the γ phase. [35Sch] found that for greater than 10 at. % Ni, the (γ Fe,Ni) \rightarrow (α Fe) transformation temperature could not be lowered by long annealing times (up to 100 h). Some early diagrams, such as that of [36Mer], were drawn showing the irreversibility of the diffusionless transformation directly.

[62Gil] reported that the diffusionless transformation is massive type for Ni contents less than about 15 at. %. For very rapid cooling and/or for higher Ni concentration, [66Hum] and [62Gil] reported that the transformation is martensitic type.

According to [49Jon], the diffusionless $\alpha_2 \rightarrow$ (γ Fe,Ni) transformations are independent of the cooling or heating rate for rates between 2 and 150 °C/min. [76Ino] and [82Ray] showed that the

Section II: Phase Diagram Evaluations

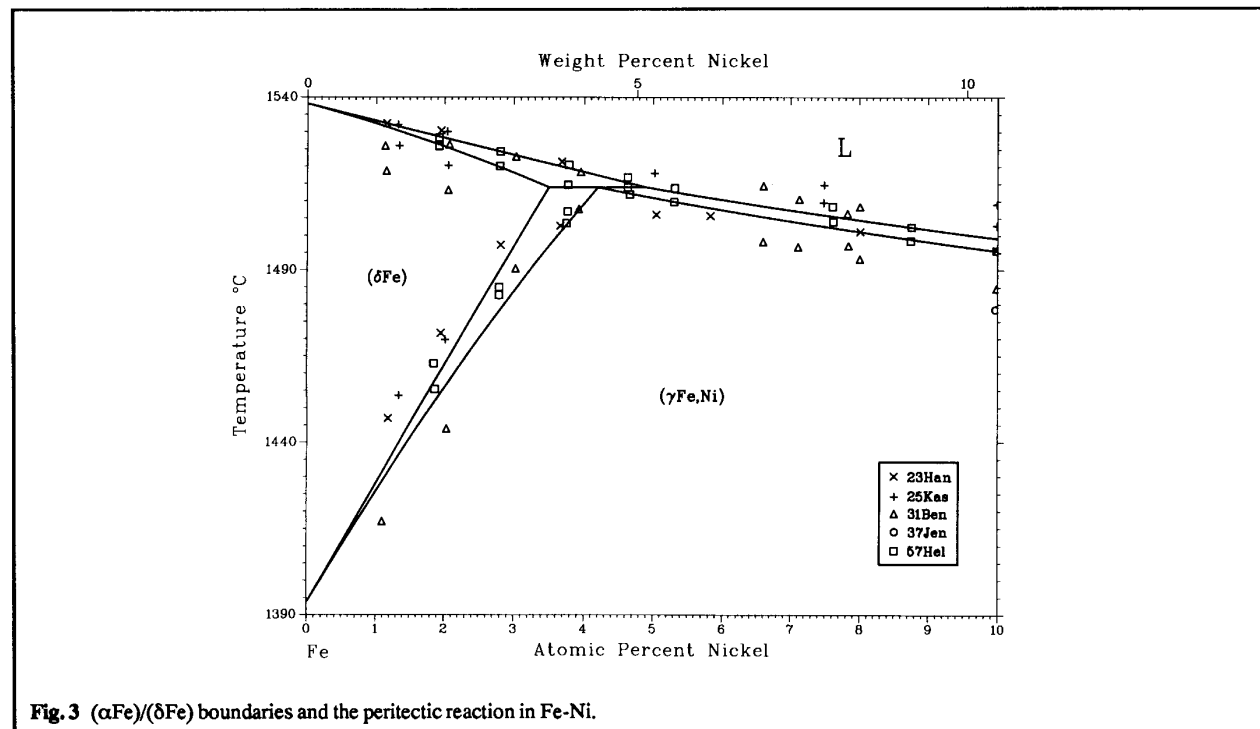
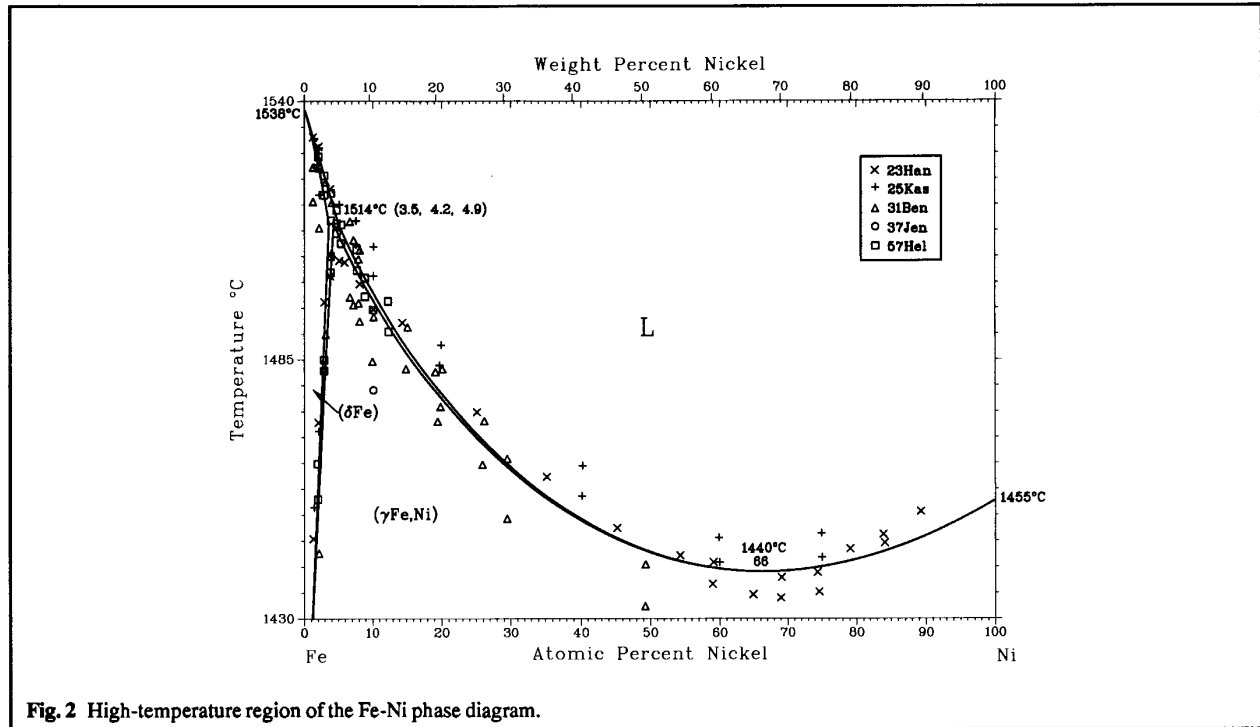


Table 2 (α Fe)/(γ Fe,Ni) Equilibrium Phase Boundary Measurements

Temperature, °C	Composition, at. % Ni		Anneal time, days	Technique	Reference
	(α Fe)/(α Fe) + (γ Fe,Ni)	(α Fe) + (γ Fe,Ni) + (γ Fe,Ni)			
817.....	1.0	X-ray	[30Rob]
806.....	...	3	...	Magnetic	[40Pic]
800.....	1.0	4.5	...	X-ray	[39Owe]
	1.9 ± 0.15	3.5 ± 0.3	31	(a)	[65Gol]
744.....	...	6	...	Magnetic	[40Pic]
721.....	...	7.6	...	Magnetic	[40Pic]
720.....	3.8 ± 0.3	8.5 ± 0.3	7	(b)	[65Gol]
717.....	2.6	X-ray	[30Rob]
705.....	...	9	...	Magnetic	[40Pic]
700.....	2.5	9	...	X-ray	[39Owe]
	3.9 ± 0.2	9.4 ± 0.2	56	(b)	[65Gol]
672.....	3.94	...	0.7	X-ray	[36Jet]
670.....	4.3 ± 0.2	12.1 ± 0.4	74	(b)	[80Rom]
668.....	...	12	...	Magnetic	[40Pic]
672.....	2.7	X-ray	[39Owe]
657.....	4.1	X-ray	[30Rob]
625.....	...	16	...	Magnetic	[40Pic]
600.....	3.5	14	...	X-ray	[39Owe]
	5.3 ± 0.3	19.3 ± 0.5	180	(a)	[65Gol]
	5.2 ± 0.5	19.4 ± 1.4	127	(b)	[80Rom]
585.....	...	26.20	457	X-ray	[36Jet]
	...	20	...	Magnetic	[40Pic]
572.....	...	23	...	Magnetic	[40Pic]
557.....	4.0	X-ray	[39Owe]
550.....	...	18.5	...	X-ray	[39Owe]
540.....	...	25	...	Magnetic	[40Pic]
526.....	...	25.9 ± 4	...	(c)	[63Heu]
523.....	11.2	X-ray	[30Rob]
557.....	4.22	...	1	X-ray	[36Jet]
518.....	12.6	X-ray	[30Rob]
500.....	5.0	26.5	...	X-ray	[39Owe]
	6.0 ± 1.0	31.5 ± 0.5	608	(a)	[65Gol]
	5.5 ± 0.4	31.7 ± 2.3	270	(b)	[80Rom]
496.....	5.0	X-ray	[39Owe]
	6.07	...	734	X-ray	[36Jet]
467.....	...	31.1 ± 4	...	(c)	[63Heu]
456.....	5.5	X-ray	[39Owe]
	5.91	33.36	3150	X-ray	[36Jet]
450.....	5.8 ± 0.5	36.4 ± 2.8	120	(b)	[80Rom]
412.....	...	37.0 ± 4	...	(c)	[63Heu]
400.....	6.5	41.5	...	X-ray	[39Owe]
	4.9 ± 0.5	43.8 ± 3.1	270	(b)	[80Rom]
370.....	...	46.3 ± 4	...	(c)	[63Heu]
365.....	...	34	...	Magnetic	[43Has]
350.....	5.8	49	28	X-ray	[39Owe]
	...	49	...	X-ray	[52Hun]
300.....	...	56.5	28	X-ray	[39Owe]
	4.0 ± 0.5	53.4 ± 4.1	430	(b)	[80Rom]

(a) Diffusion couple, analyze with electron probe. (b) Quench as α_2 , anneal, analyze with electron probe. (c) Carbonyl vapor pressure.

martensitic transformation in Fe-24 wt. % Ni can be suppressed to below room temperature by splat cooling. For alloys with less than about 30 at. % Ni, the transformation is isothermal, and the transformation temperature is strongly dependent on impurity contents. Above 30 at. % Ni, the transformation is athermal and less dependent on impurities [83Kam]. Further investigations of the nature of the $\alpha_2 \rightarrow (\gamma$ Fe,Ni) transformation were made for example by [29Gos], [30Rob], [48Fis], [47Oel], [51Smo], [62Bre], [62Yeo], [63Gol], [67Rob], [71Geo], [77Roi], [79Mat], [81Bor], [82Duf], [84Bor], [84Izm], and [84Rin].

Considerable supercooling of liquid Fe-Ni alloys is possible. [78Con] observed supercooling of up to 150 K in an alumina crucible for alloys between 6 and 90 at. % Ni. [83Abb] studied supercooling in levitation melted 25 at. % Ni samples, obtaining supercooling up to 270 °C, somewhat less than the 300 °C reported by [66Kat] for alloys surrounded by glass coatings. Transformation of (γ Fe,Ni) to (α Fe) in thin films was investigated by [78Gal].

Alloys containing approximately 20 to 50 at. % Ni—the so-called Invar alloys—exhibit anomalous thermomechanical and thermochemical behavior, including a region of very low coefficient

Table 3 FeNi₃ Equilibrium Boundary Measurements

Reference	Technique	Equilibrium	Temperature, °C	Composition, at. % Ni				
[50Jos]	Dilatometry	(γFe,Ni)/FeNi ₃	479	67				
			491	69				
			500	71				
			504	73				
			501	75				
			492	77				
			474	79				
			[53Gei]	Dilatometry	(γFe,Ni)/(γFe,Ni) + FeNi ₃	482	67	
						495	69	
						504	71	
509	73							
503	75							
494	77							
477	79							
	Dilatometry	(γFe,Ni) + FeNi ₃ /(γFe,Ni)				452	67	
						481	69	
						494	71	
			503	73				
			492	75				
			480	77				
			461	79				
			[63Heu]	Carbonyl vapor pressure	(γFe,Ni)/(γFe,Ni) + FeNi ₃	365	53 ± 4	
						(γFe,Ni) + FeNi ₃	365	62 ± 4
						FeNi ₃ /FeNi ₃ + (γFe,Ni)	300	87 ± 4
FeNi ₃ + (γFe,Ni)/(γFe,Ni)	300	92 ± 4						
(αFe) + FeNi ₃ /FeNi ₃	333	63.3						
	319	64.5						
	277	67.4						
	253	69.2						
	232	70.2						
[81Van]	Mössbauer spectroscopy	(γFe,Ni)/(γFe,Ni) + FeNi ₃				510	69	
			516	71				
			516	73				
			511	75				
			501	77				
					(γFe,Ni) + FeNi ₃ /(γFe,Ni)	505	69	
						512	71	
						515	73	
						508	75	
						494	77	

reached in alloys in which the sluggish (γFe,Ni) → (αFe) + FeNi₃ eutectoid reaction has been suppressed.

Crystal Structures and Lattice Parameters

A summary of the crystal structures found in Fe-Ni alloys is given in Table 4, and lattice parameters are listed in Table 5. Measured values of the lattice parameters for the (αFe) and (γFe,Ni) phases vs composition are shown in Fig. 7 and 8. The solid lines in Fig. 7 and 8 represent a weighted least-squares fit to these values.

[37Owe1] found that the (γFe,Ni) phase lattice parameter at room temperature (20 °C) as a function of composition reaches a maximum value of 0.3597 nm at 39 at. % Ni and then diminishes at almost the same rate at which it increases. [37Bra] made lattice spacing measurements on alloys containing 27 to 100 at. % Ni that were quenched from 700, 800 and 900 °C. This quenching gave larger lattice spacings than annealed, ordered alloys. Values shown in Fig. 8 are for their annealed alloys, which are more rep-

resentative of equilibrium. [26Osa1] and [26Osa2] measured the lattice parameters and the densities for alloys annealed at 1150 °C and then slow cooled. [63Dav] investigated the variation in lattice parameter in FeNi₃ on annealing at 480 °C for up to 1000 h.

Lattice parameters were also measured by [21And], [22Kir], [23Bai], [23Mck], [27Jun], [31Phr], [37Owe1], [37Owe2], [37Owe3], [37Owe4], [37Owe5], [41Owe], [49Hah], [53Wak], [54Lih], [55Roy], [55Sut], [66Abr], [69Ree], [69Asa], and [83Sen]. The most extensive work is that of [41Owe]. Over most of the region of the Fe-Ni diagram, lattice parameters measured at room temperature will depend on the exact heat treatment given the alloy.

Thermodynamics

[Hultgren,B] assessed the thermodynamic work on Fe-Ni through about 1972. [73Kau] and [70Pre1] reviewed thermodynamic properties of the system for use in calculations of the phase diagram. Since then, phase diagram calculations were

Section II: Phase Diagram Evaluations

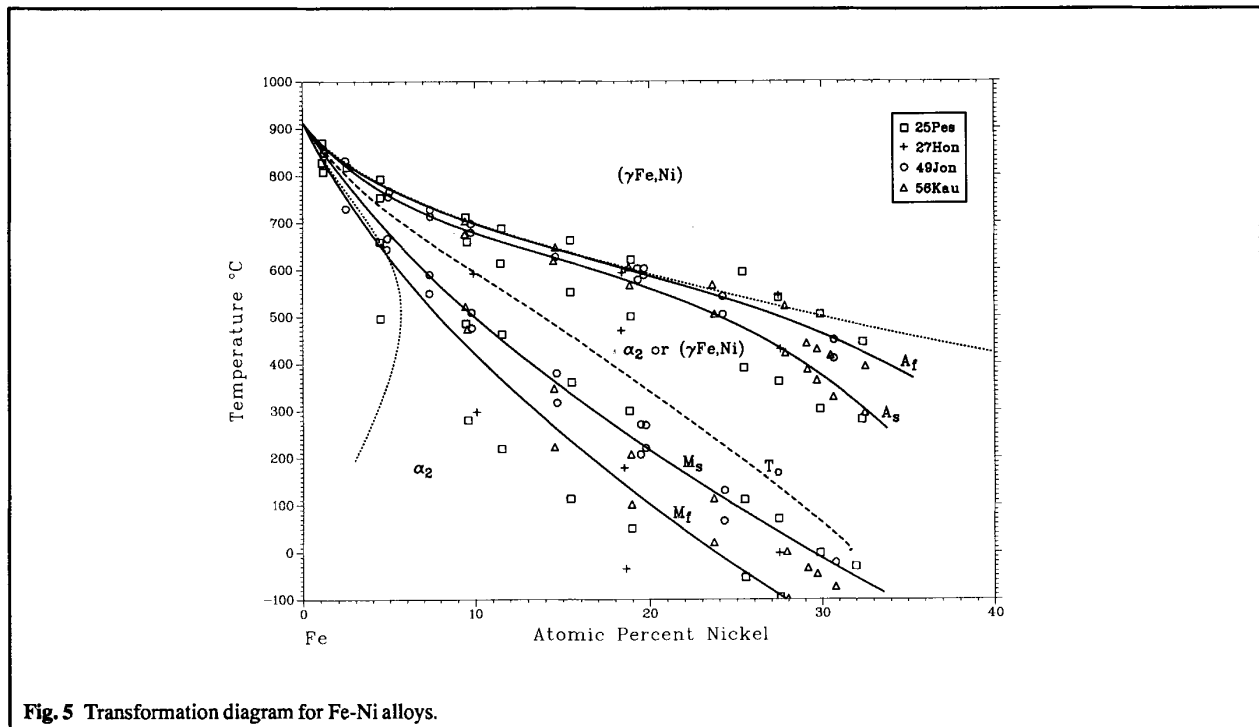


Fig. 5 Transformation diagram for Fe-Ni alloys.

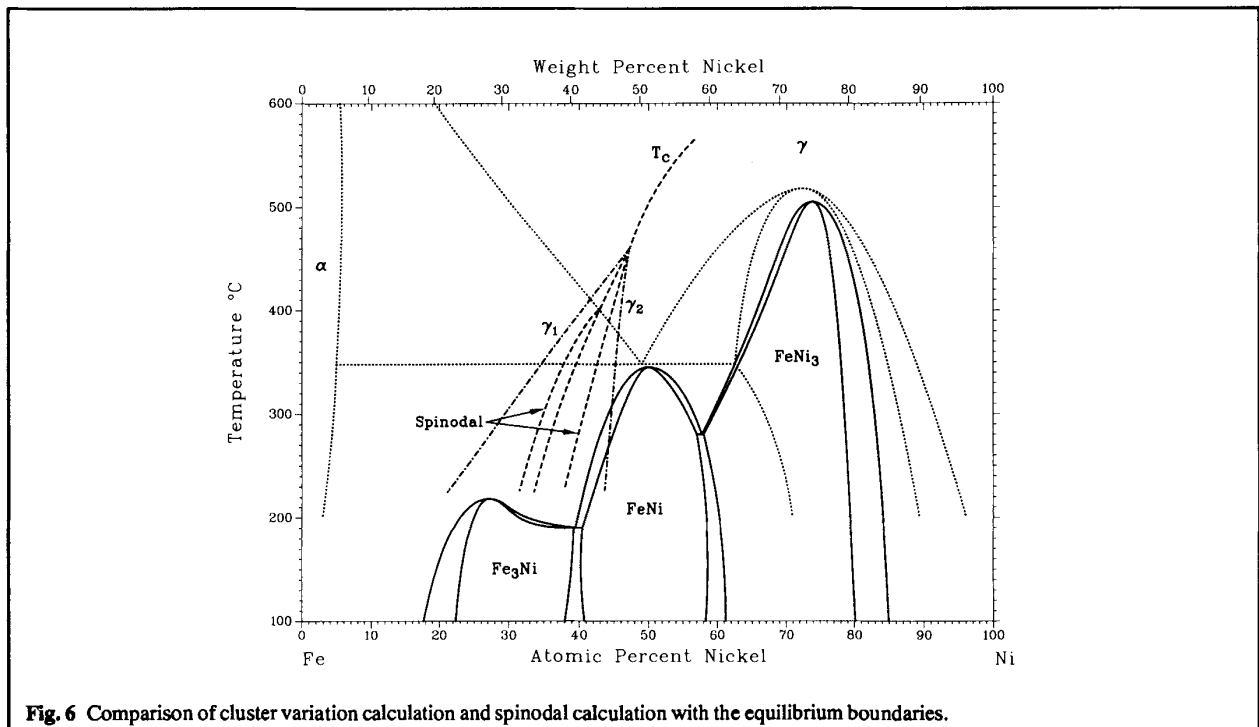


Fig. 6 Comparison of cluster variation calculation and spinodal calculation with the equilibrium boundaries.

Table 4 Fe-Ni Crystal Structure Data

Phase	Composition, at. % Ni	Pearson symbol	Space group	Strukturbericht designation	Prototype
(δ Fe)(a)	0 to 3.5	<i>cF2</i>	<i>Im$\bar{3}m$</i>	A2	W
(γ Fe,Ni)(b)	0 to 100	<i>cF4</i>	<i>Fm$\bar{3}m$</i>	A1	Cu
(α Fe)(c)	0 to 5.5	<i>cF2</i>	<i>Im$\bar{3}m$</i>	A2	W
FeNi ₃	63 to 85	<i>cP4</i>	<i>Pm$\bar{3}m$</i>	L1 ₂	AuCu ₃
Metastable phases					
FeNi	...	<i>tP2</i>	<i>P4/mmm</i>	L1 ₀	AuCu
Fe ₃ Ni	...	<i>cP4</i>	<i>Pm$\bar{3}m$</i>	L1 ₂	AuCu ₃

(a) From 1538 to 1394 °C at 0 at. % Ni. (b) From <1394 to 912 °C at 0 at. % Ni; at all temperatures at 100 at. % Ni. (c) Below <912 °C at 0 at. % Ni.

Table 5 Fe-Ni Lattice Parameter Data

Phase	Composition, at. % Ni	Lattice parameter, nm	Comment	Reference
(δ Fe)	0 to 3.5	0.29322	At 1394 °C, 0 at. % Ni	[65Pea]
(γ Fe,Ni)	0 to 100	0.36468	At 916 °C, 0 at. % Ni	[65Pea]
		0.35240	At 25 °C, 100 at. % Ni	[Massalski2]
(α Fe)	0 to 5.5	0.28664	At 20 °C, 0 at. % Ni	[65Pea]
FeNi ₃	63 to 85	0.35523	At 20 °C, 75 at. % Ni	[65Pea]
Metastable phases				
FeNi
Fe ₃ Ni

made by [74Bas], [74Rao], [77Has], [77Lar], [79Lar], [80Lar], [81Imr], [81Nis], [82Cha], [82Vel], [85Chu2], [86Chu1], and [86Chu2].

[74Rao] analyzed phase diagram data, together with thermochemical information, to deduce analytical equations for the thermodynamic functions in solutions. [77Kub] assessed partial and integral enthalpies and entropies of mixing for (γ Fe,Ni) alloys. [82Vel] derived analytical polynomial expressions for the integral enthalpies of mixing, excess entropies, and the Gibbs energies for the liquid and (γ Fe,Ni) alloys and used those expressions for the evaluation of the phase diagram.

Enthalpies of mixing of liquid alloys were measured in calorimeters by dropping one pure solid component into a bath with the other component molten. This method was used by [71Toz], [81Igu], [74Bat], and [66Elk]. [70Pre1] used differential thermal analysis for determination of the heat of mixing. The study of [66Elk] contradicts the other investigations, has considerable scatter of experimental values, and was dropped from further consideration. The study of [71Toz] gave unreasonably low values of heats of mixing; they were replaced with new values by the same authors in [81Igu]. The experimental results of [81Igu], [74Bat], and [70Pre1] agree satisfactorily (see Fig. 9).

Enthalpies of mixing for solid alloys were obtained by calorimetric measurement of the heat of reaction between powdered components at 1400 to 1600 K. This method was used by

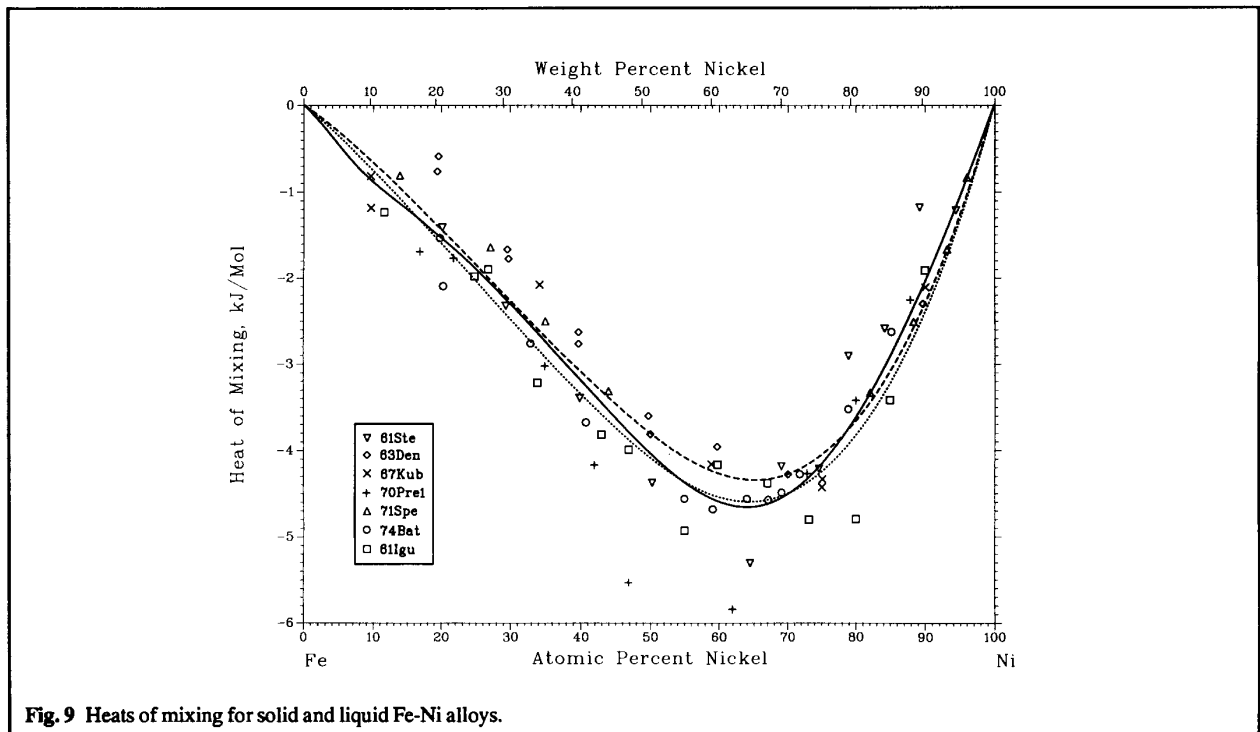
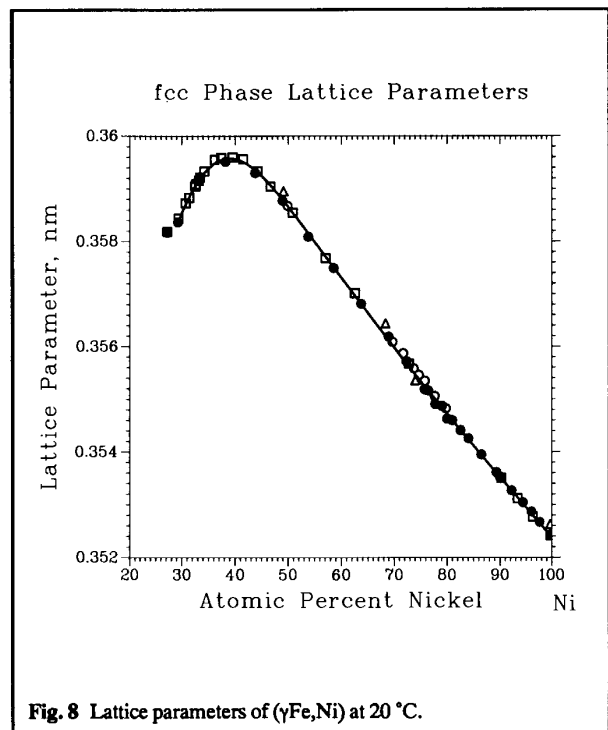
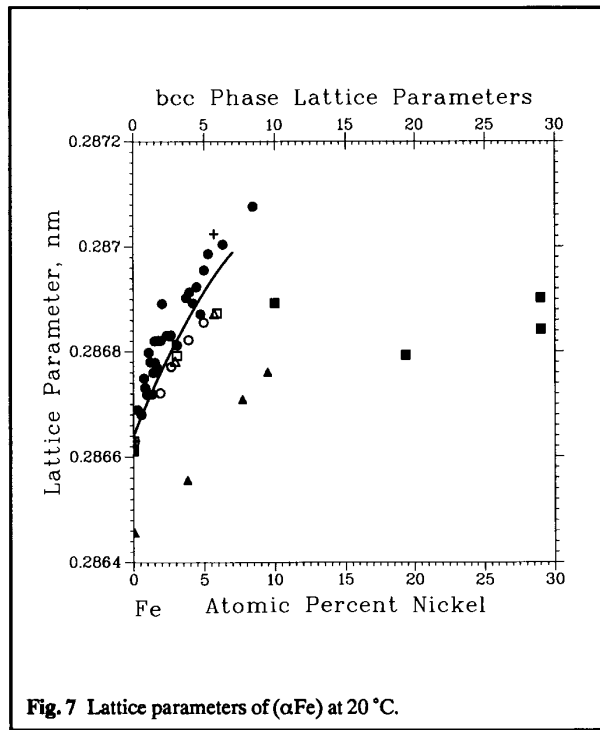
[63Den], [67Kub], and [71Spe]. [61Ste] dissolved solid components and alloys in liquid tin inside the calorimeter at 1123 K. The results of [63Den], [67Kub], [71Spe], and [61Ste] agree satisfactorily and they are also shown in Fig. 9. When all the experimental results are plotted in one graph (see Fig. 9), it is obvious that the data for solid and liquid alloys are partially overlapping, *i.e.*, the enthalpies of mixing for solid and liquid alloys are the same, within the experimental error.

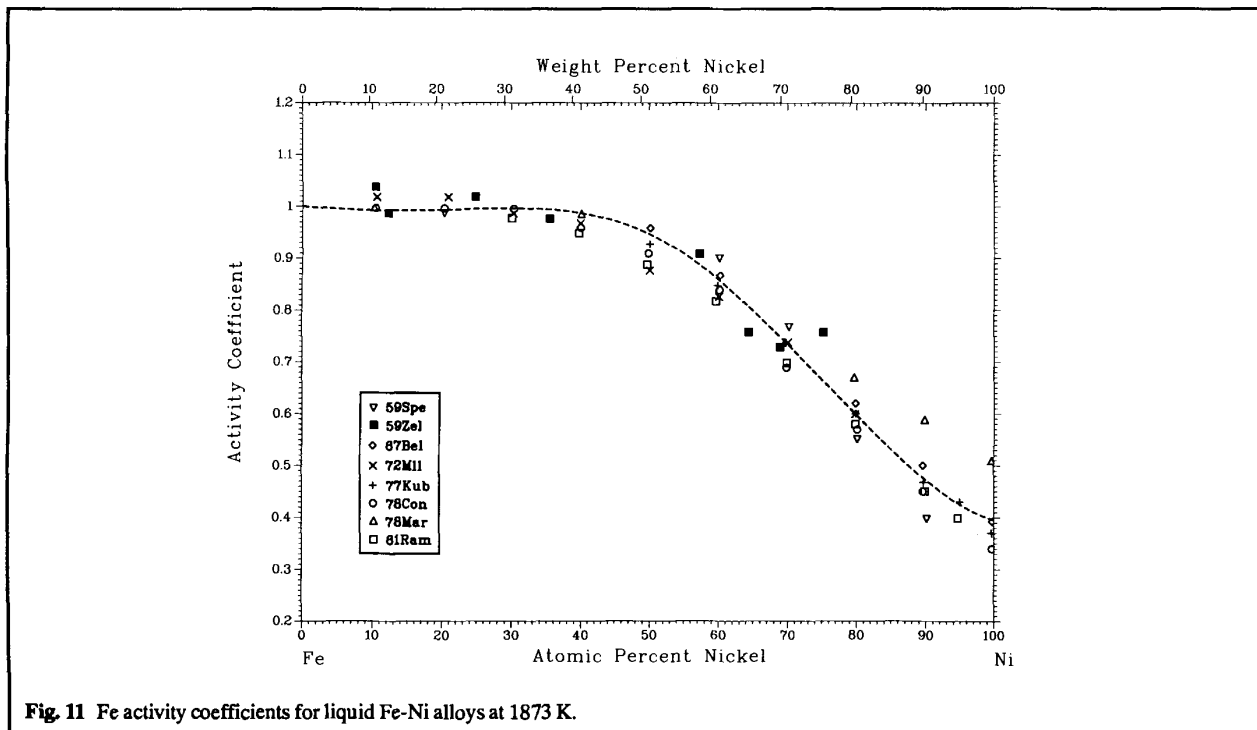
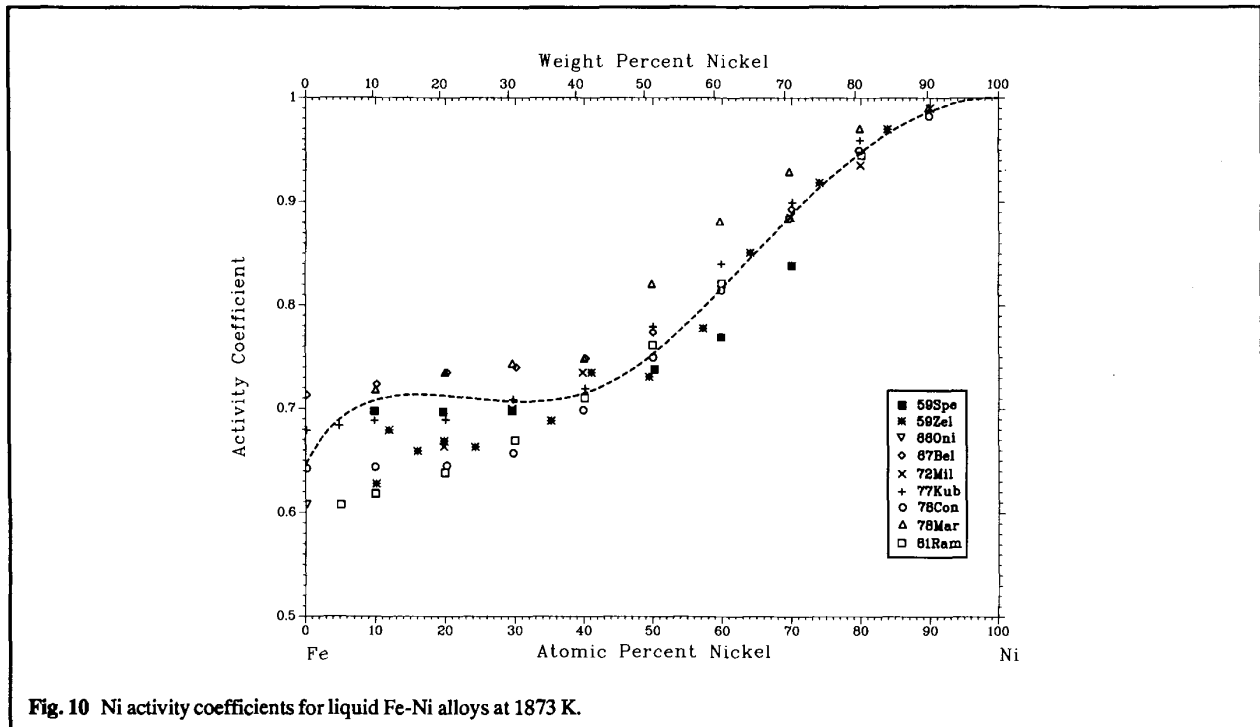
The problem of differentiating the data for liquid and solid alloys was discussed by [77Kub] and [70Pre1]. [70Pre1] measured heats of melting of ten alloys. Their results deviate from the additive value by 400 to 700 J/mol, which can be compared with the errors in determination of the heat of melting of components given by [70Pre2]: ± 750 J/mol. If the experimental data for both the solid and liquid heats of mixing are least-squares fitted to a four-term Redlich-Kister expression, the following equation is obtained for the excess enthalpy:

$$H^{ex} = X_{Fe} X_{Ni} [-16\,226 - 14\,982(X_{Fe} - X_{Ni}) + 200(X_{Fe} - X_{Ni})^2 + 11\,382(X_{Fe} - X_{Ni})^3]$$

This curve is plotted as a solid line in Fig. 9. The uncertainty in the integral values of heat of mixing is on the order of ± 600 J/mol. In Fig. 9, the dotted line represents the liquid excess enthalpies calculated from the thermodynamic model below, and the dashed line represents the solid excess enthalpies calculated from the same model.

Section II: Phase Diagram Evaluations





Section II: Phase Diagram Evaluations

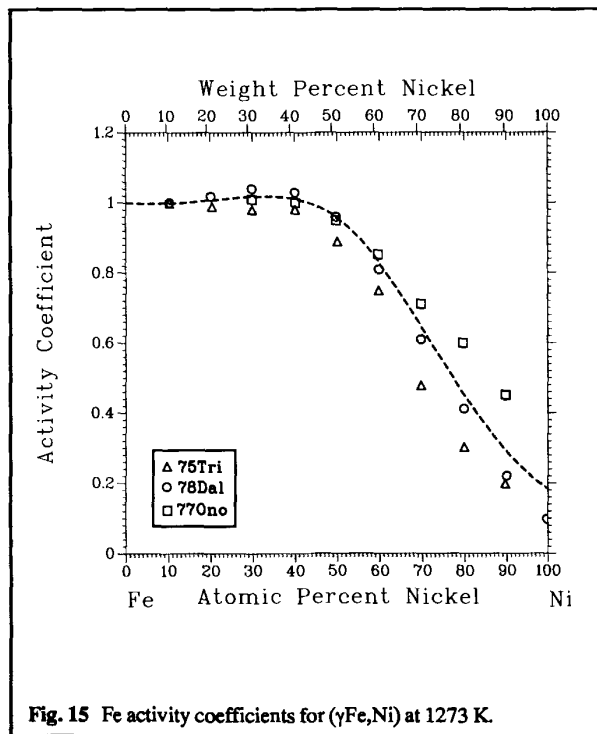
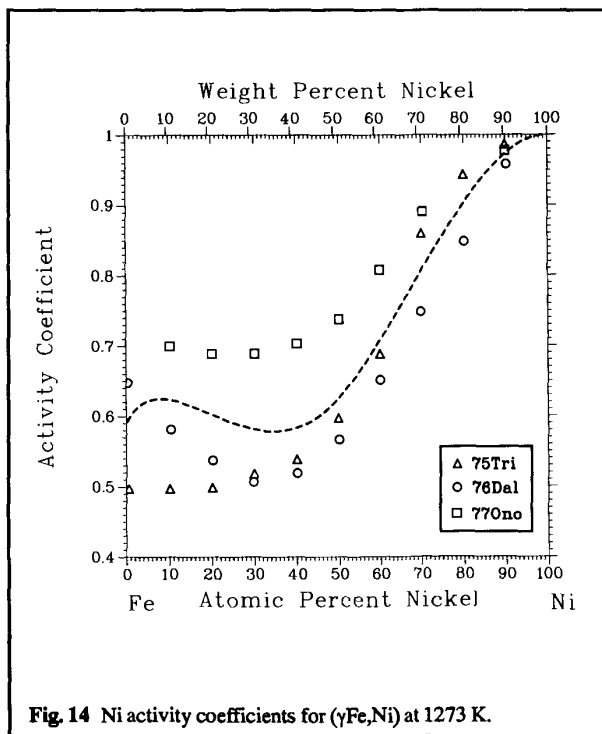
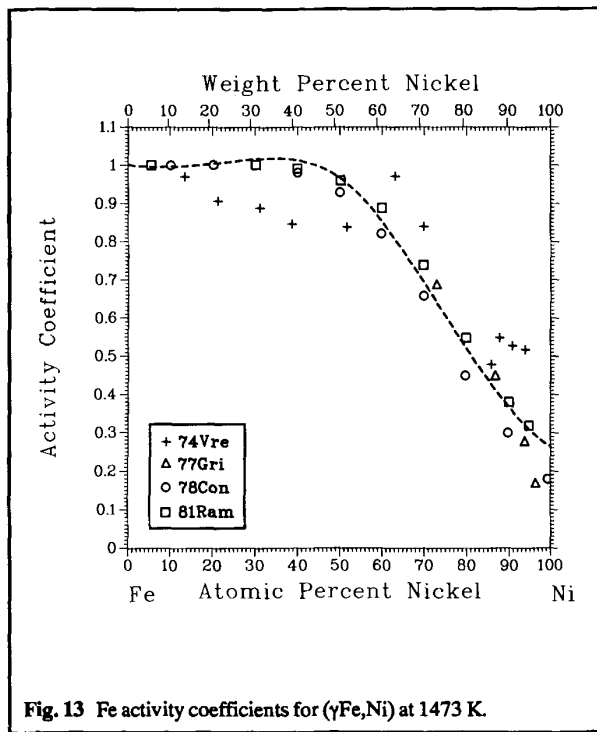
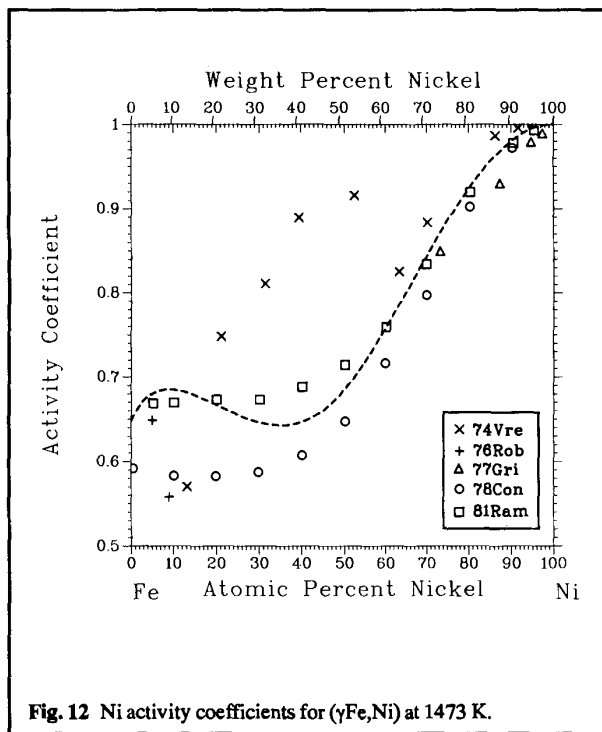


Table 6 Thermodynamic Parameters Used to Model the Fe-Ni Phase Diagram**Liquid phase**

$$G(\text{Fe,L}) = 0$$

$$G(\text{Ni,L}) = 0$$

$$G^{\text{ex}}(\text{L}) = X_{\text{Fe}} X_{\text{Ni}} [-16391 + 3.17 T + (12075 - 2.6 T)(X_{\text{Fe}} - X_{\text{Ni}}) + (-2000 + T)(X_{\text{Fe}} - X_{\text{Ni}})^2 + (-1500 - T)(X_{\text{Fe}} - X_{\text{Ni}})^3]$$

bcc phase

$$G(\text{Fe,bcc}) = 12736.4 - 17.216 T + 23.18 T \ln T - 0.0048155 T^2$$

$$G(\text{Ni,bcc}) = -12500 + 9 T$$

$$G^{\text{ex}}(\text{bcc}, T > 1667 \text{ K}) = X_{\text{Fe}} X_{\text{Ni}} [1950 - 3.05 T + (-2000 + T)(X_{\text{Fe}} - X_{\text{Ni}})^2 + (-1500 - T)(X_{\text{Fe}} - X_{\text{Ni}})^3]$$

$$G^{\text{ex}}(\text{bcc}, T < 1185 \text{ K}) = X_{\text{Fe}} X_{\text{Ni}} [13274 - 13 T + (-2000 + T)(X_{\text{Fe}} - X_{\text{Ni}})^2 + (-1500 - T)(X_{\text{Fe}} - X_{\text{Ni}})^3]$$

$$G^{\text{ex}}(\text{bcc}, 500 < T < 1850 \text{ K}) = X_{\text{Fe}} X_{\text{Ni}} (9381 - 8.775 T)$$

$$G(\text{bcc,mag}) = RT_{\text{C}}(\text{bcc}) \ln [\beta(\text{bcc}) + 1] f(t)$$

$$t = T/T_{\text{C}}(\text{bcc})$$

$$f(t < 1) = -0.9053 + t - 0.153 t^4 - 0.068 t^{10} - 0.00153 t^{16}$$

$$f(t > 1) = -0.06417 t^{-4} - 0.002037 t^{-14} - 0.0004278 t^{-24}$$

$$T_{\text{C}}(\text{bcc}) = 1043 X_{\text{Fe}} + X_{\text{Fe}} X_{\text{Ni}} [-757.6 + 1946(X_{\text{Fe}} - X_{\text{Ni}}) + 2153(X_{\text{Fe}} - X_{\text{Ni}})^2 - 2779(X_{\text{Fe}} - X_{\text{Ni}})^3]$$

$$\beta(\text{bcc}) = 2.22 X_{\text{Fe}} + X_{\text{Fe}} X_{\text{Ni}} [1.176 + 1.445(X_{\text{Fe}} - X_{\text{Ni}}) + 2.275(X_{\text{Fe}} - X_{\text{Ni}})^2 - 2.042(X_{\text{Fe}} - X_{\text{Ni}})^3]$$

fcc phase

$$G(\text{Fe,fcc}) = 11274 - 16.3878 T + 22.03 T \ln T - 0.0041755 T^2$$

$$G(\text{Ni,fcc}) = 3667.6 - 14.4177 T + 20.113 T \ln T - 0.004561 T^2$$

$$G^{\text{ex}}(\text{fcc}) = X_{\text{Fe}} X_{\text{Ni}} [-15291 + 3.47 T + (12061 - 2.5 T)(X_{\text{Fe}} - X_{\text{Ni}}) + (-2000 + T)(X_{\text{Fe}} - X_{\text{Ni}})^2 + (-1500 - T)(X_{\text{Fe}} - X_{\text{Ni}})^3]$$

$$G(\text{fcc,mag}) = RT_{\text{C}}(\text{fcc}) \ln [\beta(\text{fcc}) + 1] f(t)$$

$$t = T/T_{\text{C}}(\text{fcc})$$

$$f(t < 1) = -0.5597 - 0.6315 t - 0.09178 t^4 + 0.001872 t^{10} - 0.007715 t^{16}$$

$$f(t > 1) = -0.03184 t^{-4} + 0.002468 t^{-14} - 0.0019904 t^{-24}$$

$$T_{\text{C}}(\text{fcc}) = -80 X_{\text{Fe}} + 627.4 X_{\text{Ni}} + X_{\text{Fe}} X_{\text{Ni}} [2040.5 - 1250(X_{\text{Fe}} - X_{\text{Ni}}) - 2627(X_{\text{Fe}} - X_{\text{Ni}})^2 - 1784(X_{\text{Fe}} - X_{\text{Ni}})^3]$$

$$\beta(\text{fcc}) = -1.59 X_{\text{Fe}} + 0.62 X_{\text{Ni}} + X_{\text{Fe}} X_{\text{Ni}} [8.644 + 7.691(X_{\text{Fe}} - X_{\text{Ni}}) + 4.435(X_{\text{Fe}} - X_{\text{Ni}})^2 + 0.585(X_{\text{Fe}} - X_{\text{Ni}})^3]$$

FeNi₃ phase

$$G(\text{Fe in FeNi}_3) = 1127.4 - 16.388 T + 22.03 T \ln T + 0.0041755 T^2$$

$$G(\text{Ni in FeNi}_3) = 3667.6 - 14.418 T + 20.11 T \ln T - 0.004561 T^2$$

$$G^{\text{ex}}(\text{FeNi}_3) = X_{\text{Fe}} X_{\text{Ni}} [-24185 + 1.9 T + 21475(X_{\text{Fe}} - X_{\text{Ni}}) + (-1700 + T)(X_{\text{Fe}} - X_{\text{Ni}})^2 + (-1500 - T)(X_{\text{Fe}} - X_{\text{Ni}})^3]$$

$$G(\text{FeNi}_3,\text{mag}) = RT_{\text{C}}(\text{FeNi}_3) \ln [\beta(\text{FeNi}_3) + 1] f(t)$$

$$t = T/T_{\text{C}}(\text{FeNi}_3)$$

$$f(t < 1) = -0.5597 - 0.6315 t - 0.09718 t^4 + 0.001872 t^{10} - 0.007715 t^{16}$$

$$f(t > 1) = -0.03184 t^{-4} + 0.002468 t^{-14} - 0.0019904 t^{-24}$$

$$T_{\text{C}}(\text{FeNi}_3) = -80 X_{\text{Fe}} + 627.4 X_{\text{Ni}} + X_{\text{Fe}} X_{\text{Ni}} [2040.5 - 1250(X_{\text{Fe}} - X_{\text{Ni}}) - 2627(X_{\text{Fe}} - X_{\text{Ni}})^2 - 1784(X_{\text{Fe}} - X_{\text{Ni}})^3]$$

$$\beta(\text{FeNi}_3) = -1.59 X_{\text{Fe}} + 0.62 X_{\text{Ni}} + X_{\text{Fe}} X_{\text{Ni}} [8.644 + 7.691(X_{\text{Fe}} - X_{\text{Ni}}) + 4.435(X_{\text{Fe}} - X_{\text{Ni}})^2 + 0.585(X_{\text{Fe}} - X_{\text{Ni}})^3]$$

Note: X_{Fe} and X_{Ni} are atomic fractions; Gibbs energy values are in J/mol; and T is in K.

Measurements of the activities in liquid alloys using the transpiration method with a stream of inert gas were made by [59Zel] at 1830 to 1891 K, by [78Mar] at 1873 K, and by [66Oni] in dilute alloys at 1825 to 1930 K. The transpiration method based on analysis of condensate evaporated in vacuum was used by [59Spe] at 1783 to 1873 K, by [72Mil] at 2178 to 2558 K, and by [71Tse] at 1873 K. The Knudsen cell with a mass spectrometer was used by [77Kub] at 1773 to 1923 K, by [78Con] at 1500 to 1900 K, by [67Bel] at 1863 K, and by [81Ram] at 1373 to 1923 K. The results obtained by [71Tse] deviate considerably from other studies and were discarded. All other investigations appear to be in reasonable agreement, at least over most of the concentration range. Most of the results are plotted in Fig. 10 and 11. (In these figures, the dotted lines represent the values calculated from the thermodynamic model given below.) From the analysis of information given in the original papers, it is difficult to reject a study completely or to give preference to any particular group of investigations.

[72Dav], [78Con], and [81Ram] also made measurements of activities in the solid alloys. Solid alloy activity measurements using CO/CO₂ equilibrium over the Fe-Ni-O system were made by [77Gri] at 1573 K for alloys between 0 and 27 at.% Ni. [76Rob] reported on Ni activities in two alloys with 4.8 and 9.4 at.% Ni at 1400 to 1550 K measured by Knudsen cell with a mass spectrometer. These results agree satisfactorily and are plotted in Fig. 12 and 13. (In these figures, the dotted lines represent the values calculated from the thermodynamic model given below.) Early investigations of solid activities were made by [58Lyu], who measured vapor pressures of alloys using a mass spectrometer at 1463 to 1583 K and by [74Vre] using the transpiration method at 1509 K for alloys between 13 and 94 at.% Ni. The results of [58Lyu] are close to ideal values for both components—in considerable contradiction with the other results—and were dropped from further consideration. The results of [74Vre], plotted in Fig. 12 and 13, were given low weight because of their scatter and contradiction with the later investigations.

Section II: Phase Diagram Evaluations

Table 7 Average Magnetic Moments Measured for Ferromagnetic Fe-Ni Alloys

Phase	Composition, at. % Ni	μ , Bohr magnetons	Reference
(αFe).....	0	2.22	[63Cra]
	1.4	2.21	[25Pes]
	1.5	2.24	[63Cra]
	3.0	2.26	[63Cra]
	3.5	2.22	[25Pes]
	4.3	2.27	[63Cra]
	5.1	2.23	[25Pes]
	6.2	2.29	[63Cra]
	6.9	2.24	[25Pes]
	9.3	2.28	[63Cra]
	11.3	2.23	[25Pes]
	11.5	2.29	[63Cra]
	15.9	2.22	[25Pes]
	18.9	2.23	[63Cra]
	19.0	2.21	[25Pes]
	23.3	2.17	[63Cra]
	25.2	2.13	[25Pes]
	25.5	2.12	[25Pes]
	29.7	2.00	[25Pes]
	30.4	2.00	[63Cra]
(γFe,Ni).....	0	2.20	[25Pes]
	32.5	1.93	[63Cra]
	30.8	1.25	[63Cra]
	32.1	1.61	[63Cra]
	34.3	1.77	[63Cra]
	35.3	1.82	[63Cra]
	40.8	1.80	[25Pes]
		1.84	[63Cra]
	42.0	1.79	[25Pes]
	43.5	1.77	[25Pes]
	49.6	1.67	[25Pes]
	49.8	1.69	[63Cra]
	51.0	1.65	[25Pes]
	57.7	1.52	[25Pes]
	60.0	1.50	[63Cra]
	67.0	1.36	[25Pes]
	79.7	1.07	[63Cra]
	80.2	1.06	[25Pes]
	87.7	0.88	[25Pes]
	100	0.61	[25Pes, 63Cra]

With decreasing temperature, the vapor pressure and the reliability of activity measurements drop rapidly. The difference in values of the Ni activity coefficients at 1473 K (Fig. 12) between two similar investigations [78Con, 67Bel] looks natural, considering the probable uncertainty of the methods used. For both solid and liquid alloys, the uncertainty in determination of the activity coefficient of either of the components is on the order of ± 0.03 for a component in an alloy near the pure component, ± 0.08 in alloys around the equiatomic composition, and ± 0.15 for a component in alloy near infinite dilution.

Other reports of activities in solid alloys were provided by [49Kub], [53Ori], [69Kus], [64Roe], [70Gat], [72Dav], [75Tri], [76Dal], [77Ono], and [79Tan]. Most of these contradict each other, and it is worthwhile to plot only some of the latest studies. [75Tri] measured CO/CO₂ equilibrium over the Fe-Ni-O system at 1273 K. [76Dal] used the same technique at 1065 to 1380 K.

[77Ono] measured the Fe activities by the emf method at 1023 to 1423 K. Figures 14 and 15 show that at 1273 K, the results of three of these studies agree satisfactorily. (The dotted lines in the figures represent the values calculated from the thermodynamic model given below.)

Specific heat measurements in the Fe-Ni system at low temperatures were reported by [40Kee], [64Gup], [65Ehr], and [66Shi] and at higher temperatures by [39Lee], [73Kol], and [82Bro2].

An attempt was made to construct a thermodynamic model that represents the Fe-Ni diagram over the widest possible temperature range and agrees, within the above stated experimental errors, with the thermodynamic measurements. This model was used as an aid in the evaluation of the measured phase diagram boundaries, and greater weight was given to these boundaries than to the thermodynamic measurements. In the model, the Gibbs energy for a phase p is represented by:

$$G(p) = X_{\text{Fe}}G(p, \text{Fe}) + X_{\text{Ni}}G(p, \text{Ni}) + G(p, \text{mag}) + RT(X_{\text{Fe}} \ln X_{\text{Fe}} + X_{\text{Ni}} \ln X_{\text{Ni}}) + G(p)^{\text{ex}}$$

where $G(p, \text{Fe})$ is the Gibbs energy of pure Fe, and $G(p)^{\text{ex}}$ is the nonmagnetic excess free energy. Following [74Ind], the magnetic contribution to the Gibbs energy is of the form:

$$G(p, \text{mag}) = RT_C(p) \ln(\beta(p) + 1)f(t)$$

where t is the reduced temperature T/T_C , T_C is the Curie temperature, and β is magnetic moment in Bohr magnetons. Both T_C and β are functions of composition. In the Fe-Ni system, all three phases in the equilibrium diagram are ferromagnetic, and the magnetic contribution is significant, especially at temperatures below 912 °C. Early estimates of the magnetic contributions to phase equilibrium in the Fe-Ni system were given by [73Sch].

The functions for T_C and β for the bcc and fcc phases were obtained by least-squares fitting the literature data. For the FeNi₃ phase, T_C and β values were taken to be approximately equal to those in the fcc phase. For the bcc phase, the function $f(t)$, as expanded in a power series by [78Hil], was used (the resultant contribution to the Gibbs energy agrees well with the alternate form used by [85Chu1]). For the fcc phase, the same power series for $f(t)$ was used, with the coefficients being obtained by least-squares fitting the evaluated specific heat data of [84Des] for Ni. For pure Fe, the thermodynamic functions given by [79Agr] were used. For pure Ni, the enthalpies of melting and specific heat values given in the evaluation of [84Des] were used to construct the nonmagnetic part of the thermodynamic functions. For bcc Ni, the lattice stability estimates of [73Kau] were used. In assessing the diagram, the thermodynamic modeling and optimization procedure of [81Sun] were used. For the liquidus and solidus, greatest weight was given to the liquidus measurements, especially those of [57Hel].

The parameters found by a combination of optimization and trial and error to best fit the diagram are given in Table 6, and the calculated Fe-Ni diagram is shown in Fig. 16. Above about 500 °C, the calculated and assessed diagrams are nearly identical (± 1 °C in temperature and ± 0.5 at. % in composition). At lower temperatures, the assessed and calculated boundaries differ somewhat. Especially noticeable is the tricritical point predicted by the model and arising from the influence of the magnetic contribution

Table 8 Measured Curie Temperatures vs Composition for Fe-Ni Alloys

Phase	Composition, at. % Ni	Curie, Temperature, °C	Reference	Phase	Composition, at. % Ni	Curie, Temperature, °C	Reference	
(αFe)	0	771	[25Pes]	(γFe,Ni)(cont.)	55.0	558	[53Wak]	
		770	[29Gos]		57.7	590	[25Pes]	
	1.4	766	[25Pes]		60.0	592	[53Wak]	
	2.8	763	[29Gos]			591	[63Cra]	
	3.5	758	[25Pes]		65.0	613	[53Wak]	
	4.8	755	[29Gos]		67.0	612	[25Pes]	
	5.1	752	[25Pes]		68.0	616	[53Wak]	
	6.9	748	[25Pes]		70.0	614	[53Wak]	
	15.9	740	[25Pes]		72.0	608	[53Wak]	
	19.0	715	[25Pes]		74.0	600	[53Wak]	
	23.0	565	[43Hos]		75.0	598	[53Wak]	
	29.7	597	[25Pes]		76.0	589	[53Wak]	
	31.3	535	[25Pes]		78.0	585	[53Wak]	
	33.3	460	[25Pes]		79.7	570	[63Cra]	
	33.8	435	[25Pes]		80.0	577	[53Wak]	
	(γFe,Ni)	29.7	120		[25Pes]	80.2	576	[25Pes]
		30.8	100		[63Cra]	81.0	571	[53Wak]
		31.3	160		[25Pes]	85.0	543	[53Wak]
		31.8	174		[25Pes]	87.7	511	[25Pes]
		32.1	156		[63Cra]	100.0	360	[25Pes]
33.3		228	[25Pes]		361 ± 1	[63Cra]		
33.8		245	[25Pes]		354.3	[68Kou]		
35.3		261	[25Pes]	FeNi ₃	45.0	494 ± 5	[53Wak]	
		228	[63Cra]	50.0	543	[53Wak]		
36.1		250	[63Cra]	55.0	580	[53Wak]		
37.0		285	[25Pes]	60.0	616	[53Wak]		
38.5		300	[29Gos]	65.0	636	[53Wak]		
39.0		317	[25Pes]	68.0	668	[53Wak]		
40.8		321	[25Pes]	70.0	680	[53Wak]		
		354	[63Cra]	72.0	696	[53Wak]		
42.0		346	[25Pes]	74.0	691	[53Wak]		
43.5		403	[25Pes]	75.0	681	[53Wak]		
45.0		468	[53Wak]	76.0	654	[53Wak]		
47.1		415	[29Gos]	78.0	624	[53Wak]		
49.3		506	[25Pes]	80.0	599	[53Wak]		
49.8	513	[63Cra]	81.0	584	[53Wak]			
50.0	520	[53Wak]	85.0	543	[53Wak]			
51.0	522	[25Pes]						

to the Gibbs energy. (The tricritical point was also calculated by [77Hut].) [85Chu2] gave convincing arguments for the existence of this tricritical point, but further experimental confirmation appears necessary. In fitting the (αFe)/(δFe) and (αFe)/(γFe,Ni) experimental boundaries, better fits are obtained if the expression for the excess energy of the bcc phase is divided into two temperature regions—one for the (αFe) and one for the (δFe) region. An expression for the bcc excess energy that covers the entire temperature range, which gives a good approximation to the observed boundaries and which is more sensible from a thermodynamic point of view, is also included in Table 6.

In Fig. 9, the heats of mixing obtained from the parameters of Table 6 are compared with the measured values (the dotted line is for the liquid, the dashed line for the solid). In Fig. 10 through 15, the theoretical values of the activities calculated from the model parameters (dotted lines) are compared with measured values. In all instances, agreement is within experimental error. However, the fits are in some respects unsatisfying, especially for the Ni-rich heats of mixing and Fe-rich Ni activities. The slight oscillation in the Ni activity coefficients on the Fe-rich side (Fig. 12 and 14) evidently is unjustified by the data. This may be in part due to

the poor accuracy of the measured values of the solidus and liquidus of the Ni rich alloys.

Pressure

The equilibrium diagram for 50, 100, and 150 kbar was calculated by [61Kau1]. [61Kau2] showed that pressure lowers the (γFe,Ni) → (αFe) transformation temperatures. [66Mcq] investigated the effect of pressure on the density of Fe-Ni alloys by the shock technique up to 2000 kbar. Using XRD, [68Tak] measured the effect of pressure on the crystal structure and molar volume.

Magnetism

The saturation magnetization, average magnetic moments, and Curie temperatures for single-phase fcc alloys from 30 to 100 at.% Ni were measured by [63Cra]. They also measured the average magnetic moment for single-phase bcc alloys in the range 0 to 30 at.% Ni. Magnetic moments on individual Fe and Ni atoms were measured by [62Col], [73Cab], [74Nis], and [55Shu] between 40 and 100 at.% Ni. The use of magnetic measurements for

Section II: Phase Diagram Evaluations

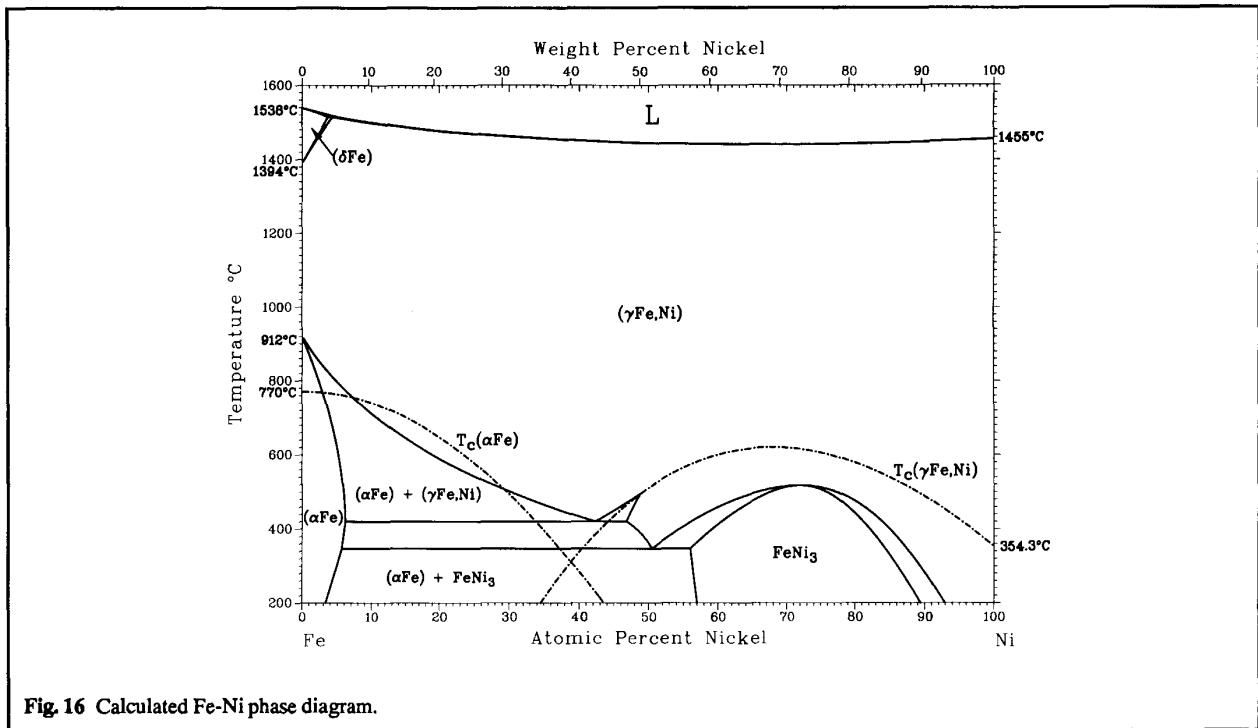


Fig. 16 Calculated Fe-Ni phase diagram.

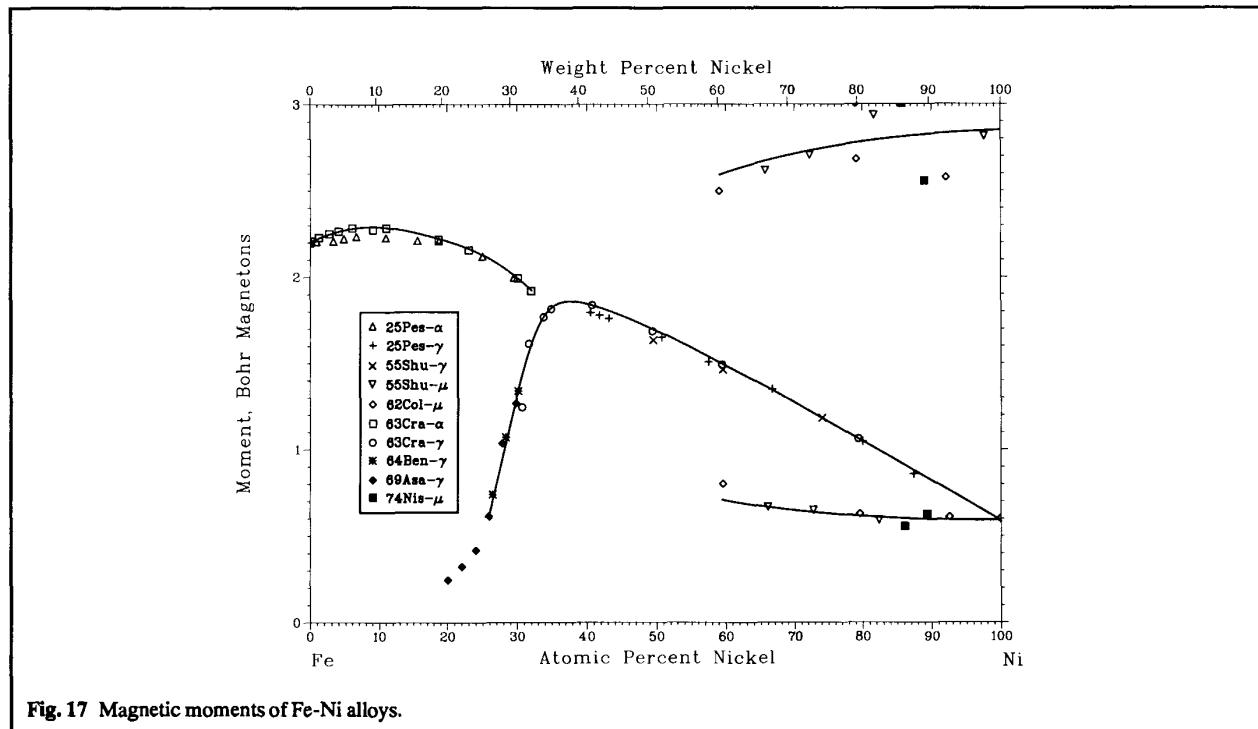


Fig. 17 Magnetic moments of Fe-Ni alloys.

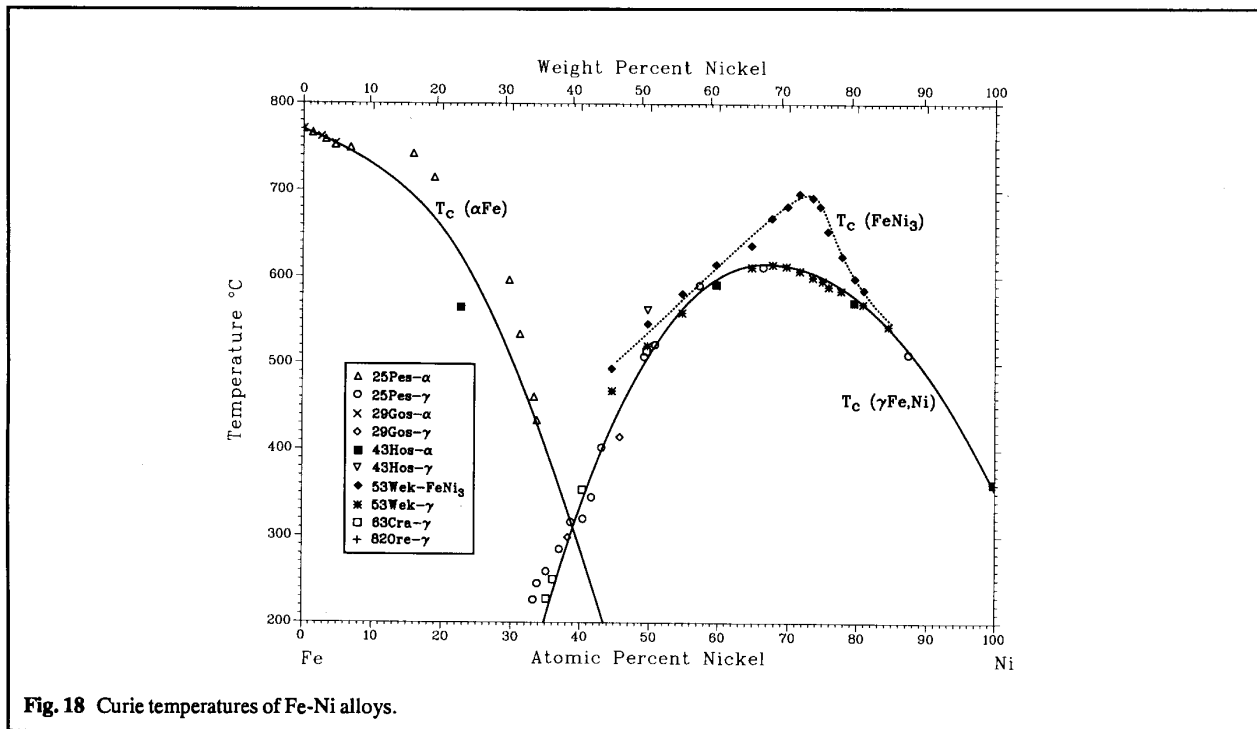


Fig. 18 Curie temperatures of Fe-Ni alloys.

studying two-phase Fe-Ni alloys was described by [39Suc] and [40Pic]. The effect of heat treatment on the magnetic properties of FeNi₃, including the maximum permeability, coercive force, remanent, and saturation magnetization was investigated by [53Wak]. By extrapolating the magnetization vs temperature curves, they estimated the Curie temperatures for ordered FeNi₃ and found a higher Curie temperature for the ordered alloys than for the disordered. A slightly higher saturation magnetization is also found for the ordered alloys ([40Gra], see Table 7). Figure 17 and Table 7 compare the various measured magnetic moments, and Fig. 18 and Table 8 compare the various measured Curie temperatures. The Curie temperature of pure Ni is taken as 627.4 K, in accordance with [68Kou] and [82Rhy].

Alloys of high maximum permeability, the so-called permalloys, can be formed by rapidly cooling alloys near the FeNi₃ composition [32Dah, 38Kay, 53Boz1, 53Boz2, 64Sch]. The magnetic properties of an equiatomic single crystal of FeNi that had been ordered metastably in the AuCu structure by neutron irradiation below 320 °C were studied by [64Nee]. Further anomalies in magnetic properties and phase separation have been observed by [51Suc], [59Dek] and [61Gor]. [75Ind] showed how the Curie temperature variation in (γFe,Ni) may be closely fitted to a Redlich-Kister form with a single interaction term. [77Mio] showed how this interaction parameter is related to the two-moment model for γFe of [63Wei]. [73Miz] measured Curie temperatures and magnetic moments in rapidly quenched amorphous quasibinary alloys with 0 to 90 at.% Ni and boron and phosphorus additions.

Cited References

- 1899Osm: F. Osmond, "On the Alloys of Iron and Nickel," *Compt. Rend.*, 128, 304-307 (1899) in French. (Equi Diagram; Experimental; #)
- 05Gue: W. Guertler and G. Tammann, "On the Alloys of Nickel and Cobalt with Iron," *Z. Anorg. Chem.*, 45, 205-216 (1905) in German. (Equi Diagram; Experimental; #)
- 10Heg: F. Hegg, "Thermomagnetic Study of Ferro-nickels," *Arch. Sci. Phys. Nat. Geneve*, 30, 15-45 (1910) in French. (Equi Diagram; Experimental; #)
- 10Rue: R. Ruer and E. Schuz, "The Iron-Nickel System," *Metallurgie*, 7, 415-470 (1910) in German. (Equi Diagram; Experimental; #)
- 20Han: D. Hanson and H.E. Hanson, "The Constitution of the Nickel-Iron Alloys," *J. Iron Steel Inst.*, 102, 39-64 (1920). (Equi Diagram, Meta Phases; Experimental)
- 21And: M.R. Andrews, "X-ray Analysis of Three Series of Alloys," *Phys. Rev.*, 18, 245-254 (1921). (Crys Structure; Experimental)
- 21Mer: P.D. Merica, "Iron-Nickel Alloys," *Chem. Met. Eng.*, 24, 375-378 (1921). (Equi Diagram; Theory; #)
- 22Kir: F. Kirchner, "Structure Determination with X-rays," *Ann. Phys.*, 69, 59-81 (1922) in German. (Crys Structure; Experimental)
- 23Bai: E.C. Bain, "The Crystal Structures of Solid Solutions," *Trans. AIME*, 68, 625-641 (1923). (Crys Structure; Experimental)
- *23Han: D. Hanson and J.R. Freeman, "The Constitution of the Alloys of Iron and Nickel," *J. Iron Steel Inst.*, 107, 301-321 (1923). (Equi Diagram; Experimental)
- 23Mck: L.W. McKeehan, "The Crystal Structure of Iron-Nickel Alloys," *Phys. Rev.*, 21, 402-407 (1923). (Crys Structure; Experimental)
- 25Kas: T. Kase, "On the Equilibrium Diagram of the Iron-Carbon-Nickel System," *Sci. Rep. Tohoku Imp. Univ.*, 14, 173-217 (1925). (Equi Diagram; Experimental)

Section II: Phase Diagram Evaluations

- *25Pes: M. Peschard, "Contribution to the Study of Ferro-nickels," *Rev. Metall.*, 22, 430-676 (1925) in French. (Meta Phases, Magnetism; Experimental)
- 25Vog: R. Vogel, "On the Structure of Iron-Nickel Meteorites," *Z. Anorg. Chem.*, 142, 193-228 (1925) in German. (Equi Diagram; Experimental; #)
- 26Kaw: M. Kawakami, "On the Specific Heat of Iron-Nickel Alloys," *Sci. Rep. Tohoku Imp. Univ.*, 15, 251-262 (1926). (Equi Diagram; Experimental)
- 26Osa1: A. Osawa, "The Relation Between Space-Lattice Constant and Density of Iron-Nickel Alloys," *Sci. Rep. Tohoku Imp. Univ.*, 15, 387-398 (1926). (Crys Structure; Experimental)
- 26Osa2: A. Osawa, "On the Relation Between the Lattice Constant and the Density of Iron-Nickel Alloys," *J. Iron Steel Inst.*, 113, 447-456 (1926). (Crys Structure; Experimental)
- 27Hon: K. Honda and S. Miura, "On the Determination of the Heterogeneous Field in the System Fe-Ni," *Sci. Rep. Tohoku Imp. Univ.*, 16, 745-753 (1927). (Meta Phases; Experimental)
- 27Jun: A.O. Jung, "The Structure and Lattice Constants of Artificial and Natural Iron Alloys," *Z. Krist.*, 65, 309-334 (1927) in German. (Crys Structure; Experimental)
- 27Vog: R. Vogel, "On the Structure of Iron Meteorites," *Arch. Eisenhüttenwes.*, 1, 605-611 (1927) in German. (Equi Diagram; Experimental)
- 28Vog: R. Vogel, "On the Structure of Iron-Nickel Meteorites," *Z. Anorg. Chem.*, 142, 193-228 (1928) in German. (Equi Diagram; Experimental; #)
- 29Gos: G. Gossels, "Investigation of the Hysteresis Stability of Iron-Nickel Alloys," *Z. Anorg. Chem.*, 182, 19-27 (1929) in German. (Meta Phases, Magnetism; Experimental)
- 30Rob: O.L. Roberts and W.P. Davey, "An X-ray Study of the A₃ Point of Iron and Some Iron-Nickel Alloys," *Met. Alloys*, 1, 648-654 (1930). (Equi Diagram, Meta Phases; Experimental)
- *31Ben: H. Bennedek and P. Schafmeister, "The Area of the Delta-Gamma Transformation in the Iron-Nickel System," *Arch. Eisenhüttenwes.*, 5, 123-125 (1931) in German. (Equi Diagram; Experimental)
- 31Phr: G. Phragmen, "X-ray Investigation of Certain Nickel Steels of Low Thermal Expansion," *J. Iron Steel Inst.*, 123, 465-477 (1931). (Crys Structure; Experimental)
- 32Dah: O. Dahl, "On the Question of Supercooled Transformations of State in Iron-Nickel Alloys (The High Permeability of Air Cooled Permalloy)," *Z. Metallkd.*, 24, 107-111 (1932) in German. (Equi Diagram, Magnetism; Experimental)
- 32Sch: E. Scheil, "On the Origin of the Transformation of Austenite into Martensite in the Vicinity of Room Temperature," *Z. Elektrochem.*, 38, 554-557 (1932) in German. (Meta Phases; Experimental)
- 33Dah: O. Dahl and J. Pfaffenberger, "A Contribution on Iron-Nickel Alloys," *Z. Metallkd.*, 25, 241-245 (1933) in German. (Equi Diagram; Experimental)
- 34Deh: V. Dehlinger, "Kinetics and Phase Diagram of the Irreversible Transformation in the Iron-Nickel System," *Z. Metallkd.*, 5, 112-116 (1934) in German. (Meta Phases; Experimental)
- 35Sch: E. Scheil, "The Irreversibility of Iron-Nickel Alloys and their Equilibrium Diagram," *Arch. Eisenhüttenwes.*, 9, 163-166 (1935). (Meta Phases; Experimental)
- 36Dah: O. Dahl, "Cold Working and Relaxation in Alloys with Ordered Atomic Distributions," *Z. Metallkd.*, 28, 133-138 (1936) in German. (Equi Diagram; Experimental)
- *36Jet: E. Jette and F. Foote, "X-ray Study of Iron-Nickel Alloys," *Trans. AIME*, 120, 259-276 (1936). (Equi Diagram; Experimental)
- 36Sam: H.O. von Samonson-Himmelstjerna, "The Heat Content and Heat of Formation of Melted Alloys," *Z. Metallkd.*, 28, 197-202 (1936) in German. (Equi Diagram; Experimental)
- 36Mer: P.D. Merica, "Constitution of Iron-Nickel Alloys," *Metals Handbook*, American Society for Metals, Cleveland, OH, 271-273 (1936). (Meta Phases; Review; #)
- 37Bra: A.J. Bradley, A.H. Jay, and A. Taylor, "The Lattice Spacing of Iron-Nickel Alloys," *Philos. Mag.*, 23, 545-547 (1937). (Crys Structure; Experimental)
- 37Jen: C.H.M. Jenkins, E.H. Bucknall, C.R. Austin, and G.A. Mellor, "Some Alloys for Use at High Temperatures," *J. Iron Steel Inst.*, 136, 187-222 (1937). (Equi Diagram; Experimental; #)
- 37Kal: O. Kallback, "Determination of the Order-Disorder Point in FeNi₃," *Ark. Mat. Astron. Fys.*, 34B, 17-21 (1947). (Equi Diagram; Experimental)
- 37Koe: F. Koerber, W. Oelsen, and H. Lichtenberg, "On the Thermochemistry of Alloys II. Direct Determination of the Heats of Formation of the Ternary Alloys Fe-Ni-Al, Fe-Co-Al, Cu-Ni-Al, Fe-Al-Si, and a Portion of the Cu-Mn-Al System," *Mitt. Kaiser Wilhelm Inst. Eisenforsch.*, 19, 131-159 (1937) in German. (Equi Diagram; Experimental)
- 37Owe1: E.A. Owen and E.L. Yates, "X-ray Investigation of Pure Iron-Nickel Alloys. Part I: Thermal Expansion of Alloys Rich in Nickel," *Proc. Phys. Soc. (London)*, 49, 17-28 (1937). (Crys Structure; Experimental)
- 37Owe2: E.A. Owen and E.L. Yates, "X-ray Investigation of Pure Iron-Nickel Alloys. Part 2: Thermal Expansion of Some Further Alloys," *Proc. Phys. Soc. (London)*, 49, 178-188 (1937). (Crys Structure; Experimental)
- 37Owe3: E.A. Owen and E.L. Yates, "An X-ray Investigation of Pure Iron-Nickel Alloys. Part 3: The Thermal Expansion of Alloys Rich in Iron," *Proc. Phys. Soc. (London)*, 49, 307-314 (1937). (Crys Structure; Experimental)
- 37Owe4: E.A. Owen, E.L. Yates, and A.H. Sully, "An X-ray Investigation of Pure Iron-Nickel Alloys. Part 4: The Variation of Lattice Parameter with Composition," *Proc. Phys. Soc. (London)*, 49, 315-322 (1937). (Crys Structure; Experimental)
- 37Owe5: E.A. Owen, E.L. Yates, and A.H. Sully, "An X-ray Investigation of Pure Iron-Nickel Alloys. Part 5: The Variation of Thermal Expansion with Composition," *Proc. Phys. Soc. (London)*, 49, 323-325 (1937). (Crys Structure; Experimental)
- 38Haw: F.E. Haworth, "An X-ray Test of Superstructure in FeNi₃," *Phys. Rev.*, 54, 693-698 (1938). (Equi Diagram; Experimental)
- 38Kay: S. Kaya, "The Superlattice in Iron-Nickel Alloys and the Permalloy Problem," *J. Fac. Sci. Hokkaido Imp. Univ.*, 2, 29-53 (1938). (Magnetism; Experimental)
- 38Mar: J.S. March, *The Alloys of Iron and Nickel*, McGraw Hill, New York, 24-55 (1938). (Equi Diagram; Review; #)
- 39Haw: F.E. Haworth, "Superstructure in FeNi₃," *Phys. Rev.*, 56, 289-231 (1939). (Equi Diagram; Experimental)
- 39Kay: S. Kaya and M. Nakayama, "The Superstructure in Iron-Nickel-Cobalt Alloys and the Perminvar Problem," *Z. Phys.*, 112, 420-429 (1939) in German. (Equi Diagram; Experimental)
- 39Kus: A. Kussmann, "Evidence for a Superstructure Phase in the Iron-Nickel System," *Z. Metallkd.*, 31, 212-214 (1939) in German. (Equi Diagram; Experimental)
- 39Lee: P. Leech and C. Sykes, "The Evidence for A Superlattice in the Nickel-Iron Alloy Ni₃Fe," *Philos. Mag.*, 27, 742-753 (1939). (Equi Diagram, Thermo; Experimental)
- 39Owe: E.A. Owen and A.H. Sully, "The Equilibrium Diagram of Iron-Nickel Alloys," *Philos. Mag.*, 27, 614-636 (1939). (Equi Diagram; Experimental; #)

- 39Suc:** W. Sucksmith, "The Measurement of Magnetic Saturation Intensities at Different Temperatures," *Proc. R. Soc. (London)*, *170*, 551-557 (1939). (Magnetism; Experimental)
- 40Gra:** E.M. Grabbe, "Ferromagnetic Anisotropy, Magnetization at Saturation, and Superstructure in Ni₃Fe and Nearby Compositions," *Phys. Rev.*, *57*, 728-734 (1940). (Magnetism; Experimental)
- 40Kee:** W.H. Keesom and B. Kurrelmeyer, "Specific Heats of Alloys of Nickel with Copper and with Iron from 1.2° to 20°K," *Physica*, *7*, 1003-1024 (1940). (Thermo; Experimental)
- 40Nix:** F.C. Nix, H.G. Beyer, and R. Dunning, "Neutron Studies of Order in Fe-Ni Alloys," *Phys. Rev.*, *58*, 1031-1034 (1940). (Equi Diagram; Experimental)
- 40Pic:** A.T. Pickles and W. Sucksmith, "A Magnetic Study of the Two-Phase Iron-Nickel Alloys," *Proc. R. Soc. (London) A*, *175*, 331-334 (1940). (Equi Diagram, Magnetism; Experimental)
- 40Zui:** A.J. Zuihoff, "The Exact Measurement of the Specific Heats of Solid Substances at High Temperature XII. The Specific Heats of Iron-Nickel Alloys of Various Compositions Between 100° and 1400 °C," *Rec. Trav. Chim.*, *59*, 131-160 (1940). (Equi Diagram; Experimental; #)
- 41Owe:** E.A. Owen and A.H. Sully, "On the Migration of Atoms in Iron-Nickel Alloys," *Philos. Mag.*, *31*, 314-338 (1941). (Equi Diagram, Crys Structure; Experimental)
- 43Hos:** K. Hoselitz and W. Sucksmith, "A Magnetic Study of the Two-Phase Iron-Nickel Alloys, II," *Proc. R. Soc. (London)*, *1*, 30 (1943). (Equi Diagram, Meta Phases, Magnetism; Experimental)
- 47Oel:** W. Oelsen and F. Wever, "On the Influence of Elements on the Polymorphism of Iron," *Arch. Eisenhüttenwes.*, *19*, 97-104 (1947) in German. (Meta Phases; Theory)
- 48Fis:** J.C. Fisher, J.H. Hollomon, and D. Turnbull, "Nucleation," *J. Appl. Phys.*, *19*, 775-784 (1948). (Meta Phases; Theory)
- 48Kal:** O. Kallback, "Determination of the Order-Disorder Point in FeNi₃," *Ark. Mat. Astron. Fys.*, *34B*(17), 1-6 (1948). (Equi Diagram; Experimental)
- 49Hah:** H. Hahn and H. Muhlberg, "The System Iron/Nickel/Nitrogen," *Z. Anorg. Chem.*, *259*, 121-134 (1949) in German. (Crys Structure; Experimental)
- *49Jon:** F.N. Jones and W.I. Pumphrey, "Free Energy and Metastable States in the Iron-Nickel and Iron-Manganese Systems," *J. Iron Steel Inst.*, *163*, 121-131 (1949). (Equi Diagram, Meta Phases; Experimental)
- 49Kub:** O. Kubaschewski and O. von Goldbeck, "The Thermodynamics of the Iron-Nickel Alloys," *Trans. Faraday Soc.*, *45*, 948-960 (1949). (Thermo; Experimental)
- *49Owe:** E.A. Owen and Y.H. Liu, "Further X-Ray Study of the Equilibrium Diagram of the Iron-Nickel System," *J. Iron Steel Inst.*, *123*, 132-136 (1949). (Equi Diagram; Experimental; #)
- *50Jos:** E. Josso, "Equilibrium Diagram for the Order to Disorder Transformation of Iron-Nickels near Ni₃Fe," *Compt. Rend.*, *230*, 1467-1469 (1950). (Equi Diagram; Experimental)
- 51Mac:** E.S. Machlin and M. Cohen, "Burst Phenomenon in the Martensitic Transformation," *Trans. AIME*, *191*, 746-754 (1951). (Meta Phases; Experimental)
- 51Smo:** R. Smoluchowski, "Statistical Properties of Solid Solutions," *Phys. Rev.*, *84*, 511-518 (1951). (Meta Phases; Theory)
- 51Suc:** W. Sucksmith, "Magnetic Saturation Intensity and Some Related Measurements," *J. Phys. Radium*, *12*, 430-436 (1951). (Magnetism; Experimental)
- 52Hun:** F. Hund, "Characterization of Nickel-Iron Alloy Powders at Low Temperature and Investigations of Lattice Changes," *Z. Elektrochem.*, *56*, 609-612 (1952) in German. (Equi Diagram; Experimental)
- 52Iid:** S. Iida, "Formation Energy of Superlattice for Ni₃Fe, (I) Cooperative Formation of Superlattice at the Critical Temperatures," *J. Phys. Soc. Jpn.*, *7*, 373-379 (1952). (Equi Diagram; Experimental)
- 53Boz1:** R.M. Bozorth and J.G. Walker, "Magnetic Crystal Anisotropy and Magnetostriction of Iron-Nickel Alloys," *Phys. Rev.*, *89*, 624-628 (1953). (Magnetism; Experimental)
- 53Boz2:** R.M. Bozorth, "The Permalloy Problem," *Rev. Mod. Phys.*, *25*, 42-48 (1953). (Magnetism; Experimental)
- *53Gei:** A.H. Geisler, "Written Discussion of [53Rhi]," *Trans. ASM*, *45*, 1051-1054 (1953). (Equi Diagram; Experimental)
- 53Ori:** R.A. Oriani, "Thermodynamic Activities in Iron-Nickel Alloys," *Acta Metall.*, *1*, 448-454 (1953). (Thermo; Experimental)
- *53Rhi:** F.N. Rhines and J.B. Newkirk, "The Order-Disorder Transformation Viewed as a Classical Phase Change," *Trans. ASM*, *45*, 1029-1046 (1953). (Equi Diagram; Theory)
- 53Wak:** R.J. Wakelin and E.L. Yates, "A Study of the Order-Disorder Transformation in Iron-Nickel Alloys in the Region FeNi₃," *Proc. Phys. Soc. (London) B*, *66*, 221-240 (1953). (Crys Structure, Magnetism; Experimental)
- 54Iid:** S. Iida, "Formation Energy of Superlattice in Ni₃Fe (II) Kinetics of the Superlattice in the Stage of Local Ordering," *J. Phys. Soc. Jpn.*, *9*, 346-354 (1954). (Equi Diagram; Experimental)
- 54Lih:** F. Lihl, "Phase Boundaries in the Iron-Nickel System at Temperatures Below 300 °C," *Arch. Eisenhüttenwes.*, *25*, 475-478 (1954) in German. (Crys Structure; Experimental)
- 54Mey:** M.R. Meyerson and S.J. Rosenberg, "The Influence of Heat Treating Variables on the Martensite Transformation in SAE 1050 Steel," *Trans. ASM*, *46*, 1225-1253 (1954). (Meta Phases; Experimental)
- 55Roy:** P. Royen and H. Reinhart, "The Influence of Alloying Iron with Gold, Silver, Copper, of Nickel on Iron Oxidation Equilibrium," *Z. Anorg. Chem.*, *281*, 18-36 (1955) in German. (Crys Structure; Experimental)
- 55Shu:** C.G. Shull and M.K. Wilkinson, "Neutron Diffraction Studies of the Magnetic Structure of Alloys of Transition Elements," *Phys. Rev.*, *97*, 304-310 (1955). (Magnetism; Experimental)
- 55Sut:** A.L. Sutton and W. Hume-Rothery, "The Lattice Spacings of Solid Solutions of Titanium, Vanadium, Chromium, Manganese, Cobalt and Nickel in Alpha-Iron," *Philos. Mag.*, *46*, 1295-1309 (1955). (Crys Structure; Experimental)
- 56Cec:** R.E. Cech, "Evidence for Solidification of a Metastable Phase in Fe-Ni Alloys," *Trans. AIME*, *206*, 585-589 (1956). (Meta Phases; Experimental)
- 56Kau:** L. Kaufman and M. Cohen, "The Martensitic Transformation in the Iron-Nickel System," *Trans. AIME*, *206*, 1393-1401 (1956). (Meta Phases; Experimental)
- 56Tino:** Y. Tino, "Possible Existence of Fe₃Ni," *Sci. Rep. Tohoku Imp. Univ.*, *40*, 17-23 (1956). (Meta Phases; Experimental)
- *57Hel:** A. Hellawell and W. Hume-Rothery, "The Constitution of Alloys of Iron and Manganese with Transition Elements of the First Long Period," *Philos. Trans. R. Soc. (London) A*, *249*, 417-459 (1957). (Equi Diagram, Thermo; Experimental)
- 57Lya:** B.G. Lyashchenko, D.F. Litvin, I.M. Puzei, and Yu.G. Abov, "Neutron Diffraction of Iron-Nickel Alloys of the Permalloy Class," *Kristallografiya*, *2*, 64-73 (1957) in Russian; TR: *Sov. Phys. Crystallogr.*, *2*, 59-67 (1957). (Equi Diagram; Experimental)
- 57Vit:** L.M. Viting, "Investigation of the Iron-Nickel-Cobalt System in the Region of the Metallic Compounds Ni₃Fe and FeCo," *Zh. Neorg. Khim.*, *2*, 367-374 (1957) in Russian; TR: *J. Inorg. Chem.*, *2*(2), 217-228 (1957). (Equi Diagram; Experimental)
- 58Kus:** A. Kussmann and K. Jessen, "Investigation of Atomic Ordering in Iron-Nickel-(Platinum) Alloys with Low Thermal Expansion,"

Section II: Phase Diagram Evaluations

- Arch. Eisenhüttenwes.*, 29, 585-594 (1958) in German. (Equi Diagram, Meta Phases; Experimental)
- 58Lyu:** A.P. Lyubimov, V.Ya. Zobens, and V.P. Rakhovskii, "A Mass Spectrometric Determination of the Thermodynamic Characteristics of Binary Metallic Systems," *Zh. Fiz. Khim.*, 32, 1804-1808 (1958) in Russian. (Thermo; Experimental)
- 58Pin:** B. Ya. Pines and I.P. Grebennils, "A New Crystalline Phase in Thin Films of Fe-Ni Alloys," *Kristallografiya*, 3¹, 461-466 (1958) in Russian; TR: *Sov. Phys. Crystallogr.*, 3, 460-464 (1958). (Meta Phases; Experimental)
- 59Ana:** N.I. Ananthanarayanan and R.J. Peavler, "Room Temperature Decomposition of Austenite in Fifty Percent Nickel-Fifty Percent Iron Magnetic Alloy Tapes," *J. Appl. Phys.*, 30, 202S-203S (1959). (Meta Phases; Experimental)
- 59Dek:** M.V. Dekhtyar and N.M. Kazantseva, "Structure Changes and Anomalous Temperature Dependence of the Magnetic Properties of Ni-Fe Alloys (50 Percent Ni)," *Fiz. Met. Metalloved.*, 8, 412-416 (1959) in Russian; TR: *Phys. Met. Metallogr.*, 8, 84-87 (1959). (Magnetism; Experimental)
- 59Sch:** F. Scheil and W. Normann, "Investigation of the Thermodynamics of the $\alpha \leftrightarrow \gamma$ Transformation in Iron-Nickel Alloys," *Arch. Eisenhüttenwes.*, 30, 751-754 (1959) in German. (Equi Diagram; Experimental)
- 59Spe:** R. Speiser, A.J. Jacobs, and J.W. Spertnak, "Activities of Iron and Nickel in Liquid Iron-Nickel Solutions," *Trans Metall. Soc. AIME*, 215, 185-192 (1959). (Thermo; Experimental)
- 59Zel:** G.R. Zellars, S.L. Payne, J.P. Morris, and R.L. Kipp, "The Activities of Iron and Nickel in Liquid Fe-Ni Alloys," *Trans. Metall. Soc. AIME*, 215, 181-185 (1959). (Thermo; Experimental)
- 60Kon:** E.J. Kondorski and V. Sedov, "Antiferromagnetism of Iron in Face-Centered Crystalline Lattice and the Causes of Anomalies in Invar Physical Properties," *J. Appl. Phys.*, 31, 331S-335S (1960). (Meta Phases; Experimental)
- 60Pau:** J. Paulene and D. Dautreppe, "Neutron Orientation Superstructure Created during Irradiation in a Magnetic Field of an Fe-Ni(50-50 Percent) Alloy," *Compt. Rend.*, 250, 3804-3806 (1960) in French. (Meta Phases; Experimental)
- 61Ana:** N.I. Ananthanarayanan and P.J. Peuler, "A New Reversible Solid State Transformation in Iron-Nickel Alloys in the Invar Range of Composition," *Nature*, 192, 962-963 (1961). (Meta Phases; Experimental)
- 61Ban:** Y. Bando, "The Formation of Superstructure in Fe₃Ni Fine Particles," *J. Phys. Soc. Jpn.*, 16, 2342-2343 (1961). (Meta Phases; Experimental)
- 61Gor:** V.I. Gorbunov, "Investigation of the Structure of Irreversible Alloys of the Iron-Nickel System," *Fiz. Met. Metalloved.*, 12, 78-83 (1961) in Russian; TR: *Phys. Met. Metallogr.*, 12(1), 68-72 (1961). (Magnetism; Experimental)
- 61Kau1:** L. Kaufman and A.E. Ringwood, "High Pressure Equilibria in the Iron-Nickel System and the Structure of Metallic Meteorite," *Acta Metall.*, 9, 941-944 (1961). (Pressure; Theory)
- 61Kau2:** L. Kaufman, A. Leyenaar, and J.S. Harvey, "The Effect of Hydrostatic Pressure on the F.C.C.-B.C.C. Reactions in Iron-Base Alloys," *Progress in Very High Pressure Research*, F. Bundy *et al.*, Eds., J. Wiley and Sons, New York, 90-108 (1961). (Pressure; Experimental)
- 61Ste:** W. Steiner and O. Krisement, "Heat of Formation of γ Iron-Nickel Alloys at 850 °C," *Arch. Eisenhüttenwes.*, 32, 701-707 (1961) in German. (Thermo; Experimental)
- 62Bre:** J.F. Breedis and C.M. Wayman, "The Martensitic Transformation in Fe-31 wt Pct Ni," *Trans. Metall. Soc. AIME*, 224, 1128-1133 (1962). (Meta Phases; Experimental)
- 62Col:** M.F. Collins, R.V. Jones, and R.D. Lawde, "On the Magnetic Moments and the Degree of Order in Iron-Nickel Alloys," *J. Phys. Soc. Jpn.*, 17, Supplement B-III, Proc. Int. Conf. on Magn. and Crys., Kyoto, Sep 25-30, 19-26 (1962). (Magnetism; Experimental)
- *62Gil:** A. Gilbert and W.S. Owen, "Diffusionless Transformation in Iron-Nickel, Iron-Chromium and Iron-Silicon Alloys," *Acta Metall.*, 10, 45-54 (1962). (Meta Phases; Experimental)
- 62Kac:** S. Kachi, Y. Bando, and S. Higuchi, "The Phase Transformations of Iron-Rich Iron-Nickel Alloy in Fine Particles," *Jpn. J. Appl. Phys.*, 1, 307-313 (1962). (Equi Diagram; Experimental)
- 62Pau1:** J. Pauleve, D. Dautreppe, J. Laugier, and L. Neel, "A New Order-Disorder Transition in Fe-Ni (50-50)," *J. Phys. Radium*, 23, 841-843 (1962) in French. (Meta Phases; Experimental)
- 62Pau2:** J. Pauleve, D. Dautreppe, J. Laugier, and L. Neel, "Establishment of an Ordered Structure in FeNi by Irradiation with Neutrons," *Compt. Rend.*, 254, 965-968 (1962) in French. (Meta Phases; Experimental)
- 62Yeo:** R.B.C. Yeo, "Isothermal Martensite Transformation in Iron Base Alloys of Low Carbon Content," *Trans. Metall. Soc. AIME*, 224, 1222-1227 (1962). (Meta Phases; Experimental)
- 63Cra:** J. Crangle and G.C. Hallam, "The Magnetization of Face-Centered-Cubic and Body-Centered-Cubic Iron and Nickel Alloys," *Proc. R. Soc. (London) A*, 272, 119-132 (1963). (Magnetism; Experimental)
- 63Dav:** R.G. Davies and N.S. Stoloff, "Order and domain Hardening in Cu₃Au Type Superlattice Alloys," *Acta Metall.*, 11, 1347-1353 (1963). (Equi Diagram, Crys Structure; Experimental)
- 63Den:** W.A. Dench, "Adiabatic High-Temperature Calorimeter for the Measurements of Heats of Alloys," *Trans. Faraday Soc.*, 59, 1279-1292 (1963). (Thermo; Experimental)
- 63Gol:** A.J. Goldman and C.N.J. Wagner, "Faulting in Deformed Austenite and Martensite," *Acta Metall.*, 11, 405-413 (1963). (Meta Phases; Experimental)
- *63Heu:** T. Heumann and G. Karsten, "Carbonyl Vapor Method for Determination of Phase Equilibria in the Low Mobility Temperature Range Applied to Iron-Nickel Alloys," *Arch. Eisenhüttenwes.*, 34, 781-785 (1963). (Equi Diagram, Meta Phases; Experimental; #)
- 63Mar:** A. Marchand, J. Pauleve, and D. Dautreppe, "Resistivity of and FeNi (50-50 Percent) Alloy Ordered by Irradiation with Neutrons," *Compt. Rend.*, 257, 2987-2989 (1963) in French. (Meta Phases; Experimental)
- 63Tre:** R.G. Treuting and B.W. Batterman, "A Diffractometer Study of Long-Range Ordering in Ni₃Fe and Associated Permalloys," *J. Appl. Phys.*, 34, 2005-2006 (1963). (Equi Diagram; Experimental)
- 63Wei:** R.J. Weiss, "The Origin of the Invar Effect," *Proc. Phys. Soc. (London)*, 82, 281-288 (1963). (Magnetism; Theory)
- 63Yeo:** R.B.G. Yeo, "The Effect of Alloying Elements on the Transformation of Fe-22.5 Pct Ni Alloys," *Trans Metall. Soc. AIME*, 227, 884-890 (1963). (Meta Phases; Experimental)
- 64Ban:** Y. Bando, "The Magnetization of Face Centered Cubic Iron-Nickel Alloys in the Vicinity of Invar Region," *J. Phys. Soc. Jpn.*, 19, 237 (1964). (Meta Phases, Magnetism; Experimental)
- 64Gup:** K.P. Gupta, C.H. Cheng, and P.A. Beck, "Low Temperature Specific Heat of F.C.C. Alloys of the 3d-Transition Elements," *J. Phys. Chem. Solids*, 25, 73-83 (1964). (Thermo; Experimental)
- 64Hum:** W. Hume-Rothery and R.A. Buckley, "Liquidus \leftrightarrow Solidus Relations in Iron Alloys: Ideal Solutions," *J. Iron Steel Inst.*, 202, 531-533 (1964). (Equi Diagram; Theory)
- 64Nee:** L. Neel, J. Paulene, R. Pauthenet, J. Laugier, and D. Dautreppe, "Magnetic Properties of an Iron-Nickel Single Crystal Ordered by Neutron Bombardment," *J. Appl. Phys.*, 35, 873-876 (1964). (Meta Phases, Magnetism; Experimental)

- 64Roe:** G. A. Roeder and W. W. Smeltzer, "The Dissociation Pressures of Iron-Nickel Alloys," *J. Electrochem. Soc.*, *111*, 1074-1078 (1964). (Thermo; Experimental)
- 64Sch:** A. D. Schindler and C. M. Williams, "Investigations of the Effects of Neutron and He(3) Irradiation on the Magnetic Properties of Permalloy Thin Films," *J. Appl. Phys.*, *35*, 877-879 (1964). (Magnetism; Experimental)
- 65Ehr:** R. Ehrat and D. Rivier, "Low Temperature Specific Heats of Dilute Nickel Alloys," *Helv. Phys. Acta*, *38*, 643-645 (1965) in French. (Thermo; Experimental)
- *65Gol:** J. I. Goldstein and R. E. Ogilvie, "A Re-Evaluation of the Iron-Rich Portion of the Fe-Ni System," *Trans. Metall. Soc. AIME*, *223*, 2083-2087 (1965). (Equi Diagram; Experimental)
- 65Gon:** V. I. Gonamkov, I. M. Puzei, and A. A. Loshmanov, "A Study of Superlattice Structure in Ni₃Fe," *Kristallografiya*, *10*, 416-418 (1965) in Russian; TR: *Sov. Phys. Crystallogr.*, *10*, 338-340 (1965). (Equi Diagram; Experimental)
- 65Pea:** W. B. Pearson, "Handbook of Lattice Spacings and Structures of Metals-2," International Series of Monographs in Metal Physics and Physical Metallurgy, Volume 8, G. V. Raynov Ed., National Research Council, Ottawa, 1965.
- 66Abr:** E. P. Abrahamson II and S. L. Lopata, "The Lattice Parameters and Solubility Limits of Alpha Iron as Affected by Some Binary Transition-Element Additions," *Trans. Metall. Soc. AIME*, *236*, 76-87 (1966). (Crys Structure; Experimental)
- 66Elk:** A. El-Khasan, K. Abdel-Aziz, A. A. Vertman, and A. M. Samarin, "Thermochemistry of Molten Nickel or Iron Alloys," *Izv. Akad. Nauk SSSR, Met.*, (3), 19-31 (1966) in Russian; TR: *Russ. Metall.*, (3), 10-16 (1966). (Thermo; Experimental)
- 66Hum:** W. Hume-Rothery, *The Structures of Alloys of Iron*, Pergamon Press, New York, NY, 121 (1966). (Meta Phases; Review)
- 66Kat:** T. Z. Kattamis and M. C. Flemings, "Dendrite Structure and Grain Size of Undercooled Melts," *Trans. Metall. Soc. AIME*, *236*, 1523-1532 (1966). (Meta Phases; Experimental)
- 66Mcq:** R. G. McQueen and S. P. Marsh, "Shock Wave Compression of Iron-Nickel Alloys and the Earth's Core," *J. Geophys. Res.*, *71*, 1751-1756 (1966). (Pressure; Experimental)
- 66Oni:** M. Onillon and M. Olette, "Determination of the Thermodynamic Functions for Dilute Solutions of Nickel in Liquid Iron," *C. R. Acad. Sci. (Paris) C*, *263*, 1122-1125 (1966) in French. (Thermo; Experimental)
- 66Shi:** S. S. Shinozaki and A. Arrott, "Electronic Specific Heat of Dilute Alloys: Fe(Ti), Fe(V), Fe(Cr), Fe(Mn), Fe(Co), Fe(Ni), Fe(Al), Fe(Si), Fe(Mo), Fe(W), and Ag(Au)," *Phys. Rev.*, *152*, 611-622 (1966). (Thermo; Experimental)
- 67Bel:** G. R. Belton and R. J. Fruehman, "The Determination of Activities by Mass Spectroscopy. I. The Liquid Metallic Systems Iron-Nickel and Iron Cobalt," *J. Phys. Chem.*, *71*, 1403-1409 (1967). (Thermo; Experimental)
- 67Hil:** M. Hillert, T. Wade, and H. Wada, "The Alpha-Gamma Equilibrium in Fe-Mn, Fe-Mo, Fe-Ni, Fe-Sb, Fe-Sn and Fe-W Systems," *J. Iron Steel Inst.*, 539-546 (1967). (Equi Diagram; Theory)
- 67Kub:** O. Kubaschewski and L. E. H. Stuart, "Heats of Formation and Heat Capacities in the System Iron-Nickel-Chromium," *J. Chem. Eng. Data*, *12*, 418-420 (1967). (Thermo; Experimental)
- 67Rob:** M. J. Roberts and W. S. Owen, "The Strength of Martensitic Iron-Nickel Alloys," *Trans. ASM*, *60*, 687-692 (1967). (Meta Phases; Experimental)
- 68Kou:** J. S. Kouvel and J. B. Comly, "Magnetic Equation of State for Nickel Near its Curie Point," *Phys. Rev. Lett.*, *20*, 1237-1239 (1968). (Magnetism; Experimental)
- 68Tak:** T. Takahashi, W. A. Bassett, and H. K. Mao, "Isothermal Compression of the Alloys of Iron up to 300 Kilobars at Room Temperature: Iron-Nickel Alloys," *J. Geophys. Res.*, *73*, 4717-4725 (1968). (Pressure; Experimental)
- 69Asa:** H. Asano, "Magnetism of Gamma Fe-Ni Invar Alloys with Low Nickel Concentration," *J. Phys. Soc. Jpn.*, *27*(3), 542-533 (1969). (Crys Structure, Magnetism; Experimental)
- 69Kus:** M. T. Kusho, V. F. Balakirev, R. Yu. Dobrovinskii, G. M. Popov, A. N. Men, and G. I. Chufarov, "The Activities of the Components of Solid Solutions in the System Nickel-Iron-Oxygen," *Zh. Fiz. Khim.*, *43*, 3095-3098 (1969) in Russian; TR: *Russ. J. Phys. Chem.*, *43*, 1739-1740 (1969). (Thermo; Experimental)
- 69Ree:** R. P. Reed and R. E. Schramm, "Lattice Parameters of Martensite and Austenite in Fe-Ni Alloys," *J. Appl. Phys.*, *40*, 3453-3458 (1969). (Crys Structure; Experimental)
- 69Sta:** R. E. Staub and J. L. McCall, "Metallographic Studies of an Iron-Nickel Meteorite Following Long-Time Heat Treatments," Proc. of the 2nd Annual Technical Meeting, Sept. 8-10, 1969 San Francisco International Metallographic Society, 337-344 (1969). (Equi Diagram; Experimental)
- 70Gat:** C. Gatellier, D. Henriot, and M. Olette, "Determination of the Thermodynamic Activities of the Constituents of Solid Fe-Ni Alloys by the Electrochemical Method," *Compt. Rend.*, *271*, 453-460 (1970) in French. (Thermo; Experimental)
- 70Gro:** Y. Grosand and J. J. Pauleve, "Mössbauer Effect Study of Order in a 50-50 Fe-Ni Alloy Irradiated by Neutrons or Electrons," *J. Phys.*, *31*, 459-470 (1970) in French. (Meta Phases; Experimental)
- 70Pre1:** B. Predel and R. Mohs, "Thermodynamic Investigations of the Fe-Ni and Fe-Co Systems," *Arch. Eisenhüttenwes.*, *41*, 143-149 (1970) in German. (Thermo; Experimental)
- 70Pre2:** B. Predel and R. Mohs, "A New High Temperature Calorimeter and its Application to the Determination of the Mixing Enthalpy of Liquid Cobalt-Nickel Alloys," *Arch. Eisenhüttenwes.*, *41*, 61-66 (1970) in German. (Thermo; Experimental)
- 71Geo:** I. Y. Georgiyeva and O. P. Maksimora, "On the Interrelation Between Kinetics and Structure During Martensitic Transformations," *Fiz. Met. Metalloved.*, *32*, 364-376 (1971) in Russian; TR: *Phys. Met. Metallogr.*, *32*(2), 135-146 (1971). (Meta Phases; Experimental)
- 71Hau:** G. Hausch and H. Warlimont, "Structural Inhomogeneity in Fe-Ni Invar Alloys Studied by Electron Diffraction," *Phys. Lett. A*, *36*, 415-416 (1971). (Meta Phases; Experimental)
- 71Spe:** P. J. Spencer, F. H. Hayes, and L. Elford, "Relationships Between Binary and Ternary Properties: A Calorimetric Investigation of the Fe-Co-Ni System," in Chemical Metallurgy of Iron and Steel, Proc. Int. Symp., London, 1971, The Iron and Steel Institute, 322-326 (1973). (Thermo; Experimental)
- 71Toz:** Y. Tozaki, Y. I. Iguchi, S. Ban-ya, and T. Fuwa, "Heat of Mixing of Iron Alloys," in Chemical Metallurgy of Iron and Steel, Proc. Int. Symp., London, 1971, The Iron and Steel Institute, 130-132 (1973). (Thermo; Experimental)
- 71Tse:** L. Sh. Tsemekhman, S. E. Vaisburd, and Z. F. Shirokova, "Activities in Iron-Nickel, Iron-Cobalt, and Nickel-Cobalt Binary Melts," *Zh. Fiz. Khim.*, *45*, 2074-2077 (1971) in Russian; TR: *Russ. J. Phys. Chem.*, *45*, 1176-1177 (1971). (Thermo; Experimental)
- 72Cal:** Y. Calvayrac and M. Fayard, "Behavior of Iron-Nickel Alloys Around the Composition 75-25 in the Neighborhood of the Order-Disorder Transformation Temperature," *Mater. Res. Bull.*, *7*, 891-901 (1972) in French. (Equi Diagram; Experimental)
- 72Dav:** H. Davies and W. W. Smeltzer, "Oxygen and Metal Activities of the Iron-Nickel-Oxygen System at 1000 °C," *J. Electrochem. Soc.*, *19*, 1362-1368 (1972). (Thermo; Experimental)

Section II: Phase Diagram Evaluations

- 72Mil:** K.C. Mills, K. Kinoshita, and P. Grieson, "A Thermodynamic Study of Liquid Iron and Nickel Alloys Using Electromagnetic Levitation," *J. Chem. Thermodyn.*, **4**, 581-590 (1972). (Thermo; Experimental)
- 72Wei:** R.J. Weiss, "The Invar Effect," *Philos. Mag.*, **26**(1), 261-263 (1972). (Meta Phases; Theory)
- 73Cab:** J.W. Cable and E.O. Wollan, "Magnetic Moment Distribution in NiFe and AuFe Alloys," *Phys. Rev. B*, **7**, 2005-2016 (1973). (Magnetism; Experimental)
- 73Cal:** Y. Calvayrac and M. Fayard, "Structural State and Mechanical Properties of Polycrystalline Ni₃Fe Alloys," *Phys. Status Solidi (a)*, **17**, 407-421 (1973). (Equi Diagram; Experimental)
- 73Kau:** L. Kaufman and H. Nesor, "Calculation of the Binary Phase Diagrams of Iron, Chromium, Nickel and Cobalt," *Z. Metallkd.*, **64**, 249-257 (1973). (Thermo; Experimental)
- 73Kol:** T.G. Kollie and C.R. Brooks, "The Heat Capacity of Ni₃Fe," *Phys. Status Solidi (a)*, **19**, 545 (1973). (Thermo; Experimental)
- 73Miz:** T. Mizoguchi, K. Yamauchi, and H. Miyajima, "Ferromagnetism of Amorphous Iron Alloys," in *Amorphous Magnetism*, H.O. Hooper and A.M. deGraaf, Ed., Plenum Press, 325-330 (1973). (Meta Phases, Magnetism; Experimental)
- 73Sch:** W.F. Schlosser, "Thermodynamics of an Invar Alloy," *Int. J. Magn.*, **4**, 49-55 (1973). (Thermo; Theory)
- 74Bas:** M.I. Baskes, "Phase Stability of Iron Alloys," *Mater. Sci. Eng.*, **15**, 195-202 (1974). (Thermo; Theory; #)
- 74Bat:** G.I. Batalin, N.N. Mineko, and V.S. Sundavtsova, "Enthalpy of Mixing and Thermodynamic Properties of Liquid Alloys of Iron with Manganese, Cobalt, and Nickel," *Izv. Akad. Nauk SSSR, Met.*, **(5)**, 99-104 (1974) in Russian; TR: *Russ. Metall.*, **(5)**, 82-86 (1974). (Thermo; Experimental)
- 74Gol:** N.S. Golosov and B.V. Dudka, "Computer Modeling of the Order-Disorder Transformation in Cu₃Au and Ni₃Fe," *Phys. Status Solidi (b)*, **66**, 439-448 (1974). (Meta Phases; Theory)
- 74Ind:** G. Inden, "Ordering and Segregation Reactions in B.C.C. Binary Alloys," *Acta Metall.*, **22**, 945-951 (1974). (Thermo; Theory)
- 74Nis:** M. Nishi, Y. Nakai, and N. Kunitomi, "Magnetic Moments in Fe-Ni Alloys," *J. Phys. Soc. Jpn.*, **37**, 570 (1974). (Magnetism; Experimental)
- 74Rao:** M.V. Rao and W.A. Tiller, "The Systems Fe-Cr and Fe-Ni: Thermochemistry and Phase Equilibria," *Mater. Sci. Eng.*, **14**, 47-54 (1974). (Thermo; Theory; #)
- 74Ume:** M. Umemoto and W.S. Owen, "Effects of Austenitizing Temperature and Austenite Grain Size on the Formation of Athermal Martensite in an Iron-Nickel-Carbon Alloy," *Metall. Trans.*, **5**, 2041-2046 (1974). (Meta Phases; Experimental)
- 74Vre:** J. Vrestal, A. Pokorna, and K. Stransky, "Determination of Thermodynamic Activities of Components in the Iron-Nickel System at T = 1509 K," *Kovové Mater.*, **1**, 3-9 (Thermo; Experimental)
- 75Bil:** L. Billard and A. Chamberod, "On the Dissymmetry of Mössbauer Spectra in Iron-Nickel Alloys," *Solid State Commun.*, **17**, 113-118 (1975). (Equi Diagram; Experimental)
- 75Ind:** G. Inden, "Determination of Chemical and Magnetic Interchange Energies in BCC Alloys," *Z. Metallkd.*, **66**, 577-582 (1975). (Magnetism; Theory)
- 75Leb:** M. Lebienvue and B. Dubois, "Study of the Order-Disorder Transformation in Ni₃Fe by Measurement of Internal Friction," *C.R. Acad. Sci. (Paris) C*, **280**, 1251-1253 (1975) in French. (Equi Diagram; Experimental)
- 75Tri:** C.C. Trinel-Dufour and M.P. Perrot, "Activities of the Constituents of Fe-Ni Alloys Determined by Equilibrium Measurements in the Presence of an Oxide Phase," *C.R. Acad. Sci. (Paris) C*, **281**, 589-592 (1975) in French. (Thermo; Experimental)
- 76Dal:** A.D. Dalvi and R. Sridhar, "Thermodynamics of the Fe-Ni-O and Fe-Ni Systems at 1065 K to 1380 K," *Can Metall. Q.*, **15**(4), 349-357 (1976). (Thermo; Experimental)
- 76Rob:** D. Robinson and B.B. Argent, "Thermodynamics of Dilute Solutions of the First-Period Transition Elements in Iron," *Met. Sci.*, **10**, 219-221 (1976). (Thermo; Experimental)
- 76Ino:** Y. Inokuti and B. Cantor, "Splat-Quenched Fe-Ni Alloys," *Scr. Metall.*, **10**, 655-659 (1976). (Meta Phases; Experimental)
- 77Gri:** E.J. Grimsey and A.K. Biswas, "The Activity of Iron in Low-Iron Liquid (Ni+Au+Fe) and Solid (Ni+Fe) Alloys at 1573 K," *J. Chem. Thermodyn.*, **9**, 415-422 (1977). (Thermo; Experimental)
- 77Has:** M. Hasebe and T. Nishizawa, "Analysis and Synthesis of Phase Diagrams of the Fe-Cr-Ni, Fe-Cu-Mn and Fe-Cu-Ni Systems," *Applications of Phase Diagrams in Metallurgy and Ceramics*, Nat. Bur. Stds. SP-496, U.S. Govt. Printing Office, Washington, DC, 1977. (Thermo; Experimental)
- 77Hut:** H. Huthmann, "Factors Influencing Chemical and Magnetic Ordering Transformations in F.C.C. Iron-Nickel Alloys," thesis, Tech. Univ., Aachen (1977) in German. (Equi Diagram, Thermo; Experimental)
- *77Kub:** O. Kubaschewski, K.H. Geiger, and K. Hack, "The Thermochemical Properties of Iron-Nickel Alloys," *Z. Metallkd.*, **68**, 337-341 (1977) in German. (Thermo; Experimental)
- 77Lar:** L.N. Larikov and Y.V. Vsov, "Thermal Properties of Fe-Ni Alloys," *Akad. Nauk Ukr. SSR, Metallofiz.*, **68**, 3-14 (1977) in Russian. (Thermo; Theory; #)
- 77Mio:** A.P. Miodownik, "The Calculation of Magnetic Contributions to Phase Stability," *Calphad*, **1**, 133-158 (1977). (Magnetism; Theory)
- 77Ono:** K. Ono, Y. Veda, Y. Yamaguchi, and J. Moriyama, "Thermodynamic Study of Fe-Ni Solid Solution," *Trans. Jpn. Inst. Met.*, **18**, 610-616 (1977). (Thermo; Experimental)
- 77Pet:** J.F. Petersen, A. Aydin, and J.M. Knudsen, "Mössbauer Spectroscopy of an Ordered Phase (Superstructure) of FeNi in an Iron Meteorite," *Phys. Lett. A*, **62**, 192-194 (1977). (Meta Phases; Experimental)
- 77Roit:** A.L. Roitburd, "Predominant Effect of the Internal Stress Relaxation on Microstructural and Kinetic Features of Martensitic Transformation," *Phys. Status Solidi (a)*, **40**, 333-342 (1977). (Meta Phases; Experimental)
- 78Alb1:** J.F. Albertsen, G.B. Jensen, and J.M. Knudsen, "Structure of Taenite in Two Meteorites," *Nature*, **273**, 453-454 (1978). (Meta Phases; Experimental)
- 78Alb2:** J.F. Albertsen, M. Aydin, and J.M. Knudsen, "Mössbauer Effect Studies of Taenite Lamelle of Iron Meteorite Cape York (III.A)," *Phys. Scr.*, **17**, 467-472 (1978). (Meta Phases; Experimental)
- 78Cha:** A. Chamberod, M. Roth, and L. Billard, "Small Angle Scattering in Invar Alloys," *J. Magn. Magn. Mater.*, **7**, 101-103 (1978). (Meta Phases; Experimental)
- 78Con:** B.R. Conrad, T.S. McAneney, and R. Sridhan, "Thermodynamics of Iron-Nickel Alloys by Mass Spectroscopy," *Metall. Trans. B*, **9**, 463-468 (1978). (Meta Phases, Thermo; Experimental)
- 78Gal:** G. Galeczki and A.A. Hirsch, "Gamma Phase Dispersions in Fe-Ni Alloys Below the Critical Concentration," *J. Magn. Magn. Mater.*, **7**, 110-112 (1978). (Meta Phases; Experimental)
- 78Hil:** M. Hillert, "Prediction of Iron-Base Diagram," in *Hardenability Concepts with Applications to Steel*, TMS-AIME, Warrendale, Pa, 5-27 (1978). (Thermo; Theory)
- 78Kat:** A. Katsuki, "Physics and Applications of Invar Alloys," Honda Memorial Series on Materials Science No. 3 (1978). (Meta Phases, Thermo, Magnetism; Review)
- 78Mar:** N. Maruyama and S. Ban-ya, "Measurements of Activities in Liquid Fe-Ni, Fe-Co, and Ni-Co Alloys by a Transportation Method,"

- J. Inst. Met. Jpn.*, 42, 992-999 (1978) in Japanese. (Thermo; Experimental)
- 79Agr:** J. Agren, "A Thermodynamic Analysis of the Fe-C and Fe-Ni Phase Diagram," *Metall. Trans. A*, 10, 1847-1852 (1979). (Thermo; Theory)
- 79Bos:** O. Bostanjoglo, U. Heinecke, and R. Liedtke, "Possible Stabilization of Amorphous FeNi Films by Conduction Electrons," *Phys. Status Solidi (a)*, 56, 569-572 (1979). (Meta Phases; Experimental)
- 79Cha:** A. Chamberod, J. Laugier, and J.M. Penisson, "Electron Irradiation Effects on Iron-Nickel Invar Alloys," *J. Magn. Magn. Mater.*, 10, 139-144 (1979). (Meta Phases; Experimental; #)
- 79Des:** M.C. Desjonqueres and M. Lavanga, "Effects of Order on the Electronic Structure of Ferromagnetic Transition Metal Alloys: Application to FeCo and Ni₃Fe," *J. Phys. F, Met. Phys.*, 9, 1733-1743 (1979). (Equi Diagram; Experimental)
- 79Lar:** J.M. Larrain and H.H. Kellogg, "Use of Chemical Species for Correlation of Solution Properties," in *Calculation of Phase Diagrams and Thermochemistry of Alloy Phases*, TMS-AIME, Warrendale, PA, 130-144 (1979). (Thermo; Theory; #)
- 79Lin:** L.S. Lin, J.I. Goldstein, and D.B. Williams, "Analytical Electron Microscopy Study of the Plessite Structure in Four III CD Iron Meteorites," *Geochim. Cosmochim. Acta*, 43, 725-737 (1979). (Meta Phases; Experimental)
- 79Mat:** M. Matsui and K. Adachi, "Low Temperature Structure of Fe-Ni Alloys," *J. Magn. Magn. Mater.*, 10, 152-154 (1979). (Meta Phases; Experimental)
- 79Sco:** E.R.D. Scott and R.S. Clarke, "Identification of Clear Taenite in Meteorites as Ordered FeNi," *Nature*, 281, 360-362 (1979). (Meta Phases; Experimental)
- 79Shi:** M. Shimizu, "Origin of the Anomalies and Thermodynamic Aspects of Iron-Nickel Invar Alloys," *J. Magn. Magn. Mater.*, 10, 231-235 (1979). (Meta Phases; Theory)
- 79Tan:** Y. Tanji, Y. Nakagawa, Y. Saito, K. Nishimura, and K. Nakatzuka, "Anomalous Thermodynamic Properties of Iron-Nickel (F.C.C.) Alloys," *Phys. Status Solidi (a)*, 56, 513-519 (1979). (Thermo; Experimental)
- 80Lar:** J.M. Larrain, "High Temperature Thermodynamic Properties of Iron-Nickel Alloys," *Calphad*, 4, 155-171 (1980). (Thermo; Theory; #)
- 80Meh:** S. Mehta, P.M. Novotny, D.B. Williams, and J.I. Goldstein, "Electron-Optical Observations of Ordered Fe-Ni in the Estherville Meteorite," *Nature*, 284, 151-153 (1980). (Meta Phases; Experimental)
- 80Rom:** A.D. Romig and J.I. Goldstein, "Determination of the Fe-Ni and Fe-Ni-P Phase Diagrams at Low Temperatures (700 to 300 °C)," *Metall. Trans. A*, 11, 1151-1159 (1980). (Equi Diagram; Experimental)
- 80Van:** J.K. Van Deen and F. Van der Woude, "Phase Diagram of the Order-Disorder Transition in Ni₃Fe," *J. Phys.*, 41, C1-367-C1-368 (1980). (Equi Diagram; Experimental)
- 81Bor:** G. Bordin, G.C. Cecchi, and G.B. Fratucello, "Remarks on the Martensitic Transformation in Some Iron-Nickel Alloys," *Nuovo Cimento B*, 61, 338-346 (1981). (Meta Phases; Experimental)
- 81Igu:** Y. Iguchi, Y. Tozaki, M. Kakizaki, T. Fuwa, and S. Ban-ya, "A Calorimetric Study of Heat of Mixing of Liquid Iron Alloys," *J. Iron Steel Inst. Jpn.*, 67, 925-932 (1981) in Japanese. (Thermo; Experimental)
- 81Imr:** G. Imrich-Swartz and H. Gamsjager, "Computer-Supported Evaluation of the Gibbs-Duhem Equation," *Ber. Hüttenmänn. Monatsh.*, 126, 275-277 (1981) in German. (Thermo; Theory)
- 81LeF:** S. Lefebvre, F. Bleu, M. Fayard, and M. Roth, "Neutron Diffuse Scattering Investigation of Different States of Local Order in ⁶²Ni_{0.765}Fe_{0.235}," *Acta Metall.*, 29, 749-761 (1981). (Equi Diagram; Experimental)
- 81Nis:** T. Nishizawa and M. Hasebe, "Computer Calculation of Phase Diagrams of Iron Alloys," *J. Iron Steel Inst. Jpn.*, 67, 2086-2097 (1981) in Japanese. (Thermo; Theory; #)
- 81Ram:** W. Rammensee and D.G. Fraser, "Activities in Solid and Liquid Fe-Ni and Fe-Co Alloys Determined by Knudsen Cell Mass Spectrometry," *Ber. Bunsenges. Phys. Chem.*, 85, 558-592 (1981). (Thermo; Experimental)
- 81Sun:** B. Sundman, "A Computer Program for Optimizing Parameters in Thermodynamic Model," R. Inst. Stockholm, Sweden, Rep. D28 (1981). (Thermo; Theory)
- *81Van:** J.K. Van Deen and F. Van der Woude, "Phase Diagram of the Order-Disorder Transition in Ni₃Fe," *Acta Metall.*, 29, 1255-1262 (1981). (Equi Diagram; Experimental)
- 82Bro1:** P.J. Brofman and G.S. Asell, "On The Morphology of Martensite in Fe-27 Ni Alloys," Proc. Int. Conf. on Solid-Solid Phase Transformations, TMS-AIME, Warrendale, PA, 1373-1377 (1982). (Meta Phases; Experimental)
- 82Bro2:** C.R. Brooks, P.J. Meschter, and T.G. Kollie, "The Magnetic Heat Capacity of the Configurationally Disordered Ni-25 at% Fe Alloy," *Phys. Status Solidi (a)*, 73, 189-198 (1982). (Thermo; Experimental)
- *82Cha:** T.G. Chart, D.D. Gohil, and Z.S. Xing, "Calculated Phase Equilibria for the Cu-Ni-Fe System," NPL Rep. DMA(A) 54, National Physical Laboratory, Middlesex, UK, Aug (1982). (Thermo; Theory; #)
- 82Duf:** F. Duflos and B. Cantor, "The Microstructure and Kinetics of Martensite Transformation in Splat-Quenched Fe and Fe-Ni Alloys-I. Pure Fe," *Acta Metall.*, 30, 323-342 (1982). (Meta Phases; Experimental)
- 82Gol:** J.I. Goldstein and D.B. Williams, "Low Temperature Phase Transformations in the Metallic Phases of Meteorites," Proc. Int. Conf. on Solid-Solid Phase Transformations, TMS-AIME, Warrendale, PA, 715-719 (1982). (Meta Phases; Experimental)
- 82Jag:** R.A. Jago, P.E. Clark, and P.L. Rossiter, "The Santa Catharina Meteorite and the Equilibrium State of Fe-Ni Alloys," *Phys. Status Solidi (a)*, 74, 247-254 (1982). (Meta Phases; Experimental)
- 82Kub:** O. Kubaschewski, *Iron Binary Phase Diagrams*, Springer-Verlag, New York, NY, 73-78 (1982). (Equi Diagram; Review)
- 82Ore:** J. Orehotsky, J.B. Sousa, and M.F. Pinheiro, "Critical Behavior in Ni₃Fe and Ni₃Mn," *J. Appl. Phys.*, 53, 7939-7941 (1982). (Equi Diagram, Magnetism; Experimental)
- 82Ray:** J.J. Rayment, O. Ashira, and B. Cantor, "The As-Quenched Microstructure of Rapidly Solidified Fe-25 wt.% Ni," Proc. Int. Conf. Solid-Solid Phase Transformations, TMS-AIME, Warrendale, PA, 1385-1389 (1982). (Meta Phases; Experimental)
- 82Rhy:** J.J. Rhyne, "Magnetic Transition Temperatures of the Elements," *Bull. Alloy Phase Diagrams*, 3, 402 (1982). (Magnetism; Review)
- 82Rod:** A. Rodrigues, C. Prioul, J. Plusquellec, and P.Y. Azou, "The Effects of Carbon and Time-Related Parameters on the Reheat Martensite Transformations in Fe-Ni-C Alloys at Subzero Temperatures," Proc. Int. Conf. Solid-Solid Phase Transformations, TMS-AIME, Warrendale, PA 1391-1395 (1982). (Meta Phases; Experimental)
- 82Vel:** J. Velisek, "Correlation of Selected Thermodynamic and Phase Data in the Fe-Ni System," *Kovové Mater.*, 20, 257-265 (1982). (Thermo; Theory; #)

Section II: Phase Diagram Evaluations

- 83Abb:** G.J. Abbaschian and M.C. Flemings, "Supercooling and Structure of Levitation Melted Fe-Ni Alloys," *Metall. Trans. A*, *14*, 1147-1157 (1983). (Meta Phases; Experimental)
- 83Kam:** D.S. Kamenetskaya, O.P. Maksimora, and V.I. Shirayev, "Features of the Martensite Transformation in High Purity Iron-Nickel Alloys," *Fiz. Met. Metalloved.*, *55*(5), 967-972 (1983) in Russian; TR: *Phys. Met. Metallogr.*, *55*(5), 121-127 (1983). (Meta Phases; Experimental)
- 83Sen:** A. Sen Gupta and B.K. Banarjee, "High Temperature X-ray Study of Some Iron-Nickel Alloys," *Indian J. Phys. A*, *57*, 196-199 (1983). (Crys Structure; Experimental)
- 84Bor:** G. Bordin, G.C. Cecchi, and I. Montanari, "Some Transport Properties in Martensitic Iron—Nickel Alloys," *Nuovo Cimento D*, *3*(2), 436-446 (1984). (Meta Phases; Experimental)
- 84Cen:** P. Cenedese, F. Bley, and S. Lefebvre, "Atomic Short Range Order in a Fe-Ni Invar Alloy," *Phase Transformations in Solids*, Mater. Res. Symp. Proc., T. Tsakalakos, Ed., North-Holland, New York, 351-353 (1984). (Meta Phases; Experimental)
- 84Des:** P.D. Desai and M.S. Desphande, "Thermodynamic Properties of Nickel," CINDAS Rep. 80, Purdue University, Lafayette, IN, Aug (1984). (Thermo; Review)
- 84Gor:** A.M. Gorovol, A.I. Ushakov, V.G. Kazakov, Yu.L. Raodionov, and V.N. Goloborod'ko, "The Approach to the Equilibrium State in Films of Iron—Nickel Alloys," *Fiz. Met. Metalloved.*, *58*(1), 113-118 (1984) in Russian. (Meta Phases; Experimental)
- 84Izm:** E.A. Izmailov, "The Transformation of Martensite into Austenite in Iron-Nickel Alloys," *Fiz. Met. Metalloved.*, *58*(1), 39-97 (1984). (Meta Phases; Experimental)
- 84Lef:** S. Lefebvre, F. Bley, and P. Cenedese, "Determination of Short Range Order Parameters in $^{62}\text{Ni}_{0.765}\text{Fe}_{0.235}$ at 600 °C Effect of a Quench," *Phase Transformations in Solids*, Mater. Res. Symp. Proc., T. Tsakalakos, Ed., North-Holland, New York, 351-353 (1984). (Equi Diagram; Experimental)
- 84Miu:** H. Miura, S. Isa, K. Omuro, "Production of Amorphous Iron—Nickel Based Alloys by Flame-Spray Quenching and Coatings on Metal Substrates," *Trans. Jpn. Inst. Met.*, *25*(4), 284-291 (1984). (Meta Phases; Experimental)
- 84Rin:** O.S. Rinkevich and V. Zel'dovich, "An Analysis of the Growth Kinetics of New Austenite Grains During the Alpha-Gamma Transformation in an Iron-Nickel Alloy," *Fiz. Met. Metalloved.*, *58*(1), 142-148 (1984). (Meta Phases; Experimental)
- 84Ros1:** P.L. Rossiter and R.A. Jago, "Towards a True Fe-Ni Phase Diagram," *Phase Transformation in Solids*, Mater. Res. Symp. Proc., T. Tsakalakos, Ed., 409-411, North Holland, New York (1984). (Meta Phases; Experimental; #)
- 84Ros2:** P.L. Rossiter and P.J. Lawrence, "Phase Transformations in Fe-Ni Invar Alloys," *Philos. Mag. A*, *49*(4), 535-546 (1984). (Meta Phases; Experimental)
- 84Yam:** H. Yamauchi and S. Radelaar, "Cu-Ni-Fe Coherent Phase Diagram," TMS-AIME, Warrendale, PA (1984). (Meta Phases; Theory)
- 85Chu1:** Y.Y. Chuang, R. Schmid, and Y.A. Chang, "Magnetic Contributions to the Thermodynamic Functions of Pure Ni, Co, and Fe," *Metall. Trans. A*, *16*, 153-165 (1985). (Thermo; Theory)
- 85Chu2:** Y.Y. Chuang, Y.A. Chang, and R. Schmid, "Magnetic Contribution to the Thermodynamic Functions of Alloys and the Phase Diagram of Fe-Ni System Below 1200 K," *Metall. Trans. A*, *16*, 153-165 (1985). (Meta Phases, Thermo; Theory)
- 85Tom:** J. Tomiska and A. Neckel, "Thermodynamic Investigation of Fe-Ni Alloys: Mass Spectrometric Determination of Thermodynamic Mixing Effects and Calculation of the Melting Diagram," *Ber. Bunsenges. Phys. Chem.*, *89*, 1104-1109 (1985). (Equi Diagram; Thermo; Experimental)
- 86Chu1:** Y.Y. Chuang, K.C. Hsieh, and Y.A. Chang, "A Thermodynamic Analysis of the Phase Equilibrium of the Fe-Ni System Above 1200 K," *Metall. Trans. A*, *17*, 1373-1379 (1986). (Meta Phases; Theory)
- 86Chu2:** Y.Y. Chuang, Y.A. Chang, R. Schmid, and J.C. Lin, "Magnetic Contributions to the Thermodynamic Functions of Alloys and the Phase Equilibria of Fe-Ni System below 1200 K," *Metall. Trans. A*, *17*, 1361-1371 (1986). (Meta Phases; Equi Diagram; Theory)
- 89Reu:** K.B. Reuter, D.B. Williams, and J.I. Goldstein, "Determination of the Fe-Ni Phase Diagram Below 400 °C," *Metall. Trans. A*, *20*, 719-724 (1989). (Equi Diagram, Meta Phases; Experimental)

Fe-Ni evaluation contributed by L.J. Swartzendruber, Metallurgical Structures Group, National Institute of Standards and Technology, Gaithersburg, MD 20899; V.P. Itkin, Department of Metallurgy and Materials Science, University of Toronto, Ontario M5S 1A4, Canada; and C.B. Alcock, Center for Sensor Materials, University of Notre Dame, 114 Cushing Hall, Notre Dame, IN 46556. This work was supported by ASM International. Literature searched through 1989. Dr. Swartzendruber is the former Alloy Phase Diagram Category Editor for binary iron alloys.

ROBERT SINCLAIR

Professor

Department of Materials Science and Engineering
Stanford University
Stanford, California 94305-4034

Telephone: 650-723-1102
FAX: 650-725-4034
E-mail: bobsinc@stanford.edu

EDUCATION

B.A.	Materials Science	Cambridge University	1968
Ph. D., M.A.	Materials Science	Cambridge University	1972

CAREER

Permanent Positions

University of Newcastle-upon-Tyne, U.K.	Research Associate	1971 – 73
University of California, Berkeley	Research Engineer	1973 – 77
Stanford University		
Department of Materials Science and Engineering	Assistant Professor	1977 – 80
	Associate Professor	1980 – 84
	(with tenure)	
	Professor	1984 – present
	Chair	2004 – 2014
	Charles M. Pigott Professor in the School of Engineering	2009 – present
Stanford Nanocharacterization Laboratory	Director	2003 – 13
Bing Overseas Studies Program	Director	2010 – 12
Wallenberg Research Link	Associate Director	2013 – present

Visiting Positions

Centre d'Etudes Nucleaires, Grenoble	1981
HREM Laboratory, Cambridge University	1985
Matsushita Electric Industrial Company, Osaka	1987, 1989, 1991 – 94
Stanford Center for Japanese Studies, Kyoto	1997
Stanford Center in Oxford, U.K.	2001, 2010
Adjunct Advisor for International Center for Young Scientists, NIMS, Tsukuba	2004
Visiting Professor in the World Class University Project, Seoul National University, Korea	2008 – 2010

AWARDS

First Prize, Modern Metallography Micrograph Competition, 1972
First Prize Physical Science, Electron Microscopy Society of America Scientific Exhibit, 1975, 1976
Robert Lansing Hardy Gold Medal, The Metallurgical Society of AIME, 1976
Eli Franklin Burton Award, Electron Microscopy Society of America, 1977
Alfred P. Sloan Foundation Fellowship, 1979
Marcus E. Grossman Award, American Society for Metals, 1982
Excellence in Undergraduate Teaching, Stanford University Society for Black Scientists and Engineers, 1984, Stanford Society of Chicano/Latino Engineers and Scientists, 1993
Yamaha Prize for Best Poster, 1st International Conference on Metallic Multilayers, Kyoto, 1993
Fellow, (inaugural class) Microscopy Society of America, 2009
Distinguished Scientist, Physical Sciences, Microscopy Society of America, 2009
David Turnbull Lectureship Award, Materials Research Society, 2012
John M. Cowley Distinguished Lecture, Arizona State University, 2015

SELECTED PROFESSIONAL ACTIVITIES

Electron Microscopy Society of America: Program Committee, 1979, 1980, 1990, 1993; Bulletin Editorial Board, 1975-1981; Northern California Society President, 1980; Executive Committee, 1979-1982; Twelfth International Congress (ICEM) Program Committee, 1988-1990; Fourteenth ICEM Program Committee, 1997-1998; Fifteenth ICEM Program Committee, 2001-2002.

The Metallurgical Society of AIME: Alloy Phases Committee, 1977-1992; Northern California Section Chairman, 1979.

Materials Research Society: Symposium Organizer, 1987, 1990, 1994, 1995, 2010.

Organizer: Stanford Symposium on Applications of Contemporary Electron Microscopy, 1979-1994.

Organizer: US-France Asilomar Symposium on Amorphous Nickel-Titanium 1987.

A.S.U. National HREM Facility: Outside Proposal Review Committee, 1982-1990; Winter School Instructor, 1982-2006, 2011.

Electron Microscopy Short Courses: Harbin Institute of Technology, China, 1980; Linkoping University, Sweden, 1980, 1985; Korea Advanced Institute of Science and Technology, Seoul, 1988; Samsung Advanced Institute of Technology, Suwon, Korea, 2001, 2002.

Stanford University Short Course for Philips Technicians, 1989-1992, 1994.

Editorial Board: Journal of Applied Physics, 1994-1996; Journal of Electron Microscopy, 1996-present; and other journals.

Organizer: U.S.-Japan Workshop on "The Contributions of *In Situ* Electron Microscopy to the Understanding and Creation of Advanced Materials", Stanford Japan Center, Kyoto, Japan, 2000.

Co-Organizer: United Engineering Foundation Conference on Nanostructured Magnetic Materials, Irsee, Germany, 2002.

Co-Organizer: 70th Birthday Symposium in honor of Professor Gareth Thomas, ICEM XV, Durban, South Africa, 2002.

Organizer: *In Situ* Electron Microscopy Symposium, ICEM XV, Durban, South Africa, 2002.

Co-Organizer: Symposium on Semiconductor and Magnetic Materials, Microscopy and Microanalysis Conference, Quebec, Canada, 2003.

Chair: National Research Council Committee on Smaller Facilities, 2003-2006.

Organizer: ECI Conference: "Innovative Dynamic Studies of Materials at the Nanoscale", Gyeong-ju, Korea, 2008

Co-Organizer: "International Workshop on Remote Electron Microscopy for *In Situ* Studies": Stanford University, Stanford, California, 2008; Chalmers University of Technology, Gothenburg, Sweden, 2009; Carnegie Mellon University, Pittsburgh, Pennsylvania, 2011.

Organizer: Symposium on Medical Applications of Nanotechnology, 11th International Congress on Advanced Materials, Rio de Janeiro, Brazil, 2009.

Co-Organizer: Symposium on Microscopy of Biological, Biomimetic and Medical Materials, 17th International Microscopy Congress, Rio de Janeiro, Brazil, 2010.

Co-Organizer: Symposium on Nanofunctional Materials, Nanostructures, and Nanodevices for Biomedical Applications II, Materials Research Society Fall 2010 Meeting, Boston, Massachusetts, 2010.

Co-Organizer: Stanford – Chalmers Workshop on Advancing Materials Innovatively, Stanford, California, 2012
Gothenburg, Sweden, 2013, Stanford 2014

Committee Member: National Science Foundation Materials 2022 Committee, 2012

Co-Organizer: Symposium on Nanoparticles: Applications and Bio-safety Issues, 18th International Microscopy Congress Prague, 2014

Co-Organizer: IAMNano 2014, International Workshop on Advanced and In-situ Microscopies of Functional Nanomaterials and Devices, Rio de Janeiro, 2014

COURSES TAUGHT (*present offerings)

Atomic Arrangements in Solids (G1); X-ray Diffraction Laboratory (UG1-4); Transmission Electron Microscopy (G2+)*; Nano-Characterization of Materials (G2+)*; Nanostructure and Characterization (UG1-4); Imperfections in Crystalline Solids (G1); Introduction to Materials Science: Nanotechnology Emphasis (UG1-4)*; Microscopic World of Technology (UG1-4); Japanese Companies and Japanese Society (UG2)*; Infrastructure of British Science and Technology (UG 3); Soccer and English Society (UG 3)

RESEARCH INTERESTS

Structure-property-processing correlations in materials, using high-resolution microscopy and diffraction techniques, application to development of integrated circuit and magnetic recording materials. Introduction of in situ high resolution electron microscopy.

PUBLICATIONS

1 NAS government report, 5 edited works, 6 book chapters, 238 archival journal articles, 204 conference articles, 2 patents. (List available on request).

PUBLICATIONS

A. EDITED WORKS AND BOOK CHAPTERS

(a) Government Reports

1. Committee on Smaller Facilities: R. Sinclair (chair), A. Aprahamian, A. I. Bienenstock, J. P. Bradley, D. R. Clarke, J. W. Davenport, F. J. DiSalvo, C. A. Evans, Jr., W. P. Lowe, F. M. Ross, D. J. Smith, J. M. Soures, L. Spicer, D. M. Tennant. National Research Council of the National Academy of Sciences. *Midsized Facilities: the Infrastructure for Materials Research*. Washington: National Academies Press, pp. 1-230 2006.

(b) Edited Works

1. "Report of Workshop on High Resolution Electron Microscopy," edited by G. Thomas, R. M. Glaeser, J. M. Cowley and R. Sinclair (Lawrence Berkeley Laboratory, Special Publication #106, 1976).
2. "Characterization of Defects in Materials", edited by R. W. Siegel, J. R. Weertman and R. Sinclair, *Mat. Res. Soc. Symp. Proc.* **82**, pp. 1-532 (1987).
3. "High Resolution Electron Microscopy of Defects in Materials", edited by R. Sinclair, D. J. Smith and U. Dahmen, *Mat. Res. Soc. Symp. Proc.* **183**, pp. 1-391 (1990).
4. "Polycrystalline Thin Films-Structure, Texture, Properties and Applications", edited by K. Barmak, M. A. Parker, J. F. Floro, R. Sinclair and D. A. Smith, *Mat. Res. Soc. Symp. Proc.* **343**, pp. 1-769 (1994).
5. "In Situ Electron and Tunneling Microscopy of Dynamic Processes", edited by R. Sharma, P. L. Gai, M. Gajdardziska-Josifovska, L. J. Whitman and R. Sinclair, *Mat. Res. Soc. Symp. Proc.* **404**, pp. 1-226 (1996).

(c) Book Chapters

1. "Direct Observation and Characterization of Lattice Defects in Materials," R. Sinclair, in *Treatise on Materials Science and Technology*, Volume 11, edited by R. K. McCrone (Academic Press, New York, 1977) pp. 1-45.
2. "Microanalysis by Lattice Imaging," R. Sinclair, in *Analytical Electron Microscopy*, edited by J. J. Hren, J. I. Goldstein and D. C. Joy (Plenum Press, New York, 1979) pp. 507-534.
3. "Recent Developments in Lattice Imaging of Materials", R. Sinclair, in *Annual Reviews of Materials Science*, Volume 11, edited by R. A. Huggins (Annual Reviews, Inc., Palo Alto, California, 1981) pp. 427-439.
4. "High Resolution Electron Microscopy", R. Sinclair, in *Quantitative Electron Microscopy*, edited by J.N. Chapman and A.J. Craven (SUSSP Publications, Edinburgh, 1984) pp. 341-350.
5. "Electron Microscope", R. Sinclair, in *1987 Yearbook of Science and Technology*, (McGraw-Hill, New York, 1986) pp. 173-176.
6. "Thermochemical Properties and Phase Diagrams", R. Sinclair, R. Madar and M. Setton, in *Properties of Metal Silicides*, edited by K. Maex and M. van Rossum (Inst. Elec. Eng'rs, London, 1995), pp. 95 - 152.
7. "A Brief History of Controlled Atmosphere Transmission Electron Microscopy", A. L. Koh, S. C. Lee and R. Sinclair, in: *Controlled Atmosphere Transmission Electron Microscopy – Principles and Practices*, edited by T. W. Hansen and J. B. Wagner (Springer Publishing Company), under review.

B. JOURNAL PUBLICATIONS (refereed)

1. "Structural Studies on the Ni-Ni₃Ti System", R. Sinclair, Ph.D. Thesis, University of Cambridge, England (1972).
2. "Measurement of Relative Bond Energies in Some Ordered Nickel-Based Alloys by Field-Ion Microscopy", R.J. Taunt, R. Sinclair and B. Ralph, *Phys. Status Solidi A*, **16**, pp. 469-484 (1973).
3. "On the Determination of a Local Order Parameter in a Nickel-Titanium Alloy", R. Sinclair, B. Ralph and J.A. Leake, *Philos. Mag.*, **28**, pp. 1111-1123 (1973).
4. "Spinodal Decomposition of a Nickel-Titanium Alloy", R. Sinclair, J.A. Leake and B. Ralph, *Phys. Status Solidi A*, **26**, pp. 285-298 (1974).
5. "Antiphase Domains and Diffraction Spot Splitting in Cu₃Au", R. Sinclair and G. Thomas, *J. Appl. Crystallography*, **8**, pp. 206-211 (1975).
6. "On the Lattice Parameter of Non-Random Solid Solutions", A. Krawitz and R. Sinclair, *Philos. Mag.*, **31**, pp. 697-712 (1975).

7. "Analysis of Ordering in Cu₃Au, Utilizing Lattice Imaging Techniques", R. Sinclair, K. Schneider and G. Thomas, *Acta Metall.*, **23**, pp. 873-883 (1975).
8. "Applications of the Critical Voltage Effect for the Study of Ordering", R. Sinclair, M.J. Goringe and G. Thomas, *Philos. Mag.*, **32**, pp. 501-512 (1975).
9. "Optical Diffraction from Lattice Images of Alloys", R. Sinclair, R. Gronsky and G. Thomas, *Acta Metall.*, **24**, pp. 789-795 (1976).
10. "Observations of B19 Ordering in Mg₃Cd Thin Foils", J. Dutkiewicz and R. Sinclair, *Scripta Met.*, **10**, pp. 489-493 (1976).
11. "Discussion of An Electron Diffraction Study of Short-Range Order in Quenched Ni₄Mo Alloy", G. Thomas and R. Sinclair, *Acta Metall.*, **25**, pp. 231-234 (1977).
12. "Lattice Image Studies of B19 Ordering and Interfacial Structures in Mg₃Cd", R. Sinclair and J. Dutkiewicz, *Acta Metall.*, **25**, pp. 235-249 (1977).
13. "The Importance of Electron Diffraction to Transmission Electron Imaging", R. Sinclair, *Trans. Am. Cryst. Soc.*, **13**, pp. 101-126 (1977).
14. "Structure of Ordered Alloys", R. Sinclair and G. Thomas, *J. Phys. (Paris)*, **38**, C7, pp. 165-171 (1977).
15. "A Preliminary Lattice Image Investigation of Nickel-Titanium Martensite", R. Sinclair, *J. Phys. (Paris)*, **38**, C7, pp. 453-456 (1977).
16. "Lattice Imaging and Optical Microanalysis of a Cu-Ni-Cr Spinodal Alloy", C. K. Wu, R. Sinclair and G. Thomas, *Met. Trans.*, **9A**, pp.381-387 (1978).
17. "Determination of Local Composition by Lattice Imaging", R. Sinclair and G. Thomas, *Met. Trans.*, **9A**, pp. 373-380 (1978).
18. "Lattice Imaging Study of a Martensite-Austenite Interface", R. Sinclair and H.A. Mohamed, *Acta Metall.*, **26**, pp. 623-628 (1978).
19. "Modulated Substitutional-Interstitial Solute-Atom Clustering in Nitrided Austenitic Fe-34 Ni-V Alloys", J.H. Driver, R. Sinclair and K.H. Jack, *Proc. R. Soc. London*, **A367**, pp. 99-115 (1978).
20. "Comments on 'The Early Stages of the Transformation in Dilute Alloys of Titanium in Nickel'", D.E. Laughlin, R. Sinclair, and L.E. Tanner, *Scripta Met.*, **14**, pp. 373-376 (1980).
21. "A Quantitative Assessment of the Capabilities of 2 1/2 D Microscopy for Analyzing Crystalline Solids", G. M. Michal and R. Sinclair, *Philos. Mag.*, **A42**, pp. 691-704 (1980).
22. "Metallurgical Applications of the 2 1/2 D TEM Technique", R. Sinclair, G.M. Michal and T. Yamashita, *Met. Trans.*, **12A**, pp. 1503-1512 (1981).
23. "Atomic Motion on the Surface of a Cadmium Telluride Single Crystal", R. Sinclair, T. Yamashita and F.A. Ponce, *Nature*, **290**, pp. 386-388 (1981).
24. "Room Temperature Deformation Mechanisms and the Defect Structure of Tungsten Carbide", M.K. Hibbs and R. Sinclair, *Acta Metall.*, **29**, pp. 1645-1654 (1981).
25. "Native Tellurium Dioxide Layer on Cadmium Telluride: A High Resolution Electron Microscopy Study", F.A. Ponce, R. Sinclair and R.H. Bube, *Appl. Phys. Lett.*, **39**, pp. 951-953 (1981).
26. "The Effect of Orientation, Grain Size and Polymorphism on Magnetic Properties of Sputtered Co-Re Thin Film Media", T. Chen, T. Yamashita and R. Sinclair, *IEEE Trans. Magn.*, **MAG-17**, pp. 3187-3189 (1981).
27. "The Structure of TiNi Martensite", G.M. Michal and R. Sinclair, *Acta Crystallogr. B*, **37**, pp. 1803-1807 (1981).
28. "A Morphological Study of 'Premartensitic' Effects in TiNi," P. Moine, G.M. Michal and R. Sinclair, *Acta Metall.*, **30**, pp. 109-123 (1982).
29. "Characterization of the Lattice Displacement Waves in Premartensitic TiNi", G.M. Michal, P. Moine and R. Sinclair, *Acta Metall.*, **30**, pp. 125-138 (1982).
30. "Electron Irradiation Induced Crystalline Amorphous Transitions in Ni-Ti Alloys", G. Thomas, H. Mori, H. Fujita and R. Sinclair, *Scripta Met.*, **15**, pp. 589-592 (1982).
31. "High Resolution Lattice Imaging of Cadmium Telluride", T. Yamashita, F.A. Ponce, P. Pirouz and R. Sinclair, *Philos. Mag.*, **A45**, pp. 693-711 (1982).
32. "Dynamic Observation of Defect Annealing in CdTe at Lattice Resolution", R. Sinclair, F.A. Ponce, T. Yamashita, D.J. Smith, R.A. Camps, L.A. Freeman, S.J. Erasmus, W.C. Nixon, K.C.A. Smith and C.J.D. Catto, *Nature*, **298**, pp. 127-131 (1982).
33. "Martensitic Transformations in a TiNi Thin Foil", P. Moine, E. Goo and R. Sinclair, *J. Phys. (Paris)*, **43**, C4, pp. 243-248 (1982).

34. "Transmission Electron Microscopy of Annealed $ZrO_2+8Mol\%Sc_2O_3$ ", F.K. Moghadam, T. Yamashita, R. Sinclair and D.A. Stevenson, *J. Am. Ceram. Soc.*, **66**, pp. 213-217 (1983).
35. "Intergranular Cracking in WC-6%Co: An Application of the von Mises Criterion", V. Jayaram, R. Sinclair and D.J. Rowcliffe, *Acta Metall.*, **31**, pp. 373-378 (1983).
36. "Transmission Electron Microscopy Studies of the Polycrystalline Silicon – SiO_2 Interface", J.C. Bravman and R. Sinclair, *Thin Solid Films*, **104**, pp. 153-161 (1983).
37. "Detection of Thin Intergranular Cobalt Layers in WC-Co Composites by Lattice Imaging", V. Jayaram and R. Sinclair, *J. Am. Ceram. Soc.*, **66**, pp. C137-C139 (1983).
38. "Defect Interactions in Deformed WC", M.K. Hibbs, R. Sinclair and D.J. Rowcliffe, *Acta Metall.*, **32**, pp. 941-947 (1984).
39. "The Preparation of Cross-Section Specimens for Transmission Electron Microscopy", J.C. Bravman and R. Sinclair, *J. Electron Microsc. Tech.*, **1**, pp. 53-61 (1984).
40. "Cadmium Telluride Films and Solar Cells" R.H. Bube, A. Fahrenbruch, R. Sinclair, T.C. Anthony, C. Fortmann, W. Huber, C-T. Lee, T. Thorpe and T. Yamashita, *IEEE Trans. Electron Devices*, **ED-31**, pp. 528-538 (1984).
41. "Thin Foil Artifacts Observed in Electron Diffraction on a TiNi Alloy", P. Moine, E. Goo and R. Sinclair, *Scripta Met.*, **18**, pp. 1143-1147 (1984).
42. "Phase Equilibria in Thin-Film Metallizations", R. Beyers, R. Sinclair and M.E. Thomas, *J. Vac. Sci. Technol.*, **B2**, pp. 781-784 (1984).
43. "Metastable Phase Formation in Titanium-Silicon Thin Films", R. Beyers and R. Sinclair, *J. Appl. Phys.*, **57**, pp. 5240-5245 (1985).
44. "*In Situ* TEM Study of Martensitic NiTi Amorphization by Ni Ion Implantation", P. Moine, J. P. Riviere, M.O. Ruault, J. Chaumont, A. Pelton and R. Sinclair, *Nucl. Instrum. Methods B*, **7/8**, pp. 20-25 (1985).
45. "Precipitation of Phosphorus and Tin in Temper Embrittled Low Alloy Steel", J.E. Wittig, R. Sinclair and R. Viswanathan, *Scripta Met.*, **19**, pp. 111-116 (1985).
46. "Displacement Boundaries in TiNi Alloys", E. Goo and R. Sinclair, *Scripta Met.*, **19**, pp. 1257-1259 (1985).
47. "Silicon Nitride Joining", M. L. Mecartney, R. Sinclair and R. E. Loehman, *J. Am. Ceram. Soc.*, **68**, pp. 472-478 (1985).
48. "Mechanical Twinning in $Ti_{50}Ni_{47}Fe_3$ and $Ti_{49}Ni_{51}$ Alloys", E. Goo, T. Duerig, K.N. Melton and R. Sinclair, *Acta Metall.*, **33**, pp. 1725-1733 (1985).
49. "The B2 to R Transformation in $Ti_{50}Ni_{47}Fe_3$ and $Ti_{49.5}Ni_{50.5}$ Alloys", E. Goo and R. Sinclair, *Acta Metall.*, **33**, pp. 1717-1723 (1985).
50. "Delineation of Emitter-Collector Shorts in Bipolar Test Structures by Voltage Contrast Scanning Electron Microscopy", A.H. Carim, R. Sinclair and W.T. Stacy, *SEM 1985: III*, pp. 1047-1053 (1985).
51. "Lattice Images of Defect Free Silicon-On-Sapphire Prepared by Ion Implantation", M.A. Parker, R. Sinclair and T.W. Sigmon, *Appl. Phys. Lett.*, **47**, pp. 626-628 (1985).
52. "Deformation Enhanced Decarburization of WC-Co", V. Jayaram, R. Sinclair and D.J. Rowcliffe, *Scripta Met.*, **20**, pp. 55-60 (1986).
53. "Plastic Deformation of WC-Co at High Confining Pressure", V. Jayaram, A. Kronenberg, S.H. Kirby, D.J. Rowcliffe and R. Sinclair, *Scripta Met.*, **20**, pp. 701-705 (1986).
54. "High Resolution Transmission Electron Microscope Observations of Silicon Regrowth at Controlled Elevated Temperatures", R. Sinclair and M.A. Parker, *Nature*, **322**, pp. 531-533 (1986).
55. "The Evolution of Si/ SiO_2 Interface Roughness", A.H. Carim and R. Sinclair, *J. Electrochem. Soc.*, **134**, pp. 741-746 (1987).
56. "Amorphous Ti-Si Alloy Formed by Interdiffusion of Amorphous Si and Crystalline Ti Multilayers", K. Holloway and R. Sinclair, *J. Appl. Phys.*, **61**, pp. 1359-1364 (1987).
57. "Phase Equilibria in Metal-Gallium-Arsenic Systems: Thermodynamic Considerations for Metallization Materials", R. Beyers, K.B. Kim and R. Sinclair, *J. Appl. Phys.*, **61**, pp. 2195-2202 (1987).
58. "Kinetics & Oxide Composition for Thermal Oxidation of Cadmium Telluride", F. Wang, A. Schwartzman, A.L. Fahrenbruch, R. Sinclair, R.H. Bube and C.M. Stahle, *J. Appl. Phys.*, **62**, pp. 1469-1476 (1987).
59. "High-Resolution Electron Microscopy of Structural Features at the Si/ SiO_2 Interface", A.H. Carim and R. Sinclair, *Mater. Letts.*, **5**, pp. 94-98 (1987).
60. "High-Resolution Electron Microscopy and Scanning Tunneling Microscopy of Native Oxides on Silicon", A.H. Carim, M.M. Dovek, C.F. Quate, R. Sinclair and C. Vorst, *Science*, **237**, pp. 630-633 (1987).

61. "In Situ HREM of Interface Reactions in Semiconductors", R. Sinclair, M.A. Parker and K.B. Kim, *Ultramicroscopy*, **23**, pp. 383-396 (1987).
62. "Disordered Intermixing at the Platinum-Silicon Interface Demonstrated by High-resolution Cross-sectional Transmission Electron Microscopy, Auger Electron Spectroscopy and MeV Ion Channeling", J.R. Abelson, K.B. Kim, D.E. Mercer, C. R. Helms, R. Sinclair and T.W. Sigmon, *J. Appl. Phys.*, **63**, pp. 689-692 (1988).
63. "High-resolution and *In Situ* TEM Studies of Annealing of Ti-Si Multilayers", K. Holloway and R. Sinclair, *J. Less Common Metals*, **140**, pp. 139-148 (1988).
64. "Structural Determination of Small Amorphous Volumes by Electron Diffraction", P. Moine, A.R. Pelton and R. Sinclair, *J. Non-Cryst. Solids*, **101**, pp. 213-222 (1988).
65. "Interfacial Reactions in the Ti/GaAs System", K.B. Kim, M. Kniffin, R. Sinclair and C. R. Helms, *J. Vac. Sci. Technol. A*, **6**, pp. 1473-1477 (1988).
66. "The Development of *In Situ* High Resolution Electron Microscopy", R. Sinclair, T. Yamashita, M.A. Parker, K.B. Kim, K. Holloway and A.F. Schwartzman, *Acta Crystallogr. Sec. A*, **44**, pp. 965-975 (1988).
67. "Interfacial Reactions on Annealing Molybdenum-Silicon Multilayers", K. Holloway, K.B. Do and R. Sinclair, *J. Appl. Phys.*, **65**, pp. 474-480 (1989).
68. "A High-Resolution Electron Microscopy Study of the Fine Structure in a Trench Capacitor", R. Sinclair, K.B. Kim, O. Shippou and H. Iwasaki, *J. Electrochem. Soc.*, **136**, pp. 511-518 (1989).
69. "Structure and Electrical Properties of Interfaces Between Silicon Films and n+ Silicon Crystals", S. Ogawa, S. Okuda, T. Yoshida, T. Kouzaki, K. Tsukamoto and R. Sinclair, *J. Appl. Phys.*, **65**, pp. 668-671 (1989).
70. "Amorphous Silicide Formation by Thermal Reaction: A Comparison of Several Metal-Silicon Systems", K. Holloway, R. Sinclair and M. Nathan, *J. Vac. Sci. Technol. A*, **7**, pp. 1479-1483 (1989).
71. "Morphology of the Silicon Implanted Interface of a Polysilicon/Single Crystal Silicon Structure", S. Okuda, S. Ogawa, T. Kouzaki, T. Yoshida, F. Toujou and R. Sinclair, *Jpn. Nucl. Instr. Meth. Phys. Res. B*, **39**, pp. 334-337 (1989).
72. "Thickness Measurements and Growth Kinetics of Thin SiO₂ Layers", A.H. Carim and R. Sinclair, *J. Electrochem. Soc.*, **137**, pp. 279-283 (1990).
73. "Metastable Phase Formation in Thin Films and Multilayers", B.M. Clemens and R. Sinclair, *MRS Bull.*, **15** (2), pp. 19-28 (1990).
74. "Deformation, Twinning and Thermo-Mechanical Strengthening of Ti₅₀Ni₄₇Fe₃", W.J. Moberly, J.L. Proft, T.W. Duerig and R. Sinclair, *Acta Metall.*, **38**, pp. 2601-2612 (1990).
75. "A Thermodynamic Approach for Interpreting Metallization Layer Stability and Thin-Film Reactions Involving Four Elements: Application to Integrated Circuit Contact Metallurgy", A.S. Bhansali, R. Sinclair and A.E. Morgan, *J. Appl. Phys.*, **68**, pp. 1043-1049 (1990).
76. "Phase Reactions at Semiconductor Metallization Interfaces", A.S. Bhansali, D.H. Ko and R. Sinclair, *J. Electron. Mater.*, **19**, pp. 1171-1175 (1990).
77. "Study of Interfacial Reactions in Metal-Silicon and Related Interfacial Reactions by High Resolution Electron Microscopy and Thermodynamic Analysis", R. Sinclair, *Mater. Trans. Jpn. Inst. Met.*, **31**, pp. 628-635 (1990).
78. "SiO₂/Si Interfaces Studied by STM and HRTEM (II)", M. Niwa, M. Onoda, M. Matsumoto, H. Iwasaki and R. Sinclair, *Jpn. J. Appl. Phys.*, **29**, pp. 2665-2670 (1990).
79. "Interface Microstructure of Titanium Thin-Film / Silicon-Crystal Single Substrate, Correlated with Electrical Barrier Heights", S. Ogawa, T. Yoshida, T. Kouzaki and R. Sinclair, *J. Appl. Phys.*, **70**, pp. 827-832 (1991).
80. "Structure of an Amorphous Ti-Si Alloy Formed by Thermal Reaction", K. Holloway, P. Moine, J. Delage and R. Sinclair, *J. Non-Cryst. Solids*, **134**, pp. 133-140 (1991).
81. "Amorphous Phase Formation in an As-Deposited Platinum-GaAs Interface", D.H. Ko and R. Sinclair, *Appl. Phys. Lett.*, **58**, pp. 1851-1853 (1991).
82. "Metastable and Equilibrium Defect Structure of II/VI GaAs Interfaces", A.F. Schwartzman and R. Sinclair, *J. Electron. Mater.*, **20**, pp. 805-814 (1991).
83. "SiO₂/Si Interfaces Studied by Scanning Tunneling Microscopy and High Resolution Transmission Electron Microscopy", M. Niwa, M. Onoda, M. Matsumoto, H. Iwasaki and R. Sinclair, *J. Electrochem. Soc.*, **139**, pp. 901-906 (1992).
84. "Modeling of Agglomeration in Polycrystalline Thin Films: Application to TiSi₂ on a Silicon Substrate", T.P. Nolan, R. Sinclair and R. Beyers, *J. Appl. Phys.*, **71**, pp. 720-724, (1992).
85. "Structural Determination of Amorphous Ni-Ti Thin Films, Using Electron Diffraction Analysis", P. Moine, J. Delage, A.R. Pelton and R. Sinclair, *Acta Metall.*, **40**, pp. 1855-1863 (1992).

86. "Amorphous Phase Formation and Initial Interfacial Reaction in the Pt/GaAs System", D.H. Ko and R. Sinclair, *J. Appl. Phys.*, **72**, pp. 2036-2042 (1992).
87. "Epitaxial Pt (001), Pt (110) and Pt (111) Films on MgO (001), MgO (110), MgO (111) and Al₂O₃ (0001)", B.M. Lairson, M.R. Visokay, R. Sinclair, S. Hagstrom and B.M. Clemens, *Appl. Phys. Lett.*, **61**, pp. 1390-1392 (1992).
88. "Microstructure and Crystallography of Textured CoCrTa/Cr Sputtered Thin Film Media for Longitudinal Recording", T.P. Nolan, R. Sinclair, R. Ranjan and T. Yamashita, *Ultramicroscopy*, **47**, pp. 437-446 (1992).
89. "Crystallization of Silicon in Aluminum/Amorphous-Silicon Multilayers", T.J. Konno and R. Sinclair, *Philos. Mag. B*, **66**, pp. 749-765 (1992).
90. "Epitaxial PtFe (001) Thin Films on MgO (001) with Perpendicular Magnetic Anisotropy", B.M. Lairson, M.R. Visokay, R. Sinclair and B. M. Clemens, *Appl. Phys. Lett.*, **62**, pp. 639-641 (1993).
91. "TEM Analysis of Co-Gd and Cr-Gd Multilayer Structures", G.A. Bertero, T.C. Hufnagel, B.M. Clemens and R. Sinclair, *J. Mater. Res.*, **8**, pp. 771-774 (1993).
92. "Transmission Electron Microscopic Analysis of Microstructural Features in Magnetic Recording Media", T.P. Nolan, R. Sinclair, R. Ranjan and T. Yamashita, *IEEE Trans. Magn.*, **29**, pp. 292-299 (1993).
93. "Direct Observation of Crystallization in Silicon by *In Situ* High Resolution Electron Microscopy", R. Sinclair, J. Morgiel, A.S. Kirtikar, I.W. Wu and A. Chiang, *Ultramicroscopy*, **51**, pp. 41-45 (1993).
94. "Crystallographic Orientation of Textured CoCrTa/Cr Recording Media", T.P. Nolan, R. Sinclair, R. Ranjan and T. Yamashita, *J. Appl. Phys.*, **73**, pp. 5117-5124 (1993).
95. "Effect of Microstructural Features on Media Noise in Longitudinal Recording Media", T.P. Nolan, R. Sinclair, R. Ranjan and T. Yamashita, *J. Appl. Phys.*, **73**, pp. 5566-5568 (1993).
96. "Microstructural Analysis of Magnetic Fe/Pt Multilayer Thin Films by Transmission Electron Microscopy", M. R. Visokay, B.M. Lairson, B.M. Clemens and R. Sinclair, *J. Magn. Magn. Mater.*, **126**, pp. 136-140 (1993).
97. "Influence of Interfacial Doping with Rare Earth Elements on the Magnetic Properties of Selected Co/Pt Multilayers", G.A. Bertero and R. Sinclair, *J. Magn. Mag. Mater.*, **126**, pp. 275-278 (1993).
98. "Annealing of Metal Multilayers Studied by *In Situ* High Resolution Electron Microscopy", R. Sinclair and T.J. Konno, *J. Magn. Magn. Mater.*, **126**, pp. 108-112 (1993).
99. "Crystallization and Decomposition of Co-sputtered Amorphous Silicon-Aluminum Thin Films", T.J. Konno and R. Sinclair, *Mater. Chem. Phys.*, **35**, pp. 99-113 (1993).
100. "Epitaxial PtFe and PtCo(001) Thin Films with Perpendicular Magnetic Anisotropy", B.M. Lairson, M. R. Visokay, R. Sinclair and B.M. Clemens, *J. Magn. Mag. Mater.*, **126**, pp. 577-579 (1993).
101. "Epitaxial Tetragonal PtCo(001) Thin Films with Perpendicular Magnetic Anisotropy", B.M. Lairson, M.R. Visokay, E.E. Marinero, R. Sinclair and B.M. Clemens, *J. Appl. Phys.*, **74**, pp. 1922-1928 (1993).
102. "Annealing Effect on Structure of Fe/Zr Multilayers", K. Yamamoto, T. Nakayama, H. Sato, T.J. Konno and R. Sinclair, *J. Magn. Magn. Mater.*, **126**, pp. 128-130 (1993).
103. "Structure and Corrosion Properties of Al/Si Multilayers", T. Nakayama, T.J. Konno, H. Satoh and R. Sinclair, *J. Magn. Magn. Mater.*, **126**, pp. 167-169 (1993).
104. "Structure and Corrosion Properties of Fe/Zr Multilayers", T. Nakayama, H. Sato, T. J. Konno, B.M. Clemens, D.A. Stevenson, R. Sinclair and S.B. Hagstrom, *J. Magn. Mag. Mater.*, **126**, pp. 105-107 (1993).
105. "Atomic-scale Planarization of SiO₂/Si(001) Interfaces", M. Niwa, M. Udagawa, K. Okada, T. Kouzaki and R. Sinclair, *Appl. Phys. Lett.*, **63**, pp. 675-677 (1993).
106. "Crystallization of Co-sputtered Amorphous Cobalt-Carbon Alloys", T.J. Konno and R. Sinclair, *Acta Metall. Mater.*, **42**, pp. 1231-1247 (1994).
107. "Crystallization of Co-sputtered Amorphous Cobalt-Carbon Alloys: Morphology and Kinetics of Spherulitic Growth", T.J. Konno and R. Sinclair, *Mater. Sci. Eng.*, **A179/A180**, pp. 297-302 (1994).
108. "Metal-Contact Induced Crystallization of Semiconductors," T.J. Konno and R. Sinclair, *Mater. Sci. Eng. A*, **A179/A180**, pp. 426-432 (1994).
109. "*In-Situ* , Dynamic High Resolution Transmission Electron Microscopy: Application to Pt/GaAs Interfacial Reactions", D.H. Ko and R. Sinclair, *Ultramicroscopy*, **54**, pp. 166-178 (1994).
110. "Noise Properties and Microstructure of Oriented CoCrTa/Cr Media", R. Ranjan, W. R. Bennett, G.J. Tarnopolsky, T. Yamashita, T.P. Nolan and R. Sinclair, *J. Appl. Phys.*, **75**, pp. 6144-6146 (1994).
111. "Thermochemical Stability of BaFe₁₂O₁₉ and BaFe₂O₄ and Phase Relations in the Ba-Fe-O Ternary System". J. Li, T.M. Gur, R. Sinclair, S.S. Rosenblum and H. Hayashi, *J. Mater. Res.*, **9**, pp. 1499-1512 (1994).

112. "Structure-Property Correlations in Pt/Co Multilayers for Magneto-Optic Recording", G.A. Bertero and R. Sinclair, *J. Magn. Magn. Mater.*, **134**, pp. 173-184 (1994).
113. "Studies of Material Reactions by *In-Situ* High Resolution Electron Microscopy (HREM)," R. Sinclair, *MRS Bull.*, **19** (6), pp. 26-31 (1994).
114. "Oxygen Coulometric Titration Study of M Ba-Ferrite", J. Li, T.M. Gur, R. Sinclair, S.S. Rosenblum and H. Hayashi, *Solid State Ionics*, **73**, pp. 185-188 (1994).
115. "*In Situ* HREM: Application to Metal-Mediated Crystallization," R. Sinclair and T.J. Konno, *Ultramicroscopy*, **56**, pp. 225-232 (1994).
116. "(Pt/Co/Pt)/X Multilayer Films With High Kerr Rotations and Large Perpendicular Magnetic Anisotropies", G.A. Bertero and R. Sinclair, *Appl. Phys. Lett.*, **64**, pp. 3337-3339 (1994).
117. "Temperature and Orientation Effects on Magnetic Properties of Barium Ferrite Thin Films", J. Li, R. Sinclair, S.S. Rosenblum and H. Hayashi, *IEEE Trans. Magn.*, **30**, pp. 4050-4052 (1994).
118. "Longitudinal Recording Performance of Doped Barium Ferrite Magnetic Thin Films", S. S. Rosenblum, J. Li, H. Hayashi and R. Sinclair, *IEEE Trans. Magn.*, **30**, pp. 4047-4049 (1994).
119. "Atomic-Order Planarization of Ultra-Thin SiO₂/Si (001) Interfaces," M. Niwa, T. Kouzaki, K. Okada, M. Udagawa and R. Sinclair, *Jpn. J. Appl. Phys.*, **33**, pp. 388-394 (1994).
120. "Metal-Mediated Crystallization of Amorphous Silicon in Silicon-Silver Layered Systems," T.J. Konno and R. Sinclair, *Philos. Mag. B*, **71**, pp. 163-178 (1995).
121. "Metal-Mediated Crystallization of Amorphous Germanium in Germanium-Silver Layered Systems," T.J. Konno and R. Sinclair, *Philos. Mag. B*, **71**, pp. 179-199 (1995).
122. "Crystallization of Amorphous Carbon in Carbon-Cobalt Layered Thin Films," T. J. Konno and R. Sinclair, *Acta Metall. Mater.*, **43**, pp. 471-484 (1995).
123. "Direct Formation of Ordered CoPt and FePt Compound Thin Films by Sputtering", M.R. Visokay and R. Sinclair, *Appl. Phys. Lett.*, **66**, pp. 1692-1694 (1995).
124. "Interface Structure and Perpendicular Magnetic Anisotropy in Pt/Co Multilayers", G.A. Bertero, R. Sinclair, C.-H. Park and Z.X. Shen, *J. Appl. Phys.*, **77**, pp. 3953-3959 (1995).
125. "High Density Recording Characteristics of Sputtered Barium Ferrite Thin Films", J. Li, S.S. Rosenblum, W. Nojima, H. Hayashi and R. Sinclair, *IEEE Trans. Magn.*, **31**, pp. 2749-2751 (1995).
126. "As-deposited Crystalline Barium Ferrite Thin Film Media for Longitudinal Recording", J. Li, S.S. Rosenblum, H. Hayashi and R. Sinclair, *J. Magn. Mag. Mater.*, **153**, p. 246 (1995).
127. "Reaction Mediated Texturing of Barium Ferrite Magnetic Thin Films", J. Li, S. S. Rosenblum, H. Hayashi and R. Sinclair, *J. Mater. Res.*, **10**, pp. 2343-2349 (1995).
128. "Interfacial Reactions in the Zr/Si System Studied by *In-Situ* TEM", H. Tanaka, T.J. Konno, R. Sinclair and N. Hiroshita, *J. Appl. Phys.*, **78**, pp. 4982-4987 (1995).
129. "Kerr Rotations and Anisotropy in (Pt/Co/Pt)/X Multilayers", G.A. Bertero and R. Sinclair, *IEEE Trans. Magn.*, **31**, pp. 3337-3342 (1995).
130. "Magnetic and Structural Characteristics of Sputtered Barium Ferrite Thin Films" J. Li, S.S. Rosenblum, H. Hayashi and R. Sinclair, *J. Magn. Magn. Mater.*, **155**, pp. 157-160 (1995).
131. "Microstructural Evolution of NiFe/Ag Multilayers Studied by X-ray Diffraction and *In Situ* TEM", E. Snoeck, R. Sinclair, M.A. Parker, T.L. Hylton, K.R. Coffey, J.K. Howard, A. Lessmann and A.I. Bienenstock, *J. Magn. Magn. Mater.*, **151**, pp. 24-32 (1995).
132. "Anomalous Moment and Anisotropy Behavior in Fe₃O₄ Films", D.T. Margulies, F.T. Parker, F.E. Spada, J. Li, R. Sinclair, R.S. Goldman and A.E. Berkowitz, *Phys. Rev. B*, **53**, p. 9175-9187 (1996).
133. "Micromagnetic and Experimental Studies of CoPtCr Polycrystalline Thin Film Media with Bicrystal Microstructure", Q. Peng, H.N. Bertram, N. Fussing, M.F. Doerner, M. Mirzamaani, D. Margulies, R. Sinclair and S. Lambert, *IEEE Trans. Magn.*, **31**, pp. 2821-2823 (1995).
134. "Structural Comparisons of Ion-Beam and RF Sputter-Deposited GMR Spin Valves by High Resolution Transmission Electron Microscopy", W.E. Bailey, N.C. Zhu, R. Sinclair and S.X. Wang, *J. Appl. Phys.*, **79**, pp. 6393-6395 (1996).
135. "Effects of Pt Addition on the Magnetic and Crystallographic Properties of Co-Cr-Pt Thin Film Media," A. Ishikawa and R. Sinclair, *J. Magn. Magn. Mater.*, **152**, pp. 265-273 (1996).
136. "Analyses of Stacking Fault Density in Co-Alloy Thin Films by High-Resolution Transmission Electron Microscopy," A. Ishikawa and R. Sinclair, *IEEE Trans. Magn.*, **32**, pp. 3605-3607 (1996).
137. "Measurements of Crystalline Anisotropy on Longitudinal Media," J.K. Chang, Q. Peng, H.N. Bertram and R. Sinclair, *IEEE Trans. Magn.*, **32**, pp. 4902-4904 (1996).

138. "Thin Film Media With and Without Bicrystal Cluster Structure on Glass Ceramic Structures," Q. Chen, J.K. Chang, G.L. Chen and R. Sinclair, *IEEE Trans. Magn.*, **32**, pp. 3599-3601 (1996).
139. "Microstructure-Magnetic Property Relationships in CoCrPt Magnetic Thin Films," S. McKinlay, N. Fussing, R. Sinclair, and M.F. Doerner, *IEEE Trans. Magn.*, **32**, pp. 3587-3589 (1996).
140. "Lorentz Transmission Electron Microscopy Study of Micromagnetic Structures in Real Computer Hard Disks," K. Tang, M. R. Visokay, R. Sinclair, C. Ross, R. Ranjan and T. Yamashita, *IEEE Trans. Magn.*, **32**, pp. 4130-4132 (1996).
141. "Growth of α' Nitrogen-Martensite and Fe₁₆N₂ Films Using (001) Silicon Substrates," T.E. Clark, M. R. Visokay, N. Zhu, and R. Sinclair, *IEEE Trans. Magn.*, **32**, pp. 3503-3505 (1996).
142. "*In Situ* Observation of the C₄₉-to-C₅₄ Phase Transformation in TiSi₂ Thin Films by Transmission Electron Microscopy", H. Tanaka, N. Hirashita and R. Sinclair, *Jpn. J. Appl. Phys. Lett.*, **35**, pp. L479-481 (1996).
143. "*In Situ* Atomic Resolution Electron Microscopy of Metal-Mediated Crystallization of Semiconductors", T.J. Konno and R. Sinclair, *Materials Science Forum*, **204-206**, pp. 749-754 (1996).
144. "Evolution of Bicrystal Media," J.K. Chang, Q. Peng, Q. Chen, G.-L. Chen, H.N. Bertram and R. Sinclair, *IEEE Trans. Magn.*, **33**, pp. 885-890 (1997).
145. "Magnetic Clusters, Intergranular Exchange Interaction and Their Microstructural Basis in Thin Film Longitudinal Media", K. Tang, M.E. Schabes, C.A. Ross, L. He, R. Ranjan, T. Yamashita and R. Sinclair, *IEEE Trans. Magn.*, **33**, pp. 4074-4076 (1997).
146. "Wear Effects on the Microstructural Features of Amorphous Carbon Thin Film", A. Ramirez and R. Sinclair, *Surf. Coat. Tech.*, **94-95**, pp. 549-554 (1997).
147. "Nano-roughness Effect on Cr Growth Mechanism", J.K. Chang, Q. Chen, G.-L. Chen and R. Sinclair, *J. Appl. Phys.*, **81** (8), pp. 3943-3946 (1997).
148. "Interfacial Reaction in the poly-Si/Ta₂O₅/TiN Capacitor System", H.-J. Lee, M.-B. Lee, H.-D. Lee and R. Sinclair, *J. Appl. Phys.*, **82** (12), pp. 139-144 (1997).
149. "Evidence of Heteroepitaxial Growth of Copper on β -Tantalum", K.W. Kwon, C. Ryu, R. Sinclair and S.S. Wong, *Appl. Phys. Lett.*, **71**, pp. 3069-3071 (1997).
150. "Chromium Segregation in CoCrTa/Cr and CoCrPt/Cr Thin Films for Longitudinal Recording Media", J.E. Wittig, T.P. Nolan, C.A. Ross, M.E. Schabes, K. Tang, R. Sinclair, and J. Bentley, *IEEE Trans. Magn.*, **34**, pp. 1564-1566 (1998).
151. "Effects of Ultra-High Vacuum on Crystallographic, Recording and Magnetic Properties of Thin Film Media", C. Gao, S. Wu, J.-P. Chen, R. Malmhall, C. Habermeier, R. Sinclair, H. Laidler and K. O'Grady, *IEEE Trans. Magn.*, **34**, pp. 1576-1578 (1998).
152. "Kinetic Analysis of the C₄₉-to-C₅₄ Phase Transformation in TiSi₂ Thin Films by *In Situ* Observation", H. Tanaka, N. Hirashita and R. Sinclair, *Jpn. J. Appl. Phys.*, **37**, pp. 4284-4287 (1998).
153. "Crystallization of Amorphous Carbon Thin Films in the Presence of Magnetic Media", A. G. Ramirez, T. Itoh and R. Sinclair, *J. Appl. Phys.*, **85**, pp. 1508-1513 (1999).
154. "A Study of the Failure Mechanism of a Titanium Nitride Diffusion Barrier", H.-J. Lee, P. Li, B. Roberts and R. Sinclair, *J. Appl. Phys.*, **86** (6), pp. 3096-3103 (1999).
155. "Solid-state Amorphization at tetragonal-Ta/Cu Interfaces", K.-W. Kwon, H.-J. Lee and R. Sinclair, *Appl. Phys. Lett.*, **75** (7), pp. 935-937, (1999).
156. "Wear-induced Modifications of Amorphous Carbon in the Presence of Magnetic Media", A. G. Ramirez and R. Sinclair, *J. Appl. Phys.*, **85** (8), pp. 5597-5599, (1999).
157. "Thermal Stability of a Cu/Ta Multilayer: an Intriguing Interfacial Reaction", H.-J. Lee, K. W. Kwon, C. Ryu and R. Sinclair, *Acta Mater.*, **47** (15/16), pp. 3965-3975, (1999).
158. "Growth and Characterization of Epitaxial NiMnSb/PtMnSb C1_b Heusler Alloy Superlattices", F. B. Mancoff, J. F. Bobo, O. Richter, K. Bessho, P. R. Johnson, R. Sinclair, W. D. Nix, R. L. White and B. M. Clemens, *J. Mater. Res.*, **14** (4), pp. 1560-1569, (1999).
159. "Case Study of Media Noise Mechanisms in Longitudinal Recording", E. T. Yen, S.Z. Wu, T. Thomson, R. Ristau, R. Ranjan, G. C. Rauch, C. Habermeier and R. Sinclair, *IEEE Trans. Magn.*, **35** (5), pp. 2730-2732, (1999).
160. "Study of DC Plasma Oxidized Al₂O₃ Barriers in Spin Dependent Tunneling Junctions Using High Resolution Transmission Electron Microscopy", T. E. Clark, F. B. Mancoff, S. X. Wang, B.M. Clemens and R. Sinclair, *IEEE Trans. Magn.*, **35** (5), pp. 2922-2924, (1999).
161. "Grain Size Analysis of Longitudinal Thin Film Media", D.W. Park, R. Sinclair, B.B. Lal, S.S. Malhotra and M.A. Russak, *J. Appl. Phys.*, **87** (9), pp. 5687-5689, (2000).

162. "In Situ TEM Studies of Metal-Carbon Reactions", R. Sinclair, T. Itoh and R. Chin, *Microscopy and Microanalysis* **8**, pp. 288-304, (2002).
163. "Transmission Electron Microscopy Analysis of Computer Hard Disc, Magnetic Thin Films", J. Risner, U. Kwon, D.W. Park and R. Sinclair, *Mater. Chem. Phys.* **81**, pp. 241-243, (2003)
164. "Thermal Stability of Epitaxial Pt Films on Y₂O₃ in a Metal-Oxide-Si Structure", M.-H. Cho, D.W. Moon, K.H. Min, R. Sinclair, S.A. Park, Y.K. Kim, K. Jeong, S.K. Kang and D.-H. Ko, *Appl. Phys. Lett.*, **83** (23), pp. 4758-4760, (2003).
165. "Change in the Chemical State and Thermal Stability of HfO₂ by the Incorporation of Al₂O₃", M.-H. Cho, H.S. Chang, Y.J. Cho, D.W. Moon, K.-H. Min, R. Sinclair, S.K. Kang, D.-H. Ko, J.H. Lee, J.H. Gu and N.I. Lee, *Appl. Phys. Lett.*, **84** (4), pp. 571-573, (2004).
166. "Carbide Evolution in Temper Embrittled NiCrMoV Bainitic Steel", J.E. Wittig and R. Sinclair, *Steel Res. Int.*, **75** (1), pp. 47-54, (2004).
167. "Investigation of the Chemical State of Ultrathin Hf-Al-O Films during High Temperature Annealing", M.-H. Cho, H. S. Chang, Y.J. Cho, D.W. Moon, K.-H. Min, R. Sinclair, S.K. Kang, D.-H. Ko, J.H. Lee, J.H. Gu, et al., *Surface Science*, **554** (1), pp. L75-L80, (2004).
168. "Recent Developments in Nano-Characterization of Materials", R. Sinclair, H. Li, J. Risner, U. Kwon, J.U. Huh, R.W. Chin and K.H. Min, *J. Ceram. Proc. Res.*, **5** (1), pp. 5-9 (2004).
169. "Crystallization and Anisotropic Dielectric Properties of Tantalum Oxide Thin Films", K.-H. Min and R. Sinclair, *J. Ceram. Proc. Res.*, **6**, pp. 17-19, (2005).
170. "Application of In Situ HREM to Study Crystallization in Materials", R. Sinclair, K.-H. Min, and U. Kwon, *Materials Science Forum*, **494**, pp. 7-12, (2005).
171. "Crystallization Behavior of ALD-Ta₂O₅ Thin Films: An Application of In-situ TEM", K.-H. Min, R. Sinclair, I.-S. Park, S.-T. Kim, and U.-I. Chung, *Philos. Mag.*, **85** (18), pp. 2049-2063, (2005).
172. "Ru/Ru-oxide Interlayers for CoCrPtO Perpendicular Recording Media", U. Kwon, R. Sinclair, E.M.T. Velu, S. Malhotra, and G. Bertero, *IEEE Trans. Magn.*, **41** (10), pp. 3193-3195, (2005).
173. "Observation of the Effect of Grain Orientation on Chromium Segregation in Longitudinal Magnetic Media", J.D. Risner, R. Sinclair and J. Bentley, *J. Appl. Phys.*, **99**, pp. 033905-1-7, (2006).
174. "FIB and TEM Studies of Interface Structure in Diamond-SiC Composites," J.S. Park, R. Sinclair, D. Rowcliffe, M. Stern, and H. Davidson, *J. Mater. Sci.*, **41** (14), pp. 4611-4616, (2006).
175. "Effect of Magnetic Recording Layer Thickness on Media Performance in CoCrPt-Oxide Perpendicular Media," U. Kwon, H.S. Jung, M. Kuo, E.M.T. Velu, S.S. Malhotra, W. Jiang, G. Bertero, and R. Sinclair, *IEEE Trans. Magn.*, **42** (10), pp. 2330-2332, (2006).
176. "Microstructure and Exchange Coupling of Segregated Oxide Perpendicular Recording Media", T.P. Nolan, J.D. Risner, S.D. Harkness, E. Girt, S.Z. Wu, G.P. Ju and R. Sinclair, *IEEE Trans. Magn.*, **43** (2), pp. 639-644, (2007).
177. "Orientation Relationship in Diamond and Silicon Carbide Composites", J.S. Park, R. Sinclair, D. Rowcliffe, M. Stern and H. Davidson, *Diamond Rel. Mater.*, **16** (3), pp. 562-565, (2007).
178. "Analytical TEM Examinations of CoPt-TiO₂ Perpendicular Magnetic Recording Media", J.D. Risner, T.P. Nolan, J. Bentley, E. Girt, S.D. Harkness IV, and R. Sinclair, *Microsc. Microanal.*, **13**, pp. 70-79, (2007).
179. "High-Moment Antiferromagnetic Nanoparticles with Tunable Magnetic Properties", W. Hu, R. J. Wilson, A.L. Koh, A. Fu, A.Z. Faranesh, C. M. Earhart, S.J. Osterfeld, S-J. Han, L. Xu, S. Guccione, R. Sinclair and Shan X. Wang, *Advanced Materials* **20**, pp. 1479-1483 (2008).
180. "Real-Time Intravital Imaging of RGD-Quantum Dot Binding to Luminal Endothelium in Mouse Tumor Neovasculature", B. R. Smith, Z. Cheng, A. De, A. L. Koh, R. Sinclair and S. S. Gambhir, *Nano Letters* **8**(9), pp. 2599-2606, (2008).
181. "Synthesis and characterization of PVP-coated large core iron oxide nanoparticles as an MRI contrast agent", H-Y. Lee, S-H Lee, C. Xu, J. Xie, J-H. Lee, B. Wu, A. L. Koh, X. Wang, R. Sinclair, S. X. Wang, D. G. Nishimura, S. Biswall, S. Sun, S. H. Cho and X. Chen, *Nanotechnology* **19** (2008) 165101
182. "TEM Analyses of Synthetic Anti-Ferromagnetic (SAF) Nanoparticles Fabricated Using Different Release Layers", A.L. Koh, W. Hu, R.J. Wilson, S.X. Wang and R. Sinclair, *Ultramicroscopy* **108**, pp. 1490-1494 (2008).
183. "Improved QD-BRET Conjugates for Detection and Imaging", Y. Xing, M-K. So, A.L. Koh, R. Sinclair and J. Rao, *Biochemical and Biophysical Research Communications* **372**, pp. 388-394 (2008).

184. "Electron Microscopy Localization and Characterization of Functionalized Composite Organic-Inorganic SERS Nanoparticles on Leukemia Cells", A. L. Koh, C.M. Shachaf, S. Elchuri, G.P. Nolan and R. Sinclair, *Ultramicroscopy* **109**, pp. 111-121 (2008)
185. "Preparation, Structural and Magnetic Characterization of Synthetic Anti-ferromagnetic (SAF) Nanoparticles", A.L. Koh, W. Hu, R.J. Wilson, S.X. Wang and R. Sinclair, *Philosophical Magazine* **88**:36 pp. 4225-4241 (2008).
186. "Multiplex detection of protease activity with quantum dot nanosensors prepared by intein-mediated specific bioconjugation", Z. Xia, Y. Xing, M-K. So, A.L. Koh, R. Sinclair and J. Rao, *Anal. Chem.* **80**, pp. 8649–8655 (2008).
187. "Particle Size, Surface Coating, and PEGylation Influence the Biodistribution of Quantum Dots in Living Mice", M.L. Schipper, G. Iyer, A.L. Koh, Z. Cheng, Y. Ebenstein, A. Aharoni, S. Keren, L.A. Bentolila, J. Li, J. Rao, X. Chen, U. Banin, A.M. Wu, R. Sinclair, S. Weiss, and S.S. Gambhir, *Small* **5** (1) (2009): 126-34.
188. "Synthetic Antiferromagnetic Nanoparticles with Tunable Susceptibilities", W. Hu, R. J. Wilson, C. M. Earhart, A.L. Koh, R. Sinclair and S. X. Wang, *J. Appl. Phys.* **105**, 2009, pp. 07B508 1-3.
189. "Formation and properties of magnetic chains for 100 nm nanoparticles used in separations of molecules and cells", R.J. Wilson, W. Hu, C. P.F. Wong, A.L. Koh, R. Gaster, C.M. Earhart, A. Fu, S.C. Heilshorn, R. Sinclair and S. X. Wang, *J. Magn. Magn. Mat.* **321** (2009), pp.1452–1458.
190. "No Titan, No Excuse" (T.J. Konno, 1 April 2008) A Report on an International Workshop on Remote Electron Microscopy for In Situ Studies", R. Sinclair, R. Chin, A.L. Koh and G. Solorzano, *Acta Microscopica* **18**(1) (2009) pp. 33–38.
191. "A novel method for detection of phosphorylation in single cells by Surface Enhanced Raman Scattering (SERS) using Composite Organic-Inorganic Nanoparticles (COINs)", C. M. Shachaf, S. Elchuri, A.L. Koh, J. Zhu, L. Nguyen, D.J. Mitchell, J. Zhang, K. Swartz, L. Sun, S. Chan, R. Sinclair and G.P. Nolan, *PLoS One* **4**(4) (2009) doi:10.1371/journal.pone.0005206
192. "Structural and Magnetic Characterization of High Moment Synthetic Antiferromagnetic Nanoparticles Fabricated Using Self-Assembled Stamps", A.L. Koh, W. Hu, R.J. Wilson, C. M. Earhart, S. X. Wang and R. Sinclair, *J. Appl Phys.* **107** (2010), pp. 09B522 1-3.
193. "Atomic layer deposition of ZnS via in situ production of H₂S", J.R. Bakke, J.S. King, H.J. Jung, R. Sinclair and S.F. Bent, *THIN SOLID FILMS.* **518** (2010) pp. 5400–5408.
194. "Atomic Layer Deposition of CdS Films", J. R. Bakke, H. J. Jung, J. T. Tanskanen, R. Sinclair and S. F. Bent, *Chem. Mater.* **22** (2010), pp. 4669–4678.
195. "Laser-Synthesized Epitaxial Graphene", S. Lee, M.F. Toney, W. Ko, J.C. Randel, H.J. Jung, K. Munakata, J.Lu, T.H. Geballe, M.R. Beasley, R. Sinclair, H.C. Manoharan, A. Salleo, *ACS Nano*, **4** (12) pp. 7524-7530 (2010).
196. "Scanning Tunneling Spectroscopy of Lead Sulfide Quantum Wells Fabricated by Atomic Layer Deposition for Band Gap Engineering", W. Lee, N. P. Dasgupta, H.J. Jung, J.-R. Lee, R. Sinclair and F.B. Prinz, *Nanotechnology*, **21**, 485402, 4pp. (2010).
197. "Atomic Layer Deposition of Cd_xZn_{1-x}S Films", J.R. Bakke, J.T. Tanskanen, H.J. Jung, R. Sinclair and S.F. Bent, *J. Mater. Chem.*, **21**, 743–751 (2011). doi: 10.1039/c0jm02786c.
198. "Thermal conductivity anisotropy and grain structure in Ge₂Sb₂Te₅ films", J. Lee, Z. Li, J.P. Reifenberg, S. Lee, R. Sinclair, M. Asheghi and K.E. Goodson. *J. Appl. Phys.* **109** (8) pp. 084902-084908 (2011). doi: 10.1063/1.3573505.
199. "Atomic Layer Deposition of Lead Sulfide Quantum Dots on Nanowire Surfaces", H.J. Jung, N. Dasgupta, O. Trejo, M.T. McDowell, A. Hryciw, M. Brongersma, R. Sinclair and F.B. Prinz, *Nano Lett.*, **11** (3), pp 934–940 (2011). doi: 10.1021/nl103001h.
200. "Crater Patterned 3-D Protonic Fuel Cell with Ultra Thin Y:BaZrO₃ Ceramic Membrane", Y.B. Kim, T.M. Gur, S. Kang, H.J. Jung, R. Sinclair, F.B. Prinz, *Electrochem. Comm.*, **13** (5), pp. 403-406 (2011). doi: 10.1016/j.elecom.2011.02.004.
201. "Effect of crystallinity on ionic conductivity of Y-doped Barium Zirconate", Y.B. Kim, T.M. Gur, H.J. Jung, S. Kang, R. Sinclair, F.B. Prinz, *Solid State Ionics*, **Vol. 198**, Issue 1, 19, 39-46 (2011).
202. "Fabrication of planar, layered nanoparticles using tri-layer resist templates", W. Hu, M. Zhang, R.J. Wilson, A.L. Koh, J.-S. Wi, M. Tang, R. Sinclair and S.X. Wang, *Nanotechnology* **22** (18) pp. 185302-185308 (2011). doi. 10.1088/0957-4484/22/18/185302.

203. "Oxidative Stress Mediates the Effects of Raman Active Gold Nanoparticles in Human Cells", A.S. Thakor, R. Paulmurugan, P.J. Kempen, C.L. Zavaleta, R. Sinclair, T.F. Massoud, and S.S. Gambhir, *Small*, **7**: 126–136 (2011).
204. "The Fate and Toxicity of Raman Active Silica-Gold Nanoparticles in Mice", A.S. Thakor, R. Luong, R. Murugan, F. Lin, P.J. Kempen, C.L. Zavaleta, P. Chu, T.F. Massoud, R. Sinclair and S.S. Gambhir, *Sci Transl Med*, **3**:79ra33, (2011).
205. "Preclinical Evaluation of Raman Nanoparticle Biodistribution for their Potential Use in Clinical Endoscopy Imaging", C.L. Zavaleta, K.B. Hartman, Z. Miao, M.L. James, P. Kempen, A.S. Thakor, C.H. Nielsen, R. Sinclair, Z. Cheng and S.S. Gambhir, *Small*, **7** (15), pp. 2232-2240, (2011). doi: 10.1002/sml.201002317
206. "Scanning Transmission Electron Microscopy Analysis of Grain Structure in Perpendicular Magnetic Recording Media", F. Hossein-Babaei, R. Sinclair, K. Srinivasan and G. A. Bertero, *Nano Lett.*, **11** (9), pp 3751–3754 (2011).
207. "A Brain Tumor Molecular Imaging Strategy Using a Novel Triple Modality Nanoparticle", M.F. Kircher, A. De La Zerda, J.V. Jokerst, C.L. Zavaleta, P.J. Kempen, E.S. Mittra, F.G. Habte, R. Sinclair and S.S. Gambhir, *Nature Medicine*, **18**, pp. 829-834 (2012)
208. "Effects of Thermal Cycling on Microstructure and Properties in Nitinol", A.R. Pelton, G.H. Huang, P. Moine and R. Sinclair, *Mater. Sci. Eng. A*, **532**, pp. 130-138 (2012).
209. "Oxygen Surface Exchange at Grain Boundaries of Oxide Ion Conductors", W. Lee, H.J. Jung, M.H. Lee, Y.B. Kim, J.S. Park, R. Sinclair and F.B. Prinz, *Adv. Funct. Mater.*, **22** (5), pp. 965–971 (2012).
210. "Smart-cut Layer Transfer of Single-crystal SiC using Spin-on-Glass", J.H. Lee, I. Bargatin, J. Park, K.M. Milaninia, L.S. Theogarajan, R. Sinclair and R.T. Howe, *J. Vac. Sci. Technol. B*, **30** (4), pp. 0420010 1-6 (2012).
211. "Nickel Silicide Nanowire Arrays for Anti-Reflective Electrodes in Photovoltaics", N.P. Dasgupta, S.Xu, H.J. Jung, A. Iancu, R. Fasching, R. Sinclair and F.B. Prinz, *Adv. Funct. Mater.*, **22** (17), pp. 3650–3657 (2012).
212. "In Situ Cycle-by-Cycle Flash Annealing of Atomic Layer Deposited Materials", M. Langston, N. Dasgupta, H.J. Jung, M. Logar, Y. Huang, R. Sinclair and F.B. Prinz, *J. Phys. Chem. C*, **116** (45), pp. 24177–24183 (2012).
213. "Photoacoustic Imaging of Mesenchymal Stem Cells in Living Mice via Silica-Coated Gold Nanorods," J.V. Jokerst, M. Thangaraj, P.J. Kempen, R. Sinclair and S.S. Gambhir, *ACS Nano*: **6** (7), pp. 5920-30, (2012). PMID: 22681633
214. "Shape Matters: Intravital Microscopy Reveals Surprising Geometrical Dependence for Nanoparticles in Tumor Models of Extravasation," B.R. Smith, P.J. Kempen, D. Bouley, Z. Liu, H. Dai, R. Sinclair and S.S. Gambhir, *Nano Letters*: **12** (7), pp. 3369-77, (2012). PMID: PMC3495189
215. "Aberration Corrected Transmission Electron Microscopy of the Intergranular Phase in Magnetic Recording Media," F. Hossein-Babaei, A. L. Koh, K. Srinivasan, G. A. Bertero and R. Sinclair, *Nano Lett.* **12** (5), pp. 2595–2598 (2012).
216. "Interfacial Alloy Hydride Destabilization in Mg/Pd Thin Films," C.J. Chung, S.C. Lee, J.R. Groves, E.N. Brower, R. Sinclair and B.M. Clemens, *Phys. Rev. Lett.*, **108**, pp. 106102 1-4 (2012).
217. "Spatial Variation of Available Electronic Excitations Within Individual Quantum Dots," H.J. Jung, N.P. Dasgupta, P.B. Van Stockum, A.L. Koh and R. Sinclair, *Nano Lett.* **13** (2), pp. 716-721, DOI: 10.1021/nl304400c (2013).
218. "Observations of Carbon Nanotube Oxidation in an Aberration-Corrected, Environmental Transmission Electron Microscope," A. L. Koh, E. Gidcumb, O. Zhou and R. Sinclair, *ACS nano* **7**(3), pp. 2566-2572, DOI: 10.1021/nn305949h (2013).
219. "HREM Analysis of Graphite-Encapsulated Metallic Nanoparticles for Possible Medical Applications," R. Sinclair, H. Li, S. Madsen and H. Dai, *Ultramicroscopy* **134**, pp. 167-174, (2013).
220. "Atomic Layer Deposition of CdO and Cd_xZn_{1-x}O Films", J.R. Bakke, C. Häggglund, H.J. Jung, R. Sinclair and S.F. Bent, *Materials Chemistry and Physics* **140**, pp. 465-471, (2013).
221. "Aberration-Corrected TEM Imaging of Oxygen Occupancy in YSZ", J. An, A. L. Koh, J. S. Park, R. Sinclair, T. M. Gür and F. B. Prinz, *J. Phys. Chem. Lett.* **4** (7), pp. 1156-1160, DOI: 10.1021/jz4002423 (2013).
222. "Codoping Titanium Dioxide Nanowires with (W, C) for Enhancing Photoelectrochemical Performance," I.S. Cho, C.H. Lee, Y. Feng, M. Logar, P.M. Rao, L. Cai, D.R. Kim, R. Sinclair and X. Zheng, *Nature Communications* **4**, 1723, DOI: 10.1038/ncomms2729 (2013).

223. "Amorphous Thin Film TaWSiC as a Diffusion Barrier for Copper Interconnects", R. Wongpiya, J. Ouyang, T. R. Kim, M. Deal, R. Sinclair, Y. Nishi and B. Clemens, *Appl. Phys. Lett.* **103**, 022104, DOI: 10.1063/1.4813396 (2013).
224. "Atomic Scale Verification of Oxide-Ion Vacancy Distribution near a Single Grain Boundary in YSZ", J. An, J.S. Park, A.L. Koh, H.B. Lee, H.J. Jung, R. Sinclair, T.M. Gür and F.B. Prinz, *Scientific Reports* **3**, 2680, DOI:10.1038/srep02680 (2013).
225. "A Scanning Transmission Electron Microscopy (STEM) Technique to Analyze 'Large' Volumes of Tissue to Detect Nanoparticles," P.J. Kempen, A.S. Thakor, C.L. Zavaleta, S.S. Gambhir and R. Sinclair, *Microscopy and Microanalysis* **19** (5) pp. 1290-1297, (2013).
226. "Approaching the Limits of Dielectric Breakdown for SiO₂ Films Deposited by Plasma-Enhanced Atomic Layer Deposition", T. Usui, C. A. Donnelly, M. Logar, R. Sinclair, J. Schoonman and F. B. Printz, *Acta Materialia* **61** (20) pp. 7660-7670, (2013).
227. "*In Situ* High-Resolution Transmission Electron Microscopy of Materials Reactions", R. Sinclair, *Mat. Res. Soc. Bull.* **38**, pp. 1065-1071, (2013).
228. "Effects of Germanium Incorporation on Optical Performances of silicon Germanium Passive Devices for Group-IV Photonic Integrated Circuits", S. Cho, J. Park, H. Kim, R. Sinclair, B.-G. Park and J. S. Harris Jr., *Phot. Nano. Fund. Appl.* **12** (1), pp. 54-68, (2014).
229. "The Stanford Nanocharacterization Laboratory (SNL) and Recent Applications of an Aberration-Corrected Environmental Transmission Electron Microscope", R. Sinclair, P. J. Kempen, R. Chin and A. L. Koh, *Adv. Eng. Mater.*, **16** (5), pp. 476-481, (2014).
230. "A Tunable Silk-alginate Hydrogel Scaffold for Stem Cell Culture and Transplantation", K. Ziv, H. Nuhn, Y. Ben-Haim, L. S. Sasportas, P. J. Kempen, T. P. Niedringhaus, M. Hrynyk, R. Sinclair, A. E. Barron and S. S. Gambhir, *Biomaterials*, **35** (12), pp. 3736-3743, (2014).
231. "RESET-First Unipolar Resistance Switching Behavior in Annealed Nb₂O₅ Films", K. Lee, J. Kim, I.-S. Mok, H. Na, D.-H. Ko, H. Sohn, S. Lee and R. Sinclair, *Thin Solid Films* **558**, pp. 423-429, (2014).
232. "Tuning Interlayer Coupling in Large-Area Heterostructures with CVD-grown MoS₂ and WS₂ Monolayers", S. Tongay, W. Fan, J. Kang, J. Park, U. Koldemir, J. Suh, D. S. Narang, K. Liu, J. Ji, J. Li, R. Sinclair and J. Wu, *Nano Lett.*, **14** (6), pp. 3185-3190, (2014).
233. "Redox-Triggered Self-Assembly of Gadolinium-Based MRI Probes for Sensing Reducing Environment", D. Ye, P. Pandit, P. Kempen, J. Lin, L. Xiong, R. Sinclair, B. Rutt and J. Rao, *Bioconjugate Chem.*, **25** (8), pp. 1526-1536, (2014).
234. "Ultrafast Polarization Response of an Optically Trapped Single Ferroelectric Nanowire", S. Nah, Y.-H. Kuo, F. Chen, J. Park, R. Sinclair and A. M. Lindenberg, *Nano Lett.*, **14** (8), pp. 4322-4327, (2014).
235. "Designing Active and Stable Silicon Photocathodes for Solar Hydrogen Production Using Molybdenum Sulfide Nanomaterials", J. D. Benck, S. C. Lee, K. D. Fong, J. Kibsgaard, R. Sinclair and T. F. Jaramillo, *Adv. Energy Mater.*, **4** (18), pp. 1400739, (2014).
236. "Controlling Sulphur Precursor Addition for Large Single Crystal Domains of WS₂", Y. Rong, Y. Fan, A. L. Koh, A. W. Robertson, K. He, S. Wang, H. Tan, R. Sinclair and J. H. Warner, *Nanoscale* **6** (20), pp. 12096-12103, (2014).
237. "Doping against the Native Propensity of MoS₂: Degenerate Hole Doping by Cation Substitution", J. Suh, T.-E. Park, D.-Y. Lin, D. Fu, J. Park, H. J. Jung, Y. Chen, C. Ko, C. Jang, Y. Sun, R. Sinclair, J. Chang, S. Tongay and J. Wu, *Nano Lett.*, **14** (12), pp. 6976-6982, (2014).
238. "A Correlative Optical Microscopy and Scanning Electron Microscopy Approach to Locating Nanoparticles in Brain Tumors", P. J. Kempen, M. F. Kircher, A. de la Zerda, C. L. Zavaleta, J. V. Jokerst, I. K. Mellinghoff, S. S. Gambhir and R. Sinclair, *Micron*, **68**, pp. 70-76, (2015).
239. "Control of Rubrene polymorphs via polymer binders: applications in Organic Field Effect Transistors", P. S. Jo, D. T. Duong, J. Park, R. Sinclair and A. Salleo, *Adv. Funct. Mater.*, (2014) submitted.
240. "Scalable Assembly of Densely Aligned Single-Walled Carbon Nanotubes using Solution Shearing and their Application to Field-Effect Transistors", S. Park, G. Pitner, G. Giri, J. H. Koo, J. Park, K. Kim, H. Wang, R. Sinclair and Z. Bao, *Nano Lett.*, (2014) submitted

C. PATENTS

1. "Multilayered Thin Films for Perpendicular Magnetic Recording", G. A. Bertero and R. Sinclair, filed April 1994.

2. "Method for Producing Uniaxial Tetragonal Thin Films of Ternary Intermetallic Compounds", M. R. Visokay, B. M. Lairson and R. Sinclair, filed February 1995.

D. CONFERENCE ARTICLES, ETC.(non-refereed and refereed)

1. "High Resolution Transmission Electron Microscopy", R. Sinclair, Industrial Research, pp. 62-65 (October 1973).
2. "Lattice Image Contrast of Ordered Domains in Cu_3Au ", R. Sinclair and G. Thomas, 32nd Proc. EMSA, pp. 500-501 (1974).
3. "A New 1000°C Double Tilt Stage for the Hitachi 650 kV Microscope", W. Worthington, T. Kosel and R. Sinclair, 32nd Proc. EMSA, pp. 442-443 (1974).
4. "Lattice Imaging of Ordered Alloys", R. Sinclair, K. Scheider and G. Thomas, Proc. ICEM-VIII, pp. 520-521 (1974).
5. "Lattice Image Studies of Ordered Alloys", R. Sinclair and J. Dutkiewicz, 33rd Proc. EMSA, pp. 10-11 (1975).
6. "Lattice Imaging of Spinodal Alloys", R. Gronsky, M. Okada, R. Sinclair and G. Thomas, 33rd Proc. EMSA, pp. 22-23 (1975).
7. "Studies of Atomic Scattering Factors from the Critical Voltage in Ordered Alloys: Applications to Cu_3Au ", A. Rocher, R. Sinclair and G. Thomas, *Proc. 4th Int'l Congress on High Voltage Electron Microscopy*, pp. 125-128 (1975).
8. "Preliminary Observations of Electron Irradiation Damage in Short-Range Ordered Ni_4Mo ", R. Sinclair, D.S. Gelles and G. Thomas, 34th Proc. EMSA, pp. 600- 601 (1976).
9. "Optical Microdiffraction in Lattice Image Analysis", R. Gronsky, R. Sinclair, and G. Thomas, 34th Proc. EMSA, pp. 494-495 (1976).
10. "Lattice Image and Optical Diffraction Studies of Alloys", G. Thomas, R. Sinclair, and R. Gronsky, *Proc. 6th European Congress on Electron Microscopy*, Jerusalem, pp. 114-119 (1976).
11. "Applications of High Resolution Electron Microscopy in Materials Science", *Report of Workshop on High Resolution Electron Microscopy*, eds. G. Thomas, R.M. Glaeser, J.M. Cowley and R. Sinclair, Lawrence Berkeley Laboratory Special Publication #106, pp. 71-79 (1976).
12. "Fine Structure of Interfaces as Revealed by Lattice Fringe Imaging", R. Sinclair, 35th Proc. EMSA, pp. 110-113 (1977).
13. "Aspects of Microanalysis in a TEM", R. Sinclair and B.E. Jacobson, Proc. ICEM-IX **1**, pp. 510-511 (1978).
14. "Applications of Lattice Fringe Imaging", R. Sinclair, Proc. ICEM-IX **3**, pp. 140-146 (1978).
15. "Growth Relationships in $\text{Nb}_3\text{Sn-Cu}$ Superconducting Composites", B.E. Jacobson and R. Sinclair, *New Developments and Applications in Composites*, eds. D. Kuhlman-Wilsdorf and W.C. Harrigan (Met. Soc., AIME), pp. 204-221 (1979).
16. "*In-Situ* Observations of Diffusionless Transformations in NiTi ", G.M. Michal and R. Sinclair, ICOMAT 79, pp. 136-141 (1979).
17. "Origin of Stacking Faults in NiTi Martensite", R. Sinclair, *Modulated Structures 1979*, eds. J.M. Cowley, J.B. Cohen, M.B. Salamon and B.J. Wuensch, AIP Proc. #53, pp. 269-271 (1979).
18. "Lattice Fringe Imaging of Alloys", R. Sinclair, 37th Proc. EMSA, pp. 404-407 (1979).
19. "Physical Properties of Ion-Implanted SEM-Annealed Silicon", J.L. Regolini, N.M. Johnson, R. Sinclair, T.W. Sigmon and J.F. Gibbons, *Laser and Electron Beam Processing of Materials*, eds. C.W. White and P.S. Percey, Academic (New York), pp. 297-302 (1980).
20. "High Resolution Imaging of Cadmium Telluride", R. Sinclair, F. Ponce, T. Yamashita and P. Pirouz, *Proc. 7th European Congress on Electron Microscopy*, pp. 312-313 (1980).
21. "Structure Imaging of Defects in Cadmium Telluride", F. Ponce, T. Yamashita and R. Sinclair, 38th Proc. EMSA, pp. 320-321 (1980).
22. "A Transmission Electron Microscopical Investigation of Phase Transformations in TiNi ", P. Moine, G.M. Michal and R. Sinclair, 38th Proc. EMSA, pp. 340-341. (1980).
23. "Defect Structure of Deformed WC", M.K. Hibbs and R. Sinclair, 38th Proc. EMSA, pp. 216-217 (1980).
24. "Analytical Electron Microscopy of Ferroelectric BaTiO_3 ", M.L. Mecartney and R. Sinclair, 38th Proc. EMSA, pp. 364-365 (1980).

25. "Combined High Resolution and Analytical TEM Studies of Phase-Separated Alloys", C.K. Wu, A.F. Marshall, G. Thomas and R. Sinclair, 38th Proc. EMSA, pp. 176-177 (1980).
26. "Chemical and Microstructural Analyses of Grain Boundaries in BaTiO₃-Based Dielectrics". M.L. Mecartney, R. Sinclair and G.J. Ewell, *Advances in Ceramics*, Volume 1, edited by L.M. Levinson, (American Ceramic Soc. Columbus, OH) pp. 207-214 (1981).
27. "Imaging of Defects in Cadmium Telluride Using High Resolution Transmission Electron Microscopy", F.A. Ponce, T. Yamashita, R.H. Bube and R. Sinclair, in *Defects in Semiconductors*, eds. J. Narayan and T.Y. Tan, (1981).
28. "High Resolution Transmission Electron Microscopy of Semiconductor Materials", R. Sinclair, F.A. Ponce, J.C. Bravman, T. Yamashita and P. Pirouz, *Proc. of the 2nd Conference on Microscopy of Semiconducting Materials*, Oxford, England, pp. 147-152 (1981).
29. "High Resolution Imaging of Semiconductor Interfaces", R. Sinclair, F.A. Ponce, T. Yamashita and J.C. Bravman, 39th Proc. EMSA, pp. 124-127 (1981).
30. "The Premartensitic State in TiNi", R. Sinclair, P. Moine and G.M. Michal, *Proc. of the Int'l Conference on Solid-Solid Phase Transformations*, pp. 1253-1257 (1981).
31. "Applications of the 2 1/2 D TEM Technique", R. Sinclair, EMAG1981, Inst. Phys. Conference Series 61, pp. 341-342 (1982).
32. "Lattice Resolution Movie of Defect Modification in Cadmium Telluride", R. Sinclair, D.J. Smith, S.J. Erasmus and F.A. Ponce, Proc. ICEM-X 2, pp. 47-48 (1982).
33. "The Effect of Oxygen in Cosputtered (Titanium + Silicon) Films", R. Beyers, R. Sinclair and M.E. Thomas, in *Defects in Semiconductors*, eds. J.W. Corbett and S. Mahajan, (Elsevier North-Holland), pp. 423-427 (1982).
34. "Dynamic Observation of Atomic-Level Events in Cadmium Telluride by High Resolution TEM", T. Yamashita and R. Sinclair, in *Defects in Semiconductors*, eds. J.W. Corbett and S. Mahajan, (Elsevier North-Holland), pp. 295-299 (1982).
35. "High Resolution Electron Microscopy II-VI Compound Semiconductors", R. Sinclair, F.A. Ponce, T. Yamashita and David J. Smith, Inst. Phys. Conference Series 67, pp. 103-108 (1983).
36. "Defect Structure of WC Deformed at Room and High Temperatures", M.K. Hibbs, D.J. Rowcliffe and R. Sinclair, *Proc. of the Int'l Conference on the Science of Hard Materials*, eds. R.K. Viswanathan, D.J. Rowcliffe and J. Gurland, pp. 121-135 (1983).
37. "Microstructural Characterization of Deformation and Precipitation in (W, Ti)C", S.L. Shinde, V. Jayaram and R. Sinclair, *Proc. of the Int'l Conference on the Science of Hard Materials*, eds. R.K. Viswanathan, D.J. Rowcliffe and J. Gurland, pp. 137-154 (1983).
38. "High Voltage High Resolution Electron Microscopy of Compound Semiconductors", R. Sinclair, F.A. Ponce, T. Yamashita and David J. Smith, *Proc. 7th Int'l Conference on High Voltage Electron Microscopy*, LBL Report #16031, pp. 31-34 (1983).
39. "HREM of Interfaces and Defects in Semiconductors", R. Sinclair, 41st Proc. EMSA, pp. 130-133 (1983).
40. "Lattice Imaging of CdS/CdTe Solar Cell Interface", T. Yamashita, J.G. Werthen, R.H. Bube and R. Sinclair, 41st Proc. EMSA, ed. G.W. Bailey, San Francisco Press, San Francisco, pp. 124-125 (1983).
41. "Observation of Dislocation Reactions in CdTe at Lattice Resolution", T. Yamashita and R. Sinclair, 41st Proc. EMSA, pp. 112-113 (1983).
42. "Structural Determination of Amorphous Ti-Ni Alloys" A.R. Pelton, P. Moine, and R. Sinclair, 42nd Proc. EMSA, pp. 508-509 (1984).
43. "The Morphology of the Polysilicon-SiO₂ Interface", J.C. Bravman and R. Sinclair, *Mat. Res. Soc. Symp. Proc.*, **25**, pp. 311-316 (1984).
44. "Silicon on Sapphire of Single Crystal Quality Obtained by Double Solid Phase Exptaxial Regrowth", M.A. Parker, T.W. Sigmon and R. Sinclair, *Mat. Res. Soc. Symp. Proc.*, **37**, pp. 211-216 (1985).
45. "Morphological Studies of Polysilicon Emitter Contacts", J.C. Bravman, G.L. Patton, R. Sinclair and J.D. Plummer, *Mat. Res. Soc. Symp. Proc.*, **37**, pp. 461-466 (1985).
46. "Characterization of Emitter-Collector Shorts by Anodization, Voltage Contrast SEM and TEM", A.H. Carim, R. Sinclair and W.T. Stacy, *Mat. Res. Soc. Symp. Proc.*, **41**, pp. 375-380 (1985).
47. "Direct Observation of Defect Motion in Silicon By High Resolution Transmission Electron Microscopy", M.A. Parker and R. Sinclair, 43rd Proc. EMSA, pp. 358-359 (1985).

48. “*In-Situ* High Resolution Transmission Electron Microscopy of Dynamic Events During the Amorphous to Crystalline Phase Transformation in Silicon”, M.A. Parker, T.W. Sigmon and R. Sinclair, *Mat. Res. Soc. Symp. Proc.*, **62**, pp. 311-321 (1985).
49. “The Evolution of Si/SiO₂ Interface Roughness”, A.H. Carim and R. Sinclair, in *Semiconductor Silicon 1986*, eds. H.R. Huff, T. Abe, and B. Kolbesen, The Electrochemical Soc. Inc., Pennington, NJ, pp. 458-469 (1986).
50. “*In Situ* HREM and HVEM Studies of Silicon Epitaxial Regrowth”, M.A. Parker and R. Sinclair, *Proc. ICEM-XI 2*, pp. 991-992 (1986).
51. “Crystalline-To-Amorphous Transitions in Ti-Ni Alloys”, A.R. Pelton, P. Moine, M.A. Noak and R. Sinclair, *Mat. Res. Soc. Symp. Proc.*, **62**, pp. 291-302 (1986).
52. “Interfacial Reactions in Titanium-Silicon Multilayers”, K. Holloway and R. Sinclair, *Mat. Res. Soc. Symp. Proc.*, **77**, pp. 357-362 (1987).
53. “*In Situ* High Resolution Electron Microscopy for Interface Studies”, M.A. Parker and R. Sinclair, *Mat. Res. Soc. Symp. Proc.*, **82**, pp. 379-382 (1987).
54. “*In-Situ* and High-Resolution TEM Observation of Interfacial Reactions in Metal- Silicon Multilayers”, K. Holloway, K.B. Do and R. Sinclair, *Mat. Res. Soc. Symp. Proc.*, **103**, pp. 167-172 (1988).
55. “Microstructures of Polysilicon”, R. Sinclair, A.H. Carim, J. Morgiel and J.C. Bravman, *Mat. Res. Soc. Symp. Proc.*, **106**, pp. 27-38 (1988).
56. “Compressive Deformation and Fracture in WC Materials”, D.J. Rowcliffe, V. Jayaram, M.K. Hibbs and R. Sinclair, *Mat. Sci. and Eng. A*, **105-106**, pp. 299-303 (1988).
57. “Phase Equilibria at Semiconductor Interfaces”, R. Sinclair, A.S. Bhansali and A.F. Schwartzman, *Proc. 2nd Advanced Materials Institute Conf.*, pp. 11-17, ed. by F. W. Smith (AMI) (1989).
58. “*In Situ* High Resolution Electron Microscopy”, R. Sinclair, 47th Proc. EMSA, pp. 448-449 (1989).
59. “Reactions at Metal-Semiconductor Interfaces”, R. Sinclair, 47th Proc. EMSA, pp. 638-639 (1989).
60. “Transmission Electron Microscopy and High Resolution Scanning Electron Microscopy of Co-Ni-Pt Thin Film Magnetic Recording Media”, L. Chan, T. Yamashita and R. Sinclair, 47th Proc. EMSA, pp. 570-571 (1989).
61. “HREM *In Situ* Annealing of the CdTe/GaAs Heterojunction”, A.F. Schwartzman and R. Sinclair, *Mat. Res. Soc. Symp. Proc.*, **139**, pp. 205-210 (1989).
62. “Reaction and Structure at Metal-Semiconductor Interfaces”, R. Sinclair, K. Holloway, K.B. Kim, D.H. Ko, A.S. Bhansali, A.F. Schwartzman and S. Ogawa, *Inst. Phys. Conference Series 100*, pp. 599-607 (1989).
63. “*In Situ* Annealing Transmission Electron Microscopy (TEM) Study of Ti/GaAs and Ni/GaAs Interfacial Reactions”, K.B. Kim and R. Sinclair, *Mat. Res. Soc. Symp. Proc.*, **148**, pp. 21-26 (1989).
64. “Quaternary Phase Equilibria in the Ti-Si-N-O System: Stability of Metallization Layers and Prediction of Thin Film Reactions”, A.S. Bhansali and R. Sinclair, *Mat. Res. Soc. Symp. Proc.*, **148**, pp. 71-76 (1989).
65. “High-Resolution TEM of Metal-Semiconductor Interfaces”, R. Sinclair, *Proc. 2nd Int’l Conf. Solid St. Int. Circ. Techn.*, in press (1989).
66. “*In Situ* HREM Observation of Crystallization in Amorphous Silicon”, J. Morgiel, I.W. Wu, A. Chiang and R. Sinclair, *Proc. 2nd Int’l Conf. Solid St. Int. Circ. Techn.*, in press (1989).
67. “Twinless Martensite in TiNiCu Shape Memory Alloys”, W.J. Moberly, T.W. Duerig, J.L. Proft and R. Sinclair, *Proc. ICOMAT-89*, pp. 605 (1989).
68. “Structure and Reaction at Metal-Semiconductor Interfaces”, R. Sinclair and S. Ogawa, *Jpn. Soc. Appl. Phys.*, Catalog No. AP892228, No. 431, pp. 29-33 (1989).
69. “Mechanical Twinning and Plasticity in Ti-Ni-Fe(3%)”, W.J. Moberly, T.W. Duerig, J.L. Proft and R. Sinclair, *Proc. ICOMAT-89*, edited by B.C. Muddle, Trans Tech. Publications Ltd., pp. 759 (1990).
70. “Twinning in Ternary Ti₅₀Ni(50-x)M_x Alloys”, W.J. Moberly, R. Sinclair and T.W. Duerig, *Proc. ICEM-XII 4*, pp. 186-187 (1990).
71. “*In Situ* High-Resolution Electron Microscopy”, R. Sinclair, *Proc. ICEM-XII 4*, pp. 512-513 (1990).
72. “A Phase Diagram Approach for Predicting Reactions in Al/TiW (-Nitride) Thin-Film Systems”, A.S. Bhansali, I.J.M.M. Raaijmakers, R. Sinclair, A.E. Morgan, B.J. Burrow and M. Arst, *Mat. Res. Soc. Symp. Proc.*, **187**, pp. 15-20 (1990).
73. “Microstructure-Property Studies for Semiconductor Interfaces Using High- Resolution Electron Microscopy”, R. Sinclair, *SPIE Conf. Proc.*, edited by H.G. Craighead and J.M. Gibson, 1284, pp. 225-227 (1990).
74. “Characterization of Metal Silicide/Silicon Interfaces”, R. Sinclair, *Proc. Semicon/Kansai*, pp. 95-101 (1990).
75. “Thermodynamic Stability of PtAl Thin Films on GaAs”, D.H. Ko and R. Sinclair, *Mat. Res. Soc. Symp. Proc.*, **181**, pp. 333-338 (1990).

76. "Structure of the Ti-Single Crystal Si Interface", S. Ogawa, T. Kouzaki, T. Yoshida and R. Sinclair, *Mat. Res. Soc. Symp. Proc.*, **181**, pp. 139-144 (1990).
77. "SiO₂/Si Interfaces Studied by STM and HRTEM", M. Niwa, M. Onoda, H. Iwasaki and R. Sinclair, *Mat. Res. Soc. Symp. Proc.*, **183**, pp. 141-146 (1990).
78. "*In Situ* HREM Observations of Crystallization in LPCVD Amorphous Silicon", J. Morgiel, I.W. Wu, A. Chiang and R. Sinclair, *Mat. Res. Soc. Symp. Proc.*, **182**, pp. 191-194 (1990).
79. "HRTEM and Nano-scale Microanalysis of the Titanium/Silicon Interfacial Reaction Correlated with Electrical Properties", S. Ogawa, T. Kouzaki, T. Yoshida and R. Sinclair, *Proc. I.C.S.S.D.M.-90*, **22**, pp. 429-432 (1990).
80. "Structure and Thermodynamics of Amorphous Titanium-Silicon Produced by Solid- State Interdiffusion", K. Holloway, P. Moine, J. Delage, R. Bormann, R. Sinclair and L. Capuano, *Mat. Res. Soc. Symp. Proc.*, **187**, pp. 71-76 (1991).
81. "An *In Situ* HREM Study of Crystal Nucleation in Amorphous Silicon Thin Films", A.S. Kirtikar, J. Morgiel, R. Sinclair, I.W. Wu and A. Chiang, *Mat. Res. Soc. Symp. Proc.*, **202**, pp. 627-632 (1991).
82. "Low-Temperature Reactions at Metal-Semiconductor Interfaces", R. Sinclair, T.J. Konno, D.H. Ko and S. Ogawa, *Inst. Phys. Conf. Ser.* 117, pp. 283-287 (1991).
83. "*In Situ* Heating Studies at High Resolution", R. Sinclair, 49th Proc. EMSA, pp. 656-657 (1991).
84. "Crystallization of Amorphous Si in Si/Al Multilayers", T.J. Konno and R. Sinclair, 49th Proc. EMSA, pp. 824-825 (1991).
85. "Amorphous-Phase Formation and Initial Reactions at Pt/GaAs Interfaces", D.H. Ko and R. Sinclair, 49th Proc. EMSA, pp. 858-859 (1991).
86. "Reaction and Stability at Material Interfaces", R. Sinclair, 25th Proc. MAS 26, pp. 229-231 (1991).
87. "Evidence for a Grain Boundary Grooving Model of Agglomeration in Polycrystalline TiSi₂ Thin Films", T. Nolan, R. Beyers and R. Sinclair, *Mat. Res. Soc. Symp. Proc.*, **202**, pp. 95-100 (1991).
88. "A Highly Reliable Sub-Half Micron Via and Interconnect Technology Using Al Alloy High-Temperature Sputter Filling", H. Nishimura, T. Yamada, R. Sinclair and S. Ogawa, *VLSI Tech. Dig.*, pp. 74-75 (1992).
89. "Reaction and Stability at VLSI Contact Interfaces", S. Ogawa and R. Sinclair, *Jpn. Soc. Appl. Phys.*, Catalog No. AP921108-00, 29p-NC-3, pp. 1268 (1992).
90. "Crystallization of Amorphous Si in Al/Si Multilayers", T.J. Konno and R. Sinclair, *Mat. Res. Soc. Symp. Proc.*, **230**, pp. 189-194 (1992).
91. "Amorphous Phase Formation and the Initial Reactions at Pt/GaAs Interfaces", D.H. Ko and R. Sinclair, *Mat. Res. Soc. Symp. Proc.*, **230**, pp. 33-38 (1992).
92. "Crystallization of Amorphous Silicon-Aluminum Thin Films: *In-Situ* Observation and Thermal Analysis", T.J. Konno and R. Sinclair, *Mat. Res. Soc. Symp. Proc.*, **237**, pp. 609-614 (1992).
93. "Reactions at Solid Interfaces", R. Sinclair, D.H. Ko, T.J. Konno and T.P. Nolan, *Mat. Res. Soc. Symp. Proc.*, **238**, pp. 269-272 (1992).
94. "Two-Step Martensitic Transformations in TiNi (10% Cu) Shape Memory Alloys", W.J. Moberly, T.W. Duerig, J.L. Proft and R. Sinclair, *Mat. Res. Soc. Symp. Proc.*, **246**, pp. 55-60 (1992).
95. "Pt/GaAs Interfacial Reactions: Ex-Situ and *In-Situ* Annealing TEM Study", D.H. Ko and R. Sinclair, *Mat. Res. Soc. Symp. Proc.*, **260**, in press (1992).
96. "Reaction and Stability at ULSI Circuit Interfaces", R. Sinclair and S. Ogawa, *Mat. Res. Soc. Proc. ULSI-VII*, pp. 273-276 (1992).
97. "Study of Semiconductor Metallization Problems by High Resolution Electron Microscopy and Thermodynamic Analysis", R. Sinclair, *Proc. 3rd ICSICT*, pp. 122-123 (1992).
98. "Transmission Electron Microscopy of Epitaxial Fe/Pt Multilayers", M.R. Visokay, B.M. Lairson, B.M. Clemens and R. Sinclair, *J. Magn. Soc. Jap.*, **17**, S1, pp. 113-116 (1993).
99. "Production of c-Axis Oriented PtFe Thin Film with Perpendicular Magnetic Anisotropy", B.M. Lairson, M.R. Visokay, R. Sinclair and B.M. Clemens, *J. Magn. Soc. Jap.*, **17**, S1, pp. 40-43 (1993).
100. "Reactions at the Ti-Si Interface Studied Using Hot Stage TEM", A.S. Kirtikar and R. Sinclair, *Mat. Res. Soc. Symp. Proc.*, **260**, pp. 227-231 (1993).
101. "*In-Situ* High Resolution Electron Microscopy of Metal-Contact Induced Crystallization of Semiconductors", T.J. Konno and R. Sinclair, *Inst. Phys. Conf. Ser.* 134, pp. 173-176 (1993).
102. "Reactions in Metal-Metalloid Multilayers", R. Sinclair and T.J. Konna, *Mat. Res. Soc. Symp. Proc.*, **311**, pp. 3-8 (1993).

103. "Crystallization of Amorphous Germanium in Silver-Germanium Layered Systems", T.J. Konno and R. Sinclair, *Mat. Res. Soc. Symp. Proc.*, **311**, pp. 99-104 (1993).
104. "Structure and Magnetic Properties of Fe/Zr Multilayer Films", T.J. Konno, T. Nakayama, B.M. Clemens and R. Sinclair, *Mat. Res. Soc. Symp. Proc.*, **313**, pp. 731-736 (1993).
105. "Deposition of Barium Ferrite Thin Films by RF Off-Axis Magnetron Sputtering", J. Li, R. Sinclair, S.S. Rosenblum and H. Hayashi, 3rd Euro. Ceram. Soc. Conf. Proc., **2**, pp. 751-756 (1993).
106. "A Solid State Electrochemical Technique to Study Barium Ferrite Thermodynamic Stability". J. Li, T.M. Gur, R. Sinclair, S.S. Rosenblum and H. Hayashi, 3rd Euro. Ceram. Soc. Conf. Proc., **2**, pp. 413-418 (1993).
107. "Correlation of Microstructural and Magnetic Properties of Longitudinal Recording Media Using TEM", T.P. Nolan, R. Sinclair, T. Yamashita and R. Ranjan, 51st Proc. MSA, pp. 1016-1017 (1993).
108. "Grain Separation Enhanced Magnetic Coercivity in Pt/Co Multilayers", G.A. Bertero and R. Sinclair, 51st Proc. MSA, pp. 1038-1039 (1993).
109. "*In Situ* HREM of Interface Reactions", R. Sinclair and T.J. Konno, 51st Proc. MSA, pp. 830-831 (1993).
110. "Transmission Electron Microscopy Study of PtCo(001) and PtFe(001) Films Formed from Epitaxial Pt/Co and Pt/Fe Multilayers", M.R. Visokay, B.M. Lairson, B.M. Clemens and R. Sinclair, *Mat. Res. Soc. Symp. Proc.*, **311**, pp. 15-20 (1993).
111. "Evolution of Gd Thin Film Structure Due to Amorphization by Co-Deposition", T.C. Hufnagel, G.A. Bertero, R. Sinclair and B.M. Clemens, *Mat. Res. Soc. Symp. Proc.*, **311**, pp. 73-78 (1993).
112. "Structural Properties of Uniaxial Tetragonal PtCo(001) and PtFe(001) Thin Films on MgO(001)", B.M. Lairson, M.R. Visokay, R. Sinclair, S.M. Brennan and B.M. Clemens, *Mat. Res. Soc. Symp. Proc.*, **311**, pp. 9-14 (1993).
113. "Magnetic and Magneto-Optic Properties of PtFe(001) and PtCo(001) Thin Films", B.M. Lairson, M.R. Visokay, R. Sinclair, and B.M. Clemens, *Mat. Res. Soc. Symp. Proc.*, **313**, pp. 805-810 (1993).
114. "Magnetic Properties and Crystallography of Selected Co/Pt Multilayers with Rare-Earth Doped Interface", G.A. Bertero and R. Sinclair, *Mat. Res. Soc. Symp. Proc.*, **313**, pp. 817-822 (1993).
115. "Application of High Resolution Electron Microscopy to the Study of Magnetic Thin Films and Multilayers", R. Sinclair, T.P. Nolan, G.A. Bertero and M.R. Visokay, *Mat. Res. Soc. Symp. Proc.*, **313**, pp. 705-712 (1993).
116. "Real Time Lattice Imaging of Crystallization in Amorphous Silicon", J. Morgiel, I.W. Wu, A. Chiang and R. Sinclair, *VIII El. Microsc. Conf. on Sol. St. Phys. Proc.*, pp. 131-139 (1993).
117. "TEM and *In Situ* HREM for Studying Metal-Semiconductor Interfacial Reactions", R. Sinclair, T.J. Konno, and D.-H. Ko, *Reactive Phase Formation at Interfaces and Diffusion Processes*, eds. Y. Limoge and J.L. Bocquet, V. 155-156 of Materials Science Forum, Trans Tech Pub., pp. 111-120 (1994).
118. "Reactions at Semiconductor Metal Interfaces", R. Sinclair, T.J. Konno and D.-H. Ko, First International Symposium on Control of Semiconductor Interfaces, Elsevier, New York, pp. 247-254 (1994).
119. "Roughness Control and Electrical Properties of SiO₂/Si (001) Interfaces," M. Niwa, K. Okada, T. Kouzaki and R. Sinclair, First International Symposium on Control of Semiconductor Interfaces, Elsevier, New York, pp. 405-410 (1994).
119. "Direct Solid State Phase Transformation from Co to Epitaxial CoSi₂ in Co/Thin Ti/(100) Si Structure and its Application for Shallow Junction Formation", S. Ogawa, J.A. Fair, T. Kouzaki, R. Sinclair, E.C. Jones, N.W. Cheung and D.B. Fraser, *Mat. Res. Soc. Symp. Proc.*, **320**, pp. 355-360 (1993).
120. "Atomic-Order Planarization of Ultra-Thin SiO₂/Si (001) Interfaces," M. Niwa, T. Kouzaki, K. Okada and R. Sinclair, *Proc. SSDM '93*, pp. 621-623 (1993).
121. "*In Situ* HREM of Phase Reactions", R. Sinclair, T.J. Konno and D.-H. Ko, *Proc. ICEM XIII*, pp. 429-430 (1994).
122. "Observation of Ferroelectric Domain Walls in KTP by HREM", E. Snoeck and R. Sinclair, *Proc. ICEM XIII*, pp. 233-234 (1994).
123. "Microscopic Interfacial Phenomena During Solid Phase Crystallization of Amorphous Silicon Thin Films: *In-Situ* CTEM and HREM Studies", J.P. Guillemet, B. de Mauduit, B. Peiraggi, R. Sinclair and T.J. Konno, *Proc. ICEM XIII*, pp. 449-450 (1994).
124. "*In-Situ* TEM Observation of Interfacial Reactions in the Zr/Si System", H. Tanaka, T.J. Konno and R. Sinclair, *Mat. Res. Soc. Symp. Proc.*, **337**, pp. 481-485 (1994).
125. "Transmission Electron Microscopy of MOCVD Titanium Nitride Films", T. Itoh, T.J. Konno, R. Sinclair, I.J.M.M. Raaijmakers and B.E. Roberts, *Mat. Res. Soc. Symp. Proc.*, **337**, pp. 735-740 (1994).

126. "Characterization of Sputtered Magnetic Barium-Ferrite Thin Films on Silicon Nitride Coated High Density Amorphous Carbon Substrates", J. Li, R. Sinclair, S.S. Rosenblum and H. Hayashi, *Mat. Res. Soc. Symp. Proc.*, **341**, pp. 59-64 (1994).
127. "Effect of Interlayers Upon Texture and Magnetic Properties in Co Alloy Multilayers for Longitudinal Magnetic Recording", M.R. Visokay, M. Kuwabara, H. Saffari, H. Hayashi, R. Sinclair and Y. Onishi, *Mat. Res. Soc. Symp. Proc.*, **343**, pp. 381-386 (1994).
128. "On The Perpendicular Magnetic Anisotropy of Co/Pt Multilayers: Structure-Property Relationships", G.A. Bertero and R. Sinclair, *Mat. Res. Soc. Symp. Proc.*, **343**, pp. 369-374 (1994).
129. "Correlation of Structure and Properties in Thin-Film Magnetic Media", T.P. Nolan, R. Sinclair, T. Yamashita, R. Ranjan, G. Tarnopolsky and W. Bennett, *Mat. Res. Soc. Symp. Proc.*, **343**, pp. 297-302 (1994).
130. "Atomically Layered Structures for Magnetic Information Storage", B.M. Lairson, M.R. Visokay, R. Sinclair, S.N. Brennan and B.M. Clemens, *Mat. Res. Soc. Symp. Proc.*, **343**, pp. 359-367 (1994).
131. "Effects of Substrate Temperature on Magnetic and Crystallographic Properties of Co-Cr-Pt/Cr Films Deposited by Laser Ablation Method", A. Ishikawa, Y. Shiroishi and R. Sinclair, *Mat. Res. Soc. Symp. Proc.*, **343**, pp. 345-350 (1994).
132. "Nickel Mediated Transformation of Amorphous Carbon to Graphite", T. Itoh and R. Sinclair, *Mat. Res. Soc. Symp. Proc.*, **349**, pp. 31-36 (1994).
133. "Correlation of Micro-structural, Micro-chemical and Micro-magnetic Properties of Longitudinal Recording Media Using CM20 FEG Lorentz TEM", T.P. Nolan, R. Sinclair, T. Yamashita and R. Ranjan, *52nd Proc. MSA*, pp. 892-893 (1994).
134. "Formation of Epitaxial (001) Ordered FePd Films from Multilayer Precursors", M.R. Visokay, B.M. Lairson, B.M. Clemens and R. Sinclair, *J. Mag. Soc. Jpn.*, **19**, S1, pp. 399-403 (1995).
135. "(Pt/Co/Pt)/X Multilayer Thin Films for Magneto-Optic Media", G.A. Bertero and R. Sinclair, *J. Mag. Soc. Jpn.*, **19**, S1, pp. 201-204 (1995).
136. "Microstructural, Magnetic and Magneto-Optical Properties of (100) and (111) Oriented Thick 'FCC' Cobalt Single Crystal", M. Ozkan, T. Suzuki, D. Miller, A. Kellock, C.-A. Chang and R. Sinclair, *J. Mag. Soc. Jpn.*, **19**, S1, pp. 267-270 (1995).
137. "Interface Reaction Enhanced Epitaxial Growth of Barium Ferrite Magnetic Thin Films", J. Li, R. Sinclair, S.S. Rosenblum and H. Hayashi, *Mat. Res. Soc. Symp. Proc.*, **357**, pp. 165-170 (1995).
138. "*In Situ* Electron Microscopy and its Application to Semiconductor Reactions at High Resolution", R. Sinclair, *Proc. MSA*, **53**, pp. 222-223 (1995).
139. "*In Situ* TEM Study of Reactions in Iron/Amorphous Carbon Layered Thin Films", T. Itoh and R. Sinclair, *Mat. Res. Soc. Symp. Proc.*, **382**, p. 45-50 (1995).
140. "Observation of Micromagnetic Structure in Computer Hard Disks by Lorentz Transmission Electron Microscopy", K. Tang, M.R. Visokay and R. Sinclair, *Mat. Res. Soc. Symp. Proc.*, **384**, p. 21-26 (1995).
141. "Growth and Characterization of FePt Compound Thin Films", M.R. Visokay and R. Sinclair, *Mat. Res. Soc. Symp. Proc.*, **384**, p. 91-96 (1995).
142. "TEM study of Crystallization of a-SiC in Contact with Silver", N.C. Zhu and R. Sinclair, *Mat. Res. Soc. Symp. Proc.*, **382**, pp. 206-209 (1995).
143. "Study of Diffusion Barrier Performance of MOCVD-TiN", H.-J. Lee, R. Sinclair, B.E. Roberts and R. Jackson, *Mat. Res. Soc. Symp. Proc.*, **391**, pp. 205-209 (1995).
144. "Crystallization in Metal-Metalloid Multilayers", R. Sinclair, T.J. Konno, T. Itoh and N.C. Zhu, *Mat. Res. Soc. Symp. Proc.*, **382**, pp. 3-8 (1995).
145. "HREM of Ultra-thin Oxides", R. Sinclair, M. Niwa and T. Kouzaki, *Proc. 4th ICSICT, Publishing House of the Electronics Industry, China* pp. 739-741 (1995).
146. "Strategies and Opportunities for *In-Situ* Electron Microscopy", R. Sinclair, *3rd Congreso de la Asociacion Mexicana de Microscopia*, ed. E.M. Rivera Munoz, pp. 89-90, (1996).
147. "A Failure Mechanism of MOCVD TiN Diffusion Barriers at High Temperatures", H.-J. Lee, P. Li, B. Roberts and R. Sinclair, *Mat. Res. Soc. Symp. Proc.*, **428**, pp. 295-300, (1996).
148. "Structure-Property Relationships in Sputtered Magneto-optic Multilayers", R. Sinclair, G.A. Bertero and M.R. Visokay, *55th Proc. MSA*, **3**, pp. 397-398, (1997).
149. "Micromagnetic and Microstructure-Property Relationships in Magnetic Recording Media", R. Sinclair, K. Tang and S.E. McKinlay, *55th Proc. MSA*, **3**, pp. 513-514, (1997).
150. "Applications of TEM for Analysis of Local Failures Occurring During Si Metallization Process", H.-J. Lee and R. Sinclair, *55th Proc. MSA*, **3**, pp. 465-466, (1997).

151. “*In Situ* HREM of Reactions at Interfaces”, R. Sinclair, T. Itoh, H.-J. Lee and K.W. Kwon, 55th Proc. MSA, **3**, pp. 621-622 (1997).
152. “Characterization of Ta as an underlayer for Cu Interconnects”, K.W. Kwon, H.-J. Lee, C. Ryu, R. Sinclair and S.S. Wong, Proc. Advanced Metallization for ULSI Applications, pp. 711-716 (1997).
153. “Diffusion Barrier Stability in ULSI Applications”, R. Sinclair, H.-J. Lee and K.W. Kwon, Proc. 4th International Conference on Materials and Process Characterization for VLSI, Shanghai, China, pp. 305-308 (1997).
154. “Chromium Distribution in CoCrTa/Cr Longitudinal Recording Media”, J.E. Wittig, T.P. Nolan, R. Sinclair and J. Bentley, Mat. Res. Soc. Symp. Proc., **517**, pp. 211-216 (1998).
155. “Roughness Measurements of Thin SiO₂ and poly-Si Interfaces Using High Resolution Cross-Sectional TEM”, M. Yamaguchi, R. Sinclair, and M. Niwa, Proc. of the Symposium on Silicon Nitride and Silicon Dioxide Thin Insulating Films, pp. 232-239 (1998).
156. “Magnetic Imaging of Recording Media”, R. Sinclair and K. Tang, Proc. Microscopy and Microanalysis, **5**, pp. 28-29 (1999).
157. “Thermal Stability of the Copper/Tantalum Interfaces in Advanced Microelectronic Metallization”, K.W. Kwon, H.-J. Lee, and R. Sinclair, Proc. Microscopy and Microanalysis, **5**, pp. 176-177 (1999).
158. “*In Situ* HREM of Interface Reactions”, R. Sinclair, Proc. 5th International Symp. on Advance Physical Fields, NRIM Japan, edited by K. Yoshihara, pp. 47-48 (2000).
159. “Grain Size Relationship Between the Magnetic Layer and the Underlayer in CoCrPtTa Recording Media”, K. Ma, R. Sinclair, G. Bertero, and W. Cao, Mat. Res. Soc. Symp. Proc., **614**, pp. 141-146 (2001).
160. “Microstructural Characterization of Longitudinal Magnetic Recording Media”, R. Sinclair, D.W. Park, C. Habermeier, and K. Ma, Mat. Res. Soc. Proc., **589**, pp. 3-12 (2001).
161. “Quantitative EFTEM of Cr Grain Boundary Segregation in CoCrTa”, J.E. Wittig, J.F. Al-Sharab, J. Bentley, N.D. Evans, T.P. Nolan, and R. Sinclair, Proc. Microscopy and Microanalysis, **7**, pp. 298-299 (2001).
162. “*In Situ* Transmission Electron Microscopy of Materials”, R. Sinclair and K.H. Min, Proc. 2001 International Workshop on Adv. Microscopy, ed. L.J. Chen, pp. I-O-12-13 (2001).
163. “Transmission Electron Microscopy of Computer Hard Disc, Magnetic Thin Films”, R. Sinclair, Proc. 4th International COE Symposium on Atomic Scale Processing and Novel Prop. in Nanoscopic Materials, ed. T. Kawaii, p. 12 (2001).
164. “*In Situ* HREM of Crystallization Reactions”, R. Sinclair and K.H. Min, Proc. Microscopy and Microanalysis, **8**, Supplement 2, pp. 416-417 (2002).
165. “TEM Microstructure Studies of Thin Film Magnetic Recording Media”, R. Sinclair, U. Kwon and J.D. Risner, Proc. Microscopy and Microanalysis, **8**, Supplement 2, pp. 368-369 (2002).
166. “*In-Situ* Heating Study of Materials”, R. Sinclair and K.H. Min, Proc. ICEM XV, pp. 931-932 (2002).
167. “Reactions in Metal-Carbon Systems”, R. Sinclair, T. Itoh and R. Chin, Proc. ICEM XV, pp. 153-154 (2002).
168. “Failure Analysis of Ferroelectric RAM Device by Transmission Electron Microscopy”, H.S. Baik, G.S. Park, S.A. Song, J.K. Lee, and R. Sinclair, Proc. ICEM XV, pp. 805-806 (2002).
169. “Characterization for crystallization of SrBi₂Nb₂O₉ thin films on Si substrates”, D.C. Yoo, J.Y. Lee, R. Sinclair, I.S. Kim, Y.T. Kim, J. Korean Phys. Soc., **42** Supp (1), pp. S450-453 (2003).
170. “High Resolution and Analytical TEM of Cr Grain Boundary Segregation in Co-alloy Longitudinal Hard Disk Magnetic Recording Media”, J. Risner, R. Sinclair and J. Bentley, Proc. Microscopy and Microanalysis, **10**, Supplement 2, pp. 14-15 (2004).
171. “High-Resolution Analytical TEM and Energy-Filtered Imaging of CoPt-Oxide Perpendicular Magnetic Recording Media”, J.D. Risner, T.P. Nolan, J. Bentley, S.Z. Wu, S.D. Harkness, and R. Sinclair, Proc. Microscopy and Microanalysis, **11**, Supplement 2, pp. 1806-1807 (2005).
172. “HRTEM and Nano-probe EDS Studies on the Microstructure of CoCrPtO Perpendicular Recording Media with Ru/Ru-oxide Interlayers”, U. Kwon, and R. Sinclair, Proc. Microscopy and Microanalysis, **11**, Supplement 2, pp. 1834-1835 (2005).
173. “Synthesis and Characterization of Fe-C Core-shell Nanoparticles”, H. Li, H. Dai, and R. Sinclair, Proc. Microscopy and Microanalysis, **11**, Supplement 2, pp. 1902-1903 (2005).
174. “Characterization of AuFe-C Core-shell Nanoparticles”, H. Li, H. Dai, L. Xing, and R. Sinclair, Proc. Microscopy and Microanalysis, **12**, Supplement 2, pp. 524CD-525CD (2006).
175. “Information Storage Technology: The Role of the TEM”, R. Sinclair, J. Risner, and U. Kwon, Proc. Microscopy and Microanalysis, **12**, Supplement 2, pp. 76-77 (2006).
176. “TEM Studies of Reactions in Thin Films and their Interfaces”, R. Sinclair, Proc. ICEM XVI, p. 1322 (2006).

177. "FIB and TEM Studies of Interface Structure in Diamond-SiC Composites", J.S. Park, R. Sinclair, D. Rowcliffe, M. Stern, and H. Davidson, Proc. ICEM XVI, p. 1965 (2006).
178. "TEM Observations of Bio-conjugated Streptavidin-Gold Particles", A. L. Koh and R. Sinclair, Mat. Res. Soc. Symp. Proc., **1019E**, p. 1019-FF05-01 (2007).
179. "TEM Studies of Iron Oxide Nanoparticles for Cell Labeling and Magnetic Separation", A. L. Koh and R. Sinclair, Technical Proceedings of the 2007 Nanotechnology Conference and Trade Show, **4**, pp. 101-104 (2007).
180. "Grain Size Distribution in CoCrPtO-based Perpendicular Magnetic Recording Media", F. Hossein-Babaei, U. Kwon and R. Sinclair, Technical Proceedings of the 2007 Nanotechnology Conference and Trade Show, **4**, pp. 547-550 (2007).
181. "Characterization of Magnetic Nanoparticles by High Resolution TEM Methods", R. Sinclair, H. Li, and A. L. Koh, Proc. Microscopy and Microanalysis, **13**, Supplement 2, p. 66CD (2007).
182. "TEM Studies of Synthetic Anti-ferromagnetic (SAF) Nanoparticles", A. L. Koh, W. Hu, R. Wilson, S. X. Wang, and R. Sinclair, Proc. Microscopy and Microanalysis, **13**, Supplement 2, p. 622CD (2007).
183. "Electron Microscopy Characterization of Composite Organic-Inorganic Nanoparticles (COINs) as Raman Labels for Extra-Cellular Analyses", A. L. Koh, C.M. Shachaf, S. Elchuri, G.P. Nolan and R. Sinclair, Microsc. Microanal. **14**, Supplement 2, p. 670CD (2008).
184. "Electron Energy-Loss Spectrometry (EELS) and Energy-Filtered TEM (EFTEM) Analyses of Organic-Inorganic Nanoparticles", A.L. Koh, M. Watanabe and R. Sinclair, Microsc. Microanal. **15** (Suppl. 2) (2009) p.432CD.
185. "In Situ and High Resolution TEM Studies of Nano-scale Materials", R. Sinclair, A.L. Koh, P.J. Kempen and H.J. Jung, Microscopy and Microanalysis 2009 Meeting, Microsc. Microanal. **15** (Suppl. 2) (2009) 1200CD.
186. "Electron Microscopy Characterization of Gold-Silica Core-Shell Nanoparticle Raman Labels (Nanoplex™ Biotags) and their Conjugation to Cells", P.J. Kempen, A.L. Koh, C. Zavaleta, K. Hartman, S. Gambhir and R. Sinclair, Microscopy and Microanalysis 2009 Meeting, *late-breaking poster*
187. "Direct Microscale Visualization of Targeted Quantum Dot Binding in Multiple Tumor Models of Living Mice using Intravital Microscopy", B. Smith, Z. Cheng, A. de la Zerda, A.L. Koh, R. Sinclair, 2009 World Molecular Imaging Congress, (2009) <http://search.proquest.com/docview/42472036?accountid=14026>.
188. "Organic-Inorganic Particles as Labels to Trace Biological Signaling Pathways", A. L. Koh and R. Sinclair, Microsc. Microanal. **16** (Suppl. 2) 1130-1131 (2010) doi:10.1017/S143192761005899X.
189. "TEM Study on PbS Quantum Dots Made by Atomic Layer Deposition and Their Behavior Under E-beam Irradiation", H. J. Jung, N. P. Dasgupta, F. B. Prinz and R. Sinclair, Microsc. Microanal. **16** (Suppl 2), pp 1376-1377 (2010).
190. "Nanostructural correlation between Co magnetic layer and its Ru seed layer in a PMR medium", F. Hossein-Babaei (Jr.), R. Sinclair, G. Bertero, and K. Srinivasan, Microsc. Microanal. **16** (Suppl. 2), pp. 1522-1523 (2010).
191. "Utilizing Scanning Transmission Electron Microscopy to Locate and Image Raman Active Gold Core Nanoparticles in Mouse Tissue", P.J. Kempen, A.S. Thakor, C.L. Zavaleta, S.S. Gambhir, and R. Sinclair, Microsc. Microanal. **16** (Suppl. 2) pp. 1116-1117 (2010).
192. "Utilizing Scanning Transmission Electron Microscopy to Locate and Image Raman Active Gold Core Nanoparticles in Mouse Tissue", P.J. Kempen, A.S. Thakor, C.L. Zavaleta, S.S. Gambhir, and R. Sinclair, IMC XVII, M16.4 (2010).
193. "Developing Remote Microscopy at a University User Facility", R. Chin and R. Sinclair, IMC XVII, I17.3 (2010).
194. "Scanning Electron Microscopy and Surface Enhanced Raman Spectroscopy Correlation Studies of Functionalized Composite Organic-Inorganic SERS Nanoparticles on Cancer Cells", A.L. Koh and R. Sinclair, Mater. Res. Soc. Symp. Proc. 1316: mrsf10-1316-qq11-06 (2011) doi: 10.1557/opi.2011.664.
195. "Correlative Microscopy of Tumor Vasculature", P.J. Kempen, B.R. Smith, M.F. Kircher, S.S. Gambhir, and R. Sinclair, Microsc. Microanal. **17** (Suppl 2), 2011 pp. 360-361 (2011).
196. "Proton Conduction in Epitaxial and Polycrystalline Yttrium-doped Barium Zirconate Thin Films", Y.B. Kim, T.M. Gür, H.-J. Jung, S. Kang and F.B. Prinz, Abstract 271, 219th ECS Meeting, The Electrochemical Society, ECS Meeting Abstracts, 1101, 271 (2011).
197. "A Brain Tumor Molecular Imaging Strategy Using a New Triple-Modality MRI-Photoacoustic-Raman Nanoparticle", A. de la Zerda, M.F. Kircher, J.V. Jokerst, C.L. Zavaleta, P.J. Kempen, E. Mittra, K. Pitter, R.

- Huang, C. Campos, F. Habte, R. Sinclair, C.W. Brennan, I.K. Mellinghoff, E.C. Holland and S.S. Gambhir, Proc. SPIE 8581, Photons Plus Ultrasound: Imaging and Sensing, (2013) doi: 10.1117/12.2001719.
198. "Advanced Characterization Techniques for Nanoparticles for Cancer Research: Applications of SEM and NanoSIMS for Locating Au Nanoparticles in Cells", P.J. Kempen, C. Hitzman, L.S. Sasportas, S.S. Gambhir and R. Sinclair, MRS Online Proceedings Library 1569 (2013): mrss 13-1569.
 199. "NorTEMnet 2013 Workshop on Advanced Transmission Electron Microscopy", E. Olsson, R. Sinclair, W. Jaeger, Microscopy and Analysis EMEA 8, pp. 30 (2013).
 200. "Locating and Characterizing Self-Assembled Gadolinium Chelate Nanoparticles in Stem Cells Using TEM", P.J. Kempen, H. Nejadnik, D. Ye, B.K. Rutt, J. Rao, H.E. Daldrup-Link and R. Sinclair, Microsc. Microanal. **19** (Suppl 2), pp. 178-179 (2013).
 201. "Characterization of E-Beam Fabricated Gold Nanoparticles", S. Madsen, P.J. Kempen and R. Sinclair, Microsc. Microanal. **19** (Suppl 2), pp. 1554-1555 (2013).
 202. "Oxidation Studies of Carbon Nanotubes for Applications as X-Ray Field Emitters Using an Aberration-Corrected, Environmental TEM", Microsc. Microanal. **19** (Suppl 2), pp. 466-467 (2013).
 203. "Hybrid Graphene-crystalyst Nanostructures: elucidating the Nature of the Interface", G. Diankov, J. An, J. Park, F. Prinz and D. Goldhaber-Gordon, Bull. Am. Phys. Soc. **59** (1) (2014): BAPS.2014.MAR.H1.200.
 204. "Phonon Thermal Conduction in Periodically Porous Silicon Nanobeams", W. Park, A.M. Marconnet, T. Kodama, J. Park, R. Sinclair, M. Asheghi and K.E. Goodson, Thermal and Thermomechanical Phenomena in Electronic Systems (ITherm), 2014 IEEE Intersociety Conference on, pp. 637-640 (2014).
 205. "Imaging Perpendicular Magnetic Domains in Plan-view Using Lorentz Transmission Electron Microscopy", T.R. Kim, A.L. Koh and R. Sinclair, Microsc. Microanal. **20** (Suppl 3), pp. 286 (2014).
 206. "Observing Plasmon Damping Effects of Metallic Adhesion Layers in E-Beam Synthesized Nanostructures Using STEM-EELS and Raman Spectroscopy", S. Madsen, P. Kempen and R. Sinclair, Microsc. Microanal. **20** (Suppl 3), pp. 558 (2014).
 207. "Gareth Thomas (9 August 1932—6 February 2014)", R. Sinclair, Microscopy **63** (3), pp.175-176 (2014).
 208. "Characterizing the effectiveness of antibody labeled nanoparticle targeting of cancer cells using scanning and transmission electron microscopy", P.J. Kempen, D.M. Kurtz, S.J. Madsen, S.S. Gambhir and R. Sinclair, International Microscopy Congress, **18** (2014): ID-5-O-2827.
 209. "Aberration-Corrected, Environmental TEM Studies on Carbon Nanotube Oxidation and the Influence of the Imaging Electron Beam", A.L. Koh, E. Gidcumb, O. Zhou and R. Sinclair, International Microscopy Congress, **18** (2014): IT-6-P-2451.
 210. "Using STEM-EELS to Observe Effects of Metallic Adhesion Layers on Plasmon Resonance in Electron Beam Lithographically Patterned Gold Thin Films", S.J. Madsen, A.L. Koh, P.J. Kempen and R. Sinclair, International Microscopy Congress, **18** (2014): MS-3-P-3411.